Hans-Georg Weber
Masataka Nakazawa

OPTICAL AND FIBER COMMUNICATIONS REPORTS 3

Ultrahigh-Speed Optical Transmission Technology

Springer

Hans-Georg Weber Masataka Nakazawa
Editors

Ultrahigh-Speed Optical Transmission Technology

With 350 Figures

Springer

Hans-Georg Weber
Fraunhofer Institute for
Telecommunications
Heinrich-Hertz-Institut
Einsteinufer 37
10587 Berlin, Germany
hgweber@hhi.fhg.de

Masataka Nakazawa
Research Institute of Electrical
Communication
2-1-1 Katahira
Sendai-shi, Miyagiken 980-8577
Aoba-Ka, Japan
nakazawa@riec.tohoku.ac.jp

Library of Congress Control Number:

ISBN-13: 978-3-540-23878-2 e-ISBN-13: 978-3-540-68005

Printed on acid-free paper.

9 8 7 6 5 4 3 2 1

springer.com

Contents

Introduction to ultra-high-speed optical transmission technology

Hans-Georg Weber[1] and Masataka Nakazawa[2]

[1] Fraunhofer Institute for Telecommunications, Heinrich-Hertz-Institut
Einsteinufer 37, 10587 Berlin, Germany
Email: hgweber@hhi.fhg.de
[2] Research Institute of Electrical Communication, Tohoku University
2-1-1 Katahira, Aoba-ku, Sendai-shi, Miyagi-ken 980-8577, Japan
Email: nakazawa@riec.tohoku.ac.jp

Abstract. This paper serves as an introduction to this volume on ultra-high-speed optical transmission technology. It reviews ultra-high-speed data transmission in optical fibers, which is essentially the same as optical time division multiplexing (OTDM) transmission technology. The research work in this field is driven by the need to increase the transmission capacity and controllability of fiber optic networks as well as by an interest in investigating the feasibility of high-speed data transmission in fiber. The chapter summarizes OTDM components and describes results of OTDM-transmission experiments. In addition, it outlines the chapters of this volume, which describe the considered topics in detail.

1. The Challenge of OTDM

The rapid increase in data traffic in communication networks has led to a demand for higher transmission capacities. New fibers may need to be installed from time to time. However, the costs are high and lead times may be long. Therefore, finding a way to increase the fiber transmission capacity is the target of many studies. The transmission capacity per fiber is given by the number of wavelength division multiplexing (WDM) channels multiplied by the time division multiplexing (TDM) bit rate per channel. The past has seen considerable interest in the use of WDM to increase the total transmission capacity. For instance, a 10-Tbit/s transmission capacity was achieved in 2001 using WDM systems with about 260 wavelength channels and a TDM bit rate of 40 Gbit/s [1,2]. However, for very large numbers of wavelength channels (e.g., a few thousand), such factors as wavelength management, power consumption, and footprint will probably limit the usefulness of increasing the number of WDM channels

and will favor a higher TDM bit rate in terms of increasing the total transmission capacity. The motivation for higher TDM bit rates also arises from the effort to reduce the cost per transmitted information bit. A higher TDM bit rate will make it possible to reduce the number of transmitters and receivers and to increase both the spectral and space efficiency of WDM systems. Indeed, in the past the TDM bit rate was steadily increased in installed fiber transmission systems. In the early 1990s and in about 1995, respectively, TDM bit rates of 2.5 and 10 Gbit/s were introduced in commercial fiber transmission systems. This TDM bit rate has now been increased to 40 Gbit/s. These bit rates are all based on electrical signal processing (electrical TDM, ETDM). The next generation TDM bit rate will be 160 Gbit/s. As electrical signal processing is currently unavailable at this bit rate, many laboratories are investigating optical TDM (OTDM) technology. The basics of OTDM technology have been described in several review articles [3–5] and will be discussed below.

The most challenging view as regards OTDM technology is that optical networks will evolve into "photonic networks", in which ultrafast optical signals of any bit rate and modulation format will be transmitted and processed from end to end without optical-electrical-optical conversion. With this as the target, OTDM technology presents us with the challenge of investigating and developing high-speed optical signal processing and exploring the ultimate capacity for fiber transmission in a single wavelength channel. We must study how the advantages of high TDM bit rates are eventually eroded by an increase in detrimental effects. A higher TDM bit rate makes transmission systems more vulnerable to chromatic dispersion (CD) and polarization-mode dispersion (PMD), as well as creating the need for a higher optical signal-to-noise ratio (OSNR) in the wavelength channel. A higher OSNR is obtained by employing a higher signal power, and this will make the system more sensitive to fiber non-linearity. On the other hand, the need for a high signal power may be reduced by other means such as distributed Raman amplification, advanced optical modulation formats and the use of forward error correction (FEC).

From another viewpoint, OTDM technology is considered to be an interim technique with which to study high-speed data transmission in fiber. In this sense, OTDM will be replaced by ETDM as soon as electrical signal processing becomes available at the required TDM bit rate. This is currently the case with a TDM bit rate of 40 Gbit/s and will probably reach a TDM bit rate of 160 Gbit/s in the future. Recent advances in high-speed electronic ICs based on SiGe technology [6], broadband low drive voltage modulators [7] and waveguide pin detectors [8] indicate that full electronic TDM systems operating at 80 Gbit/s and above are already feasible. For example, an ETDM receiver working at 85 Gbit/s has recently been demonstrated [9]. From this standpoint, the main task as regards OTDM technology is to investigate the feasibility of ultrahigh-speed data transmission as a prerequisite to the development of ETDM technology.

The "photonic network" appears to be a task for the distant future and ETDM technology will dominate commercial transmission systems in the near future. Nevertheless, some OTDM components may find applications in current ETDM systems. Optical pulse sources will be used in ETDM systems with an RZ-modulation format. OTDM demultiplexers already perform better than ETDM receivers at data rates of 80 Gbit/s. We may expect communication networks to be based on an appropriate combination of WDM, ETDM and OTDM technologies. Also, OTDM components, such

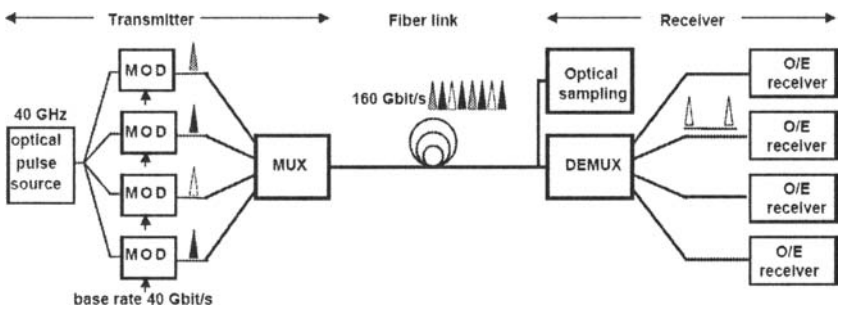

Fig. 1. Schematic view of a 160-Gbit/s OTDM transmission system.

as pulse sources, optical gates and clock recovery devices are already being employed in optical sampling systems for waveform and signal quality monitoring.

2. OTDM Transmission System

Figure 1 is a schematic illustration of a 160-Gbit/s OTDM transmission system as an example. The essential component on the transmitter side is an optical pulse source. The repetition frequency of a generated pulse train depends on the base data rate (ETDM data rate). The system shown in Fig. 1 has a base data rate of 40 Gbit/s. The 40-GHz optical pulse train is coupled into four optical branches, in which modulators (MOD) driven by 40 Gbit/s electrical data signals generate 40 Gbit/s optical return to zero (RZ) data signals. The modulation formats include on-off keying (OOK), differential phase shift keying (DPSK), and differential quadrature phase shift keying (DQPSK). The format depends on the modulation format of the electrical data signal and the appropriate modulator. The four optical data signals (TDM channels) are bit-interleaved by a multiplexer (MUX) to generate a multiplexed 160-Gbit/s optical data signal. Multiplexing can be such that all bits of the multiplexed data signal have the same polarization (SP multiplexing) or adjacent bits have alternating (orthogonal) polarization (AP multiplexing). Moreover, the controllability of the optical phases of pulses in adjacent bit slots is an important feature of an OTDM system. On the receiver side, the essential component is an optical demultiplexer (DEMUX), which separates the four base rate data signals (TDM channels) for subsequent detection and electrical signal processing.

The laboratory systems described in this book are frequently simplified on the transmitter side by adopting a set-up with only one modulator, which is combined with a pulse source for a 40-Gbit/s optical transmitter. This optical data signal is then multiplexed by a fiber delay line multiplexer to a 160-Gbit/s data signal using SP or AP multiplexing (see Fig. 2). The laboratory systems described in this book are also frequently simplified on the receiver side. That is, only one 40-Gbit/s TDM channel is selected and detected by one 40-Gbit/s optoelectric receiver at a given time. In a proper experiment all TDM channels are measured successively in this way.

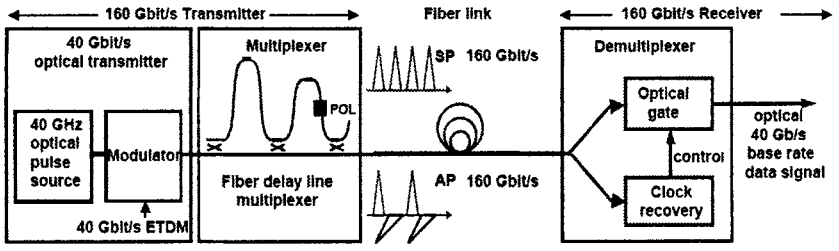

Fig. 2. Schematic view of a simplified 160-Gbit/s OTDM transmission system.

The DEMUX shown in Fig. 2 comprises two parts, an optical gate and a clock recovery device. The optical gate is a fast switch with a switching time that is shorter than the bit period (6.25 ps for 160 Gbit/s) of the multiplexed data signal. The clock recovery device provides the timing signal for the optical gate. Very often in papers on OTDM technology, the DEMUX is identified with the optical gate, and the clock recovery is considered as a separate unit next to the DEMUX.

The transmission system must be capable of compensating for chromatic dispersion (CD) and polarization mode dispersion (PMD), which both depend on the type of single-mode fiber used in the transmission system. For advanced high-speed transmission systems, it is desirable to employ techniques such as optical sampling to monitor the optical data signal with picosecond resolution. Chapter 17 ("Optical sampling techniques", by Schmidt-Langhorst and Weber) reviews the techniques used in optical sampling systems to perform the ultrafast sampling of the signal under investigation.

For even more advanced systems, high-speed optical signal processing techniques must be developed not only for the point-to-point transmission shown in Fig. 1, but also for transmission nodes. Components and subsystems such as add-drop multiplexers [e.g., 10–13], wavelength converters [e.g., 14–17], modulation format converters [e.g., 18] and optical regenerators [e.g., 19,20] are also required. These topics are partly dealt with in chapter 6 ("Optical signal processing using nonlinear fibers", by Watanabe) in the context of fiber-based optical signal processing and in chapters 5 ("High-speed optical signal processing using semiconductor optical amplifiers", by Schubert et al.) and 8 ("Optical nonlinearities in semiconductor optical amplifier and electro-absorption modulator: their applications to all-optical regeneration", by Usami and Nishimura) in the context of semiconductor optical amplifier and electroabsorption modulator based optical signal processing.

Figures 1 and 2 show the set-up of a one wavelength channel OTDM system. Chapters 13 ("Application of electroabsorption modulators for high-speed transmission systems", by Lach et al.) and 15 ("Ultrafast optical technologies for large-capacity TDM/WDM photonic networks", by Morioka) also provide examples of WDM/OTDM transmission systems comprising several wavelength channels.

3. Transmitter: Optical Pulse Source, Modulator, Multiplexer

High bit rate transmission demands reliable short pulse generation at high repetition frequencies. The pulse source must provide the following: a well-controlled repetition frequency and wavelength, transform limited pulses, a pulse width shorter than the bit period of the multiplexed data signal, a timing jitter much less than the pulse width, low amplitude noise, and a high extinction ratio (pedestal suppression). The pulse width should be less than one quarter of the bit period (1.5 ps for 160 Gbit/s) for SP multiplexing and less than one half of the bit period for AP multiplexing to avoid coherent beat noise between adjacent bits. Moreover, if some sort of phase modulation format such as a DPSK is used, there are further pulse source requirements, namely it must be highly stable in terms of phase and carrier wavelength.

Various pulse sources were used in the OTDM transmission experiments. Semiconductor mode-locked lasers (ML-LD) are becoming increasingly attractive, as they are stable, compact and viable for OTDM applications. In chapter 2 ("Semiconductor mode-locked lasers as pulse sources for high bit rate data transmission", by Jiang et al.), the ML-LD is evaluated as a pulse source for high bit rate data transmission. This chapter compares various OTDM source technologies, explains the impact of timing jitter and amplitude noise on OTDM performance, and illustrates how to characterize OTDM source noise. Another important pulse source is the mode-locked fiber ring laser (ML-FRL). Chapter 3 ("Ultrafast mode-locked fiber lasers for high-speed OTDM transmission and related topics", by Nakazawa) provides a detailed description of several types of ML-FRL, which are capable of generating picosecond to femtosecond optical pulse trains at repetition rates of 10 to 40 GHz in the 1.55 μm region. The ML-FRL is a harmonically mode-locked laser, whereas the ML-LD is generally operated at the fundamental mode repetition frequency. Recently, a solid-state mode-locked laser, known as an erbium-glass oscillator pulse generating laser (ERGO-PGL), was successfully operated in a 160 Gbit/s transmission experiment [12]. This laser operates at the fundamental mode repetition frequency. It has very low amplitude and phase noise and a pulse width that is slightly larger than those of the ML-LD and ML-FRL.

Another pulse source is a CW laser externally modulated (CW-Mod) by a Mach-Zehnder modulator or an electroabsorption modulator (EAM). The application of this pulse source in 160 and 320 Gbit/s (AP multiplexing) OTDM transmission experiments is described in chapter 13 ("Application of electroabsorption modulators for high-speed transmission systems", by Lach et al.). In general this type of pulse source does not provide optical pulses with a pulse width of less than about 3 ps. Some sort of subsequent pulse compression (PuC) and optical regeneration are needed to generate shorter pulses.

A pulse source of particular interest for WDM/OTDM applications is the supercontinuum pulse generation (SC-pulse) described in chapter 15 ("Ultrafast optical technologies for large-capacity TDM/WDM photonic networks", by Morioka). This pulse source provides short (<1 ps) optical pulses, whose pulse width and wavelength are both tunable. Moreover, this pulse source can be used as a multi-wavelength pulse source for WDM/OTDM systems.

The generated pulse train is modulated by using an EAM or a lithium-niobate ($LiNbO_3$) modulator. Chapter 4 ("Ultra-high-speed $LiNbO_3$ modulators", by Noguchi) discusses state of the art ultrahigh-speed $LiNbO_3$ modulators. The $LiNbO_3$ modulator covers a very broad band. Moreover, its modulation characteristics, such as insertion

loss, driving voltage (half-wave voltage), and frequency response, have little dependence on wavelength in the 1.3 to 1.5 μm range. In addition, the frequency chirping of a modulated optical signal can be reduced to almost zero. $LiNbO_3$ modulators have been used as amplitude and phase modulators in many high bit rate transmission experiments. Chapter 13 ("Application of electroabsorption modulators for high-speed transmission systems", by Lach et al.) describes the application of the EAM in OTDM experiments for data modulation as well as pulse carving, and this chapter also compares the EAM and the $LiNbO_3$ modulator.

Most optical multiplexers (MUX) are of the kind depicted in Fig. 2. They are realized by using 2×2 optical couplers and optical delay lines either as fiber devices or as planar lightwave circuits. These multiplexers are not "real" multiplexers, which combine TDM channels generated, for example, by different modulators (see Fig. 1) to provide a multiplexed data signal. The delay line multiplexers generate a high bit rate test signal for laboratory experiments by combining several replicas of one data signals with different relative delays. An important requirement for these "test multiplexers" is that there is no correlation between the adjacent bits of the multiplexed data signal. This is obtained by employing a delay time, which is long compared with the bit period of the input signal. These test multiplexers are described in more detail in chapter 13 ("Application of electroabsorption modulators for high-speed transmission systems", by Lach et al.). An example of a "real" multiplexer is provided in chapter 15 ("Ultrafast optical technologies for large-capacity TDM/WDM photonic networks", by Morioka). This multiplexer enables the multiplexing of eight different 20 Gbit/s data signals to one multiplexed 160 Gbit/s data signal by using an integrated planar lightwave circuit [21, 22]. Yet another "real" multiplexer is reported in [23] and described in chapter 13 ("Application of electroabsorption modulators for high-speed transmission systems", by Lach et al.). It provides independent modulation of all TDM-channels and optical phase alignment between adjacent bits.

4. OTDM-Receiver: Optical Demultiplexer, Clock Recovery Device, O/E-Receiver

Various switching devices have been used for demultiplexing. In very high-speed transmission experiments, optical switching was based on fiber nonlinearity using cross phase modulation (XPM) or four wave mixing (FWM) in fibers [3–5]. A well-known example is the nonlinear optical loop mirror (NOLM) [24]. Chapter 14 ("Ultrafast OTDM transmission using novel fiber devices for pulse compression, shaping, and demultiplexing", by Yamamoto and Nakazawa) describes the application of the NOLM as a DEMUX for a data rate of 640 Gbit/s, the fastest DEMUX reported so far. The advantage of fiber based switching devices is their potential for ultrafast switching due to the fast non-resonant nonlinearity of the fiber. The main drawback of these devices stems from the small optical nonlinearity of glass. For an optical switch, the product of control power times the fiber length of conventional fiber must be about 1 W km. In recent years, however, new fibers have been developed called "highly non-linear fibers" (HNLF). At present, the product of control power times fibre length of HNLF needs only to be about 0.1 W km mainly because of the smaller effective area of the HNLF. Chapter 6 ("Optical signal processing using nonlinear fibers", by Watanabe) reports on all-optical signal processing using HNLF for demultiplexing and other ap-

plications. Another type of new optical fiber is the photonic crystal fiber [25]. Optical signal processing based on photonic crystal fiber is not explicitly reported in this book.

Another class of optical switching devices uses the high resonant nonlinearity in active semiconductor structures. Chapter 5 ("High-speed optical signal processing using semiconductor optical amplifiers", by Schubert et al.) reports on optical gating devices based on XPM and FWM in a semiconductor optical amplifier (SOA). Examples of XPM based optical gates include the SOA in a Mach-Zehnder interferometer (SOA-MZI), the SOA in a polarization discriminating switch (SOA-UNI), and the SOA in a Sagnac interferometer (SLALOM). These devices have been used as DEMUX in several high-speed transmission experiments. Examples are the SOA-MZI DEMUX in transmission experiments at bit rates of up to 320 Gbit/s [26,27], and the SLALOM DEMUX in a 640-Gbit/s demultiplexing experiment, where 8 WDM channels, each carrying an 80-Gbit/s TDM data signal, were simultaneously demultiplexed in the time domain to 8 further WDM channels, each carrying a 10-Gbit/s TDM data signal [28]. The advantage of the SOA based switching devices is their small size and their low optical power requirement for all-optical switching. Moreover, these devices can be realized as photonic integrated circuits.

SOA- and fiber-based optical gates use all-optical switching. An optical signal controls the gate, which switches an optical data signal. Another optical gate used in many high-speed transmission experiments is the electroabsorption modulator (EAM). In this device an electrical control signal controls the gate that switches the optical data signal. This switch has been used for demultiplexing in many transmission experiments as described in chapter 13 ("Application of electroabsorption modulators for high-speed transmission systems", by Lach et al.). Recently, an EAM was monolithically integrated with a photodiode and an electrical signal from the photodiode drove the EAM directly [29, 30].

The demultiplexers described above are capable of selecting only one TDM channel of the multiplexed data signal (single channel output operation). Multiple channel output operation can be achieved by a serial-parallel configuration of several of these switches. An example is reported in [31] and discussed in chapter 15 ("Ultrafast optical technologies for large-capacity TDM/WDM photonic networks", by Morioka). This chapter also reports on the realization of optical switches that provide a multiple channel output directly in a single device. The reported examples utilize XPM-assisted chirp compensation in an optical fiber or FWM by employing linearly chirped square control pulses to generate different frequency components corresponding to independent TDM channels.

SOA- and EAM-based optical switching devices operate well at data rates of up to 160 Gbit/s. Their performance worsens considerably at higher data rates. Chapter 16 ("New optical device technologies for ultrafast OTDM systems", by Sakurai and Kobayashi) reports on investigations into new optical device technologies, which will enable faster switching devices to be realized for future ultrafast OTDM transmission systems.

Clock recovery or timing extraction from a transmitted data signal is another key function in an OTDM receiver and in other subsystems such as add-drop multiplexers and 3R-regenerators. Several timing extraction techniques have been developed including phase-locked loops (PLL), the injection locking of pulse sources, and resonant oscillator circuits [4,5]. At data rates of 160 Gbit/s and beyond, clock recovery was most successfully achieved by using PLL configurations with an optical or opto-

electrical phase comparator. Chapters 5 ("High-speed optical signal processing using semiconductor optical amplifiers", by Schubert et al.) and 15 ("Ultrafast optical technologies for large-capacity TDM/WDM photonic networks", by Morioka) report on the application of SOAs as optical phase comparators using either FWM or XPM in an SOA and chapter 13 ("Application of electroabsorption modulators for high-speed transmission systems", by Lach et al.) reports on the application of EAMs as optoelectrical phase comparators in a clock recovery circuit. SOA-based and EAM-based clock recovery devices have been operated at up to 400 [32] and 320 Gbit/s [33], respectively.

Many transmission experiments were also performed without recovering the clock signal from the multiplexed data signal, because an appropriate clock recovery device was unavailable. Two alternative approaches were used. A clock signal was generated at the transmitter and transmitted together with the data signal over the fiber at a separate wavelength ("clock transmitted"), or the multiplexer at the transmitter end was adjusted for slightly different pulse amplitudes ("clock modulation") such that a simple photo detector was able to detect the clock signal at the receiver end.

In the OTDM experiments reported to date, the O/E receivers were operated at up to 40 Gbit/s. However, in laboratory experiments O/E receivers have already operated at data rates of up to about 80 Gbit/s [9]. Chapter 7 ("Ultrafast photodetectors and receivers", by Bach) reports on ultrafast photodetectors and receivers. It is expected that ETDM transmission systems will soon be available for data rates up to 100 Gbit/s. This will most likely increase the base rate of OTDM systems from 40 to 100 Gbit/s.

5. Transmission Fiber, Compensation of Chromatic Dispersion and Polarization Mode Dispersion, 2R/3R-Regeneration

A data signal is degraded along a transmission line by attenuation, fiber non-linearity, chromatic dispersion (CD) and the polarization mode dispersion (PMD) of the fiber, and the accumulation of noise generated in the amplifier stages. These impairments can be partly compensated for, depending on the type of transmission fiber used.

For a 160-Gbit/s system, it is necessary to compensate not only for chromatic dispersion (D or β_2) at the center wavelength of the pulse but also for the dispersion slope ($dD/d\lambda$ or β_3). The dispersion slope produces oscillations near the trailing edge of the data pulse even if the center wavelength of the pulse is adjusted to the zero-dispersion point of the path-averaged dispersion. Currently, the most mature dispersion compensation technique is based on dispersion compensating fibres (DCF), which compensate simultaneously for both D and $dD/d\lambda$. DCF, also sometimes known as high-slope dispersion compensating fiber (HS-DCF), has become an essential optical component supporting high-speed large capacity optical transmission. DCF has further evolved into dispersion-managed optical fiber transmission lines. Chapter 9 ("Optical fibers and fiber dispersion compensators for high-speed optical communication", by Nishimura) reports on DCF and dispersion-managed optical transmission lines as well as on advanced optical fiber such as ultra-low loss or ultra-low nonlinearity fiber and various types of dispersion-modified fiber.

Dispersion compensation using DCF is insufficient for very high bit rate transmission (640 Gbit/s and beyond) in most fibers. Higher order dispersion terms (β_4) have to be taken into account. This is dealt with in chapter 11 ("Higher-order dispersion compensation using phase modulators", by Pelusi and Suzuki). This chapter focuses

on the use of a phase modulation technique that has been effectively employed in the fastest OTDM fiber transmission experiments using OOK modulation format reported to date [see chapter 14 ("Ultrafast OTDM transmission using novel fiber devices for pulse compression, shaping, and demultiplexing", by Yamamoto and Nakazawa)]).

Various types of transmission fiber and their associated DCF have been investigated for high-speed data transmission. Examples are standard single-mode fiber (SMF, $D \cong 17$ ps/km/nm at $\lambda = 1550$ nm), dispersion shifted fiber (DSF, $D \cong 0.1$ ps/km/nm), and various types of non-zero dispersion shifted fiber (NZDSF, $D \cong 4$–8 ps/km/nm), e.g., TrueWave^{TM}, LEAF^{TM} and TeraLight^{TM}. Additionally, there are several types of dispersion-managed fiber (DMF) such as "TeraLight^{TM}-Reverse TeraLight^{TM}", SMF-reverse dispersion fiber (SMF-RDF) and "Ultrawave^{TM} Fiber" (SLA-IDF). The DMF represents a pair of transmission fibers, which together compensate for D and $dD/d\lambda$ over a wide wavelength range. For example Ultrawave^{TM} Fiber comprises Super Large Area fiber (SLA, $D \cong 20$ ps/km/nm) and Inverse Dispersion Fiber (IDF, $D \cong -44$ ps/km/nm).

The tolerances as regards residual dispersion or residual DCF length are particularly crucial for high-speed systems. For instance, for a data rate of 160 Gbit/s over 160 km of SMF, the 3 dB tolerance (an increase in the pulse width by a factor of two) is $\pm$ 1.2 ps/nm. This corresponds to a DCF fiber length tolerance of $\pm$ 12 m or an SMF fiber length tolerance of $\pm$ 75 m. To maintain such small tolerances over a large environmental temperature range requires automatic dispersion compensation in addition to the DCF fiber. Various tunable dispersion compensators have been proposed [34–37]. In particular, the chirped fiber Bragg grating (FBG) is a key device for tunable dispersion compensation. Chapter 10 ("Fiber Bragg gratings for dispersion compensation in optical communication systems", by Sumetsky and Eggleton) presents an overview of FBG fabrication principles and applications with emphasis on the chirped FBG used for dispersion compensation in high-speed optical communication systems. An example of a tunable dispersion compensator is also discussed in chapter 15 ("Ultrafast optical technologies for large-capacity TDM/WDM photonic networks", by Morioka).

High-speed transmission experiments are commonly performed in the quasi-linear (pseudo-linear) transmission regime, where the nonlinear length is much greater than the dispersion length [e.g., 38]. A high local dispersion is advantageous for this transmission regime, provided that the path-averaged dispersion and dispersion slope are close to zero. The short pulses of the data signal disperse very quickly in the fiber, spreading into many adjacent timeslots before the original pulse sequence is restored by dispersion compensation. Therefore, the peak power of the pulses is low for most of the path along the fiber. Consequently, fibers with high dispersion D are most appropriate for high-speed transmission. For example, with 160 Gbit/s data transmission, impressive results with transmission spans of up to 2,000 km have been obtained using NZDSF [39]. However, 160 Gbit/s data transmission over the Ultrawave^{TM} Fiber with its high local dispersion and low non-linearity achieved a transmission distance of more than 4,000 km [40]. In these experiments, intra-channel FWM is the main degradation factor as regards data signals with high optical powers.

PMD is also a severe limitation with respect to high bit rate data transmission. PMD is caused by a slight birefringence of the fiber and of other components in the transmission link. Based on the example cited above, a PMD value of less than 0.07 ps/$\sqrt{\text{km}}$ is needed to realize a low penalty 160 Gbit/s transmission over a 160-km fiber link. Modern fiber such as Ultrawave^{TM} Fiber has a PMD value of less than 0.05

Table 1. Examples of ultra-high-speed optical transmission experiments.

Date	TDM bit rate (Gbit/s)	WDM channel	Modulation format	Transmission length (km, fiber)	Span length (km, repeater)	Pulse source	Demux	Clock Recovery	Institute	Ref.
03/95	160	1	OOK, AP	200 DSF	25, EDFA	ML-FRL+PuC	POL+NOLM	clock modulation	NTT	46
05/95	200	1	OOK, SP	100 DSF	20, 40,EDFA	SC-pulse	FWM in Fiber	PLL, FWM in SOA	NTT	47
05/96	400	1	OOK,SP	40 SMF	unrepeatered	SC-pulse	FWM in Fiber	PLL, FWM in SOA	NTT	48
09/97	200	7	OOK, SP	50 DSF	unrepeatered	SC-pulse	FWM in Fiber	PLL, FWM in SOA	NTT	52
04/98	640	1	OOK, SP	60 SMF	unrepeatered	ML-FRL+PuC	NOLM	clock modulation	NTT	49
05/99	160	19	OOK, SP	40 DSF	unrepeatered	SC-pulse	FWM in Fiber	PLL, FWM in SOA	NTT	53
09/99	160	1	OOK, AP	300 TW	100, EDFA	CW+Mod+PuC	2 EAM	resonant-oscillator	Lucent	61
03/00	320	1	OOK, AP	200 TW	100, Raman	CW + Mod	POL+2 EAM	resonant-oscillator	Lucent	38
09/00	160	1	OOK, SP	160 SMF	unrepeatered	ML-LD	SOA-MZI	transmitted	HHI	54
11/00	1280	1	OOK, AP	70 SMF +RDF	unrepeatered	ML-FRL+PuC	POL+NOLM	transmitted	NTT	51
03/01	160	6	OOK, AP	400 TW	100, Raman	SC-pulse	2 EAM	resonant-oscillator	Lucent	67
03/01	160	1	OOK, SP	116 SMF, field trial	unrepeatered	ML-LD	SOA-UNI	transmitted	HHI	55
09/01	160	1	OOK, SP	200 TW-RS,LEAF	unrepeatered	CW+Mod+PuC	3 EAM	resonant-oscillator	Agere	62
08/03	160	4	OOK, AP, CS-RZ	225 NZ-DSF	75, EDFA	CW + Mod	POL+ 2 EAM	resonant-oscillator	KDDI	71
09/03	160	1	OOK, SP,CS-RZ	640 SMF	80, Raman	CW + Mod	2 EAM	PLL	OKI	23
09/03	160	8	OOK, AP, CS-RZ	85 TeraLight-Ultra	unrepeatered	CW + Mod	1 EAM +POL	resonant-oscillator	Alcatel	69
09/03	160 +7%FEC	7	OOK, AP, CS-RZ	600 SMF	100, Raman	CW + Mod	1 EAM +POL	transmitted	Alcatel	70
09/03	160	8	OOK, SP	140 SMF	unrepeatered	SC-pulse	SOA-MZI	transmitted	FESTA /OKI/NEC	57
10/03	160	1	DPSK, SP	410, SLA+IDF	80, EDFA	ML-LD	1 EAM	EO-PLL, EAM	HHI	75
11/03	160+7%FEC	6	DPSK, AP	2000 TW-RS	100, Raman	CW + Mod	1 EAM,40Gb/s	clock modulation	Lucent	39
02/04	160	1	OOK, SP	160, SMF+RDF	80, Raman	SC-pulse	all channel	transmitted	NTT/ Stanford Univ.	22
07/04	160	1	DPSK, SP	200 SMF,field trial	50, EDFA	CW+Mod+PuC	2 EAM,40Gb/s	EO-PLL, EAM	KDDI/ NICT	77
09/04	160	1	OOK, SP	275 SMF, field trial	69, EDFA	solid state	FWM in SOA	EO-PLL, EAM	Siemens/ BT	58
09/04	160+7%FEC	8	OOK, AP, CS-RZ	430 SMF, field trial	71, EDFA	CW + Mod	1 EAM +Pol	resonant-oscillator	Alcatel/ FT/ DT	45
09/04	320	10	OOK, SP	40, SMF	unrepeatered	SC-pulse	SOA-MZI	transmitted	FESTA /OKI/NEC	26
09/04	640	1	DPSK, AP	160 SLA+IDF	80, EDFA	ML.-FRL	POL+NOLM	EO-PLL, EAM	HHI / Fujitsu	80
09/05	160+7%FEC	1	DPSK, AP	4300 SLA+IDF	80, Raman	ML.-LD	1 EAM,40Gb/s	EO-PLL, EAM	HHI/ Lucent(G)	40
09/05	640	1	DQPSK, AP	480 SLA+IDF	80, EDFA	ML.-LD	POL+ 1 EAM	EO-PLL, EAM	HHI	84
02/06	1280	1	DQPSK, AP	240 SLA+IDF	80, EDFA	solid state	POL+NOLM	EO-PLL, EAM	HHI/Fujitsu	85
02/06	2400+7%FEC	1	DQPSK, AP	160 SLA+IDF	80, EDFA	solid state	POL+NOLM	clock modul.+PLL	HHI/Fujitsu	85

ps/$\sqrt{\text{km}}$. On the other hand, older installed fiber generally has a larger PMD value. Unlike CD, PMD is much more difficult to compensate for because it changes greatly with time and wavelength in a non-deterministic way. Therefore, automatic (adaptive) PMD compensation is required. Chapter 12 ("PMD-compensation techniques", by Rosenfeldt and Brinkmeyer) deals with PMD compensation techniques. Adaptive PMD compensation has been demonstrated for data rates of up to 160 Gbit/s [41–45]. In most ultrahigh bit rate transmission experiments, PMD (first order) was compensated for by manually adjusting the polarization of the data signal at the transmission link input.

For advanced transmission systems, 3R-regeneration (re-amplification, re-shaping, re-timing) is needed to reduce the transmission impairments, which are associated with waveform distortions caused by fiber transmission as well as with noise and jitter accumulation. There has been little experimental work on this topic as regards high bit rate data transmission. Chapter 6 ("Optical signal processing using nonlinear fibers", by Watanabe) reports on a 160-Gbit/s 3R-regenerator experiment [19]. Chapter 8 ("Optical nonlinearities in semiconductor optical amplifier and electro-absorption modulator: their applications to all-optical regeneration", by Usami and Nishimura) provides some references to 2R and 3R regenerator experiments for data rates below 160 Gbit/s.

6. Transmission Experiments

In this review we focus on the recent developments with respect to OTDM transmission experiments as early transmission experiments have been discussed in previous review articles [3–5]. Table 1 is a summary of important and recent high bit rate transmission experiments at TDM bit rates of 160 Gbit/s and beyond. Many of the pioneering OTDM-transmission experiments were performed by NTT and are described in chapter 15 ("Ultrafast optical technologies for large-capacity TDM/WDM photonic networks", by Morioka). Examples include 160 Gbit/s soliton transmission over 200 km DSF [46], 200 Gbit/s transmission over 100 km DSF [47], 400 Gbit/s over 40 km SMF [48], 640 Gbit/s over 60 km and 92 km SMF [49,50] and finally 1.28 Tbit/s over 70 km DMF (SMF+RDF) [51]. In addition to these single wavelength channel transmission experiments, chapter 15 ("Ultrafast optical technologies for large-capacity TDM/WDM photonic networks", by Morioka) also describes pioneering OTDM/WDM experiments performed by NTT such as 1.4 Tbit/s (200 Gbit/s $\times$ 7 λ) over 50 km DSF [52] and 3 Tbit/s (160 Gbit/s $\times$ 19 λ) over 40 km DSF [53]. These experiments combine ultrafast OTDM and ultra-wideband WDM technologies.

In these experiments, the terminal equipment mainly comprised fiber devices. The pulse source in the transmitter was either a mode-locked fiber ring laser (ML-FRL) followed by an optical pulse compressor (PuC) or a pulse source based on supercontinuum generation (SC-pulse). The demultiplexer in the OTDM-receiver was an optical gate based either on a nonlinear optical loop mirror (NOLM) or on four-wave-mixing (FWM) in fiber. An exception was the optical clock recovery device, which comprised a PLL with a phase comparator based on FWM in a semiconductor optical amplifier (SOA). EDFAs were used as in-line amplifiers.

The NTT work represents investigations on the physical limits of high-speed fiber transmission and the search for appropriate data generation, transmission and demultiplexing techniques to extend these limits. An extraordinary 1.28 Tbit/s (640 Gbit/s $\times$

2 polarization-division multiplexing) single wavelength channel transmission experiment is described in detail in chapter 14 ("Ultrafast OTDM transmission using novel fiber devices for pulse compression, shaping, and demultiplexing", by Yamamoto and Nakazawa). This chapter covers the adiabatic soliton compression technique, which compresses the optical pulses of an ML-FRL, a technique for eliminating the pedestals of the compressed optical pulses, and an all-optical demultiplexing technique employing a NOLM with very small walk-off.

An alternative to fiber-based optical signal processing is the employment of semiconductor devices for optical signal processing in the transmitter and receiver of the OTDM system. In particular, the SOA has long been considered a key device for optical signal processing. Chapter 5 ("High-speed optical signal processing using semiconductor optical amplifiers", by Schubert et al.) describes the technology of SOA-based devices such as optical gates, optical clock recovery devices and optical add-drop multiplexers. These devices have been used in several transmission experiments [54–58,26,12,22]. Examples of single wavelength channel transmission include unrepeatered 160 Gbit/s transmission over 160 km SMF using a hybrid SOA-MZI DEMUX [54], the first 160-Gbit/s field trial involving unrepeatered transmission over 116 km field-installed SMF using an SOA-UNI DEMUX [55] and a 160 Gbit/s field trial over various link lengths of installed fiber of up to 275 km SMF using a DEMUX based on FWM in a SOA [58,12]. The latter field experiment is of particular interest because it also includes a 160 Gbit/s add-drop node based on gain-transparent operation of a SOA [see chapter 5 ("High-speed optical signal processing using semiconductor optical amplifiers", by Schubert et al.)]. This is the first OTDM networking experiment using deployed fiber. Also of particular importance is the first 160 Gbit/s OTDM transmission experiment with all-channel independent modulation and all-channel simultaneous demultiplexing achieved by using a multiplexer and a demultiplexer based on periodically poled lithium niobate and SOA hybrid integrated planar lightwave circuits [22]. This transmission experiment is described in detail in chapter 15 ("Ultrafast optical technologies for large-capacity TDM/WDM photonic networks", by Morioka). A hybrid-integrated SOA-MZI DEMUX was operated in two OTDM/WDM transmission experiments, namely, 1.28 Tbit/s (160 Gbit/s $\times$ 8λ) unrepeatered transmission over 140 km SMF [57] and 3.2 Tbit/s (320 Gbit/s $\times$ 10λ) transmission over 40 km SMF [26]. In these experiments the spectral efficiencies were 0.4 and 0.8 bit/s/Hz, respectively.

At present, the SOA based optical gate is probably not the most popular choice for demultiplexing applications in 160 Gbit/s transmission systems. Another semiconductor device, the EAM, has been developed into a very effective component for optical signal processing. In pioneering experiments, British Telecom (BT) demonstrated the application of the EAM for OTDM data generation and demultiplexing [59,60]. Lucent Technologies reported the first 160 Gbit/s transmission experiment, which used the EAM as a key device in the transmitter and the receiver [61]. This investigation also stimulated similar experiments in many other laboratories [62–65], because 160 Gbit/s transmission became viable without such sophisticated devices for demultiplexing as interferometric optical gates or FWM configurations based on SOAs or fibers, and without sophisticated optical pulse sources. The EAM was used as an optical gate in the demultiplexer, as a basic element in the clock recovery circuit and as a device for optical pulse generation (CW + Mod). Moreover, the EAM-based demultiplexer is polarization insensitive, which is difficult to achieve with the fiber-

based and SOA-based demultiplexers. Also, the EAM-based demultiplexer does not need an optical pulse source to operate the optical gate. The simpler technology of the EAM-based OTDM-system also stimulated 320 Gbit/s transmission experiments using AP-multiplexing [66,38] and several $N\times$ 160 Gbit/s OTDM/WDM transmission experiments [67–71,45]. Chapter 13 ("Application of electroabsorption modulators for high-speed transmission systems", by Lach et al.) focuses on OTDM transmission technology based on EAMs. This chapter reviews the various applications of the EAM in the transmitter and receiver in ultra-high speed OTDM-transmission systems and also presents the results of single channel and WDM/OTDM fiber transmission experiments.

In the experiments mentioned above, the modulation format was on-off-keying (OOK). Moreover, in most of these experiments the relative phase of adjacent pulses (RZ-signals) was arbitrary, because in general no effort was made in these experiments to adjust and stabilize the delay line multiplexers for a well-defined relative phase of the adjacent pulses. However, the controllability of the optical phase alignment between adjacent bits is an important feature of an OTDM system [72]. The effect of a well-defined relative phase of adjacent data pulses in the multiplexed data signal is expected to increase the tolerance of the transmission system with respect to CD and fiber nonlinearity and it will increase the spectral efficiency. Techniques for realizing optical phase alignment have been introduced [73,74] and several OTDM and OTDM/WDM transmission experiments have been performed using such formats as "carrier-suppressed return-to-zero (CS-RZ)", in which the optical pulses in adjacent bit slots have a relative phase shift of π [23,69–71,45].

Recently, several OTDM-transmission experiments have been performed using modulation format differential phase shift keying (DPSK) [75–80, 39,40]. In combination with balanced detection, 160 Gbit/s DPSK transmission provided a system performance that was more than 3 dB better than transmission with the OOK modulation format [76]. The increased system margin can be used to extend the transmission length or to reduce the optical power requirements. On the other hand, additional components are needed in the transmitter and receiver. In particular, the DPSK demodulator in the receiver needs to be actively matched to the transmitter wavelength, which increases the system complexity. Nevertheless, the improvement in the system performance is significant and worth the additional system cost and complexity. The increased system margin also made it possible to realize a 640-Gbit/s DPSK, AP transmission over a 160 km dispersion managed fiber link [80].

In the past, many high-bit-rate transmission experiments were "proof of feasibility" experiments. It was sufficient simply to obtain a system that was stable for the few minutes needed to perform BER measurements. Recently, it was also shown that OTDM transmission systems can have long-term stability [78,79]. In a 160-Gbit/s DPSK transmission over a 320-km fiber link, BER measurements revealed, that the system operated without any error for more than 5 hours. This corresponds to a BER of about 10^{-15}. The first errors were detected after 5 hours and these were caused by a slight drifting of some parts of the system with increases in the environmental temperature. There were 32 errors within 10 hours. After 10 hours the system was readjusted and error-free performance was again obtained. No PMD compensator was required in this experiment because of the high quality of the Ultrawave^{TM} Fiber used. Similar results were also obtained using a 334-km SMF fiber link including a PMD mitigation scheme [79]. In both experiments, the transmission system comprised a

semiconductor mode-locked laser (ML-LD) in the transmitter and two EAMs in the demultiplexer (one in the optical gate and one in the clock recovery). If this system is equipped with an automatic stabilization circuit and FEC, it can probably be operated error free for many years. The system has a stability appropriate for applications in a deployed transmission link.

Some further recent transmission experiments concern DQPSK transmission with data rates of 160 Gbit/s and higher [82-85]. DQPSK transmission provides a bit rate that is twice the symbol bit rate. Based on 40 Gbit/s ETDM technology, the application of DQPSK provides 80 Gbit/s data transmission. In [82,83] this was further combined with polarization-division multiplexing (AP multiplexing) to generate a 160-Gbit/s data signal. In this experiment, 40 WDM channels, each carrying a 160 Gbit/s data signal generated in this way, were transmitted over a 324-km SMF fiber link. The system was operated above the FEC limit. This corresponds to a 5.94-Tbit/s error-free transmission conditional on the use of FEC. A spectral efficiency of 1.6 bit/s/Hz was obtained. In another experiment, the 160-Gbit/s OTDM-SP-multiplexing transmission technology was upgraded to 640 Gbit/s by applying the modulation format DQPSK and polarization-division multiplexing (AP multiplexing). A 640-Gbit/s DQPSK data signal was transmitted over 480 km DMF (SLA-IDF) error-free without FEC [84].

Most recently, DQPSK transmission with AP multiplexing was also realized at 1.28 Tbit/s over 240 km and 2.56 Tbit/s over 160 km fiber link [85]. For 1.28 Tbit/s, error-free (BER $< 10^{-9}$) transmission was obtained for all tributaries of the 1.28 Tbit/s data signal. For 2.56 Tbit/s transmission, the system performed nearly error-free (BER $\approx 10^{-9}$) in the back-to-back configuration and revealed BER-values $\leq 10^{-5}$ after 160 km transmission. BER values of less than 10^{-4} result in an effective BER $< 10^{-12}$ if standard FEC (assuming a 7% overhead) is used. This FEC would reduce the payload to 2.4 Tbit/s.

References

1. K. Fukuchi, T. Kasamatsu, M. Morie, R. Ohhira, T. Ito, K. Sekiya, D. Ogasahara, and T. Ono, "10.92 Tb/s (273 × 40 Gb/s) triple-band/ultra-dense WDM optical-repeatered transmission experiment" in Proc. Optical Fiber Communication Conference, OFC 2001, postdeadline papers, PD 24 (2001).
2. S. Biego, Y. Frignac, G. Charlet, W. Idler, S. Borne, H. Gross, R. Dischler, W. Poehlmann, P. Tran, C. Simonneau, D. Bayart, G. Veith, A. Jourdan, J.-P. Hamaide, "10.2 Tbit/s (256 × 42.7 Gbit/s PDM/WDM) transmission over 100 km TeraLight fiber with 1.28 bit/s/Hz spectral efficiency" in Proc. Optical Fiber Communication Conference, OFC 2001, postdeadline papers, PD 25 (2001).
3. S. Kawanishi, "Ultrahigh-speed optical time-division-multiplexed transmission technology based on optical signal processing", IEEE J. Quantum Electron. **34**, 2064–2079 (1998).
4. M. Saruwatari, "All-optical signal processing for Tera bit/s optical transmission", IEEE J. Select Topics Quantum Electron. **6**, 1363–1374 (2000).
5. M. Saruwatari, "All-optical time-division multiplexing technology" in *Fiber Optic Communication Devices*, edited by N. Grote, H. Venghaus (Springer-Verlag, Berlin, 2001).
6. A. Joseph, D. Coolbaugh, D. Harame, G. Freeman, S. Subbanna, M. Doherty, J. Dunn, C. Dickey, D. Greenberg, R. Groves, M. Meghelli, A. Rylyakov, M. Sorna, O. Schreiber, D. Herman, and T. Tanji, "0.13 μm 210 GHz f_T SiGe HBTs—expanding the horizons of

SiGe BiCMOS", International Solid-State Circuits Conference, ISSCC, Digest of Technical papers, pp. 180–181 (2002).

7. Y. Yu, R. Lewen, S. Irmscher, U. Westergren, L. Thylen, U. Eriksson, and W.S. Lee, "80 Gb/s ETDM Transmitter with a Traveling-Wave Electroabsorption Modulator", in Proc. Optical Fiber Communication Conference, OFC 2005, Paper OWE1 (2005).
8. H.-G. Bach, A. Beling, G.G. Mekonnen, R. Kunkel, D. Schmidt, W. Ebert, A. Seeger, M. Stollberg, and W. Schlaak, "InP-Based Waveguide-Integrated Photodetector with 100 GHz Bandwidth", IEEE J. Select. Topics on Quantum Electron. **10** (4), 668–672 (2004).
9. K. Schuh, B. Junginger, E. Lach, A. Klekamp, E. Schlag, "85.4 Gbit/s ETDM receiver with full rate electronic clock recovery", in Proc. European Conference on Optical Communication, ECOC 2004, PDP Th4.1.1 (2004).
10. O. Kamatani and S. Kawanishi, "Add/drop operation for 100 Gbit/s optical signal based on optical wavelength conversion by four-wave mixing", Electron. Lett. **32**, 911–913 (1996).
11. C. Schubert, C. Schmidt, S. Ferber, R. Ludwig, and H.G. Weber, "Error-free all-optical add-drop multiplexing at 160 Gbit/s", Electron. Lett. **39**, 1074–1076 (2003).
12. J.P. Turkiewicz, E. Tangdiongga, G. Lehmann, H. Rohde, W. Schairer, Y.R. Zhou, E.S.R. Sikora, A. Lord, D.B. Payne, G.-D. Khoe, and H. de Waardt, "160 Gbit/s OTDM networking using deployed fiber", J. Lightwave Technol. **23**, 225–235 (2005).
13. H.F. Chou, J.E. Bowers, and D.J. Blumenthal, "Compact 160-Gb/s Add-Drop Multiplexing with a 40-Gb/s Base-Rate", Optical Fiber Communication Conf., 2004, PDP28 (2004).
14. S. Nakamura, Y. Ueno, and K. Tajima, "168-Gb/s all-optical wavelength conversion with a symmetric-Mach-Zehnder-type switch", Photon. Technol. Lett. **13**, 1091–1093 (2001).
15. J. Leuthold, C. Joyner, B. Mikkelsen, G. Raybon, J. Pleumeekers, B. Miller, K. Dreyer, and C. Burrus, "100 Gbit/s all-optical wavelength conversion with integrated SOA delayed-interference configuration", Electron. Lett. **36**, 1129–1130 (2000).
16. J. Hansryd, P.A. Andrekson, M. Westlund, J. Li, and P.-O. Hedekvist, "Fiber-based optical parametric amplifiers and their applications", IEEE J. Select. Topics Quantum Electron. **8**, 506–520 (2002).
17. F. Futami, R. Okabe, Y. Takita, and S. Watanabe, "Transparent wavelength conversion at up to 160 Gb/s by using supercontinuum generation in a nonlinear fiber", Proc. Optical Amplifiers and Applications, OAA 2003 at Otaru, Japan, Paper MD07 (2003).
18. S. Ferber, R. Ludwig, F. Futami, S. Watanabe, C. Boerner, C. Schmidt-Langhorst, L. Molle, K. Habel, M. Rohde, and H.G.Weber, "160 Gbit/s regenerating conversion node", in Proc. Optical Fiber Communication Conference, OFC 2004, Los Angeles, CA, USA, paper ThT2 (2004).
19. S. Watanabe, R. Ludwig, F. Futami, C. Schubert, S. Ferber, C. Boerner, C. Schmidt-Langhorst, J. Berger, and H.G. Weber, "Ultrafast all-optical 3R-regeneration", IEICE Trans. Electron. **E87-C** (7), 1114–1118 (2004).
20. P.V. Mamyshev, "All-optical data regeneration based on self-phase modulation effect", in Proc. European Conference on Optical Communications, ECOC 1998, Madrid, Spain, Volume 1, pp. 475–476 (1998).
21. T. Ohara, H. Takara, I. Shake, K. Mori, S. Kawanishi, S. Mino, T. Yamada, M. Ishii, T. Kitoh. T. Kitagawa, K.R. Parameswaran, and M.M. Fejer, "160 Gbit/s optical-time-division multiplexing with PPLN hybrid integrated planar lightwave circuit", IEEE Photon. Technol. Lett. **15**, 302–304 (2003).

22. T. Ohara, H. Takara, I. Shake, K. Mori, K. Sato, S. Kawanishi, S. Mino, T. Yamada, M. Ishii, I. Ogawa, T. Kitoh, K. Magari, M. Okamoto, R.V. Roussev, J.R. Kurz, K.R. Parameswaran, and M.M. Fejer, "160-Gb/s OTDM transmission using integrated all-optical MUX/DEMUX with all-channel modulation and demultiplexing", IEEE Photon. Technol. Lett. **16**, 650–652 (2004).
23. H. Murai, K. Masatoshi, H. Tsuji, and K. Fujii, "Single Channel 160 Gbit/s Carrier-Suppressed RZ Transmission over 640 km with EA Modulator based OTDM Module", ECOC 2003, paper Mo.3.6.4, Rimini.
24. K.J. Blow, N.J. Doran, and B.P. Nelson, "Demonstration of the nonlinear fibre loop mirror as an ultrafast all-optical demultiplexer", Electron. Lett. **26**, 962–963 (1990).
25. A. Bjarklev, J. Broeng, and A.S. Bjarklev, *Photonic Crystal Fibers* (Kluwer Academic Publishers, Dordrecht, The Netherlands, 2003).
26. A. Suzuki, X. Wang, Y. Ogawa, and S. Nakamura, "10 × 320 Gbit/s (3.2 Tbit/s) DWDM/ OTDM transmission by semiconductor based devices", Proc. ECOC 2004, paper Th4.1.7.
27. K. Tajima, S. Nakamura, and A. Furukawa, "Hybrid-integrated symmetric Mach-Zehnder all-optical switches and ultrafast signal processing" IEICE Trans. Electron. **E87-C** (7), 1119–1125 (2004).
28. S. Diez, R. Ludwig, and H.G. Weber, "All-optical switch for TDM and WDM/TDM systems demonstrated in a 640 Gbit/s demultiplexing experiment", Electron. Lett. **34**, 803 (1998).
29. S. Kodama, T. Yoshimatsu, and H. Ito, "320 Gbit/s error-free demultiplexing using ultrafast optical gate monolithically integrating a photodiode and electroabsorption modulator", Electron. Lett. **39** (17), 1269–1270 (2003).
30. S. Kodama, T. Yoshimatsu, and H. Ito, "500-Gbit/s demultiplexing operation of monolithic PD-EAM gate", postdeadline paper Th4.2.8, ECOC 2003, Rimini.
31. I. Shake, H. Takara, K. Uchiyama, I. Ogawa, T. Kitoh, T. Kitagawa, M. Okamoto, K. Magari, Y. Suzuki, and T. Morioka, "160 Gbit/s full optical time-division demultiplexing using FWM of SOA-array integrated on PLC", Electron Lett. **38**, 37–38 (2002).
32. O. Kamatani and S. Kawanishi, "Prescaled Timing extraction from 400 Gbit/s optical signal using a phase lock loop based on four-wave mixing", IEEE Photon. Technol. Lett. **8**, 1094–1096 (1996).
33. C. Boerner, V. Marembert, S. Ferber, C. Schubert, C. Schmidt-Langhorst, R. Ludwig, and H.G. Weber, "320 Gbit/s clock recovery with electro-optical PLL using a bidirectionally operated electroabsorption modulator as phase comparator" in Proc. Optical Fiber Communication Conference, OFC 2005, paper OTuO3 (2005).
34. B. J. Eggleton, B. Mikkelsen, G. Raybon, A. Ahuja, J.A. Rogers, P.S. Westbrook, T.N. Nielsen, S. Stulz, and K. Dreyer, "Tunable dispersion compensation in a 160 Gb/s TDM system by voltage controlled chirped fiber Bragg grating" IEEE Photon.Technol. Lett. **12**, 1022–1024 (2000).
35. C.K. Madsen, "Integrated waveguide allpass filter tunable dispersion compensator", OFC' 2002, TuT1.
36. T. Inui, T. Komukai, M. Nakazawa, K. Suzuki, K.R. Tamura, K. Uchiyama, and T. Morioka, "Adaptive dispersion slope equalizer using a nonlinearly chirped fiber Bragg grating pair with a novel dispersion detection technique", IEEE Photon. Technol. Lett. **14**, 549–551 (2002).
37. S. Wakabayashi, A. Baba, H. Moriya, X. Wang, T. Hasegawa, and A. Suzuki, "Tunable dispersion and dispersion slope compensator based on two twin chirped FBGs with temperature gradient for 160 Gbit/s transmission." IEICE Trans. Electron. **E87-C**, 1100–1105 (2004).

38. B. Mikkelsen, G. Raybon, R.-J. Essiambre, A.J. Stentz, T.N. Nielsen, D.W. Peckham, L. Hsu, L. Gruner-Nielsen, K. Dreyer, and J.E. Johnson, "320 Gbit/s single-channel pseudolinear transmission over 200 km nonzero-dispersion fiber", IEEE Photon. Technol. Lett. **12**, 1400–1402 (2000).

39. A.H. Gnauck, G. Raybon, P.G. Bernasconi, J. Leuthold, C.R. Doerr, and L.W. Stulz, "1 Tb/s 6×170.6 Gb/s) transmission over 2000 km NZDF using OTDM and RZ-DPSK", IEEE Photon. Technol. Lett. **15** (11), 1618–1620 (2003).

40. S. Weisser, S. Ferber, L. Raddatz, R. Ludwig, A. Benz, C. Boerner, H.G. Weber, "Single- and Alternating Polarization 170 Gbit/s Transmission up to 4000 km using Dispersion-Managed Fiber and All-Raman Amplification", IEEE Photon. Technol. Lett. **18** (12), 1320–1322 (2006).

41. M. Westlund, H. Sunnerud, J. Li, J. Hansryd, M. Karlsson, P.O. Hedekvist, and P.A. Andrekson, "Long-term automatic PMD compensation for 160 Gbit/s RZ transmission", Electron. Lett. **38**, 982–983 (2002).

42. T. Miyazaki, M. Daikoku, I. Morita, T. Otani, Y. Nagao, M. Suzuki, and F. Kubota, "Stable 160 Gbit/s DPSK transmission using a simple PMD compensator on the field photonic network test bed of JGN II", Proc. OECC 2004, PD-1-3.

43. F. Buchali, W. Baumert, M. Schmidt, and H. Buelow, "Dynamic distortion compensation in a 160 Gb/s RZ OTDM system: adaptive 2 stage PMD compensation", Optical Fiber Communication Conf., pp. 589–590 (2003)

44. S. Kieckbusch, S. Ferber, H. Rosenfeldt, R. Ludwig, A. Ehrhardt, E. Brinkmeyer, and H.G. Weber, "Automactic PMD compensator in a single-channel 160 Gb/s transmission over deployed fiber using RZ-DPSK modulation format" J. Lightwave Technol. **23** (1), 165–171 (2005).

45. M. Schmidt, M. Witte, F. Buchali, E. Lach, E. Le Rouzic, S. Salaun, S. Vorbeck, and R.Leppla, "8×170 Gbit/s DWDM Field Transmission Experiment over 430 km SSMF Using Adaptive PMD Compensation", ECOC 2004 Stockholm, PDP Th4.1.2.

46. M. Nakazawa, K. Suzuki, E. Yoshida, E. Yamada, T. Kitoh, and M. Kawachi, "160 Gbit/s soliton data transmission over 200 km", Electron. Lett. **31**, 565–566 (1995).

47. S. Kawanishi, H. Takara, T. Morioka, O. Kamatani, and M. Saruwatari, "200 Gbit/s, 100 km time-division-multiplexed optical transmission using supercontinuum pulses with prescaled PLL timing extraction and all-optical demultiplexing", Electron. Lett. **31**, 816–817 (1995).

48. S. Kawanishi, H. Takara, T. Morioka, O. Kamatani, K. Takiguchi, T. Kitoh, and M. Saruwatari, "Single channel 400 Gbit/s time-division-multiplexed transmission of 0.98 ps pulses over 40 km employing dispersion slope compensation", Electron. Lett. **32**, 916 (1996).

49. M. Nakazawa, E. Yoshida, T. Yamamoto, E. Yamada, and A. Sahara, "TDM single channel 640 Gbit/s transmission experiment over 60 km using 400 fs pulse train and walk-off free, dispersion flattened nonlinear optical loop mirror", Electron. Lett. **34**, 907–908 (1998).

50. T. Yamamoto, E. Yoshida, K.R. Tamura, K. Yonenaga, and M. Nakazawa, "640 Gbit/s optical TDM transmission over 92 km through a dispersion managed fiber consisting of single-mode fiber and reverse dispersion fibre", IEEE Photon. Technol. Lett. **12**, 353–355 (2000).

51. M. Nakazawa, T. Yamamoto, and K. R. Tamura, "1.28 Tbit/s–70 km OTDM transmission using third-and fourth-order simultaneous dispersion compensation with a phase modulator, Electron. Lett. **36**, 2027–2029 (2000).

52. S. Kawanishi, H. Takara, K. Uchiyama, I. Shake, O. Kamatani, and H. Takahashi, "1.4 Tbit/s (200 Gbit/s × 7 ch) 50 km optical transmission experiment", Electron. Lett. **33**, 1716–1717 (1997).

53. S. Kawanishi, H. Takara, K. Uchiyama, I. Shake, and K. Mori, "3 Tbit/s (160 Gbit/s × 19 channel) optical TDM and WDM transmission experiment", Electron. Lett. **35** (10), 826–827 (1999).

54. R. Ludwig, U. Feiste, S. Diez, C. Schubert, C. Schmidt, H.J. Ehrke, and H.G. Weber, "Unrepeatered 160 Gbit/s RZ single-channel transmission over 160 km of standard fibre at 1.55 μm with hybrid MZI optical DEMUX", Electron. Lett. **36**, 1405–1406 (2000).

55. U. Feiste, R. Ludwig, C. Schubert, J. Berger, C. Schmidt, H.G. Weber, B. Schmauss, A. Munk, B. Buchold, D. Briggmann, F. Kueppers, and F. Rumpf, "160 Gbit/s transmission over 116 km field-installed fibre using 160 Gbit/s OTDM and 40 Gbit/s ETDM", Electron. Lett. **37**, 443–445 (2001).

56. T. Yamamoto,U. Feiste, J. Berger, C. Schubert, C. Schmidt, R. Ludwig, and H.G. Weber, "160Gbit/s demultiplexer with clock recovery using SOA-based interferometric switches and its application to 120 km fiber transmission", ECOC'01, Amsterdam, Tu.L.2.6.

57. A. Suzuki, X. Wang, T. Hasegawa, Y. Ogawa, S. Arahira, K. Tajima, and S. Nakamura, "8×160Gb/s (1.28Tb/s) DWDM/OTDM unrepeatered transmission over 140 km standard fiber by semiconductor-based devices", ECOC 2003, Rimini, paper Mo3.6.1.

58. J.P. Turkiewicz, E. Tangdiongga, G.-D. Khoe, H. de Waardt, W. Schairer, H. Rohde, G. Lehmann, E.S.R. Sikora, Y.R. Zhou, A. Lord, and D.B. Payne, "Field trial of 160 Gbit/s OTDM add/drop node in a link of 275 km deployed fiber", in Proc. Optical Fiber Commun. Conf. 2004, Los Angeles, CA, PDP1.

59. D.D. Marcenac, A.D. Ellis, and D.G. Moodie, "80 Gbit/s OTDM using electroabsorption modulators", Electron. Lett. **34** (1), 101–103 (1998).

60. A.D. Ellis, J.K. Lucek, D. Pitcher, D.G. Moodie, and D. Cotter, "Full 10×10 Gbit/s OTDM data generation and demultiplexing using electroabsorption modulators", Electron. Lett. **34** (18), 1766–1767 (1998).

61. B. Mikkelsen, G. Raybon, R.-J. Essiambre, K. Dreyer, Y. Su, L.E. Nelson, J.E. Johnson, G. Shtengel, A. Bond, D.G. Moodie, and A.D. Ellis, "160 Gbit/s single-channel transmission over 300 km nonzero-dispersion fiber with semiconductor based transmitter and demultiplexer", ECOC 1999, postdeadline paper 2-3, Nice (1999).

62. J. Yu, K. Kojima, N. Chand, M.C. Fischer, R. Espindola, and T.G.B. Mason, "160 Gb/s single-channel unrepeatured transmission over 200 km of non-zero dispersion shifted fiber", Proc. ECOC 2001 paper PD M.1.10 (2001).

63. J-L. Augé, M. Cavallari, M. Jones, P. Kean, D. Watley, and A. Hadjifotiou, "Single channel 160 Git/s OTDM propagation over 480 km of standard fiber using a 40 GHz semiconductor mode-locked laser pulse source", OFC 2002, paper TuA3, Anaheim (2002).

64. E. Lach, M. Schmidt, K. Schuh, B. Junginger, G. Veith, and P. Nouchi, "Advanced 160 Gb/s OTDM system based on wavelength transparent 4×40 Gb/s ETDM transmitters and receivers", OFC 2002 Anaheim, paper TuA2.

65. H. Murai, M. Kagawa, H. Tsuji, K. Fujii, Y. Hashimoto, and H. Yokoyama, "Single Channel 160 Gbit/s (40 Gbit/s × 4) 300 km Transmission Using EA Modulator based OTDM Module and 40 GHz External Cavity Mode-locked LD", ECOC 2002, paper 2.1.4, Copenhagen.

66. M. Schmidt, E. Lach, K. Schuh, M. Schilling, P. Sillard, and G. Veith, "Unrepeatered 320 Gbit/s (8×40 Gbit/s) OTDM transmission over 80 km TeraLight^{TM}-reverse TeraLight^{TM} fiber link", ECOC 2003, We.4.P.117, Rimini.

67. B. Mikkelsen, G. Raybon, B. Zhu, R.-J. Essiambre, P.G. Bernasconi, K. Dreyer, L.W. Stulz, and S.N. Knudsen, "High spectral efficiency (0.53 bit/s/Hz) WDM transmission of 160 Gb/s per wavelength over 400 km of fiber", OFC 2001, paper ThF2-1, Anaheim.

68. K. Schuh, M. Schmidt, E. Lach, B. Junginger, A. Klekamp, G. Veith, and P. Sillard, "4×160 Gbit/s DWDM / OTDM transmission over 3×80 km TeraLight^{TM}-Reverse TeraLight^{TM}-fibre", ECOC 2002, paper 2.1.2, Copenhagen (2002).

69. M. Schmidt, K. Schuh, E. Lach, M. Schilling, and G. Veith, "8×160 Gbit/s (1.28 Tbit/s DWDM transmission with 0.53 bit/s/Hz spectral efficiency using single EA-modulator based RZ pulse source and demux", ECOC 2003, paper Mo3.6.5, Rimini.

70. E. Lach, K. Schuh, M. Schmidt, B. Junginger, G. Charlet, P. Pecci, and G. Veith, "7×170 Gbit/s (160 Gbit/s + FEC overhead) DWDM transmission with 0.53 bit/s/Hz spectral efficiency over long haul distance of Standard SMF", Proc. ECOC 2003 paper PD Th4.3.5.

71. M. Daikoku, T. Otani, and M. Suzuki, "160 Gb/s Four WDM Quasi-linear transmission over 225 km NZ-DSF with 75 km spacing", IEEE Photon. Technol. Lett. **15** (8), 1165–1167 (2003).

72. S. Randel, B. Konrad, A. Hodzic, and K. Petermann, "Influence of bitwise phase changes on the performance of 160 Gbit/s transmission systems", ECOC 2002 Copenhagen Proc., Vol.3, paper P3.31 (2002).

73. M. Kagawa, H. Murai, H. Tsuji, and K. Fujii, "Performance comparison of bitwise phase-controlled 160 Gbit/s signal transmission using an OTDM multiplexer with phase-correlation monitor", in Proc. ECOC 2004, paper We 4.P.109 (2004).

74. Y. Su, L.Moller, C. Xie, R. Ryf, X. Liu, X. Wei, and S. Cabot, "Ultra high-speed data signals with alternating and pairwise alternating optical phases", J. Lightwave Technol. **23** (1), 26–31 (2005).

75. A. Beling, H.-G. Bach, D. Schmidt, G.G. Mekonnen, R. Ludwig, S. Ferber, C. Schubert, C. Boerner, B. Schmauss, J. Berger, C. Schmidt, U. Troppenz, and H.G. Weber, "Monolithically integrated balanced photodetector and its application in OTDM 160 Gbit/s DPSK transmission", Electron. Lett. **39**, 1204–1205 (2003).

76. S. Ferber, R. Ludwig, C. Boerner, A.Wietfeld, B. Schmauss, J. Berger, C. Schubert, G. Unterboersch, and H.G. Weber, "Comparison of DPSK and OOK modulation format in 160 Gbit/s transmission system", Electron. Lett. **39** (20), 1458–1459 (2003).

77. T. Miyazaki, M. Daikoku, I. Morita, T. Otani, Y. Nagao, M. Suzuki, and F. Kubota, "Stable 160 Gbit/s DPSK transmission using a simple PMD compensator on the field photonic network test bed of JGN II", Proc. OECC 2004, PD-1-3.

78. S. Ferber, R. Ludwig, C. Boerner, C. Schubert, C. Schmidt-Langhorst, M. Kroh, V. Marembert, and H.G. Weber, "160 Gbit/s DPSK transmission over 320 km fibre link with high long-term stability" Electron. Lett. **41**, 200–202 (2005).

79. F. Ferber, C. Schmidt-Langhorst, R. Ludwig, C. Boerner, C. Schubert, V. Marembert, M. Kroh, and H.G. Weber, "160 Gbit/s OTDM long-haul transmission with long-term stability using RZ-DPSK modulation format" IEICE Trans. Commun. **E88-B** (5), 1947–1954 (2005).

80. V. Marembert, C. Schubert, S. Ferber, K. Schulze, C. Schmidt-Langhorst, C. Boerner, M. Kroh, R. Ludwig, S. Watanabe, F. Futami, R. Okabe, and H.G. Weber, "Single-channel 640 Gbit/s DPSK Transmission over a 160 km Fibre Link", Proc. Europ. Conf. on Opt. Comm. (ECOC'04), Stockholm, Sweden, 2004. Post-deadline paper Th4.4.2.

81. A.H. Gnauck and P.J. Winzer, "Optical phase-shift-keyed transmission", J. Lightwave Technol. **23** (1), 115–130 (2005).

82. A.Fauzi Abas Ismail, D. Sandel, A. Hidayat, B. Milivojevic, S. Bhandare, H. Zhang, and R. Noe, "2.56 Tbit/s,1.6 bit/s/Hz, 40 Gbaud RZ-DQPSK polarization division multiplex transmission over 273 km of fiber", OptoElectronic and Communication Conference, OECC 2004, Yokohama, Japan, PD-paper PD1-4 (2004).

83. B. Milivojevic, A.F. Abas, A. Hidayat, S. Bhandare, D. Sandel, R. Noé, M. Guy, and M. Lapointe, "1.6-bit/s/Hz, 160-Gbit/s, 230-km RZ-DQPSK Polarization Multiplex Transmission with Tunable Dispersion Compensation", IEEE Photon. Technol. Lett. **17** (2), 495 (2005).

84. S. Ferber, C. Schubert, R. Ludwig, C. Boerner, C. Schmidt-Langhorst, and H.G. Weber, "640 Gbit/s DQPSK Single-channel Transmission over 480 km Fibre Link", Electron. Lett. **41**, (22), 1234–1235 (2005).

85. H.G. Weber, S. Ferber, M. Kroh, C. Schmidt-Langhorst, R. Ludwig, V. Marembert, C. Boerner, F. Futami, S. Watanabe, C. Schubert, "Single Channel 1.28 Tbit/s and 2.56 Tbit/s DQPSK Transmission", Electron. Lett. **42**, 178–179 (2006).

DOI: 10.1007/s10297-004-0022-0
Originally published in J. Opt. Fiber. Commun. Rep. 2, 1–31 (2005)

Semiconductor mode-locked lasers as pulse sources for high bit rate data transmission

Leaf A. Jiang[1], Erich P. Ippen[1], and Hiroyuki Yokoyama[2]

[1] Research Laboratories of Electronics
Massachusetts Institute of Technology
Cambridge, MA 02139, USA

[2] New Industry Creation Hatchery Center (NICHe)
Tohoku University
10 Aramaki-Aza-Aoba, Aoba-ku, Sendai, Miyagi 980-8579, Japan

Abstract. Semiconductor mode-locked lasers are evaluated as pulse sources for high bit rate data transmission. This chapter describes the requirements of OTDM sources for high bit rate data transmission, compares various OTDM source technologies, describes three semiconductor mode-locked laser cavity designs, explains the impact of timing jitter and amplitude noise on OTDM performance, illustrates how to characterize noise of OTDM sources using rf and optical techniques, shows how to interpret the noise measurements, and finally discusses semiconductor mode-locked laser cavity optimizations that can achieve low noise performance.

A critical part of the design of a communication system is the choice of the transmitter or source laser. High bit rate optical time-division multiplexed (OTDM) systems in particular demand reliable short pulse generation at high repetition rates and turn-key operation. Semiconductor mode-locked lasers are becoming increasingly attractive and viable for such applications.

Semiconductor mode-locked lasers can be compact sources of picosecond, high-repetition rate pulses of light at the popular telecommunication wavelength of 1.5 μm [1, 2]. Recent advances in semiconductor processing and cavity design have led to the advent of ultra-stable [3] and ultralow-noise [4, 5] performance. With proper temperature control of the semiconductor device and a clean electric supply for the bias and injection current, the diode can remain mode-locked for days. Single-channel, single-polarization transmission rates up to 160 Gb/s [6] have been successfully demonstrated using mode-locked semiconductor lasers, and detailed characterization of their noise

properties [4] indicate that they may be useful sources for transmission rates beyond 1 Tb/s.

The next two sections will discuss several mode-locked semiconductor laser designs and how the performance of these lasers impacts the bit error rates of OTDM systems. The latter sections will show how to measure the noise of these lasers, describe the physical origins of the measured noise spectra, and discuss the ultimate limits of their timing jitter performance.

1. Requirements for OTDM Sources

The requirements for an OTDM pulse source can be listed as follows

1. **Short pulses.** Single channel rates of 160 Gbit/s (6.25 ps/bit-slot) and 1.28 Tbit/s (0.78 ps/bit-slot) require pulses that are a fraction of the repetition period.
2. **High repetition rate.** The source repetition rate should ideally match the rate at which opto-electronic modulators can impress data onto a pulse train. Currently, this rate is typically 10 or 40 GHz. These 10 or 40 Gbit/s data streams can then be multiplexed up to higher repetition rates using passive delay lines. For example, a 10 Gbit/s data pulse train was multiplexed up to a 640 Gbit/s signal using a planar lightwave circuit multiplexer [7]. The highest aggregate repetition rate is limited by the pulse width.
3. **Low pedestal, high extinction ratio.** A low extinction ratio between intensity of the peak of a data pulse and intensity in the wings causes channel crosstalk and interferometric noise due to the fluctuating phase difference of neighboring pulses [8]. For example, a 40-dB extinction ratio is required to interleave four 10 Gbit/s OTDM channels with negligible penalty due to interference [9]. This extinction ratio is easily achieved with Erbium-doped fiber lasers ($>$ 40 dB), but difficult to achieve with electro-absorption modulators and $LiNbO_3$ modulators (15-25 dB) [10].
4. **Low timing jitter.** Experiments and theory [8] have shown that the timing jitter should be less than 1/12 of the switching window width of the demultiplexer to achieve a bit error rate (BER) of less than 10^{-9} for a signal pulse whose width is equal to 1/5 the time slot width. For example, a 100-Gbit/s OTDM system with a demultiplexer that has a 5-ps switching window should have a signal source with better than 0.42 ps rms timing jitter [11].
5. **Low amplitude noise.** The amplitude noise of a pulse source is directly related to the BER of an OTDM system. Often the amplitude noise of a cw laser source is characterized by its relative intensity noise (RIN), which is the ratio of the variance to the squared mean of the output intensity.
6. **Locked to standard clock rate.** The repetition rate of the pulse source must be able to lock to a standard repetition rate, e.g., the synchronous digital hierarchy (SDH) frequencies of 9.953, 19.906, and 39.813 GHz [12]. For mode-locked laser sources, the laser cavity must either be actively or hybridly mode-locked, or passively mode-locked with feedback to stabilize the repetition rate to a known rf reference.

7. **Highly reliable and stable.** The ability to have turn-key operation with reliable performance, minimal tweaking, and long-term operation is desirable. Long-term stability has been demonstrated with both semiconductor [1, 3] and fiber lasers [13, 14, 15].

Erbium-doped mode-locked fiber lasers, compressor sources, gain-switched laser diodes, and mode-locked semiconductor lasers have each been shown to satisfy most, if not all, of the above requirements. The next section will compare the performance of these sources for OTDM applications.

2. Comparison of OTDM Sources

2.1. Mode-locked Erbium-Doped Fiber Laser (ML-EDFL)

ML-EDFLs are typically ring cavities that consist of the erbium-doped fiber, an electro-optic phase or amplitude modulator, isolators for unidirectional operation, and additional fiber for nonlinear/pulse-shaping effects. The erbium-doped fiber can be pumped at 980 or 1480 nm and typically provides gain from 1530-1610 nm [16]. Since these wavelengths correspond to the low attenuation wavelength region in silica-core fiber, erbium-doped fibers have been used extensively in optical transmission systems for amplification and laser sources.

ML-EDFLs are capable of generating picosecond pulses at multi-gigahertz repetition rates. Examples include 1.6 ps pulse generation at 40 GHz [17], 0.7-1.3 ps pulses at 10 GHz in the 1536-1569 nm wavelength region [18], 1.2-1.9 ps pulses at 40 GHz tunable over 40 nm [19], 1.3 ps pulses at 10 GHz [20], and 0.85 ps pulses at 40 GHz [21]. The reported pulse widths are transform-limited or near-transform-limited for hyperbolic secant pulses. Output average powers of ML-EDFL are typically on the order of 10 mW.

The advantages of the ML-EDFLs are that they have good pulse quality (typically transform-limited hyperbolic secant pulses), high extinction-ratio, low noise, and are a mature technology [13, 14, 15]. On the other hand, the ML-EDFLs are relatively large ($18 \times 48 \times 38$ cm are typical dimensions), are sensitive to environmental changes, require feedback circuits to stabilize the long fiber cavity length, and may suffer from pulse drop-outs.

2.2. Compressor Sources

A compressor source typically starts with a long pulse (tens of picoseconds) that is generated by a gain-switching a laser diode or modulating the output of a cw laser source. Compression of these long pulses through adiabatic soliton compression can result in sub-picosecond pulses [22]. Compressor sources have drawn much attention due to the simplicity of operation and availability of commercial components.

Adiabatic pulse compression by propagating amplified pulses through dispersion decreasing fiber (DDF) has been used to obtain short pulses [22]. The decreasing dispersion should be gradual on the timescale of the soliton period, which means that the required length of fiber grows quadratically with initial pulse width [23]. For a sinusoidal modulation at 10 GHz, the required DDF length to generate picosecond pulse

trains is close to thousands of kilometers [24]. Using a shorter length of DDF results in significant pedestals which need to be removed using a nonlinear amplifying loop mirror (NALM); but this reduces the required DDF length from hundreds of kilometers to less than 30 km [24]. The quadratic dependence of DDF length on the initial pulse width means that it is desirable to start with a short pulse, so that the length of the DDF length can be a reasonable length (less than several tens of kilometers). When an EAM was used to directly generate 6 ps pulses, only 2 km and 1.6 km of DDF were needed to obtain 1.2 ps (2.5 GHz, < -25 dB pedestal) and 0.19 ps (10 GHz, -23 dB pedestal) pulses [25, 26]. It has been difficult to date to obtain DDF with a consistently uniform dispersion profile. To overcome this limitation, comb-like dispersion profiled fiber (CDPF) has also been used [27]. CDPF consists of fusion-spliced sections of commercially available high and low dispersion fiber. Modest compression factors of 1:5 or 1:9 can be obtained since the maximum practical number of segments that can be included in a CDPF is $\approx$ 30 [28]. A new type of pulse compression using Raman gain in 6.75 km of standard Corning SMF-28 fiber has recently been shown to yield 1.3 ps pulses at 10 GHz that were nearly transform limited (TBWP = 0.32) [23]. This technique yielded an excellent pedestal of -27 dB without the use of a NOLM or DDF.

The advantages of compressor sources is that they can require little tweaking, yield high output powers, yield transform-limited pulses, can produce sub-picosecond pulses, and are readily constructible from standard telecom equipment. The disadvantages are that they require several large optical components, require several kilometers of single-mode fiber which is temperature and polarization sensitive, and may require hard-to-obtain specialty DDF. The amplitude and timing noise of these sources is not well characterized, and they can have large pedestals (although that can be fixed with a NOLM or clever design). Furthermore, fluctuations of the effective length of the kilometer-long pulse compressor fiber necessitates the use of active stabilization of the fiber length to allow effective multiplexing of several compressor sources into one high data-rate OTDM source.

2.3. Gain-Switched Laser Diode

Short pulses can be obtained from laser diodes by biasing the gain region below threshold and using a pulse or sinusoidal injection current [11]. The achievable modulation frequency in a gain-switched laser diode is limited by its relaxation frequency, which is usually less than 30 GHz [11]. Short, chirped pulses of 20-30 ps duration can be obtained and can be compressed to 2-6 ps by passing them through a normal dispersion medium [11]. In one experiment, 20 fs pulses were generated using a four-stage soliton compression technique [29], but there were significant pedestals containing half the pulse energy that extended for approximately 100 fs.

Pulses with a pulse width of 0.42 ps at a 100-MHz PRF with 1.3 ps of pulse-to-pulse timing jitter were obtained by using a gain-switched DFB-LD with CW light injection and nonlinear optical loop mirror [30]. The timing jitter was reduced from 7.1 to 1.3 ps with the CW light injection. Loss-switching instead of gain-switching of a two-section laser diode at 5 GHz with 30 ps pulses yielded an uncorrelated timing jitter of 0.25 ps. The better performance is presumably due to the better extinction ratio and sharper modulation curvature of loss-modulation. Similar timing jitter performance can be obtained by gain-switching and employing optical and electrical feedback [31].

At high modulation frequencies (> 10 GHz), the timing jitter of a gain-switched laser diode is almost the same as that of the RF oscillator used to drive the LD [11]. The timing jitter gets worse at lower modulation frequency (< 1 GHz) since the spontaneous emission noise can build up over a larger time. It was also found experimentally [32], that the timing jitter becomes worse as the DC bias is adjusted to obtain short pulse operation. The timing jitter of a DFB-LD driven at 5 GHz had uncorrelated jitter of 2 ps with a pulse width of 6 ps and a jitter of 0.5 ps with a pulse width of 10 ps [32]. The uncorrelated timing jitter from the driving synthesizer remained at a constant 0.2 ps. Uncorrelated timing jitter is the pulse-to-pulse timing jitter that arises from the random turn-on process from ASE buildup.

The advantages of gain-switched laser diodes are that they are turn-key ready, reliable, compact, and repetition-rate tunable. The disadvantages are that they require a bulky normally dispersive element such as dispersion compensating fiber to compress the pulses, pulse widths of gain-switched lasers are typically 20-30 ps, and they suffer from significant uncorrelated timing jitter, which is typically on the order of 1-2 ps. In addition, the shape, width, and frequency of every pulse is different and depends on the statistics of the spontaneous emission at the time the gain is increased, especially for very short pulses [33].

2.4. Mode-locked Semiconductor Laser

The first mode-locked semiconductor laser in AlGaAs was demonstrated by P. T. Ho in 1978 [34]. Since then, the pulse widths of mode-locked semiconductor lasers have dropped from 30 ps down to 1 ps [1, 3, 35].

Semiconductor mode-locked lasers can directly yield short pulses of durations ≈ 1 ps. They are widely wavelength tunable since the semiconductor gain medium can be designed to encompass a broad range of wavelengths. Their compact size allows fundamental modelocking, which results in stable operation and prevents pulse drop-outs that may occur in harmonically mode-locked lasers. Small packaging allows integration of a thermoelectric cooler and thermistor to regulate the temperature of the diode chip and to allow long, reliable operation.

The disadvantages are that the output is slightly chirped (TBWP < 0.45 are typical), the output power of current devices are on the order of 1 mW, and the limited ability to create perfect AR coatings yields small satellite pulses that are typically 20 dB smaller than the main pulse.

A comparison of these various OTDM pulse sources are tabulated in Table 1.

3. Semiconductor Mode-locked Laser Designs

Semiconductor mode-locked lasers can be classified into three categories: the type of cavity (monolithic or external), the type of modelocking (passive, active, or hybrid), and the order of modelocking (fundamental or harmonic). A monolithic cavity is one in which all laser elements are integrated on the chip: modulator, saturable absorber, gain section, and gratings. An external cavity is one in which the cavity is formed by the laser diode device plus a free space section and mirror or grating. External cavities are desirable for low-repetition rates (2-10 GHz) where the monolithic device

Table 1. A comparison of various OTDM pulse sources. SL = Semiconductor Laser. CS = Compressor Source. EL = Erbium-fiber Laser. EC = External Cavity. M = Monolithic. FM = Fundamentally Mode-locked. HM = Harmonically Mode-locked. NR = Not Reported. † = coupled into single-mode fiber. ‡ = obtained by integrating the first supermode. ♣ = 1545-1560 nm tunable for 1 ps pulse widths. ♡ = 90 fs free-run

Pulse Source Type	Output Power	Pulse Width	TBWP	Repetition Rate	Wavelength	Timing Jitter	RIN	Ref.
Semiconductor laser (EC-FM)	-6 to 6 dBm	> 1.5 ps	< 0.45	2-10 GHz	1520-1560 nm	86-500 fs	< 140 dB/Hz	[3, 4]
(EC-HM)	-6 to 6 dBm	> 1.5 ps	< 0.45	40 GHz	1530-1570 nm	86-500 fs	< 140 dB/Hz	[36]
Semiconductor laser (EC-FM)	-5 dBm	0.2-20 ps	???	1-20 GHz	1480-1580 nm	300-800 fs	NR	[1]
Semiconductor laser (M-FM)	0.5 mW	1.6 ps	0.52	80 GHz	1554 nm	230 fs	< -125 dB/Hz	[37]
	NR	2.4 ps	0.45	102 GHz	1554 nm	230 fs	< -125 dB/Hz	[37]
	2.9 dBm †	4 ps	0.5	20 GHz	1556 nm	200 fs	-129 dB/Hz @ 1.8 GHz	[38]
	NR	2 ps	1.2	16.3 GHz	1590 nm	NR	NR	[39]
Semiconductor laser (M-FM)	NR	4 ps	1.4	40 GHz	1.5 μm	NR	NR	[40]
Semiconductor laser (M-FM)	-8 dBm	0.95 ps	0.32	38.5 GHz	1.5 μm	NR	NR	CPM [41, 42]
Semiconductor laser (M-FM)	0.183 mW†	6.7 ps	0.38	10 GHz	1551 nm	0.3 ps	NR	Rep-rate tunable [12]
	NR	8.3 ps	0.32	20 GHz	1548.5 nm	0.18 ps	-140 dB/Hz	Rep-rate tunable [12]
	NR	NR	NR	40 GHz	NR	0.2 ps	NR	Rep-rate tunable [12]
Semiconductor laser (M-FM)	0.1 mW†	8 ps	0.30	4.9 GHz	1565.4 nm	NR	NR	[43]
	NR	20 ps	0.34	8.1 GHz	1550 nm	NR	NR	[44]
Semiconductor laser (M-FM)	0.5 mW	1.4 ps	NR	15 GHz	1.3 μm	NR	NR	[45]
Semiconductor laser (M-FM)	0.63 mW	2.2 ps	1.1	21 GHz	1.58 μm	NR	NR	[46]
Semiconductor laser (M-FM)	≥ 1 mW†	2-2.5 ps	0.37-0.5	37.5GHz$\pm$250MHz	1.5μm$\pm$2.5nm	300 fs(100Hz-80MHz)	NR	[?]
Compressor source	27 dBm	1.2 ps	0.32	10 GHz	1547-1558 nm	NR	NR	[23]
Compressor source	> 40 mW	190 fs	0.38	10 GHz	1566 nm	NR	1%	[47]
Compressor source	NR	130 fs	0.313	6.67-18 GHz	1550 nm	NR	NR	[48]
Compressor source	120 mW	560 fs	NR	10 GHz	1534-1560 nm	NR	NR	5% pedestals [49]
Erbium-fiber laser (HM=9960)	8.3 mW	1.3 ps	0.62	10 GHz	1564 nm	0.16 ps ‡	1.1% ‡	AM sigma laser [20]
Erbium-fiber laser (HM=200000)	NR	1.6 ps	Near TL	40 GHz	1556 nm	0.46 ps ‡	NR	AM [17]
Erbium-fiber laser (HM=6500)	3.4-5.2 mW	0.7-1.3 ps	0.31-0.33	10 GHz	1536-1569 nm	110 fs ‡	NR	AM [18]
(HM=24000)	14 dBm	1.2-1.9 ps	0.32-0.35	40 GHz	1530-1570 nm	< 0.1 ps ‡	NR	AM [19]
Erbium-fiber laser (HM=44444)	4 mW	0.85-1.1 ps	0.37-0.42	40 GHz	1540-1555 nm	NR	NR	Regen [21]
(HM=44444)	2-4 mW	0.9-1.3 ps	0.3	40 GHz	1530-1560 nm	< 0.1 ps ‡	NR	Regen [50]
(HM=11111)	NR	1 ps	TL	10 GHz	NR	120 fs PLL ‡♡	0.2% ‡	Regen [51]
(HM=11111)	1 mW	1-1.1 ps	0.35	10 GHz	1530-1555 nm	NR	NR	Regen [52]
Erbium-fiber laser (HM)	> 10 mW	1.6-10 ps	0.36	1-40 GHz	1530-1560 nm ♣	NR	NR	[13]
Erbium-fiber laser (HM)	> 20 mW	1.2-10 ps	NR	5-40 GHz	1530-1560 nm ♣	< 100 fs ‡	1.5% ‡	[14]
Erbium-glass laser (FM)	> 10 mW	3-5 ps	< 0.60	9.95328 GHz	1535 nm	< 100 fs	< 1.0 %	[15]

size becomes too large. Broad-band wavelength tuning is possible through the use of an optical filter or end-mirror grating, and precise tuning of the repetition rate by translating the end mirror or grating. A fundamentally mode-locked laser only has one pulse in the cavity at any instant of time. A harmonically mode-locked laser has several pulses in the cavity and the repetition rate of the pulses is at an integer multiple (> 1) of the fundamental cavity round-trip frequency. The preferable configuration for a mode-locked semiconductor laser is a monolithic cavity (for compact packaging) that is fundamentally (to prevent pulse drop-outs) and hybridly mode-locked (for short pulses).

This section is broken up into three parts which address external-cavity mode-locked lasers, monolithic mode-locked lasers and harmonically mode-locked lasers.

3.1. External-Cavity Mode-locked Laser

The basic design of an external-cavity mode-locked laser is shown in Fig. 1. The laser diode chip contains a saturable absorber section and a gain section (typically InGaAsP-based for operation in 1.3 or 1.5-μm wavelength regions). The external cavity contains a GRIN lens, an optical bandpass filter, and an end-mirror. The filter and mirror can be replaced by a grating for wavelength and repetition-rate tunability. Although bulk optics are used, these devices can be packaged into compact 33 x 21 x 10 mm boxes [3].

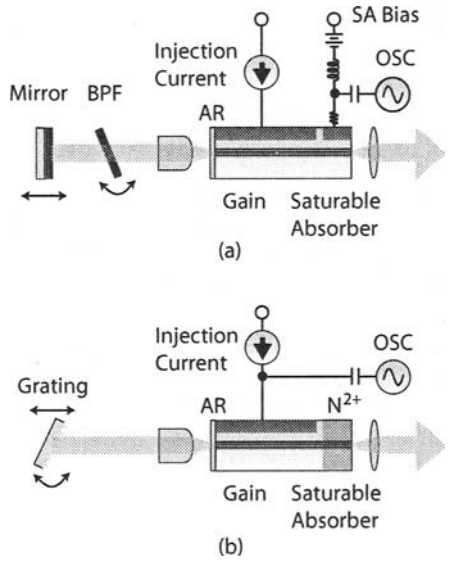

Fig. 1. Basic design of an external cavity mode-locked semiconductor laser with (a) optical bandpass filter [3] and (b) grating [35].

External-cavities allow broad wavelength tuning(120 nm) as well as repetition-rate tuning (1-14 GHz) [1, 35]. Fundamental modelocking is possible to 14 GHz, beyond which the cavity length becomes too small for bulk components. Higher modulation rates require either harmonic modelocking or monolithic devices.

Pulse widths down to 180 fs with external-cavity mode-locked lasers have been demonstrated [35], but repeatability of the saturable absorber properties and short pulse instabilities have limited practically obtainable pulse widths to > 1 ps.

The saturable absorber in the mode-locked semiconductor laser allows pulse widths shorter than the usual Siegman-Kuizenga limit [53, p. 1067]. One facet of the laser diode can be N^+-ion implanted to create a saturable absorber [35]. Alternatively, the saturable absorber can also be created by reverse biasing a short segment of the laser to create a waveguide saturable absorber [3, 46]. The second method can be manufactured more reliably but may yield absorbers with slower recovery times. The mode-locked laser yielding 180 fs pulses had an ion-implantation-type saturable absorber [35].

A schematic of a bi-section MLLD device is shown in Fig. 2. The device is a double-channel planar buried heterostructure laser diode with a separate confinement heterostructure with InGaAs/InGaAsP strained MQWs for the active layer [54]. The gain section is 500 μm long and the saturable absorber section is 40 μm long. Typical operating specifications for these mode-locked lasers is shown in Table 1, Ref. [3].

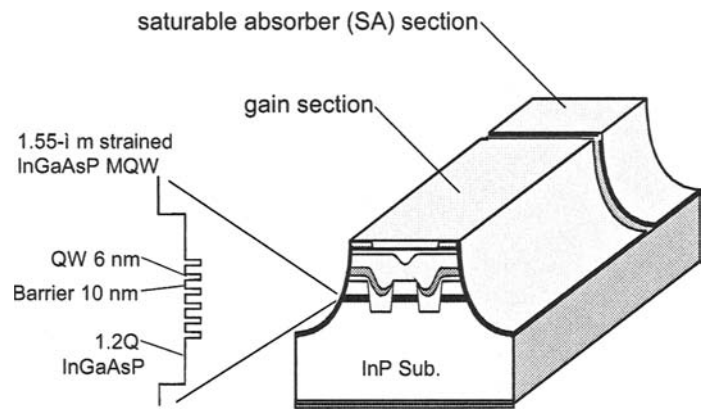

Fig. 2. The double-channel buried heterostructure MLLD device with a separate confinement heterostructure with InGaAs/InGaAsP strained MQWs for the active layer [3].

3.2. Monolithic Mode-locked Laser

Ideally, the OTDM pulse source should be a monolithic device that does not consist of external components [39, 41, 43, 44]. Such a source would be more compact, permit reduced cost in fabricating a number of devices, and not have the mechanical instabilities associated with bulk optical elements. Monolithic mode-locked lasers have multiple segments, often including a waveguide saturable absorber, gain section, electro-absorption modulator, and DBR section. Figure 3 shows an example of a repetition-rate tunable mode-locked laser diode.

The main challenge with monolithic devices is to achieve precise repetition-frequency control by cleaving a precise cavity length. To tune the cavity length of

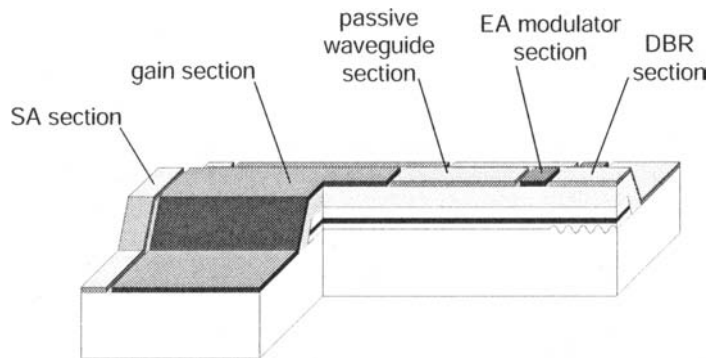

Fig. 3. Monolithic MLLD device structure [12].

a monolithic device to an exact frequency of 9.953, 19.906, or 39.813 GHz, an electrically tuned DBR section can be integrated into the device to fine-tune the effective cavity length [12, 55]. A typical fabrication error in cleaving a diode chip is 10 μm. Ogura et al. have shown that it is possible to compensate for this error with a small change in the absorption loss in the DBR section of about 20 cm^{-1} [12]. The detuning range of a monolithic mode-locked laser at 20 GHz repetition rate can be 0.22 GHz (corresponding to an error of 22 μm) due to the retiming function of the electroabsorption modulation gate [38, 56]. Over this detuning range, this particular laser emitted 4 ps pulses with a TBWP of 0.5. The downside of this technique is that the detuning is accompanied by a wavelength shift. To overcome this problem, multiple tuning elements consisting of electronic and thermal phase tuning sections were used [**?**]. Recently, a 2-2.5 ps pulse width, 220 fs (100 Hz to 10 MHz) timing jitter, 40 GHz monolithic mode-locked laser with a 500 MHz repetition-rate tuning range has been demonstrated [**?**].

Typical performances of monolithic mode-locked semiconductor devices is shown in Table 1. The pulse widths of mode-locked semiconductor lasers are still far from the inherent gain bandwidth limit of $\approx$ 50 fs [57], and there remains work to be done in designing fast saturable absorbers to achieve shorter pulses.

3.3. Harmonically Mode-locked Laser

For ultimate flexibility in the design of the cavity elements, semiconductor ring lasers have been used [5]. These lasers are typically several meters long since they incorporate bulk devices such as a semiconductor optical amplifier (SOA), Faraday isolator, polarization controllers, and electro-optic modulator (see Fig. 4). Harmonic modelocking allows pulse repetition rates of 10 GHz and beyond, similar to that in mode-locked Erbium-doped fiber ring lasers. Repetition rates as high as 20 GHz and pulse widths as short as 1.2 ps have been demonstrated [5].

One inherent problem of harmonically-mode-locked lasers is the occurrence of pulse drop-outs and supermode noise. However, the incorporation of a high finesse Fabry-Perot (F-P) etalon removes the supermode noise by distributing the pulse energy of one pulse to many other time slots [58, 59, 60]. Timing jitter as low as 165 fs from

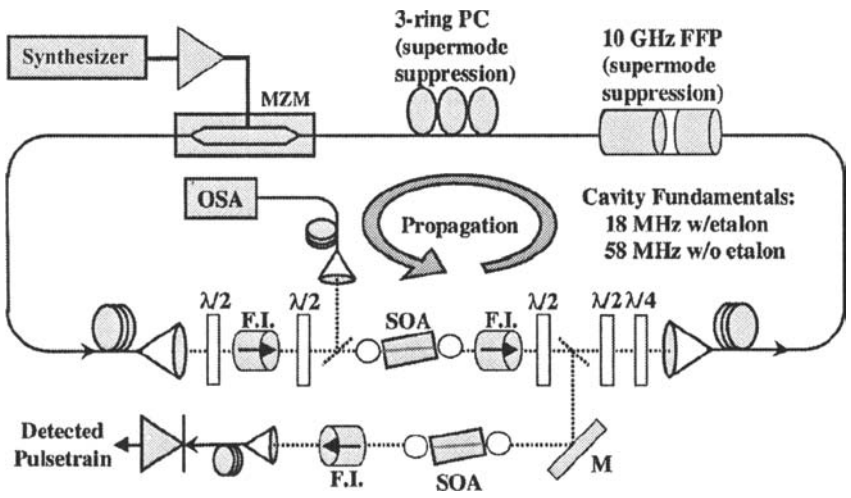

Fig. 4. Harmonically mode-locked semiconductor diode ring laser with intracavity Fabry-Perot etalon [58].

10 to 5 GHz of a 10-GHz semiconductor diode ring laser with a F-P etalon has been reported [58]. Higher finesse F-P etalons may enable even lower timing jitters on the order of tens of femtoseconds. If a mode-locked laser source has 500 fs of timing jitter, incorporating a F-P etalon with finesse F, the timing jitter improves according to that shown in Table 2. The main difficulty with the incorporation of the Fabry-Perot etalon is matching the cavity modes with the F-P modes, and the alignment becomes more difficult as the finesse increases.

Table 2. Timing jitter improvement with Fabry-Perot etalon. σ = rms timing jitter, N = harmonically modelocking order, $\mathcal{F}$ = finesse.

N	$\sigma \propto N^{-1/2}$	$\mathcal{F} \propto N$
1	500 fs	–
180	37 fs	180
10000	5 fs	10000

The benefit of a harmonically mode-locked laser is the flexibility of cavity design which allows for picosecond pulses at high repetition rates with low noise. The drawback of using harmonically mode-locked lasers is their large size and mechanical sensitivity.

4. Noise of Semiconductor Mode-locked Lasers

This section will cover the impact of timing jitter and amplitude noise on OTDM performance, review techniques to characterize and interpret noise measurements, and present a brief overview of low noise laser design.

4.1. Impact of Timing Jitter and Amplitude Noise on OTDM Performance

Amplitude noise and timing jitter degrades the performance of OTDM transmission systems. This subsection derives the values of timing jitter and RIN needed to achieve a given transmission rate.

4.1.1. Timing Jitter

Often the rms timing jitter is quoted as a single number without indication of the integration range of the timing jitter noise power spectral density. Unfortunately, the rms timing jitter integration range is not standardized, and reported values can cover ranges of 100 Hz to 1 MHz [61], 10 Hz to 5 GHz [4, 62], etc. This makes it difficult to directly compare the noise of different mode-locked laser sources. So what integration range is important for OTDM systems? Since it is timing jitter relative to the recovered clock, not relative to the universe, that is important for evaluation of the BER, one must carefully interpret how the quoted timing jitter (relative to the universe) relates to the jitter relative to the recovered clock.

The recovered clock is derived from a data pulse train with timing jitter. The best performance of a clock recovery circuit occurs when all the incoming data bits are ones. Typically the low-pass filter, of bandwidth B, after the optical, electro-optical [63] or microwave [64] phase comparator determines the number of pulses (assuming all ones) over which the recovered clock is defined. Therefore, the recovered clock follows slow timing drifts and errors arise from fast timing fluctuations that occur faster than $1/B$, where B is typically 10 or 100 Hz. Slow timing fluctuations are important, since neighboring channels should not drift into each others time slots, but this slow drift can be actively compensated with feedback and is generally not a fundamental limitation.

Experiments and theory [8] have shown that the timing jitter (integrated for frequency offsets greater than B) should be less than 1/12 of the switching window width of the demultiplexer to achieve a bit error rate (BER) of less than 10^{-9} for a signal pulse whose width is equal to 1/5 the time slot width. For example, at 640 Gbit/s, the time slot width is 1.56 ps. A signal pulse 1/5 this duration has a duration of 313 fs and a switching window of half the time-slot has a duration of 781 fs. This would imply that the timing jitter should be less than $1/12 \times 781$ fs $= 66$ fs! See Table 3 for the required timing jitter performance at different repetition-rates. Therefore, at high aggregate bandwidth, timing jitter is a critical factor in the performance of an OTDM system. One can partially overcome the stringent timing jitter requirements by transmitting the clock with the data. Transmission at 640 Gbit/s $\times 2$ (for polarization multiplexing) has been demonstrated using regeneratively mode-locked fiber lasers [7]. The fact that the clock was transmitted with the signal alleviated the problem of timing jitter, since the jitter between the transmitted clock and laser is very small. One

can use a noisy laser, as long as one also transmits the noisy clock as well. Clock recovery from a 160 Gbit/s data stream typically yields timing jitters of 300 fs [63] and 230 fs [64], which is too large for 640 Gbit/s transmission. Therefore, transmission rates at 640 Gbit/s are possible, but may require the broadcasting of a master clock (to the receiver and other transmitting lasers) due to timing jitter. It will in any case be a challenge to lock multiple transmitting lasers to a master clock (derivable from one of the regeneratively mode-locked fiber lasers) with a residual jitter of less than 66 fs. In the reported 640 Gbit/s $\times 2$ transmission experiment [7], the high-repetition-rate OTDM transmission was derived by transmitting a 10 Gbit/s pulse train through a PLC MUX, rather than multiplexing 64 independent mode-locked laser sources. Therefore, it is important to develop sources with low residual phase noise [4, 5, 65]. The lowest reported residual phase noise for gigahertz-repetition-rate semiconductor lasers is 50 fs (100 Hz to 100 MHz, 12 ps pulse width) [65], 86 fs (10 Hz to 4.5 GHz, 6.7 ps pulses) [4], and 94 fs (10 Hz to 5 GHz, 3.5 ps) [58]. Even though the gigahertz-repetition-rate mode-locked erbium-doped fiber laser literature reports timing jitters of $<$ 10 fs (100 Hz to 1 MHz, 1 ps pulse width) [61], 16 fs (100 Hz to 100 kHz, 3 ps) [66], 120 fs (100 Hz to 10 MHz, 1 ps) [51], the total timing jitter should be integrated out to half the repetition-rate of the laser (i.e. 10 Hz to 5 GHz) [58, 67], and hence the total timing jitter of these sources are not well characterized since these integration ranges do not include the supermode timing jitter. In section 4.4, the design path towards sub-66 fs timing jitter sources will be outlined to enable multi-terabit per second transmission rates.

Table 3. Bitrate versus required timing jitter performance for a BER $< 10^{-9}$.

Bit rate (GHz)	Time Slot (ps)	Switching Window (ps)	Pulse Width (ps)	Allowable Timing Jitter (ps)
1	1000	500	200	42
10	100	50	20	4.2
40	25	12.5	5	1.05
160	6.25	3.13	1.25	0.26
640	0.16	0.78	0.31	0.66
1280	0.08	0.04	0.16	0.03

4.1.2. Amplitude Noise

In addition to timing jitter, amplitude noise can also worsen the BER of OTDM transmission. The relative intensity noise (RIN) is defined as the variance over the squared mean of the output intensity. For a BER $< 10^{-9}$, the laser must have a RIN < -21.6 dB [68, p.222], which corresponds to an rms power fluctuation of 6.9×10^{-2} times the average power. Table 4 shows the maximum RIN per unit bandwidth (dB/Hz) for a BER $< 10^{-9}$ at several bit rates. The table shows that as the system bandwidth is increased, the laser RIN per unit bandwidth must decrease for the same BER.

Typical values for the amplitude noise are: 0.21% or -26.78 dB (10 Hz to 5 GHz) for harmonically mode-locked semiconductor ring lasers [5], 0.01% or -40 dB (10 MHz to 10 GHz) for monolithic hybridly mode-locked semiconductor lasers [12], -48 dB (10 Hz to 5 GHz)[3], 1.1% or -19.59 dB ($<$ 200 kHz) for mode-locked erbium fiber

Table 4. Digital transmission RIN requirements for a given bit rate and BER = 10^{-9}.

Bit rate (Gbit/s)	System Bandwidth (GHz)	RIN (dB/Hz)
1	0.5	-108.6
2	1	-111.6
10	5	-118.6
40	20	-124.6
160	80	-130.6
640	320	-136.7
1280	640	-139.7

sigma laser [20], 0.2% or -26.99 dB (10 Hz to 10 MHz) for PLL regeneratively mode-locked erbium-doped fiber laser [51].

4.2. Characterization of Timing Jitter

The measurement and interpretation of timing jitter for mode-locked semiconductor lasers is presented in this section. Special attention will be given to the correct interpretation of the harmonically mode-locked laser rf spectrum.

4.2.1. Overview of Measurement Techniques

Three techniques for the measurement of mode-locked laser noise will be presented: RF spectrum analyzer, residual phase noise measurement, optical cross-correlation.

RF Spectrum Analyzer The experimentally easiest, but most difficult to interpret, method for amplitude and timing noise characterization is detecting the optical pulse train with a photodiode and observing the resulting electronic current on an rf spectrum analyzer. To extract timing jitter and amplitude noise values from the rf spectrum, one must first assume a model for the correlation of the pulse-to-pulse timing jitter and amplitude noise for the laser. The model is different for

gain-switched lasers [32, 69, 70] – Each pulse builds up independently from ASE. Therefore, the timing jitter of each pulse is *uncorrelated* with all other pulses. There is also a smaller correlated noise component in gain-switched lasers that is attributed to the correlated noise of the driving microwave signal.

fundamentally mode-locked lasers [70, 71, 72] – The same pulse recirculates through the laser cavity, each time giving up a fraction of its photons. Therefore, the position and amplitude of neighboring pulses are highly *correlated.*

harmonically mode-locked lasers [67] – Neighboring pulses arise independently from ASE similar to a gain-switched laser (assuming that there are no coupling effects such as gain saturation effects and reflections), but the pulses are highly correlated every round-trip since it is the same pulse, similar to a fundamentally mode-locked laser. Hence the noise correlation function in a harmonically mode-locked laser is a mix between the gain-switched laser and fundamentally mode-locked laser correlation functions.

Fitting the model to the measured rf spectrum yields the timing jitter and amplitude noise.

The calculated rf spectrum of a gain-switched laser is shown in Fig. 5. The pulse shape is assumed be delta-function-like and hence the power at all harmonic frequencies is constant. In a real laser with finite pulse width, the harmonics are multiplied by an envelope function that decreases with increasing frequency. The rf spectrum of a delta-function-like pulse was plotted to reveal the frequency dependence of timing and amplitude noise. The timing jitter increases with the square of the frequency and the amplitude noise is constant with frequency.

The rf spectrum of a fundamentally mode-locked laser is similar to that of a gain-switched laser, except that the spectral envelope limitation is not usually observable since the pulse width of a fundamentally mode-locked laser is typically much shorter than the inverse bandwidth of the electronics, and the uncorrelated noise of a fundamentally mode-locked laser is typically well-below the noise floor of the rf spectrum analyzer. Figure5 shows that when the pulses are totally uncorrelated, the rf spectrum contains a background that increases as the square of the frequency. The correlated noise energy appears as skirts around the harmonics of the repetition rate. The noise skirts are proportional to the amplitude noise power spectral density plus the timing jitter power spectral density times the harmonic number squared. An important consequence is that the noise skirts at the higher harmonics of the repetition rate reveal the timing jitter of the laser.

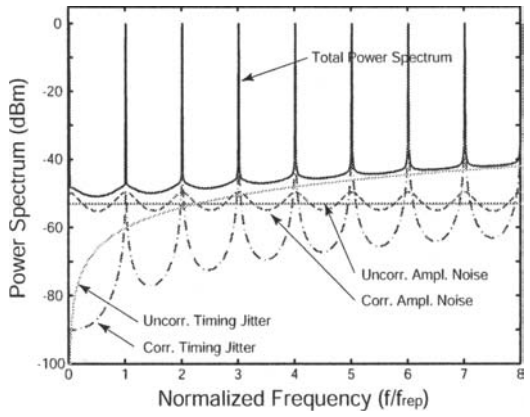

Fig. 5. The calculated rf spectrum of a gain-switched laser with correlated and uncorrelated noise. These calculations assumed that the pulse period $T_R = 100$ ps, the pulse width $FWHM \rightarrow 0$ ps, the rms correlated timing jitter $\sigma_{T,\mathrm{corr}} = 39.6$ fs, the rms correlated amplitude noise $\sigma_{A,\mathrm{corr}} = 1.77 \times 10^{-3}$, the uncorrelated timing jitter $\sigma_{T,\mathrm{uncorr}} = 100$ fs, the uncorrelated amplitude noise $\sigma_{A,\mathrm{uncorr}} = 2.24 \times 10^{-3}$. The correlated timing and amplitude noise spectra were assumed to be Lorentzian with a 3-dB bandwidth of 200 MHz and 4 GHz, respectively.

Harmonically mode-locked lasers have the addition of supermode noise that occurs at multiples of the cavity round-trip frequency. The power spectral density (psd) of the amplitude noise contributes equally to each supermode in the rf spectrum and the psd of the timing jitter contributes a noise skirt at each supermode whose magnitude increases as the square of the supermode number.

Rather than explain how to interpret the rf spectra in detail, we refer the reader to recent papers in the literature [67, 70]. The main point is that one must make assumptions about correlations of the pulse-to-pulse timing jitter and amplitude noise before the rf spectrum can be interpreted correctly and a valid rms timing jitter number can be obtained.

When using an rf spectrum analyzer to measure the noise of the laser, the measured result for the noise spectral density underestimates the noise by about 2 dB due to the effect of envelope detection, log averaging, and shape of the resolution filter of the rf spectrum analyzer [73].

Even though this method seems to be simple, actually measuring the power spectral density over many harmonics is not trivial. One must measure over several tens of gigahertz for a multiple number of spans and resolution bandwidths to capture the uncorrelated and correlated jitter. In addition, the frequency response of the detector plus spectrum analyzer from 0 to 50 GHz is not flat and must be calibrated. Figure 6 shows the power spectrum around the first harmonic of a fundamentally mode-locked external-cavity semiconductor laser [74]. The timing jitter noise can be upper-bounded by assuming that all the noise around the first harmonic is due to correlated timing jitter (we assume that the amplitude noise fluctuations are small) and the tails fit well to a Lorentzian shape.

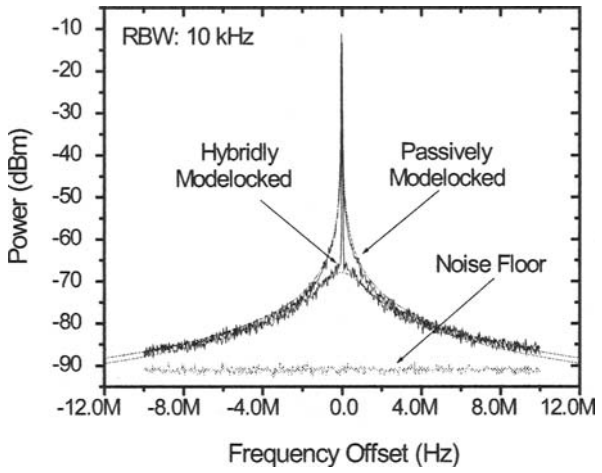

Fig. 6. RF measurements and Lorentzian fits. The span is 10 MHz [74].

Residual Phase Noise Measurement A residual phase noise measurement yields the timing jitter of the pulses relative to the driving microwave oscillator and is a good indication of the inherent quantum and technical noise of the mode-locked laser. The residual phase noise measurement method is illustrated in Fig. 7. A microwave oscillator drives a laser whose pulses are detected with a photodiode. The photodiode signal is then mixed with the original microwave oscillator signal. If the path length between the RF and IF ports of the mixer to the microwave oscillator are equal, then

the noise from the microwave source cancels. The mixer is operated as a phase detector by tuning the delay in one arm until the sinusoidal inputs to the IF and RF ports are in quadrature. The resulting phase noise can be measured with a rf spectrum or vector signal analyzer.

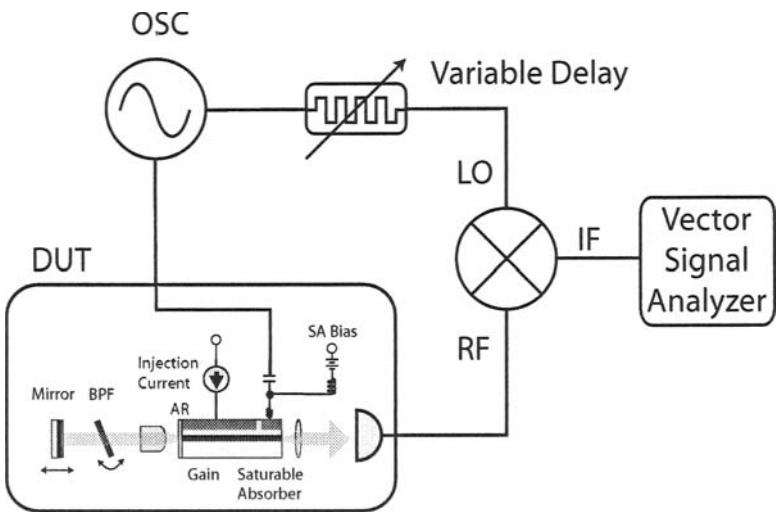

Fig. 7. The residual phase noise measurement of a optical pulse source.

The noise floor of the residual phase noise measurement is obtained by replacing the pulse source with an equivalent microwave loss. This loss was 51 dB in the case of an external-cavity hybridly-mode-locked semiconductor laser [4].

It is difficult to do residual phase noise measurements on a pulse train after fiber compression since it is difficult to match the length of the two arms to the mixer. In one arm there are several kilometers of single-mode fiber. Installing several kilometers of microwave cable in the other arm is impractical due to the large loss (typically 1 dB/m for SMA coaxial cables).

Until the advent of the ultralow-phase noise microwave sapphire-loaded crystal oscillator (SCLO) in 1996 (Poseidon Scientific Instruments), the noise of mode-locked lasers have been limited by the driving microwave source [65, 61]. At 10 GHz, the integrated timing jitter of the SCLO is $\approx$ 6 fs from 10 Hz to 5 GHz. This means that it is now possible to obtain mode-locked lasers with absolute timing jitters that are limited by their quantum noise [4].

Some residual phase noise measurements of mode-locked semiconductor lasers and the interpretation of the plots will be shown in section 4.2.2. The measurement of the noise of harmonically mode-locked lasers is especially difficult and will be discussed later.

Optical Cross-Correlation Optical cross-correlation techniques have been used extensively for characterizing the timing jitter between two lasers [75], the timing jitter of a gain-switched diode [30], and for mode-locked lasers [74]. The optical cross-correlation measurement is useful for measuring the timing jitter at high frequency

offsets (which is the same as the "uncorrelated jitter") and for directly measuring the timing jitter between pulses separated by time T. Several optical cross-correlation measurements with different values of T allows one to reconstruct the timing-jitter correlation function. Correlations between pulses that are separated by tens of thousands of pulse periods is possible at high repetition rates (10 or 40 GHz) using less than a kilometer of single-mode fiber as an optical delay line [74].

An optical cross-correlator is shown in Fig. 8. The input optical pulse train is split into two arms. Propagation in one arm is delayed relative to the other arm with a spool of fiber. The pulses from both arms are then recombined through a nonlinear crystal and the SHG is observed on a photomultiplier tube. The results of cross-correlation measurements made with a 1000-m delay are shown in Fig. 9. The three traces show the autocorrelation, cross-correlation, and autocorrelation preceded by the same 1000-m fiber spool. The broadening of the cross-correlation over the autocorrelation yields the timing jitter. The autocorrelation preceded by the same 1000-m fiber spool allows one to remove the broadening effects in the cross-correlation due to the dispersion of the fiber. The recovered rms timing jitter fluctuations as a function of fiber delay lengths from 20 to 500 m are plotted in Fig. 10 for both passively and hybridly mode-locked lasers. These two curves show that the timing jitter of the hybridly mode-locked laser is bounded due to the restoring force of the active modulator whereas the timing jitter of the passively mode-locked laser continues to increase as a function of delay, which is the theoretically expected result. Figure 10 shows a maximum timing jitter of approximately 700 fs, which also agrees with the integration of the rf spectrum measurement shown in Fig. 6. For higher modelocker modulation depths, the hybridly mode-locked laser can be as low as 159 fs (10 Hz to 10 MHz, see Fig. 11) with 2 ps pulses or 45 fs (10 Hz to 10 MHz, see Fig. 12) with 7 ps pulses [76].

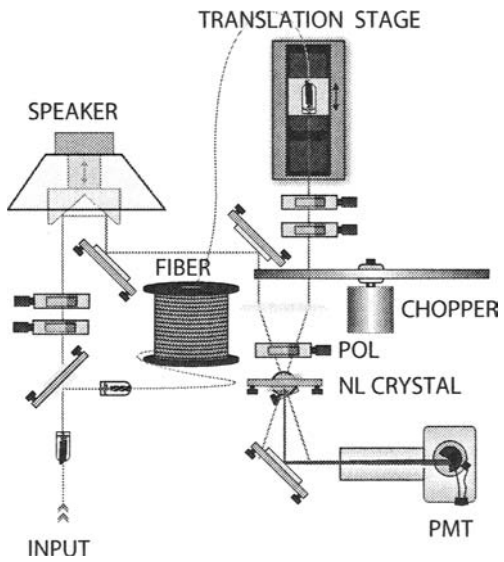

Fig. 8. An optical cross-correlator that measures the background-free SHG signal from a nonlinear crystal [74].

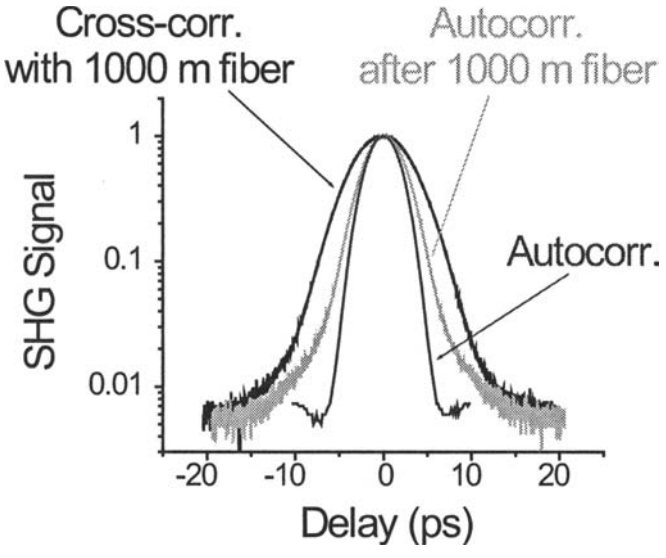

Fig. 9. Cross-correlation measurements.

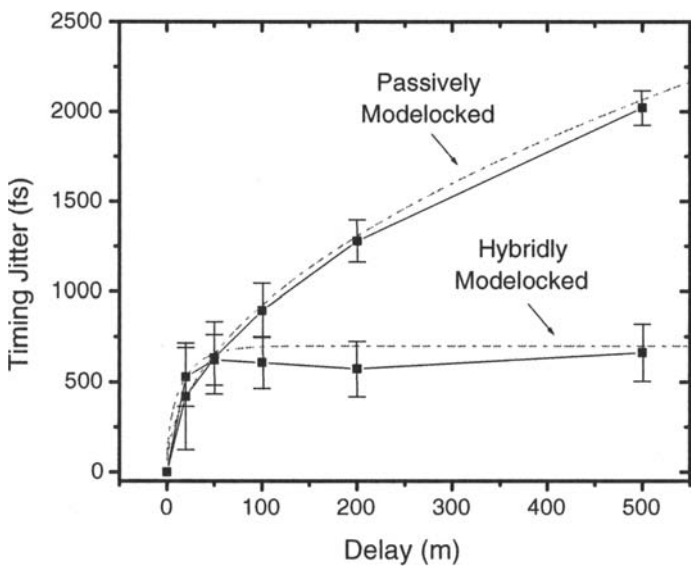

Fig. 10. Cross-correlation measurements of the timing jitter as a function of delay. The dashed lines indicate the theoretically predicted dependence [74].

Optical cross-correlations have also revealed the different timing jitter correlation functions of harmonically mode-locked lasers. In these lasers, the timing jitter is

highly correlated when T equals a multiple of the cavity round-trip time, but is highly uncorrelated otherwise.

4.2.2. Application of Measurement Techniques

The last subsection outlined three noise measurement techniques to determine the timing jitter of OTDM pulse sources. The interpretation of these measurements can be complicated, and in this subsection several important cases will be discussed.

Fundamentally and Actively Mode-locked Laser The pulse position perturbation in an actively mode-locked laser is analogous to that of a mass on a spring with damping but subject to white noise perturbations [77]. For dispersionless and AM modulated mode-locked lasers, the timing restoration of the pulses is critically damped. This means that once the pulse is perturbed from its equilibrium position, it moves back to its equilibrium position exponentially in time [78]. The power spectral density of a noise process with exponential retiming has a Lorentzian functional form.

The residual phase noise plots for a 2-ps-pulsewidth, 10-GHz, hybridly mode-locked external-cavity laser diode is shown in Fig. 11 [76]. The residual phase noise fits well to the theoretically expected Lorentzian shape plotted with a dashed line. Integrating from 10 Hz to 10 MHz yields rms timing jitters of 159 fs and 500 fs for an rf modulation strength of 24 and 15 dBm, respectively. The residual phase noise of an ultralow noise mode-locked semiconductor laser is shown in Fig. 12, which shows the noise spectral energy from 10 Hz to 4.5 GHz. The integrated values over each decade are shown in Fig. 13 and indicate that most of the integrated timing jitter arises around the spectral roll-off from 10 to 100 MHz. The integrated timing jitter from 10 Hz to 4.5 GHz is only 86 fs. At low offsets, flicker noise of the driving current source appears in the noise spectrum, but the effect on the integrated timing jitter is very small (< 8 fs).

Near-Lorentzian single-sideband phase noise has also been observed in other fundamentally and actively mode-locked external-cavity mode-locked laser diodes [1, 62]. For lasers that have dispersion in the cavity, active phase modulation, and other technical noise [37, 77], the phase noise spectra can be more complicated than a simple Lorentzian function.

Harmonically and Actively Mode-locked Laser The calculated rf spectrum of a harmonically mode-locked laser is shown in Fig. 14, and the calculated residual phase noise is shown in Fig. 15. The residual phase noise plot exhibits Lorentzian-shaped noise spectra that repeat at multiples of the cavity round-trip frequency. The high-frequency fluctuations are due to pulse-to-pulse fluctuations. Here it is assumed that each of the N pulses inside the laser cavity is uncorrelated with respect to all others[3] but is correlated with itself after an integer number of round-trips. Integrating the residual phase noise spectrum from 10 Hz to 5 GHz (half the repetition-rate) yields the timing jitter. Note that this measurement is difficult for two reasons:

1. Each Lorentzian spectrum should be measured over several decades 10-100 Hz, 100-1 kHz, ... 1-10 MHz, etc. If we measure 7 decades of offset, then $7N$ measurements are needed. For EDFLs, N is typically on the order of 10000, which

[3] This is a good approximation in EDFLs where the gain-lifetime is long, but may be less appropriate for semiconductor lasers where the gain strongly correlates neighboring pulses.

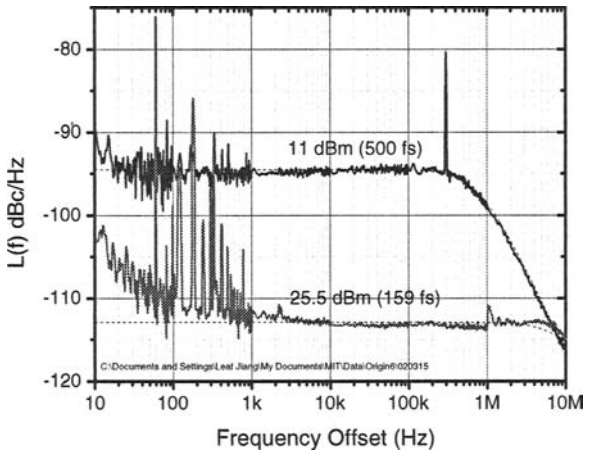

Fig. 11. Temperature-controlled external cavity mode-locked semiconductor laser with 5-nm filter for two different modulation depths.

means that to correctly measure the noise, one must run 70000 measurements! If we assume that neighboring pulses are uncorrelated, then all the Lorentzian spectra have the same height and only 7 measurements are needed.

2. The first supermode is most likely contaminated by the noise of the RF oscillator [79]. Assuming that a $N = 10000$ harmonically mode-locked laser has < 500 fs of jitter at a 10 GHz repetition rate (we know that this must be true from sampling scope measurements), then each Lorentzian supermode phase noise spectrum has only $\sqrt{500^2/N} = 5$ fs of timing jitter (assuming the pulses in the cavity are uncorrelated with respect to each other). If the FWHM of each Lorentzian is 50 kHz, then the phase noise is less -116 dBc/Hz from 10 Hz to 5 GHz! For the Agilent 83732B, the phase noise is only that good at offsets above 100 kHz. This means that the first supermode is mainly rf oscillator noise, as has been measured by several groups [61, 66].

To summarize, the procedure to measure the phase noise of a harmonically mode-locked laser is

1. measured one of the supermodes, but not the first few which are contaminated by the rf oscillator noise, over several decades
2. keeping the resolution bandwidth fixed, measure the relative heights of each supermode, assume that they all have the same shape as the one measured in the first step
3. integrate the supermodes from 10 Hz to half the repetition rate.

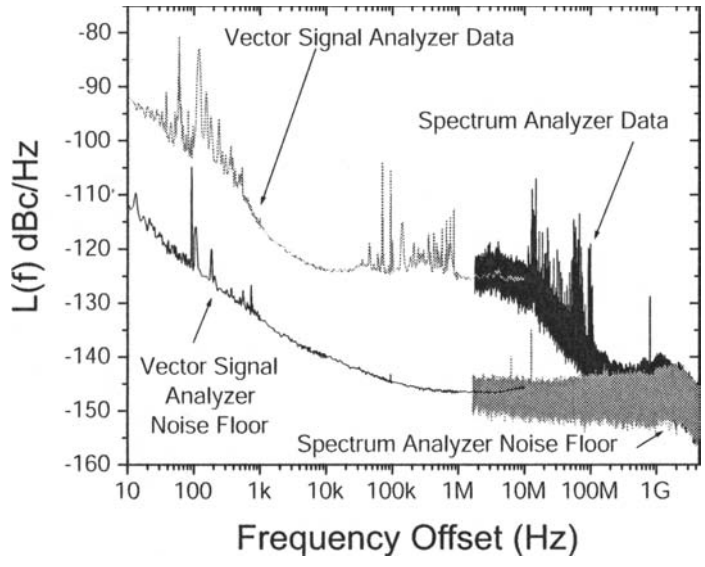

Fig. 12. Single-sideband phase noise of the hybridly mode-locked laser diode and corresponding noise floor. The plot is pieced together from vector signal analyzer measurements at low offsets and radio frequency spectrum analyzer measurements at high offsets. The measurement noise floor was obtained by bypassing the mode-locked laser and substituting it with an equivalent microwave loss (51 dB in this case) and was given by the thermal noise of the amplifiers after the photodiode. The mixer IF bandwidth was 2 GHz, which was wide enough to view the noise energy before it dipped below the measurement noise floor [4].

4.3. Characterization of Amplitude Noise

The intensity noise of an OTDM source can be measured by a fast photodiode and rf spectrum analyzer or by an AM noise measurement. The theory of RIN in cw semiconductor lasers is described in [68], but does not entirely apply to mode-locked lasers. The amplitude noise spectrum of mode-locked lasers also includes the correlated amplitude noise from the driving rf microwave oscillator.

4.3.1. Direct Detection and RF Spectrum Analyzer

The amplitude noise of cw laser diodes is often measured by detection with a fast photodiode followed by a low-noise rf amplifier and an rf spectrum analyzer. Using this technique, the RIN of a widely tunable sampled-grating DBR laser was measured to have less than -160 dB/Hz (at frequencies below the relaxation oscillation frequency) for optical powers above 1 mW [80].

The measurement of the amplitude noise of a mode-locked laser is more difficult since the rf power spectrum contains both amplitude and timing noise. Therefore, one must assume a model for the laser noise before interpreting the amplitude noise [70]. The uncorrelated amplitude noise for a fundamentally mode-locked laser appears as noise skirts around each harmonic with the same magnitude [71]. Since the measured

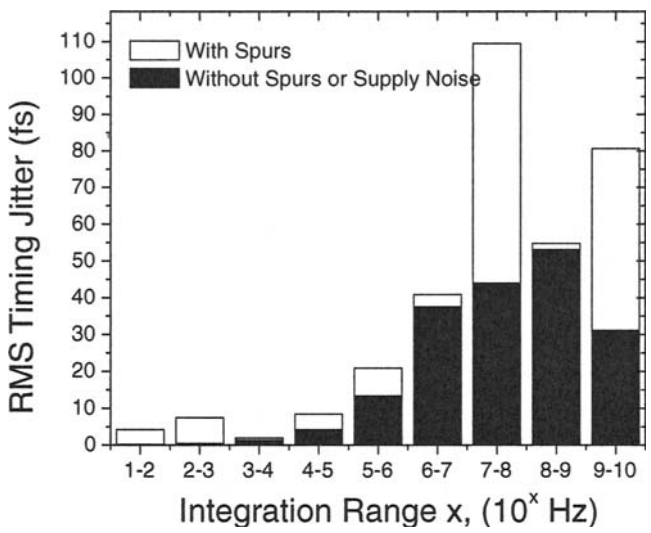

Fig. 13. The integrated timing jitter in each decade of the phase noise shown in Fig. 12. The square root of the sum of the squares of the numbers above yields the jitter over multiple decades. In the last decade, from 1 to 4.5 GHz, the white bar corresponds to the timing jitter where we assume that the noise is equal to the noise floor and the black bar corresponds to a theoretically expected -20 dB/decade rolloff [4].

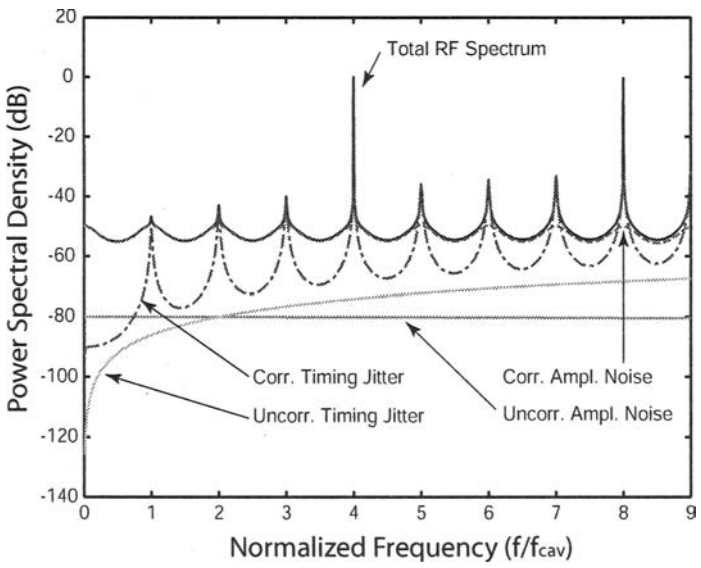

Fig. 14. RF spectrum of a harmonically mode-locked laser.

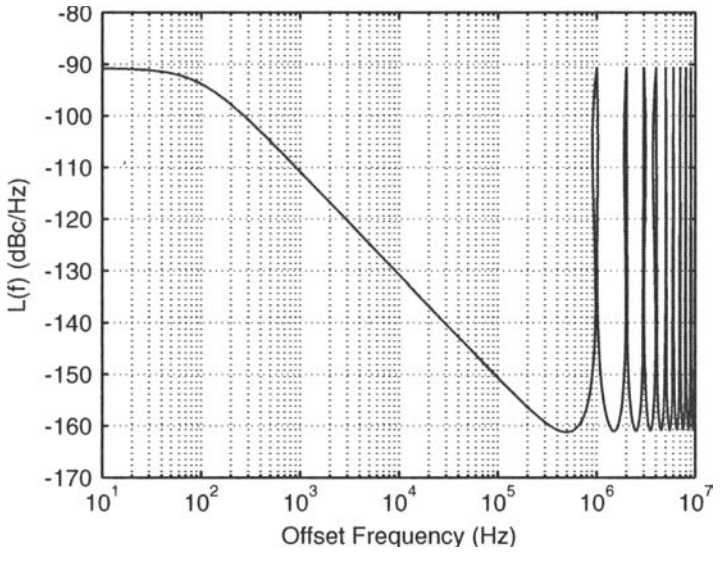

Fig. 15. Power spectral density of the timing jitter for an AM actively and harmonically mode-locked laser.

noise is a combination of both amplitude and timing fluctuations, it is difficult to extract the amplitude noise from this measurement alone.

4.3.2. AM Noise Measurement

The AM noise can be measured by downconverting the photodetected signal using the same rf oscillator used to drive the OTDM pulse source. The method relies on using a low noise mixer biased so that the LO and RF ports are in phase. The IF port yields a signal proportional to the amplitude noise.

The AM noise measurements of harmonically mode-locked [5] and fundamentally mode-locked [62] semiconductor lasers show that the amplitude noise of a mode-locked semiconductor medium has the usual broad band RIN noise spectrum with a peak at the relaxation oscillation frequency [68] plus correlated noise from the driving rf oscillator.

An overview of sensitive AM noise measurements of femtosecond Ti:sapphire lasers is presented in [81].

4.4. Low Noise Mode-locked Laser Design

4.4.1. Cavity Optimizations

The rms timing jitter of an actively mode-locked laser is [76]

$$\sigma_t^2 = \frac{\mathcal{E}_{\mathrm{ASE}}}{w_0} \frac{1}{2M\omega_M^2}, \tag{1}$$

where $\mathcal{E}_{\mathrm{ASE}}$ is the spontaneous emission energy in one time-slot, w_0 the the pulse energy (note that $\mathcal{E}_{\mathrm{ASE}}/w_0$ can be thought of as 1/SNR), M is the modulation depth of the amplitude modulation defined ($M = \pi/4$ corresponds to full modulation), and ω_M is the modulation angular frequency. Typical values in a mode-locked semiconductor laser are $\mathcal{E}_{\mathrm{ASE}} = P_{\mathrm{ASE}}T_R = h\nu B n_{\mathrm{sp}}(G-1)T_R = h(2\times 10^{14})(0.7\text{ nm}\times 133\text{ GHz/nm})(100-1)\times 100\text{ ps} = 1.22\times 10^{-16}$ pJ = 922 noise photons, $w_0 = 0.7$ pJ $= 5.28\times 10^6$ signal photons, $M = \pi/4$, and $\omega_M = 2\pi\times 10$ GHz, yielding a total rms timing jitter of $\sigma_t = 168$ fs. The inclusion of a saturable absorber improves the signal-to-noise ratio since it cleans up the ASE between pulses and hence results in a timing jitter value smaller than this expression predicts.

To design a low timing jitter mode-locked laser, Eq. (1) shows that it is necessary to increase the number of signal photons compared to noise photons, maximize the modulation depth of the rf oscillator, and operate at high-repetition rates (large ω_M). To improve the SNR ratio of the number of photons, one can (1) increase the modulation depth (see Figs. 16 and 11) and decrease the recovery time of the saturable absorber (see Fig. 17) to clean up ASE photons between pulses, (2) minimize cavity losses, and (3) operate at high output powers, many times the threshold value. High output powers are desirable since the carrier density clamps at a constant average value above threshold and hence the spontaneous emission rate is clamped. Additional current added above the threshold current directly results in signal photons and improves the SNR. In addition to the quantum noise of the laser, there are several technical noise sources that must be minimized: (1) vibrations, (2) thermal gradients, (3) ground-loops leading to variations at multiples of the wall-current frequency (50 or 60 Hz), (4) flicker noise of the current and voltage sources used to bias the laser, and (5) AM and PM noise of the rf oscillator.

The timing jitter power spectral density due to ASE for a dispersionless, AM modulated, fundamentally and actively mode-locked laser is Lorentzian. Measurements of the residual phase noise of external-cavity mode-locked semiconductor lasers is tabulated in Table 5. This data indicates that extremely low noise microwave oscillators are needed to have a low absolute phase noise. For example, a good synthesizer at 10 GHz (Agilent 83732B) has a phase noise of -90 dBc/Hz at an offset of 10 kHz, which is well above the phase noise of most of the laser sources listed in Table 5. It is possible to achieve quantum-limited performance by using a quiet rf oscillator such as the PSI SCLO at 10 GHz, which has a phase noise of -160 dBc/Hz at an offset of 10 kHz.

Table 5. Nearly Lorentzian phase noise spectra for various external-cavity mode-locked semiconductor lasers.

Plateau) (dBc/Hz)	Knee Freq.	Rolloff (dB/decade)	Timing Jitter	Pulse Width	Ref.
-110	55 MHz	-25	670 fs (10 Hz to 5 GHz)	NR	[62]
-82	200 kHz	-18	850 fs (100 Hz to 10 MHz)	0.6 ps	[1]
-94	350 kHz	-17.5	390 fs (100 Hz to 10 MHz)	1.3 ps	[1]
-124	10 MHz	-17	86 fs (10 Hz to 4.5 GHz)	6.7 ps	[4]
-113	10 MHz	-17	159 fs (10 Hz to 10 MHz)	2 ps	[76]

The timing jitter performance of an OTDM pulse source can be improved with feedback and feed-forward techniques. Using phase modulation plus dispersion [82],

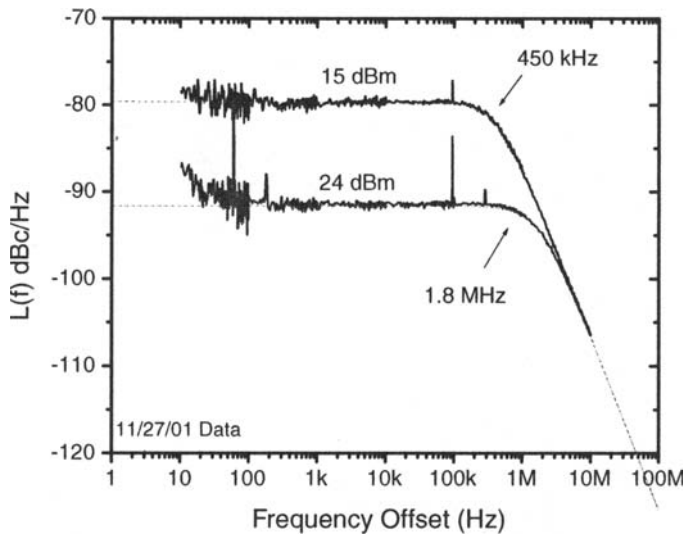

Fig. 16. Single-sideband phase noise of the temperature controlled external-cavity mode-locked semiconductor laser at 10 GHz with a 5-nm optical BPF. The phase noise increases as the microwave driving power to the saturable absorber decreases from 24 dBm to 15 dBm. The dashed lines show the theoretical values.

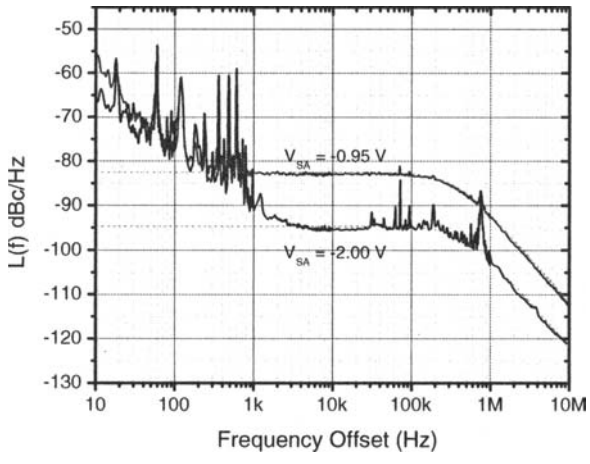

Fig. 17. Residual phase noise of mode-locked semiconductor laser as a function of saturable absorption.

it has been shown that the timing jitter can be improved by over 12 dB [83, 84]. In addition electrical, feedback can reduce the timing jitter when there a stable, low-noise rf oscillator is available. Using the error signal from a residual phase noise measurement, feedback to the saturable absorber bias in an external-cavity mode-locked semiconductor laser shows improvement in the phase noise performance in Fig. 18. The improvement in the phase noise is directly related to the gain-bandwidth product of the feedback circuit. For AM noise, a feed-forward technique has demonstrated the ability to reduce the AM noise by as much as 25 dB [85].

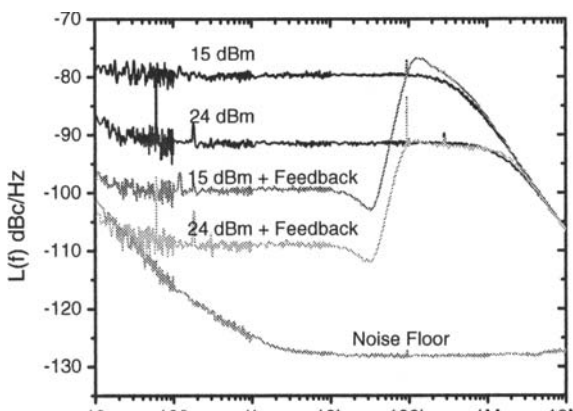

Fig. 18. Timing jitter noise of temperature controlled external-cavity MLLD with and without electronic feedback. The power level refers to the microwave power applied to the saturable absorber.

5. Conclusions

Semiconductor mode-locked lasers are excellent sources for OTDM since they are compact, yield picosecond pulses at high repetition rates at 1.5 μm wavelengths, and can have extremely low timing jitter. Mode-locked semiconductor lasers have yet to reach their full potential in performance: gain-bandwidth-limited pulses as short as 50 fs, high output powers above 10 mW, and sub-picosecond 10 or 40 GHz monolithic mode-locked semiconductor lasers that can be fabricated reliably for a specified wavelength and repetition-rate have yet to be demonstrated and are exciting topics for further research and development.

References

1. R. Ludwig, S. Diez, A. Ehrhardt, L. Küller, W. Pieper, and H. G. Weber, "A tunable femtosecond modelocked semiconductor laser for applications in OTDM-systems," IEICE Trans. Electron., **E81-C**, 140–145 (1998), IEICE transactions on electronics.
2. H. Yokoyama, "Highly stabilized mode-locked semiconductor diode lasers," Rev. Laser Eng., **27**, 750–755, 1999.
3. H. Yokoyama, "Highly reliable mode-locked semiconductor lasers," IEICE Trans. Electron., **E85-C** (1), 27–36 (January 2002).
4. L. A. Jiang, M. E. Grein, E. P. Ippen, C. McNeilage, J. Searls, and H. Yokoyama, "Quantum-limited noise performance of a modelocked laser diode," Opt. Lett., **27** (1), 49–51 (2002).
5. C. M. DePriest, T. Yilmaz, A. Braun, J. H. Abeles, and P. J. Delfyett Jr., "High-quality photonic sampling streams from a semiconductor diode ring laser," IEEE J. Quant. Electron., **38** (4), 380–389 (2002).
6. U. Feiste, R. Ludwig, C. Schubert, J. Berger, C. Schmidt, H. G. Weber, B. Schmauss, A. Munk, B. Buchold, D. Briggmann, F. Kueppers, and F. Rumpf, "160 Gbit/s transmission over 116 km field-installed fibre using 160 Gbit/s OTDM and 40 Gbit/s ETDM," Electron. Lett., **37** (7), 443–445 (March 2001).
7. M. Nakazawa, T. Yamamoto, and K. R. Tamura, "Ultrahigh-speed OTDM transmission beyond 1 Ter-bit-per-second using a femtosecond pulse train," IEICE Trans. Electron., **E85-C** (1), 117–125 (2002).
8. J. Zhang, M. Yao, X. Chen, L. Xu, M. Chen, and Y. Gao, "Bit error rate analysis of OTDM system based on moment generation function," J. Lightwave Technol., **18** (11, pp. 1513–1518 (November 2000).
9. K. S. Jepsen, H. N. Poulsen, A. T. Clausen, and K. E. Stubkjer, "Investigation of cascadability of add-drop multiplexers in OTDM systems," in Proc. ECOC'98, 1998, vol. 1.
10. M. L. Nielsen, B.-E. Olsson, and D. J. Blumenthal, "Pulse extinction ratio improvement using SPM in an SOA for OTDM system applications," IEEE Photon. Technol. Lett., **14** (2), 245–247 (2002).
11. E. Hashimoto, A. Takada, and Y. Katagiri, "High-frequency synchronized signal generation using semiconductor lasers," IEEE Transactions on Microwave Theory and Techniques, **47** (7), 1206–1218 (1999).
12. I. Ogura, H. Kurita, T. Sasaki, and H. Yokoyama, "Precise operation-frequency control of monolithic mode-locked laser diodes for high-speed optical communication and all-optical signal processing," Opt. Quant. Electron., **33**, 709–725 (2001).
13. PriTel, Naperville, IL, USA, Datasheet for UOC series Ultrafast Optical Clocks.
14. Calmar Optcom, Sunnyvale, CA, USA, Datasheet for PSL series picosecond lasers, 2001.
15. GigaTera, Lerzenstrasse 16, CH-8953 Dietikron, Switzerland, Datasheet for ERGO pulse generating laser, September 2002.
16. Emmanuel Desurvire, *Erbium-doped fiber amplifiers: principles and applications* (John Wiley and Sons, New York, 1994).
17. A. D. Ellis, R. J. Manning, I. D. Phillips, and D. Nesset, "1.6 ps pulse generation at 40 GHz in phaselocked ring laser incorporating highly nonlinear fibre for application to 160 Gbit/s OTDM networks," Electron. Lett., **8** (35), 645–646 (1999).
18. J. Li, A. Andrekson, and B. Bakhshi, "Direct generation of subpicosecond chirp-free pulses at 10 GHz from a nonpolarization maintaining actively mode-locked fiber ring laser," IEEE Photon. Technol. Lett., **12** (9), 1150–1152 (2000).

19. B. Bakhshi and P. A. Andrekson, "40 GHz actively modelocked polarisation-maintaining erbium fibre ring laser," Electron. Lett., **36** (5), 411–413 (2000).

20. T. F. Carruthers and I. N. Duling III, "10-GHz, 1.3 ps erbium fiber laser employing soliton pulse shortening," Opt. Lett., **21** (23), 1927–1929 (1996).

21. M. Nakazawa and E. Yoshida, "A 40-GHz 850-fs regeneratively FM mode-locked polarization-maintaining erbium fiber ring laser," IEEE Photon. Technol. Lett., **12** (12), 1613–1615 (2000).

22. P. V. Mamyshev, S. V. Chernikov, and E. M. Dianov, "Generation of fundamental soliton trains for high-bit-rate optical fiber communication lines," IEEE J. Quant. Electron., **27** (10), 2347–2355 (1991).

23. T. E. Murphy, "10-GHz 1.3-ps pulse generation using chirped soliton compression in a Raman gain medium," IEEE Photon Technol. Lett., **14** (10), 1424–1426, (2002).

24. D. Lee, H. Yoon, and N. Park, "Extension of dispersion decreasing fiber – pulse shaping method for the optical time division multiplexing system source applications," in CLEO Pacific Rim'99, 1999.

25. M. J. Guy, S. V. Chernikov, J. R. Taylor, D. G. Moodie, and R. Kashyap, "200 fs soliton pulse generation at 10 GHz through nonlinear compression of transform-limited pulses from an electroabsorption modulator," Electron. Lett., **31** (9), 740–741 (1995).

26. M. J. Guy, S. V. Chernikov, J. R. Taylor, D. G. Moodie, and R. Kashyap, "1.2 ps pulses at low base repetition rates for 100 Gbit/s per channel optical communication networks," Electron. Lett., **31** (25), 2190–2191 (1995).

27. S. V. Chernikov, J. R. Taylor, and R. Kashyap, "Comb-like dispersion-profiled fibre for soliton pulse-train generation," Opt. Lett., **19** (8), 539–541 (1994).

28. M. Guy, S. Chernikov, and R. Taylor, "Electroabsorption modulators for high speed ultrashort pulse generation and processing," IEICE Trans. Electron., **E81-C** (2), 169–174 (1998).

29. Y. Matsui, M. D. Pelusi, and A. Suzuki, "Generation of 20-fs optical pulses from a gain-switched laser diode by a four-stage soliton compression technique," IEEE Photon. Technol. Lett., **11** (10), 1217–1219 (1999).

30. H. Ohta, S. Nogiwa, and H. Chiba, "Generation of low timing jitter, sub-picosecond optical pulses using a gain-switched DFB-LD with CW light injection and a nonlinear optical loop mirror," IEICE Trans. Electron., **E81-C** (2), 166–168 (1998).

31. K. A. Wiliams, I. H. White, D. Burns, and W. Sibbett, "Jitter reduction through feedback for picosecond pulsed InGaAsP lasers," IEEE J. Quant. Electron., **32** (11), 1988–1994 (1996).

32. M. Jinno, "Correlated and uncorrelated timing jitter in gain-switched laser diodes," IEEE Photon. Technol. Lett., **5** (10), 1140–1143 (1993).

33. Y. Arakawa, T. Sogawa, M. Nishioka, M. Tanaka, and H. Sakaki, "Picosecond pulse generation ($<$ 1.8 ps) in a quantum well laser by a gain switching method," Appl. Phys. Lett., **51** (17), 1295–1297 (1987).

34. P. T. Ho, L. A. Glasser, E. P. Ippen, and H. A. Haus, "Picosecond pulse generation with a cw GaAlAs laser diode," Appl. Phys. Lett., **33** (3), 241–242 (1978).

35. R. Ludwig and A. Ehrhardt, "Turn-key-ready wavelength-, repetition rate- and pulsewidth-tunable femtosecond hybrid modelocked semiconductor laser," Electron. Lett., **31** (14), 1165–1167 (1995).

36. Y. Hashimoto, H. Yamada, R. Kuribayashi, and H. Yokoyama, "40-GHz tunable optical pulse generation from a highly-stable external-cavity mode-locked semiconductor laser module," in OFC'02, OSA, 2002.

37. K. Sato, A. Hirano, N. Shimizu, and I. Kotaka, "High-frequency and low-jitter optical pulse generation using semiconductor mode-locked lasers," IEEE Transactions on Microwave Theory and Techniques, **47** (7), 1251–1256 (1999).

38. K. Sato, I. Kotaka, Y. Kondo, and M. Yamamoto, "Actively mode-locked strained-InGaAsP multiquantum-well lasers integrated with electroabsorption modulators and distributed Bragg reflectors," IEEE J. Select. Topics Quant. Electron., **2** (3), 557–565 (1996).

39. K. Sato, K. Wakita, I. Kotaka, Y. Kondo, M. Yamamoto, and A. Takada, "Monolithic strained-InGaAsP multiple-quantum-well lasers with integrated electroabsorption modulators for active mode locking," Appl. Phys. Lett., **65** (1), 1–3 (1994).

40. R. S. Tucker, U. Koren, G. Raybon, C. A. Burrus, B. I. Miller, T. L. Koch, G. Eisenstein, and A. Shahar, "40 Ghz active mode-locking in a 1.5 μm monolithic extended-cavity laser," Electron. Lett., **25** (10), 621–622 (1989).

41. M. C. Wu, Y. K. Chen, T. Tanbun-Ek, R. A. Logan, M. A. Chin, and G. Raybon, "Transform-limited 1.4 ps optical pulses from a monolithic colliding-pulse mode-locked quantum well laser," Appl. Phys. Lett., **57** (8), 759–761 (1990).

42. Y. K. Chen and M. C. Wu, "Monolithic colliding-pulse mode-locked quantum-well lasers," IEEE J. Quant. Electron., **28** (10), 2176–2185 (1992).

43. P. B. Hansen, G. Raybon, U. Koren, B. I. Miller, M. G. Young, M. A. Newkirk, M.-D. Chien, B. Tell, and C. A. Burrus, "Monolithic semiconductor soliton transmitter," J. Lightwave Technol., **13** (2), 297–301 (1995).

44. P. B. Hansen, G. Raybon, U. Koren, B. I. Miller, M. G. Young, M. Chien, C. A. Burrus, and R. C. Alferness, "5.5-mm long InGaAsP monolithic extended-cavity laser with an integrated bragg-reflector for active mode-locking," IEEE Photon. Technol. Lett., **4** (3), 215–217 (1992).

45. P. A. Morton, J. E. Bowers, L. A. Koszi, M. Soler, J. Lopata, and D. P. Wilt, "Monolithic hybrid mode-locked 1.3 μm semiconductor lasers," Appl. Phys. Lett., **56** (2), 111–113 (1990).

46. D. J. Derickson, R. J. Helkey, A. Mar, J. R. Karin, J. G. Wasserbauer, and J. E. Bowers, "Short pulse generation using multisegment mode-locked semiconductor lasers," IEEE J. Quant. Electron., **28** (10), 2186–2202 (1992).

47. M. J. Guy, S. V. Chernikov, and J. R. Taylor, "A duration-tunable, multiwavelength pulse source for OTDM and WDM communications," IEEE Photon. Technol. Lett., **9** (7), 1017–1019 (1997).

48. M. D. Pelusi, Y. Matsui, and A. Suzuki, "Frequency tunable femtosecond pulse generation from an electroabsorption modulator by enhanced higher order soliton compression in dispersion decreasing fibre," Electron. Lett., **35** (9), 734–735 (1999).

49. P. C. Reeves-Hall and J. R. Taylor, "Wavelength and duration tunable subpicosecond source using adiabatic Raman compression," Electron. Lett., **37** (7), 417–418 (2001).

50. E. Yoshida and Nakazawa M., "A 40-GHz 0.9-ps regeneratively mode-locked fiber laser with a tuning range of 1530-1560," IEEE Photon. Technol. Lett., **11** (12), 1587–1589 (December 1999).

51. E. Yoshida and Nakazawa M., "Measurement of the timing jitter and pulse energy fluctuation of a PLL regeneratively mode-locked fiber laser," IEEE Photon. Technol. Lett., **11** (5), 548–550 (May 1999).

52. E. Yoshida and Nakazawa M., "Wavelength tunable 1.0 ps pulse generation in 1.530-1.555 μm region from PLL regeneratively modelocked fibre laser," Electron. Lett., **34** (18), 1753–1754 (1998).

53. A. E. Siegman, *Lasers* (University Science Books, Mill Valley, CA, 1986).

54. H. Yokoyama, T. Shimizu, T. Ono, and Y. Yano, "Synchronous injection locking operation of monolithic mode-locked diode lasers," Opt. Rev., **2**, 85–88 (1995).

55. I. Ogura, T. Sasaki, H. Yamada, and H. Yokoyama, "Precise sdh frequency operation of monolithic laser diodes with frequency tuning function," Electron. Lett., **35** (15), 1275–1277 (1999).

56. K. Sato, I. Hiroyuki, I. Kotaka, K. Yasuhiro, and M. Yamamoto, "Frequency range extension of actively mode-locked lasers integrated with electroabsorption modulators using chirped gratings," IEEE J. Select. Topics Quant. Electron., **3** (2), 250–255 (1997).

57. J. E. Bowers, P. A. Morton, A. Mar, and S. W. Corzine, "Actively mode-locked semiconductor lasers," IEEE J. Quant. Electron., **25** (6), 1426–1439 (1989).

58. C. M. DePriest, T. Yilmaz, P. J. Delfyett Jr., S. Etemad, A. Braun, and J. H. Abeles, "Ultralow noise and supermode suppression in an actively mode-locked external-cavity semiconductor diode ring," Opt. Lett., **27** (9), 719–721 (2002).

59. G. T. Harvey and L. F. Mollenauer, "Harmonically mode-locked fiber laser with an internal Fabry-Perot stabilizer for soliton transmission," Opt. Lett., **18** (2), 107–109 (1993).

60. K. K. Gupta, N. Onodera, and M. Hyodo, "Technique to generate equal amplitude, higher-order optical pulses in rational harmonically modelocked fibre ring lasers," Electron. Lett., **37** (15), 948–950 (2001).

61. T. R. Clark, T. F. Carruthers, P. J. Matthews, and I. N. Duling III, "Phase noise measurements of ultrastable 10 GHz harmonically modelocked fibre laser," Electron. Lett., **35** (9), 720–721 (1999).

62. T. Yilmaz, C. M. DePriest, and P. J. Delfyett Jr., "Complete noise characterisation of external cavity semiconductor laser hybridly modelocked at 10 GHz," Electron. Lett., **37** (22), 1338–1339 (2001).

63. T. Yamamoto, L. K. Oxenlowe, C. Schmidt, C. Schubert, E. Hilliger, U. Feiste, J. Berger, R. Ludwig, and H. G. Weber, "Clock recovery from 160 Gbit/s data signals using phase-locked loop with interferometric optical switch baseed on semiconductor optical amplifier," Electron. Lett., **37** (8), 509–510 (2001).

64. D. T. L. Tong, K.-L. Deng, B. Mikkelsen, G. Raybon, K. F. Dreyer, and J. E. Johnson, "160 Gbit/s clock recovery using electroabsorption modulator-based phase-locked loop," Electron. Lett., **36** (23), 1951–1952 (2000).

65. D. J. Derickson, A. Mar, and J. E. Bowers, "Residual and absolute timing jitter in actively mode-locked semiconductor lasers," Electron. Lett., **26** (24), 2026–2028 (November 1990).

66. W. Ng, R. Stephens, D. Persechini, and K. V. Reddy, "Ultra-low jitter modelocking of er-fibre laser at 10 GHz and its application in photonic sampling for analogue-to-digital conversion," Electron Lett., **37**, 113–115 (2001).

67. F. Rana, H. L. T. Lee, M. E. Grein, L. A. Jiang, and R. J. Ram, "Characterization of the noise and correlations in harmonically mode-locked lasers," to be published in JOSA B.

68. L. A. Coldren and S. W. Corzine, *Diode lasers and photonic integrated circuits* (John Wiley and Sons, New York, 1995).

69. D. A. Leep and D. A. Holm, "Spectral measurement of timing jitter in gain-switched semiconductor lasers," Appl. Phys. Lett., **60** (20), 2451–2453 (1992).

70. M. C. Gross, M. Hanna, K. M. Patel, and S. E. Ralph, "Spectral method for the simultaneous determination of uncorrelated and correlated amplitude and timing jitter," Appl. Phys. Lett., **80** (20), 3694–3696 (2002).

71. D. von der Linde, "Characterization of noise in continuously operating mode-locked lasers," Appl. Phys. B, **39**, 201–217 (1986).

72. Ursula Keller, Kathryn D. Li, Mark Rodwell, and David M. Bloom, "Noise characterization of femtosecond fiber raman soliton lasers," IEEE Journal of Quantum Electronics, **25** (3), 280–288 (March 1989).

73. Blake Peterson, "Spectrum analysis, application note 150," Tech. Rep., Agilent Technologies, 1989.

74. L. A. Jiang, M. E. Grein, S. T. Wong, H. A. Haus, and E. P. Ippen, "Measuring timing jitter with optical cross-correlations," submitted to IEEE J. Quant. Electron.

75. S. A. Crooker, F. D. Betz, J. Levy, and D. D. Awschalom, "Femtosecond synchronization of two passively mode-locked Ti:sapphire lasers," Rev. Sci. Instrum., **67** (6), 2068–2071 (June 1996).

76. L. A. Jiang, Ultralow-noise modelocked lasers, Ph.D. thesis, MIT, 2002.

77. M. E. Grein, L. A. Jiang, Y. Chen, H. A. Haus, and E. P. Ippen, "Timing restoration dynamics in an actively mode-locked fiber ring laser," Opt. Lett., **24** (23), 1687–1689 (1999).

78. L. A. Jiang, K. S. Abedin, M. E. Grein, and E. P. Ippen, "Retiming dynamics of a mode-locked semiconductor laser," Electron. Lett., **38** (22), 1446–1447 (2002).

79. L. A. Jiang, M. E. Grein, and E. P. Ippen, "Region of validity for residual phase noise measurements of actively modelocked lasers," submitted to Electron. Lett.

80. H. Shi, D. Cohen, J. Barton, M. Majewski, L. A. Coldren, M. C. Larson, and G. A. Fish, "Relative intensity noise measurements of a widely tunable sampled-grating DBR laser," IEEE Photon. Technol. Lett., **14** (6), 759–761 (2002).

81. R. P. Scott, C. Langrock, and B. H. Kolner, "High-dynamic-range laser amplitude and phase noise measurement techniques," IEEE. J. Select. Topics Quant. Electron., **7** (4), 641–655 (2001).

82. M. E. Grein, H. A. Haus, L. A. Jiang, and E. P. Ippen, "Action on pulse position and momentum using dispersion and phase modulation," Opt. Express, **8** (12), 664–669 (2001).

83. L. A. Jiang, M. E. Grein, H. A. Haus, E. P. Ippen, and H. Yokoyama, "Timing jitter eater for optical pulse trains," Opt. Lett., **28** (2), 78–80, 2003.

84. L. Mollenauer and C. Xu, "Time-lens timing-jitter compensator in ultra-long haul dwdm dispersion managed soliton transmissions," in CLEO'02 Postdeadline Papers, 2002.

85. Thomas R. Clark Irl N. Duling III, Robert P. Moeller, "Active filtering of the amplitude noise of a mode-locked fiber laser," in Conference on Lasers and Electro-Optics, San Francisco, California, USA, May 2000, OSA.

DOI: 10.1007/s10297-004-0029-6
Originally published in J. Opt. Fiber. Commun. Rep. 2, 462–496 (2005)

Ultrafast mode-locked fiber lasers for high-speed OTDM transmission and related topics

Masataka Nakazawa

Research Institute of Electrical Communication
Tohoku University
2-1-1 Katahira, Aoba-ku, Sendai-shi, Miyagi-ken 980-8577, Japan
E-mail: nakazawa@riec.tohoku.ac.jp

Abstract. Ultrashort optical pulse sources in the 1.5-μm region are becoming increasingly important in terms of realizing ultrahigh-speed optical transmission and signal processing at optical nodes. This paper provides a detailed description of several types of mode-locked erbium-doped fiber laser, which are capable of generating picosecond–femtosecond optical pulses in the 1.55-μm region. In terms of ultrashort pulse generation at a low repetition rate ($\sim$100 MHz), passively mode-locked fiber lasers enable us to produce pulses of approximately 100 fs. With regard to high repetition rate pulse generation at 10–40 GHz, harmonically mode-locked fiber lasers can produce picosecond pulses. This paper also describes the generation of a femtosecond pulse train at a repetition rate of 10–40 GHz by compressing the output pulses from harmonically mode-locked fiber lasers with dispersion-decreasing fibers. Finally, a new Cs optical atomic clock at a frequency of 9.1926 GHz is reported that uses a regeneratively mode-locked fiber laser as an opto-electronic oscillator instead of a quartz oscillator. The repetition rate stability reaches as high as 10^{-12}–10^{-13}.

1. Introduction

Since the advent of the erbium-doped fiber amplifier (EDFA) pumped by 1.48 μm InGaAsP semiconductor lasers, there has been marked progress on fiber lasers because they offer ease of cavity construction and stable oscillation characteristics. The oscillation wavelength is tunable from 1.52 to 1.60 μm. Of the many types of erbium-doped fiber lasers providing, for example, CW, Q-switched, and high-repetition-rate oscillations, short optical pulse generation from erbium-doped fiber lasers operating at 1.55 μm is particularly attractive for high-speed optical communication, because

this source can generate transform-limited pico-subpicosecond pulses in the minimum loss region of silica fibers.

In general, fiber lasers consist of an active fiber medium with a pumping optical source supplied through a WDM coupler, a loop of fiber that forms a ring cavity, an optical output coupler, and an isolator that makes the cavity unidirectional. When the goal is pulse oscillation, a saturable absorber or optical modulator is installed in the cavity. A fiber cavity is particularly suitable as a laser cavity because

1. The fiber loss is low, which makes it possible to form a low-loss cavity (low threshold).
2. The optical intensity in the fiber cavity becomes very high, which enables us to obtain fiber nonlinearity and laser oscillation even in a three level system such as an erbium ion ($^4I_{15/2}$–$^4I_{13/2}$).
3. Nonlinear optical effects such as soliton propagation and nonlinear polarization rotation are available to generate ultrashort pulses.
4. The dispersion control of the cavity is very easily achieved by connecting fibers with different group velocity dispersions (GVD).
5. As the cavity length can be extended to the order of a kilometer, the Q value of the cavity becomes much higher than that of conventional lasers.

In particular, the EDFA has excellent characteristics as a laser medium:

1. It has a high gain that exceeds 30 dB and a high energy conversion efficiency.
2. A large saturation output power can be obtained by increasing the pumping power because the erbium ion is a three level system.

With the above characteristics, erbium fiber lasers generally have the following laser characteristics:

1. Wideband wavelength tunability from 1.5 to 1.6 μm.
2. Easy single longitudinal mode oscillation under a unidirectional ring cavity.
3. High output power.
4. Easy ultrashort pulse generation with a simple cavity configuration.

There are two schemes for generating short pulses as shown in Fig. 1: passive and active mode-locking. Passive mode-locking is the preferred technique for generating the shortest possible pulse in the femtosecond regime, while the repetition rate is of the order of 100 MHz. One method by which to construct a passively mode-locked fiber laser is to use a nonlinear amplifying loop mirror (NALM) [1, 2]. A NALM is a kind of nonlinear optical loop mirror (NOLM) with an EDFA, which acts as an ultrafast saturable absorber in the fiber cavity by using self-phase modulation (SPM) [3]. An alternative approach to passive mode-locking is to use nonlinear polarization rotation (NPR) [4,5]. NPR is a phenomenon in which a polarization ellipse, composed of two orthogonal components (x and y axis components) in a birefringent fiber, rotates at an ultrahigh speed depending on the light intensity when light propagates through the fiber. A new technique, named stretched pulse mode-locking, is also very interesting because it can emit stable high power pulses in the femtosecond regime [6,7].

A stable optical pulse source that operates in the GHz region is important to the development of ultrahigh speed optical communication. For high repetition-rate pulse

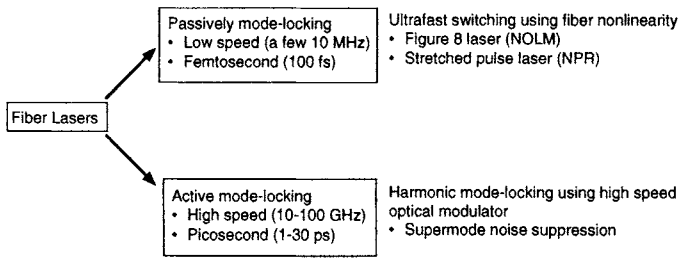

Fig. 1. Classification of mode-locked fiber lasers. Passive mode-locking and active mode-locking.

generation, the preferred technique is active mode-locking. Conventional active mode-locking uses an optical modulator as an optical gate in the time domain, which is driven at the harmonic of the fundamental frequency determined by the cavity length [8,9]. An interesting technique, regenerative mode-locking [10], was adopted in a harmonically mode-locked fiber laser [11]. This laser has been used for various high-speed optical communication systems [12–14].

This paper begins with a description of passive and active mode-locked fiber lasers. Then it moves on to describe a harmonically and regeneratively mode-locked fiber laser operating at a repetition rate of 10 GHz. In section 3 we report phase-locked-loop (PLL) operation and repetition-rate stabilization, and the suppression of supermode noise. Section 4 deals with topics related to high-speed fiber lasers such as FM mode-locking and pulse compression using a dispersion decreasing fiber (DDF). Finally, as an important application of regenerative mode-locking, we describe a Cs optical atomic clock, which may be applicable to a new era of frequency standards.

2. Mode-Locked Fiber Lasers

2.1. Passively Mode-Locked Fiber Laser

NALMs [1,2], nonlinear polarization rotation (NPR) [4,5], and dispersion-managed stretched pulse propagation [6,7] have been used for passively mode-locked fiber lasers. A typical pulse width with passive mode-locking is 100–300 fs. Here, a nonlinear loop mirror (NOLM) is a fundamental fiber switching device that employs the phase rotation resulting from the difference between the SPM of the clock and counter-clock directions. The NALM enables low intensity optical switching (three or four times less power than with NOLM switching). NALM, NOLM and NPR act as ultrafast saturable absorbers, which shorten the pulse by removing its wing components. Moreover, the NPR cavity configuration for passive mode-locking, is much simpler than that of a NALM.

Let us consider a case where an optical fiber has a weak birefringence. A linearly polarized light that passes through a polarizer is elliptically polarized by a polarization controller. When a low intensity light is launched into the optical fiber, there is no NPR. Therefore this light experiences a significant loss at an analyzer whose polarization

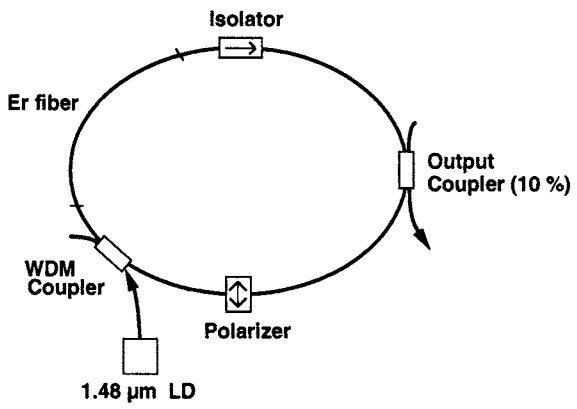

Fig. 2. Configuration of passively mode-locked femtosecond fiber laser using nonlinear polarization rotation (NPR). A polarizer is installed at a point-symmetric position in relation to the isolator.

direction is orthogonal to the polarizer. By contrast, when a high intensity light is launched into the optical fiber, NPR occurs and the polarization ellipse rotates. As a result, this light passes through the analyzer without loss. Therefore NPR can be used for short pulse generation or pulse shaping because it allows high intensity light to pass but blocks low intensity light. That is, polarization switching acts as a fast saturable absorber.

The configuration of a femtosecond fiber laser using NPR is shown in Fig. 2 [15]. The laser is composed of a polarization dependent isolator, an output coupler, a WDM coupler, erbium-doped fiber, and a polarizer. We use ordinary fiber in which the intrinsic birefringence is very small to make it easy to obtain an NPR angle of π. The pumping source is 1.48 μm InGaAsP laser diodes. The erbium-doped fiber is 1 m long with an erbium ion doping concentration of 8900 ppm. The total cavity length is only 3.6 m. A polarizer is installed in the cavity at a point symmetric position in relation to the isolator. The polarization axis of the polarizer is orthogonal to that of the isolator, so that only a $\pi/2$ (or an odd integral multiple of $\pi/2$) polarization-rotated component can pass through the polarizer without loss [15,16].

The output pulses thus obtained are shown in Fig. 3, where Fig. 3(a) shows an autocorrelation waveform for a pump power of 63 mW. The corresponding spectrum is shown in Fig. 3(b). The pulse width was 145 fs and had no pedestal. The central wavelength was 1.555 μm and the spectral width was 18 nm. This gives a bandwidth-pulse width product $\Delta\nu\Delta\tau$ of 0.32, which indicates that the output pulse was a transform-limited sech (secant hyperbolic) pulse. The peak power of the output pulse was 25 W. The shortest pulse width was 136 fs for a pump power of 74 mW as shown in Fig. 3(c). The repetitive feature of the output pulse is shown in Fig. 3(d), which reveals that a uniformly repetitive oscillation was successfully obtained at 56 MHz.

Another interesting passive mode-locking technique is stretched pulse mode-locking [6,7], in which the fiber cavity consists of two fibers with different group

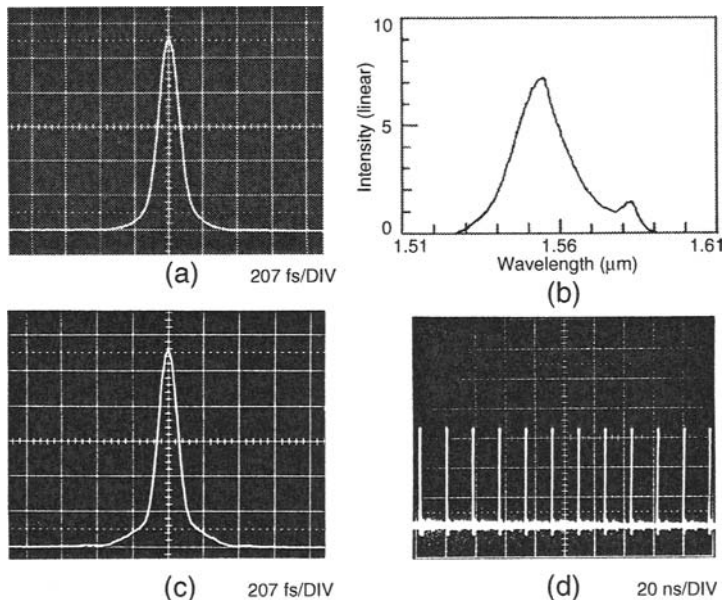

Fig. 3. Output characteristics of the passively mode-locked fiber laser using NPR. (a): 145 fs autocorrelation waveform for a pump power of 63 mW, (b): corresponding spectrum, (c): shortest pulse waveform of 136 fs for a pump power of 74 mW, and (d): stable repetitive feature of the output pulse (the repetition rate is 56 MHz). The spectrum in (b) has the appearance of a continuum profile, but it is due to a mode separation of as small as 56 MHz.

velocity dispersions (GVDs). One is a fiber with large normal GVD and the other is a fiber with large anomalous GVD. It has been shown that a high energy pulse can survive in such a cavity as a steady-state pulse, which is related to dispersion-managed soliton transmission [17–19]. Recently, these passively mode-locked fiber lasers have attracted considerable interest in relation to an optical frequency comb (application to frequency standards and direct measurement of optical frequency) and an optical sampling scope [20].

2.2. *Actively Mode-Locked Fiber Laser*

An actively mode-locked fiber laser consists of a mode-locker for shaping a pulse in the cavity, a signal source that generates RF whose frequency is equal to a longitudinal mode spacing (the free spectral range of the fiber cavity), an active medium, and a bandwidth-limiting optical filter. Active mode-locking can be achieved in two ways. One is mode-locking at a fundamental frequency, in which there is only one pulse in the cavity at any one time. In this case the repetition rate is limited by the fiber length. If the cavity length is increased, the repetition rate becomes low. When the fiber cavity is shortened, as with the mode-locking of laser diodes, this eliminates such advantages

as the inclusion of fiber nonlinearity. The other interesting way of achieving active mode-locking is mode-locking at higher harmonics of the fundamental mode spacing. This technique is particularly useful as it provides high repetition-rate pulses even in long cavities.

If we are to realize ultrahigh-speed optical communication, we need stable optical short pulse sources that operate in the GHz region. In this sense, a harmonically and actively mode-locked fiber laser is simple to construct and can easily produce pulses shorter than 10 ps in the GHz region [8,9]. With conventional harmonic active mode-locking, a synthesizer is used to generate an RF signal, which drives the modulator. This modulation frequency is tuned to a high harmonic of the fundamental cavity frequency. If the modulation frequency of the synthesizer is not equal to a harmonic of the fundamental frequency, the phases of the cavity modes are not locked and eventually unstable pulsation occurs. When temperature variations and/or mechanical vibrations are applied to the cavity, the cavity length or the fundamental cavity frequency changes. This causes a mismatch between the modulation frequency and the cavity modes. A conventional harmonic actively mode-locked fiber laser that operates in the GHz region is especially sensitive to temperature variations and/or mechanical vibrations because the cavity length (a few meters to hundreds of meters) is typically longer than that of other mode-locked lasers. Therefore, it is possible to generate clean pulses for a short period, but it is difficult to maintain an optimum operational condition over a long period.

3. Harmonically and Regeneratively Mode-Locked Fiber Lasers

3.1. Laser Configuration and Output Characteristics

Difficulties that accompany conventional harmonic mode-locking can be overcome with a regenerative mode-locking technique [11]. Figure 4 shows a regeneratively mode-locked erbium-doped fiber laser with a repetition rate of 10 GHz. This laser consists of a polarization-maintaining erbium-doped fiber (PM-EDF), a WDM coupler, a polarization-maintaining dispersion-shifted fiber (PM-DSF), a 15% output coupler, a polarization dependent isolator, a $LiNbO_3$ intensity modulator and an optical bandpass filter. The pumping source is 1.48 μm laser diodes. The dispersion-shifted fiber is 180 m long and the group velocity dispersion (GVD) is 3.3 ps/km/nm. The optical filter has a bandwidth of 2.5 nm. All the fibers in the cavity are polarization-maintaining to prevent polarization fluctuation. The clock extraction circuit is composed of a high-speed photodetector, a high Q dielectric filter ($Q \sim 1400$) and a high gain amplifier. The center frequency of the dielectric filter is set at 10 GHz.

Part of the laser output beam is coupled into the clock extraction circuit. A longitudinal self-beat signal near 10 GHz, which is one of the harmonic longitudinal modes of the cavity, is detected with the clock extraction circuit. This harmonic beat signal is amplified through an electrical amplifier and fed back to the $LiNbO_3$ intensity modulator. The phase between the pulse and the clock signal is adjusted using a phase controller.

The laser starts from noise and regenerative mode-locking is accomplished automatically by adjusting the phase between the pulse and the clock signal. Once mode-locking is achieved, stable operation continues for a long period because the clock signal always follows the changes in the cavity length.

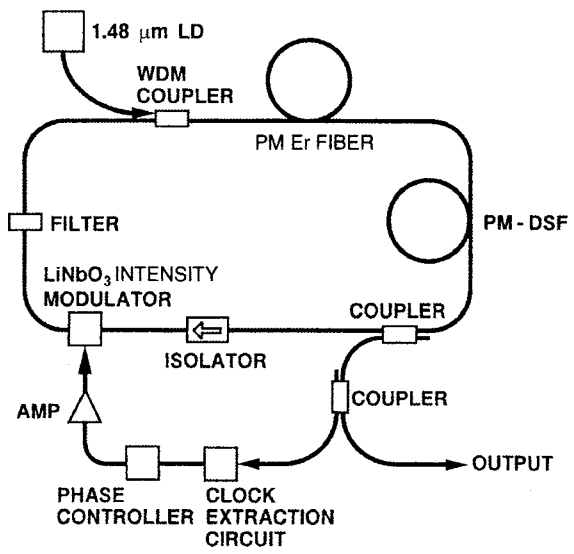

Fig. 4. Configuration of a regeneratively and harmonically mode-locked erbium-doped fiber laser operating at a repetition rate of 10 GHz. AM mode-locking is used in the unidirectional ring cavity.

Figure 5 shows the laser oscillation characteristics at 10 GHz. An autocorrelation waveform of the output pulse for a pump power of 50 mW is shown in Fig. 5(a). The pulse width was 2.7 ps. The corresponding spectrum is shown in Fig. 5(b). The center wavelength was 1.552 μm and the spectral width was 1.0 nm. The fine structure with a spectral separation of 0.08 nm corresponds to a longitudinal mode separation of 10 GHz. The bandwidth-pulse width product is 0.34, indicating that the output pulse is almost a transform-limited sech pulse. Figure 5(c) shows the extracted clock spectrum. It is important to note that there is no other spectrum (supermode) or parasitic noise in Fig. 5(c).

3.2. Phase-Locked-Loop (PLL) Operation and Repetition-Rate Stabilization

As described in section 3.1, regenerative mode-locking is accomplished by feeding back the self-beat signal. Thus, complete mode-locking is achieved automatically because an ideal feedback signal, which reflects the instantaneous frequency change between the longitudinal beats, is used as the modulation frequency, even when large perturbations are applied.

The otherwise excellent regenerative mode-locking technique has one drawback, which is that the repetition rate fluctuates with time in a free-running condition when the optical path length in the cavity is not stabilized. Therefore, there is an urgent need to stabilize the repetition rate of the regeneratively mode-locked fiber laser at a fixed frequency. For this purpose an offset locking technique was developed in which

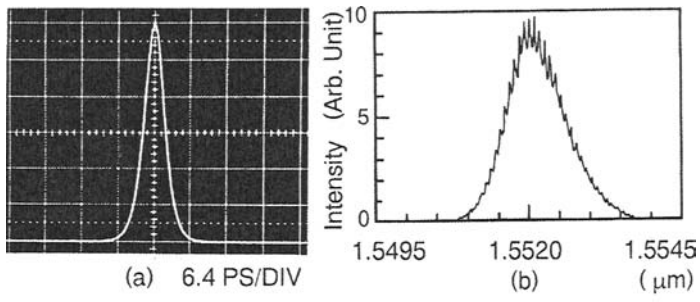

Fig. 5. Oscillation characteristics of a 10 GHz regeneratively and harmonically mode-locked fiber laser. (a) an autocorrelation waveform of the output pulse for a pump power of 50 mW, (b) corresponding spectrum (the resolution is limited by the spectrum analyzer), (c) extracted 10 GHz clock spectrum.

the repetition rate is stabilized at a fixed frequency [21]. The repetition rate stability thus obtained was better than 1×10^{-9}, and this value was mainly determined by the stability of the synthesizer. However, with this scheme, it was still not possible to lock the repetition rate to an external clock signal with a zero offset frequency. There have been several interesting reports on the repetition rate stabilization of fiber lasers [22,23].

Here, we describe the phase-locked-loop (PLL) operation of a fiber laser that uses a voltage controlled regenerative mode-locking technique [24]. The key to success is that the regeneratively mode-locked fiber laser, whose cavity length is controlled with a PZT on which part of the fiber cavity is wound, operates as an optical voltage controlled oscillator (OVCO). A basic PLL generally consists of a self-oscillatory circuit such as a voltage controlled crystal oscillator (VCO), a mixer, a synthesizer (as an external clock), and a feedback control circuit. To date, in order to achieve PLL operation in a mode-locked fiber laser, an external clock signal had to be simultaneously fed back to the laser cavity to maintain the oscillation. Without the modulation signal, oscillation was not completed. That is, no voltage-controlled self-oscillatory laser, such as an electrical VCO at microwave frequencies, has been reported. However, a regeneratively mode-locked fiber laser operates as an OVCO when part of the fiber

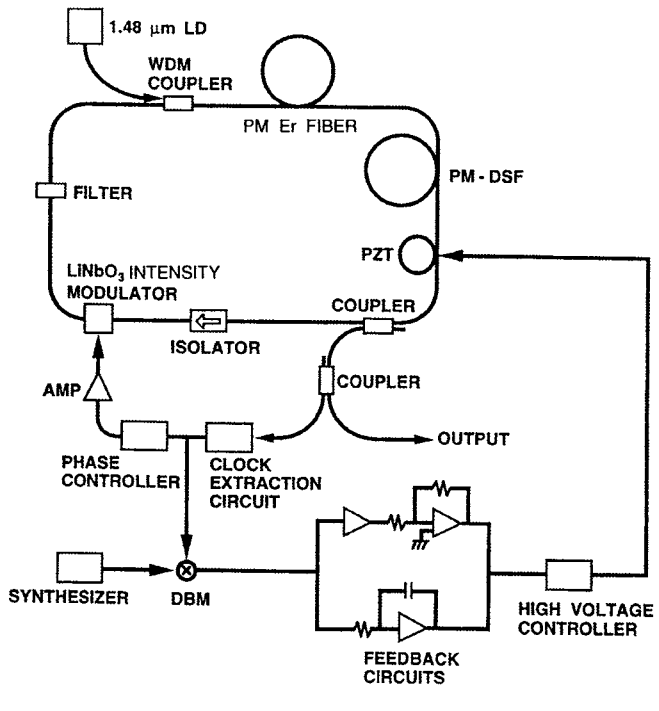

Fig. 6. Experimental set-up for a phase locked loop (PLL) fiber laser using voltage controlled regenerative mode-locking. The repetition rate is 10 GHz.

cavity is wound on a PZT and the cavity length is tuned by applying a DC voltage to the PZT.

The configuration for a PLL fiber laser using voltage controlled regenerative mode-locking is shown in Fig. 6. This laser operates as a harmonically mode-locked fiber laser where part of the fiber cavity is wound on a PZT so that the repetition rate of the regenerative laser can be varied by applying a DC voltage. That is, this oscillator is an optical self oscillatory circuit (OVCO) in which the repetition rate changes very smoothly when the DC voltage is changed.

To achieve PLL operation, a sinusoidal clock signal from the laser is mixed with a signal from a synthesizer and its beat frequency is set at nearly zero. That is, if the laser clock signal has the same frequency as the synthesizer and the phase difference between the laser clock and the synthesizer is $\theta(t)$, the output signal from the double-balanced mixer (DBM) becomes $\sin(\theta(t))$ when there is an appropriate phase bias between the laser clock and the synthesizer. In this case, the phase retardation of the laser clock is linearly converted to a voltage signal, which can be utilized as an error signal for phase change detection. This signal is fed back to the PZT after proportional or integral control. It is important to note that there is no need to install a phase controller to obtain a $\sin(\theta(t))$ signal as the regenerative laser itself is automatically phase-shifted.

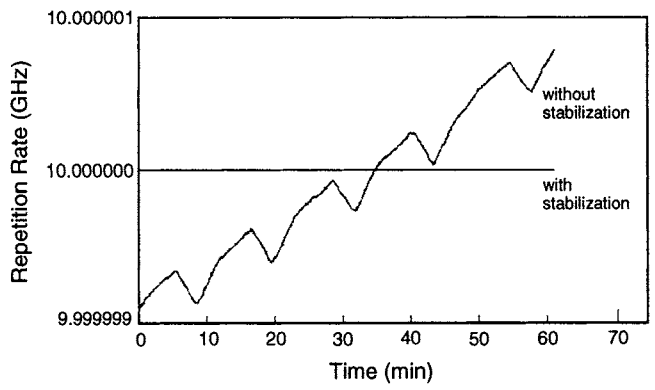

Fig. 7. Change in the repetition-rate frequency of a mode-locked fiber laser with and without PLL operation.

Once the system is locked, the laser repetition rate will accurately track that of the synthesizer by tuning the cavity length such that $\theta(t)$ is always zero.

The laser cavity configuration was almost the same as that described in Fig. 4 except for the PLL. Part of the fiber cavity is wound on a PZT in order to change the cavity length by applying a voltage signal. When the voltage applied to the PZT is changed, the repetition frequency change per volt is 120 Hz/V. The PLL circuit comprises a frequency synthesizer, a double balanced mixer, proportional and integral feedback circuits, and a high voltage controller. Thus, by feeding this error signal back to the PZT after it has passed through a proportional and integral control circuit, the repetition rate of the laser is PLL-stabilized. Although the use of the PLL is similar to that described in [22], the synthesizer signal has to be simultaneously fed back to the laser modulator itself, which does not form an OVCO.

Figure 7 shows the change in the repetition-rate frequency with time. Without PLL stabilization, there was a frequency difference of approximately 2–10 kHz over the course of an hour with a temperature change of 0.5 deg. However, when the laser was PLL-stabilized, the repetition rate was completely locked to that of the synthesizer within the stability of the synthesizer itself. The repetition rate stability was better than 1×10^{-9} and the tracking range was approximately 40 kHz. The resolution of the counter was better than 7×10^{-10}. As the frequency stability of the synthesizer is the same as that of the output repetition rate, the stability of the repetition rate is mainly determined by the synthesizer itself.

The single polarization average output power was 1.5 mW and the output pulse width was 5.7 ps. An output waveform monitored with an autocorrelator is shown in Fig. 8(a) and its spectral profile is shown in Fig. 8(b). A fine structure, which indicates a mode separation of 10 GHz, is clearly seen in Fig. 8(b). The spectral width of the output pulse is 0.6 nm, resulting in a pulse width-bandwidth product of 0.43. The 10-GHz clock extracted from the laser output is shown in Fig. 8(c) and a pulse waveform monitored with a high-speed photodetector is shown in (d). As shown in (c) and (d), the

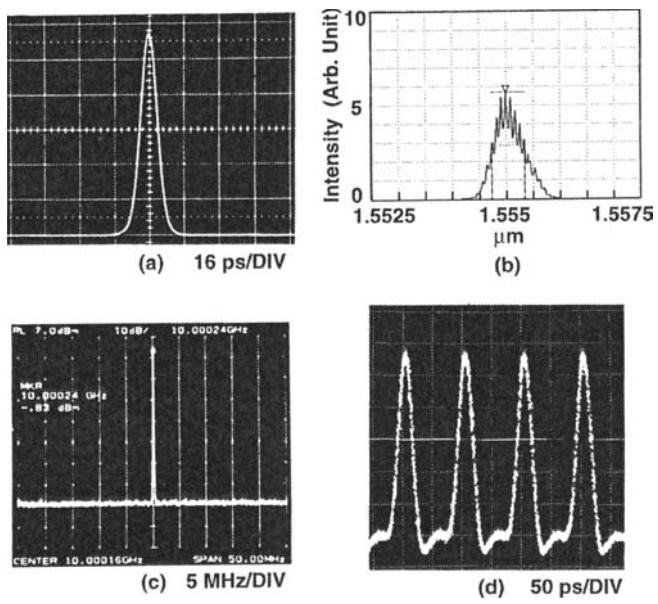

Fig. 8. Output characteristics of a 10-GHz PLL regeneratively mode-locked fiber laser. (a) output waveform monitored with an autocorrelator, (b) corresponding spectral profile, (c) extracted 10 GHz clock, and (d) pulse waveform electrically monitored with a high-speed photodetector.

amplitude of the pulse train is very stable and the pulse train contains no supermode noise (see details in section 3.3).

This PLL regeneratively mode-locked laser is highly advantageous as a data transmission source and can be used to provide a control pulse for demultiplexing and for many optical measurement techniques.

3.3. Suppression of Supermode Noise in Harmonic Mode-Locking

When a fiber laser is harmonically mode-locked, many longitudinal modes appear and the amplitude of the output pulse fluctuates with time. Because the recovery time of the erbium amplifier is of the order of 10 ms (the lifetime of $^4I_{13/2}$), there is no high-speed gain response that recovers within the repetition rate. Therefore, a fluctuation induced by amplified spontaneous emission (ASE) noise results in a steady-state non-uniform amplitude. This noise is called supermode noise. Several techniques have been reported for removing the noise [25,26]. In this section, we report that the combination of SPM and spectral filtering provides a fast intensity dependent loss in the cavity, which equalizes the pulse energies and completely suppresses the supermode noise [27].

Here, we describe how the noise is removed. First, we prepare two types of harmonically mode-locked fiber lasers operating at 10 GHz. One is an ordinary actively

mode-locked erbium fiber laser, in which a synthesizer supplies the mode-locking frequency, which is one of the harmonic cavity modes. The other is a regeneratively mode-locked erbium fiber laser [11]. We prepared two polarization-maintaining fiber cavities with different lengths. The cavities were 27 and 220 m long and are denoted as "short" and "long" cavities, respectively. A 2.5-nm optical filter was installed in both configurations.

The mode-locking characteristics of the short cavity laser are shown in Fig. 9. The oscillation wavelength is 1.552 μm. Figures 9 (a-1), (a-2), and (a-3) show the pulse peak envelope, electrical spectrum, and optical spectrum of the output pulse train of the actively mode-locked fiber laser, respectively. Figures 9 (b-1), (b-2) and (b-3) are the corresponding measurements for the regeneratively mode-locked laser. Both output pulse widths are 7.0 ps. It is clearly seen in both Fig. 9 (a-2) and (b-2) that a lot of supermode noise appears and it is impossible to remove. Because of the many supermodes, the pulse train amplitudes have unequal pulse energies as shown in Figs. 9 (a-1) and (b-1). In both cases, the peak power inside the cavity is 280 mW. The spectral width of the output pulse is 20% of the filter bandwidth and the nonlinear phase shift is as small as $\pi/100$ rad. Thus these lasers are operating in the linear regime. The time-bandwidth product is 0.44, which means that the output pulses are transform-limited Gaussian pulses.

However, with a long cavity, the situation is completely different. These results are shown in Fig. 10. The oscillation wavelength was also set at 1.552 μm at which the GVD is 3 ps/km/nm in the anomalous region. Figures 10 (a-1), (a-2), and (a-3) show the pulse peak envelope, electrical spectrum, and optical spectrum of the output pulse train from the actively mode-locked fiber laser, respectively. Figures 10 (b-1), (b-2) and (b-3) are the corresponding measurements for the regeneratively mode-locked laser. In both cases, the output pulse width has shortened to 3.0 ps. As seen in Figs. 10 (a-2) and (b-2), the supermode noise disappears completely and a single line is clearly seen at 10 GHz. Correspondingly, the amplitude of the output pulse train is very stable (Figs. 10 (a-1) and (b-1)), which also suggests that there is no supermode noise. In both cases, the peak power of the pulse inside the cavity is 420 mW, which corresponds to an $N = 1.15$ soliton. The spectral width of the output pulses is approximately 36% of the filter bandwidth and the estimated nonlinear phase shift is approximately $\pi/7$ rad. The time-bandwidth products are 0.34 and the output pulses are close to sech pulses.

The physical interpretation of supermode noise suppression is as follows. When the peak power of the pulse in a long cavity increases through the AM mode-locking process, SPM is generated and the wing of the pulse is frequency chirped. However, the spectral component with a large amount of chirp, which is located at the wings of the pulse in the time domain, is removed by passing it through an optical filter. Thus the pulse can be shortened by a combination of SPM and the filter. It is important to note that the filter also limits the spectral width of the pulse. Therefore, the peak intensity of a high power pulse with a short pulse width is eventually limited to within the filter bandwidth. That is, the energy at the pulse centers shifts to the wings due to SPM and is eliminated by the filter. Hence, the pulse amplitude is clipped to a certain intensity level at which the pulse energy is stabilized when the pulse spectral width reaches a certain ratio of the filter bandwidth. This process acts as an intensity dependent gain limit or loss increase.

Under such a condition, if the pulse amplitude is further increased by perturbations, the excess pulse energy is eliminated by the combination of the filter and the excess

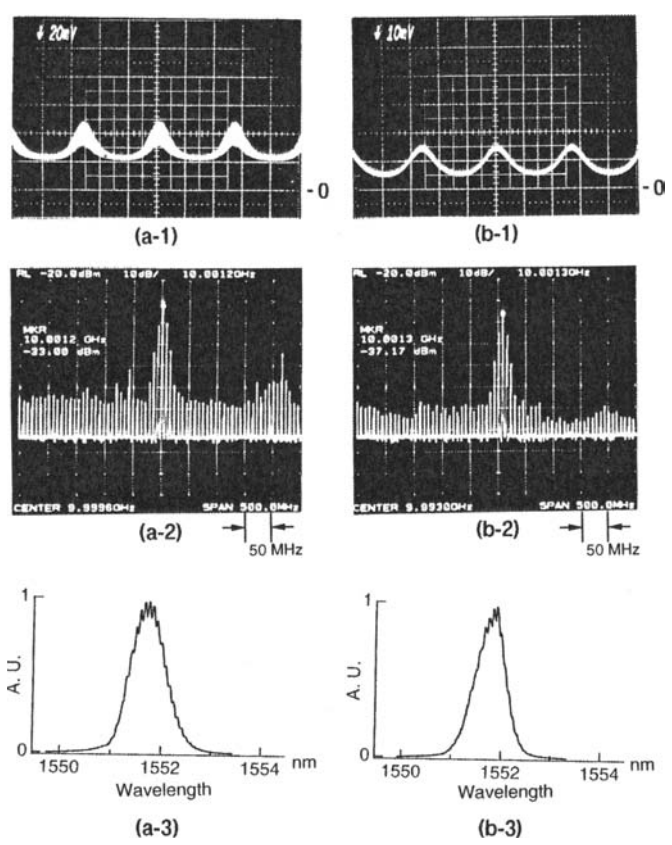

Fig. 9. Mode-locking characteristics of the short cavity laser (27 m). (a-1), (a-2), and (a-3): the pulse peak envelope, electrical spectrum, and optical spectrum of the output pulse train of an ordinary actively mode-locked fiber laser, respectively. (b-1), (b-2) and (b-3): the corresponding measurements for the regeneratively mode-locked laser. Supermode noise appears in (a) and (b).

SPM. By contrast, if the pulse amplitude decreases, the pulse energy is increased by the filter and the smaller SPM (a smaller spectral width experiences a smaller loss through the filter). A pulse with a small amplitude automatically builds up through the erbium gain and is shortened through the AM modulator until the SPM becomes effective. Thus, there is a steady state condition with a fixed amplitude, which means that the supermode noise can be suppressed. When the SPM is strong enough, stabilization occurs. Therefore it is important to make the cavity long enough to generate sufficient SPM.

The supermode noise appeared when the cavity was shorter than 100 m, but when the peak intensity was doubled, the noise was suppressed as in the 220-m cavity. This means that the nonlinear phase shift plays an important role in suppressing the supermode noise. Furthermore, when the 2.5-nm filter is removed, the supermodes

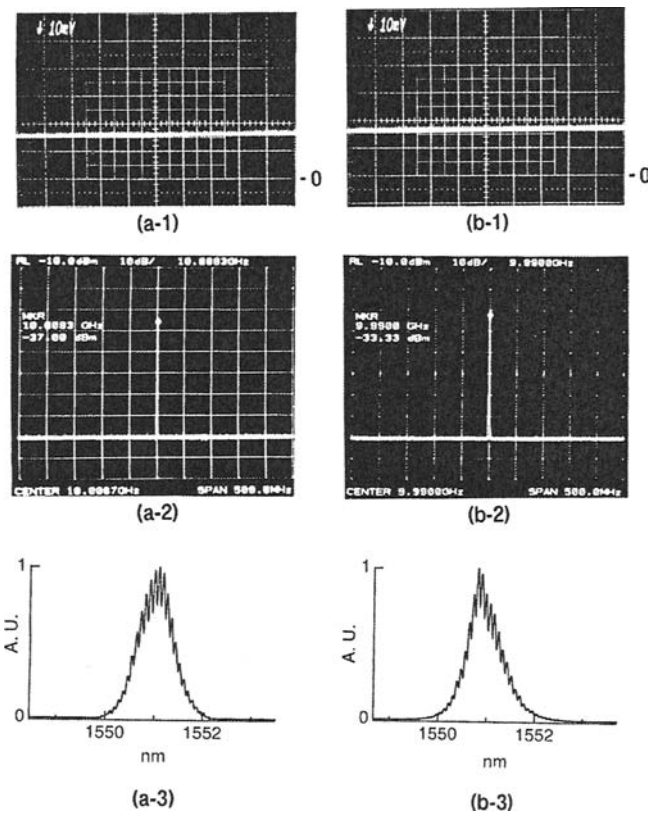

Fig. 10. Mode-locking characteristics of the long cavity laser (220 m). (a-1), (a-2), and (a-3): the pulse peak envelope, electrical spectrum, and optical spectrum of the output pulse train of an ordinary actively mode-locked fiber laser, respectively. (b-1), (b-2) and (b-3): the corresponding measurements for the regeneratively mode-locked laser. Supermode noise are suppressed in (a) and (b).

appear even in the "long" cavity, which means that the filter also plays an important role in limiting the energy and stabilizing the pulse.

We have also examined the GVD dependence of the supermode noise suppression by changing the carrier wavelengths to anomalous, zero, and normal GVDs. There was no significant change for the three regimes. However, strictly speaking, soliton standardization can be achieved in the anomalous GVD regime by using a filter [28], resulting in better stability. In the normal GVD region, if the pulse width is broadened and the peak intensity is lower than that of the soliton, the noise suppression becomes weaker. However, as long as the peak intensity is sufficient to generate SPM, suppression can be achieved.

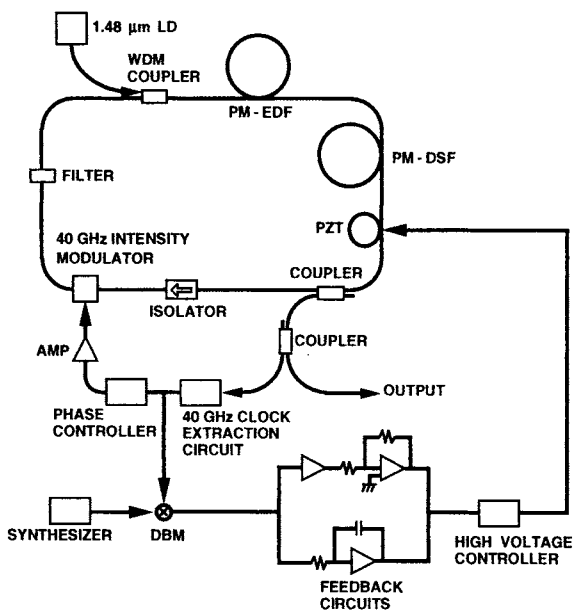

Fig. 11. Experimental setup for a 40 GHz regeneratively and harmonically AM mode-locked fiber laser with a 0.9-ps pulse width. PLL operation was employed.

3.4. 40-GHz Regeneratively and Harmonically PLL Mode-Locked Fiber Laser

Recently many 40 Gbit/s optical transmission experiments [29,30] have been reported because electronics at 40 Gbit/s has matured. A stable optical pulse source at such a high repetition rate is very desirable for future ultrafast TDM and WDM optical transmissions. This section describes a 40-GHz regeneratively mode-locked fiber laser, where the laser was also locked to an external signal by a phase-locked loop (PLL) operation [24].

The configuration of the PLL 40-GHz laser is shown in Fig. 11. The laser consists of a PM-EDF, a WDM coupler, a PM-DSF, a 10% output coupler, a polarization dependent isolator, an LN intensity modulator and a 5-nm optical bandpass filter. The average GVD of the cavity was 1 ps/km/nm at 1.55 μm. The cavity length was 230 m. Part of the laser output was coupled into the clock extraction circuit, which was composed of a uni-traveling-carrier (UTC) PD [31], a high Q electric filter ($Q \sim 1200$) with a center frequency of 40 GHz and a high-gain amplifier. A longitudinal self-beat signal near 40 GHz was detected with the clock extraction circuit and fed back to the intensity modulator.

Figure 12 shows typical output pulse characteristics. Figures 12(a) and (b) are autocorrelation waveforms. Figure 12(a) shows the repetitive feature of the output pulse. The interval between the two pulses is 25 ps, which corresponds to a repetition rate of 40 GHz. Figure 12(b) is the expanded waveform of 12(a) and the pulse width is as short as 0.9 ps. Figure 12(c) is an optical spectrum. The spectrum has a symmetric profile and the longitudinal modes of 40 GHz (0.32 nm in the frequency domain) are

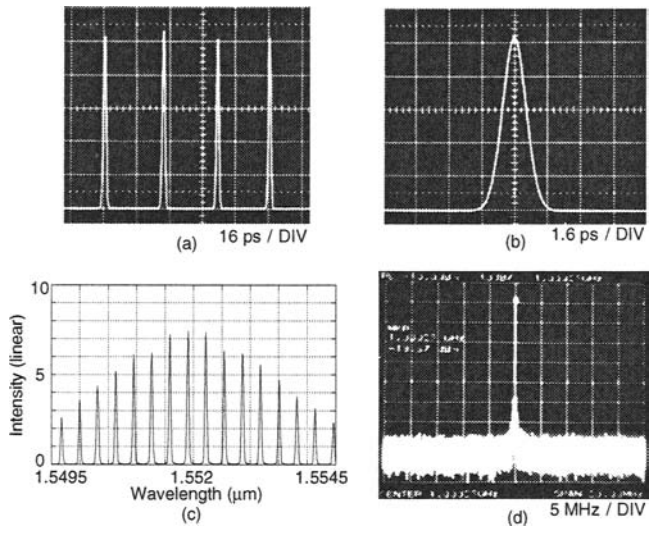

Fig. 12. Typical output pulse characteristics of a 40-GHz regeneratively AM mode-locked fiber laser. (a) repetitive feature of the output pulse, (b) expansion waveform of (a), (c) optical spectrum, (d) 1 GHz beat RF spectrum obtained from the difference between a 40 GHz original clock signal and a 39-GHz synthesizer signal.

clearly seen. The center wavelength is 1.552 μm and the spectral width is 2.7 nm. Thus, the bandwidth-pulse width product ($\Delta\nu\Delta\tau$) is 0.3, which indicates that the output pulse is close to a transform-limited sech pulse. The shortest pulse width of 0.9 ps was obtained for a pump power of 110 mW. The average output power was 3.9 mW. Figure 12(d) is a 1-GHz beat RF spectrum that we obtained from the difference between the 40-GHz original clock signal and a 39-GHz synthesizer signal. There was only one clock component and the supermode noise was suppressed to 70 dB down from the peak.

3.5. Jitter Characteristics of a 10-GHz Regeneratively Mode-Locked Fiber Laser

This section describes the timing jitter and pulse energy fluctuations of the output pulse of a regeneratively mode-locked fiber laser. We measured the single-sideband (SSB) phase noise to evaluate timing jitter [32]. The noise power spectrum of the output pulse of the laser was measured electrically with a high speed photodetector and an RF spectrum analyzer. The noise spectrum, which appears on the wing of the carrier frequency peak, corresponds to timing jitter and amplitude fluctuation. Figure 13 shows SSB noise versus frequency offset from the 10-GHz carrier frequency. Figure 13(a)-(c) correspond to the synthesizer, PLL fiber laser, and free-running fiber laser, respectively. The integration region of the SSB spectrum is from 100 Hz to 10 MHz. The low frequency end is set at 100 Hz in consideration of the resolution bandwidth of the spectrum analyzer.

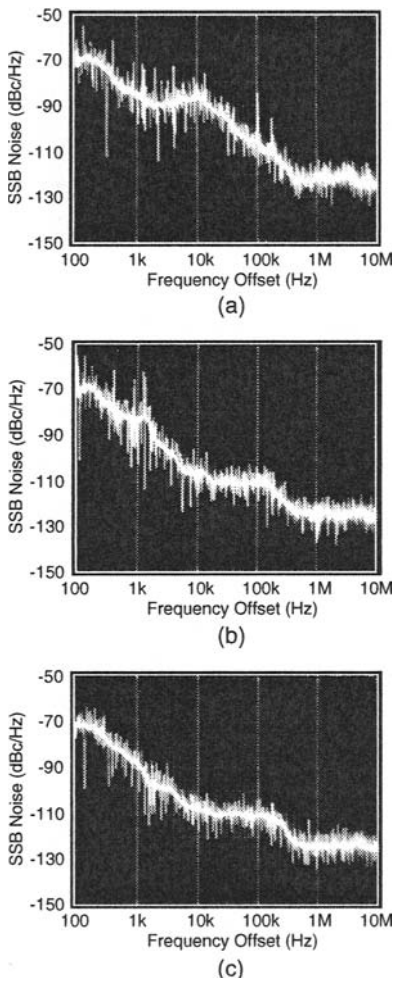

Fig. 13. Single side band (SSB) phase noise of the repetition rate frequency versus frequency offset from the 10-GHz carrier frequency. (a) the synthesizer, (b) PLL fiber laser, and (c) free-running fiber laser. The estimated jitter values for the corresponding SSB noise are 180, 120, and 90 fs, respectively.

The timing jitter of the synthesizer (a) is estimated to be 180 fs from this data. By contrast, the timing jitter of the PLL laser and the free-running laser are as low as 120 and 90 fs, respectively. The timing jitter of the PLL laser is lower than that of the synthesizer. This is because the high-frequency jitter components in the synthesizer are not fed back to the laser cavity since the response frequency of the PLL is several kHz, which is limited by the PZT response time. The SSB phase noise of the high-frequency components at frequencies greater than 10 MHz is less than 120 dBc/Hz and

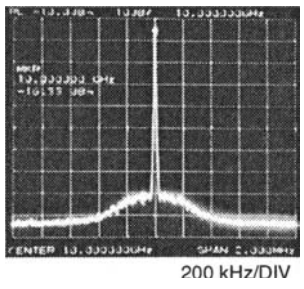

Fig. 14. The first-order (10 GHz) RF power spectrum of the output pulse from a 10-GHz PLL laser.

the contributions of these components to the timing jitter and/or amplitude fluctuations are negligible.

To confirm the above results, we made a second jitter measurement as described below. According to [33], the pulse energy fluctuation and the timing jitter are related to the ratio of the noise band power to the carrier peak power P_1 in the nth-order component as follows:

$$\Delta E/E = [(P_2/P_1)_{n=0}\Delta f_A/\Delta f_{\text{res}}]^{1/2} \tag{1}$$

$$\Delta T/T = (2\pi n)^{-1}[(P_2/P_1)_n \Delta f_J/\Delta f_{\text{res}}]^{1/2}, \tag{2}$$

where Δf_A, Δf_J, and Δf_{res} are the energy noise bandwidth, timing jitter bandwidth, and resolution bandwidth, respectively. All widths correspond to the full-width at half-maximum (FWHM). When the timing jitter is assumed to be small ($\Delta T/T \approx 0.1\%$ from Fig. 13), $\Delta E/E$ can be approximated as $[(P_2/P_1)_{n=1}\Delta f_A/\Delta f_{\text{res}}]^{1/2}$ [34].

The first-order (10 GHz) RF power spectrum of the output pulse from a PLL laser is shown in Fig. 14. The span range and the resolution bandwidth Δf_{res} are 2 MHz and 3 kHz, respectively. With $(P_2/P_1)_{n=1} = 2.0 \times 10^{-8}$ and $\Delta f_A = 400$ kHz, we have $\Delta E/E = 1.6 \times 10^{-3}$. It is important to note that the amplitude stability is very high although the fiber laser operates at a high harmonic. This is because we use a pulse energy stabilization mechanism, which is a combination of SPM and spectral filtering as described in section 3.3. There was no difference between the PLL and free-running operation as regards energy fluctuation.

Figure 15 shows the 10-GHz RF power spectrum of the output from the synthesizer, the output pulse from the PLL laser, and that from the free-running laser. The span range and the resolution bandwidth are 5 kHz and 30 Hz, respectively. Single-scan detection only is used in Fig. 15(c) because the carrier frequency changes slightly during free-running operation. The dashed lines in Figs. 15(b) and (c) represent approximated noise bands. Under free-running operation, the ripples that appeared in Figs. 15(a) and (b) disappeared completely, as shown in Fig. 15(c). From the RF spectrum shown in Fig. 15(b), we can roughly estimate that $\Delta T/T = 1.2 \times 10^{-3}$. The pulse interval T is 100 ps. Thus, the PLL fiber laser exhibits a timing jitter of approximately 120 fs. In the same way, by using the values of $(P_2/P_1)_{n=1} = 2.0 \times 10^{-6}$ and $\Delta f_J = 400$ Hz in the RF spectrum shown in Fig. 15(c), we can estimate that $\Delta T/T = 0.8 \times 10^{-3}$ and

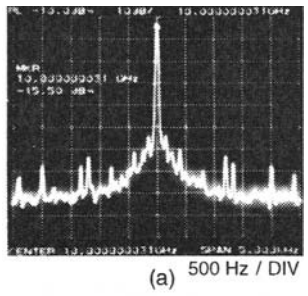
(a) 500 Hz / DIV

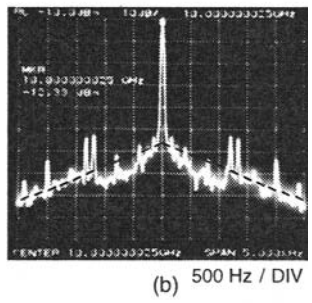
(b) 500 Hz / DIV

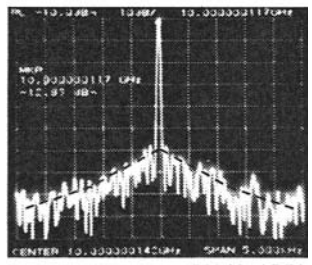
(c) 500 Hz / DIV

Fig. 15. 10-GHz RF power spectrum of the output from the synthesizer, the output pulse from the PLL laser, and that from the free-running laser. (a) synthesizer, (b) output pulse under PLL, and (c) output pulse under free-running condition.

that the timing jitter is approximately 80 fs for a free-running fiber laser. We obtained the same results even with $n = 2$ (20 GHz). The results estimated in Fig. 15 agree well with the results obtained in Fig. 13.

4. Topics in High-Speed Fiber Lasers

4.1. FM Mode-Locking of High Repetition-Rate Fiber Laser

We have shown that the output pulse of a regeneratively and harmonically mode-locked fiber laser has excellent characteristics such as a short pulse width, long term stability,

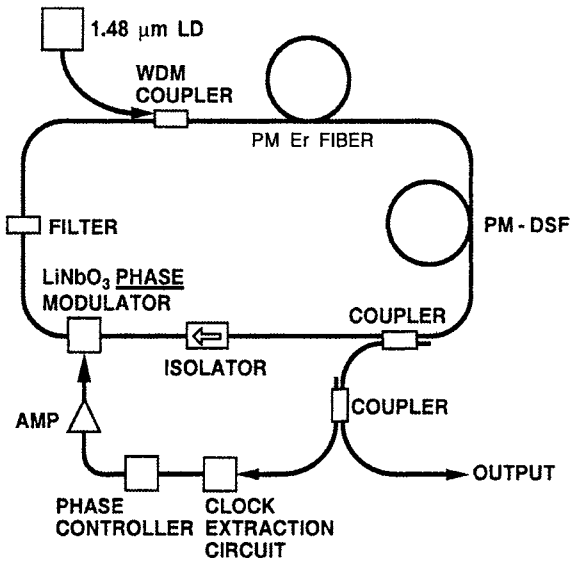

Fig. 16. Experimental set-up for the harmonically and regeneratively FM mode-locked fiber laser. A phase modulator is used instead of an intensity modulator.

and high spectral quality. An alternative approach to active mode-locking is FM mode-locking, which applies FM (phase) modulation to a cavity [35]. A phase modulator is more attractive than an amplitude modulator because it has no DC bias, which is highly advantageous as the laser is free from the DC bias drift of the modulator. Figure 16 shows the configuration of a 10-GHz harmonically and regeneratively FM mode-locked fiber ring laser. For the regenerative FM mode-locking, we replace the intensity modulator with a phase modulator. The insertion loss and V_π modulator are 3.0 dB and 5.5 V, respectively.

The output characteristics are shown in Fig. 17. A single polarization average output power of 0.8 mW was obtained at 10 GHz. The pulse width was 2 ps. Figure 17(a) shows a typical output waveform monitored with an autocorrelator and its spectral profile is shown in Fig. 17(b). The spectral width of the 2 ps output pulse was 1.4 nm, resulting in a pulse width-bandwidth product of 0.34, which means that the output pulse is nearly a sech pulse. Optimum operation was achieved by adjusting the phase controller. The extracted clock spectrum and a pulse waveform monitored with a high-speed photodetector and a sampling scope are shown in Fig. 17 (c) and (d), respectively.

The optical filter cuts off the wings of the pulse because the wing has a different spectral component due to the chirp caused by the FM. This is the main feature of the mechanism (FM mode-locking) that shapes the pulse in the time domain by means of phase modulation and an optical filter. Although one might think that a shorter pulse could be generated by using a narrower filter, instead it causes a larger decrease in the pulse amplitude, resulting in a decrease in the SPM in the cavity. In this case, stable

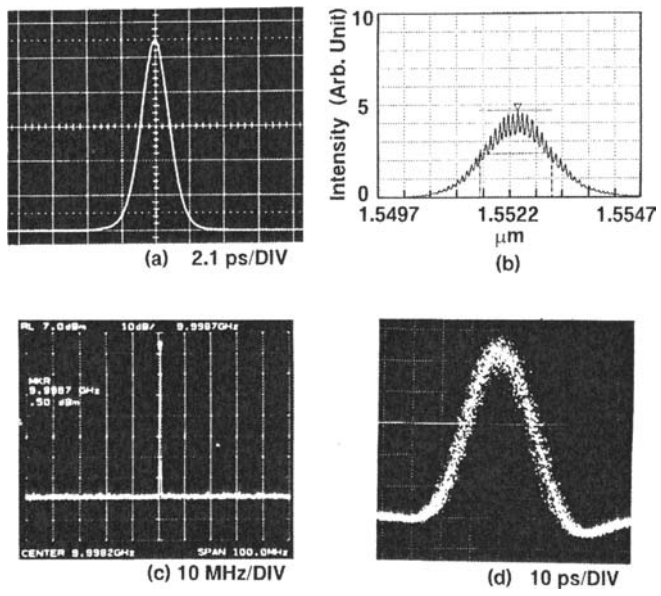

Fig. 17. Output characteristics of an FM mode-locked fiber laser. (a) typical output waveform monitored with an autocorrelator, (b) its spectral profile, (c) extracted clock spectrum, and (d) a pulse waveform monitored with a high speed photodetector.

pulse oscillation cannot be obtained. Therefore there is an optimum filter bandwidth that can maintain a stable pulse amplitude (energy) when the chirp slope is given.

One difficulty with FM mode-locked lasers is that the pulses can be generated equally well at either of the two phase positions (up- and down-chirp) that are 180 deg. apart relative to the modulation signal. Therefore, it is well known that the pulses of FM mode-locked pulses tend to jump back and forth between the two phase states; up-chirp and down-chirp [36]. However, such unstable operation does not occur for the following reason. When the fiber cavity has GVD, there is another pulse compression mechanism in addition to the phase modulator and the optical filter. When the GVD is anomalous, the up-chirped pulse caused by the phase modulator is compressed without loss, while the down-chirped pulse is broadened. The broader pulse has a larger chirp as a result of the modulation, which experiences a larger loss through the filter. Therefore, only the up-chirped modulation is stable. By contrast, when the fiber cavity has a normal GVD, the down-chirped pulse is compressed and experiences a smaller loss than the up-chirped pulse. Thus, the down-chirped pulse is stable.

When the peak intensity of the pulse increases, SPM inevitably occurs in a long fiber cavity. Therefore, the up- and down-chirp caused by the FM modulation is greatly modified. That is, there are two ways of applying an imbalanced FM modulation to a long cavity. One is where the up-chirped modulation produced by the phase modulator is in-phase with the chirp caused by the SPM. In this case, the total chirp is increased and the pulse in the cavity is further compressed by anomalous GVD. That is, the

soliton effect helps to generate a shorter pulse. The other way is where the phase modulator produces a down-chirp, and here the chirping is out-of-phase with the chirp caused by the SPM. In this case, the total down-chirp is reduced and this weakens both the pulse formation via phase modulation and filtering, and the soliton effect. Therefore, the pulse is not efficiently shortened by the FM modulation and eventually disperses out. These mechanisms explain why stable harmonic FM mode-locking is achieved in the present laser.

4.2. *Direct Generation of Subpicosecond Pulses at 10 GHz From a Fiber Laser*

This section describes the direct generation of a 750-fs, 10-GHz pulse train from a regeneratively mode-locked fiber laser, which has two synchronized amplitude modulations at 10 and 20 GHz [37]. As the two modulators are synchronized, the pulse repetition rate is determined by the lower repetition (10 GHz), while the pulse width is determined by a mixture of 10 and 20 GHz.

Figure 18 shows a regeneratively mode-locked fiber laser with two synchronized intensity modulators. To generate a shorter pulse train at the same repetition rate with active mode-locking, it is important to have a sharper curvature at the modulation peak. A higher modulation frequency gives a shorter pulse width [36,38]. This means that by applying a new modulation frequency that is an integral multiple of the harmonic mode-locking frequency to the fiber cavity, we can shorten the pulse width while keeping the repetition rate at the original frequency. Here it is important to synchronize the two modulations. To achieve this, an extracted original clock signal at 10 GHz is frequency-doubled and fed back to the other intensity modulator, which operates at 20 GHz. The phase of the 20-GHz electrical signal is adjusted so that the modulation peak at 20 GHz always passes through the modulation peak at 10 GHz. Thus the pulse experiences a larger pulse shortening velocity than that of the 10-GHz modulator. Let the fundamental modulation frequency ω and its harmonic modulation be $m\omega$. Then, the pulse width under multiple harmonic modulation, τ is shortened to $\tau = \tau_0/\sqrt[4]{(m^2+1)}$. Here τ_0 is the output pulse width of the mode-locked fiber laser with a single modulator having a modulation frequency of ω. The pulse width is expected to be shortened to 740–800 fs as m is 2.

The laser we constructed was an ordinary regeneratively mode-locked fiber laser with two modulators and a 7-nm optical filter. The experimental results are shown in Fig. 19. Figures 19 (a), (b) and (c) are an autocorrelation trace of the laser output, the clock spectrum and a 10-GHz pulse train monitored with a streak camera, respectively. We obtained a single polarization average output power of 1.5 mW at 10 GHz for a pump power of 160 mW. The loss increase due to the installation of two modulators was compensated for by the bidirectional pumping. The pulse had slight chirp characteristics and was chirp-compensated with a 15-m-long conventional single-mode fiber. After compensation, the pulse width was as short as 750 fs. Figure 19(a) clearly shows that there is no pedestal on the wing of the pulse. We obtained an output pulse train with a very clean repetitive feature as shown in Fig. 19(c).

The spectral characteristics of the laser are shown in Fig. 20. The whole spectrum is shown in Fig. 20 (a) and part of the spectrum is expanded in Fig. 20 (b) to reveal the fine structure of the longitudinal modes. A fine structure indicating a longitudinal mode separation of 10 GHz is clearly seen in Fig. 20 (b). The spectral width was typically about 4.5 nm. This indicates that the time and bandwidth product was 0.41, which is

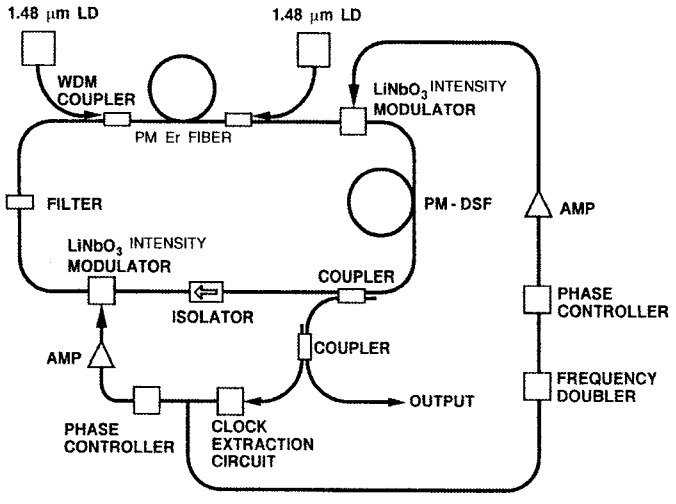

Fig. 18. Configuration of a 10-GHz, 750-fs regeneratively and harmonically mode-locked fiber laser with two synchronized intensity modulators. PM-DSF: polarization-maintained and dispersion-shifted fiber.

a nearly transform-limited Gaussian pulse. Although the laser incorporates the soliton compression effect, the pulse characteristics are mainly determined by the active mode locking characteristics because we employ strong intensity modulations. A symmetric spectrum is obtained and a spectral dip is observed at the wing of the spectrum. This is due to a four wave mixing interaction between the soliton like pulse and the dispersive waves. However, the dip exists at a wavelength where the spectral power is 20 dB down from the center spectrum, so there will be no significant deterioration in the quality of a pulse transmitted through a long fiber.

4.3. Femtosecond Pulse Compression Using a Dispersion-Decreasing Fiber

The generation of femtosecond pulses in the GHz region is especially important in terms of realizing ultrahigh speed OTDM transmission. An interesting technique using modulation instability with a two light beam configuration can produce a femtosecond pulse train at repetition rate of more than 100 GHz [39]. However, when the aim is to digitally modulate such a high-speed signal, conventional optical modulators are not applicable because they cannot respond at all in this region. Therefore, a femtosecond pulse train at a repetition rate of 10–40 GHz would seem to be the most attractive candidate for digitally modulating a signal with a conventional high-speed modulator [14]. The method for compressing the output pulse from the fiber laser is the most advantageous for the generation of a femtosecond pulse train at 10 GHz.

Here we describe an adiabatic soliton pulse compression technique for dispersion decreasing fibers (DDFs). This technique is currently one of the most practical ways of compressing high repetition rate picosecond pulses to femtosecond durations [40,41]. Such short pulse trains are needed for high-speed optical time division multiplexed

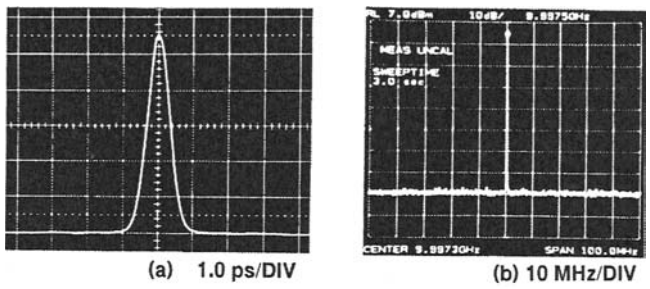

(a) 1.0 ps/DIV (b) 10 MHz/DIV

(c) 50 ps/DIV

Fig. 19. Output characteristics of a mode-locked laser with two synchronized modulators. (a) an autocorrelation trace of the laser output (750 fs), (b) a clock spectrum, and (c) a 10-GHz pulse train monitored with a streak camera.

(OTDM) transmission, all-optical sampling, and all-optical switching. The mechanism of the compression is based on the principle of keeping the soliton energy constant. The energy of an $N = 1$ soliton is proportional to D/τ. Here, D is the GVD and τ is the input pulse width. By keeping the $N = 1$ energy constant and decreasing the GVD, the pulse width τ of the soliton automatically shortens corresponding to the ratio between the decrease in the dispersion and the original dispersion. Here, adiabatic compression occurs when the dispersion decrease per soliton period is much smaller than the original GVD.

Pulses in several wavelength regimes are desirable for all of these applications. One problem with a conventional DDF constructed from step-index fibers, however, is that third-order dispersion (TOD) can cause the compressed pulse to form in a different wavelength regime from the input pulse. Another problem is that the compressed pulse spectrum varies significantly with input wavelength. In this section, we show that both of these problems are substantially reduced when we use a dispersion-flattened DDF, which has low TOD. The reduced TOD also reduces the minimum compressed pulse width.

We first compared the compression properties of a conventional DDF and a dispersion-flattened DDF with similar lengths and dispersions. The conventional DDF was constructed from step index dispersion-shifted fiber (DSF) and was 908 m long. The dispersion-flattened DDF was constructed from a 1106-m-long dispersion-

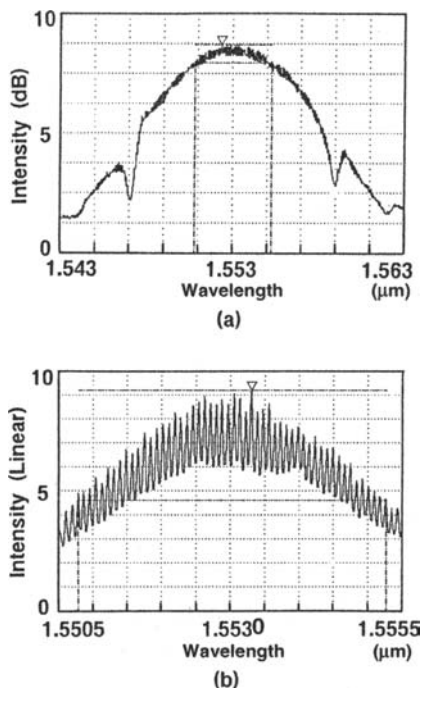

Fig. 20. Spectral characteristics of a mode-locked laser with two synchronized modulators (a) the whole spectrum and (b) expanded spectrum, which reveals the fine structure of the longitudinal modes.

flattened fiber (DFF) with a W-shaped core. In previous work, a dispersion-flattened DDF that crossed into the normal dispersion regime at the output end was used for supercontinuum (SC) generation [42]. Figure 21 shows the measured dispersions of the DDFs fitted with a 5-term Sellmeier equation. In Fig. 21, D_t is the total dispersion, and D_0 is the dispersion of a 100-m segment cut from the output end. The profile of D_0 has the most important effect on the compressed pulse, and for conventional DDF, D_0 has a slope (TOD) of approximately 4.5×10^{-2} ps/(nm^{2}km), as shown by the dotted lines. For dispersion-flattened DDF, D_0 has a slope that changes from 1.4×10^{-2} to 2×10^{-3} ps/(nm^{2}km) over a wavelength range of 1530–1565 nm, as shown by the solid lines. The changing slope indicates that the fourth-order dispersion (FOD) is -3.6×10^{-4} ps/(nm^{3}km). Both fibers had mode field diameters of approximately 6 μm. The seed pulses were generated from a 10-GHz regeneratively mode-locked fiber laser that emitted 3.0–3.6 ps duration, transform-limited pulses over a wavelength range of 1533–1565 nm. The pulses were amplified to average powers in excess of 140 mW using a high-power EDFA. The amplified pulses were launched into the DDF, and the output was characterized on an autocorrelator and a spectrum analyzer.

The compression ratio (the ratio of input to output pulse width) in each DDF varied with input power. We compared the wavelength dependence of the compression

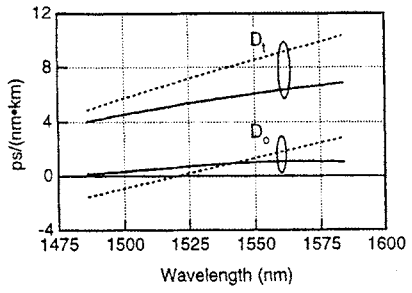

Fig. 21. Measured dispersions of the DDFs fitted with a 5-term Sellmeier equation. Conventional DDF: dashed line and dispersion-flattened DDF: solid line. D_t is the total dispersion of the DDF. D_0 is the dispersion measured in a 100-m segment cut from the output end.

at a power that gave a compression ratio of approximately 21 at the center of the tuning range. Figure 22(a) shows the output spectra from the conventional DDF as the input wavelength λ_i was varied from 1533–1565 nm. The average power at the output end was 80–85 mW. The TOD caused large variations in the spectra, which broadened asymmetrically. The spectral spike corresponds to uncompressed light at the input wavelength, and the compressed soliton is shifted to the longer wavelength side. Figure 22 (b) shows the output spectra from the dispersion-flattened DDF over the same input wavelength range. The output power was 51–55 mW. In contrast to the conventional DDF, similar and symmetrically broadened spectra were obtained over the entire range of input wavelengths, which was the result of reducing the effects of TOD.

Figure 23 compares the wavelength at the peak of the compressed soliton spectrum (λ_s), compressed pulse width $\Delta\tau$, and output time-bandwidth product $\Delta\nu\Delta\tau$ as functions of λ_i for conventional DDF (open symbols) and dispersion-flattened DDF (filled symbols). For the conventional DDF, λ_s appears to be limited to near 1550 nm, but with the dispersion-flattened DDF, λ_s and λ_i remain nearly equal. The plots of $\Delta\tau$ and $\Delta\nu\Delta\tau$ confirm that the compression properties of the dispersion-flattened DDF are uniform with λ_i. When calculating $\Delta\nu\Delta\tau$ we estimated the spectral width by fitting a squared sech to the broadened portion of the spectrum. In the auto-correlations, the peak-to-pedestal ratios (PPR) were found to be greater than 20 dB for the dispersion-flattened DDF, while for the conventional DDF, they were approximately 17 dB when λ_i was shorter than 1550 nm and greater than 20 dB when λ_i was longer than 1550 nm. The pedestal widths ranged from 6–10 ps.

We examined the pulse compression limits for each fiber by measuring the compressed pulse as a function of input power. $\Delta\nu\Delta\tau$ and PPR as functions of the output power from each DDF are plotted in Fig. 24 for an input wavelength of 1553.5 nm. The degradation in PPR with power is mainly due to increased non-adiabatic higher order soliton compression effects, which increase the pulse wings. The pulse shortening was limited to approximately 131 fs for the conventional DDF and to approximately 100 fs for the dispersion-flattened DDF. The inset shows the 98 fs compressed pulse that was generated from the dispersion-flattened DDF for an average output power of 75

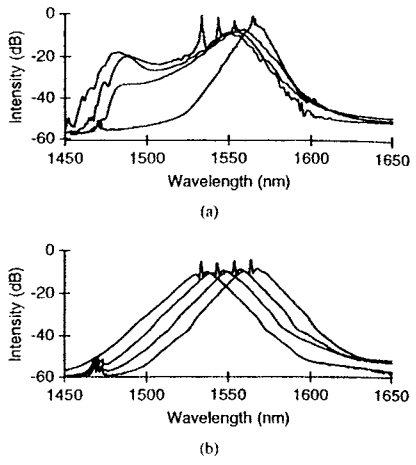

Fig. 22. Change in the spectral profile through soliton pulse compression in DDFs. (a) output spectra of the conventional DDF as the input wavelength i is varied from 1533-1565 nm and (b) output spectra of the dispersion-flattened DDF over the same input wavelength range. The input wavelength is tuned from 1533 to 1565 nm.

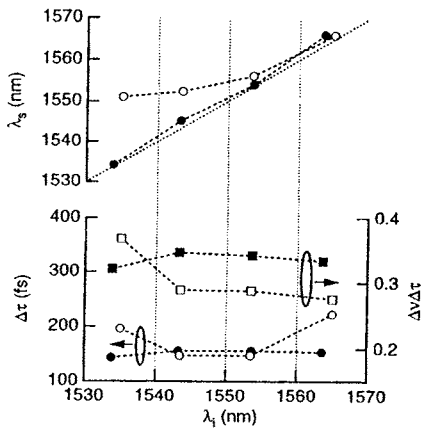

Fig. 23. Comparison of the compression characteristics of the conventional DDF and the dispersion-flattened DDF. λ_s: center of soliton spectrum, $\Delta\tau$: compressed pulse width, λ_i: input wavelength. The filled symbols show results for DF-DDF and the open symbols are for conventional DDF.

mW. The PPR is approximately 21 dB. From the spectral fit (dashed line), the bandwidth is 30.8 nm. The corresponding time-bandwidth product $\Delta\nu\Delta\tau$ is 0.37, which indicates that the pulse is nearly transform-limited. The compression properties of the dispersion-flattened DDF began to show a small wavelength dependence at these high

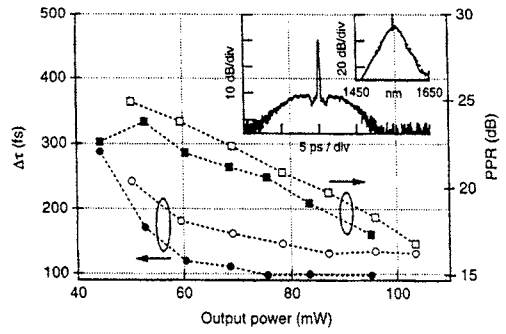

Fig. 24. $\Delta\tau$ (left) and peak-to-pedestal ratio (PPR; right) as functions of output power for conventional DDF(open symbols) and dispersion-flattened DDF (filled symbols). The input wavelength is 1553.6 nm. The inset shows the autocorrelation and corresponding spectrum for a 98-fs pulse from DF-DDF. The vertical axes indicate intensity. The dashed curve is a sech^2 fit to spectrum.

compression ratios. Nevertheless, pulses shorter than 115 fs were obtained over the entire range from 1533–1565 nm.

A variety of mechanisms may cause the limit to $\Delta\tau$ observed in Fig. 24. These include higher order dispersion, the finite nonlinear response time of the fiber (Raman effect), and polarization mode dispersion (PMD). The effective lengths associated with the Raman effect were estimated to be >150 m at the DDF outputs. The PMD was measured and found to be <0.1 ps/(km)$^{1/2}$ over the entire DDF length. Hence, higher order dispersion was expected to be the main limit to compression. Recently, we succeeded in generating a 54-fs pulse train at 10 GHz by using polarization-maintaining DF-DDF [43]. We used these compressed pulses for a terabit/s OTDM transmission experiment, and realized the first 1.28 Tbit/s OTDM transmission over 70 km [14].

4.4. Cs Optical Atomic Clock Using a Regeneratively Mode-Llocked Fiber Laser

We found that PLL operation in the fiber laser results in the jitter being less than that of the synthesizer itself [32]. This is due to the fact that the feedback circuit, which includes the PZT for the PLL operation, does not respond to the higher Fourier frequency components of the synthesizer jitter. Hence, the jitter in the high Fourier frequency region is determined solely by the jitter of the laser itself in a free-running condition, which is very low. Thus, the PLL regenerative fiber laser has little phase noise (a low repetition rate drift) over a wide Fourier frequency region.

This result suggests that we can realize a microwave signal that has better frequency stability than a synthesizer. This in turn indicates that if the laser repetition frequency can be stabilized to an atomic resonance, it will be possible to realize an ultrastable microwave source and an optical time clock. This idea is similar to the frequency stabilization of a single longitudinal-mode laser to a molecular resonance such as a 3.39-μm He-Ne laser with a CH_4 or 0.633-μm He-Ne laser with I_2.

In this section, we describe how we locked the repetition rate of our regeneratively mode-locked fiber laser to the 9.1926-GHz atomic resonance of Cs in order to obtain

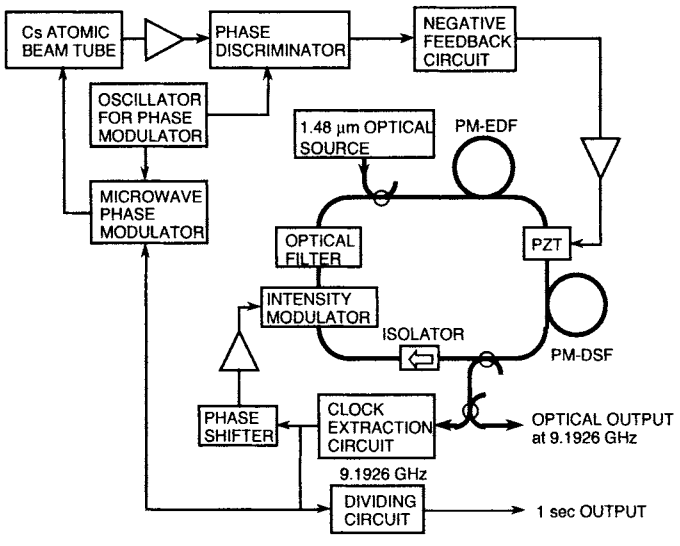

Fig. 25. Configuration of a new Cs optical atomic clock using a regeneratively mode-locked 9.1926-GHz fiber laser.

an optical time clock that is more stable than a conventional Cs atomic clock [44]. We cannot improve the long-term stability of the Cs time clock with this scheme, but we can improve its short-term stability and simultaneously obtain an ultrastable optical pulse train as stable as the Cs clock.

The new Cs optical atomic clock is shown in Fig. 25. In this scheme we replace a 5-MHz quartz oscillator and multiplexers with a regeneratively mode-locked fiber laser that oscillates directly at 9.1926 GHz. In a conventional Cs clock, multiplexers are needed to convert the 5-MHz signal to the 9.1926-GHz Cs resonance. Here a single frequency sinusoidal clock signal with a signal to noise ratio (SNR) of more than 70 dB is coupled to a microwave phase modulator to provide frequency modulation at a low frequency to discriminate the frequency detuning from the Cs resonance. The frequency modulated 9.1926-GHz signal is then coupled to a Cs atomic beam tube in which the Ramsey fringe [45] is used to detect the frequency deviation. Phase sensitive detection is achieved by using a lock-in amplifier, in which any frequency deviation from the Cs resonance can be converted to a voltage error signal. The error signal was finally fed back to the PZT of the fiber laser cavity after passing through a negative feedback circuit comprising proportional and integral (PI) circuits.

Here, it is important to note that the long-term stability of the present Cs oscillator is the same as before, but the short-term stability is greatly improved. In fact, with a conventional Cs clock, it is impossible in principle to obtain an ultrastable pure microwave at 9.1926 GHz, since frequency modulation (FM) is imposed on the 9.1926-GHz signal to obtain an error signal. In addition, the SNR of the 9.1926-GHz signal is not good since it is obtained after the signal has been multiplexed a number of times from 5 MHz by using electrical mixers. In contrast, the present scheme can

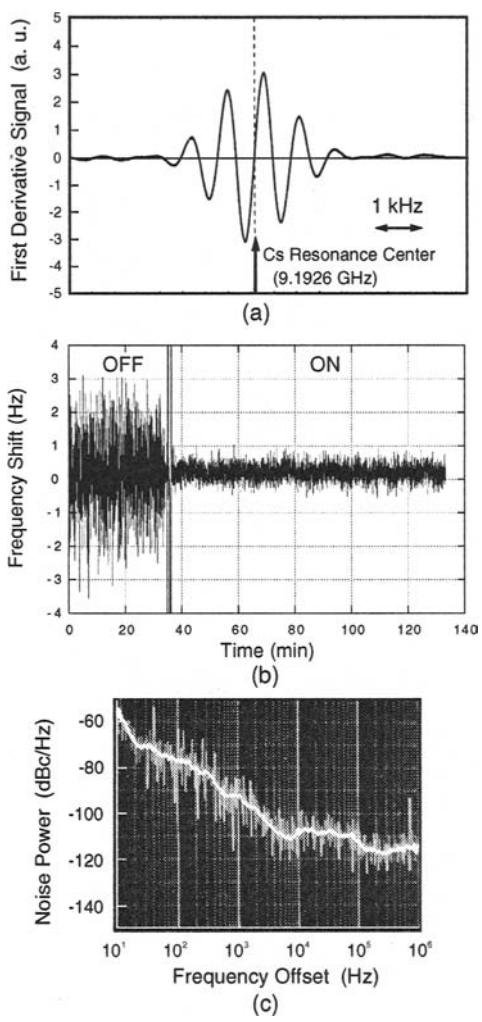

Fig. 26. Microwave characteristics of a Cs optical atomic clock. (a) First derivative signal of the Ramsey fringe pattern of a Cs resonance and (b) repetition-frequency fluctuation with feedback off and on, (c) single-sideband phase noise at 9.1926 GHz.

offer a very pure 9.1926-GHz signal with a high SNR and no FM, resulting in a better discrimination curve.

Figure 26 shows the microwave characteristics. We obtained the first derivative of the Ramsey fringe pattern of the Cs resonance by applying FM to the microwave signal. This first derivative signal is shown in Fig. 26 (a). It is important to note that a positive error signal is obtained when the signal frequency deviates to the higher frequency region and a negative error signal is obtained for the lower frequency region.

We fed the error signal back to the laser cavity after it had passed through the PI circuit. That is, an error voltage was applied to the PZT on which part of the fiber cavity was wound. In Fig. 26 (b), we show that a large frequency change is observed when the feedback signal is off. However, when the feedback loop is on, the signal frequency is well stabilized. It is clearly seen that the laser repetition frequency was well stabilized over a long period by using the Cs resonance. The Allan variance [46], which we estimated from the error signal, was approximately 7.1×10^{-12} for $\tau = 1$ second. We also evaluated the timing jitter of the signal at 9.1926 GHz from the single sideband (SSB) phase noise between 10 Hz and 1 MHz. The result is shown in Fig. 26 (c). The timing jitter was approximately 105 fs, which is much smaller than that of ordinary synthesizers. Thus, the jitter of the output signal at 9.1926 GHz is the lowest reported to date.

An interesting feature of this new Cs atomic clock is the generation of an optical pulse train with the same accuracy of repetition. Figure 27 shows the optical output pulse characteristics. Waveforms (a)-(d) correspond to a pulse train observed with an electrical sampling scope, a single optical pulse measured with an auto-correlator, a 9.1926-GHz clock spectrum measured with an electrical spectrum analyzer, and a spectral profile measured with an optical spectrum analyzer, respectively. In (b) the average output power was 1 mW and the output pulse width was 1 ps. The spectral width of the output pulse was 2.46 nm, resulting in a pulse width-bandwidth product of 0.31, which is almost a transform-limited sech pulse due to the soliton effect. From (a) and (c) the amplitude of the pulse train is very stable, resulting in an SNR of more than 70 dB as seen in (c). This also indicates that the laser has no supermode noise. This shows that a very pure clock can be successfully obtained. (d) shows many longitudinal modes with a 9.1926-GHz separation that have a mode spacing stability with an Allan variance of 7.1×10^{-12} for $\tau = 1$ second. The fact that our new Cs clock can generate an optical pulse train at 9.1926 GHz means that an ultrastable clock signal can be delivered throughout the world through the optical fiber network. In addition, by selecting an arbitrary mode spacing that is an integral multiple of 9.1926 GHz it is possible to obtain a new frequency chain or ultrastable millimeter to terahertz waves by using frequency mixing in a high-speed photo detector.

5. Summary

Passive and active mode-locked fiber lasers and related topics have been reported in detail. For passively mode-locked lasers, the repetition rate is of the order of 100 MHz, but they can generate femtosecond pulses shorter than 100 fs. These lasers are useful as optical sources for an optical sampling scope or comb generation for frequency standards. By contrast, actively mode-locked lasers have the advantage of being able to generate a GHz pulse train through the use of harmonic mode-locking. These lasers are useful for high-speed optical communication. In this chapter, we focused particularly on a regeneratively and harmonically mode-locked fiber laser, which operates very stably in the 10–40 GHz repetition rate regime. As regards soliton communication, such a pulse train is very advantageous since the fiber laser can directly generate a transform-limited sech pulse using a soliton effect in the fiber cavity. It is also useful as an input pulse for an optical pulse compressor using the adiabatic soliton compression

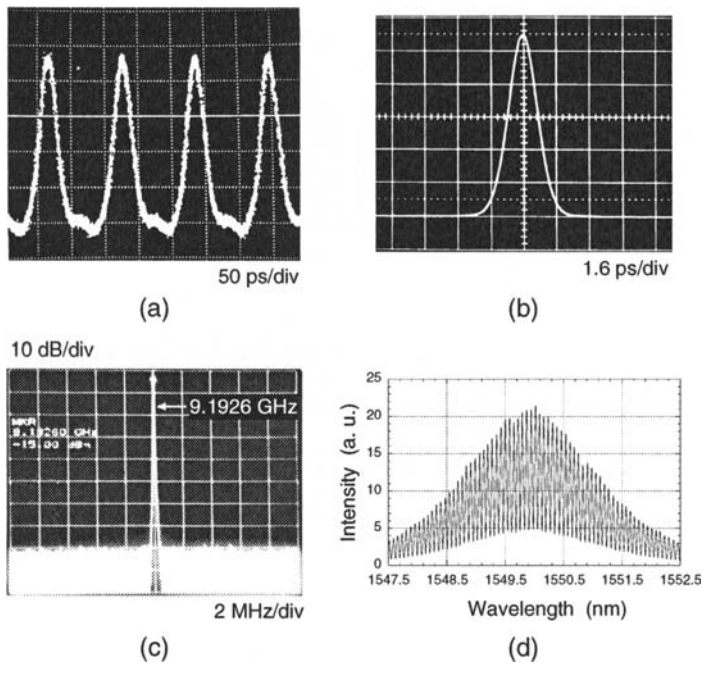

Fig. 27. Optical output pulse characteristics. (a) a pulse train observed with an electrical sampling scope, (b) a single optical pulse measured with an autocorrelator, (c) a 9.1926-GHz clock spectrum measured with an electrical spectrum analyzer, and (d) a spectral profile measured with an optical spectrum analyzer.

effect. With this technique, we were able to compress the input picosecond pulses to 50–200 fs in the GHz region.

We also described a new application of regenerative mode-locking as an ultrastable opto-microwave oscillator that we achieved by frequency-locking the laser repetition rate to the Cs resonance at 9.1926 GHz. This technique enables us to send very stable clock signals or time standards through the global optical network.

References

1. I. N. Duling III, "Subpicosecond all-fibre erbium laser," Electron. Lett., **27**, 544–545 (1991).
2. M. Nakazawa, E. Yoshida, and Y. Kimura, "Generation of 98 fs optical pulses directly from an erbium-doped fiber ring laser at 1.57 μm," Electron. Lett., **29**, 63–64 (1993).
3. M.E. Fermann, F. Haberl, M. Hofer, and H. Hochreiter, "Nonlinear amplifying loop mirror," Opt. Lett., **15**, 752–754 (1990).
4. V.J. Matsas, T.P. Newson, D.J. Richardson, and D. N. Payne, "Selfstarting passively mode-locked fibre ring soliton laser exploiting nonlinear polarisation rotation," Electron. Lett., **28**, 1391–1393 (1992).

5. K. Tamura, H.A. Haus, and E.P. Ippen, "Self-starting additive pulse mode-locked erbium fibre ring laser," Electron. Lett., **28**, 2226–2228 (1992).

6. K. Tamura, E.P. Ippen, and H.A. Haus, "Pulse dynamics in stretched pulse fiber lasers," Appl. Phys. Lett., **67**, 158–160 (1995).

7. H.A. Haus, K. Tamura, L.E. Nelson, and E.P. Ippen, "Stretched-pulse additive pulse mode-locking in fiber ring lasers: theory and experiment," IEEE, J. Quantum Electron., **31**, 591–598 (1995).

8. A. Takada and H. Miyazawa, "30 GHz picosecond pulse generation from actively mode-locked erbium-doped fibre laser," Electron. Lett., **26**, 216–217 (1990).

9. H. Takara, S. Kawanishi, and M. Saruwatari, "20 GHz transform-limited optical pulse generation and bit-error-free operation using a tunable, actively modelocked Er-doped fibre ring laser," Electron. Lett., **29**, 1149–1150 (1993).

10. G.R. Huggett, "Mode-locking of CW lasers by regenerative RF feedback," Appl. Phys. Lett., **13**, 186–187 (1968).

11. M. Nakazawa, E. Yoshida, and Y. Kimura, "Ultrastable harmonically and regeneratively modelocked polarisation-maintaining erbium fibre laser," Electron. Lett., **30**, 1603–1604 (1994).

12. M. Nakazawa, H. Kubota, K. Suzuki, E. Yamada, and A. Sahara, "Ultrahigh-speed long-distance TDM and WDM soliton transmission technologies," IEEE, J. Select. Topics Quantum Electron., **6**, 363–396 (2000).

13. *Ultrafast lasers*, edited by M.E. Fermann, A. Galvanauskas, and G. Sucha, Ch. 13 (Marcel Dekker, 2003).

14. M. Nakazawa, T. Yamamoto, and K.R. Tamura, "1.28 Tbit/s-70 km OTDM transmission using third- and fourth-order simultaneous dispersion compensation with a phase modulator," Electron. Lett., **36**, 2027–2029 (2000).

15. M. Nakazawa, E. Yoshida, T. Sugawa and Y. Kimura, "Continuum suppressed, uniformly repetitive 136 fs pulse generation from an erbium-doped fiber laser with nonlinear polarisation rotation," Electron. Lett., **29**, 1327–1328 (1993).

16. E. Yoshida, Y. Kimura and M. Nakazawa, "Femtosecond erbium-doped fiber laser with nonlinear polarization rotation and its soliton compression," Jpn. J. Appl. Phys., **33**, 5779–5783 (1994).

17. N.J. Smith, F.M. Fox, N.J. Doran, K.J. Blow, and I. Bennion, "Enhanced power solitons in optical fibres with periodic dispersion management," Electron. Lett., **32**, 54–55 (1996).

18. M. Nakazawa and H. Kubota, "Optical soliton communication in a positively and negatively dispersion-allocated optical fibre transmission line," Electron. Lett., **31**, 216–217 (1995).

19. M. Suzuki, I. Morita, S. Yamamoto, N. Edagawa, H. Taga, and S. Akiba, "Timing jitter reduction by periodic dispersion compensation in soliton transmission," OFC'95, PDP 20, San Diego, March (1995).

20. H. Ohta, N. Banjo, N. Yamada, S. Nogiwa, and Y. Yanagisawa, "Measuring eye diagram of 320 Gbit/s optical signal by optical sampling using passively modelocked fibre laser," Electron. Lett., **37**, 1541–1542 (2001).

21. M. Nakazawa, E. Yoshida, E. Yamada, and Kimura, "A repetition-rate stabilized and tunable, regeneratively mode-locked fibre laser using an offset locking technique," Jpn. J. Appl. Phys., **35**, L691–694 (1996).

22. X. Shan, D. Cleland, and A. Ellis, "Stabilising Er fibre soliton laser with pulse phase locking," Electron. Lett., **28**, 182–184 (1992).

23. H. Takara, S. Kawanishi, and M. Saruwatari, "Stabilisation of a modelocked Er-doped fibre laser by suppressing the relaxation oscillation frequency component," Electron. Lett., **31**, 292–293 (1995).

24. M. Nakazawa, E. Yoshida and K.R. Tamura, "Ideal phase-locked-loop (PLL) operation of a 10 GHz erbium-doped fibre laser using regenerative modelocking as an optical voltage controlled oscillator," Electron. Lett., **33**, 1318–1319 (1997).

25. X. Shan and D.M. Spirit, "Novel method to suppress noise in harmonically mode-locked erbium fibre laser," Electron. Lett., **29**, 979–981 (1993).

26. C.R. Doerr, H.A. Haus, E.P. Ippen, M. Shirasaki, and K. Tamura, "Additive-pulse limiting," Opt. Lett., **19**, 31–33 (1994).

27. M. Nakazawa, K. Tamura, and E. Yoshida, "Supermode noise suppression in a harmonically modelocked fibre laser by selfphase modulation and spectral filtering," Electron. Lett., **32**, 461–463 (1996).

28. K.J. Blow, N.J. Doran, and D. Wood, "Generation and stabilization of short soliton pulses in the amplified nonlinear Schrödinger equation," J. Opt. Soc. Am. B, **5**, 381–390 (1988).

29. D. Breuer, H.J. Ehrke, F. Küppers, R. Ludwig, K. Petermann, H.G. Weber, and K. Weich, "Unrepeatered 40-Gb/s RZ single-channel transmission at 1.55 μm Using various fiber types," IEEE, Photon. Technol. Lett., **10**, 822–824 (1998).

30. K. Suzuki, H. Kubota, A. Sahara, and M. Nakazawa, "40 Gbit/s single channel optical soliton transmission over 70,000 km using in-line synchronous modulation and optical filtering," Electron. Lett., **34**, 98–100 (1998).

31. T. Ishibashi, N. Shimizu, S. Kodama, H. Ito, T. Nagatsuma, and T. Furuta, "Uni-traveling-carrier photodiodes," in Proc. Ultrafast Electronics and Optoelectronics, UEO, pp. 166–168 (1997).

32. E. Yoshida and M. Nakazawa, "Measurement of the timing jitter and pulse energy fluctuation of a PLL regeneratively mode-locked fiber laser," IEEE, Photon. Technol. Lett., **11**, 548–550 (1999).

33. D. Von der Linde, "Characterization of the noise in continuously operating mode-locked laser," Appl. Phys. B, **39**, 201–217 (1986).

34. Y. Ishida and K. Naganuma, "Compact diode-pumped all-solid-state femtosecond Cr4+:YAG laser," Opt. Lett., **21**, 51–53 (1996).

35. M. Nakazawa and E. Yoshida, "A 40-GHz 850-fs regeneratively FM mode-locked polarization-maintaining erbium-doped fiber ring laser," IEEE Photon. Technol. Lett., **12**, 1613–1615 (2000).

36. A. E. Siegman, *Lasers* (University Science Books, Mill Valley, CA, 1986)

37. M. Nakazawa and E. Yoshida, "Direct generation of a 750 fs, 10 GHz pulse train from a regeneratively mode-locked fibre laser with multiple harmonic modulation," Electron. Lett., **32**, 1291–1293 (1996).

38. H.A. Haus, *Waves and fields in optoelectronics* (Prentice-Hall, Englewood Cliffs, NJ, 1984).

39. S.V. Chernikov, D.J. Richardson, E.M. Dianov, D.N. Payne, "Picosecond soliton pulse compressor based on dispersion decreasing fibre," Electron. Lett., **28**, 1842–1844 (1992).

40. S.V. Chernikov and P.V. Mamyshev, "Femtosecond soliton propagation in fibers with slowly decreasing dispersion", J. Opt. Soc. Am. B, **8**, 1633–1641 (1991).

41. M. Nakazawa, E. Yoshida, H. Kubota, and Y. Kimura, "Generation of a 170 fs, 10 GHz transform-limited pulse train at 1.55 μm using a dispersion-decreasing, erbium-doped active soliton compressor," Electron. Lett., **30**, 2038–2040 (1994).

42. K. Mori, H. Takara, S. Kawakami, M. Saruwatari, and T. Morioka, "Flatly broadened supercontinuum spectrum generated in a dispersion decreasing fiber with convex dispersion profile," Electron. Lett., **33**, 1806–1808 (1997).

43. K.R. Tamura and M. Nakazawa, "54-fs, 10 GHz soliton generation from a polarization-maintaining dispersion-flattened dispersion-decreasing fiber compressor," Opt. Lett., **26**, 762–764 (2001).

44. M. Nakazawa and K. Suzuki, "Cesium optical atomic clock: an optical pulse tells the time," Opt. Lett., **26**, 635–637 (2001).

45. N.F. Ramsey, *Molecular Beams* (Oxford University Press, England, 1956).

46. D.W. Allan, "Statistics of atomic frequency standards," Proc. IEEE, **54**, 221–230 (1966).

DOI: 10.1007/s10297-007-0080-1
Originally published in J. Opt. Fiber. Commun. Rep. 4, 1–13 (2007)

Ultra-high-speed $LiNbO_3$ modulators

Kazuto Noguchi

NTT Photonics Laboratories 3-1 Morinosato Wakamiya
Atsugi, Kanagawa 243-0198, Japan
Email: nogu@aecl.ntt.co.jp

Abstract. This paper overviews ultra-high-speed optical modulators fabricated on $LiNbO_3$ substrate, which are used in large-capacity optical transmission systems.

1. Introduction

High-speed $LiNbO_3$ optical modulators are essential components of large-capacity long-haul optical transmission systems based on time-division-multiplexing (TDM) and wavelength-division-multiplexing (WDM) technology [1–5]. Ever since their long-term stability was improved [6, 7], they have been used in commercial service for large-capacity trunk networks such as STM-64/OC-192 systems. These modulators have been used in advanced transmission experiments demonstrating large capacity optical transmission systems [1,2], an optical-time-division-multiplexing (OTDM) system [3], and carrier suppressed return-to-zero (CS-RZ) systems [4,5]. With the recent development of low-drive voltage capability [8–11], the modulators have become strong candidate for 40-Gbit/s systems of the next generation.

The $LiNbO_3$ modulator has several features that make it suitable for use as a component in both TDM and WDM systems: It works at very broadband from DC to microwave or millimeter-wave frequency range [12], and its modulation characteristics, such as insertion loss, driving voltage (half-wave voltage), and frequency response, depend little on wavelengths from 1.3 to 1.5 μm. In addition, the frequency chirping of modulated optical signal is very small or almost zero.

This paper overviews ultra-high-speed optical modulators fabricated on $LiNbO_3$ substrate, which are used in large-capacity optical transmission systems. Following a brief introduction, section 2 describes the basic structures and operation principle from the view point of high-speed modulation. Section 3 covers the concept of the

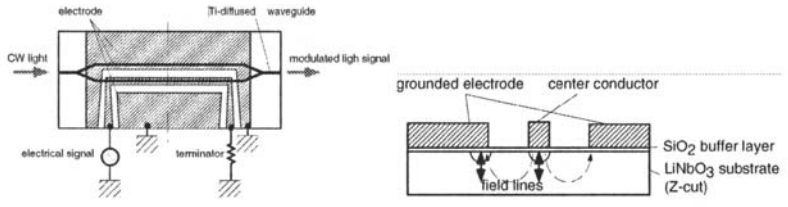

Fig. 1. (a) Top view and (b) cross-sectional configurations of an optical intensity modulator with a Mach–Zehnder optical waveguide fabricated on Z-cut $LiNbO_3$ substrate.

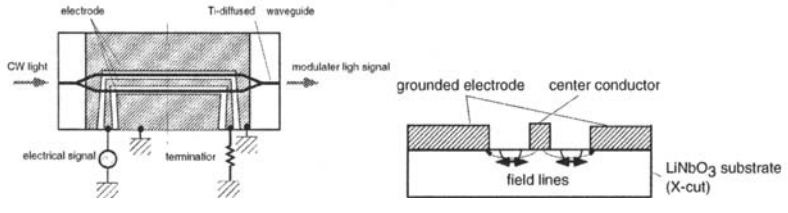

Fig. 2. (a) Top view and (b) cross-sectional configurations of an optical intensity modulator with Mach–Zehnder optical waveguide fabricated on X-cut $LiNbO_3$ substrate.

design of high-speed modulators with traveling-wave electrode. Section 4 reviews recent progress of the devices based on the analysis of electrode characteristics.

2. Structures and Operation of $LiNbO_3$ Modulators

A $LiNbO_3$ modulator consists of a $LiNbO_3$ substrate, waveguide, buffer layer, and electrode [13]. The linear electro-optic effect of the crystal is used for the modulation of light signal: When an electric field is applied to a $LiNbO_3$ crystal, the refractive index changes. The index change causes a change in optical path length of the light, and this phase change is used for the modulation of light signal.

A $LiNbO_3$ is a uniaxial crystal and two types of wafers, Z-cut and X-cut, are used for modulators. Figures 1 and 2 show the schematic structures of the components fabricated on Z-cut and X-cut $LiNbO_3$ substrates, respectively. In Z-cut substrate, waveguides are formed just under the electrode as shown in Figs. 1(a) and 1(b). The optical wave of the TM-mode in the waveguides, indicated by bi-directional arrows, suffers index change because of the vertical components of supplied electrical field. On the contrary, in X-cut substrate, waveguides are located between the center conductor and grounded electrodes as shown in Figs. 2(a) and 2(b). In this case, TE-mode optical signals are launched into the optical waveguide and the lateral component of the electrical field is used for modulation. Since there is no need for a buffer layer, it is possible to suppress the dc-drift in the modulator [9,14,15].

Optical waveguides on the $LiNbO_3$ are formed by titanium (Ti) in-diffusion on the $LiNbO_3$ substrate [16, 17]. When the optical waveguide is a single straight line, an

optical phase modulator is obtained. An intensity modulator is obtained when the optical waveguide is the Mach–Zehnder type. The mode field diameter of the waveguide is about 8 to 10 μm, which assures low coupling loss of less than 0.5 dB/facet with a single-mode fiber. The propagation loss is as small as 0.1 to 0.2 dB/cm typically. This is one of the important factors for high-speed modulation, because, as described later, it enables us to use a traveling-wave electrode with longer interaction length.

For the buffer layer, silicon oxide thin film is commonly used, because silicon oxide is stable low-index material and the film is easy to form by conventional techniques, such as electron beam evaporation or plasma chemical vapor deposition. In a $LiNbO_3$ modulator, the buffer layer separates the electrode from the optical waveguide to avoid absorbing loss of optical wave by the metal in the Z-cut modulator, and lowering the microwave index to obtain velocity and impedance matching. As described later, the buffer layer thickness is a critical parameter for fabricating high-speed modulators.

A traveling-wave electrode is used in high-speed modulators operating at above several GHz [18]. The electrode is made of gold because of gold's low conductor loss. A superconductor electrode has also been used [19]. Two types of traveling-wave electrode, co-planar waveguide (CPW) electrodes and asymmetric coplanar strip (ACPS) electrodes were studied in modulators. When a $LiNbO_3$ modulator with an ACPS electrode is fully connectorized to a packaged module, the module suffers from cavity resonance above 10 GHz and the operation at higher frequency range is hindered [20,21]. Therefore a CPW electrode is commonly used for higher operation speeds, such as 40 Gbit/s. A CPW electrode also provides a good connection with the coaxial lines for feeding the electrical signal.

3. Traveling-Wave Electrode and Modulation Speed

3.1. Limitation of Modulation Speed

A $LiNbO_3$ optical modulator is not only an optical component with an optical waveguide, but also a microwave or millimeter-wave component with an electrode. Its response is the result of interaction between the optical wave propagating in the optical waveguide and the electrical wave propagating in the traveling-wave electrode. Therefore the frequency response of a $LiNbO_3$ modulator depends on the optical characteristics of $LiNbO_3$ crystal and silicon oxide, and on the electrical characteristics of $LiNbO_3$ crystal, silicon oxide, and gold in millimeter-wave frequency range.

Since the material dispersions of silicon oxide and $LiNbO_3$ in the millimeter-wave frequency range is small and the response speed of the electro-optic effect in $LiNbO_3$ is in the THz range, the modulation speed is dominated by the electrode characteristics of the modulator. Here, the modulation speed is limited by the following factors:

1. Group velocity difference between electrical wave and optical wave (velocity mismatch).
2. Characteristic impedance of the electrode.
3. Propagation loss of the electrode.
4. Geometric dispersion of the electrode.

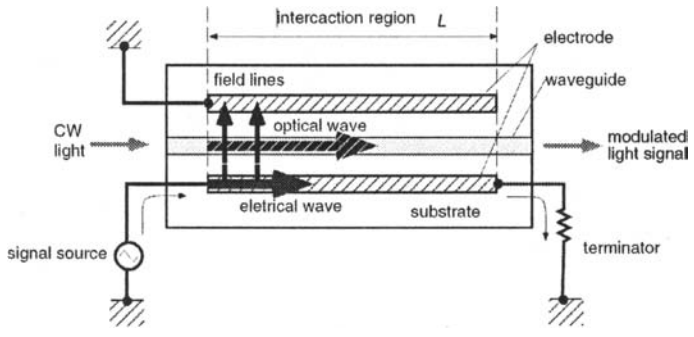

Fig. 3. Schematic structure of a modulator with a traveling-wave electrode.

Among those factors, the geometric dispersion can be neglected below millimeter-wave frequency range because the cross-sectional size of the electrode is several ten microns, which is very small compared with the wavelength of modulating electrical wave of several millimeters. Thus factors 1, 2 and 3 are main factors limiting modulation speed.

3.2. Velocity Matching

The traveling-wave electrode of the modulator acts as a transmission line as shown in Fig. 3. The optical signal in the waveguide and the modulating electric signal in the electrode propagate the same direction. Index change in the optical waveguide is induced by the electrical wave through the linear electro-optic effect of the $LiNbO_3$ crystal and the optical signal is modulated. The dielectric constants of a $LiNbO_3$ crystal along c-axis and a-axis are 28 and 44 in microwave and millimeter-wave frequency range, respectively [22]. In the case of an optical modulator with thin planar electrode on $LiNbO_3$ substrate, the effective refractive index of the electrical wave, n_m (= 4.2), is about twice that of the optical wave, n_0 (= 2.15). This difference causes velocity mismatch between the electrical wave and optical wave as they propagate through the interaction region of the modulator. When the velocity mismatch exists in a modulator, phase change is once introduced from electrical wave to optical wave, and then canceled by the reverse phase change that occurs in optical wave as it propagates through the interaction region. This degrades the frequency response characteristics of the optical modulator.

The relationship between modulation bandwidth (electrical 3-dB), B, and the effective refractive index n_m is

$$B = 1.4c/[(\pi L(n_m - n_0)], \tag{1}$$

where c is the velocity of light in a vacuum and L the interaction length. For simplification, lets assume impedance matching is obtained and neglect the conductor loss. The calculated result is shown in Fig 4. By obtaining velocity matching, modulation bandwidth can be enlarged to more than 100 GHz. When $L = 2$ cm, modulation bandwidth

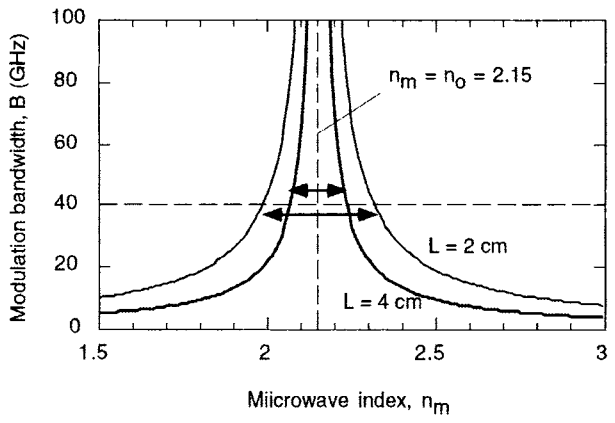

Fig. 4. Relationship between microwave index, nm, and modulation bandwidth (electrical 3-dB), B, of a modulator with a traveling-wave electrode as a parameter of interaction length, L.

of more than 40 GHz is obtained with an index difference of less than 0.16. On the contrary, the index difference must be adjusted within 0.08 for $L = 4$ cm. Therefore, a shorter electrode is preferable for high-speed modulation.

However, smaller L leads to larger driving voltage: Since the phase change of the optical wave is proportional to L, the driving voltage of the modulator is inversely proportional to L. Therefore, a trade-off exists between modulation bandwidth and driving voltage. Korotky et al. fabricated modulators with 1-cm-long ACPS electrode to minimize velocity mismatch, and obtained large modulation bandwidth of 40 GHz and high driving voltage of 25 V [23].

4. Ultra-High-Speed Modulators

4.1. Design of CPW Electrode

The basic design and characteristics of a $LiNbO_3$ modulator with a CPW electrode were first reported by Kawano et al. [24]. In their design, the width of the center conductor was 8 μm, which provided a large overlap between electrical fields and optical field to lower the driving voltage. The gaps were designed to be 15 μm to obtain impedance matching. A relatively thick buffer layer of 1.2 μm was used for the first time to lower the microwave index, and quasi-velocity matching was obtained as $n_m = 3$.

In a CPW electrode, velocity matching is obtained with an electrode thicker than 10 μm because more of the microwave field leaks into the air at the gaps. Mitomi et al. calculated the characteristics of velocity-matched modulators with a CPW electrode [25]. Figure 5 shows the dependences of the electrode thickness at velocity matching, tvm, the characteristic impedance, Z_c, the product of driving voltage and interaction length, $V_\pi L$, and the conductor loss coefficient, α_0 on the buffer layer thickness, t_b, where the parameter is the gap, G. The wider the gap, the thicker the electrode. And a thick electrode leads to low-conductor loss, which results in a larger modulation

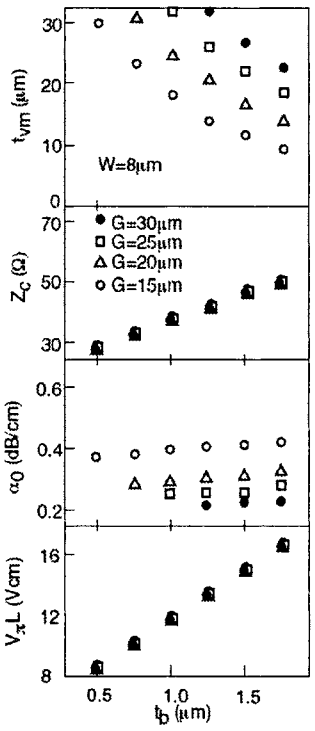

Fig. 5. Calculated characteristics of $LiNbO_3$ modulators with a CPW electrode as a function of buffer layer thickness, tb, where the width of the center conductor, W, is 8 μm, and gap, G, is the parameter.

bandwidth. In this case, the dependence of Z_c and $V_\pi L$ on G is very small. As a consequence, the wider gaps with thicker electrodes lead to larger bandwidth with lower conductor loss and a little higher driving voltage.

However, it should be noted that fabricating a thick electrode with a high aspect ratio is quite difficult. The width of the center conductor must be maintained at about 8 μm to obtain large interaction between the electrical and optical wave and lower the driving voltage [26]. Consequently, the center conductor has to be 8 μm wide, several ten micrometers high, and several centimeters long. Recently, Sugiyama et al. developed 'driver-less' modulator with wide-gap (50-μm) CPW electrode; the driving voltage is 0.9 V at push-pull drive (1.6 V at single drive) [8]. Using their excellent fabrication technique, they successfully formed a modulator with a 30-μm-thick, 50-μm gap, and 6-cm-long electrode on 4-inch $LiNbO_3$ wafer.

4.2. Low Dielectric Structures for High-Speed Operation

Lowering the effective index of the electrical wave is the best way to obtain velocity matching between microwaves and optical waves and thereby achieve broadband operation, because the resulting frequency response is flat. This situation can be realized

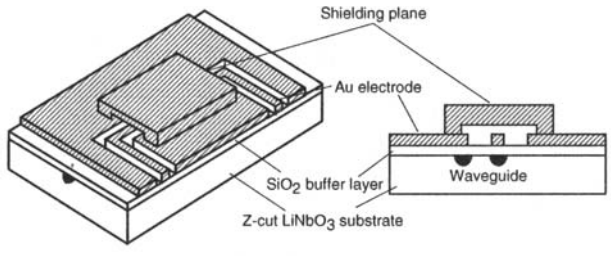

Fig. 6. Schematic and cross-sectional configurations of shielded-velocity-matched modulator.

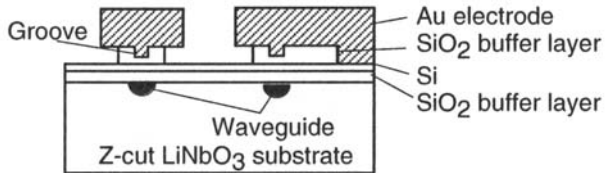

Fig. 7. Cross section of a $LiNbO_3$ modulator with electrodes buried in the buffer layer.

by using effectively low dielectric materials around the electrode: air and silicon oxide. The microwave electrical field efficiently leaks into those materials and the effective index is lowered to that of the optical wave. As shown in the previous section, thick CPW electrode is one way to obtain velocity matched modulators. It is more effective to remove high dielectric material, $LiNbO_3$ substrate, and to replace it with low dielectric material in the interaction region. This concept led to several excellent structures:

Figure 6 shows the shielded velocity matched structure reported by Kawano et al. [27]. A shielding plane is put on the CPW electrode in the interaction region and the microwave electrical field leaks into the air. Velocity matching is obtained with the gap of 4 μm, and the modulation bandwidth (electrical 3-dB) is 12 GHz.

Another way to lower the microwave index and obtain impedance matching is to etch the silicon oxide buffer layer and replace it with air. Miyamoto et al. fabricated a silicon oxide groove with an undercut between the hot electrode and ground of ACPS electrode (Fig. 7). Moreover, the bottoms of the electrodes are buried in the buffer layer in order to lower the driving voltage. They obtained a modulation bandwidth of 14 GHz with driving voltage of 3.2 V. Dolfi et al. have developed a divided buffer layer structure with 15-μm-wide ground electrodes (Fig. 8) [29]. They achieved a modulation bandwidth of 44 GHz and driving voltage of 8.3 V with 1-cm-long electrode for both 1.3 and 1.5 μm wavelengths.

Goplakrishnam et al. have developed a simple 20-μm-thick CPW electrode structure and achieved a modulation bandwidth of 40 GHz [30]. They also analyzed and carried out experiments on the microwave input/output sections, tapers and bends, as well as the interaction region, of a test electrode structure for fabrication of a fully-packaged module. Madabhushi et al. have developed low-microwave attenuation

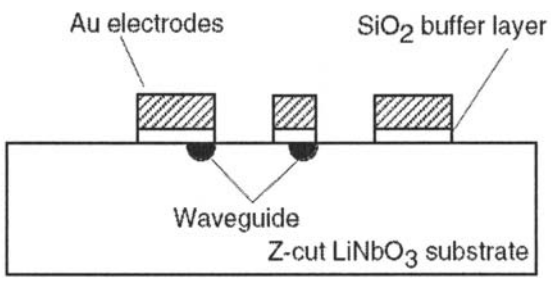

Fig. 8. Cross section of a $LiNbO_3$ modulator with an etched buffer layer and narrow ground electrodes.

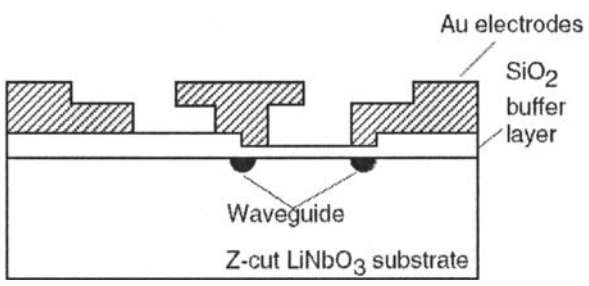

Fig. 9. Cross section of a $LiNbO_3$ modulator with a mushroom electrode and step-etched buffer layer.

electrode structures with a two-stage modified (mushroom-type) CPW electrode [31]. They also use a step-buffer layer to reduce driving voltage as shown in Fig. 9. They fabricated a fully connectorized modulator with bandwidths of 25 GHz and driving voltage of 2.5 V and confined the capability at 40 Gbit/s operation with clear eye opening.

Etching of $LiNbO_3$ substrate is the most effective for lowering the microwave index, because this enables us to replace the highest index material of $LiNbO_3$ crystal with lower index materials of air and silicon oxide. Haga et al. developed the etched grooved structure as shown in Fig. 10, which introduces air between ACPS electrodes [32]. A 4.3-μm-deep grove was fabricated on the $LiNbO_3$ substrate by reactive ion etching . The microwave index was effectively lowered to 3.8, and the modulation bandwidth is 12 GHz.

Figure 11 shows the ridge structure developed by Noguchi et al., where the $LiNbO_3$ substrate was etched between the center conductor and the ground of the CPW electrode in the interaction region [11, 12, 33]. With this structure, they obtained not only velocity- and impedance-matching but also a low driving voltage because the microwave field is concentrated in the ridged section, where the optical wave propa-

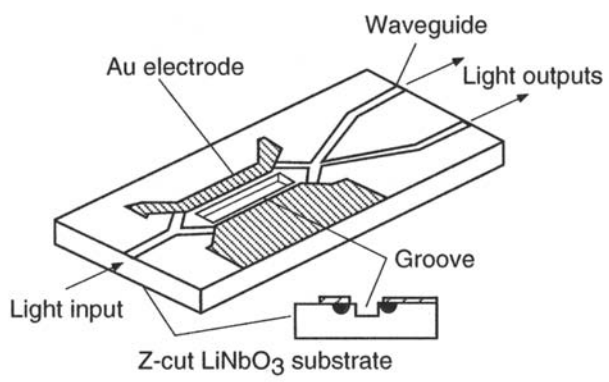

Fig. 10. Schematic structure of a modulator with a groove.

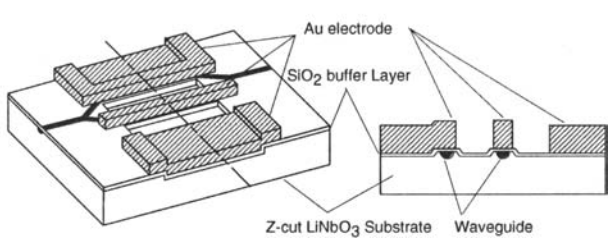

Fig. 11. Schematic and cross-sectional configurations of a ridge modulator.

gates in the Ti-diffused waveguide. Using this structure, they examined the modulation response up to 110 GHz, as described in the next section [33].

Kondo et al. reported an X-cut modulator with a two-step back-slot structure [9, 15] as shown in Fig. 12. In this structure, the thickness of the substrate around the optical waveguide is made much larger than the optical mode size to avoid the deformation and scattering. Near the ground electrodes, the thickness of the substrate is thinned for the purpose of decreasing the effective microwave index. The microwave efficiently leaks into the air not only the coplanar wave electrode but also the back slot. Using a micro-machining technique based on KrF excimer laser ablation, the substrate was thinned to 10 μm. They demonstrated a packaged modulator with 25-GHz bandwidth and 3-V driving voltage with fully suppressed DC drift.

4.3. Ultra-High-Speed Operation More Than 100 GHz

Ultra-high-speed operation up to 110 GHz has been reported by Noguchi et. al. with the ridge structure [33]. Figure 13 shows the frequency dependence of optical response from 0.1 to 110 GHz. The modulation bandwidth is 70 GHz with driving voltage of 5.1 V. The frequency dependence of the CPW electrode characteristics of the modulator

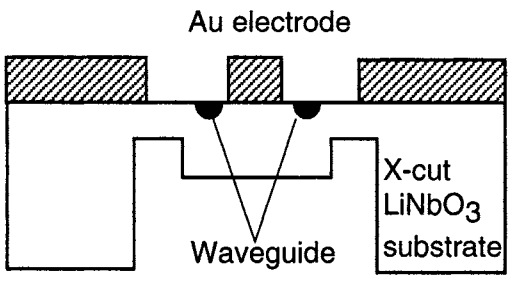

Fig. 12. Cross section of two-step back modulator on X-cut substrate.

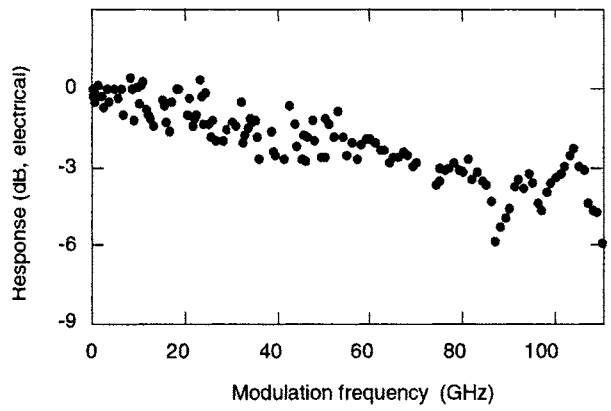

Fig. 13. Frequency dependence of the electrooptic response of a ridge modulator.

was analyzed in the 45-MHz to 110-GHz frequency range. Figure 14 shows the S-parameters of the CPW electrode measured using a vector network analyzer and probe heads. From the microwave reflection and transmission data, the frequency dependencies of nm and microwave propagation loss, α_0, were calculated, and are shown in Fig. 15. In the upper section, the dashed line shows the velocity matched line. At low frequencies, n_m is extremely large due to the finite electrode conductivity. Since n_m is almost constant above 5 GHz, geometric dispersion is not observed up to 110 GHz. The data shows that the velocity matching is maintained and that the modulator has a large bandwidth.

On the contrary, the loss increases with frequency. Below 20 GHz, the microwave propagation loss is mainly determined by the conductor loss of the electrode. Above 20 GHz, the dielectric loss increases and so does to the conductor loss [34]. The origins of the dielectric loss lie in both the $LiNbO_3$ substrate and the silicon oxide buffer layer. It should be noted that the contribution of the silicon oxide buffer layer to the dielectric loss is twice as large as that of the $LiNbO_3$ substrate because the microwave confinement factor in the buffer layer is more than 4 times as large as that in the substrate [12].

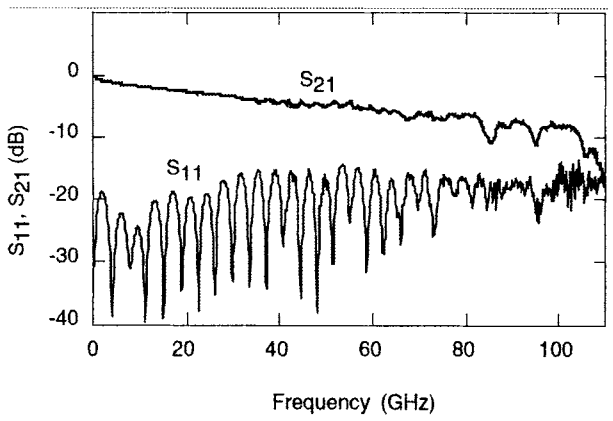

Fig. 14. Microwave reflected power (S_{11}) and transmitted power (S_{21}) of a ridge modulator.

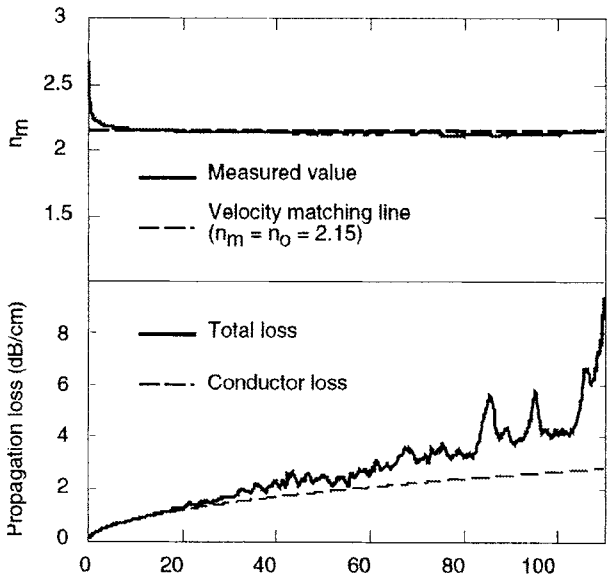

Fig. 15. Frequency dependence of microwave index and propagation loss.

5. Summary

This paper overviewed high-speed $LiNbO_3$ modulators. It has been shown that the modulator works not only as an optical component but also as a microwave or millimeter-wave component and that the operation speed is mainly determined by the electrode characteristics. Velocity- and impedance-matched structures have been developed and it has been found that lowering the microwave propagation loss is a key to achieving a

higher frequency range. The dielectric loss of the silicon oxide buffer layer should be considered in designing ultrahigh-speed modulators operating in the millimeter-wave frequency range. Further studies of polarization-independent structures or low-voltage components are required. The $LiNbO_3$ modulators are strong candidates for large-capacity and long-haul optical transmission systems operating above 40 Gbit/s in the future.

References

1. K. Hagimoto, M. Yoneyama, A. Sano, H. Hirano, T. Kataoka, T. Otsuji, K. Sato, and K. Noguchi, "Limitations and challenges of single-carrier full 40-Gbit/s repeater system based on optical equalization and new circuit design," OFC'97, ThC1, 242–243 (1997).
2. H. Onaka, H. Miyata, G. Ishikawa, K. Otsuka, H. Ooi, Y. Kai, S. Kinoshita, M. Seino, H. Nishimoto, and T. Chikama, "1.1 Tb/s WDM transmission over a 150 km 1.3 μm zero-dispersion single-mode fiber,'" OFC'96, PD19-1 (1996).
3. S. Kawanishi, H. Takara, K. Uchiyama, I. Shake, and K. Mori, "3 Tbit/s (160 Gbit/s $\times$ 19 ch) OTDM/WDM transmission experiment," OFC'99, PD1-1 (1999).
4. Y. Miyamoto, K. Yonenaga, S. Kuwahara, M. Tomizawa, A. Hirano, H. Toba, K. Murata, Y. Tada, Y. Umeda, and H. Miyazawa, "1.2 Tbit/s (30 $\times$ 42.7-Gbit/s) ETDM optical channel) WDM transmission over 376 km with 125-km spacing using forward error correction and carrier-suppressed RZ format," OFC2000, PD26-1 (2000).
5. I. Morita and N. Edagawa, "50 GHz-spaced 64 $\times$ 42.7 Gbit/s transmission over 8200 km using pre-filtered CS-RZ DPSK signal and EDFA repeaters," ECOC'03, Th4.3.1 (2003).
6. M. Seino, T. Nakazawa, Y. Kubota, M. Doi, T. Yamane, and H. Hakogi, "A low DC-drift Ti: $LiNbO_3$ modulator assured over 15 years," OFC'92, PD-3, 325–328 (1992).
7. H. Nagata and J. Nayyer, "Stability and reliability of Lithium Niobate optical modulators, IPR'95, ISaB1-1, 290-292 (1995).
8. M. Sugiyama, M. Doi, S. Taniguchi, T. Nakazawa, and H. Onaka, "Driver-less 40 Gb/s $LiNbO_3$ modulator with sub-1 V drive voltage, OFC'02 PD, FB6-1-4 (2002).
9. J. Kondo, A. Kondo, K. Aoki, M. Imaeda, T. Mori, Y. Mizuno, S. Takatsuji, Y. Kozuka, O. Mitomi, and M. Minakata, "40-Gb/s X-cut $LiNbO_3$ optical modulator with two-step back-slot structure," IEEE J. Lightwave Technol. **20**, 2110–2114 (2002).
10. M.M. Howerton, et al., "Fully packaged, broad-band $LiNbO_3$ modulator with low drive voltage," IEEE Photon. Technol. Lett. **12**, 792–794 (2000).
11. K. Noguchi, H. Miyazawa, and O. Mitomi, "Millimeter-wave Ti: $LiNbO_3$ optical modulatrs," IEEE J. Lightwave Technol. **16**, 615–619 (1998).
12. K. Noguchi, H. Miyazawa, and O. Mitomi, "Frequency-dependent propagation characteristics of a coplanar waveguide electrode on a 100-GHz-Ti: $LiNbO_3$ optical modulator," Electron. Lett. **34**, 661–662 (1998).
13. R.C.A. Alferness, "Waveguide electrooptic modulators," IEEE Trans. Microwave Theory Tech. **MTT-30**, 1121–1137 (1982).
14. H. Nagata, "DC drift failure rate estimation on 10 Gb/s X-cut lithium niobate modulators," IEEE Photon. Technol. Lett. **12**, 1477–1479 (2000).
15. J. Konodo, A. Kondo, K. Aoki, S. Takatsuji, O. Mitomi, M. Imaeda, Y. Kozuka, and M. Minakata, "A packaged 40-Gb/s X-cut $LiNbO_3$ modulator with 3-V-drive-voltage and suppressed dc-drift," ECOC'02, P2.11 (2002).

16. R.V. Schmidt and I.P. Kaminow, "Metal diffused optical waveguides in $LiNbO_3$," Appl. Phys. Lett. **25**, 458–460 (1974).

17. T. Nozawa, K. Noguchi, H. Miyazawa, and K. Kawano, "Water vapor effects on optical characteristics in Ti: $LiNbO_3$ channel waveguides," Appl. Opt. **30**, 1085–1089 (1991).

18. M. Izutsu, Y. Yamane, and T. Sueta, "Broad-band traveling-wave modulator using $LiNbO_3$ optical waveguide," IEEE J. Quantum Electron. **QE-13**, 287–290 (1977).

19. K. Yoshida, Y. Kanda, and S. Kohjiro, "A traveling-wave-type $LiNbO_3$ optical modulator with superconducting electrodes," IEEE Trans. Microwave Theory Tech. **47**, 1201 (1999).

20. M. Seino, N. Mekada, T. Yamane, Y. Kubota, M. Doi, and T. Nakazawa, "20-GHz 3 dB-bandwidth Ti; $LiNbO_3$ Mach-Zehnder modulator," ECOC'90, PD-3, 999–1002 (1990).

21. G.K. Gopalakrishnan, C.H. Bulmer, W.K. Burns, R.W. McElahanon, and A.S. Greenblatt, "40 GHz, low half-wave voltage Ti: $LiNbO_3$ intensity modulator," Electron. Lett. **28**, 826–827 (1992)

22. K.H. Hellwege, editor, *Numerical data and functional relationships in science and technology*, Vol. 16, Springer-Verlag, pp. 149–163.

23. S.K. Korotky, G. Eisenstein, R.S. Tucker, J.J. Veselka, and G. Raybon, "Optical intensity modulation to 40 GHz using a waveguide electro-optic switch, Appl. Phys. Lett. **50**, 1631–1632 (1987).

24. K. Kawano, T. Kitoh, O. Mitomi, T. Nozawa, and H. Jumonji, "A wide-band and low-driving-power phase modulator employing a Ti: $LiNbO_3$ optical wavguide at 1.5 μm wavelength," IEEE Photon. Technol. Lett. **1**, 33–34 (1989).

25. O. Mitomi, K. Noguchi, and H. Miyazawa, "Broadband and low driving-voltage $LiNbO_3$ optical modulators," IEE Proc.-Optoelectron. **145**, 360–364 (1998).

26. K. Noguchi, O. Mitomi, and H. Miyazawa, "40-Gbit/s Ti: $LiNbO_3$ optical moculator with a two-stage electrode," IEICE Trans. Electron. **E81-C**, 1316–1320 (1998).

27. K. Kawano, T. Kitoh, H. Jumonji, T. Nozawa, and M. Yanagibashi, "New traveing wave elecrode Mach-Zehnder optical modulator with 20 GHz bandwidth and 4.7 V driving voltage at 1.52 μm wavelngth," Electron. Lett. **25**, 1382–1383 (1989).

28. H. Miyamoto, H. Ohta, K. Tabuse, and Y. Miyagawa, "Evaluation of $LiNbO_3$ intensity modulator using electrodes buried in buffer layer," Electron. Lett. **28**, 976–977 (1992).

29. D. Dolfi and T. R. Ranganath, "50 GHz volocity-matched, broad wavelength $LiNbO_3$ modulator with multimode acrive section," Electron. Lett. **28**, 1197–1198 (1992).

30. G.K. Gopalakrishnan, W.K. Burns, R.W. McElhanon, C.H. Bulmer, and A.S. Greenblatt, "Performance and modeling of broadband $LiNbO_3$ traveling wave optical intensity modulators," IEEE J. Lightwave Technol. **12**, 1807–1818 (1994).

31. R. Madabhushi, Y. Uematsu, K. Fukuchi, and A. Noda, "Wide-band, low driving voltage Ti: $LiNbO_3$ optical modulators for 40 Gb/s applications," ECOC'98, 1, 547–548 (1998).

32. H. Haga, M. Izutsu, and T. Sueta, "$LiNbO_3$ traveling-wave light modulator/switch with an etched groove," IEEE J. Quantum Electron. **QE-22**, 902–906 (1986).

33. K. Noguchi, O. Mitomi, H. Miyazawa, and S. Seki, "Broadband Ti: $LiNbO_3$ optical modulator with a ridge structure," IEEE J. Lightwave Technol. **LT-13**, 1164–1168 (1995).

34. W.M. Robertson, G. Arajavalingam, and G. Kopcsay, "Broadband microwave dielectric properties of lithium niobate," Electron. Lett. **27**, 175–176 (1991).

DOI: 10.1007/s10297-005-0036-2
Originally published in J. Opt. Fiber Commun. Rep. 2, 171–208 (2004)

High-speed optical signal processing using semiconductor optical amplifiers

Colja Schubert, Reinhold Ludwig, and Hans-Georg Weber

Fraunhofer Institute for Telecommunications, Heinrich Hertz Institut
Einsteinufer 37, 10587 Berlin, Germany

Abstract. The authors report on all-optical switching devices based on semiconductor optical amplifiers (SOA) in applications for optical time division multiplexing (OTDM) transmission technology. The report includes a discussion on the basic properties of an SOA, on the nonlinear processes of cross-phase modulation and four-wave mixing in the SOA used for all-optical switching, and on the application of the SOA as demultiplexer, add-drop multiplexer, clock recovery and wavelength converter. The devices considered here operate at data rates in excess of 80 Gbit/s, where electrical signal processing is not available today.

1. Introduction

Ultrafast transmission technology requires a variety of devices or subsystems for demultiplexing, add–drop multiplexing, wavelength conversion, clock recovery, regeneration and optical sampling. The devices considered here operate at bit rates, where electrical signal processing is not available today, i.e., at data rates in excess of 80 Gbit/s. These devices can be realized in various ways for instance using passive or active nonlinear optical components. The most widely investigated active nonlinear optical component is the semiconductor optical amplifier (SOA). The main advantage of the SOA as compared to passive structures, e.g., optical fibers, is its compactness due to a resonant enhancement of the nonlinear optical effects. In this paper the properties of the SOA for applications in high-speed transmission experiments will be discussed. The focus is on its application as demultiplexer and as add–drop multiplexer in time division multiplexing transmission systems. Also, the application of the SOA for clock recovery, wavelength conversion and for dispersion compensation in transmission experiments using the mid-span spectral inversion technique will be briefly discussed.

2. Semiconductor Optical Amplifier (SOA)

First reports on SOAs date back to more than 30 years ago [1,2]. At that time, SOAs were also called "travelling-wave laser amplifiers" or "semiconductor laser amplifiers (SLA)". There was no special design for SOAs. Laser diodes developed for operation in a transmitter were provided with an anti-reflection coating on both facets and then applied as amplifiers. Today, SOAs are developed having a special design for applications as amplifier. Apart from their use as simple amplifiers, SOAs have attracted much attention for all-optical switching applications, due to their high nonlinearity. In this section the basic properties of SOAs will be discussed, mainly with respect to their use in all-optical switching configurations. A more detailed and general description of SOAs may be found in [3–8].

2.1. Fundamentals of SOA

Figure 1 shows schematically the typical structure of an SOA with input and output fibers. In this basic SOA configuration, light is coupled into the amplifier via one of the facets. Then it passes the active region once (in a single pass) before the light is coupled into the output fiber at the opposite side of the SOA. An efficient fiber-chip coupling can be achieved by use of a tapered fiber. Here, the taper acts as a micro-lens, which focuses the light onto the active region on the SOA-facet. Typical values for the optical losses associated with the fiber-chip coupling are about 3 dB per facet.

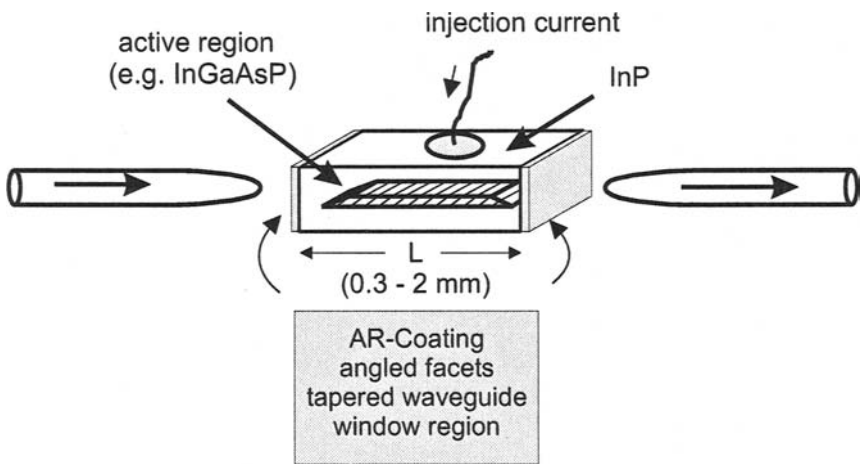

Fig. 1. Schematic of an InGaAsP/InP SOA device with fiber coupling.

Characteristic geometries of the active region are a cross section of the order of 1 mm × 0.1 mm and a length L of 0.3 to 2 mm. In the active region population inversion is achieved by current injection and light is amplified by stimulated emission. As the single-pass gain of an SOA can be as high as 30 dB, extreme care must be taken to reduce the power reflectivity at the facets to values below 10^{-4}. High reflectivity

results in multiple reflections and a gain-profile modulated by the resonator modes. There are several technological means to reduce the facet reflectivity of an SOA chip: antireflection (AR) coatings, angled facets and window regions. Often several techniques are used simultaneously. The antireflection coating comprises multiple layers to achieve wide-band low facet reflectivity. To improve fiber chip coupling, sometimes a taper region is integrated in the SOA, in which the width of the active waveguide decreases continuously towards the end facets.

The operation wavelength of SOAs for applications in optical telecommunications is generally around 1.3 or 1.55 μm [9–15]. The structure of the active region can be either bulk, multi-quantumwell (MQW) or quantum-dot (QD). An MQW-SOA has generally a larger gain bandwidth and offers a higher degree of freedom with respect to the device design. The QD-SOA is of great interest because of its unique opto-electronic properties. Despite several successful developments [16, 17], QD-SOAs are still of minor importance for all-optical signal processing and will not be discussed further in this paper.

2.2. *Basic Properties*

The active semiconductor region of an SOA has a band structure as schematically depicted in Fig. 2. It is electrically pumped with carriers by the injection current. This results in population inversion between the conduction band and the valence band.

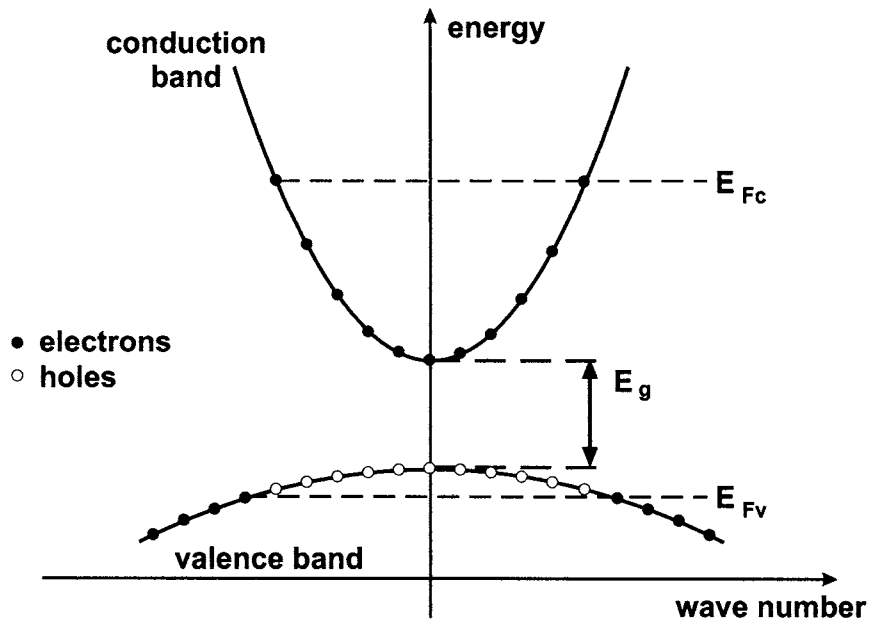

Fig. 2. Simplified band structure of a direct band-gap semiconductor in quasi-equilibrium.

A light signal with frequency ω, injected in such an active semiconductor medium, is amplified by stimulated emission, if the photon energy $\hbar\omega$ is larger than the band gap

energy E_g between valence band and conduction band and smaller than the separation $\Delta E_F = E_{Fc} - E_{Fv}$ between the quasi-Fermi levels E_{Fc} and E_{Fv} of the conduction band and valence band, respectively. The medium is transparent for photons with an energy below the band gap ($\hbar\omega < E_g$), whereas absorption dominates over stimulated emission for photon energies larger than ΔE_F. The quasi-Fermi levels depend on the current-dependent population inversion.

The propagation of light power along the z axis in an amplifying medium can be described by

$$\frac{d}{dz}P(z) = [\Gamma g(z) - \alpha_s]\, P(z). \tag{1}$$

Here, $P(z)$ is the optical power at the longitudinal coordinate z in the SOA, α_s denotes the scattering losses, Γ is the confinement factor, which characterizes the ratio of waveguide gain to material gain, and $g(z)$ is the local gain coefficient. The single-pass gain G of an SOA is defined as the ratio of the optical power $P(L)$ at the output to the optical power $P(0)$ at the input of the SOA. It is obtained by integration of Eq. (1) over the length L of the active region:

$$G = \exp\left(\int [\Gamma g(z) - \alpha_s]\, dz\right). \tag{2}$$

In the small-signal regime, $g(z)$ can be replaced by the spatially uniform, unsaturated gain coefficient g_0, which gives $G = \exp[(\Gamma g_0 - \alpha_s)L]$. The unsaturated gain coefficient is a function of optical frequency (or wavelength) and the carrier density. In general, the confinement factor Γ for the two fundamental modes TE and TM in the SOA is different [7]. As a result, the single-pass gain of the SOA depends on the state of polarization of the incoming light wave. The polarization dependence of the gain is typically 0.5–1 dB.

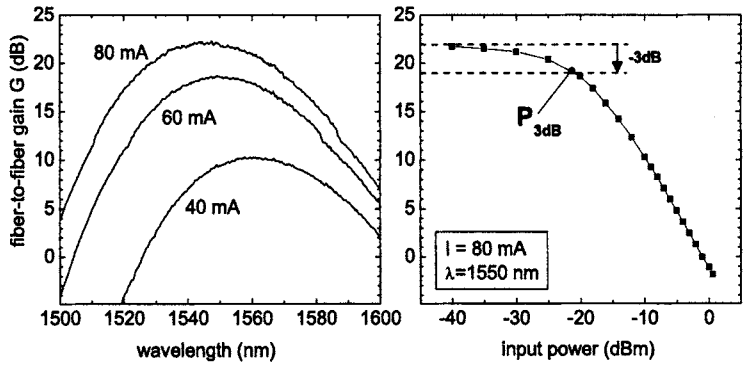

Fig. 3. Left: Spectral profiles of unsaturated SOA gain at various injection currents. Right: SOA gain versus the optical input power (λ =1550 nm). The SOA is a bulk device with a length of 500 μm.

Figure 3 (left) shows typical experimental data of unsaturated gain spectra for various injection currents. The injection current determines the carrier density N. The plotted gain values are the fiber-to-fiber gain. These gain values are defined by the ratio of the optical power in the fiber at the output to the optical power in the fiber at the input. Figure 3 (left) shows, that the maximum of the gain profile is shifted towards shorter wavelengths, if the injection current and therefore also the carrier density N are increased.

High optical power in the SOA leads to a significant depletion of carriers due to stimulated emission. As a result, the carrier density N is in general not spatially uniform and the gain coefficient becomes z-dependent. For example, the local gain coefficient in the stationary case may be written as [5, 18]:

$$g(z) = \frac{g_0}{1 + \frac{P(z)}{P_s}}. \tag{3}$$

According to this equation, the gain of the SOA saturates by the injection of an optical signal in the SOA. The saturation output power P_s is a characteristic property of the SOA. It specifies the optical output power, at which the gain coefficient reduces to half of the unsaturated value. The output power $P_{3\mathrm{dB}}$ at which the fiber-to-fiber gain is reduced to half its value, which is the actual measurement quantity, can be approximated by $P_{3\mathrm{dB}} = \ln(2)P_s$ for high single-pass gain values. Figure 3 (right) is an example of measurements of the fiber-to-fiber gain versus the optical input power to the SOA. Gain saturation causes a shift of the gain maximum towards longer wavelengths because gain saturation means reduction of carrier density N at the given injection current.

The propagation of an optical wave through the SOA is described by the complex refractive index $n_c = n - in''$. The real part n is identical with the commonly used refractive index. It determines the change of the phase Φ of the transmitted wave having the wavelength λ after passage through the medium with length L and refractive index n as $\Delta\Phi = 2\pi Ln/\lambda$. The imaginary part n'' describes the gain of the medium and is related to the gain coefficient g by $\Gamma(g - \alpha_s) = -4\pi n''/\lambda$ [19]. Both n and n'' depend on the carrier density N. Gain saturation in an SOA ($dN < 0$) leads to an increase of n and a decrease of g. Very often the linewidth-enhancement factor (or Henry-factor) $dn/dn'' = \alpha$ is used to relate the changes in both n and n'' [20].

Another important parameter of the SOA is the noise figure. It is defined by the ratio of two ratios, namely the signal to noise ratio of a data signal at the input and the signal to noise ratio of a data signal at the output of the SOA. Typical noise figure values for an SOA are between 5-10 dB. This rather high value is due to amplified spontaneous emission (ASE), which is an important characteristic of the SOA. The spontaneously emitted photons are also amplified. Therefore the ASE-spectrum has approximately the shape of the gain spectrum. The spectral power density of the ASE increases with the population inversion and therefore with the injection current.

Table 1 summarizes some characteristic parameters of an InGaAsP/InP SOA. It should be noted that not all of these values can be obtained simultaneously.

2.3. Change of Gain and Refractive Index, Nonlinear Effects

The gain coefficient g and the refractive index n of the SOA are a function of the carrier density N, i.e., they change, when the carrier density in the SOA is varied, for example

Parameters	typical values
Fiber-to-fiber small signal gain	25–30 dB
Polarization dependence of the gain	0.5–1 dB
3 dB saturation output power $P_{3\mathrm{dB}}$	10–12 dBm
3 dB gain bandwidth	≈100 nm
Noise figure	10 dB
Width × height of active region	≈ 1 μm × 0.1 μm
Length of active region	300–2000 μm

Table 1. Characteristic parameters of an InGaAsP/InP SOA for operation temperatures around 25 °C and driving currents between 100 and 500 mA.

by the injection of an optical pump signal into the SOA [6,18,21]. Another light signal (probe signal) injected in the SOA simultaneously with the pump signal experiences the change of N as a change of the gain Δg and the phase $\Delta\Phi = 2\pi L\Delta n/\lambda$.

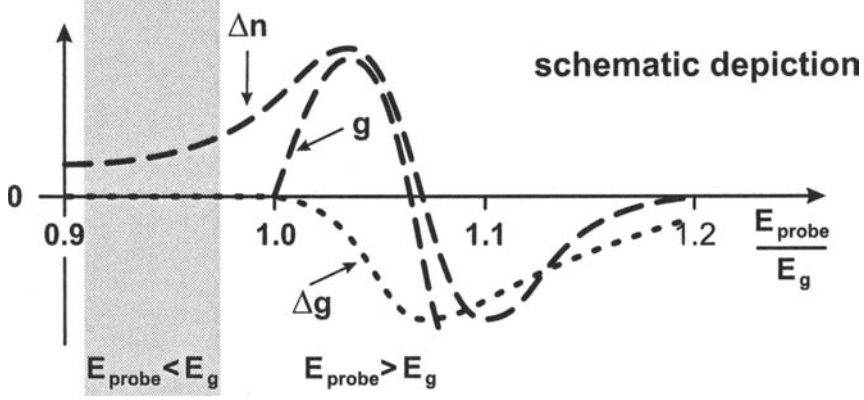

Fig. 4. Light induced change of gain and refractive index in an SOA (schematic picture) as a function of the light energy E_{probe} relative to the band gap energy E_g.

Figure 4 is a schematic depiction of the resulting gain change Δg and refractive index change Δn as seen by the probe signal with photon energy $E_{\mathrm{probe}} = \hbar\omega$ (adapted from [22]). It is assumed that the strong optical pump signal has a photon energy slightly larger than the band gap energy E_g and lies within the range of a positive gain coefficient ($g > 0$). A typical carrier density for population inversion in amplifiers with gain is $N > 10^{18}$ cm^{-3}. At this carrier density, a 1-ps pump pulse with a pulse energy of about 200 fJ results in estimated values of $\Delta g = 25$ cm^{-1} and $\Delta n = 10^{-3}$ near the maximum of the gain coefficient g. The resulting phase change can easily amount to $\Delta\Phi \approx \pi$ in a 750 μm long SOA at a wavelength of 1.5 μm. The shape of the curve of Δg illustrates that a change in the carrier density results in a large

gain change on the short wavelength side (large E_{probe}) of the SOA gain profile, while only small changes are evoked near the band edge. In fact, there is practically no gain change below the band gap, as the SOA is transparent in this wavelength range. The change of the refractive index Δn is fairly high within the whole amplification band of the SOA. Moreover, there is still a non-zero phase change below the band gap.

The dynamic of the changes Δg and $\Delta\Phi$ is important for switching applications of the SOA. The carrier density N in the conduction band is almost instantaneously reduced by stimulated emission, if an optical pulse having a narrow pulse width ($\approx$ 1 ps) is injected into the SOA. This causes an almost instantaneous change of Δg and $\Delta\Phi$. However, the recovery of the gain and of the index of refraction is governed by several processes with different time constants. There are two classes of dynamical processes [18]. The interband dynamic involves the exchange of carriers between the conduction band and the valence band. This affects the carrier density. The recovery of the carrier density N is a slow process with a time constant in the range of some 100 ps depending on the geometry and the operating conditions of the SOA. It can be reduced by an assist light beam [23]. On the other hand, the intraband dynamic denotes processes, which do not change the carrier density but change the energy distribution of carriers in the conduction band and in the valence band. The most significant intraband processes are carrier heating with a time constant in the range of 500 fs and spectral hole burning with a time constant of 50–100 fs [24–27].
The gain and phase change result in the following nonlinear optical effects:

- The gain change Δg experienced by the optical probe signal is called **Cross-Gain Modulation (XGM)**.
- The phase change $\Delta\Phi$ experienced by the optical probe signal is referred to as **Cross-Phase Modulation (XPM)**.
- If pump signal and probe signal have comparable optical power, their intensity beating modulates the carrier density at an intermediate frequency, causing the generation of dynamical gain and index gratings. Both signals are scattered at these gratings, which gives rise to additional spectral components. This effect is known as **Four-Wave Mixing (FWM)**.

The application of these nonlinear effects for all-optical switching will be discussed in this chapter.

2.4. Conventional and Gain-Transparent Operation of an SOA Switch

In the application of the SOA for all-optical switching, two modes of operation can be distinguished. Figure 5 (left) depicts schematically the "conventional" operation of an SOA switch. The control (pump) signal and the data (probe) signal have both their wavelength near the wavelength of the gain maximum of the SOA. According to Fig. 4, the data (probe) signal experiences a strong gain change Δg and a strong phase change $\Delta\Phi$. This mode of operation is required in the application of cross-gain modulation (XGM). However, in switching configurations which rely solely on cross-phase modulation (XPM), gain changes are unwanted, because they cause an adverse amplitude modulation of the transmitted data (probe) signal. In this case, it can be beneficial to choose the "gain-transparent" operation of an SOA switch [see Fig. 5 (right)]. In this mode of operation the data (probe) signal keeps its operation

wavelength (1.55 μm). However, an SOA is chosen having the gain maximum at a shorter wavelength (1.3 μm for example). Also, the pump (control) signal has a wavelength near 1.3 μm, i.e., near the gain maximum of the SOA. According to Fig. 4, the data (probe) signal has a photon energy below the band gap energy. Its wavelength is in the transparency region of the SOA. In this operation mode the refractive index change is still sufficient for switching and the gain change is strongly reduced ($\Delta g \approx 0$) [28, 29]. Switching with $\Delta g \approx 0$, i.e., gain-transparent operation of the SOA switch, has several advantages. In particular, the data (probe) signal does not affect the gain, independent of the data (probe) power. Therefore, intrachannel interference is negligible. Moreover, the data (probe) signal is outside the ASE-noise spectrum of the SOA. The gain-transparent operation of the SOA switch cannot be used for applications of XGM, but it is very beneficial for applications of XPM.

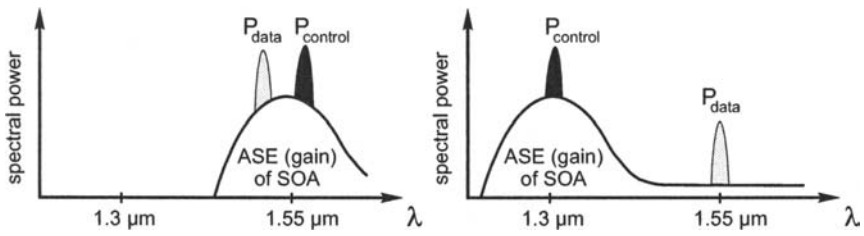

Fig. 5. Configurations of "conventional" (left) and "gain-transparent" (right) operation of an SOA switch.

2.5. *Measurements of gain and phase dynamic in an SOA*

Figure 6 shows a pump-probe set-up, which was used for measurements of both the gain and the phase dynamic in gain-transparent and conventionally operated SOAs [30]. It comprises a hybrid fiber based Mach-Zehnder interferometer (MZI) incorporating the SOA (gain maximum at 1.55 or 1.3 μm) under investigation in one arm. An attenuator (Att) provides similar power levels in both interferometer arms and an optical delay line (OD) provides adjustment of the length of both arms. A shutter in each arm enables to detect the output power of each single arm separately. The two optical pulse sources generate 10 or 40 GHz pulse trains having a pulse width of about 1 ps. Moreover, the pump pulses have a wavelength of either 1300 or 1540 nm depending on the SOA under study. The set-up contains several polarization controllers (not shown in the figure), since for instance optimal interference of the probe signal at the output of the interferometer requires equal polarization of the interfering components.

The pump-probe set-up shown in Fig. 6 relies on a dynamic sampling technique. The probe pulses have a repetition rate f_{probe} which slightly differs from the repetition rate f_{pump} of the pump pulses by the offset frequency $\Delta f = f_{\mathrm{probe}} - f_{\mathrm{pump}} \approx 100$ kHz. This enables the measurement of the SOA gain and phase dynamic directly by a slow photo-detection system consisting of a bandpass filter (BPF) centered at the probe wavelength, a photodiode (PD), and an analog-to-digital (A/D) converter triggered by a signal at the frequency Δf. The offset frequency Δf generates a variable

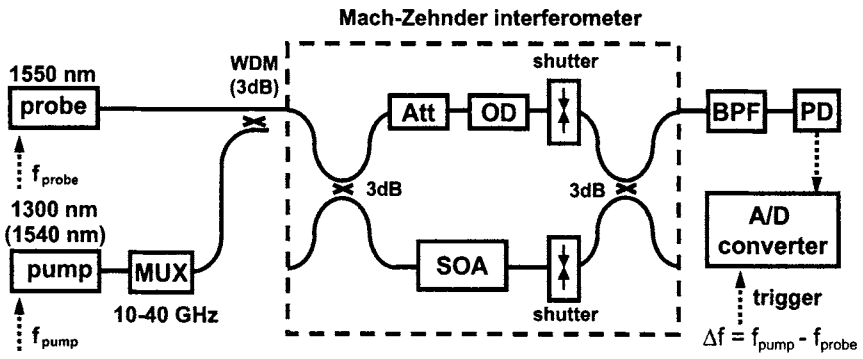

Fig. 6. Schematic of the experimental set-up for measurements of the gain and phase dynamic in a 1.3 μm SOA. For a 1.55 μm SOA, the pump wavelength is changed to 1540 nm, the WDM-coupler is replaced by a 3-dB coupler and the attenuation is applied to the lower interferometer arm, which contains the SOA, and not to the upper arm.

time delay Δt between probe and pump pulses. Details of the experimental set-up are described in [30]. The gain dynamic is measured with the upper arm of the MZI blocked. In this case the detected signal is $P_{\mathrm{out},1} = \frac{1}{4} P_{\mathrm{in}} G_1(t)$, where $P_{\mathrm{out},1}$ and P_{in} are the input and output powers of the MZI and $G_1(t)$ is the time-dependent gain in the lower arm of the interferometer. The measurements of the phase dynamic rely on the transfer function of the MZI with both arms unblocked:

$$P_{\mathrm{out}} = \frac{1}{4} P_{\mathrm{in}} \left\{ G_1(t) + G_2 - 2\sqrt{G_1(t) G_2} \cos[\Delta\Phi(t) - \Phi_0] \right\}. \qquad (4)$$

The phase shift $\Delta\Phi(t)$ induced in the SOA is obtained from the equation for P_{out} with use of the measurement of the gain dynamic $P_{\mathrm{out},1} = \frac{1}{4} P_{\mathrm{in}} G_1(t)$ and with use of the measurement of $P_{\mathrm{out},2} = \frac{1}{4} P_{\mathrm{in}} G_2$ with the lower interferometer arm blocked ($G_1(t) = 0$). The phase Φ_0 is a static phase difference in the interferometer, which can be adjusted to $\Phi_0 = 0$. Please note, that the interferometer needs an active phase stabilization for stable operation (for details see [30]).

Figure 7 shows measurements of the gain and phase dynamic at the repetition frequencies of 10 and 40 GHz of the pump pulses. The results for the gain-transparent operation were obtained with use of a 1300 nm SOA and pump pulses having a wavelength near 1300 nm and a pulse energy of 800 fJ. The results for the conventional operation were obtained with use of a 1540 nm SOA and a 1540 nm pump with a pulse energy of 800 fJ. The probe signal had a wavelength of 1550 nm in both cases.

For the conventionally operated SOA the expected fast decrease in gain, discussed in section 2.3, is observed in Fig. 7. It is followed by a fast recovery (intraband processes) and a slow recovery by electrical pumping (interband processes). A separation of the different intraband processes is not possible, due to the limited temporal resolution (about 1 ps) of the measurement technique. In the gain-transparent operated SOA the gain dynamics is mainly caused by free carrier absorption (for details see [31]).

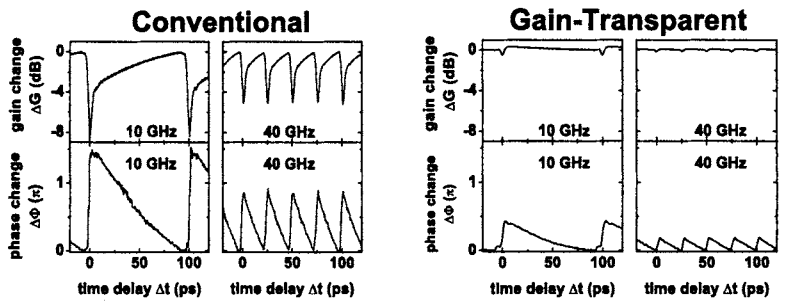

Fig. 7. Gain (upper graphs) and phase (lower graphs) dynamic for a gain-transparent and a conventionally operated SOA at repetition frequencies of the pump pulses of 10 and 40 GHz. The gain-transparent operated SOA was a multi-quantumwell device with 800 μm length, a gain maximum at 1300 nm and a fiber-to-fiber gain of about 28 dB. The conventionally operated SOA was a bulk device with 500 μm length, a gain maximum at 1550 nm and a fiber-to-fiber gain of about 20 dB.

In the phase dynamic curves no fast recovery component is observed like in the gain dynamic curves. This suggests, that the phase shift by intraband processes is smaller than the phase shift caused by interband processes.

The results in Fig. 7 also reveal that the amount of gain and phase change is different for gain-transparent and conventional operation and depends on the repetition frequency of the pump pulses. In the gain-transparent operation, the gain change is below 1 dB and the maximum phase change is 0.4 π at the repetition frequency of 10 GHz. The gain change is mainly caused by free carrier absorption. In the conventional operation, the gain change is up to 8 dB and the maximum phase change is 1.4 π at the same repetition frequency of 10 GHz. In both modes of operation, the maximum phase change decreases for the higher repetition frequency of the pump pulses. The SOAs investigated in the two modes of operation differ significantly in structure, length of the active region and in gain. Therefore, a direct comparison is difficult. Nevertheless the results agree with the expectation, that the phase change is generally smaller in the gain-transparent operation than the phase change obtained by the conventional operation.

More detailed measurements show that the phase change $\Delta\Phi$ increases with bias current and with the energy of the control pulse. Moreover, the phase change also depends on the length of the active region. Using conventional operation of the SOA, a phase change of more than 2 π was obtained at 10 GHz repetition frequency and a phase change of more than π was obtained at a repetition frequency of 40 GHz in a 1.5-mm-long device [30]. For repetition frequencies of more than 40 GHz, the maximum phase change was investigated by a spectral method [32]. The results indicate a further decrease of the maximum phase change with increasing repetition frequency. It becomes increasingly difficult to get a π phase change, but still a reasonable phase change is expected up to 160 GHz. However, high powers of the pump pulse are needed. This leads to a strong gain variation in the conventional operation. Therefore, SOA based interferometric gates using XPM are less attractive for applications like

wavelength conversion and 3R-regeneration at high bit rates (e.g., 160 Gbit/s), where high repetition rates of the pump pulses are required.

The gain-transparent operated SOA has the advantage to generate a very small gain variation compared to the conventionally operated SOA. This is advantageous in applications like add–drop multiplexing and optical sampling. However, the phase change is generally smaller than the phase change obtained by the conventionally operated SOA under comparable conditions. An increase of the maximum phase change by the use of an SOA with longer active region and a higher injection current is problematic, because the transmission loss due to free carrier absorption increases with length and injection current [33]. While a phase change less than π is acceptable in applications like demultiplexing, applications like add–drop multiplexing generally require a phase change of π and a vanishing gain change. In section 4.1.3, a special switching geometry will be presented, which makes the application of the gain-transparent SOA as add–drop multiplexer possible also for a phase change less than π.

The slow recovery of gain and phase, shown in Fig. 7, is the main obstacle for the use of SOA based switches at high bit rates, as they inhibit short switching widows (see section 3.2). The limiting effects of the slow phase recovery can be overcome by the use of a differential switching scheme (see section 3.2). A possibility to shorten the recovery time is to reduce the effective carrier lifetime, for example by clamping of the SOA with an additional cw-signal. This will be discussed in section 4.3

3. High-Speed Optical Switching Using SOA

All-optical switching based on nonlinear optical effects in an SOA relies on the application of cross-phase modulation (XPM), cross-gain modulation (XGM) or four-wave mixing (FWM). For high-speed optical switching, the application of XGM is not appropriate, in particular for applications like demultiplexing or add–drop–multiplexing, due to the limited switching contrast. Therefore, XGM will not be discussed in the following. The switching devices considered in this section rely on the application of XPM and FWM.

3.1. Pump-Probe Characterization of Switching Devices

An important property of these switching devices is the amplitude transfer characteristic, the so-called switching window. In the ideal case, the pump (control) signal changes the transmittance T for the probe (data) signal at a given time instantaneously from $T = 0$ to $T = 1$ and after a time interval τ back from $T = 1$ to $T = 0$. The switching window is the dependence of T versus time. Figure 8 depicts a pump-probe measurement set-up, which is often used to measure switching windows. The investigated switch is represented by a grey box with inputs for the pump and probe signals and an output for the switched probe signal.

The pump and probe signals are pulse trains with a repetition frequency (f_{pump}, f_{probe}) of 10 and 40 GHz for example, a pulse width of about 1 ps and the wavelengths λ_{pump} and λ_{probe}, respectively [34]. Both pulse trains are coupled into the switch with well defined polarization and with a relative time delay Δt, which is controlled by a variable optical delay-line (OD). The pulse width of the probe signal limits the

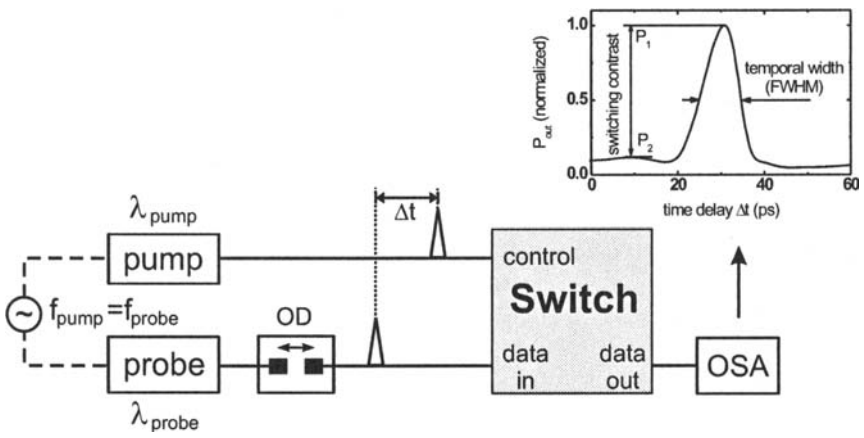

Fig. 8. Experimental set-up for the characterization of all-optical switches by pump-probe measurements. The inset shows a typical switching window of an SOA based all-optical switch measured by the pump-probe measurement technique.

temporal resolution of the measurement, while the pulse width of the pump signal determines in general the width of the switching window itself. The transmitted probe signal is detected by an optical spectrum analyzer (OSA) or by an optical power meter versus the time delay Δt between the pump and probe pulses. The inset in Fig. 8 is an example of the measurement of a switching window. The important parameters of the measured switching window are the switching contrast and the width (FWHM) of the switching window. The switching contrast is defined as the ratio of detected probe power for maximum transmittance (P_1) to the detected probe power off the maximum transmittance (P_2). Both quantities are generally used to characterize and compare different switching configurations.

3.2. Switching Based on Cross-Phase Modulation (XPM)

An optical switch based on cross-phase modulation (XPM) in an SOA is realized by incorporating the SOA in an interferometer configuration, in which the phase modulation is transferred into an amplitude modulation. The operation principle of such an interferometric switch is discussed using the Mach-Zehnder interferometer depicted in Fig. 9 as example.

The Mach-Zehnder interferometer has one 3 dB-coupler at the input and one at the output, which are both interconnected by two interferometer arms. Each interferometer arm contains an SOA and a coupler for inserting the control pulses. The data signal (data pulse) is injected into port (1) of the input 3 dB-coupler and split into both arms of the interferometer. These arms are balanced such that the data signal emerges from port 4 of the output 3 dB-coupler in the absence of a control pulse. The control pulse (port C) is split into two pulses, which are coupled with a relative time delay τ into the SOAs via the two additional couplers (ports C_1 and C_2) in the interferometer arms. Each control pulse induces a fast change and a subsequent slow recovery of the

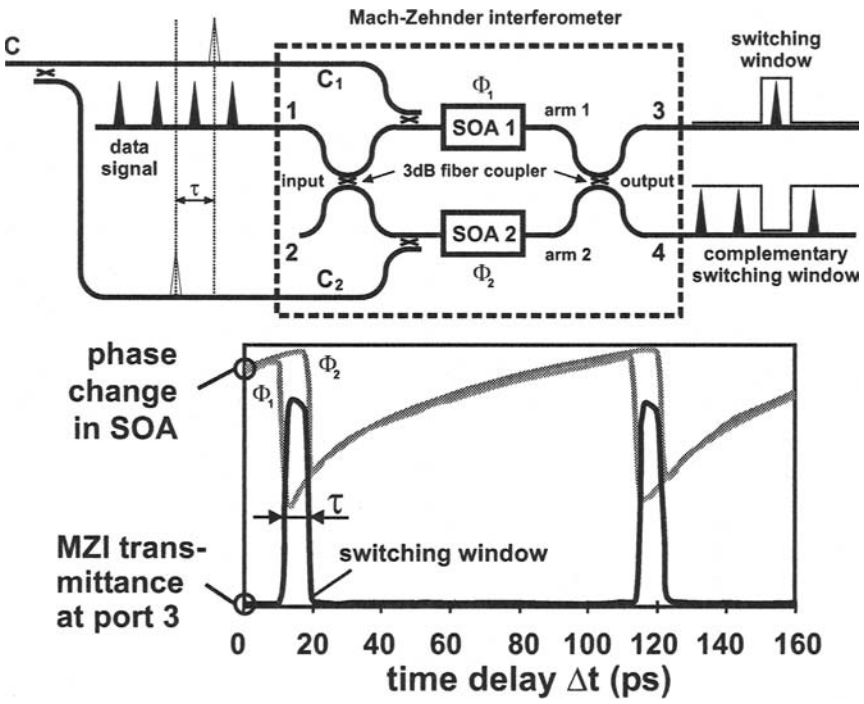

Fig. 9. Schematic depiction of a Mach-Zehnder interferometer switch based on SOAs (upper part) and the generation of the switching window from the induced phase changes Φ_1, Φ_2 (lower part).

refractive index in the SOA. The data pulses experience this change of the refractive index as a corresponding change of the phases Φ_1 and Φ_2 (depicted in the lower part of Fig. 9). The changes of Φ_1 and Φ_2 change the balance of the interferometer such that the data pulse is switched to port 3. The switching scheme in Fig. 9 is called differential switching scheme. It provides a transmission to port 3, which is only determined by the difference of Φ_1 and Φ_2 and not limited by the slow recovery. The resulting switching window is nearly symmetric and has a width determined by the relative time delay τ, because the differential phase shift $\Delta\Phi = \Phi_1 - \Phi_2$ is nearly zero outside τ by proper adjustment of the various device parameters. The change of the transmittance to the port 3 is the switching window discussed in section 3.1 and the complementary change of transmittance to port 4 is called complementary switching window. In the ideal case of a differential phase shift $\Delta\Phi = \pi$, the data pulse is completely switched to port 3 (transmittance to port 3 changes from 0 to 1). For most applications only one output (the switching window) is used, except for add–drop multiplexing, where also the complementary switching window is needed. In this case a phase change $\Delta\Phi = \pi$ is required. On the other hand, a phase change less than π is sufficient if only the switching window to the upper port is used.

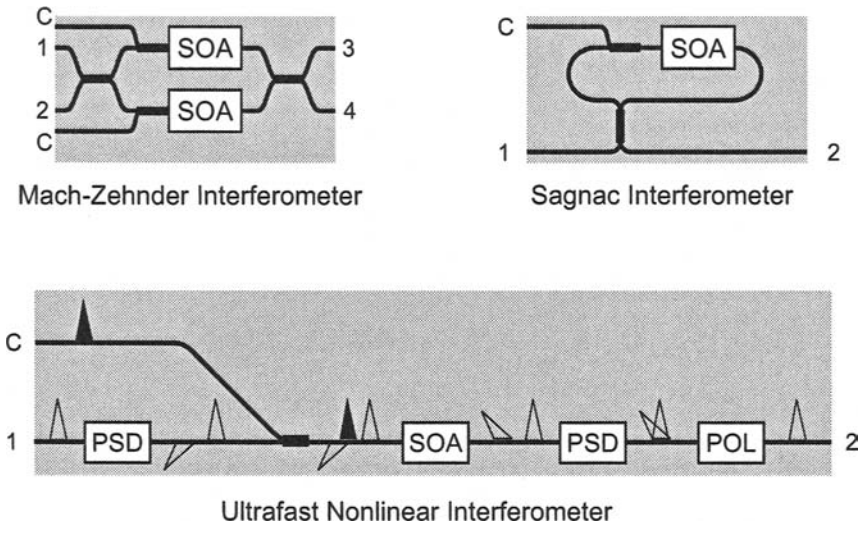

Fig. 10. Various types of interferometric switches incorporating SOAs (PSD: polarization sensitive delay, POL: polarization filter).

Besides the Mach-Zehnder interferometer also the Sagnac interferometer and the ultrafast nonlinear interferometer (UNI) are often used for XPM-switching. All three configurations are shown schematically in Fig. 10 and all use the differential switching scheme. The switching devices based on the Sagnac interferometer are known as SLALOM (semiconductor laser amplifier in a loop mirror [35,36] or TOAD (terahertz optical asymmetric demultiplexer [37,38]. In the Sagnac interferometer, the data pulses are injected into port (1) of the 3-dB coupler and propagate as clockwise and as counter-clockwise pulses in the loop. After one round trip in the loop, the clockwise and counter-clockwise pulses recombine again at the 3 dB-coupler with a phase difference, which is determined by the control pulse injected into port (C). Depending on the induced phase difference, the data pulses exit through port (1) or (2). The width of the switching window in the Sagnac configuration is determined by the position of the SOA in the fiber loop.

In the UNI switch, the two branches of the interferometer are discriminated by the state of polarization (SOP) [39,40]. The incoming data signal is equally split into two components with orthogonal SOP using a polarization sensitive delay (PSD), e.g., a highly birefringent fiber or a birefringent crystal, before passing the SOA. After the SOA, the two pulse components are recombined to a single pulse again using a second identical PSD. This pulse has an SOP, which is orthogonal to the transmission axis of the polarization filter (POL) at the output, if no control pulse is injected into the SOA. If a control pulse is injected into the SOA shortly after the first pulse component has passed the SOA, a phase change is induced in the second pulse component. This phase change results in a change of the SOP of the pulse in front of the POL, which enables transmission of the pulse through the POL. The switching window in the UNI switch is determined by the differential group delay of the PSDs.

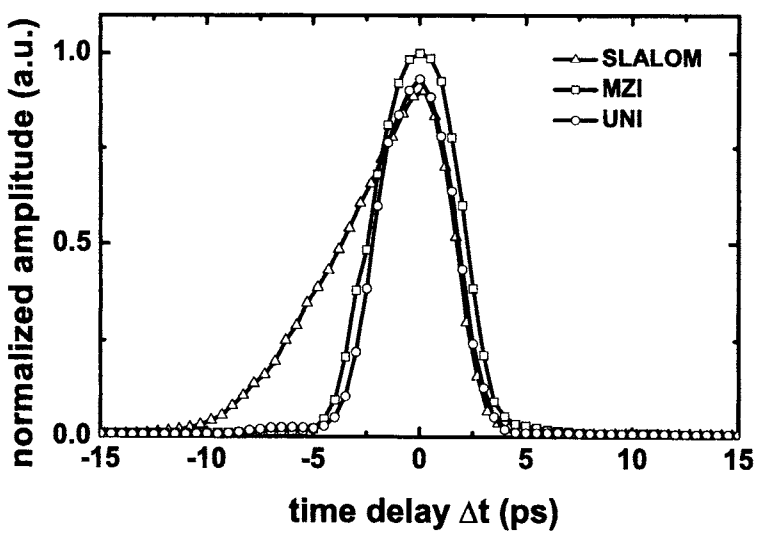

Fig. 11. Typical switching windows for a SLALOM, MZI and UNI switch, measured with a static pump-probe technique.

The switching devices based on the Sagnac interferometer are an example for an inherently stable interferometric switch. Generally, these switching devices comprise a fiber loop with a fiber length of about 10 m and with an SOA inserted into this loop. This hybrid fiber-chip set-up is inherently stable even for a variation of the optical path length by changes of the environment, because the two interferometer arms have the same spatial path. This is different with the other configurations depicted in Fig. 10. The Mach-Zehnder interferometer has two spatially separated optical arms. Stable operation is possible with this switching device only in a monolithic or hybrid integration of the interferometric configuration [41, 42]. However, with use of an additional active phase stabilization, a hybrid fiber-chip Mach-Zehnder interferometer switch was also operated as demultiplexer in a 160 Gbit/s, 160 km fiber transmission experiment [43]. The Ultrafast Nonlinear Interferometer (UNI) depicted in Fig. 10 is also not inherently stable. The polarization sensitive delays (PSD) before and after the SOA have to provide identical optical paths, which is not possible, if both are spatially separated. In section 4.1.2 a different UNI-configuration is described, which provides the same inherent stability as the Sagnac interferometer.

Figure 11 shows switching windows of XPM-switches using the Sagnac interferometer (SLALOM), the Mach-Zehnder interferometer (MZI), and the ultrafast nonlinear interferometer (UNI). The switching windows were measured using the pump-probe technique described in section 3.1 [34]. The results for the MZI and the UNI are very similar. Both switching windows have a similar shape with sharp rising and

falling flanks and a comparable switching contrast. On the other hand, the switching window of the SLALOM switch is asymmetric with different steepness of the two flanks. This is due to the configuration of the Sagnac interferometer, where one signal component is travelling in the opposite direction to the control signal through the SOA. In general, the contrast is also smaller in the SLALOM configuration. It is possible to increase the steepness of the flanks in the case of the SLAOLM by using a shorter SOA or by concatenating two SLALOM switches with opposite propagation direction of the control pulses in both SLALOM switches. However, the first method leads to a smaller phase shift, which limits the switching contrast, and the second method requires a rather complicated set-up. Therefore, the SLALOM is less appropriate for demultiplexing applications of high bit rate data signals (160 Gbit/s and above) than the interferometric switching devices based on the MZI or the UNI.

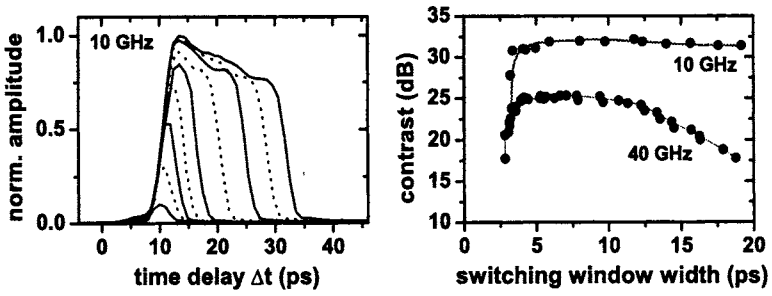

Fig. 12. Left: Measured switching windows for a GT–MZI switch at 10 GHz repetition rate of the control pulses. The relative delay τ of the control pulses (see Fig. 9) is varied, which results in different switching window widths. Right: The on-off contrast ratios derived from the measured switching windows as a function of the switching window width for control pulse repetition rates of 10 and 40 GHz.

As an example, the switching characteristic of the MZI-switch with gain-transparent operation of the SOA (GT-MZI switch) is discussed in detail in the following. We use measurements of the switching window of a hybrid MZI-switch, which is equipped with an additional phase stabilization. Figure 12 shows on the left hand side measurements of switching windows for a repetition frequency of 10 GHz of the control pulses. The relative time delay τ between the arrival times of the control pulses in SOA 1 and SOA 2 is varied in the measurements, which results in different widths of the switching windows. The on-off-contrast is determined for each switching window and plotted versus the window width on the right hand side of Fig. 12. Additionally to the results at the repetition frequency of 10 GHz, this figure shows also results at a repetition frequency of 40 GHz. For short widths the contrast decreases, because the relative time delay τ approaches the width of the optical pulses. The contrast has values above 30 dB at a window width of 3-4 ps for 10 GHz and values of 25 dB at a window width of about 4 ps for 40 GHz. The lower contrast for 40 GHz is mainly due to the lower maximum phase change in the SOA as discussed in section 2.5. For

broad switching windows the contrast is expected to decrease again due to overlapping with the adjacent switching windows. This starts earlier for 40 GHz (spacing between adjacent windows 25 ps) than for 10 GHz.

3.3. Switching based on Four-Wave Mixing (FWM)

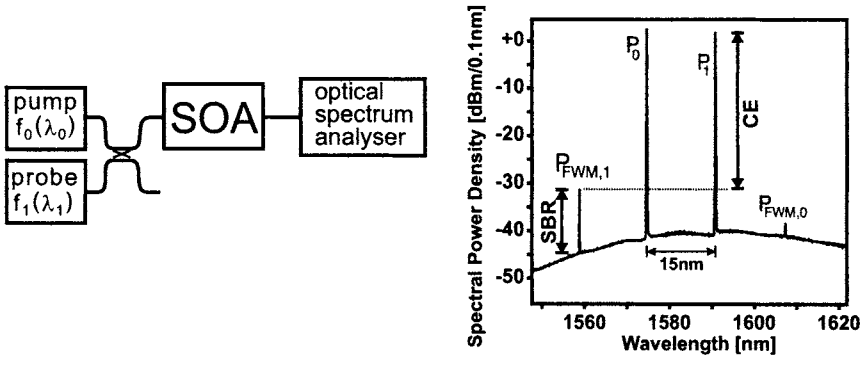

Fig. 13. Left: Schematic depiction of a typical experimental arrangement of four-wave mixing in an SOA. Right: Spectrum at the output of the SOA.

Figure 13 shows a typical experimental arrangement of four-wave mixing (FWM) in an SOA. Two optical waves, a pump (control) wave (frequency f_0, power P_0) and a probe (signal) wave (frequency f_1, power P_1) both propagating in the same direction and with the same state of polarization are coupled into an SOA. The superposition of both waves leads to a modulation of the carrier density of the SOA at the beat frequency $\Delta f = |f_1 - f_0|$ (and multiples of Δf). This modulation causes dynamic gain and refractive index gratings. Light scattering from the gain and refractive index gratings generates new light waves, the FWM-signals, with output powers $P_{\mathrm{FWM},1}$ and $P_{\mathrm{FWM},0}$. The FWM-signals are frequency shifted from the two input waves by the beat frequency Δf (see Fig. 13).

If the pump wave and the probe wave are replaced by optical pulses, the FWM-signals appear only for pump and probe pulses, which propagate simultaneously in the SOA. Hence, this scheme can be used as all-optical AND gate as experimental [44–47] and theoretical [48–50] studies showed.

Using conventional operation of the SOA (see section 2.4), the FWM-signals are generated on top of a significant background of amplified spontaneous emission (ASE) noise from the SOA as can be seen in Fig. 13. Two quantities are important for the application of FWM, the conversion efficiency CE and the signal-to-background ratio SBR, which are defined as

$$\mathrm{CE} = \frac{P_{\mathrm{FWM},1}}{P_1(0)}, \tag{5}$$

$$\mathrm{SBR} = \frac{P_{\mathrm{FWM},1}}{P_N}. \tag{6}$$

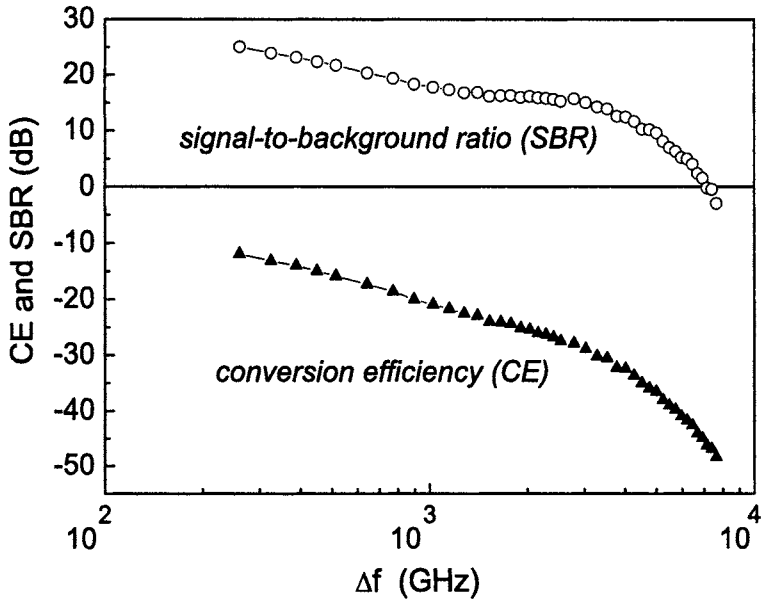

Fig. 14. Experimental data of SBR and CE versus the frequency spacing Δf between the control and data signal.

Here $P_{\mathrm{FWM},1}$ is the output power of the FWM-signal, $P_1(0)$ the signal input power and P_N the noise power in the SOA output measured at the optical frequency $f_{\mathrm{FWM},1} = f_0 - \Delta f$ of the FWM signal within a defined optical bandwidth (e.g., 0.1 nm). The SBR is mainly determined by the ASE of the SOA ($P_N \approx P_{\mathrm{ASE}}$).

The conversion efficiency CE and the signal-to-background ratio SBR depend on the location of f_1 and f_0 relative to the gain spectrum of the SOA and, as Fig. 14 shows, on the frequency spacing Δf. Strong gain modulation is obtained only near the maximum of the gain curve. The dependence on Δf originates from the finite time constants, which are associated with the gain dynamic in the SOA (see section 2.3 and [51]). More details of CE and SBR are described in [52] in terms of the dependence on the frequency spacing Δf and on the gain, and in terms of the differences of FWM using CW light or optical pulses. Phase matching is in general not a problem, because of the short length of the SOA. Experiment and theory show also, that a slight advance of the generally weaker signal pulse before the control pulse increases the CE value [48–50]. Optimum conditions for pulse width and input energy of the control pulses with respect to the switching efficiency, channel crosstalk and jitter tolerance in demultiplexer applications are investigated in [53]. Based on this technique, demultiplexing experiments of OTDM data signals with data rates of 20 Gbit/s [44], 100 Gbit/s [45] and 200 Gbit/s [46] have been reported.

The simple FWM-scheme described above is polarization sensitive. Control pulses and signal pulses have to match in polarization. However, a demultiplexer for a real OTDM system needs to be polarization insensitive. Configurations, which enable polarization insensitive FWM are known [46, 54–58], the most practical of which seems to be a polarization diversity scheme with one SOA only, that was demonstrated in a 200 Gbit/s to 6.3 Gbit/s demultiplexing experiment (see section 4.1.4).

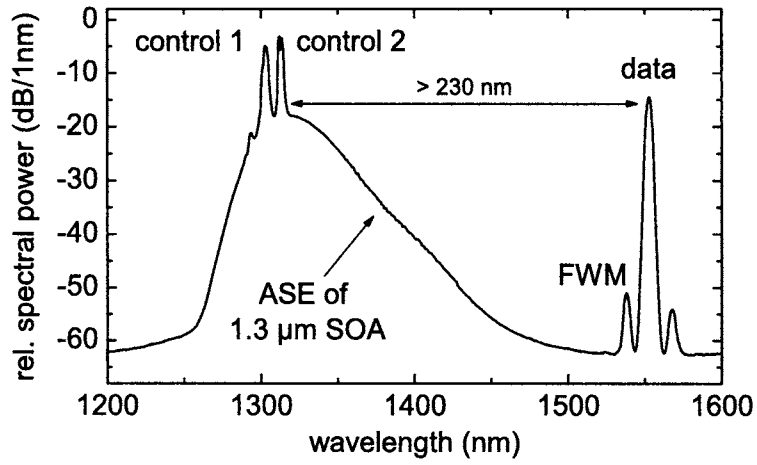

Fig. 15. Measured output spectrum of a 1300 nm SOA (gain-transparent FWM) for the case that two control signals and the data pulses overlap in time.

Up to now, the discussion on FWM was focused on the conventional SOA operation (see section 2.4). However, the beating of two optical waves (called control waves in the following) in the spectral region of positive gain causes a modulation of the refractive index also in the gain transparent region. A data signal with photon energy $\hbar\omega < E_g$ (see section 2.3) experiences this phase modulation and generates FWM-signals. This is illustrated in Fig. 15, which depicts an optical spectrum taken at the output of a 1300 nm SOA. Two control waves (control 1, control 2) are injected in the SOA with wavelengths near the gain maximum of the 1300 nm SOA and a signal wave (called data) is injected in the SOA with wavelength 1550 nm corresponding to a photon energy below the band gap energy. As there is almost no ASE noise below the band gap, the signal-to-background ratio SBR is high, despite the low conversion efficiency CE. Moreover the injected data signal itself is subject to significant loss and there is no amplification (but even attenuation) of the generated FWM-signals. In conventional FWM the amplification of the newly generated FWM-signals is considered to be a major contribution to the high CE values. Therefore, the gain-transparent FWM-switch is not suited for digital signal processing applications, such as all-optical demultiplexing. Nevertheless, this switch is of interest for analog applications, such as pulse characterization by optical sampling techniques due to its high temporal resolu-

tion and the highly linear dependence of the power of the FWM-signal on the power of the data signal over a dynamic range up to 50 dB [59].

4. Application of SOA for high-speed optical switching

The applications discussed in this section focus mainly on the use of SOA based switches in high-speed OTDM systems, namely for demultiplexing and add–drop multiplexing (section 4.1) as well as for timing extraction (section 4.2). Applications such as wavelength conversion and regeneration, which are also important signal processing functions in OTDM systems, will be addressed briefly in section 4.3. The latter section describes also applications of the SOA in "mid-span spectral inversion" experiments.

4.1. Application as Demultiplexer

The most frequently used application of an SOA in OTDM systems is an SOA-based demultiplexer. The demultiplexer (DEMUX) is a device, which enables dropping of one or more desired channels of the TDM data signal. An SOA-based optical demultiplexer, which separates several channels simultaneously (multiple output DEMUX [60]) was not convincingly realized up to now. Therefore, it is assumed that dropping of several channels simultaneously is realized by combining several demultiplexers in parallel to a multiple output DEMUX. A DEMUX has to satisfy several requirements for applications in transmission systems: stable bit-error-free operation, low control power (pulse energy of less than 1 pJ), insensitivity to the state of polarization of the data signal to be switched. The switching devices based on cross phase modulation (XPM) and four-wave mixing (FWM) in an SOA can be made to fulfill these requirements.

Among the XPM-based SOA switches, the symmetric Mach-Zehnder interferometer (MZI) configuration (see Fig. 9) is one of the most promising candidates. It enables to realize a compact and potentially low cost DEMUX by monolithic integration of the SOAs and the interferometer structure [41,61–65]. Also a hybrid-integrated SOA-MZI, called hybrid integrated symmetric Mach-Zehnder (HI-SMZ) has been realized and demultiplexing of data signals up to 336 Gbit/s was demonstrated [66–68]. The HI-SMZ comprises a Mach-Zehnder interferometer fabricated on a planar lightwave circuit (PLC) platform and an SOA array chip. These hybrid-integrated devices are a good compromise between hybrid fiber-chip devices and monolithically integrated devices because they enable the use of an optimized SOA and do not need any additional stabilization of the interferometer. The devices are however often hampered by a large insertion loss. Details on the hybrid-integrated device will be reported in "New optical device technologies for ultrafast OTDM systems" by Sakurai and Kobayashi in this publication. In section 4.1.1, a monolithically integrated SOA-MZI will be discussed as an example for a DEMUX in an MZI-configuration.

The ultrafast nonlinear interferometer (UNI) was also applied as DEMUX in many OTDM-experiments [39,69–71]. Using a "folded" geometry the UNI can be realized as hybrid device having the same intrinsic stability as the Sagnac-type optical switch. In section 4.1.2 the application of this UNI as DEMUX is described using a polarization diversity arrangement, which provides polarization independent operation.

Another key operation in a TDM system is the add–drop multiplexing. In an add–drop multiplexer (ADM), one data channel is extracted and replaced by a new

data channel. The UNI-configuration in combination with the gain-transparent SOA operation is well suited for application as ADM [72–74] and will be discussed in section 4.1.3.

Optical demultiplexers were also realized using four-wave mixing (FWM) in an SOA [46]. The application of such a DEMUX will be discussed in section 4.1.4.

4.1.1. A monolithically integrated MZI-switch as demultiplexer

In this subsection, a 160 Gbit/s all-optical demultiplexing experiment is described, based on a monolithically integrated Mach-Zehnder interferometer with SOAs [62, 75]. Figure 16 shows the experimental set-up. The monolithically integrated Mach-Zehnder interferometer has a size of 1 mm $\times$ 4.5 mm. The two SOA sections (length 1.0 mm) comprise a buried heterostructure λ = 1.50 μm InGaAsP bulk layer. The passive sections consist of a buried heterostructure λ = 1.25 μm InGaAsP bulk layer and include 3 dB multi-mode interference (MMI) couplers, S-bends, straight waveguides and spot size converters (taper).

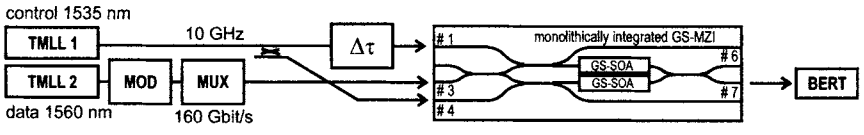

Fig. 16. Experimental set-up for 160 Gbit/s all-optical demultiplexing using a monolithically integrated MZI-switch [62].

The active waveguide is a strained bulk material with a cross-section of 0.2 μm $\times$ 0.8 μm to provide polarization insensitive gain. The passive waveguide is a wide double-mode waveguide (0.35 μm $\times$ 2 μm). In order to reduce complications due to the second order mode within the interferometer arms, small circular bends (radius 250 μm) are used as mode filters at the input of the MMI-couplers. The taper sections at the edges of the chip have nearly a square profile by reducing the width of the buried waveguides adiabatically to 0.4 μm. The taper relaxes the fiber coupling tolerances at the input and output ports. The integration of the active amplifier section with the passive waveguide network is carried out using the butt-coupling integration scheme with an angled interface to reduce reflections. The gain maximum of the two SOAs is at a wavelength of 1.5 μm, shifted away from the data wavelength, which is at 1.56 μm. Therefore, the SOA is also called "gain-shifted" SOA (GS-SOA). The purpose of this gain-shift is to get operation conditions of the SOA-MZI, which approach those of the gain-transparent operation scheme, which was explained in detail in section 2.4. However, a small gain shift was chosen in order to enable the use of a conventional Erbium doped fiber amplifier (not shown in Fig. 16) to amplify the optical control signal (λ_{control} = 1.535 μm).

The optical pulses for both the control and the data signal were generated by two 10 GHz semiconductor mode-locked lasers (TMLL), which provided sech^2-pulses having a width (FWHM) of 1.3 ps. The 160 Gbit/s data signal (RZ, OOK, PRBS = $2^7 - 1$) was generated by a 10 Gbit/s intensity modulator (MOD) and a subsequent fiber delay line multiplexer (MUX). This data signal was coupled into the MZI-switch at

port #3 with an average power of +5.5 dBm. The interferometer was balanced by proper adjustment of the injection currents into the SOAs to provide no data transmission to the port #7 in the absence of control pulses. The control signal was injected into the ports #1 and #4 of the symmetric MZI with the average powers of +15.5 and +17.7 dBm, respectively. Figure 17 (left) shows measurements of the switching window using the pump-probe technique (see section 3.1) for various delays τ between the control pulses (see Fig. 9). The minimum achievable width (FWHM) of the window was 3 ps and the highest contrast value was about 27 dB. For the demultiplexing experiments a window width of about 6 ps with a contrast of about 22 dB was chosen. Fig. 17 (right) shows the performance as demultiplexer for a data signal at 80 Gbit/s and 160 Gbit/s. The received optical power was measured before the bit-error-rate tester (BERT) at 10 Gbit/s. For the back-to-back curve the non-multiplexed 10 Gbit/s signal was used. Error-free operation (BER $< 10^{-9}$) was obtained in both cases for all 16 channels, despite an error floor at BER 10^{-11}. The power penalty was about 3.5 dB at a BER of 10^{-9} in the 160 Gbit/s demultiplexing experiment.

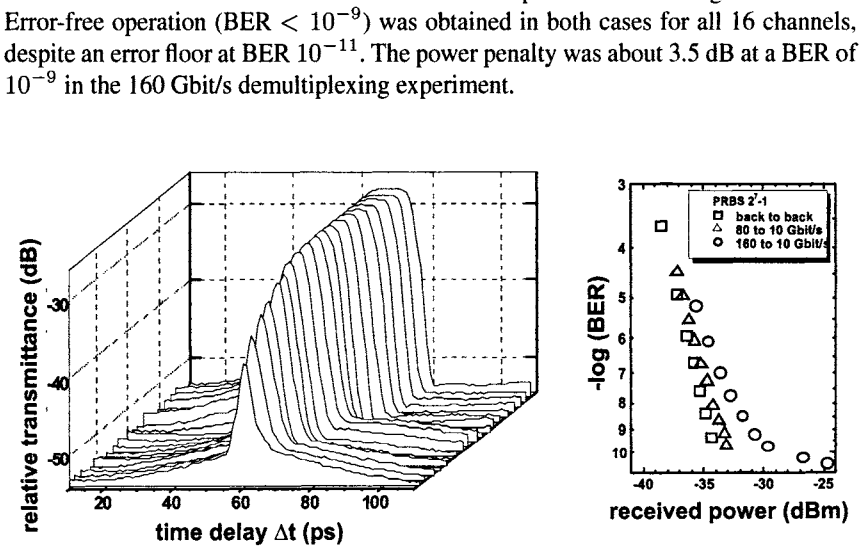

Fig. 17. Left: Switching windows of the MZI switch with gain shifted SOA (GS-MZI switch) for various delays τ between the control pulses. Right: Bit error rate measurement for a 80 and 160 Gbit/s to 10 Gbit/s demultiplexing experiment using the GS-MZI switch [62].

4.1.2. A UNI Switch as Demultiplexer

The main disadvantages of the UNI switch described in section 3.2 are the inherent polarization sensitivity and the sensitivity to changes of the environment (e.g., temperature). The sensitivity to environmental changes is due to the physical separation of the two polarization sensitive delays (PSD) before and after the SOA. The two PSD must provide the same phase shift between the two polarization components to guarantee stable operation. In the following a UNI-configuration is described, which solves both problems. Figure 18 shows schematically the set-up of this UNI switch. It is polarization insensitive by using a polarization diversity scheme [69]. At the polarizing beam splitter (PBS), the data signal (port 1) is split into two signal components (ports 2,3) with orthogonal states of polarization (SOP). Each signal component is switched in a

separate UNI-configuration. Then the two switched signal components are recombined again at the same PBS (port 4).

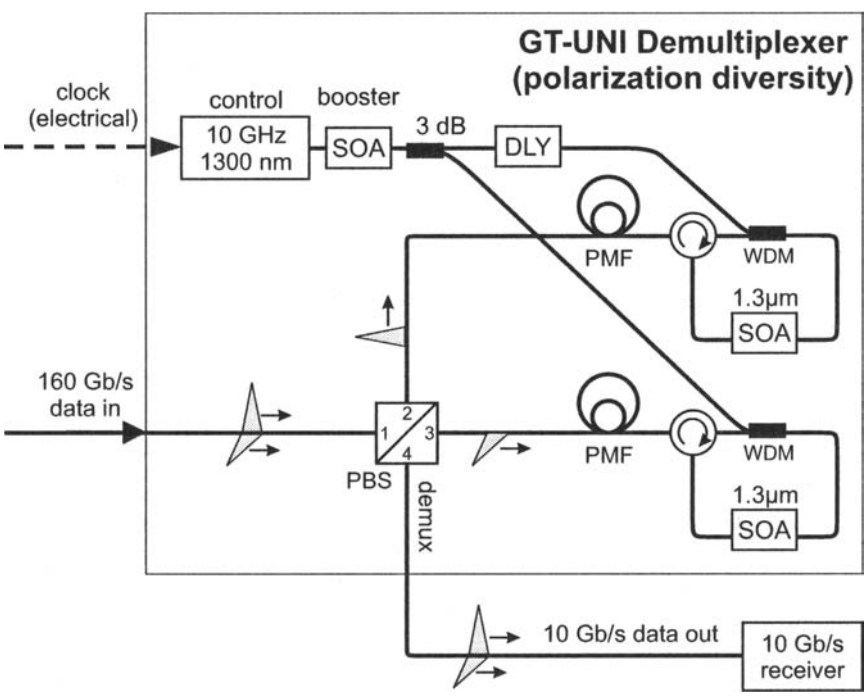

Fig. 18. Schematic of the polarization insensitive GT-UNI demultiplexer based on a polarization diversity scheme. [69]

The two UNI-configurations have a folded geometry [70], which provides insensitivity to environmental changes. The essence of this folded geometry is, that the two polarization sensitive delays (PSD) before and after the SOA are physically identical.

The operation principle of the single UNI configurations in folded geometry is as follows: An optical data pulse leaving port 2 or port 3 of the PBS is launched into a (high birefringent) polarization maintaining fiber (PMF), which operates as polarization sensitive delay (PSD). The SOP of the data pulses is such that the pulses have components of equal amplitude in both main axes of the PMF. After traversing the PMF and the circulator, both polarization components are separated in time by a delay τ, where τ depends on the differential group delay of the PMF. The two orthogonal polarization components of the pulse pass a polarization insensitive SOA and are launched again via the circulator back into the same PMF such that the "fast" component is coupled into the "slow axis" of the PMF and vice versa. Thereby, the temporal delay between both polarization components is canceled and they recombine in the PBS. Without a control pulse present, the UNI switch can be balanced such that the data pulses leave the PBS via the incoming port (port 1 for both UNI switches) and no signal will be switched to port 4 of the PBS (DEMUX output port). If a control pulse enters the SOA between the leading and the trailing polarization component, the

trailing component will experience a different phase shift as compared to the leading one. At the PBS the two polarization components recombine to a pulse having an SOP, which provides switching to port 4 of the PBS (demux output port).

The length of the PMF fiber in both UNI-switches of the diversity arrangement is about equal to get equal widths of the switching windows of both switches. Also, the overall fiber length in both UNI switches is about equal, to make sure that the separately demultiplexed signal components reach the receiver at approximately the same time (within a few picoseconds). It is not necessary to stabilize the relative phase of both signal components, because the optical power of the recombined data signal at the receiver is independent of the relative phase between both components of the diversity arrangement. As the two signal components have orthogonal SOPs, phase changes result in a random SOP of the data signal at the receiver. Therefore the receiver must be insensitive to the SOP of the data signal.

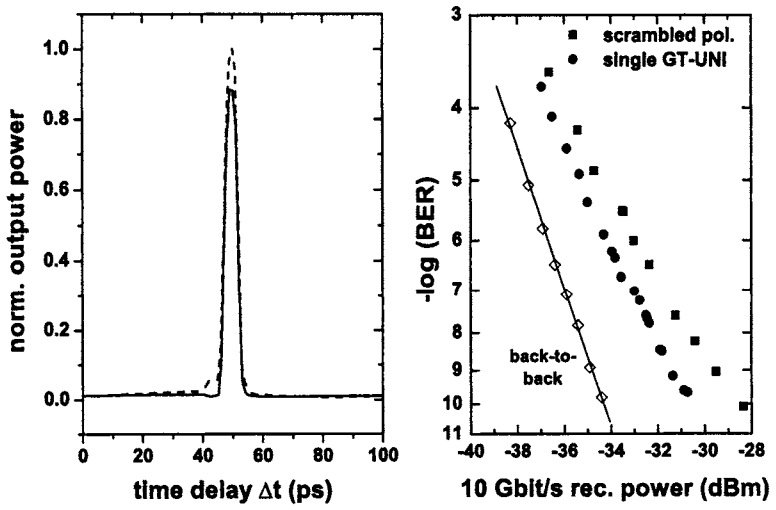

Fig. 19. Left: Switching windows of the solitary GT-UNI switches, Right: BER measurements: back-to-back (solid lines), with a single GT–UNI switch (filled circles) and with scrambled polarization (filled squares). [69]

The UNI switch can be used in conventional SOA operation or in gain-transparent SOA operation (GT–UNI) (see section 2.4). The following results refer to a UNI switch based on gain-transparent SOA operation. The data signal has a wavelength near 1.55 μm, the control pulses a wavelength near 1.3 μm and the SOA has its gain maximum around 1.3 μm.

Figure 19 shows on the left-hand side the switching windows of both GT–UNI switches in the diversity arrangement. Both switching windows differ slightly in shape and amplitude. The widths (FWHM) of the switching windows were about 5 ps and

the on-off contrasts were about 18 dB. The right-hand side of Fig. 19 shows measurements of the bit error rate (BER) in the application of the polarization insensitive GT–UNI switch as demultiplexer from 160 Gbit/s to 10 Gbit/s. The three plotted curves are: a back-to-back measurement using the non-multiplexed 10 Gbit/s signal from the receiver, a measurement at 160 Gbit/s with a single UNI-configuration and fixed (optimized) input polarization and a measurement at 160 Gbit/s with the full diversity set-up and scrambled input polarization. In the last measurement, for each BER value, the state of polarization was rapidly changed over the whole Poincaré sphere using a polarization scrambler. For the single GT–UNI switch the power penalty for error-free operation (BER = 10^{-9}) was 3.3 dB. For the full diversity set-up, error-free performance was achieved with a power penalty of 5.2 dB.

The single UNI switch (without polarization diversity) was also successfully applied in the first 160 Gbit/s field transmission experiment with 40 Gbit/s base data rate [71]. The transmission link comprised 116 km installed standard single mode fiber (SMF) of the Deutsche Telekom between the cities of Darmstadt, Gross-Gerau and Bensheim.

4.1.3. A UNI Switch as Add–Drop Multiplexer

The add–drop multiplexer (ADM) extracts (drops) a particular channel of a TDM signal and adds a new channel into the time slot of the dropped channel. In principle, an SOA-interferometric switch like the Mach-Zehnder interferometer shown in Fig. 9 offers this operation, if both output ports are used simultaneously. Thus for this application, the requirements on the switch are higher than for its application as demultiplexer. In the ADM a high on-off contrast of the switching window is needed at both output ports simultaneously (called the add port and the drop port in the following). This requires an induced phase shift of exactly π in the SOAs. Moreover, in the ADM the TDM signal appearing at the add port is used for further signal processing. Therefore, the transmitted pulses should not be affected by the switching operation. However, this cannot be avoided if conventional SOA operation is used. The gain change in the SOA leads to amplitude variations in the transmitted data signal of several dB. These amplitude modulations hampered the first ADM-experiments performed with monolithically integrated MZI switches and using conventional SOA operation at data rates up to 80 Gbit/s [64, 76–78].

Figure 20 shows schematically the set-up of the first ADM, which operated up to 160 Gbit/s [72, 73]. It is a UNI switch based on gain-transparent SOA operation. The gain-transparent SOA operation provides negligible amplitude variations of the transmitted TDM signal but in general also a phase shift less than π (see section 2.5). The set-up in Fig. 20 provides a high on-off contrast of the switching windows of both the add port and the drop-port even for a phase shift less than π.

The operation principle is similar to that of a single UNI switch, described in section 4.1.2. However, the set-up in Fig. 20 is polarization sensitive, because contrary to the set-up described in section 4.1.2 no polarization diversity arrangement is used. The ADM in Fig. 20 comprises two polarization beam splitters PBS1 and PBS2. Together with their interconnecting fibers, they form the polarization sensitive delay (PSD). At PBS1 each data pulse (port 1) having a well defined state of polarization (SOP) is split into two pulse components (ports 3,4) with orthogonal SOPs and with equal powers. The optical paths of the two pulse components to ports 1 and 2 of PBS2

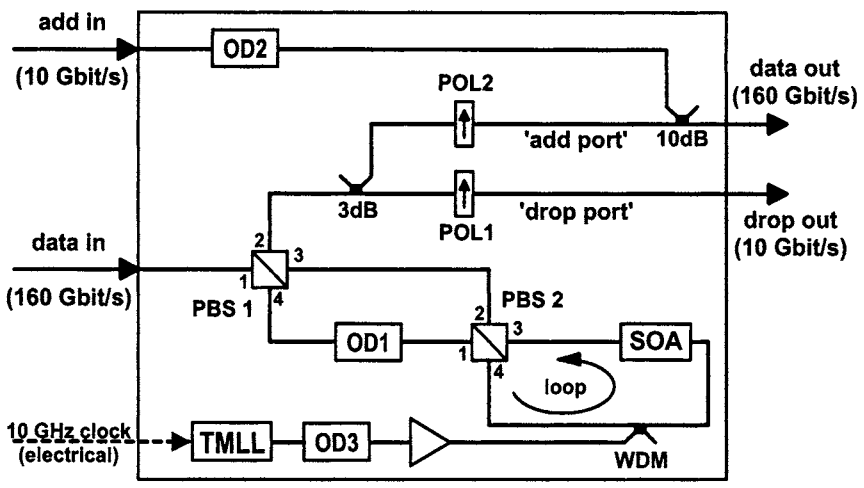

Fig. 20. Set-up of the add-drop multiplexer (ADM) based on a gain-transparent–UNI switch.

have different lengths. Both pulse components leave PBS2 at port 4 with orthogonal SOPs and with a relative time delay τ. With this time delay they pass the SOA. A control pulse injected in the SOA in the time period between the two pulse components induces a phase change in the trailing pulse component and not in the leading pulse component. Then both pulse components are coupled into port 3 of PBS2 with their SOPs adjusted such that the leading pulse component takes the longer path to PBS1 and the trailing pulse component the shorter path. Both pulse components recombine to a single pulse at port 2 of PBS1 with an SOP, which depends on the phase change induced in the trailing pulse component in the SOA by the control pulse.

The pulses at port 2 of PBS1 pass to the drop-port or the add port via a 3 dB coupler and via the polarization filters POL1 or POL2, respectively. With use of the two polarization filters POL1 or POL2 the transmittances to the add port and the drop-port are optimized independently and simultaneously to maximum on-off contrast also for a phase shift less than π.

Figure 21 shows the switching windows at the add port and the drop-port of the ADM described above. The measurements were performed with the pump-probe set-up described in section 3.1. A high on-off contrast was achieved in both cases (> 20 dB at the drop-port, > 15 dB at the add port). The width of the switching windows was 7 ps in the drop-port and 4.4 ps in the add port. The difference in the width of the switching windows can be attributed to a phase shift in the SOA of less than π.

Error-free operation of the ADM was demonstrated at a data rate of 160 Gbit/s and at a base rate of 10 Gbit/s [72, 73]. The same type of ADM was later used to demonstrated error-free performance of a 160 Gbit/s add–drop node [74]. The node was placed in between two spans of 137.5 km deployed fiber, giving an overall transmission distance of 275 km.

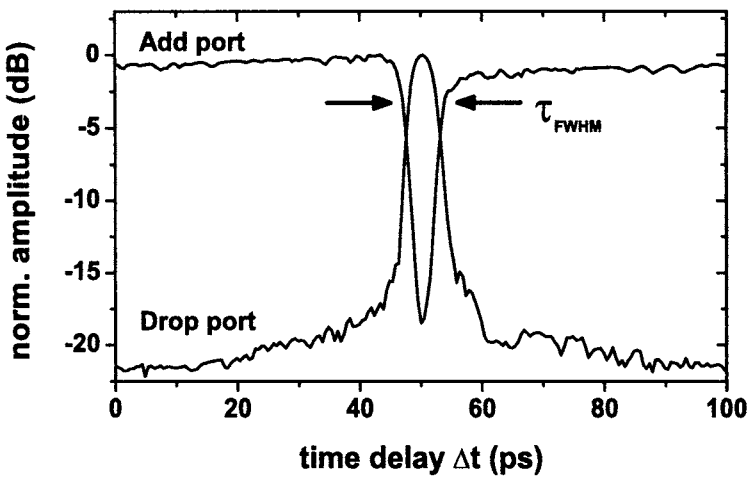

Fig. 21. Switching windows at the "add port" and "drop port" of the add-drop multiplexer depicted in Fig. 20.

4.1.4. An FWM-Switch as Demultiplexer

The first demultiplexer based on four-wave mixing (FWM) in an SOA was reported in an experiment with a data rate of 20 Gbit/s [44]. This switching device suffered from the polarization sensitivity of the FWM process. Polarization insensitive demultiplexing based on FWM in an SOA was realized by using a special configuration for 100 Gbit/s [45] and for 200 Gbit/s [46]. In the following the 200 Gbit/s demultiplexing experiment is described.

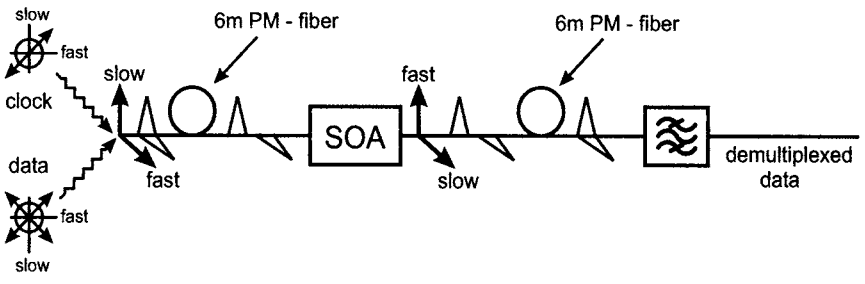

Fig. 22. FWM-based optical demultiplexer.

Figure 22 depicts the principle of the demultiplexer. The 6.3 GHz clock signal and the 200 Gbit/s data signal are input via a polarization maintaining WDM coupler (not

shown in Fig. 22) in a polarization maintaining fiber (PM-fiber) having a length of 6 m (differential group delay of 16 ps). The state of polarization (SOP) of the clock signal is linear polarized under 45 degrees with respect to the slow and fast axis of the PM-fiber. The state of polarization of the data signal is not fixed. Owing to polarization dispersion in the PM-fiber the components of clock and data signal along the fast and slow axis separate in time. The fast components of clock and data signal arrive earlier (16 ps) at the SOA and generate via FWM a new frequency component (FWM-component F). Similarly the slow components of clock and data signal generate a new frequency component (FWM-component S). At the output of the SOA is another PM-fiber (length 6 m). The axes of this fiber are adjusted such, that the FWM-component F is coupled into the slow axis and the FWM-component S in the fast axis. Thus at the output of the PM-fiber, the FWM-components F and S overlap in time and result in an FWM-signal which is independent of the state of polarization of the data signal. The resulting FWM-signal passes an optical filter, which suppresses the clock and data pulses.

In the experiment, the gain of the SOA in the TE and TM modes was slightly different ($<$ 1 dB). The adjustment of the slow and fast axes to the TE and TM modes was such that equal FWM efficiency was excited in each mode. The sources for clock and data signal were supercontinuum pulse sources providing clock pulses (λ = 1543.5 nm, pulse width 1.7 ps, average optical power 7.3 dBm) and data pulses (λ = 1553.1 nm, 1.7 ps, 2.3 dBm) at the input of the demultiplexer. Error-free, polarization-independent ($<$ 0.5 dB dependency) operation was confirmed.

4.2. Application for Timing Extraction

Timing extraction or clock recovery is an essential operation, e.g., in a receiver, in a demultiplexer or in a regenerator. Among the many methods proposed and demonstrated so far, a phase-locked loop (PLL) with an optical or opto-electrical phase comparator is a promising method especially for subharmonic clock extraction from data signals beyond 100 Gbit/s [79]. The opto-electrical phase comparator will be discussed in "Application of electroabsorption modulators for high-speed transmission systems" by Lach, Schuh and Schmidt in this publication (DOI: 10.1007/s10297-005-0032-6). In this section the optical phase comparator based on a semiconductor optical amplifier (SOA) is discussed. Clock recovery has been reported using an optical phase comparator based on four-wave mixing in an SOA at data rates up to 400 Gbit/s [80]. This is probably the most sophisticated technique of SOA-based optical phase comparators today. A simpler optical phase comparator was developed based on cross-phase modulation (XPM) in an SOA and it was operated at data rates up to 160 Gbit/s [81]. In the following the operation of this XPM-based optical phase comparator is described.

In principle any interferometric configuration described in section 3.2 can be used to convey XPM in an SOA into a signal detectable by a photodiode. In the optical phase comparator under consideration [81], the configuration of a SLALOM (see section 3.2) was used. Figure 23 shows the experimental set-up of the PLL with a SLALOM as phase comparator of the 160 Gbit/s RZ data signal and the 10 GHz optical clock signal locally generated by a tunable mode locked laser (TMLL). The output signal of the SLALOM depends on the relative phase of the data signal and the clock signal. This output signal is detected by a slow photodiode (PD1, bandwidth of about 100 MHz) and provides the error signal for the phase locked loop. However, this error signal has only one polarity. To overcome this problem, the data signal is also detected by

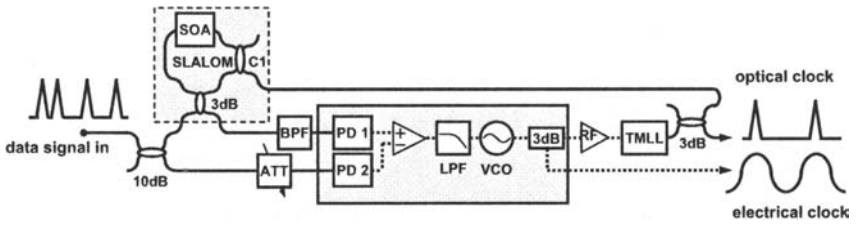

Fig. 23. Clock recovery based on a SLALOM as phase comparator. The SLALOM uses cross-phase modulation in an SOA.

a second slow photodiode (PD2). The output signal of this photodiode and the error signal are input in a difference amplifier, the output of which is supplied via a low pass filter (LPF) to the VCO. Finally the VCO controls the repetition frequency of the TMLL. This closes the loop of the PLL and locks the frequency of the VCO to the base-rate frequency of the data signal. The set-up provides an electrical clock signal as well as the optical clock pulses. The PLL does not require any initial phase adjustment.

In the experiment, the SOA in the SLALOM had its gain peak in the 1.55 μm wavelength range. The wavelengths of the clock pulses and of the data signal were 1.54 and 1.55 μm, respectively. The set-up was operated as clock recovery for OTDM data signals at 80 and 160 Gbit/s with a base data rate of 10 Gbit/s. After setting the VCO frequency almost equal to the base rate frequency without a data signal at the input, the OTDM data signal was injected and the attenuator (Att) was optimized to get the PLL locked. The locking was stable for both input data rates. Within several hours, no problems in locking were encountered independently of the word length of the pseudo-random bit stream ($2^7 - 1$ or $2^{31} - 1$). The clock recovery was also tested in 160 Gbit/s transmission experiments over a fiber link of 120 km SMF [82]. Error-free transmission was obtained with a penalty of less than 1 dB. In this experiment two cascaded EDFAs were used in front of the clock recovery unit, which were operated in the saturated region. This enabled the SLALOM based PLL to lock to the 160 Gbit/s data signals in a wide power range from -30 dBm to +5 dBm at the input of the demultiplexer (which included the clock recovery unit) without readjustment. The RMS timing jitter of the recovered optical clock was less than 0.3 ps.

4.3. Applications as Wavelength Converter, Regenerator and in Mid-Span Spectral Inversion

In this section several applications of the SOA in high-speed transmission systems are summarized, which were not included in the previous sections. The application of SOA-gates for optical sampling [83–85] are discussed in "Optical sampling techniques" by Schmidt-Langhorst and Weber in this publication (DOI: 10.1007/s10297-005-0034-4) and will not be considered here. Cross-gain modulation (XGM) and cross-phase modulation (XPM) have widely been used for all-optical wavelength conversion at data rates up to 100 Gbit/s [86]. In particular XPM in an SOA in combination with interferometric configurations, as described in section 3.2, has successfully been applied for wavelength conversion. As an example of an all-optical wavelength converter,

the SOA delayed-interference configuration (SOA-DIC) is discussed here. Figure 24 shows schematically the set-up of an SOA-DIC. It comprises an SOA followed by a delay-line interferometer with a relative delay τ. An RZ data signal (wavelength λ_1) and a CW-light (wavelength λ_2) are input in the SOA. The data signal induces a phase shift to the CW wave by the non-linear interaction in the SOA, similar to the phase shift induced by the control signals in the previously discussed switches. This phase change is then converted in an amplitude change by the subsequent interferometer. The basis of this switching is the same differential switching scheme as discussed for the Mach-Zehnder interferometer configuration in section 3.2. Depending on the relative delay τ in the interferometer, RZ to RZ or RZ to NRZ wavelength conversion is possible. The SOA-DIC was applied as all-optical wavelength converter at data rates up to 168 Gbit/s [87, 88].

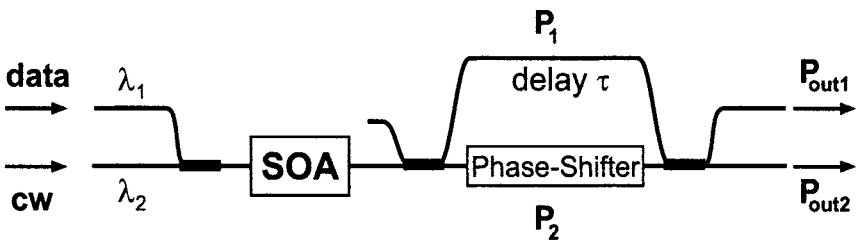

Fig. 24. Schematic of an SOA delayed-interference configuration (SOA-DIC).

Data pattern dependent effects are a problem for all-optical wavelength converters at high bit rates. In the application of the SOA as demultiplexer, the control signal, which saturates the SOA, is a periodic pulse train. This causes a periodic and regular phase change, which is constant and not dependent on the data pattern. This is different in the application as wavelength converter. In this case, the control pulses saturating the SOA are random and the time for gain recovery between successive pulses changes irregular. This causes also an irregular induced phase change. The phase change becomes dependent on the data pattern. This effect can be alleviated by a faster gain recovery, because this effect disappears if the gain is completely recovered between successive pulses. A faster recovery can be obtained by an increase of the injection current in the SOA, by reducing the carrier lifetime by stimulated emission with use of a strong CW light [23] or by using so called gain-clamped SOAs [89–92]. However, this not only reduces the carrier lifetime but also the obtainable phase shift. Therefore, some compromise has to be made. It turned out that long SOAs are advantageous for wavelength conversion.

The SOA based optical switches have also been used for optical 3R-regeneration (re-amplification, re-shaping, re-timing). Contrary to all-optical wavelength converters, in a 3R-regenerator the data signal has to switch a re-timed pulse train rather than a continuous wave signal. Many types of such switches for 3R-regeneration have been investigated over the last years [86, 93]. Using XPM in an SOA, pulse regeneration up to a data rate of 84 Gbit/s was reported [94, 95]. In the application of the SOA as 3R-regenerator, there is the same problem with the data pattern dependent saturation in the SOA as in the application as wavelength converter. However, the possibilities

to alleviate this effect are even more limited than in a wavelength converter, because the re-timed pulse train is not suitable to shorten the carrier recovery time. This can be obtained by injecting an additional CW light signal in the SOA. However, in this case the obtainable phase shift is even more reduced.

Four-wave mixing (FWM) in an SOA has widely been used for applications as wavelength converter [54, 96–99] and in mid-span spectral inversion (MSSI) experiments [55, 100–102]. One key advantage of the wavelength converter based on FWM is that several WDM channels can be handled simultaneously [54] and that the data signal can have any modulation format, including phase and frequency modulation. MSSI takes advantage of the fact, that the converted FWM signal is not only wavelength shifted, but also phase conjugated. MSSI can therefore be used to compensate for signal distortions due to chromatic dispersion and self-phase modulation effects that accumulate, when optical signals are transmitted over a long fiber length. An example of an MSSI experiment is 80 Gbit/s transmission over 106 km standard fiber [102]. This experiment also revealed that the performance of the transmission system suffered from the presence of higher order dispersion. MSSI only compensates pulse distortions due to β_2 but not due to β_3. Moreover, in contrast to fiber based MSSI devices, SOAs suffer from a poor OSNR due to the ASE of the SOA and the low conversion efficiency at large wavelength separations.

5. Conclusion

This chapter addressed the semiconductor optical amplifier (SOA) and its application in optical time division multiplexing (OTDM) transmission technology. The main focus was the application of SOAs for a TDM bit rate of 160 Gbit/s and above, because electrical signal processing is already available at a TDM bit rate up to 80 Gbit/s today.

The main application of the SOA in an OTDM-system is the optical switch in a demultiplexer. This application was experimentally verified with good performance in several transmission experiments with data rates up to 160 Gbit/s and with repetition frequencies of the control pulses at 10 and 40 GHz. There are also few experiments demonstrating the operation of an SOA based demultiplexer at a data rate of about 320 Gbit/s. However, the performance of the SOA switch is not satisfactory at data rates in excess of 160 Gbit/s, because of limitations of the required switching window of the SOA based switches at these high data rates. Moreover, an increase of the repetition frequency of the control pulses in excess of 40 GHz is very unlikely due to the limitation of the available phase shift in the SOA.

For the application of the SOA in an add–drop multiplexer the restrictions are even more severe. This application is only reasonable in the gain transparent SOA operation. Although the operation of an add–drop multiplexer was demonstrated at 160 Gbit/s, it seems unlikely, that operation at higher data rates is feasible.

In the applications as wavelength converter and 3R-regenerator, the limitation of the data rate is given by the phase shift, which the data signal induces in the SOA. Therefore, it is unlikely, that an operation at a data rate of 160 Gbit/s will be reasonable.

These conclusions refer to the bulk or multi-quantumwell SOAs, which are available today. An improvement of these devices is possible. Very recently quantum dash and quantum dot SOAs have been developed and successfully applied in high-speed

systems. These SOAs show superior gain dynamic and may be applied for high-speed signal processing in similar configurations as described in sections 3 and 4.

In addition to SOAs, there are also other devices for optical signal processing at the TDM bit rate of 160 Gbit/s. Today, the most stable 160 Gbit/s transmission experiments were performed with the electro-absorption modulator (EAM) replacing the SOA in the optical demultiplexers and in the clock recovery. These opto-electronic devices are polarization insensitive and do not require a pulse source for switching. The SOA-based subsystems are in competition with these opto-electronic devices.

References

1. J. W. Crowe and W. E. Ahearn, "Semiconductor laser amplifier," IEEE J. Quantum Electron., **2**, 283–289 (1966).
2. W. F. Kosonocky and R. H. Cornely, "Semiconductor laser amplifier," IEEE J. Quantum Electron., **4**, 125–131 (1968).
3. T. Mukai, Y. Yamamoto, and T. Kimura, "Optical amplification by semiconductor lasers," Semiconductors and Semimetals, **22** Part E, 265–321 (1985).
4. T. Saitoh and T. Mukai, "Recent progress in semiconductor laser amplifiers," J. Lightwave Technol., **6**, 1656–1988 (1988).
5. M. O'Mahony, "Semiconductor laser optical amplifier for use in future fiber systems," J. Lightwave Technol., **6**, 531–544 (1988).
6. G. Großkopf, L. Küller, R. Ludwig, R. Schnabel, and H.G. Weber, "Semicondutor laser optical amplifier in switching and distribution networks," Opt. Quant. Electron., **21**, 59–74 (1989).
7. M. J. Connelly, *Semiconductor Optical Amplifiers* (Kluwer Academic Publishers, 2002).
8. G. P. Agrawal and N. K. Dutta, *Long-Wavelength Semiconductor Lasers*. (New York: Van Nostrand Reinhold, 1986).
9. L. F. Tiemeijer, G. N. van den Hoven, P. J. A. Thijs, T. van Dongen, J. J. M. Binsma, and E. J. Jansen, "1310-nm DBR-type MQW gain-clamped semiconductor optical amplifiers with AM-CATV-grade linearity," IEEE Photon. Technol. Lett., **8** (11), 1453–1455 (1996).
10. L. F. Tiemeijer, P. J. A. Thijs, T. van Dongen, J. J. M. Binsma, E. J. Jansen, and S. Walczyk, "33 dB fiber to fiber gain +13 dBm fiber saturation power polarization independent 1310 nm MQW laser amplifier," in Optical Amplifiers and their Applications, OAA '95, Technical Digest, Davos, Switzerland, 1995, paper PD1.
11. P. Doussiére, P. Garabedian, C. Graver, D. Bonnevie, T. Fillion, E. Derouin, M. Monnot, J. G. Provost, D. Leclerc, and M. Klenk, "1.55 μm polarization independent semiconductor-optical amplifier with 25 dB fiber to fiber gain," Photon. Technol. Lett., **6**, 170–172 (1994).
12. P. Doussiére, F. Pommerau, D. Leclerc, R. Ngo, M. Goix, T. Fillion, P. Bousselet, and G. Laube, "Polarization independent 1550 nm semiconductor optical amplifier packaged module with 29 dB fiber to fiber gain," in Optical Amplifiers and their Applications, OAA '95, Technical Digest, Davos, Switzerland, pp. 119–122, 1995.
13. K. Magari, M. Okamoto, and Y. Noguchi, "1.55 μm polarisation-insensitive high-gain tensile-strained-barrier MQW optical amplifier," IEEE Photon. Technol. Lett., **3**, 998–1000 (1991).

14. M. Newkirk, B. Miller, U. Koren, M. Chien, R. Jopson, and C. Burrus, "1.5 μm multiquantum-well semiconductor optical amplifier with tensile compressively strained wells for polarisation-independent gain," IEEE Photon. Technol. Lett., **5**, 406–408 (1993).

15. A. E. Kelly, I. F. Lealman, L. J. Rivers, S. D. Perrin, and M. Silver, "Low noise figure (7.2 dB) and high gain (29 dB) semiconductor optical amplifier with a single layer ar coating," Electron. Lett., **33**, 536–538 (1997).

16. A. A. Ukhanov, A. Stintz, P. G. Eliseev, and K. J. Malloy, "Comparison of the carrier induced refractive index, gain, and linewidth enhancement factor in quantum dot and quantum well lasers," Appl. Phys. Lett., **84** (7), 1058–1060 (2004).

17. T. Akiyama, K. Kawaguchi, M. Sugawara, H. Sudo, M. Ekawa, H. Ebe, A. Kuramata, K. Otsubo, K. Morito, and Y. Arakawa, "A semiconductor optical amplifier with an extremely-high penalty-free output power of 20 dBm achieved with quantum dots," in Proc. 29th Europ. Conf. on Opt. Comm. (ECOC'03), Rimini (Italy), September 2003, post-deadline paper Th4.4.3.

18. M. J. Adams, D. A. O. Davies, M. C. Tatham, and M. A. Fisher, "Nonlinearities in semiconductor laser amplifiers," Optical and Quantum Electronics, **27**, 1–13 (1995).

19. K. J. Ebeling, *Integrierte Optoelektronik* (Berlin: Springer-Verlag, 1989).

20. C. H. Henry, "Theory of the linewidth of semiconductor lasers," IEEE J. Quantum Electron., **18** (2), 259–264 (1982).

21. J. Wiesenfeld, "Gain dynamics and associated nonlinearities in semiconductor optical amplifiers," J. High Speed Electron. Syst., **7**, 179–222 (1996).

22. B. R. Bennett, R. A. Soref, and J. A. Alamo, "Carrier-induced change in refractive index of InP, GaAs, and InGaAsP," IEEE J. Quantum Electron., **26** (1), 113–122 (1990).

23. R. Manning, A. Ellis, A. Poustie, and K. Blow, "Semiconductor laser amplifier for ultrafast all-optical signal processing," J. Opt. Soc. Am. B, **14**, 3204–3216 (1997).

24. K. L. Hall, G. Lenz, E. P. Ippen, U. Koren, and G. Raybon, "Carrier heating and spectral hole burning in strained-layer quantum-well laser amplifiers at 1.5 μm," Appl. Phys. Lett., **61**, 2512–2514 (1993).

25. K. L. Hall, A. M. Darwish, E. P. Ippen, U. Koren, and G. Raybon, "Femtosecond index nonlinearities in InGaAsP optical amplifiers," Appl. Phys. Lett., **62** (12), 1320–1322 (1993).

26. A. Uskov, J. Mørk, and J. Mark, "Wave mixing in semiconductor laser amplifiers due to carrier heating and spectral-hole burning," IEEE J. Quantum Electron., **30**, 1769–1781 (1994).

27. J. Mørk, T. W. Berg, M. L. Nielsen, and A. V. Uskov, "The role of fast carrier dynamics in SOA based devices," IEICE Trans. Electron., **E87-C**, 1126–1133 (2004).

28. S. Diez, R. Ludwig, and H.G. Weber, "Gain-transparent SOA-switch for high-bitrate OTDM Add/Drop multiplexing," IEEE Photon. Technol. Lett., **11** (1), 60–62 (1999).

29. S. Diez, R. Ludwig, and H.G. Weber, "All-optical switch for TDM and WDM/TDM systems demonstrated in a 640 Gbit/s demultiplexing experiment," Electron. Lett., **34** (8), 803–804 (1998).

30. L. Schares, C. Schubert, C. Schmidt, H.G. Weber, L. Occhi, and G. Guekos, "Phase dynamics of semiconductor optical amplifiers at 10 to 40 GHz," IEEE J. Quantum Electron., **39** (11), 1394–1408 (2003).

31. S. Diez, "All-optical signal processing by gain-transparent semiconductor switches," Ph.D. dissertation, Technical University Berlin, 2000.

32. Y. Ueno, S. Nakamura, and K. Tajima, "Nonlinear phase shifts induced by semiconductor optical amplifiers with control pulses at repetition frequencies in the 40-160 GHz range for use in ultrahigh-speed all-optical signal processing," J. Opt. Soc. Am. B, **19** (11), 2573–2589 (2002).

33. C. Schubert, "Interferometric gates for all-optical signal processing," Ph.D. dissertation, Technical University Berlin, 2004.

34. C. Schubert, J. Berger, S. Diez, H. J. Ehrke, R. Ludwig, U. Feiste, C. Schmidt, H.G. Weber, G. Toptchiyski, S. Randel, and K. Petermann, "Comparison of interferometric all-optical switches for demultiplexing applications in high-speed OTDM systems," J. Lightwave Technol., **20** (4), 618–624 (2002).

35. M. Eiselt, W. Pieper, and H.G. Weber, "All-optical demultiplexing with a semiconductor laser amplifier in a loop mirror," Electron. Lett., **29**, 1167–1169 (1993).

36. M. Eiselt, W. Pieper, and H.G. Weber, "Slalom: Semiconductor laser amplifier in a loop mirror," J. Lightwave Technol., **13**, 2099–2012 (1995).

37. J. P. Sokoloff, P. R. Prucnal, I. Glesk, and M. Kane, "A terahertz optical asymmetric demultiplexer (TOAD)," IEEE Photon. Technol. Lett., **5**, 787–790 (1993).

38. J. P. Sokoloff, I. Glesk, P. R. Prucnal, and R. K. Boncek, "Performance of a 50 Gbit/s optical time domain multiplexed system using a terahertz optical asymmetric demultiplexer," IEEE Photon. Technol. Lett., **6**, 98–100 (1994).

39. N. S. Patel, K. A. Rauschenbach, and K. L. Hall, "40 Gb/s demultiplexing using an ultrafast nonlinear interferometer (UNI)," IEEE Photon. Technol. Lett., **8** (12), 1695–1697 (1996).

40. N. S. Patel, K. L. Hall, and K. A. Rauschenbach, "Interferometric all-optical switches for ultrafast signal processing," Appl. Optics, **37**, 2831–2842 (1998).

41. R. Hess, M. Caraccia-Gross, W. Vogt, E. Gamper, P. A. Besse, M. Dülk, E. Gini, H. Melchior, B. Mikkelsen, M. Vaa, K. S. Jepsen, K. E. Stubkjaer, and S. Bouchoule, "All-optical demultiplexing of 80 to 10 Gb/s signals with monolithic integrated high-performance Mach-Zehnder interferometers," IEEE Photon. Technol. Lett., **10** (1), 165–167 (1998).

42. K. Tajima, S. Nakamura, A. Furukawa, and T. Sasaki, "Hybrid-integrated symmetric Mach-Zehnder all-optical switches and ultrafast signal processing," IEICE Trans. Electron., **E87-C**, 1119–1125 (2004).

43. R. Ludwig, U. Feiste, S. Diez, C. Schubert, C. Schmidt, H. J. Ehrke, and H.G. Weber, "Unrepeatered 160 Gbit/s RZ single-channel transmission over 160 km of standard fiber at 1.55 μm with hybrid MZI optical demultiplexer," Electron. Lett., **36** (16), 1405–1406 (2000).

44. R. Ludwig and G. Raybon, "All-optical demultiplexing using ultrafast four-wave mixing in a semiconductor laser amplifier at 20 Gbit/s," in ECOC '93, Montreux, Switzerland, 1993, pp. 57–60.

45. S. Kawanishi, T. Morioka, O. Kamatani, H. Takara, J. M. Jacob, and M. Saruwatari, "100 Gbit/s all-optical demultiplexing using four-wave mixing in a travelling wave laser diode amplifier," Electron. Lett., **30**, 981–982 (1994).

46. T. Morioka, H. Takara, S. Kawanishi, K. Uchiyama, and M. Saruwatari, "Polarisation-independent all-optical demultiplexing up to 200Gbit/s using four-wave mixing in a semiconductor laser amplifier," Electron. Lett., **32** (9), 840–842 (1996).

47. R. Ludwig, W. Pieper, R. Schnabel, S. Diez, and H.G. Weber, "Four-wave mixing in semiconductor laser amplifiers: application for optical communication systems," Fiber and Integrated Optics, **16**, 211–223 (1996).

48. M. Shtaif and G. Eisenstein, "Analytical solution of wave mixing between short optical pulses in a semiconductor optical amplifier," Appl. Phys. Lett., **66**, 1458–1460 (1995).
49. M. Shtaif, R. Nagar, and G. Eisenstein, "Four-wave mixing among short optical pulses in semiconductor optical amplifiers," Photon. Technol. Lett., **7**, 1001–1003 (1995).
50. J. Mørk and A. Mecozzi, "Theory of nondegenerate four-wave mixing between pulses in a semiconductor waveguide," IEEE J. Quantum Electron., **33** (4), 183–195 (1997).
51. S. Scotti and A. Mecozzi, "Frequency converters based on FWM in traveling-wave optical amplifiers: Theoretical aspects," in Fiber and Integrated Optics, **15** (3), 243–256 (1996).
52. S. Diez, C. Schmidt, R. Ludwig, H.G. Weber, K. Obermann, S. Kindt, I. Koltchanov, and K. Petermann, "Four-wave mixing in semiconductor optical amplifiers for frequency conversion and fast optical switching," IEEE J. Selected Top. Quantum Electron., **3**, 1131–1145 (1997).
53. M. Eiselt, "Optimum pump pulse selection for demultiplexer application of four-wave mixing in semiconductor laser amplifiers," Photon. Technol. Lett., **7**, 1312–1314 (1995).
54. R. Schnabel, U. Hilbk, T. Hermes, P. Meissner, C. von Helmholt, K. Magari, F. Raub, W. Pieper, F. J. Westphal, R. Ludwig, L. Küller, and H.G. Weber, "Polarization insensitive frequency conversion of a 10-channel OFDM signal using four-wave mixing in a semiconductor-laser amplifier," Photon. Technol. Lett., **6**, 56–58 (1994).
55. U. Feiste, R. Ludwig, E. Dietrich, S. Diez, H. J. Ehrke, D. Razic, and H.G. Weber, "40 Gbit/s transmission over 434 km standard fibre using polarisation independent mid-span spectral inversion," Electron. Lett., **34** (21), 2044–2045 (1998).
56. J. P. R. Lacey, M. A. Summerfield, and S. J. Madden, "Tunability of polarization-insensitive wavelength converters based on four-wave mixing in semiconductor optical amplifiers," J. Lightwave Technol., **16** (12), 2419–2427 (1998).
57. S. Diez, R. Ludwig, E. Patzak, H.G. Weber, G. Eisenstein, and R. Schimpe, "Four-wave mixing in semiconductor-laser amplifiers: phase matching in configurations with three input waves," in CLEO '96, Anaheim, USA, pp. 505–506, 1996.
58. P. Cortes, M. Chbat, S. Artigaud, J. Beylat, and J. Chesnoy, "Below 0.3 dB polarization penalty in 10 Gbit/s directly modulated DFB signal over 160 km using mid-span spectral inversion in a semiconductor laser amplifier," in ECOC '95, pp. 271–274, 1995.
59. S. Diez, R. Ludwig, C. Schmidt, U. Feiste, and H.G. Weber, "160-Gb/s optical sampling by gain-transparent four-wave mixing in a semiconductor optical amplifier," IEEE Photon. Technol. Lett., **11** (11), 1402–1404 (1999).
60. T. Morioka, S. Kawanishi, H. Takahara, and M. Saruwatari, "Multiple output, 100 Gbit/s all-optical demultiplexer based on multichannel four-wave mixing pumped by a linearly chirped square pulse," Electron. Lett., **30**, 1959–1961 (1994).
61. E. Jahn, N. Agrawal, M. Arbert, D. Franke, R. Ludwig, W. Pieper, H.G. Weber, and C. M. Weinert, "40 Gbit/s all-optical demultiplexing using a monolithically integrated Mach-Zehnder interferometer with semiconductor laser amplifiers," Electron. Lett., **31**, 1857–1858 (1995).
62. T. Tekin, C. Schubert, J. Berger, M. Schlak, B. Mau, W. Brinker, R. Molt, H. Ehlers, M. Gravert, and H.-P. Nolting, "160 Gbit/s error-free all-optical demultiplexing using monolithically integrated band gap shifted Mach-Zehnder interferometer (GS-MZI)," in Techn. Dig. of Conf. on Integrated Photonics Research, IPR'02, Vancouver, Canada, July 2002, paper IWC4.
63. M. Heid, S. Spälter, G. Mohs, A. Färbert, W. Vogt, and H. Melchior, "160-Gbit/s demultiplexing based on a monolithically integrated Mach-Zehnder interferometer," in Proc. 27th Europ. Conf. on Opt. Comm. (ECOC'01), Amsterdam, The Netherlands, 2001, pp. 82–83, post-deadline paper PD.B.1.8.

64. R. Hess, M. Duelk, W. Vogt, E. Gamper, E. Gini, P. A. Besse, H. Melchior, K. S. Jepsen, B. Mikkelsen, M. Vaa, H. N. Poulsen, A. T. Claussen, K. E. Stubkjaer, S. Bouchoule, and F. Devaux, "Simultaneous all-optical add and drop multiplexing of 40 Gbit/s OTDM signals using monolithically integrated Mach-Zehnder Interferometer," Electron. Lett., **34**, 579–580 (1998).

65. M. Vaa, B. Mikkelsen, K. S. Jepsen, K. E. Stubkjaer, M. Schilling, K. Daub, E. Lach, G. Laube, W. Idler, K. Wünstel, S. Bouchoule, C. Kazmierski, and D. Mathoorasing, "A bit-rate flexible and power efficient all-optical demultiplexer realized by monolithically integrated Michelson interferometer," Proc. 22nd Europ. Conf. Opt. Commun. (ECOC'96), 1996, paper ThB 3.3.

66. S. Nakamura, Y. Ueno, K. Tajima, J. Sasaki, T. Sugimoto, T. Kato, T. Shimoda, M. Itoh, H. Hatakeyama, T. Tamanuki, and T. Sasaki, "Demultiplexing of 168 Gb/s data pulses with a hybrid-integrated symmetric Mach-Zehnder all-optical switch," IEEE Photon. Technol. Lett., **12** (4), 425–427 (2000).

67. S. Nakamura, Y. Ueno, and K. Tajima, "Error-free all-optical demultiplexing at 336 Gb/s with a hybrid-integrated Symmetric-Mach-Zehnder switch," in OSA Trends in Optics and Photonics (TOPS) Vol. 55, Optical Fiber Commun. Conf., Technical Digest, Postconference Edition, Anaheim, USA, March 2002, post-deadline paper FD3.

68. A. Suziki, X. Wang, Y. Ogawa, and S. Nakamura, "10x320Gb/s (3.2Tb/s) DWDM/OTDM transmission in C-band by semiconductor-based devices," in Proc. 30th Europ. Conf. on Opt. Comm. (ECOC'04), Stockholm (Sweden), 2004, pp. 14–15 (PD–Papers), post-deadline paper Th4.1.7.

69. C. Schubert, J. Berger, U. Feiste, R. Ludwig, C. Schmidt, and H.G. Weber, "160 Gb/s polarization insensitive all-optical demultiplexing using a gain-transparent Ultrafast-Nonlinear Interferometer (GT-UNI)," IEEE Photon. Technol. Lett., **13** (11), 1200–1202 (2001).

70. C. Schubert, S. Diez, J. Berger, R. Ludwig, U. Feiste, H.G. Weber, G. Toptchiyski, K. Petermann, and V. Krajinovic, "160 Gb/s all-optical demultiplexing using a gain-transparent Ultrafast-Nonlinear Interferometer (GT-UNI)," IEEE Photon. Technol. Lett., **13** (5), 475–477 (2001).

71. U. Feiste, R. Ludwig, C. Schubert, J. Berger, C. Schmidt, H.G. Weber, A. Munk, B. Schmauss, B. Buchhold, D. Briggmann, F. Kueppers, and F. Rumpf, "160 Gbit/s transmission over 116 km field-installed fiber using 160 Gbit/s OTDM and 40 Gbit/s ETDM," Electron. Lett., **37** (7), 443–445 (2001).

72. C. Schubert, C. Schmidt, S. Ferber, R. Ludwig, and H.G. Weber, "Error-free all-optical add-drop multiplexing at 160 Gbit/s," Electron. Lett., **39** (14), 1074–1076 (2003).

73. C. Schubert, C. Schmidt, S. Ferber, R. Ludwig, and H.G. Weber, "Error-free all-optical add-drop multiplexing at 160 Gbit/s," in OSA Trends in Optics and Photonics (TOPS) Vol. 86, Optical Fiber Commun. Conf., Technical Digest, Postconference Edition, Atlanta, Georgia, USA, March 23-28 2003, postdeadline paper PD17.

74. J. P. Turkiewicz, E. Tangdiongga, G. D. Khoe, H. de Waardt, W. Schairer, H. Rohde, G. Lehmann, E. S. R. Sikora, Y. R. Zhou, A. Lord, and D. Payne, "Field trial of 160 Gbit/s OTDM add/drop node in a link of 275 km deployed fiber," in Proc. 29th Opt. Fiber Commun. Conf. (OFC'04), Los Angeles (USA), February 2004, post-deadline paper PDP1.

75. T. Tekin, M. Schlak, C. Schmidt, and C. Schubert, "The influence of gain and phase dynamics in the integrated GS-SOA on the switching performance of the monolithically integrated GS-MZI," in Integrated Photonics Research, July 2004, p. paper IWC4.

76. E. Jahn, N. Agrawal, H. J. Ehrke, R. Ludwig, W. Pieper, and H.G. Weber, "Monolithically integrated asymmetric Mach-Zehnder interferometer as a 20 Gbit/s all-optical add/drop multiplexer for OTDM systems," Electron. Lett., **32**, 216–217 (1996).

77. S. Fischer, M. Dulk, E. Gamper, W. Vogt, W. Hunziker, E. Gini, H. Melchior, A. Buxens, H. N. Poulsen, and A. T. Clausen, "All-optical regenerative OTDM add-drop multiplexing at 40 Gb/s using monolithic InP Mach-Zehnder interferometer," IEEE Photon. Technol. Lett., **12** (3), 335–337 (2000).

78. H. N. Poulsen, A. T. Clausen, A. Buxens, L. Oxenloewe, C. Peucheret, A. Kloch, T. Fjelde, D. Wolfson, and P. Jeppesen, "Ultra fast all-optical signal processing in semiconductor and fiber based devices," in Proc. 26th Europ. Conf. Opt. Commun. (ECOC'00), Munich (Germany), September 2000, vol. 3 paper 7.4.1.

79. M. Saruwatari, "All-optical signal processing for terabit/ second optical transmission," IEEE J. Sel. Top. Quant., **6** (6), 1363–1374 (2000).

80. O. Kamatani and S. Kawanishi, "Prescaled timing extraction from 400 Gb/s optical signal using a phase lock loop based on four-wave-mixing in a laser diode amplifier," IEEE Photon. Technol. Lett., **8** (8), 1094–1096 (1996).

81. T. Yamamoto, L. Oxenløwe, C. Schmidt, C. Schubert, E. Hilliger, U. Feiste, J. Berger, R. Ludwig, and H.G. Weber, "Clock recovery from 160 Gbit/s data signals using phase-locked loop with interferometric optical switch based on semiconductor optical amplifier," Electron. Lett., **37** (8), 509–510l (2001).

82. T. Yamamoto, U. Feiste, J. Berger, C. Schubert, C. Schmidt, R. Ludwig, and H.G. Weber, "160 Gbit/s demultiplexer with clock recovery using SOA-based interferometric switches and its application to 120 km fiber transmission," in Proc. 27th Europ. Conf. on Opt. Comm. (ECOC'01), Amsterdam, The Netherlands, Sep. 30–Oct. 4 2001, pp. 192–193.

83. C. Schubert, C. Schmidt, C. Börner, E. Dietrich, S. Ferber, R. Ludwig, and H.G. Weber, "A gain-transparent ultrafast-nonlinear interferometer (GT-UNI) in a 160 Gb/s optical sampling system," in Techn. Dig. of Optical Amplifiers and their Applications, OAA, 2002, paper OTuD5.

84. C. Schmidt, C. Schubert, S. Watanabe, F. Futami, R. Ludwig, and H.G. Weber, "320 Gb/s all-optical eye diagram sampling using gain-transparent ultrafast nonlinear interferometer (GT-UNI)," in Proc. 28th Europ. Conf. on Opt. Comm. (ECOC'02), Copenhagen, Denmark, 2002, paper 2.1.3.

85. L. A. Jiang, E. P. Ippen, U. Feiste, S. Diez, E. Hilliger, C. Schmidt, and H.G. Weber, "Sampling pulses with semiconductor optical amplifiers," IEEE J. Quantum Electron., **37** (1), 118–126 (2001).

86. K. E. Stubkjaer, "Semiconductor optical amplifier-based all-optical gates for high-speed optical processing," IEEE J. Sel. Top. Quant., **6** (6), 1428–1435 (2000).

87. J. Leuthold, C. Joyner, B. Mikkelsen, G. Raybon, J. Pleumeekers, B. Miller, K. Dreyer, and C. Burrus, "100 Gbit/ all-optical wavelength conversion with integrated SOA delayed-interference configuration," Electron. Lett., **36** (13), 1129–1130 (2000).

88. S. Nakamura, Y. Ueno, and K. Tajima, "Error-free all-optical data pulse regeneration at 84 Gbps and wavelength conversion at 168 Gbps with Symmetric Mach-Zehnder all-optical switches," in Techn. Dig. of Optical Amplifiers and their Applications, OAA'00, 2000, pp. PD 4–1.

89. L. F. Tiemeijer, P. J. A. Thijs, T. v. Dongen, J. J. M. Binsma, E. J. Jansen, and H. R. J. R. van Helleputte, "Reduced intermodulation distortion in 1300 nm gain-clamped MQW laser amplifiers," IEEE Photon. Technol. Lett., **7** (3), 284–286 (1995).

90. M. Bachmann, P. Doussière, J. Y. Emery, R. N'Go, F. Pommereau, L. Goldstein, G. Soulage, and A. Jourdan, "Polarisation-insensitive clamped-gain SOA with integrated spot-size convertor and DBR gratings for WDM applications at 1.55μm wavelength," Electron. Lett., **32** (22), 2076–2077 (1996).

91. C. Holtmann, P. A. Besse, and H. Melchior, "Gain-clamped semiconductor optical amplifier for 1300 nm wavelength an 20 dB polarization independent fiber-to-fiber gain and significantly reduced pulse shape and intermodulation distortions," Proc. 21st Europ. Conf. Opt. Commun. (ECOC'95), pp. 1031–1034, 1995.

92. P. Doussiere, F. Pommereau, J. Y. Emery, R. Ngo, J. L. Lafragette, P. Aubert, L. Goldstein, G. Soulage, T. Ducellier, and M. Bachmann, "1550 nm polarization independent DBR gain clamped SOA with high dynamic input power range," in Proc. 22nd Europ. Conf. Opt. Commun. (ECOC'96), vol. 3, Oslo, Norway, 1996, pp. 169–172, paper WeD.2.4.

93. J. C. Simon, L. Billes, A. Dupas, and L. Bramerie, "All optical regeneration techniques," in Proc. 25th Europ. Conf. Opt. Commun. (ECOC'99), Nice (France), September 1999, vol. II, pages 256-259.

94. A. E. Kelly, I. D. Phillips, R. J. Manning, A. D. Ellis, D. Nesset, D. G. Moodie, and R. Kashyap, "80 Gbit/s all-optical regenerative wavelength conversion using semiconductor optical amplifier based interferometer," Electron. Lett., **35** (17), 1477–1478 (1999).

95. Y. Ueno, S. Nakamura, and K. Tajima, "Penalty-free error-free all-optical data pulse regeneration at 84 Gbps with Symmetric-Mach-Zehnder-type regenerator," in OSA Trends in Optics and Photonics (TOPS) Vol. 54, Optical Fiber Commun. Conf., Technical Digest, Postconference Edition, 2001, pp. MG 5–1.

96. G. Grosskopf, R. Ludwig, and H.G. Weber, "140 Mbit/s DPSK transmission using an all-optical frequency converter with a 4000 GHz range," Electron. Lett., **24**, 1106–1107 (1988).

97. T. Morgan, J. Lacey, and R. Tucker, "Widely tunable four-wave mixing in semiconductor optical amplifiers with constant conversion efficiency," IEEE Photon. Technol. Lett., **10**, 1401–1403 (1998).

98. D. F. Geraghty, R. B. Lee, K. J. Vahala, M. Verdiell, M. Ziari, and A. Mathur, "Wavelength conversion up to 18 nm at 10 Gb/s by four-wave mixing in a semiconductor optical amplifiers," Photon. Technol. Lett., **9**, 452–454 (1997).

99. A. E. Kelly, A. D. Ellis, D. Nesset, R. Kashyap, and D. G. Moodie, "100 Gbit/s wavelength conversion using FWM in an MQW semiconductor optical amplifier," Electron. Lett., **34** (20), 1955–1956 (1998).

100. A. Ellis, M. Tatham, D. Davies, D. Nesset, D. Moodie, and G. Sherlock, "40 Gbit/s transmission over 202 km of standard fibre using midspan spectral inversion," Electron. Lett., **31**, 299–301 (1995).

101. D. D. Marcenac, D. Nesset, A. E. Kelly, M. Brierley, A. D. Ellis, D. G. Moodie, and C. W. Ford, "40 Gbit/s transmission over 406 km of NDSF using mid-span spectral inversion by four-wave-mixing in a 2 mm long semiconductor optical amplifier," Electron. Lett., **33** (10), 879–880 (1997).

102. U. Feiste, R. Ludwig, C. Schmidt, E. Dietrich, S. Diez, H.-J. Ehrke, E. Patzak, H.G. Weber, and T. Merker, "80-Gb/s transmission over 106-km standard-fiber using optical phase conjugation in a sagnac-interferometer," IEEE Photon. Technol. Lett., **11** (8), 1063–1065 (1999).

DOI: 10.1007/s10297-005-0039-z
Originally published in J. Opt. Fiber. Commun. Rep. 3, 1–24 (2005)

Optical signal processing using nonlinear fibers

Shigeki Watanabe

Fujitsu Laboratories Ltd., Photonics Networking Laboratories (L-50)
4-1-1 Kamikodanaka, Nakahara-ku, Kawasaki 211-8588, Japan
Email: shigeki@labs.fujitsu.com

Abstract. Ultra-fast optical signal processing is a promising technology for future photonic networks. This paper describes possible applications of nonlinear fibers to optical signal processing. The third-order optical nonlinearities in a fiber are discussed by analyzing the interaction of co-propagating optical waves. The properties of a nonlinear fiber are then considered in terms of optimizing the dispersion for achieving phase matching and decreasing walk-off. A highly nonlinear fiber (HNLF) is a practical candidate for an ultra-high-speed signal processor. Using HNLF, the following experiments are successfully demonstated: ultra-broadband wavelength conversion/optical phase conjugation by four-wave mixing, 160 Gb/s optical 3R-regeneration, and optical switching up to 640 Gb/s using a parametric amplified fiber switch. Steps for further improvements are also discussed.

1. Introduction

Optical signal processing is a key technology for making flexible photonic networks. [1] Advanced photonic networks need various kinds of signal processing in optical nodes including optical regeneration, wavelength conversion, optical add-drop multiplexing (OADM) and signal monitoring. [1–35] Fully transparent features in both the time and wavelength domain are required for optical signal processors because the future wavelength-division multiplexed (WDM) networks will utilize ultra-broad bandwidth over 100 nm and the data rate will range from 2.5 to 160 Gb/s or even higher. All-optical signal processors are essential for high-speed networks. Better transparency with ultra-high-speed performance over 160 Gb/s and simultaneous multi-channel processing capabilities clearly distinguish all-optical processors from opto-electronic (O-E) types. [1–11]

An attractive way to realize such transparent optical signal processors is to exploit the third-order nonlinearity in optical fibers. Fiber-based signal processors offer an

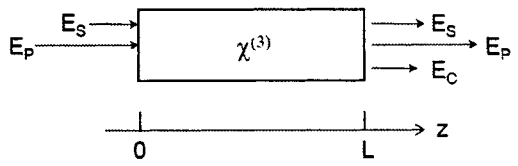

Fig. 1. Generation of optical Kerr-effect in a third-order nonlinear material.

ultra-broad conversion band [3] and ultra-high speed operation at data rates up to Tb/s and above [11] owing to the ultra-fast response time of fiber nonlinearities (several femtoseconds). In order to enable a practical use of fiber-based signal processors, an increase of the nonlinearity coefficient of the fiber and progress in the control of the chromatic dispersion characteristics are necessary. Fibers with high nonlinearity are promising candidates to fulfill the demanding requirements.

This paper describes optical signal processing based on the optical Kerr-effect in nonlinear fibers. Section 2 discusses the third-order optical nonlinearities in a fiber by analyzing the interaction of co-propagating optical waves. Section 3 investigates the properties of a nonlinear fiber for the signal processing in terms of optimizing the chromatic dispersion to achieve the phase matching and to decrease the walk-off among interacting waves. In section 4 a highly nonlinear fiber (HNLF) is shown to be a practical candidate for the ultra-high-speed signal processors. Section 5 reports on examples for the systematic applications. Using the HNLF, ultra-broadband wavelength conversion and optical phase conjugation by four-wave mixing, fiber-based 160 Gb/s optical 3R-regeneration and optical switching up to 640 Gb/s with an optical parametric amplified fiber switch were successfully demonstrated. Steps for further improvements are also discussed in this paper.

2. Third-Order Optical Nonlinearities in a Fiber

Here we analyze the interaction of co-propagating waves in the third-order nonlinear medium with a length L [36]. The schematic configuration is shown in Fig. 1. We consider optical nonlinearities induced by the pump (control) wave E_P with frequency ω_P, assuming the response time of the nonlinear interaction to be faster than the signal pulse duration. Here the "nonlinearities" include self-phase modulation (SPM), cross-phase modulation (XPM) and four-wave-mixing (FWM). E_P interacts with a co-propagating ($+z$ direction) signal wave E_S and an idler wave E_C, where $\omega_P - \omega_C = \omega_S - \omega_P = \delta\omega \neq 0$.

We assume here that we can neglect the wave-vector mismatch. In the slowly varying envelope approximation and supposing all waves to be linearly polarized in the same direction, the differential equations describing the propagation and interaction of these waves are [36,37]

$$\frac{\partial E_P}{\partial z} = \left(-\frac{\alpha}{2} + i\kappa \mid E_P \mid^2\right) E_P \tag{1}$$

$$\frac{\partial E_C}{\partial z} = \left(-\frac{\alpha}{2} + 2i\kappa \mid E_P \mid^2\right) E_C + i\kappa E_P^2 E_S^* \tag{2}$$

$$\frac{\partial E_S^*}{\partial z} = \left(-\frac{\alpha}{2} - 2i\kappa \mid E_P \mid^2\right) E_S^* - i\kappa E_P^{*2} E_C, \tag{3}$$

where α is the loss constant and

$$\kappa = \frac{3\omega\chi^{(3)}}{2nc} \tag{4}$$

denotes the coupling coefficient where $\chi^{(3)}$ denotes the real part of the third-order optical nonlinear susceptibility, ω the optical carrier frequency, n the index of refraction and c the velocity of light. To derive Eqs. (1)–(3), we assumed i) the pump beam depletion is negligible, ii) $\mid E_C \mid^2 \ll \mid E_P \mid^2$ under the initial condition of $E_C(0) = 0$, and iii) the pump power is sufficiently strong where the nonlinearities are essentially due to the pump beam ($\mid E_S \mid^2 \ll \mid E_P \mid^2$). The right-hand terms in Eqs. (1)–(3) describe linear absorption, self and induced optical Kerr effect, and parametric gain by transfer of the two photons from E_P to E_S and E_C. These equations indicate, that induced XPM is twice as effective as SPM; see the factor 2 on the second term of Eqs. (2) and (3). Equation (2) also indicates that the generated idler wave is a complex-conjugate (phase-conjugate) of the signal wave. Following the discussion for these equations [36], first the nonlinear phase shift of E_P is obtained by solving Eq. (1) as

$$E_P(z) = \exp\left(-\frac{\alpha}{2}z\right) \exp[i\phi(z)] E_P(0), \tag{5}$$

where

$$\phi(z) = \kappa \mid E_P(0) \mid^2 \ell(z) \tag{6}$$

is the nonlinear phase shift where $\ell(z) = [1 - \exp(-\alpha z)]/\alpha$ is an effective interaction length. Equations (5)–(6) indicate that the phase of the pump wave changes through propagation in proportion to the power of itself (self-phase modulation).

Substituting Eqs. (5) and (6) in Eqs. (2) and (3), the output waves are obtained under the initial condition of no idler wave input ($E_C(0) = 0$) as

$$E_S(L) = \exp\left(-\frac{\alpha}{2}L\right) \exp[i\phi(L)][1 + i\phi(L)] E_S(0) \tag{7}$$

$$E_C(L) = \exp\left(-\frac{\alpha}{2}L\right) \exp[i\phi(L)][i\phi(L)] E_S^*(0). \tag{8}$$

These equations show parametric amplification with the internal gain factors for E_S and E_C given by

$$G_S = 1 + \phi^2(L) \tag{9}$$

$$G_C = \phi^2(L) = G_S - 1. \tag{10}$$

The conversion efficiencies η_S and η_C are defined by the power ratios of output waves to that of input signal wave ($\eta_S \equiv P_S(L)/P_S(0) = \mid E_S(L) \mid^2 / \mid E_S(0) \mid^2$, $\eta_C \equiv P_C(L)/P_S(0) = \mid E_C(L) \mid^2 / \mid E_S(0) \mid^2$) and are written with use of Eqs. (9) and (10) as

$$\eta_S = \exp(-\alpha L) G_S \tag{11}$$

$$\eta_C = \exp(-\alpha L)(G_S - 1). \tag{12}$$

Equations (6) and (9)–(12) show the parametric amplification process by FWM [36]. Under the condition of using a strong pump wave, where the Kerr-phase shift $\phi(L)$ is sufficiently larger than 1, the power of the signal wave could be increased by the parametric amplification with the gain, which is almost proportional to the square of $\phi(L)$, whereas η_C increases exactly proportional to the square of $\phi(L)$. It is interesting to consider a special model in which XPM only occurs without generating idler wave. If there is no idler wave ($E_C = 0$), the nonlinear phase shift by XPM of E_S is given from Eq. (3) as

$$E_S(L) = \exp\left(-\frac{\alpha}{2}L\right) \exp[i2\phi(L)] E_S(0). \tag{13}$$

As already mentioned, Eqs. (5) and (13) indicate that XPM is twice as effective as SPM as we can see by the factor 2 in the phase term in Eq. (13). The phase shift by XPM can be applied to an optical Kerr-switch.

3. Optical Switching Using Nonlinear Fibers

Signal processing in an optical fiber is based mainly on application of SPM, XPM and FWM. Since these nonlinear optical effects have a response time of several femto seconds, ultra-high-speed and ultra-broadband signal processing is possible.

3.1. Optical Switching by Four-Wave Mixing

Here we discuss signal processing using FWM in fibers. The key issue for applications using fiber-based four-wave mixing is to find condition for increasing the bandwidth.

3.1.1. Phase Matching

To obtain the FWM with sufficiently broad bandwidth, phase matching between interacting waves is required. Considering FWM generated by a signal wave E_S and a pump wave E_P into a dispersion-shifted fiber (DSF) with the length L as depicted in Fig. 1, the phase mismatch, Δk, is approximately written as [3,4,37]

$$\Delta k = \delta\omega^2 \beta_2(\omega_P), \tag{14}$$

where $\beta_2(\omega_P)$ is the second-order dispersion or the group-velocity dispersion (GVD) at the pump frequency ω_P and $\delta\omega$ is a frequency detuning from ω_P. Here we assume that the term of nonlinear phase shift is neglected and the states of polarization (SOP) of the waves E_S and E_P are completely coincided. Equation (14) indicates that the best phase matching ($\Delta k = 0$) is achieved by tuning the pump wavelength λ_P to the average zero-dispersion wavelength λ_0. [3,4,38] However, in an actual fiber, λ_0 usually varies over several nano meters along the line. Fine control of λ_0 is thus indispensable for increasing the conversion bandwidth. The shorter the length of the fiber, the easier it is to control the variance of the dispersion.

Once we achieve the phase-matching, the efficiency of FWM generation is approximately written from Eqs. (6) and (9)–(12) with the input pump power $P_P(0)$ as [3,4]

$$\eta_C(L) = \exp(-\alpha L)[\gamma P_P(0)\ell(L)]^2, \tag{15}$$

where

$$\gamma = \frac{\omega n_2}{cA_{\text{eff}}} \tag{16}$$

denotes the third-order nonlinear coefficient with the nonlinear refractive index n_2 and the effective area of the fiber Aeff.

To obtain a larger η_C, the product $\gamma P_P(0)\ell(L)$ should be increased. It is evident from Eqs. (15) and (16) that the best way to obtain a highly efficient and broadband four-wave mixing in a fiber is to increase γ in order to shorten the necessary fiber length. A highly nonlinear dispersion-shifted fiber (HNLF) is a practical candidate because γ in HNLF increases by germanium doping in the core and by reducing the effective area A_{eff} (mode field area) by a stronger confinement. The HNLF provides highly efficient conversion with a short length, which facilitates control of the λ_0. So far, a HNLF with $\gamma \sim 20\ \text{W}^{-1}\text{km}^{-1}$, which is approximately eight times larger than that of conventional DSF, has been developed. [39]

3.1.2. Bandwidth Increase by Dispersion Arrangement

When we obtain a fiber having a typical bandwidth with some dispersion variance, we can widen the bandwidth by rearranging the dispersion in the fiber [3,5]. In this method, we first measure λ_0 of short sections in which the variance of λ_0 is sufficiently small, then we select sections with similar λ_0 and splice them together. Figure 2 (a) shows the four-wave mixing arrangement using dispersion rearranged 750-m-long HNLF consisting of three 250-m-long sections of HNLF. [5] The 250-m-long sections had the λ_0 values 1547.3, 1546.3 and 1548.4 nm, respectively [see Fig. 2 (b)]. The resultant average λ_0 of the 750-m-long HNLF was 1547.2 nm. The composition of the three sections was arranged such that the first fiber matched with $\lambda_0 = 1547.2$ nm the average zero-dispersion at most while the others were allocated symmetric with this wavelength.

Figure 3 shows the dependence of the conversion efficiency (η_C) versus the signal wavelength measured using the dispersion arranged set-up for four-wave mixing shown in Fig. 2. The 3-dB bandwidth was 34 nm (1530.2–1564.2 nm), which covers almost the entire C-band. The symmetric and flat characteristics show that FWM in HNLF can be applied for wavelength up- and down-conversion of WDM signals.

3.1.3. Ultra-Broad Bandwidth Achieved by a Polarization-Maintained Nonlinear Fiber

For large separation of the wavelengths of the signal wave E_S and the pump wave E_P, polarization-mode dispersion (PMD) appears as a residual limiting factor of the bandwidth. PMD limits the bandwidth because it deteriorates the phase matching between interacting waves. The SOP of the wave transmitted in the fiber depends on the frequency (and so on the wavelength) as [40]

$$\frac{d\mathbf{s}}{d\omega} = \Omega \times \mathbf{s}, \tag{17}$$

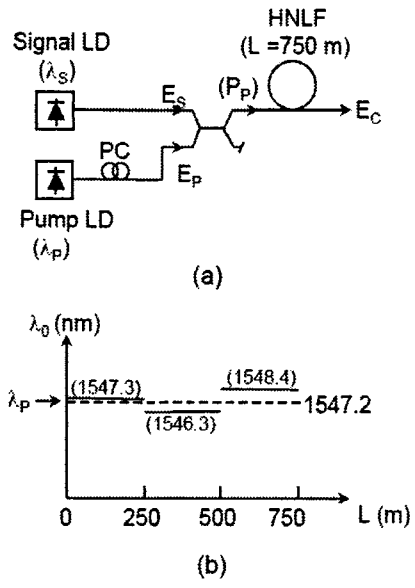

Fig. 2. Four-wave mixing wavelength converter using 750 m HNLF. (a) Configuration, (b) Arrangement of the average zero-dispersion wavelength.

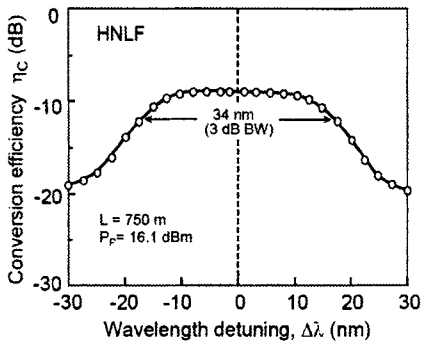

Fig. 3. Dependence of the conversion efficiency, η_C, on the signal wavelength detuning from the pump wavelength, $\Delta\lambda = \lambda_S - \lambda_P$, for a 750-m HNLF four-wave mixer.

where **s** is the unit Stokes vector representing the SOP of the wave and Ω is the rotation vector of the polarization on the Poincare sphere. The rate of rotation of the Stokes vector is equal to the differential group delay time $\delta\tau$ experienced by spectrally narrow pulses having polarizations aligned with the two orthogonal principle states of polarization, [40] i.e.,

$$| \Omega | = | \delta\tau | . \tag{18}$$

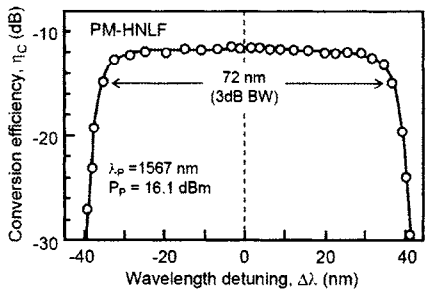

Fig. 4. Conversion efficiency dependence on $\Delta\lambda$ for 1-km PM-HNLF four-wave mixer.

Equations (17) and (18) indicate that the SOP of the largely detuned E_S and E_P change differently in the transmission due to PMD. This severely degrades the phase matching of interacting waves. The bandwidth of FWM, therefore, is limited by the PMD for large detuning condition.

The best way to overcome the PMD problem is the use of a polarization-maintaining (PM) nonlinear fiber.

Figure 4 shows the bandwidth of four-wave mixing using the PM-HNLF. [6] The fiber had a length of 1-km, the third-order nonlinear coefficient of $\sim$11 $W^{-1}km^{-1}$, the zero-dispersion wavelength at 1567.0 nm and a dispersion slope of 0.03 $ps/nm^2/km$. The crosstalk between the two polarization modes of the fiber was $\sim$25 dB. The 3-dB bandwidth of 72 nm (1532–1604 nm) was obtained with a flattened range of 66 nm. The result clearly shows the bandwidth broadening effect of fixing the SOP in the fiber by reducing the PMD.

3.2. Optical Switching by Cross-Phase Modulation

The phase shift by cross-phase modulation (XPM) in a nonlinear fiber can be applied for optical gating, e.g. in a switch based on a nonlinear optical loop mirror (NOLM) [3,11–13] or in an optical Kerr-switch with XPM-induced polarization rotation. [8,24–26] As shown in Eq. (13) the phase shift by XPM is proportional to the product, $\gamma P_P(0)\ell(L)$, where $P_P(0)$ denotes the input power of a control pulse. A nonlinear fiber with a larger nonlinearity is thus mostly appropriate.

As control pulses become shorter at higher bit rate, the walk-off between the control pulse and the probe light due to group-velocity difference is no longer negligible. The conversion efficiency as well as the speed of switching signal is limited. One way to make the group velocities at both wavelengths the same is to employ a dispersion-flattened fiber (DFF) with a small dispersion. Another way is to utilize specific wavelength allocation using a fiber with dispersion slope.

In a XPM-switch, the walk-off, Δt, between a probe light at a wavelength λ_c and control pulses at λ_s is expressed with the group velocity of the probe light, v_C, and that of control pulses, v_S, as $\Delta t = L[(1/v_C) - (1/v_S)]$, where L denotes the fiber length and group velocities are related with the GVDs as $d(1/v_C)/d\omega = \beta_{2C}$ and $d(1/v_S)/d\omega = \beta_{2S}$. The walk-off is minimized when both group velocities are equal.

Using a DSF with a dispersion slope, walk-off free condition is thus achieved when the wavelengths of the probe light and control pulses are allocated symmetric with respect to λ_0.

In a switching condition in which the phase shift by XPM is π, the effective length $\ell(L)$ is set to

$$\ell(L) = \frac{\pi}{2}\frac{1}{\gamma P_P(0)}. \tag{19}$$

In this equation, it is assumed that the peak power of the control pulses is maintained in the fiber. However, when the required fiber length for the switching condition is longer than the dispersion length, the waveform of the control pulses may be changed by the GVD and SPM. [37] A HNLF with a larger γ is a good candidate for avoiding waveform change since it is effective for shortening the required length L. In addition, a short L is preferable to suppress the walk-off even when the group velocities are not exactly the same.

4. Highly Nonlinear Fibers

From the discussions above it is evident that the best way to obtain a highly efficient and broadband fiber processor is to increase γ, to shorten the necessary length and to achieve fine control of dispersion. Increasing the nonlinearity coefficient reduces the length required to achieve a certain magnitude of nonlinearity, thus enabling more compact devices. Moreover, a shorter fiber length relaxes the requirements regarding the dispersion characteristics, which typically limit the wavelength range of optical signal processing applications. A highly-nonlinear fiber (HNLF) is, therefore, a practical candidate for optical signal processing devices. By germanium doping in the silica-core and reducing the mode field area, a HNLF with $\gamma \sim 20$ $W^{-1}km^{-1}$ has been fabricated. [39] It showed a very good nonlinear feature with finely controlled dispersion profile.

The nonlinearity of fibers can be further increased by reducing the mode field area and by using a core material with a high nonlinear refractive index. Photonic crystal fibers (PCFs) are very promising alternatives to conventional step-index HNLFs. In PCFs, a much stronger confinement of light can be achieved because of the high refractive index contrast between the core and the holey cladding. The majority of highly nonlinear fibers investigated so far are silica-based because of the mature fabrication technology and the low material absorption loss. Nonlinearity coefficients of up to 70 $W^{-1}km^{-1}$ have been reported. [41,42] Other materials such as lead-, [43] chalcogenide-, [44] or Bismuth-oxide-based glasses, [45] however, have a much larger nonlinear refractive index n_2. In a lead glass based PCF, γ-value of 640 $W^{-1}km^{-1}$ has been achieved. [43] An even higher nonlinearity coefficient of 1360 $W^{-1}km^{-1}$ has recently been reported for a Bismuth-oxide-based fiber with a conventional step index design. [45] Decreasing big losses and improving method for a fine control of dispersion are the key issues for these higher nonlinear fibers to be practical.

5. System Applications

Many system applications using the third-order nonlinearities in fiber have so far been demonstrated. Here we show recent results on simultaneous wavelength conversion

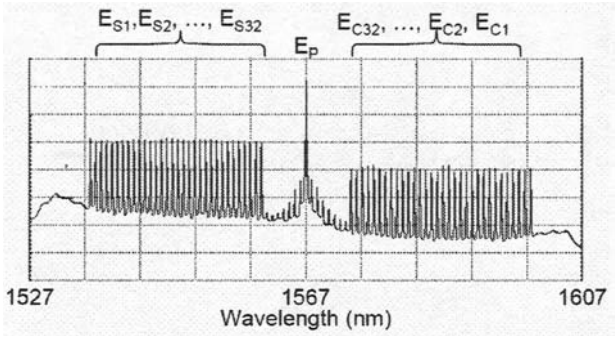

Fig. 5. Optical spectrum of simultaneous conversion of 32 × 10 Gb/s WDM signals output from PM-HNLF four-wave mixer. Res.: 0.2 nm, Vertical scale: 0.2 dB/div.

of WDM signal by FWM, 160 Gb/s optical 3R-regeneration and optical switching up to 640 Gb/s by parametric amplified fiber switch. All of these demonstrations used highly-nonlinear fibers (HNLFs).

5.1. Wavelength Conversion by Four-Wave Mixing

Simultaneous multi-channel wavelength conversion is attractive because it can reduce the number of converters. Using the PM-HNLF four-wave mixer having the bandwidth shown in Fig.4, we performed a simultaneous wavelength conversion of 32×10 Gb/s WDM signal between C-band and L-band. [3,6] The 32 WDM signals E_{Sj} (j=1,...,32) with wavelength at 1535.8 nm (λ_{S1}), 1536.6 nm (λ_{S2}),..., 1560.6 nm (λ_{S32}) (a channel spacing of 100 GHz) were input to the PM-HNLF converter and wavelength converted simultaneously to E_{Cj} at 1599.4 nm (λ_{C1}), 1598.6 nm (λ_{C2}),..., 1573.4 nm (λ_{C32}).

Figure 5 shows the spectrum at the output of the converter. The variance of the conversion efficiency was less than 2 dB for all 32 channels. The FWM crosstalk level between channels were less than −30 dB and no degradation was induced. All channels were converted simultaneously with a power penalty of less than 2.6 dB.

5.2. Optical Phase Conjugation (OPC)

As discussed in section 2, a wave, which is phase-conjugate to the input signal wave, can be generated by FWM [see Eq. (2)]. Using such an optical phase conjugation (OPC) in a transmission link, distortions due to GVD and fiber nonlinearities such as SPM, XPM, FWM and the Raman effect are compensated for. OPC compensates for both positive and negative dispersions and the effects do not depend on the bit rate, pulse shapes and the optical modulation formats. Because of these transparent features OPC has potential to extends flexibility and capacity of future photonic network.

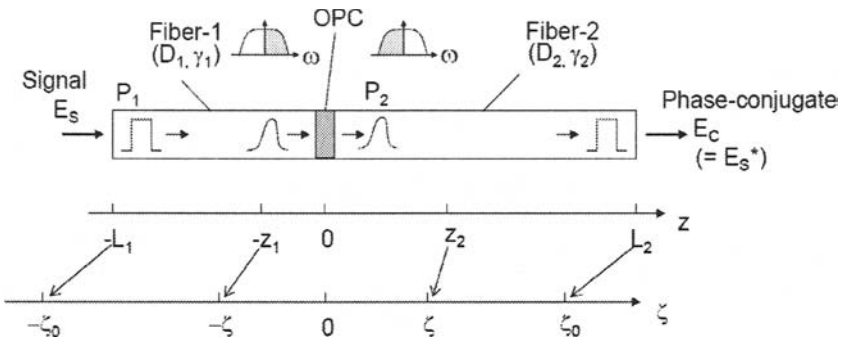

Fig. 6. Schematic configuration of GVD and SPM compensation by OPC. z: actual distance, ζ: normalized distance.

5.2.1. Waveform Distortion Compensation by OPC

Figure 6 illustrates compensation for waveform distortion due to GVD and SPM using optical phase conjugation (OPC). [46] The transmission fiber employs optical amplifiers to compensate for the fiber loss. The signal wave E_S, with optical power P_1 is transmitted through Fiber-1 of length L_1, which has a loss α_1, a dispersion D_1, and an optical nonlinear coefficient γ_1. The optical phase conjugator then converts the wave to a phase-conjugate wave E_C ($\propto E_S^*$) through which the spectrum is inverted with respect to the pump frequency. E_C with optical power P_2 is then transmitted through Fiber-2 with parameters L_2, α_2, D_2 and γ_2. By taking the complex conjugate of the wave, OPC inverts the phase change (modulation) accumulated during transmission over Fiber-1. Waveform distortion is compensated for by giving E_C the same distortion in Fiber-2.

The condition for compensation is approximately achieved when the total GVD in both fibers is identical, [47,48]

$$D_1 L_1 = D_2 L_2, \tag{20}$$

and when the path-averaged SPM-induced phase shift along both fibers is almost the same, [36,46] such that

$$\gamma_1 \overline{P_1} L_1 = \gamma \overline{P_2} L_2. \tag{21}$$

Here, $\overline{P_j} = (1/L_j) \int P_j(z) dz (j = 1, 2)$ indicates the path-averaged power. When SPM can be neglected, as in a transmission with lower signal power level, Eq. (20) is the condition for GVD compensation.

Equations (20) and (21) show the transparent characteristics of OPC, where the compensation conditions do not depend on the modulation format or the bit-rate.

SPM compensation by OPC is limited by the asymmetric distribution of the Kerr-effect along the fiber with respect to the OPC position. This is caused by the asymmetric light intensity change due to fiber loss and amplifier gain. Therefore above approximation applies only when the change of SPM along the fiber is small. An approximate criterion is such that the amplifier spacing is sufficiently shorter than the nonlinear length $L_{\mathrm{NL}} \equiv (\gamma \overline{P})^{-1}$, to keep the optical Kerr phase shift in fiber span small.

A method for the exact compensation of GVD and SPM using OPC has been proposed [46] in which the ratio of dispersion to the strength of the optical Kerr effect is designed to be the same at two corresponding positions, $-z_1$ and z_2, with respect to OPC as follows

$$\frac{D_1(-z_1)}{\gamma_1(-z_1)P_1(-z_1)} = \frac{D_2(z_2)}{\gamma_2(z_2)P_2(z_2)}. \tag{22}$$

Corresponding positions $-z_1$ and z_2 are the points at which the optical Kerr effect or the dispersion (when $D_j(z) \neq 0 (j = 1, 2)$) from the OPC position ($z = 0$) are the same as

$$\zeta = -\int_0^{z_1} \gamma_1(z)P_1(z)dz = \int_0^{z_2} \gamma_2(z)P_2(z)dz \tag{23}$$

or

$$\zeta' = -\int_0^{z_1} D_1(z)dz = \int_0^{z_2} D_2(z)dz. \tag{24}$$

Under the conditions in Eqs. (22) and (23) or Eqs. (22) and (24), the output wave from the second fiber is exactly the complex conjugate of the input wave into the first fiber. The sign of the phase change caused by GVD and SPM at any position $-z_1$, in the fiber is inverted by OPC. Thus the waveform distortion due to above phase shift at position $-z_1$ in the first fiber is exactly compensated for by the distortion due to the phase shift at position z_2 in the second fiber. By providing the equal ratio of the dispersion and the nonlinearity at the corresponding positions throughout the fibers, we can exactly compensate for the waveform distortion due to GVD and SPM. Note that positions $-z_1$ and z_2 are symmetric with respect to OPC if we measure in the normalized distance (see Fig. 6).

The effect of this method was demonstrated in 3000 km transmission system [49] in which the total distortion due to GVD and SPM in a transmission line was given before OPC in the transmitter using dispersion-decreased dispersion compensating fiber.

5.2.2. Simultaneous Compensation of WDM Signals

Using the four-wave mixer with HNLF shown in Figs. 2 and 3, a simultaneous wavelength conversion of 5-channels 40 Gb/s WDM signal were successfully transmitted through 105-km standard fiber using midway OPC. [5] Also using the four-wave mixer with PM-HNLF shown in Fig. 4, 32×10 Gb/s WDM signals were transmitted over a 100-km standard fiber with midway OPC at the 50-km point and additional dispersion compensation at the receiver. [6] Note that only small amount of dispersion compensating fiber (DCF) was required when we used OPC. Since OPC compensates for even-order dispersions (2, 4, ...) and the optical nonlinearities, the spectrum of WDM signals broadened through transmission can be recovered to the original. The simultaneous wavelength conversion and OPC thus can effectively apply for ultra-dense WDM and ultra-high speed transmission in/between future phonic networks.

5.3. Optical 3R Regeneration

An optical 3R-regeneration is an essential technology for optical nodes in future photonic networks. An all-optical 3R-regenerator is especially attractive for high-capacity

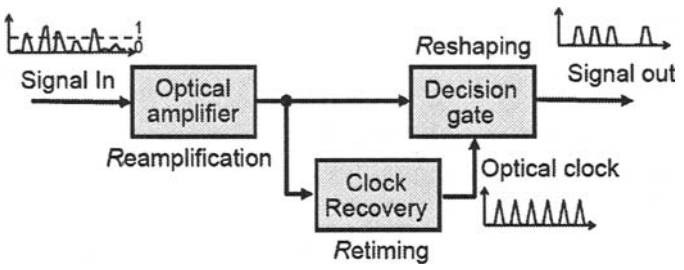

Fig. 7. Basic configuration of an optical 3R-regenerator.

networks, where an opto-electronic (O/E) regenerator will no longer be appropriate. Several methods of all-optical 3R regeneration have been investigated over the last years. [13–26]

Contrary to all-optical 2R-regeneration, e.g., in wavelength converter, in a 3R-regenerator the data signal has to switch a retimed pulse train rather than a continuous wave signal. Therefore, when we apply an optical 3R-regenerator to the 160 Gb/s and higher bit-rate signal, an ultra-high speed and transparent optical gate switch is required. One typical problem of such an ultra-high speed optical switch is that the phase noise or the jitter of the data pulses is converted to the amplitude noise of the output pulses. To overcome this problem, a method was introduced to change the pulse shape of input data signal to a flattened-top shape. [24–26] Another important issue is that the wavelength of the regenerated signal should be the same as that of the input data signal in order to make the design of the transmission link and of switching nodes simple. [25,26]

5.3.1. Optical 3R Regenerator

Figure 7 shows the basic configuration of an all-optical 3R regenerator. Three functions are required for the 3R regenerator: (i) re-amplification, (ii) re-timing and (iii) re-shaping of the input data signal. The operation of re-amplification is basically the same as that of linear amplification.

The re-timing and re-shaping functionalities are achieved in two steps, firstly by synchronizing a train of well shaped optical pulses (optical clock pulses) generated locally by a high-quality pulse source at a repetition frequency corresponding to the line rate of the data signal with the input data signal, and secondly by switching thus generated optical clock pulses in the decision gate by the data signal. For clock recovery, the most popular method is based on converting the optical signal to an electric signal for extracting the clock signal and then on generating the optical clock pulses using a pulse laser. But some electro-optical and all-optical re-timing methods were also proposed. [50–52]

In the decision gate, the data signal switches the locally generated optical clock pulses. For the optical decision gate, a semiconductor-based Mach-Zehnder interferometer, [1,7,18,20] an electro-absorption (EA-) modulator, [21] a nonlinear optical loop mirror (NOLM) [3,13] etc. have so far been proposed. For the operation of the

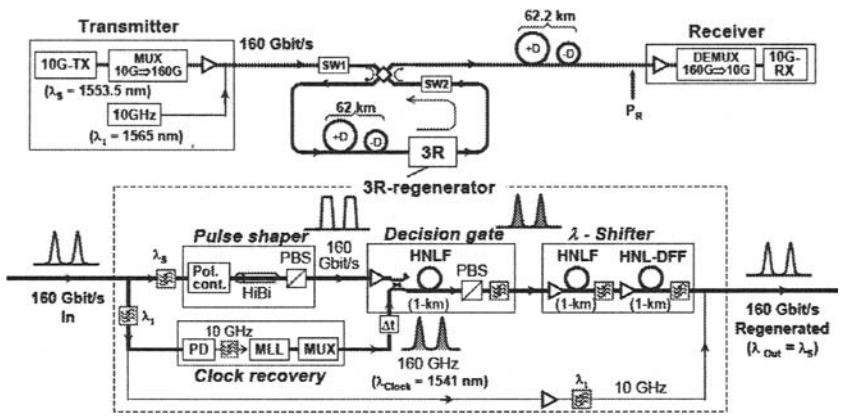

Fig. 8. Experimental setup for 160 Gb/s 3R-regenerating transmission. Inset shows the optical 3R-regenerator.

decision gate it is important that timing fluctuation or jitter of the data signal do not affect the shape of the switched pulses and, more preferably, jitter should be reduced.

Transparent operation is most important for the devices to be applied to optical 3R regenerators. The performance of the regenerator should not depend on the bit-rate, pulse shape and data pattern. The optical nonlinear effects used in the regenerator components should be faster compared with the data rate. If we operate the 3R-regenerator at 160 Gb/s and higher bit rates, the processing speed of the components of the regenerator should be less than 1 pico second. Ultra high-speed optical switches using optical fibers [3,4,11] are candidates for realizing the optical gates. One promising candidate is an optical gate based on cross-phase modulation (XPM) in an optical fiber. [24–26]

5.3.2. 160 Gb/s Optical 3R Regeneration Experiment

Figure 8 shows the setup for the 160 Gb/s 3R-regenerating transmission in a circulating loop comprising a 62-km long fiber span and the optical 3R-regenerator. [25,26] In the transmitter, a mode-locked laser generated a 10-GHz optical pulse train (~1.6 ps FWHM) at λ_s = 1553.5 nm, which was modulated by a $LiNbO_3$ intensity modulator (10 Gb/s, PRBS: $2^{23} - 1$) and optically time-division multiplexed (OTDM) to a 160-Gb/s single-polarization data signal. In the receiver, the 160-Gb/s data signal was demultiplexed to a10-Gb/s signal and detected.

The inset in Fig. 8 shows the configuration of the 160-Gb/s optical 3R-regenerator. It comprised four distinct elements: the pulse shaper, the decision gate, the optical clock recovery and the wavelength shifter.

The pulse shaper shapes input pulses into flattened-top ones using a piece of highly birefringent fiber (HiBi-fiber) and the polarization beam splitter. As shown in Fig. 9 the pulse shaper generated pulses having a well-flattened top (FWHM ~2.7 ps) and with leading and trailing edges as given by the input pulses. An optical Kerr-switch utilizing XPM induced polarization rotation in a HNLF ($\gamma = 20\ W^{-1}km^{-1}$) functioned as

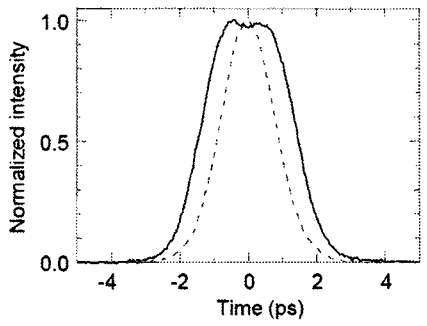

Fig. 9. Cross-correlation traces measured with a 650-fs sech^2 pulse (- - - input, — output signal of the pulse shaper).

decision gate, in which the 160-Gb/s flattened-top signals switched the locally retimed 160-GHz optical clock pulses. Owing to the pulse shaper, the decision gate was less sensitive to the jitter of the incoming data pulses (more than four times enlargement of the phase margin) and effectively suppressed the jitter as well as the amplitude noise. At the output end of the decision gate, the wavelength shifter reset the wavelength of the regenerated signal to that of the input data signal. A fiber-based wavelength shifter was employed, which broadened the signal spectrum followed by optical filtering. A regenerator with no wavelength shift is advantageous to make the design of the transmission link (dispersion compensation) and of switching nodes simpler. Note that the wavelength shift using spectrum broadening can further improve the performance of the regenerator by its 2R-regeneration effect. [53]

Figure 10 shows the power penalties (at BER = 10^{-9}) for all the 16 OTDM channels with and without 3R-regenerator measured at 62, 124 and 186 km. Compared with the results without the 3R-regenerator, 3R-regenerator well improved system performance with suppressing noise of the signal, and 160-Gbit/s optical 3R-regenerating transmission in a circulating loop was successfully demonstrated. The results indicate that the quality as well as the wavelength of the regenerated signal is almost the same as that of the original signal, which is an essential prerequisite of the 3R-regenerator.

5.4. Optical Parametric Amplified Fiber Switch

An ultra-high speed optical switch is one of the key devices for optical signal processing. [1] For practical applications, the switch should operate with high efficiency, be fully transparent in the data rate and in a wavelength range covering at least one band, e.g., the whole C or L-band. For applications such as optical add-drop multiplexing or optical 3R-regeneration, the input and output wavelengths should be same.

This section shows a fiber based optical switch operating in a full transmission band without wavelength shift and having a very high S/N ratio because it provides parametric gain. [54] Contrary to switching devices based solely on parametric gain, [55] the switch has also a very high contrast ratio. Its good and stable performance is shown in 160, 320, and 640 Gb/s optical demultiplexing and optical sampling experiments.

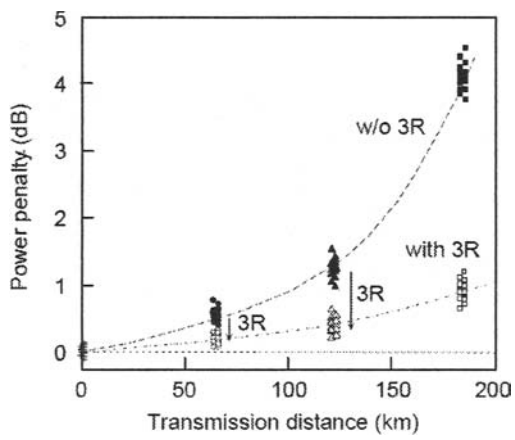

Fig. 10. Power penalty at BER = 10^{-9} versus transmission distance measured at 62, 124, and 184 km points with and without optical 3R-regeneration.

5.4.1. Principle and Operation of the Switch

The scheme of the optical switch is shown in Fig. 11. [54] The optical signal E_S (data pulses, wavelength λ_S and pulse peak power P_S) and control (pump) pulses E_P (λ_P, P_P) are input to a highly-nonlinear fiber (HNLF). Behind the HNLF is a polarizer, which transmits only light linearly polarized along the main axis of the polarizer (vertical axis in Fig. 11). Using a polarization controller, the state of polarization of E_S at the input of the HNLF is set linear and orthogonal (in the absence of a control pulse) to the main axis of the polarizer, so that no light is transmitted. The state of polarization of E_P is aligned at $\sim$45. E_P causes a change of the state of polarization of E_S by FWM and therefore transmission of the data signal with increasing P_P. The distinguished feature of the proposed switch is that it uses optical parametric amplification by FWM. The parametric amplification of the polarization component of E_S along E_P leads to an amplification of E_S and an additional change of the state of polarization. The polarization of E_S clamps at a linear polarization state with an angle θ near $\sim$45°, even if P_P is further increased.

This switch does not shift the wavelength of the signal. It has a good extinction ratio of more than 30 dB, and the switched pulses have a very high optical S/N ratio because they are parametrically amplified. Note that the peak power P_S of the output signal is increased even if we count the 3-dB loss added by the polarizer in the condition of θ $\sim$45°. Considering the ultra-fast response time of FWM of several femto seconds, the proposed switch can be applied to ultra-high speed (>Tb/s) signal processing.

5.4.2. Ultra-Broadband and Highly Efficient Switching

The switch was tested using a 20-m-long HNLF with $\gamma = 20.4\ \mathrm{W^{-1}km^{-1}}$, $\lambda_0 \sim 1579$ nm and a dispersion slope of 0.03 ps/nm^2/km. [3] Figure 12 shows the experimental setup. [54] A mode-locked fiber laser (MLFL1) generated a 10-GHz optical pulse train

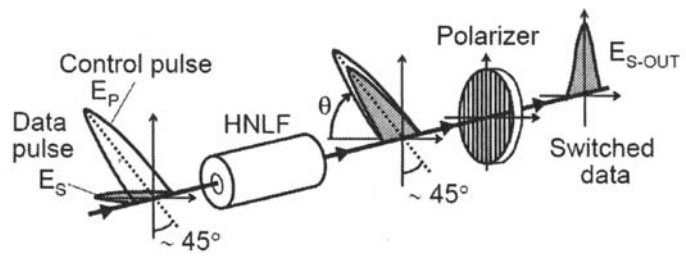

Fig. 11. Schematic of optical parametric amplified fiber switch.

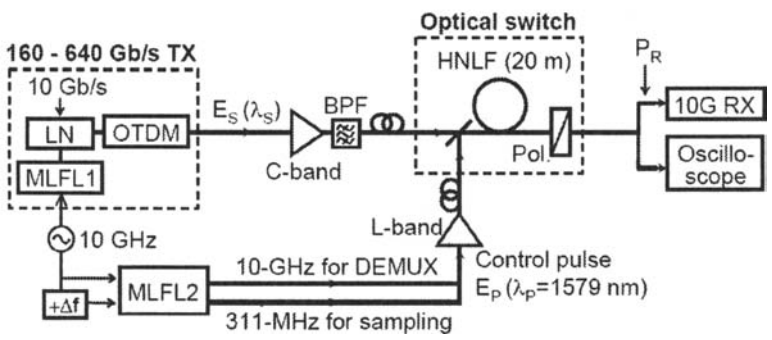

Fig. 12. Experimental setup for optical parametric amplified fiber switch.

at the wavelength λ_S in the C-band, which was modulated at 10 Gb/s (PRBS: $2^{23}-1$) and then OTDM-multiplexed to a single polarization 160–640 Gb/s data signal E_S. E_S was input to the HNLF together with the control pulses E_P generated by the second MLFL2. E_P had a wavelength located at the L-band ($\sim \lambda_0$) and $\sim$45°-aligned polarization.

Figure 13 shows the switching gain versus the control peak power P_P of 10 GHz control pulse at λ_S = 1550 nm. The pulse widths (FWHM) of E_S and E_P were 1.6 and 0.9 ps, respectively. Here the switching gain is defined as the ratio of P_S at the output of the polarizer to P_S at the input of the HNLF. Since dominant parametric gain was given in parallel polarization condition for both pulses, the output power of E_S increased proportional to P_P^2 by optical parametric amplification as discussed in section 2. The highest switching gain of 7.6 dB at $P_P \sim 15$ W (averaged power of $\sim$+21 dBm for used 10 GHz pulses) was obtained with 20-m HNLF. Figure 14 shows the switching gain versus the wavelength of E_S at P_P 15 W confirming almost flat gain over the full C-band owing to a good phase-matching and small walk-off in 20-m HNLF. Note that by allocating the wavelength of E_P in the C-band, we can provide an optical switch operating over the full L-band.

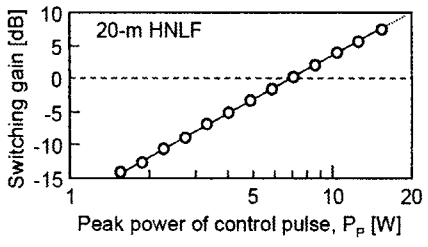

Fig. 13. Switching gain dependence on the control power.

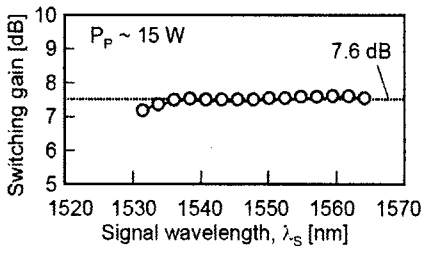

Fig. 14. Switching gain dependence on the signal wavelength.

5.4.3. Ultra-High-Speed Switching Demonstration

Using the optical fiber switch above, we performed optical demultiplexing experiments of 160, 320 and 640 Gb/s OTDM signals E_S to 10 Gb/s. [54] The pulse width of E_S was 1.6 ps for 160 Gb/s, 0.75 ps for 320 Gb/s and 0.65 ps for 640 Gb/s, whereas that of E_P was fixed at 0.9 ps. Figure 15 shows BER measurements versus the received power P_R of the demultiplexed signal at an average control power of +21.8 dBm (corresponding to $P_P \sim 15$ W). For 160 Gb/s, we measured BERs at signal wavelengths of $\lambda_S = 1535$, 1540, 1550 and 1560 nm.

Error free operation with power penalties (at BER = 10^{-9}, compared to the 10-Gb/s reference) of less than 0.2 dB was achieved for all wavelengths, demonstrating operation of this switch in the full C-band. We confirmed the error free operation at the input powers larger than -5 dBm of the 160-Gb/s signal. Error free operation was also achieved for 320 and 640 Gb/s signals with a slight increase of the power penalty of 1.1 and 2.5 dB, respectively, mainly caused by a residual cross-talk due to insufficiently short pulse widths.

5.5. Optical Sampling

Monitoring the quality of ultra-short pulses is an important issue in high-speed networks. Electrical sampling systems are commonly used to observe optical signals using O-E conversion. However, the bandwidth determined by the operation speed of the electronics is so far limited up to ~100 GHz at most. By using the ultra short pulse

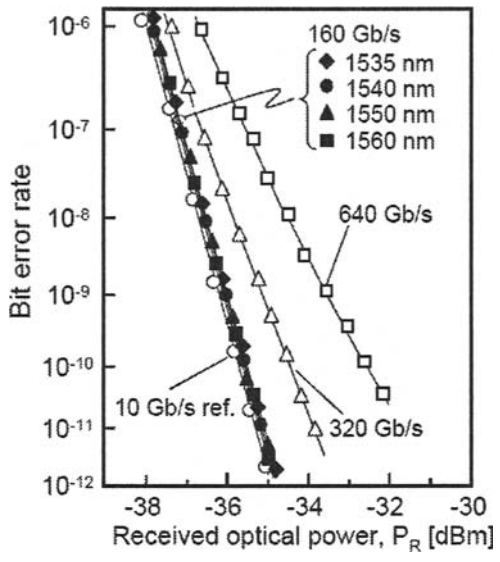

Fig. 15. Bit-error rate characteristics for the demultiplexed 10 Gb/s signal from 160, 320 and 640 Gb/s OTDM signal.

technology, optical sampling enables the direct observation of the waveform of 160 Gb/s and higher bit-rate signals. [30–35] A fiber-based optical gate is attractive for optical sampling. [30–31] because it offers higher conversion efficiency compared to optical gates based on nonlinear crystals and it also provides less than pico second time resolution.

Using the parametric amplified fiber switch described in the former section, a 160–640 Gb/s optical sampling system was demonstrated [54] using an all-optical clock recovery based on an optical phase locked loop (PLL). Figures 16 (a)–(e) show the eye-patterns observed with the same pulse widths as used in the BER measurements shown in Fig. 15. With an excellent high contrast and ultra-fast response provided by the fiber switch, clear eye-patterns of 160–640 Gb/s data were monitored with an excellent time resolution. The results indicate the possibility of optical sampling with high contrast and coverage of the entire C-band.

5.6. Supercontinuum Generation

Supercontinuum (SC) light can be generated using nonlinear fibers. [27–29] An impressive example of SC generation is the realization of a multi-wavelength source with more than 1000 channels. [27] SC with high spectral density is highly desirable for practical reasons. It can be achieved in the normal dispersion regime of fibers where chirping by self-phase modulation (SPM) is accumulated. When a part of the generated SC is filtered out with an optical filter, wavelength conversion is realized. Using a

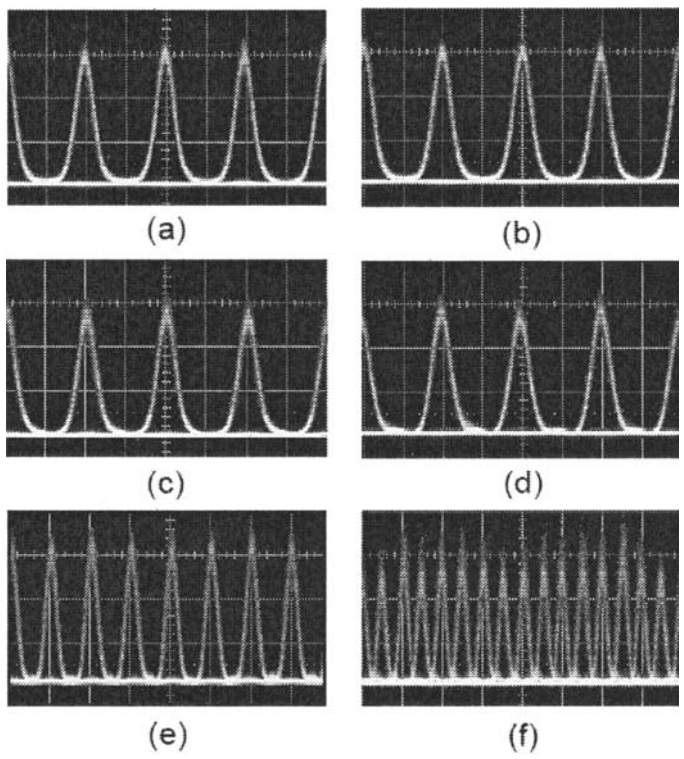

Fig. 16. Eye patterns of OTDM signal monitored by the optical sampling oscilloscope configuration using the optical parametric amplified fiber switch as a sampling gate. 160 Gb/s signal at (a) 1535 nm, (b) 1540 nm, (c) 1550 nm and (d) 1560 nm; (e) 320 Gb/s at 1550 nm and (f) 640 Gb/s at 1550 nm. Sampling rate: 311 MHz; Horizontal scale: 3.125 ps/div.

dispersion-flattened fiber with normal dispersion for SC generation, wavelength conversion at 160 Gb/s was demonstrated. [25,26,56] SC also provides a 2R regeneration function, which improves the quality of the signal. [53] This 2R effect was confirmed in a 160-Gbit/s regenerating conversion node. [57]

6. Summary

The effectiveness of nonlinear fibers for all-optical signal processing and the potential applications were described. The highly-nonlinear fiber (HNLF) is presently the most practical fiber so far developed and applied to optical signal processing. Various systematic applications have so far been demonstrated using HNLFs. Most of these demonstrations showed unique and attractive features which could not achieved without using the third-order optical nonlinearity in fiber.

By using four-wave mixing, WDM signals over almost entire C-band were simultaneously wavelength-converted to L-band. Fine control of a chromatic dispersion

as well as polarization-mode dispersion is essential to realize sufficiently broadband wavelength converter. Optical phase conjugation was also applied to WDM signal and well compensated for waveform distortion of all the channels simultaneously. The configuration and operation of an optical 3R regenerator, especially for 160 Gb/s data transmission, were described. One critical issue of using an ultra-fast optical gate switch is the conversion of timing jitter in the incoming data signal to amplitude noise in the output data signal. By using a pulse shaper at the input of the optical Kerr-switch used as a decision gate, we successfully reduced this detrimental effect and demonstrated 160 Gb/s optical 3R-regenerating transmission. Finally, an optical parametric amplified fiber switch was shown. The switch operated in a full transmission band without wavelength shift and having a very high S/N ratio and contrast ratio because it provides optical parametric gain. Using a 20-m-long highly-nonlinear fiber, optical demultiplexing and optical sampling of up to 640 Gb/s signals were successfully demonstrated over the whole C-band by using a fixed control pulse located in the L-band.

The ultra-broadband and ultra-high speed features of fiber-based optical signal processors enable us to realize Tb/s order optical switching in future photonic networks. Further increase in the nonlinearity is the key issue in realizing breakthrough fiber-based optical signal processors. Rapid development in nano-optical devices such as photonic crystal fibers, holey fibers and quantum dot amplifiers [58] is thus being demanded.

Acknowledgment

The author acknowledges F. Futami, S. Takeda, and R. Okabe at Fujitsu Laboratories Ltd. for their useful discussion and contribution in the systematic demonstrations, H.G. Weber, R. Ludwig and their colleagues at the Heinrigh-Hertz Institut (HHI) for their collaboration and useful discussion, and Sumitomo Electric Industries for producing highly-nonlinear fibers.

References

1. K.E. Stubkjaer, Semiconductor optical amplifier-based all-optical gates for high-speed optical processing, IEEE J. Select Top Quantum Electron, **6**, 1428–1435 (2000).
2. S.J.B. Yoo, Wavelength conversion technologies for WDM network applications, J. Lightwave Technol., **14**, 955–966 (1996).
3. S. Watanabe and F. Futami, All-optical signal processing using highly-nonlinear optical fibers, IEICE Trans., **E84-B**, 1179–1189 (2001).
4. S. Watanabe and F. Futami, All-optical wavelength conversion using ultra-fast nonlinearities in optical fiber, IEICE Trans., **E85-C**, 889–895 (2002).
5. S. Watanabe, S. Takeda, G. Ishikawa, H. Ooi, J.G. Nielsen, and C. Sonne, Simultaneous wavelength conversion and optical phase conjugation of 200 Gb/s (5×40 Gb/s) WDM signal using a highly nonlinear fiber four-wave mixer, Proc. Integrated Optics and Optical Fiber Communications/24th European Conference on Optical Communications (IOOC/ECOC'97) at Edinburgh, UK, September 1997, Post-deadline Paper TH3A, pp.1–4.

6. S. Watanabe, S. Takeda, and T. Chikama, Interband wavelength conversion of 320 Gb/s (32×10 Gb/s) WDM signal using a polarization-insensitive fiber four-wave mixer, Proc. 24th European Conference on Optical Communications (ECOC'98) at Madrid, Spain, September 1998, Post-deadline paper, p. 85.
7. S. Nakamura, Y. Ueno, and K. Tajima, 168-Gb/s all-optical wavelength conversion with a symmetric-Mach-Zehnder-type switch, Photon. Technol. Lett., **13**, 1091–1093 (2001).
8. J. Yu and P. Jeppesen, 80-Gb/s wavelength conversion based on cross-phase modulation in high-nonlinearity dispersion-shifted fiber and optical filtering, IEEE Photon. Tech. Lett., **13**, 833–835 (2001).
9. U. Feiste, R. Ludwig, C. Schubert, J. Berger, C. Schmidt, H.G. Weber, B. Schmauss, A. Munk, B. Buchold, D. Briggmann, F. Kueppers, and F. Rumpf: 160 Gbit/s transmission over 116 km field-installed fiber using 160 Gbit/s OTDM and 40 Gbit/s ETDM, Electron. Lett., **37**, 443–445 (2001).
10. S. Kawanishi, H. Takara, K. Uchiyama, I. Shake, K. Mori, 3 Tbit/s (160 Gbit/s x 19 channel) optical TDM and WDM transmission experiment, Electron. Lett., **35**, 826–827 (1999).
11. M. Nakazawa, T. Yamamoto, and K. R. Tamura, 1.28 Tbit/s-70 km OTDM transmission using third- and fourth-order simultaneous dispersion compensation with a phase modulator, Electron. Lett., **36**, 2027–2029 (2000).
12. M. Jinno, Effects of group velocity dispersion on self/cross phase modulation in a nonlinear Sagnac interferometer switch, J. Lightwave Technol., **10**, 1167–1178 (1992).
13. J.K. Lucek and K. Smith, All-optical signal regenerator, Opt. Lett., **18**, 1226–1228 (1993).
14. J.C. Simon, L. Billes, A. Dupas, and L. Bramerie, All optical regeneration techniques, Proc. 25th European Conference on Optical Communication (ECOC'99) at Nice, France, 1999, II, pp. 256–257.
15. B. Sartorius, All-optical 3R signal regeneration, Proc. 26th European Conference on Optical Communication (ECOC2000) at Munich, Germany, September 2000, Paper 9.4.1, pp. 293–294.
16. H. Yokoyama, H. Kurita, T. Shimizu, I. Ogura, Y. Hashimoto, R. Kuribayashi, M. Shirane, and H. Yamada, All-optical clock extraction and signal regeneration with mode-locked laser diodes, Proc. 7th International Workshop on Femtosecond Technology (FST 2000) at Tukuba, Japan, June 30, 2000, p. 71.
17. B. Sartorius, C. Bornholdt, S. Bauer, M. Moehrle, P. Brindel, and O. Leclerc, System application of 40 GHz all-optical clock in a 40 Gbit/s optical 3R regenerator, Proc. Optical Fiber Communication Conference (OFC 2000) at Baltimore, USA, 2000, Paper PD11.
18. D. Wolfson, A. Kloch, T. Fjelde, C. Janz, B. Dagens, and M. Renaud, 40-Gb/s all-optical wavelength conversion, regeneration, and demultiplexing in a SOA-based all-active Mach-Zehnder interferometer, IEEE Photon. Technol. Lett., **12**, 332–334 (2000).
19. A.E. Kelly, I.D. Phillips, R.J. Manning, A.D. Ellis, D. Nesset, D.G. Moodie, and R. Kashyap, 80 Gbit/s all-optical regenerative wavelength conversion using semiconductor optical amplifier based interferometer, Electron. Lett., **35**, 1477–1478 (1999).
20. Y. Ueno, S. Nakamura, and K. Tajima, Penalty-free error-free all-optical data pulse regeneration at 84 Gbps with Symmetric-Mach-Zehnder-type regenerator, Proc. Optical Fiber Communication Conference (OFC 2001) at Anaheim, CA, USA, 2001, Paper MG5-1.
21. T. Otani, T. Miyazaki, and S. Yamamoto, Optical 3R regenerator using wavelength converters based on electroabsorption modulator for all-optical network applications, IEEE Photon. Technol. Lett., **12**, 431–433 (2000).

22. M. Nakazawa, E. Yamada, H. Kubota, and K. Suzuki, 10 Gbit/s soliton data transmission over million kilometers, Electron. Lett., **27**, 1270–1272 (1991).

23. S. Bigo, O. Leclerc, and E. Desurvire, All-optical fiber signal processing and regeneration for Soliton communications, IEEE J. Select. Top. Quantum Electron., **3**, 1208–1223 (1997).

24. R. Ludwig, C. Schubert, S. Watanabe, F. Futami, C. Schmidt, J. Berger, C. Boerner, S. Ferber, and H. G. Weber, 160 Gbit/s 3R-regenerating wavelength converter, Proc. 7th Opto-Electronics and Communications Conference (OECC'02) at Yokohama, Japan, 2002, Post-deadline paper, PD1-3.

25. S. Watanabe, F. Futami, R. Okabe, Y. Takita, S. Ferber, R. Ludwig, C. Schubert, C. Schmidt, and H.G. Weber, 160 Gbit/s Optical 3R-Regenerator in A Fiber Transmission Experiment, Proc. Optical Fiber Communication Conference (OFC2003) at Atlanta, Georgia, USA, March 2003, Post-deadline Paper, PD16.

26. S. Watanabe, R. Ludwig, F. Futami, C. Schubert, S. Ferber, C. Boerner, C. Schmidt-Langhorst, J. Berger, and H.G. Weber, Ultrafast all-optical 3R-regeneration, IEICE Trans., **E87-C**, 1114–1118 (2004).

27. H. Takara, T. Ohara, K. Mori, K. Sato, E. Yamada, Y. Inoue, T. Shibata, M. Abe, T. Morioka, and K-I. Sato, More than 1000 channel optical frequency chain generation from single supercontinuum source with 12.5 GHz channel spacing, Electron. Lett., **36**, 2089–2090 (2000).

28. F. Futami, S. Watanabe, and T. Chikama, Simultaneous recovery of 20 × 20 GHz WDM optical clocks using supercontinuum in a nonlinear fiber: Proc. 26th European Conference on Optical Communication (ECOC2000) at Munich, Germany, September 2000, Post-deadline paper 2.8.

29. F. Futami and S. Watanabe, All-optical data addition to a time slot in 160-Gb/s OTDM signal using wavelength conversion by supercontinuum generation: Proc. 27th European Conference on Optical Communication (ECOC2001) at Amsterdam, Netherlands, September 2001, Paper WeB2, pp.306–307.

30. C. Schmidt, F. Futami, S. Watanabe, T. Yamamoto, C. Schubert, J. Berger, M. Kroh, H.-J. Ehrke, E. Dietrich, C. Boerner, R. Ludwig, and H.G. Weber, Optical Q-factor monitoring at 160 Gb/s using an optical sampling system in an 80 km transmission experiment, Proc. Conference on Lasers and Electro-Optics (CLEO 2002) at Long Beach, 2002, CThU3.

31. J. Li, J. Hansryd, P. O. Hedekvist, P. A. Andrekson, and S. N. Knudsen: 300 Gbit/s eye-diagram measurement by optical sampling using fiber based parametric amplification, Proc. Optical Fiber Communication Conference (OFC2001) at Anaheim, CA, 2001, Post-deadline paper.

32. N. Yamada, N. Banjo, H. Ohta, S. Nogiwa, and Y. Yanagisawa, 320-Gb/s eye diagram measurement by optical sampling system using a passively mode-locked fiber laser, Proc. Optical Fiber Communication Conference (OFC2002) at Anaheim, CA, 2002, Paper ThU3.

33. M. Shirane, Y. Hashimoto, H. Kurita, H. Yamada, and H. Yokoyama, Optical sampling measurement with all-optical clock recovery using mode-locked diode lasers, Proc. Optical Fiber Communication Conference (OFC2001) at Anaheim, CA, 2001, Paper MG2.

34. H. Takara, S. Kawanishi, A. Yokoo, S. Tomaru, T. Kitoh, and M. Saruwatari, 100 Gbit/s optical signal eye-diagram measurement with optical sampling using organic nonlinear optical crystal, Electron. Lett., **32**, 2256–2258 (1996).

35. K. Igawa, A. Otani, and Y. Tsuda, Novel Optical Sampling Oscilloscope without traditional trigger technique and measurement of optical short pulse modulated PRBS pattern, Proc. Optical Fiber Communication Conference (OFC 2004) at Los Angeles, 2004, CA, 2004, Paper MF73.

36. S. Watanabe, G. Ishikawa, T. Naito, and T. Chikama, Generation of optical phase-conjugate waves and compensation for pulse shape distortion in a single-mode fiber, J. Lightwave Technol., **12**, 2139–2146 (1994).

37. G. P. Agrawal, *Nonlinear Fiber Optics*, 2nd. ed. (Academic Press, San Francisco, CA, 1995).

38. K. Inoue, Four-wave mixing in an optical fiber in the zero-dispersion wavelength region, J. Lightwave Technol., **10**, 1553–1561 (1992).

39. M. Onishi, T. Okuno, T. Kashiwada, S. Ishikawa, N. Akasaka, and M. Nishimura, Highly nonlinear dispersion shifted fiber and its application to broadband wavelength converter, Proc. Integrated Optics and Optical Fiber Communications/24th European Conference on Optical Communications (IOOC/ECOC'97) at Edinburgh, UK, September 1997, Paper TU2C, pp.115–118.

40. C.D. Poole, and D.L. Favin: Polarization-mode dispersion measurements based on transmission spectra through a polarizer, J. Lightwave Technol., **12**, 917–929 (1994).

41. J.H.Lee, W. Belardi, K. Furusawa, P. Petropoulos, Z. Yusoff, T.M. Monro, D.J. Richardson, Four-wave mixing based 10-Gb/s tunable wavelength conversion using a holey fiber with a high SBS threshold, IEEE Photon. Technol. Lett., **15**, 440–442 (2003).

42. R. Hainberger, and S. Watanabe, Wavelength dependence of the nonlinear coefficient of highly nonlinear photonic crystal fibers, 9th Opto-Electronics and Communications Conference/3rd International Conference on Optical Internet (OECC/COIN2004) at Yokohama, Japan, July 2004, Paper 16E1-3.

43. P. Petropoulos, T.M. Monro, H. Ebendorff-Heidepriem, K. Frampton, R.C. Moore, H.N. Rutt, and D.J. Richardson, Soliton-self-frequency-shift effects and pulse compression in an anomalously dispersive high nonlinearity lead silicate holey fiber, Proc. Optical Fiber Communication Conference (OFC2003) at Atlanta, Georgia, USA, March 2003, Post-deadline paper PD3 Atlanta.

44. M. Asobe, H. Kobayashi, and H. Itoh, Laser-diode-driven ultrafast all-optical switching by using highly nonlinear chalcogenide glass fiber, Opt. Lett., **18**, 1056–1058 (1993).

45. N. Sugimoto, T. Nagashima, T. Hasegawa, S. Ohara, K. Taira, and K. Kikuchi, Bismuth-based optical fiber with nonlinear coefficient of 1360 $W^{-1}km^{-1}$, Proc. Optical Fiber Communication Conference (OFC 2004) at Los Angeles, 2004, CA, Post-deadline paper PD26.

46. S. Watanabe and M Shirasaki, Exact compensation for both chromatic dispersion and Kerr effect in a transmission fiber using optical phase conjugation, J. Lightwave Technol., **14**, 243–248 (1996).

47. A. Yariv, D. Fekete, and D.M. Pepper, Compensation for channel dispersion by nonlinear optical phase conjugation, Opt. Lett., **4**, 52–65 (1979).

48. S. Watanabe, T. Naito and T. Chikama, Compensation of chromatic dispersion in a single-mode fiber by optical phase conjugation, IEEE Photon. Technol. Lett., **5**, 92–95 (1993).

49. S. Watanabe, S. Kaneko, and T. Chikama, Long-haul fiber transmission using optical phase conjugation, Optical Fiber Technologies, **2**, 169–178 (1996).

50. T. Yamamoto, L.K. Oxenlowe, C. Schmidt, C. Schubert, E. Hilliger, U. Feiste, J. Berger, R. Ludwig, and H.G. Weber, Clock recovery from 160 Gbit/s data signals using phase-locked loop with interferometric optical switch based on semiconductor optical amplifier, Electron. Lett., **37**, 509–510 (2001).

51. O. Kamatani and S. Kawanishi, Prescaled timing extraction from 400 Gb/s optical signal using a phase lock loop based on four-wave-mixing in a laser diode amplifier, IEEE Photon. Technol. Lett., **8**, 1094–1096 (1996).

52. C. Boerner, S. Watanabe, F. Futami, R. Okabe, S. Ferber, C. Schubert, R. Ludwig, C. Schmidt-Langhorst, and H.G. Weber, 160 Gbit/s clock recovery in a 3R-regenerating wavelength converter, Proc. 30th European Conference on Optical Communication (ECOC2004) at Stochholm, Sweden, September 2004, Paper We3.5.6, pp. 440–441.

53. P.V. Mamyshev, All-optical data regeneration based on self-phase modulation effect, Proc. 24th European Conference on Optical Communications (ECOC'98) at Madrid, Spain, September 1998, 1, p. 475.

54. S. Watanabe, R. Okabe, F. Futami, R. Hainberger, C. Schmidt-Langhorst, C. Schubert, and H.G. Weber, Novel fiber Kerr-switch with parametric gain: Demonstration of optical demultiplexing and sampling up to 640 Gb/s, Proc. 30th European Conference on Optical Communication (ECOC2004) at Stockholm, Sweden, September 2004, Post-deadline paper Th4.1.6, pp.12–13.

55. J. Hansryd, P.A. Andrekson, M. Westlund, J. Li, P.-O. Hedekvist, Fiber-based optical parametric amplifiers and their applications, IEEE J. Select. Top. Quantum Electron., **8**, 506–520 (2002).

56. F. Futami, R. Okabe, Y. Takita, and S. Watanabe, Transparent wavelength conversion at up to 160 Gb/s by using supercontinuum generation in a nonlinear fiber, Proc. Optical Amplifiers and Applications (OAA 2003) at Otaru, Japan, 2003, Paper MD07.

57. S. Ferber, R. Ludwig, F. Futami, S. Watanabe, C. Boerner, C. Schmidt-Langhorst, L. Molle, K. Habel, M. Rohde, H.-G. Weber, 160 Gb/s regenerating conversion node, Proc. Optical Fiber Communication Conference (OFC2004) at Los Angeles, 2004, CA, 2004, Paper ThT2.

58. T. Akiyama, M. Ekawa, M. Sugawara, H. Sudo, K. Kawaguchi, A. Kuramatsu, H. Ebe, H. Imai, and Y. Arakawa, An ultrawide-band (120 nm) semiconductor optical amplifier having an extremely-high penalty-free output power of 23 dBm realized with quantum-dot active layers, Proc. Optical Fiber Communication Conference (OFC2004) at Los Angeles, 2004, CA, Post-deadline paper, PD12.

DOI: 10.1007/s10297-005-0038-0
Originally published in J. Opt. Fiber. Commun. Rep. 2, 293–344 (2005)

Ultrafast photodetectors and receivers

Heinz-Gunter Bach

Fraunhofer Institute for Telecommunications
Heinrich-Hertz-Institut Einsteinufer 37
D-10587 Berlin, Germany
Email: bach@hhi.fhg.de

Abstract. A family of ultrafast photodetectors and photoreceivers, based on evanescently coupled photodiodes, is described. The waveguide-integrated detectors are monolithically integrated with HEMTs, employing semi-insulating optical waveguides on a semi-insulating InP:Fe substrate. The integration scheme is explained and demonstrated by several examples of broadband and narrowband photodetectors, balanced detectors and photoreceivers, focussing on applications at data rates from 80 to ~160 Gbit/s.

1. Introduction to Photodetectors and Photoreceivers

Leading system providers upgrade their long-haul optical communication systems for single channel bit rates of 40 Gbit/s, aiming to exploit the transport capacities of the SMF of about 10 Tbit/s by joint progress in combining TDM and WDM techniques. System developers currently start experimenting employing 80 Gbit/s data rates. High-bit rate (40 Gbit/s) photodetectors and photoreceivers are key components for optical network extensions on all system levels (transport, metro, storage area networks).

Worldwide a few players, e.g., NTT and the UCSB, push on further the developments of ultra-high-speed photodetectors towards data rates of 160 Gbit/s and even higher. Recently FhI-HHI developed a family of 40–160 Gbit/s photodetectors and receivers, focussed on various high-power waveguide-integrated photodiodes, including those of special structure (twin-type or balanced) and InP-based monolithically integrated *pin*TWA photoreceivers (OEIC receiver) for 40 and 80 Gbit/s data rates. Those developments are based on a flexible integration concept, using semi-insulating substrates and semi-insulating optical waveguide layer stacks.

Section 2 summarizes some basics on optical detection and important parameters of photodiodes. Section 3 discusses the materials aspects for long wavelength photodetectors. Section 4 presents several types of photodetectors, mostly perpendicular illuminated, with special emphasis laid on high-speed aspects. Based on the waveguide-integrated concept, in section 5 various types of high-power photodetectors are presented in detail; the ultra-broadband types of which are now approaching a 3-dB cut-off frequency of 110 GHz.

In section 6 photoreceiver concepts are discussed, leading to the distributed amplifier type for achieving highest speed in electronic amplification. In section 7, the general receiver integration concept will be explained in detail, which allows the monolithic integration of waveguides, MMI splitters, evanescently coupled *pin* photodiodes, HEMTs and distributed amplifiers. An advanced ultra-broadband *pin*TWA receiver OEIC for 80 Gbit/s detection is presented. The detectors and photoreceivers described are suitable for ETDM with high data rates (actually up to 80 Gbit/s) within the single channel as well as for even higher data rates in transmission schemes employing OTDM techniques, e.g., up to 640 Gbit/s data rates.

To support for bit rates beyond 40 Gbit/s advanced modulation formats, like DPSK/DQPSK, also balanced detectors with 70 GHz bandwidth are treated in section 5.5. A first monolithically integrated balanced receiver OEIC for 40 Gbit/s applications is reported in section 8.

Section 9 concludes this chapter and gives an outlook on various future developments, e.g., towards concepts for receiver front-end integration for 100–160 Gbit/s data rates.

2. Characteristic Parameters of Photodetectors

2.1. Quantum Limit, Responsivity and Quantum Efficiency (Internal, External)

Ultrafast photodetectors are optimized mainly with respect to a high bandwidth-quantum efficiency product ($B \times \eta_{\text{ext}}$) and a high-output saturation power. Further the polarization dependent loss has to be kept below the half dB range. The latter aspect is only critical for side-illuminated detectors, while perpendicular illuminated detectors achieve normally PDL values below 0.1 dB easily.

The maximum achievable responsivity is determined by the wavelength of the absorbed light. Therefore the responsivity R, defined by the ratio

$$R = \frac{I_{\text{photo}}}{P_{\text{opt}}} = \frac{I_{\text{photo}}}{W_{\text{ph}}/t} = \frac{I_{\text{photo}}t}{h\nu} = \frac{\eta_{\text{ext}}e}{h\nu} = \eta_{\text{ext}}\frac{e\lambda}{hc} = \eta_{\text{ext}}R_{\text{ideal}}, \qquad (1)$$

can be deduced for arbitrary wavelengths or respective photon energies. $R_{\text{ideal}} = e\lambda/(hc)$ is the maximum responsivity for a given wavelength and corresponds to an external quantum efficiency $\eta_{\text{ext}} = 1$, which means, that every photon produces one electron-hole pair, which is transferred without losses to the contact electrodes of the photodiode. For some selected wavelengths the values of the maximum ideal responsivities are given in Table 1. The right-hand column lists appropriate semiconductor materials, suitable for effective absorption, for the given photon energies.

In real photodiodes the above listed ideal values are not reached exactly, because different losses according to limited absorption in finite absorption layer thicknesses,

Table 1. Responsivity values of ideal photodiodes for different wavelengths according to the three optical windows; the active layer materials in the right-hand-side column are selected for proper absorption according to their band-gaps related to the photon energies.

Wavelength (μm)	Photon energy (eV)	Responsivity R_{ideal}(A/W)	Suitable photon absorption layer
0.85	1.459	0.686	GaAs
1.3	0.9537	1.048	GaInAsP
1.55	0.8	1.250	GaInAs

residual optical reflection of the incident light at the semiconductor surface, losses due to the fiber-chip coupling, losses in internal contact layers and carrier recombination (before the contacts are reached) serve for external quantum efficiency values $\eta_{\text{ext}} < 1$. This leads, according to Eq. (1), to $I_{\text{photo}} = \eta_{\text{ext}} R_{\text{ideal}} P_{\text{opt}} = R P_{\text{opt}}$.

Figure 1 shows measured responsivity values of photodiodes with an absorption layer of Si, Ge and GaInAs vs. the operating wavelength [1]. Comparable quantum efficiency values have been chosen, which show, that the responsivity increases with the wavelength of the incident radiation [compare with Eq. (1)]. The reduced value of the photocurrent with respect to the ideal one in the stationary case will be diminished further in the high frequency range of operation due to further bandwidth limiting effects, like the RC-limit and the transit time limitation, to be discussed in the following sections. For a compilation of general, instructive references to detectors and receivers and their system applications, see, e.g., [49–61].

2.2. *Bandwidth (RC Limitation, Transit Time Limitation)*

In perpendicular illuminated photodetectors, e.g., *pin* diodes, a compromise in designing these elements has to be considered with respect of choosing the proper thickness of the active photon absorbing layer. The bandgap of this layer is assumed to be already properly chosen small enough with respect to the photon energy to be absorbed. A large layer thickness will be needed according to Lambert's and Beer's law of absorption, to achieve a high quantum efficiency related directly to a high responsivity of the photodetector. Unfortunately, a large absorption layer thickness directly leads to a long carrier drift time, even if the absorption layer is fully depleted by a sufficient reverse bias value, depending on the residual doping level, to be depleted. This bandwidth-efficiency trade-off is typical for all perpendicular illuminated photodetectors of the *pin*-type and of the MSM-type, and the accurate value for the bandwidth-efficiency product depends on the absorbed wavelength. According to [3] for absorption coefficients α : 1.16 μm^{-1} (0.68 μm^{-1}), the ideal bandwidth efficiency product amounts to 34 GHz (20 GHz) for wavelength values of 1.3 μm and 1.55 μm, respectively (single-pass absorption).

A rough estimation on the 3-db cut-off frequency f_t limited by the effective carrier transit time can be made applying [2]:

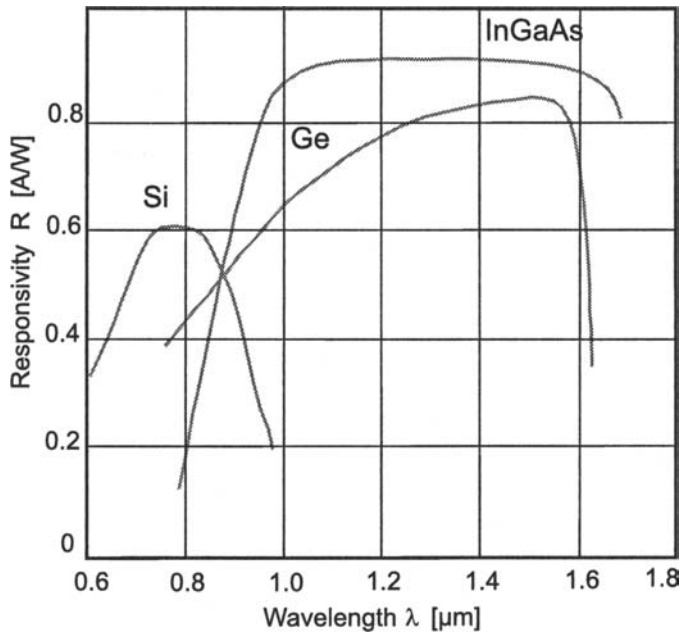

Fig. 1. Photodiode responsivities vs. the illumination wavelength, shown for different absorbing layer materials, plotted for comparable quantum efficiencies.

$$f_t = \frac{3.5 * \nu}{2 * \pi * d} \tag{2}$$

with d = carrier transit time distance (i.e., the fully depleted depletion region) and $v^{-4} = 1/2 * (v_e^{-4} + v_h^{-4})$, the effective drift velocity, with v_e, v_h being the electron and hole saturation drift velocities.

2.3. Leakage and Dark Currents

In *pin* photodiodes the total dark current is composed of several contributions. Often surface currents dominate over bulk currents, which can be identified experimentally, by plotting for a series of diodes the reverse current density at a certain fixed reverse bias level vs. the diameter in double logarithmic scale. A linear relationship indicates surface leakage predominance, while a quadratic relation proves predominance of bulk currents. Ideally a high quality of the passivation of the mesa edges should reduce the surface current level below the bulk current level, or planar photodiode structures should be considered. When surface currents have been reduced successfully by improved technology and bulk current dominance is verified, the various contributions to bulk leakage can be analyzed. The current to be seen in all diodes, is the diffusion current, described by the minority carrier contributions [51,52]. This current is in the order of 20 pA/cm^2 for GaInAs photodiodes and is most likely masked by other, higher-level leakage contributions.

In most real diodes this diffusion current is masked by several orders of magnitude by the generation current according to Shockley, Read and Hall, produced in the depleted absorption layer. The generation current level is regulated by trap concentrations (energetic position within the bandgap and capture cross sections) in the absorption layer and can be lowered to be less than 100 nA/cm^2 in GaInAs photodiodes, but often levels of 1 μA/cm^2 or even more are observed.

The discussion so far is valid for moderate reverse bias levels. If the bias is further increased to high-field values around 100 kV/cm and more, then two additional leakage current contributions can be observed, these are the tunnelling current and the impact ionization current. The tunnelling current is generally unwanted in all designs. This current dominates especially in low band gap absorption layers (needed for long wavelength detection) and with smaller effective masses of the electrons and can be reduced by lowering the doping level. The dominance of tunnelling at higher bias levels can be identified by a positive temperature coefficient of the reverse current, experimentally. The impact ionization current is characterized by a negative coefficient of the reverse current at a fixed bias level and can thus be distinguished easily from tunnelling contributions. Impact ionization can help favorably to provide an internal gain of the photocurrent, this leads to the avalanche photodetector type.

2.4. Noise Sources

Several sources of noise exist in photodetectors and receivers. For a subsequent estimation of the sensitivity of photoreceivers it is common practice, to map all sources of noise from the different sites of the circuit scheme of the photoreceiver to the electrical input of the receiver and sum up their electrical power contributions in the usual case of considering no correlation of the individual contributions. In this section the most important individual sources of noise are discussed.

The quantum noise of the incident optical radiation sets the detection limit of an otherwise noise-free ideal detector. The quantum noise stems from the discrete nature of radiation, which is composed of a stream of light particles, i.e., the photons, described by their photon energy $h\nu$ with $\nu = c/\lambda$ corresponding to the optical frequency of the radiation, which propagates with the speed of light c in vacuum. λ is the free space wavelength of the incident radiation.

The quantum limit of detection $P_{\min}$ is defined by $h\nu 2\Delta f$, with Δf denoting the electrical noise power measurement bandwidth. Quantum-limited detection can be achieved applying homodyne or heterodyne detection schemes, or nearly approached by using optical pre-amplification. In these cases any thermally generated excess noise in amplifying electronics following the photodiode is surpassed by a sufficient enhancement of the optical signal by one of the mentioned pre-amplification mechanisms.

The shot noise, accompanying any generated current within a photodetector, is not only generated by the signal current but also by the dark current of the photodiode. It is related to the statistical nature of the carrier transport across an energy barrier and to the quantum detection process itself and can be calculated for a given bandwidth Δf by evaluating the expression $\langle i^2_{\text{shot}} \rangle = 2eI\Delta f$, with e denoting the elementary charge and I the DC current, i.e., the dark current, if no optical signal would be present. For the components of the dark current see section 2.3.

In the series resistance components R of the photodiode thermal noise is generated. It is calculated for the open circuit voltage noise of a resistor by Nyquist's formula

for a given bandwidth Δf : $\langle u^2_{\mathrm{therm}} \rangle = 4k_B T R \Delta f$, with k_B denoting Boltzmann's constant and T the absolute temperature in Kelvin. A similar expression holds for the short circuit current noise of conductances. As all noise sources are uncorrelated, they have to be added in terms of their contributing power or quadratically at an adequate summation point, which often is chosen at the input of the electrical amplifier, following the photodiode.

2.5. *Noise Equivalent Power (NEP) and Detectivity in Analog Applications*

Although for ultra-fast photodetectors in telecommunications the definition of the sensitivity for digital signals under various modulations formats is more adequate, this section resumes some important definitions of the detection limit of infrared radiation for a photodetector itself (without considering subsequent electronics) in analog applications within a considered bandwidth Δf. For a signal-to-noise ratio of one at the output of the photodetector the minimum detectable signal equals the generated noise power without the optical signal, more accurately the detector output signal current equals the r.m.s. noise current produced within the unit bandwidth, e.g., for $\Delta f = 1$ Hz. The dominating noise contribution of the detector is its dark current shot noise current. For a detector with a quantum efficiency η_{ext} and a dark current I_d the spectral NEP, in units of W/Hz$^{0.5}$, amounts to

$$\mathrm{NEP} = \frac{hc\sqrt{2eI_d}}{e\lambda\eta_{\mathrm{ext}}} \tag{3}$$

per unit bandwidth of $\Delta f = 1$ Hz. In general the absolute NEP scales with the bandwidth Δf as NEP. $\sqrt{\Delta f}$ and is then given in units of W.

The detectivity D is defined as the inverse of the noise equivalent power, see Eq. (3), $D = 1/\mathrm{NEP}$, given in unit of Hz$^{0.5}$/W. The specific detectivity $D^* = D\sqrt{A}$, in units of cmHz$^{0.5}$/W, is related to the usual assumption, that in high-quality engineered photodiodes the thermal resistive noise is negligible and the surface leakage current is reduced well below the generation current, the latter of which is proportional to the area A of the detector.

In practical digital photoreceivers especially at higher bandwidth (data rates of Gbit/s and higher) the photodiode operates into a low-ohmic load resistor (50 Ω–kΩ, to extend the RC limit) and requires a minimum signal current which usually exceeds the photodiode dark current by orders of magnitude, caused by the additional electronic noise in the subsequent amplifier chain.

2.6. *Sensitivity of Optical Receivers to Digital Optical Signals*

The most common modulation formats in optical transmission schemes are NRZ and RZ, i.e., non-return-to-zero and return-to-zero formats. The main goal of optimising optical receivers is, beside to assure a necessary bandwidth (e.g., at least 70% of the bit rate for NRZ modulation), to provide a low minimum optical receiving power to detect signals at a given bit rate for a given modulation format out of the noise level of the receiver for a given maximum bit error ratio (BER), e.g., 10^{-9}. In this case the photodiode is considered together with the subsequent broadband amplifier and the respective additional electronic noise.

The noise of the amplifier is re-mapped to its input and given in terms of the equivalent input current noise [pA/Hz$^{0.5}$]. The noise of the photodiode (i.e., mainly the noise current due to the dark current) is added quadratically, to deduce the total equivalent input noise current $< i_{na}^2 >$ at the summation point at the amplifier's input for signal and noise. At this point now the achieved signal-to-noise ratio Q is considered:

$$Q = \frac{i_1 - i_0}{\sqrt{\langle \sigma_1^2 \rangle} - \sqrt{\langle \sigma_0^2 \rangle}}, \tag{4}$$

where i_0 and i_1 are the input current levels to represent the "1" and "0" of the opto-electronic converted signal, and $\langle \sigma_1^2 \rangle$ and $\langle \sigma_2^2 \rangle$ are the variances of the Gaussian distributed signal levels. The bit error ratio BER is related to the signal-to-noise ratio Q by an integral [52], which delivers for a BER $= 10^{-9}$ an necessary factor of $Q = 6$ and for BER $= 10^{-12}$ a value for $Q = 7$. The discriminator level of the decision circuit is adjusted between the signal levels i_0 and i_1 for a minimum BER. As the signal-to noise-ratio Q is fixed according to the bit error ratio BER, the minimum detectable power $P_{\min}$ of the photoreceiver can be deduced according to

$$P_{\min} = \frac{1}{R} Q \sqrt{\langle i_{na}^2 \rangle}, \tag{5}$$

with R being the responsivity [A/W] of the photodiode and $\langle i_{na}^2 \rangle$ the total equivalent input noise current density [pA/Hz$^{0.5}$] at the amplifier input.

2.7. Polarization Dependent Loss (PDL)

The responsivity of photodiodes may depend on the polarization of the incident light. This polarization dependent loss (PDL) is negligible for perpendicular illuminated photodiodes (< 0.05 dB), due to the symmetry of the structure, but it may be considerable in case of side-illuminated or waveguide-integrated photodiodes, where the optical waveguide supports more or less elliptically shaped spot profiles. In those cases special design measures have to be taken, to reduce the PDL to values below 0.5 dB. Also higher PDL values may occur in MSM type photodetectors with sub-micron finger design, where the incident wavelength is in comparable order of the finger width and space. In this case a circular electrode design may help to reduce unwanted PDL effects.

3. Materials for Ultrafast Photodetectors

The bandwidth and speed of ultrafast photodetectors are mainly determined by the material's properties of the active absorption region, and, depending on the structure of the detector (avalanche photodetector), on the properties of the drift region, too, which usually exhibits a higher bandgap than the absorption region. The material properties under consideration are the electron and hole mobilities, saturation drift velocities, and the absorption coefficient α at the wavelength under consideration. Direct bandgap materials exhibit higher absorption coefficients, thus absorption regions can be made narrower for the same high responsivities and internal quantum efficiencies. Consequently III/V materials are advantageous compared to silicon, the latter offering

only an indirect bandgap. GaInAs, e.g. exhibits for $\alpha = 0.68\ \mu\text{m}^{-1}$ at 1.55 μm and $\alpha = 1.16\ \mu\text{m}^{-1}$ at 1.3 μm wavelength [3]. For a given absorption region (optimized according to the specified internal quantum efficiency) the saturation drift velocities v_e, v_h for electrons and holes, respectively, are the next important numbers to be noted. For GaInAs values of v_e: 6.5×10^6 cm/s and v_h: 4.8×10^6 cm/s may be assumed, leading to an effective saturated drift velocity of 5.35×10^6 cm/s. Finally, high mobilities at the ohmic contacts regions should lead to small contact resistances, which also favors GaInAs to be used at the contact regions, compared to InP, which may be preferred as an adjacent cladding material to the absorption region of GaInAs.

4. Photodetectors: Structures and Devices Types

4.1. Perpendicular Illuminated Detectors

Perpendicular illuminated photodetectors are the standard types of photodetectors, often built as planar devices in silicon technology for the first optical windows around 850 nm and of the mesa type in case of the III/V heterostructure detectors for long wavelength detection purposes around 1.3/1.55 μm. Their bandwidth-efficiency product is limited to about 15 GHz, because a trade-off has to be made with respect to the thickness of the absorption region and the illuminated area (RC-limit). A thick absorption region gives a good quantum efficiency and responsivity, but at the same time also a longer carrier transit time, especially for the slower carriers, i.e., the holes. Perpendicular illuminated photodiodes dominate in bit rate applications up to 10 Gbit/s and are also used in 40 Gbit/s systems, due to their negligible polarization dependent loss, but at 40 Gbit/s and higher the side-illuminated and evanescent field illuminated photodiodes gain advantages offering a higher bandwidth-efficiency product ($>$ 50 GHz) and a better high-power linearity and saturated output power values ($>$ +12 dBm).

4.1.1. Equivalent Circuit

The equivalent circuit diagram of a *pin* photodiode, which can be adapted to other types of diodes, too, is given in Fig. 2. The most important elements are I_{pd} (proportional to the incident optical power and the responsivity) and C_{pd}, which represent the photodiode's *pn*-junction and the current excitation due to the illumination. The current source I_{pd} is frequency dependent due to the drift time delay of the carriers crossing parts of the *pin* structure. In circuit simulators favorably a Laplace transform expression can be used for modelling this transit time limitation. The *pin* capacitance C_{pd} (10 fF–pF) is defined by the depleted absorption layer thickness and the total area of the photodiode. This capacitance together with the external load impedance Z_{load} (often equal to 50 Ω) result into a first order low-pass filter behavior of the RC limitation [bandwidth = $1/(2\pi C_T R_T)$, with $C_T = C_{\text{pd}} + C_{\text{stray}}$ and $R_T = R_s + Z_{\text{load}}$; C_{stray}: external stray capacitance (some fF)] due to the packaging, usually in parallel to the load impedance).

The other elements are added for improved accuracy of the description of the frequency behavior: G_{leak} is the leakage conductance of the *pn*-junction (nS$\cdots\mu$S range), R_s is the series resistance of the photodiode (some ohms), L_{pd} is a residual

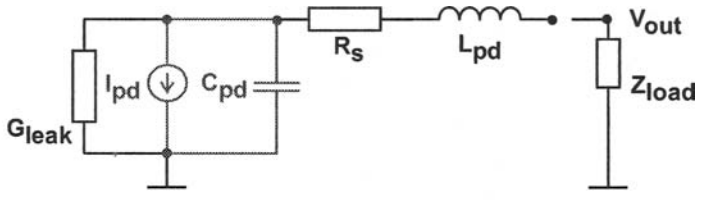

Fig. 2. *pin* photodiode small signal equivalent circuit diagram.

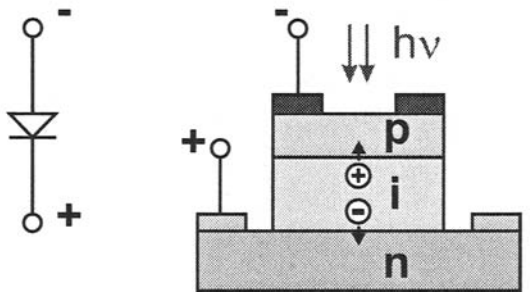

Fig. 3. Homojunction *pin*-photodiode, top-illuminated.

inductance (pH$\cdots$nH) of the wiring from the *pn*-junction to the bonding pads and gains increased importance for 10 GHz bandwidth and higher.

4.1.2. *pin* Photodiode

Photodiodes of the *pin*-type can be build as homojunction diodes (mainly in silicon, for the first optical windows around 850 nm) or as heterostructure photodiodes, normally based on InP substrate, employing a GaInAs absorption layer, to cover the second and third optical windows around 1.3 μm and 1.55 μm. Because this paper on the ultrafast photodetectors is mainly dedicated to the side-illuminated evanescent-field coupled detectors, only short overviews are given to these standard perpendicular illuminated detector types to understand their main design aspects and properties.

Homojunction Photodiode The top-illuminated homojunction *pin* photodiode, shown as a mesa structured device in Fig. 3, is the simplest basic photodiode structure. The thin highly p^{++}-doped anode contact serves also as the illuminated window layer into the intrinsic absorption layer; all layers are grown with the same bandgap. Although the structure is easy to fabricate and has no problems with metal ohmic contacting the p^{++}-doped window layer, it shows some drawbacks with respect to the total effective series resistance, because the photocurrent has to flow from the middle of the structure to the ring contact within a relatively thin layer.

The absorbing p^{++}-window layer has to be designed with a highest possible doping to reduce the lateral sheet resistance, but concerning its thickness a compromise has

to be made, because a large thickness reduces the light intensity, which reaches the intrinsic high-field absorption layer. Otherwise, a thin window layer exhibits too much effective lateral series resistance. Consequently this simple structure is acceptable in materials with high doping capability (like p^{++}-silicon) but comparably low absorption coefficients (compared to direct bandgap III-V materials), like the indirect bandgap silicon. The simple structure exhibits a further problem: the reduction or suppression of slower diffusion currents from the contact layers into the intrinsic high-field layer are highly desirable, if high-speed response is needed. The diffusion contribution, especially from the slower holes, results in early frequency decays in the opto-electronic conversion characteristics.

Thus, in III-V based materials, e.g. GaInAs/InP the heterostructure type photodiode, discussed in the next section, is used more commonly.

Heterostructure Photodiode Heterostructure photodiodes eliminate the negative effects of window absorption and slow diffusion contributions. The intrinsic high-field absorption layer, fitted to the wavelength to be detected, is embedded between the ohmic p-, and n-contact layers with higher bandgaps, e.g., InP layers cladding a GaInAs absorption layer. The structure looks similar to Fig. 3; often an additional thin low-bandgap p^{++}-contact (e.g., GaInAs) layer on-top of the structure is added directly under the p-metal, which is etched away in the window area. Further a side-wall passivation of, e.g., benzocyclobuthene (BCB) is used, to lower and to stabilize the total dark current. In mesa-type structures of those GaInAs/InP heterostructure photodiodes the dark current density can be reduced to less than 1 μA/cm^2, while in high quality planar diffused heterostructure photodiodes the dark current density can reach lowest values of 50 nA/cm^2. The bandwidth can be designed for 40 Gbit/s applications, while the responsivity cannot be much higher than 0.6 A/W due to the limited thickness of the absorption layer, due to transit time considerations. The bandwidth-efficiency product for perpendicular illuminated GaInAs/InP-based 1.55 μm heterostructure photodiodes amounts to about 15 GHz. This value can be further increased into the 50-GHz range by applying side-illuminated concepts, see section 5.

4.2. MSM Photodiode

MSM (metal-semiconductor-metal) photodiodes are potential high-speed devices (40 Gbit/s and higher), when their finger widths and electrode gaps are reduced well into the sub-micron range by applying e-beam direct writing for the definition of the electrodes [4]. Their responsivity is often lower than for pin-diodes, due to the shadowing effect of the front gate electrodes (reduction by, e.g., 50%). In case of necessity for large-area detection MSM photodiodes may be advantageous compared to pin photodiodes, due to their potential lower capacitance, if a larger electrode gap can be used, thus their RC limit can be extended for the same illuminated area somewhat higher, compared to pin photodiodes. MSM photodiodes often suffer from excess gain at low frequencies due to charge trapping effects, so their usability for broadband detection, starting from the kHz range up to 40 GHz (in case of the NRZ modulation format) and higher may be limited, because they may show spreading effects in the "zeros" and "ones" of the eye pattern for long lasting bits and PRBS sequences with low-frequency spectral contents (frame clock in SDH systems).

4.3. Avalanche Photodiode (APD)

In an avalanche photodiode (APD) the carriers, which have been generated in the absorption region by the incident light, are accelerated in a neighboring high-field drift region so intensively, that they generate new electron-hole pairs by impact ionization. Thus, a single photon is able to produce a current peak, corresponding to hundreds of electron-hole pairs, which leads to an amplification factor M. This internal gain mechanism is accompanied by an excess noise, which depends on the carrier multiplication statistics, see the section below on APD Noise.

APD Bandwidth APDs (avalanche photodiodes) use a small-gap absorption region and, in the case of heterostructure III/V diodes, a wide-bandgap drift and multiplication region to achieve an additional gain M (up to typically $10 \cdots 100$). The bandwidth of long-wavelength InP-based APDs is quite sufficient for 10 GHz operation, so APDs are standard solutions in 10 Gbit/s systems. For 40 Gbit/s systems there is still room for necessary improvements of the multiplication value to achieve higher values than three to four in the design of a necessary bandwidth above 30 GHz. The gain-bandwidth product can be increased by using InP-based APDs comprising a superlattice structure in the multiplication region to values around 120 GHz [5] by further improving the electron-hole ionization ratio α_i/β_i.

APD Noise Usually, the combined multiplication statistics by electrons and holes depends on their field-dependent ionization coefficients α_i (electrons) and β_i (holes). This leads to a larger mean value of M^2, compared to the square of the mean value of M. The excess noise factor F is defined by $F = \langle M^2 \rangle / \langle M \rangle^2$. As compared to inherent low-noise photomultipliers, it would be highly desirable, that the multiplication cascade in an APD would be induced by a single carrier type to reduce the excess noise.

So, the ratio of the ionization coefficients $k = \beta_i/\alpha_i$ should be either much smaller than one or much larger than one. For silicon based APDs values of k around 0.04 are achievable, which means, that impact ionization is mainly induced by electrons. Consequently the layer structure should be designed for electron multiplication. In APDs suitable for the longer wavelengths around 1.55 μm InP-based heterojunctions with a GaInAs absorption layer are used. InP as a multiplication layer is favorable for low dark currents due to the large bandgap of 1.35 eV, but the ionization coefficient ratio $k \approx 2$ is of comparable order for holes and electrons, thus a higher excess noise factor is expected and observed experimentally. In order to reduce the excess noise factor also for the long-wavelength APDs, the multiplication layer is composed of a heterostructure layer stack, built of a GaInAlAs/AlInAs superlattice. In this case the ionization coefficient ratio $k = \beta_i/\alpha_I$ is reduced considerably, compared to a bulk multiplication layer, so again electrons are the carriers to induce the multiplying cascade of further electron-hole pairs.

The excess noise factor $F(M_e)$ for APDs amounts in the case of an electron induced impact ionization process [6] $F(M_e) = M_e[1 - (1-k)(M_e - 1)^2/M_e^2]$, with k to be as low as possible ($k \ll 1$). For an hole induced impact ionization cascade the excess noise factor is to be evaluated by $F(M_h) = M_h[1 + (1-k)/k(M_h - 1)^2/M_h^2]$, with k to be considerably higher than one. Typical good values of InP-based photodiodes are $F(M = 10) = 5$, while silicon-based APDs achieve $F(M = 10) = 2$, a graph of which can be found in, e.g., [7].

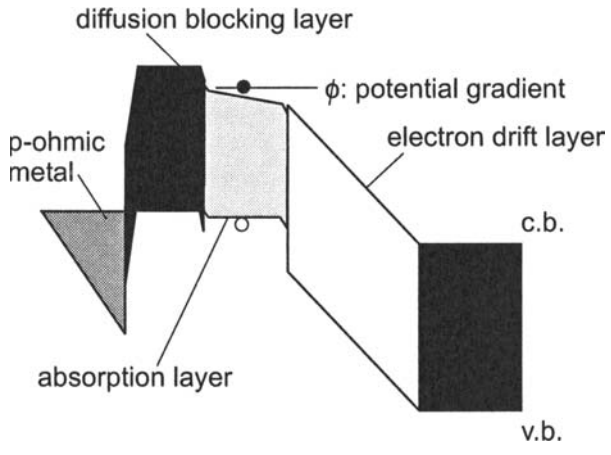

Fig. 4. Band diagram of an uni-travelling carrier photodiode showing an electron in the conduction band (c.b.) drifting/diffusing into the drift layer and a hole in valence band (v.b.) of the absorption layer moving as a majority carrier to the *p*-ohmic metal contact.

4.3.1. Uni-Travelling-Carrier Photodiode

Uni-travelling-carrier (UTC) photodiodes show a very good potential for ultra-broadband detection in the 100 to 160 Gbit/s data range even at high power levels [2]. Unlike conventional *pin* photodiodes, UTC photodiodes employ a highly doped photoabsorption layer, thus the optically generated holes are moving as majority carriers quite fast into the metal *p*-contact with an ultra-short relaxation time constant, see Fig. 4. The transit time limit of UTC diodes is consequently defined by the fast saturated electron drift velocity process, which is supported further by a potential gradient (e.g., 50 meV) in the slightly composition graded absorption layer. This structure is also beneficial for the suppression of space charge effects, which usually limit the high-power behavior of perpendicular illuminated photodetectors early. Aggressively scaled devices demonstrated pulse responses of 0.97 ps (FWHM) and FFT-deduced -3 db bandwidth of 310 GHz [8].

Because such down-scaled devices of the perpendicular illuminated type show only limited responsivities of less than 0.1 A/W (due to the narrow absorption layer), the evanescent illumination of an UTC structure proved promising to increase the responsivity up to 0.48 A/W [9]. The resulting structure, employing an angled refracting-facet evanescent illumination, is shown in Fig. 5.

These detector structures have been optimized further up to D-band (up to 160 GHz) operation in pig-tailed modules, exhibiting RF output powers in the +3 dBm range [10]. These device are used for telecom, datacom and millimeter-wave generator applications.

4.3.2. Resonant Cavity Enhanced (RCE) Photodetectors

Resonant cavity enhanced (RCE) photodetectors are based on multiple reflections of the incident light between distributed Bragg reflectors/mirrors, embracing a thin active

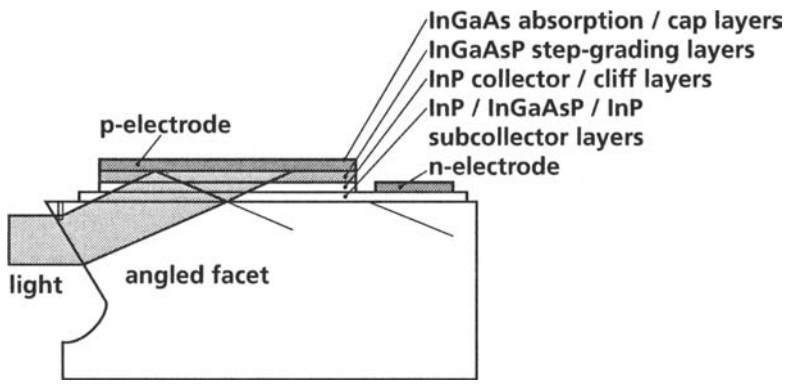

Fig. 5. Structure of a uni-travelling carrier photodiode with refracting-facet and evanescent illumination [9].

absorption region (e.g., 250 nm). In perpendicular illuminated photodiodes such a thin absorption region results into a low absorption efficiency (e.g., only about 12%). In RCE detectors the effective absorption path is much longer than the physical thickness of the absorption layer, consequently the quantum efficiency increases up to about 60%. The optical multi-reflection concept causes a distinct wavelength selectivity of this type of photodetector. The ultimate speed of the device is given by the transit time across the thin absorption layer. In almost all cases the optical path time constant is negligible, considering even the multiple reflections. Thus RCE detectors can be used in applications, where the strong wavelength selectivity of the responsivity is demanded and a good quantum efficiency is needed at high-speed response. However, the much increased technological efforts due to the additional mirrors and the problems of achieving low-ohmic contacts should be acceptable. For long wavelength detection material stacks composed of AlGaInAs/AlInAs/GaInAs/InP are preferable.

Also APDs can be built as RCE detectors, see Fig. 6, with 70% quantum efficiency and a gain-bandwidth product of 290 GHz [11].

4.4. Photoconductor Type Detectors

Photoconductors are electrically symmetric, ohmic devices, the resistance of which depends of the illumination intensity. Owing to very low background doping (and sometimes also cooling) their dark resistivity is very high (MΩ to GΩ). In the illuminated case, when the photon energy exceeds the band gap of the photoconductor (intrinsic type), an internal photo current, which is not measurable externally, is produced, which represents the number of electron-hole pairs according to the illumination intensity and absorption properties of the semiconductor (internal quantum efficiency ≤ 1). The external photocurrent, which is measured under biasing to a certain lateral field strength, is a multiple value (10 to 1000) of the internal photocurrent (i.e., external quantum efficiency $\gg 1$). The exploitable gain between these both currents reflects the ratio of the longer minority carrier recombination time and the short majority carrier drift transit time to the lateral electrodes. If the electrode distance is kept in the

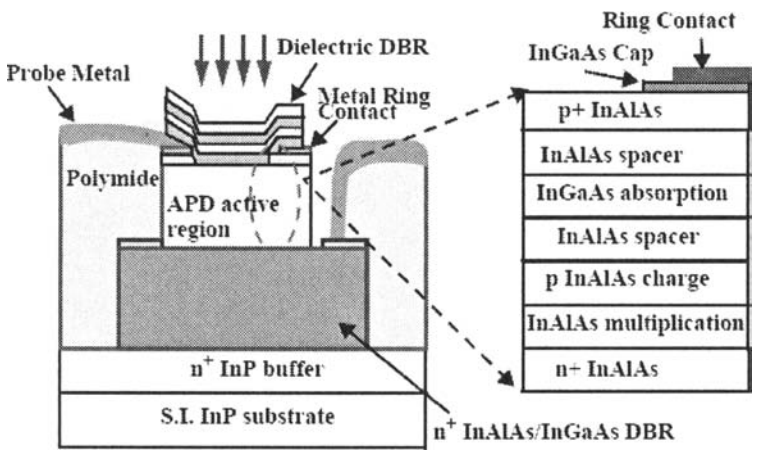

Fig. 6. Structure of a resonant cavity enhanced APD with dielectric mirror stack on-top and a semiconductor mirror below the APD active region after [11].

sub-micron range by employing electron-beam lithography for the electrodes, the drift time and thus the pulse width of photoconductors can be quite small, resulting in ultra-high bandwidth, comparable to fast *pin* photodiodes. In 1.3 μm to 1.55 μm telecom applications, where a very flat frequency response is needed, photoconductors play a minor role, because their internal gain mechanism often leads to early frequency decay effects. Also, they show generation/recombination noise, which leads to worse noise equivalent power values. They are mainly used in the farer infrared regions, $\lambda > 2$ μm, where Si- und Ge-based photodiodes are insensitive, e.g., InSb (T: 77 K) around $\lambda = 5$ μm, PbSe (T: 77 K) around $\lambda = 6$ μm and Ge/Hg (T: 30 K) around $\lambda = 10$ μm. CdS is suitable for the visible region around $\lambda = 0.4$–0.5 μm, e.g., for photoelectric barrier applications. Extrinsic photoconductors are among the most sensitive devices for far infrared detection purposes. They use undoped, at room temperature nearly semi-insulating semiconductor material and comprise additional deep level impurities to be activated by the light under detection and need cooling, often below 77 K.

5. Side-Illuminated Detectors

Side-illuminated detectors avoid the early compromise between high quantum efficiency and transit-time-limited bandwidth, which limits the quantum efficiency-bandwidth product of perpendicular illuminated long-wavelength photodetectors to around 15 GHz. In side-illuminated detectors the optical absorption path is oriented perpendicular to the electric field lines of the *pin* junction diode, as the light is injected from the side into the multimode absorption region. Side-illuminated detectors can be built by applying different schemes: waveguide-photodiodes and waveguide-integrated photodiodes.

A waveguide photodiode contains a multimode waveguide absorption region, embedded between two higher bandgap cladding layers. The light is coupled directly from the side into the absorption layer, using a tapered or lensed fiber; this photodetector type is shortly described in section 5.1.

The waveguide-integrated photodiode employs a rib-waveguide, the light from which is coupled evanescently from the lower side into the small-gap absorption layer. This type of detector, comprising also a monolithic taper at its input waveguide facet, can be monolithically integrated to more complex types of detectors (twin, balanced) and is described comprehensively in sections 5.2–5.5. The monolithic integration with amplifiers is treated in sections 7 [12] and 8.

Side-illuminated photodetectors show an improved high-power behavior, because the absorption is distributed laterally into a larger length of a thinner absorption layer in a controlled manor, compared to perpendicular illuminated detectors.

5.1. Waveguide Photodetectors

An early prototype of a waveguide photodetector with a bandwidth of 110 GHz and a responsivity of 0.5 A/W at 1.55 μm wavelength is described in [13]. The detector size was reduced down to 1.5 μm width and 10 μm length by three-dimensional mesa structuring the device. The bandwidth-efficiency product amounts to 44 GHz for this edge-coupled device. For further increasing the bandwidth-efficiency product of such devices the use of exciton absorption in a multiquantum well (MQW) photoabsorption layer was proclaimed [2]. From a practical view, the necessity to couple the light with a focussed beam from a lensed fiber may be some drawback, a point, which is solved efficiently within the next approach described in section 5.2, the waveguide-integrated photodetector.

5.2. Ultra Broadband Waveguide-Integrated Photodetectors

In a waveguide-integrated photodetector the waveguide is separated from the absorption layer, thus both components can be optimized separately. A waveguide-integrated ultra broadband photodetector is discussed below, exhibiting a bandwidth in excess of 100 GHz, based on the integration scheme on semi-insulating InP. By adding passive coplanar waveguide-based circuitry, narrowband photodetectors are designed (section 5.3). By implementing two photodetectors and 3 dB couplers, Twin-type (5.4) and balanced photodetectors (5.5) are constructed. All OEICs were packaged into modules comprising 1.85 or 1 mm connectors.

5.2.1. A 100-GHz Waveguide-Integrated Photodetector

Uni-travelling-carrier (UTC) photodiodes show a very good potential for ultra-broadband detection in the 100–160 Gbit/s data range even at high power levels [14]. Owing to the good potential for monolithic integration, the ability to form twin-type and balanced type detectors and the good linearity from low signal levels to high power values, the side-illuminated waveguide-integrated photodetector types are promising [15–17]. This basic detector type was optimized, now to achieve a 3-dB bandwidth in excess of 100 GHz.

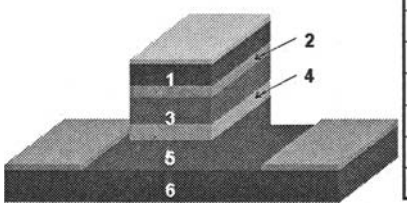

Region	Material	Doping (cm^{-3})
1	InGaAs	$N_A = 1 \times 10^{19}$
2	$InGaAsP_{1.3}$	$N_A = 5 \times 10^{18}$
3	$InGaAsP_{1.15}$	$N_A = 5 \times 10^{17}$
4	$InGaAsP_{1.3}$	$N_A = 1 \times 10^{17}$
5	InGaAs	$N_D = 3 \times 10^{14}$
6	$InGaAsP_{1.33}$	$N_D = 2 \times 10^{18}$

Fig. 7. Layer sequence of the waveguide-integrated heterostructure photodiode grown by one-step MOVPE.

The photodetector chip comprises a p-i-n photodiode, a spot-size converter for effective fiber-chip coupling, a biasing network and a 50-Ω termination resistor. This termination resistor was applied to guarantee a good signal integrity and to quentch at the detector's port any bouncing reflections from the subsequent amplifier or DEMUX. This circuit engineering aspect, which is already important at 40 Gb/s data rates, will be of increasing relevance for 80/85 Gb/s data transmission setups. The consequence of this 50-Ω matching termination at the otherwise high-impedance photodetector side is a halved AC responsivity compared to the DC responsivity, commonly accepted to provide excellent signal integrity.

The evanescently coupled photodiode with an active area of $5 \times 20\ \mu m^2$ and a GaInAsP/GaInAs heterostructure absorption layer stack is located on top of a semi-insulating ($5 \times 10^7\ \Omega$ cm) optical waveguide stack [18].

The GaInAs absorption layer (5), see Fig. 7, determines the frequency characteristics with respect to transit time limitations, and is grown nominally with 0.42 μm thickness. The effective space-charge region thickness is reduced to about 0.35 μm by deep in-diffusion of Zn, as a result of assuring a high p-type contact doping level, starting with some 10^{19} cm^{-3} from the GaInAs surface layer. Also some outdiffusion of the Si-doped n-contact has to be taken into accout, to reduce the effective space charge region in layer 5. Lateral structuring is done by combined wet and dry chemical etching steps.

The viewgraph of the final chip is given in Fig. 8 which shows the photodiode p-mesa, coupled via an air-bridge to the 50-Ω terminating resistance. The RF output signal is provided by a coplanar waveguide (CPW) taper to the contact pads, compatible with 110 GHz on-wafer probing heads. The cathode of the p-i-n diode is connected to 55 pF MIM capacitors for efficient low-inductance RF blocking at the biasing terminal V_{pd}. A BCB layer is used for the passivation of the mesa p-i-n diode.

The circuit elements of the photodetector, i.e., the p-i-n junction equivalent circuit, the air-bridge and its impedance representation, the stray elements of the terminating resistors and the CPW taper, were modelled by a circuit simulator in conjunction with anticipated damping losses and small additional inductances of bonding wires in the final packaging. The aim is to pre-compensate on-chip for the known losses of a short quartz-based CPW line in the module. These external losses were determined by network analyzer measurements of CPW test lines to about 0.5 dB for frequencies of up to 100 GHz. The idea behind this approach is to introduce a reproducible control of on-chip impedance up to the 1-mm connector in the packaging, and to avoid scatter of

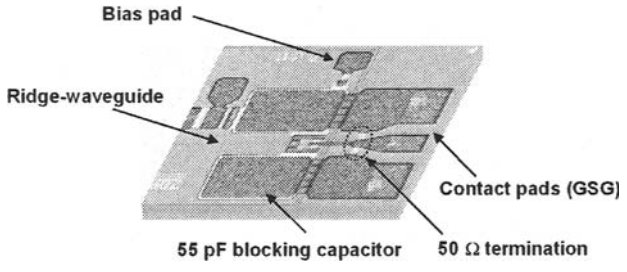

Fig. 8. Micrograph of the photodetector chip including a bias-T at the cathode and 50-Ω termination.

inductive peaking due to interconnections between the chip, the CPW on quartz, and the 1-mm connector.

5.2.2. Measurement and Device Characterization

Network analyzer (NA) measurements of the photodetector chip up to 110 GHz using on-wafer probing techniques were performed. These measurements served for identifying the equivalent circuit of the photodiode including all parasitic elements, namely the series resistance of about 5 Ω and impedance parameters of the air-bridge. Together with the implementation of an additional transit time formulation for electrons and holes it allowed to calculate the optoelectronic transfer function of the photodiode, see Fig. 9. The frequency response of the photodetector was determined by an optical heterodyne measurement technique employing two tuneable-wavelength lasers operating around 1.55 μm serving as a RF-modulated light source up to 110 GHz. The optical input signal was fed into the chip's tapered waveguide by a butt-ended fiber. The electrical output of the detector was contacted using a coplanar probe connected to a short coaxial cable, specified for operation up to 110 GHz.

Up to 50 GHz the output power using an electrical spectrum analyzer was measured. For the measurements from 50 to 110 GHz a power meter with two different sensor heads for the V- and W-band, respectively, was used. Owing to sufficient overlap of the three frequency ranges continuous transitions between the different measurements were achieved. In all cases the losses of the connecting cable and adapters were subtracted from the measured values. The uncertainty of this calibration was estimated to be less than 1 dB.

The measured O/E conversion function is also shown in Fig. 9. A 3-dB bandwidth of 100 GHz is obtained for this waveguide-integrated photodiode with a responsivity

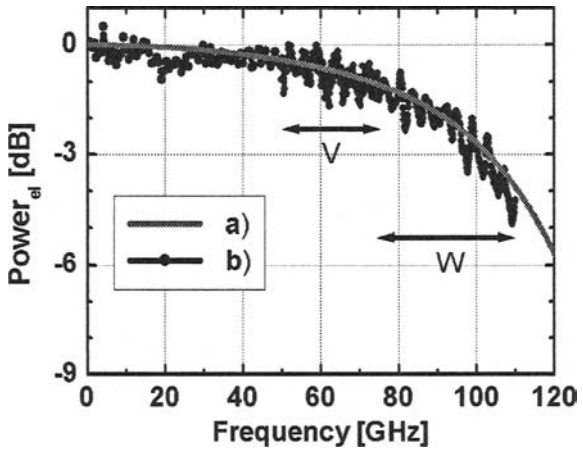

Fig. 9. Optoelectronic conversion characteristics of the photodetector chip: a) obtained from the circuit simulator, supported by NA parameter extraction, b) measured by the optical heterodyne technique, see text.

of 0.66 A/W and a low PDL of 0.9 dB. The bandwidth–quantum efficiency product is as high as 53 GHz due to the low resistance of the Zn-diffused p-type heterostructure top contact, the optimized effective absorption layer thickness and the impedance control of the air-bridge.

Figure 10 shows the DC photocurrent and the electrical output power of the photodiode measured at 100 GHz vs. the average optical input power up to +17 dBm. The DC photo current behaves linearly over the whole input power range up to output current values of 22 mA. A maximum RF power of −7 dBm at 100 GHz is obtained for a bias voltage of −2 V. The 1-dB compression point at 100 GHz measurement frequency occurs for an optical input power of larger than +12 dBm.

The compression curve is quite constant over the lower-to-mediate power range up to +8 dBm, which compares favorably with UTC-type (uni-traveling-carrier) photodiodes, which often show an increasing RF responsivity when the input power is raised from low to medium values [19].

For the estimation of the phase and group delay Hilbert's transform [20] can be used by integrating the magnitude of the O/E conversion characteristics over the whole frequency band, until values of −30 dB are reached. For this aim, the measured frequency characteristics in Fig. 9 were extrapolated into the 200-GHz range according to a circuit simulator model, including the transit limitation and the RLC limitation, the detailed parameters of which were determined by network analysis of the photodiode's equivalent circuit. After integrating the magnitude of the O/E conversion characteristics according to Hilbert's transform [20] the group delay scatter was derived from the calculated phase. The group delay exhibits a low scatter of less than 2 ps over the

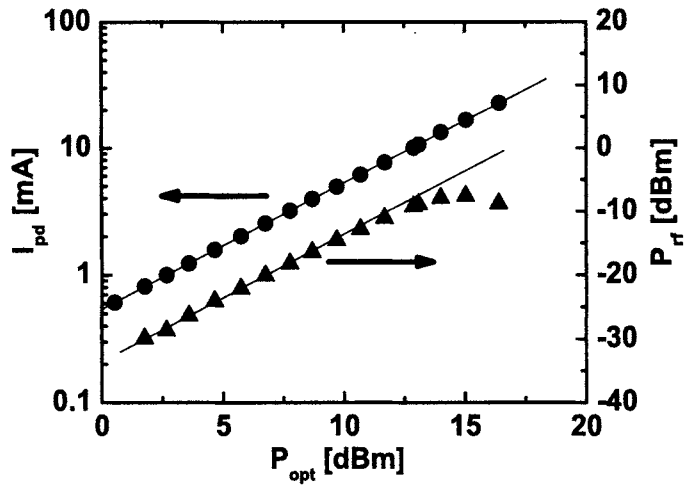

Fig. 10. DC photocurrent and RF output power into 50 Ω at 100 GHz vs. optical input power, reverse bias: -2 V, wavelength: 1.55 μm.

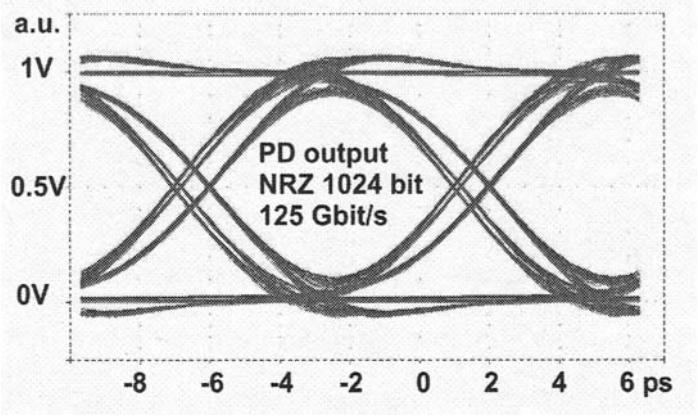

Fig. 11. Photodetector's synthesized NRZ 1024-bit eye pattern at 125 Gbit/s.

measured range up to 110 GHz and behaves smoothly at the boundary and within the extrapolated range of the transit time and RLC-limited region up to 200 GHz.

To demonstrate the benefits obtained from the low group delay scatter, synthesized eye pattern with 1024 bit are deduced from the heterodyne measured O/E characteristics [20] for a bit rate of 125 Gbit/s, given in Fig. 11. A well opened eye is obtained at this very high bitrate.

In the module, into which the chip will be packaged later, a slight further damping of the O/E characteristics is expected. Keeping this in mind, the small overshoot effects

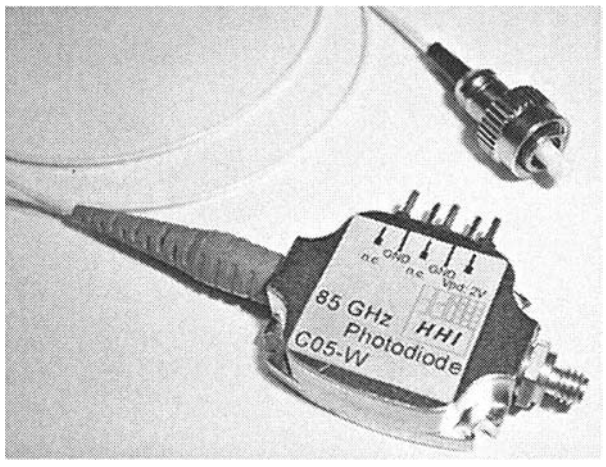

Fig. 12. Photograph of the PD module with fiber pigtail and 1-mm output connector.

to be noted from the synthesized eye diagrams for the chip may be reduced further in a well engineered module. Thus, this new photodetector appears to be well suited for the operation in the 100-Gbit/s region. Owing to the monolithically integrated taper, which adapts the fiber circular beam profile to the waveguide optical profile, the misalignment tolerances for fiber-chip coupling amount to about ± 2 mm for a 1-dB coupling loss. These rather relaxed tolerance values are twice as high as for edge-coupled waveguide photodiodes for the critical y-direction of the fiber-chip coupling [19]. Hence a cheaper packaging process and a better long-term stability can be expected.

The detector chip was assembled into a standard housing equipped with a fiber pigtail and a 1-mm coaxial output connector [21]. Figure 12 shows a photograph of the fabricated PD module.

The DC responsivity of the fabricated PD module amounts to 0.63 A/W with a polarization dependant loss (PDL) of only 0.64 dB at 1.55 μm wavelength. The frequency characteristic of the photodetector module was determined with an optical heterodyne measurement.

Figure 13 shows the calibrated frequency response of the photodetector module at +2.3 dBm optical input power and 2 V reverse bias (V_{bias}). A smooth decay of 2 dB up to 70 GHz is observed. At 100 GHz signal frequency the response has dropped by 6 dB. The -3 dB bandwidth amounts to 85 GHz. Using the same experimental setup, the power linearity of the photodetector module at a fixed frequency of 90 GHz was measured. The DC photocurrent is linear over the whole input power range up to +16 dBm up to output current values of 24 mA for $V_{\text{bias}} > 1$ V. A maximum RF power of -4 dBm at 90 GHz is obtained for a bias voltage of 2.5 V. At lower bias voltages the electrical output power is reduced significantly which may be attributed to carrier screening effects weakening the effective internal field in the intrinsic layer. At 2.5 V, the RF 1-dB compression point occurs for a photocurrent of 13 mA, corresponding to an optical input power of nearly +13 dBm. The power compression curve behaves constantly over the entire working range up to 10 mA, in contrast to UTC photodiodes,

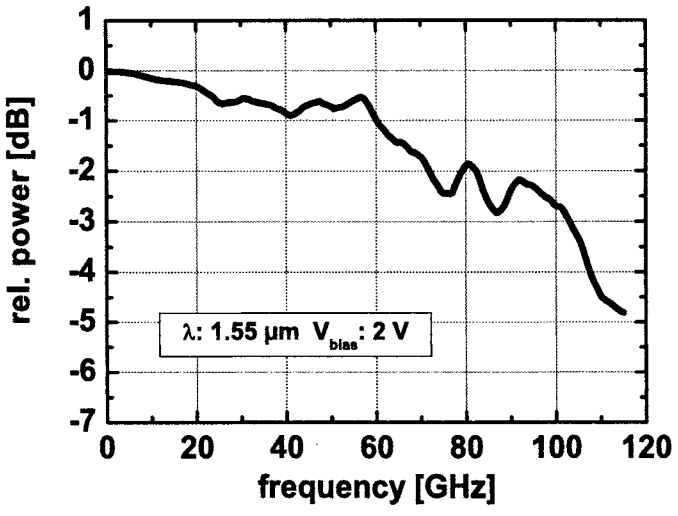

Fig. 13. Relative frequency response of the PD module measured at +2.3 dBm optical input power.

which often show an increasing RF response when the input power is raised from low to medium values [19].

In order to characterize the detector module in the time domain, the eye diagrams were measured with a 70-GHz sampling scope (Agilent 86100B with Agilent 86118A). The input pulses, generated by a 10-GHz mode locked semiconductor laser, had pulse widths of 1.7 ps. The detected electrical pulse had a FWHM of 6.8 ps and an undershoot of less than 10%, including the bandwidth limitation of the sampling scope.

By using optical time domain multiplexing techniques 80 Gbit/s and 160 Gbit/s return-to-zero (RZ) modulated data streams (PRBS) with $2^7 - 1$ pattern length were generated. Figure 14(a) shows the received electrical 80 Gbit/s eye pattern at +11 dBm optical input power. The eye diagram is opened widely with a peak voltage of ~ 0.6 V at a moderate reverse bias of 2.5 V, corresponding to an average photocurrent of 8 mA.

Figure 14(b) shows the detected 160-Gbit/s RZ data stream at +11 dBm optical input power. Owing to the insufficient bandwidth of the sampling head and the photodetector module an RZ-to-NRZ conversion is observed. The eye opening is still remarkable and the amplitude amounts to 0.3 V [29]. The slight asymmetry between adjacent eye patterns is attributed to some minor imbalances in the optical multiplexer.

5.3. Narrowband Waveguide-Integrated Photodetectors

In this section the fabrication and the characterization of InP-based narrowband photodetector OEICs and modules, covering the frequency range 38–90 GHz, is reported. The reverse bias tuneable detectors exhibit 0.55 A/W peak responsivities at 80 GHz, equal to the DC value.

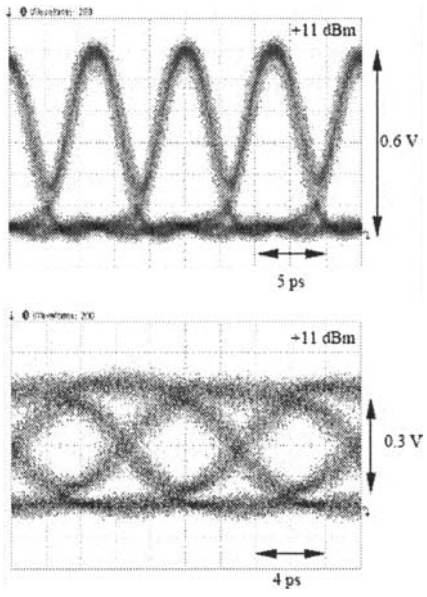

Fig. 14. (a) Electrical 80 Gbit/s RZ eye pattern at +11 dBm optical input power detected by the photodetector module at 2.5 V reverse bias, x-axis: 2.5 ps/div, y-axis: 100 mV/div. (b) Detected eye pattern under 160 Gbit/s RZ excitation at +11 dBm optical input power, $V_{\mathrm{bias}} = 2.5$ V; x-axis: 2 ps/div, y-axis: 100 mV/div.

The generation of millimeter-wave signals by photonic technologies is advantageous for a variety of applications like fiber radio wireless communication systems, remotely controlled optically steered antenna systems, clock recovery in photonic-based telecommunication networks, and high-speed measurement systems. Where ever possible, electrical post-amplification should be avoided for cost reduction by applying optical pre-amplification. Thus, high RF output power, linearity over several decades of signal strength and good conversion efficiency are needed at the operating frequency, which varies from approx. 38 to 85 GHz, depending on the application. A recent development [22] shows results on photonic millimeter wave generation by applying UTC photodiodes in an impedance transform network. In this work waveguide-integrated photodiodes with increased responsivity between 0.55 and 1 A/W (depending on the operating frequency) are applied. Further advantageous aspects of applying waveguide-integrated photodiodes with monolithic input taper are their convenient coupling to a butt-ended fiber, their capability to be used within optical waveguide networks for optical signal pre-processing, and their ability to be monolithically integrated in an array configuration. The design, fabrication and characterization of an InP-based narrowband photodetector family, covering the frequency range from 38 to 90 GHz is reported. The detectors comprise a waveguide-integrated photodiode and a short stub circuit CPW-based transformer network [23]. Furthermore, results on fully packaged detector modules for 80 GHz resonance are reported.

5.3.1. Device Design

The evanescently coupled waveguide-integrated photodiode is located on-top of a monomode rib waveguide, which ends with a tapered region at the chip edge to allow direct fiber butt-coupling. The cathode of the photodiode is coupled to an integrated biasing network. The electrical output signal of the photodiode's anode is fed to a coplanar waveguide based transformer network, comprising a short stub for transmission curve tuning and for the DC path. The exact CPW length dimensions for resonance frequencies of 40, 60, 80, 85 GHz were determined by applying standard circuit simulation; see, e.g., [23].

The transformer network produces an effective gain by allowing the photodiode to feed its output current not into the 50-Ω system but, at resonance, into a transformed higher impedance in the range of about 200–250 Ω. Thus, an effective power gain is produced at resonance, which equalizes the usual magnitude's decay around the 3-dB cut-off frequency of broadband detectors. At the same time an output impedance of 50 Ω at resonance is designed into the circuit, by proper choosing the CPW waveguide's impedance with respect to the CPW waveguide losses. Thus, a well matched power transfer to subsequent booster amplifiers or antenna systems is provided.

5.3.2. Fabrication

The OEICs (see Fig. 15) were fabricated employing a single-step MOVPE epitaxial approach for the WG-integrated PD layer stack, used within the integration scheme of broadband photoreceivers [12].

The photodetector OEIC comprises a p-i-n mesa photodiode, a spot-size converter for effective fiber-chip coupling, a biasing network, and the coplanar transformer network. All devices are integrated on a semi-insulating waveguide layer stack being composed of three quaternary optical guiding layers embedded within InP and an upper thicker waveguide layer. The evanescently coupled photodiode is grown on-top of this stack by a single MOVPE growth run. The rib waveguide and the photodiode are structured using dry and wet etching techniques. Finally the passive mm-wave devices are implemented, which involves evaporation of interconnect and NiCr resistor layers, PECVD deposition of the MIM dielectric and the formation of gold-plated air bridges. The spot size converter is integrated by exploiting the additional diluted waveguide formed by the buried semi-insulating GaInAsP guiding layers beneath the more confining GaInAsP:Fe waveguide, which feeds the InGaAs absorption region of the photodiode. The spot size transformer is vertically tapered with a ramp of less than 1 μm over a length of approx. 1 mm to provide a quasi adiabatic conversion of the spot size. The spot size converter increases the fiber alignment tolerances by one order of magnitude into the 2-μm range and enables the use of a cleaved instead of a lensed fiber [24]. The definition of the spot size converter is carried out prior to the MMIC process and has no impact on it.

5.3.3. Characterization

Network analyzer measurements of the output reflection coefficient S_{22} at 2 V reverse bias were carried out, which showed the resonance behavior near the operating frequencies mentioned above. Also the good match to an external 50-Ω load was demonstrated by return losses of better than 15 dB at resonance.

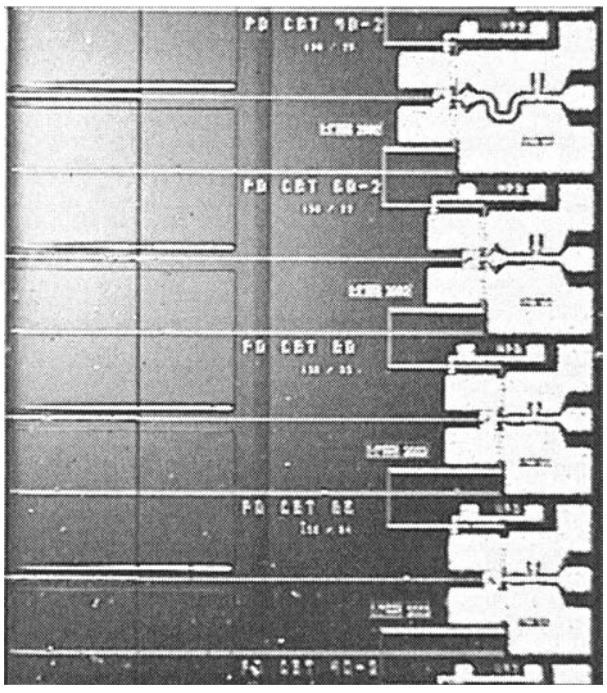

Fig. 15. Microphotograph of bar of four fabricated narrowband photodiodes, designed for 40, 60, 80 and 85 GHz resonance; left-hand side: tapered AR coated input waveguides, right-hand side: coplanar RF outputs.

The frequency response of the photodetector was determined by an optical heterodyne measurement technique employing two tuneable-wavelength lasers operating around 1.55 μm serving as an RF-modulated light source up to 110 GHz. The optical input signal was fed into the chip's tapered waveguide by a butt-ended fiber. The electrical output of the detector was contacted using a coplanar probe connected to a short coaxial cable, specified for operation up to 110 GHz. Up to 50 GHz the output power was measured using an electrical spectrum analyzer. For the measurements from 50 to 110 GHz a power meter with two different sensor heads for the V- and W-band, respectively, was used.

Heterodyne measurements were carried out, see Fig. 16, comparing the RF output power at equal photocurrents of the new narrowband detectors to an unterminated ultra-broadband detector with a bandwidth of 60 GHz available on the same wafer.

The frequency dependent gain of the transforming network at resonance can be directly seen from the peak power values at the different operating frequencies as compared to the output power of the broadband detector. Gain values of 7 dB are typically extracted. The effective gain would be even higher by further 6 dB if compared to commercial broadband detectors with internal 50 Ω termination.

The photodetectors have been designed with a low doping level in the absorption layer to exhibit deep depletion already at about 1–2 V reverse bias. Nevertheless a

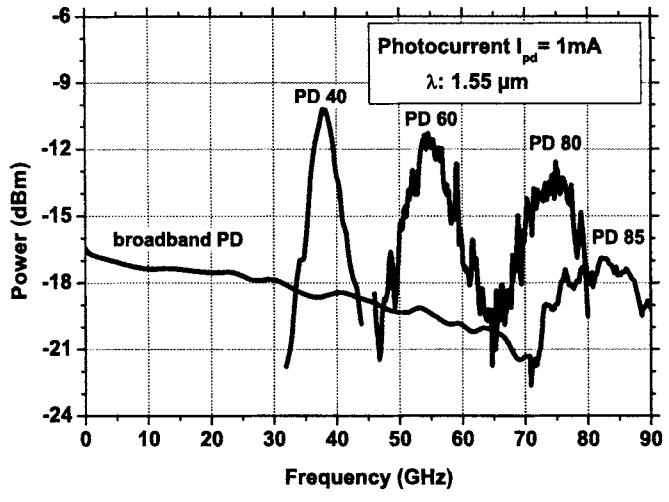

Fig. 16. Comparison of the RF power efficiency of unterminated broadband (PD) and narrowband photodiodes (PD40/60/80/85) for equal DC photocurrents of 1 mA at 2 V reverse bias.

certain tuneability of the resonance frequency by some GHz by affecting the diode's capacitance by the changing reverse bias from 2 to 12 V was detected for all detectors, operating in the 60/80/85 GHz regime.

From this finding it may be concluded that some outdiffusion of the Zn doping in the highly doped p-type heterostructure contact layer stack has taken place, which converted about 50 nm of the unintentionally doped native n-type absorption layer into p-type. This converted region may be additionally depleted with increasing reverse bias, with the consequence of a slight additional capacitance reduction under high reverse bias. Also a doping tail from the silicon-doped n-contact has to be taken into account. Obviously this small capacitance reduction can be exploited to tune the resonance of a detector, designed for, e.g,. 80 Gbit/s clock recovery purposes, also to 85 GHz resonance to serve as a clock recovery circuit in a FEC configuration, needing an about 7% higher raw data rate of about 85 Gbit/s.

Furthermore the signal peak responsivity at resonance in comparison to the DC value was investigated. Normal broadband detectors loose several dB of magnitude, depending on their 3-dB cut-off frequency. The effective responsivity at resonance of the narrowband detectors, see Fig. 17, approaches with 1 A/W nearly twice the DC value at 40 GHz and still conserves the DC value with 0.5 A/W at 80 GHz.

Especially in the latter case, the cut-off decay loss at this quite high operating frequency is effectively equalized due to the built-in gain of the resonant transformer network.

A fully packaged narrowband photodetector module similar to the one in Fig. 12 was realized for 80 Gbit/s clock recovery purposes. In the module optical coupling is done by fixing the butt fiber directly at the OEIC's tapered waveguide facet by UV curable resin. The optical return loss was better than 30 dB. This coupling type

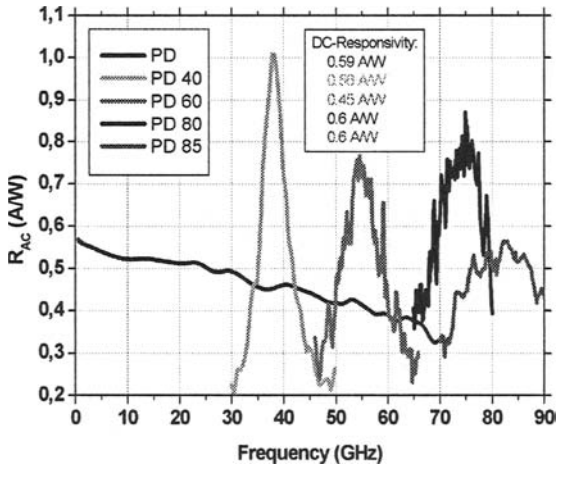

Fig. 17. Resonant photodiodes with peak responsivities at resonance of 1 A/W (40 GHz type chip), exhibiting twice of its DC responsivity; and of 0.55 A/W (80 GHz type module), exhibiting an equal value as in the DC case.

provides high robustness against vibration and thermal cycling under field operating conditions. The RF output of the OEIC was connected via multiple bonding wires to a short coplanar waveguide on a 100-μm-thin quartz substrate, which leads to a 1- or 1.85-mm connector at the end, depending on the operating frequency of the module. A return loss of better than 10 dB was measured over 40 GHz bandwidth in case of the 40 GHz type module with the 1.85 mm connector. The same good return loss is achieved over 100 GHz bandwidth in case of the 1 mm connector.

Figure 18 shows the reverse bias tuneable O/E conversion behavior of a narrowband detector module with a 1-mm connector for 80 Gbit/s clock recovery purposes.

By increasing the reverse bias from 1 to 4 V the resonance peak is shifted from 76 to 82 GHz. The resonance position for a fixed bias value was proven to be stable when the optical input power level was varied from -3 dBm to +12 dBm. When the reverse bias was kept high enough, e.g., at 3 V, the output return loss was better than 10 dB over the full range of optical input power levels. The 3-dB bandwidth around 13 GHz matches well with the expectations from the circuit simulator. Corresponding typical Q values of the narrowband detectors range between 6–8.

For a variety of applications the linearity of the detector in the higher optical input power range is of interest, e.g., using the narrowband detectors as O/E converters in fiber-based mm-wave distribution networks, to feed directly an antenna structure or a booster amplifier. Another application is the clock recovery applying an optically pre-amplified system scheme. Up to a level of +14 dBm optical input power no compression of the DC current can be noticed. At quite moderate reverse bias values of only 3 V an RF output level of approximately -2 dBm can be achieved at +14 dBm input power level [30].

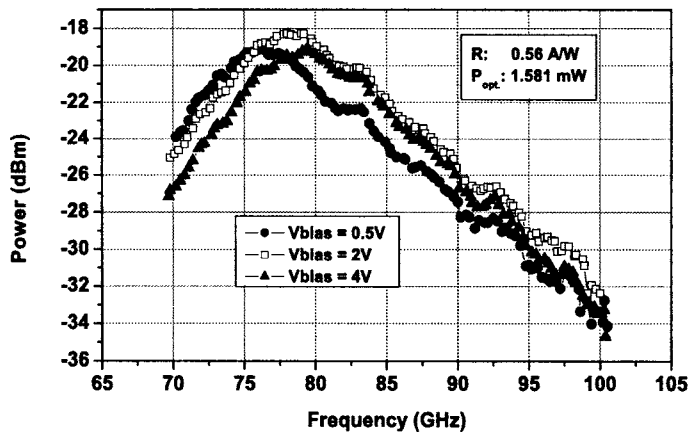

Fig. 18. Opto-electronic frequency response of a 80-GHz module, showing slight resonance tuning with reverse bias of 0.5–4 V.

5.4. Twin-Type Waveguide-Integrated Photodetectors With Differential Output

This section treats the fabrication of monolithically integrated twin-type photodetector OEICs and their successful mounting into butt-coupled modules. With regard to differential broadband operation the devices were characterized revealing 45 GHz bandwidth and a responsivity of 0.41 A/W.

For compact integration of 40 Gbit/s optical front-ends a distortion robust detector type is useful, which suppresses effectively all radiated or electromagnetically coupled interference signals from digital circuitry mounted within the same housing. Therefore it is desirable to provide directly from the detector two symmetrical electrical signals with inverse polarity at the inputs of the differential amplifier at the demultiplexer stage. In this work the first realization and characterization of twin-photodiode modules featuring broadband differential operation at $\lambda = 1.55$ μm is presented.

5.4.1. Integrated Differential Photodetector Modules

The InP-based photonic integrated twin-photodetector comprises a vertically tapered spot size converter, a multimode interference (MMI) coupler for optical 3 dB power splitting and two waveguide-fed evanescently coupled high-speed p-i-n photodiodes [24,16], one with inverse polarity. The design of the differential detector is described in [25] and is schematically depicted in Fig. 19.

To realize a robust packaging the photodetector was mounted on ceramic substrate and connected via bonding wires to the coplanar stripes (CPS) leading to the two V-connector output ports. Two types of modules have been fabricated: One type contains solely the already described twin-PD OEIC (type A), the other type B comprises additional 50 Ω thin film termination resistors very near to the OEIC's bonding pads. Network analyzer measurements of module B determining $S_{22} < -10$ dB up to 50 GHz validated the suitability of this electrical configuration. In order to minimize

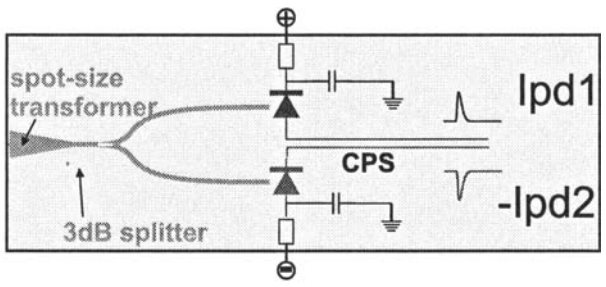

Fig. 19. Basic design of the twin-photodiode.

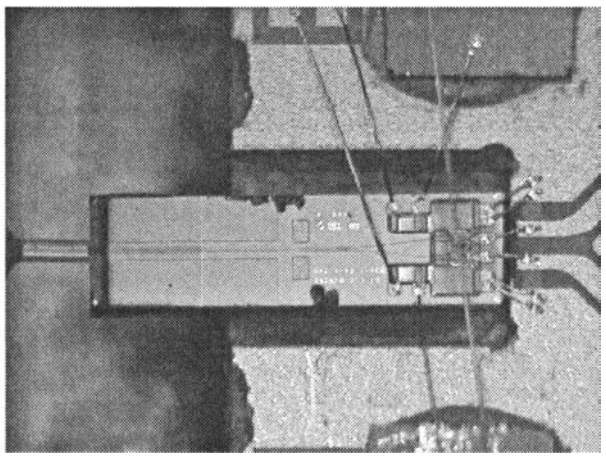

Fig. 20. OEIC after mounting, bonding and optical coupling.

optical reflection the input facet of the chip was TiO_2-coated and a low-reflective butt-fiber with optical return loss better than 27 dB was used.

Figure 20 shows a top view into the twin-photodiode module (type B) with the fiber-coupled, wire-bonded OEIC.

5.4.2. Device Characterization

For differential operation of a subsequent electronic circuit (e.g., demux stage) it is necessary to receive equal absolute photocurrents from both photodiodes. Therefore the ratio IPD1/IPD2 in dependence of the fiber-chip coupling was examined for both states of TE and TM polarizations. Owing to the integrated spot-size transformer large alignment tolerances are obtained, revealed by the sum of both photocurrents leading to more than ± 2 μm 1 dB additional loss for both states of polarization. The photocurrent ratios remain within 1 dB for all applicable offset positions indicating that values of less than 0.5 dB are achievable by minor lateral detuning during the fiber-chip coupling.

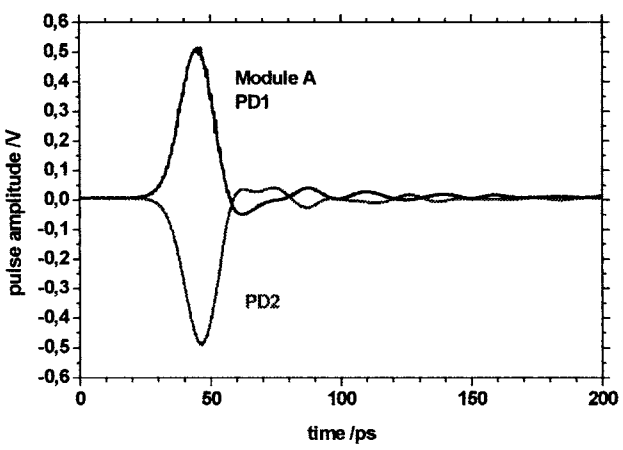

Fig. 21. Pulse measurements showing a differential amplitude of 1 V.

To estimate the polarization dependence of the device both photocurrents at different polarization angles of the incoming light are measured. Both total photocurrent and photocurrent ratio exhibit little deviations of less than 0.5 dB promising balanced polarization insensible operation.

Pulse responses of the twin-photodetector module were performed in the time domain using a picosecond laser source (FWHM: 3 ps, repetition rate: 16 MHz) and a 50-GHz sampling scope. Symmetric narrow pulses and negligible ringing are observed. Figure 21 shows the received pulses of both photodiodes with 500 mV peak voltage corresponding to a photocurrent of 10 mA, which is sufficiently high to drive directly the demultiplexer stage.

At a reverse bias of 2 V the FWHM of 13.97 and 14.36 ps remained constant up to optical input energies of 0.94 pJ, demonstrating the high power capability of the photodiodes.

A heterodyne setup consisting of two external cavity lasers was utilized to study the power transfer functions of the photodetector module. Figure 22 depicts identical flat frequency responses of the two photodiodes (denoted module A) up to 30 GHz, revealing a 3 dB cut-off frequency of 35 GHz, suited for balanced 40 Gbit/s operation. The total responsivity adds up to 0.41 A/W. In order to expand the RC limitation 50-Ω load resistances in a second module B were implemented. The measurement shows again identical responses of both photodiodes but less ripple and the effect of slight inductive peaking. The bandwidth is extended up to more than 45 GHz. The total responsivity amounts to 0.31 A/W.

The eye pattern characterizations at 42.66 Gbit/s are shown in Fig. 23. For a bit error ratio of 10^{-9} the necessary the OSNR amounts to 27 dBm, which is approximately 3 dB less than needed in case of a comparable single-ended photodetector, driving only one input of the demultiplexing electronics [31].

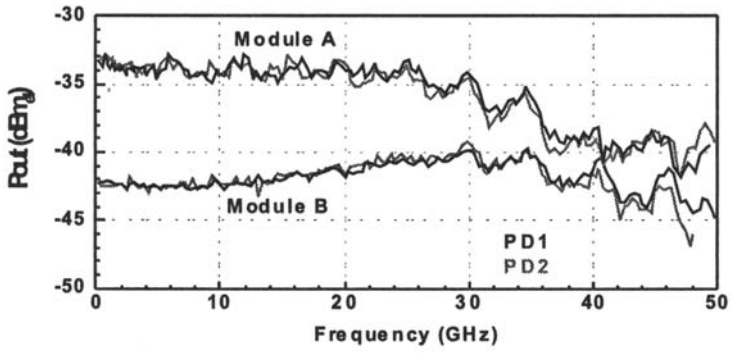

Fig. 22. Frequency responses of modules A and B at optical input powers of 643 and 650 μW, respectively.

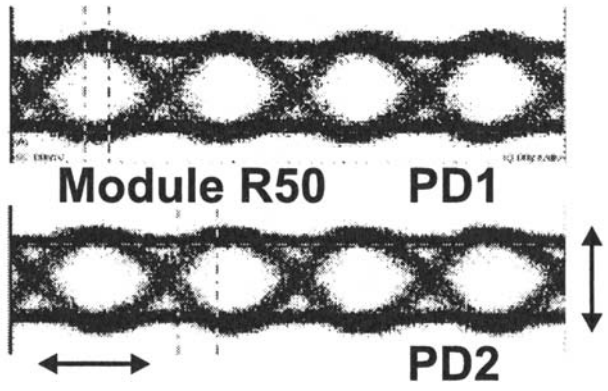

Fig. 23. Received NRZ eye pattern at 42.66 Gbit/s for FEC systems, PRBS $2^{31}-1$, x: 20 ps/div, y: 150 mV/div.

5.5. Waveguide-Integrated Balanced Photodetectors

5.5.1. Introduction

A balanced photodetector is a key element for direct detection in differential phase shift keying (DPSK) transmission formats, where a bipolar reception scheme is desired [26,27]. Furthermore it is a useful component in high-performance radio-frequency (RF) photonic systems with heterodyne detection for effective noise suppression resulting in an enhanced signal-to-noise ratio [28]. One important parameter of the balanced photodetector required by these applications is the common-mode rejection

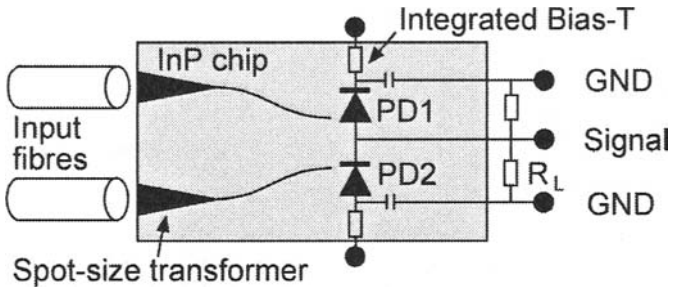

Fig. 24. Schematic view of the integrated balanced photodetector.

ratio (CMRR), which specifies the symmetry of the two photodiodes over the entire bandwidth, defined as $(I_{PD1} - I_{PD2})/(I_{PD1} + I_{PD2})$. Monolithically integrated balanced waveguide-photodetectors provide excellent RF matching of both photodiodes, broad bandwidth, high power capability and reduced packaging cost. In this section the design, fabrication, packaging and characterization of a fully packaged high-speed balanced photodetector module, suitable for operation in 40 Gbit/s transmission systems, is reported.

5.5.2. Design, Fabrication and Packaging

The design of the integrated balanced photodetector based on InP is schematically depicted in Fig. 24. It contains two spot-size transformers, two waveguide S-bends and a pair of high-speed pin-photodiodes (PD1 and PD2) with high power capability [16]. Grown by MOVPE, the evanescently coupled photodiodes with an active area of $5 \times 25\ \mu m^2$ are located on top of the semi-insulating waveguide layer stack and are biased by means of integrated bias-circuits. The photodiodes are electrically connected in an anti-parallel configuration; hence the currents are subtracted directly on chip, essentially improving the RF performance at high frequencies.

To achieve a robust packaging the chip was mounted on a ceramic substrate and all electrical connections were realized by wire bonding. The RF output is provided via a short coplanar waveguide (CPW) transmission line on TMM 10i substrate leading to the output port.

Using a standard double-fiber array with 250 μm pitch the optical coupling was performed simultaneously for both inputs. The fiber array was aligned while monitoring both photocurrents. Once the position with maximum currents was reached, the array was laterally fixed by two glass blocks. In this way a responsivity of 0.24 A/W for each PD with a polarization dependent loss of less than 0.8 dB in a first prototype module was achieved. At least 0.5 A/W, as known from chip-based measurements, should be possible by the use of a more suitable fiber array and a further improved fiber-to-chip coupling procedure, respectively. Compared to a single pin-photodiode, the described balanced detector suffers from a reduced 3-dB bandwidth due to the two pn-junction capacitances in parallel. In order to expand the RC limitation an additional load resistor chip was implemented between the detector chip and the CPW output transmission

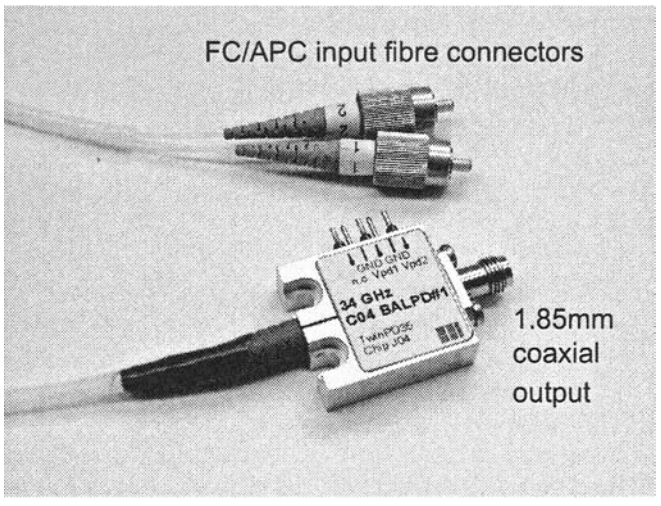

Fig. 25. Balanced photodetector module.

line. The load resistor R_L consists of two 100-Ω NiCr resistors on InP connected in parallel to the signal line. The module provides two fiber pigtails for the optical input, two pins for +2 and −2 V biasing, and one coaxial 1.85 mm connector output port (Fig. 25).

5.5.3. Experiments

An optical heterodyne setup consisting of two tuneable external cavity lasers at 1.55 μm and a 50-GHz electrical spectrum analyzer were used to study the frequency behavior of the module. The upper traces in Fig. 26 show the relative frequency responses of both PDs in unbalanced operation mode, illuminating only one PD at a time. In both cases we measured a 3-dB cut-off frequency of 34 GHz, which remained constant for reverse voltages > 1.5 V at 850 μW optical input power. Around 20 GHz, both traces show the effect of inductive peaking in terms of an increased response of 2 dB. This effect is mainly caused by the additional bonding wires required by the hybrid load resistor chip. Integrating the load resistor directly on the detector chip could further flatten the frequency response and expand the bandwidth. The agreement of the two measured frequency characteristics is determined to be within 1 dB up to 30 GHz, indicating the superior symmetry of both PDs at high signal frequencies. In order to determine the CMRR, the optical heterodyne signal was split by a 3-dB coupler to feed both photodiodes of the module. Amplitude and phase matching of the optical signals is essential for operation in balanced mode.

To compensate for phase mismatching at the inputs of the photodiodes caused by minor differences in fiber lengths a variable optical delay line in one branch of the setup was used. A variable attenuator in the second branch ensured amplitude matching. Taking the external losses of the setup into account, the optical power of one input was adjusted to equalize the dc photocurrents of both photodiodes within

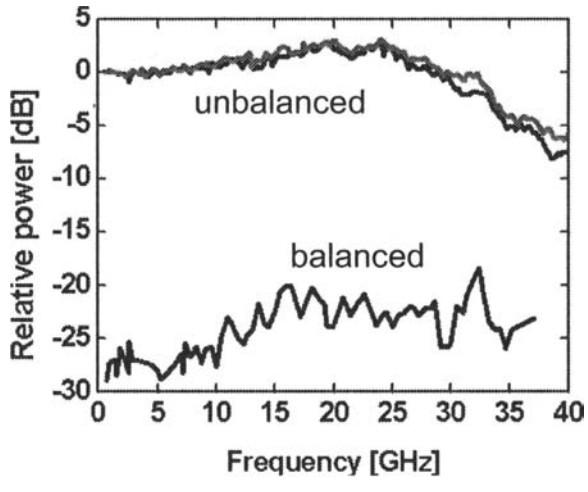

Fig. 26. Frequency responses of both photodiodes in unbalanced (upper traces) and CMRR in balanced mode (lower trace).

1%. In Fig. 26 the lower trace shows the relative CMRR vs. frequency at optical input powers of about 850 μW. Up to 10 GHz the CMRR is better than 25 dB, from 10 GHz to 30 GHz the CMRR amounts to at least 20 dB, proving that there is no significant electrical asymmetry between the two photodiodes, even at high frequencies.

Replacing the heterodyne source by an optical pulse source with a FWHM less than 4 ps, the same optical experimental setup to characterize the module in the time domain was employed. Now the electrical output signal was fed into a 50-GHz sampling scope limited by its intrinsic pulse width of 7 ps. From the received bipolar electrical pulses their FWHM was determined to 15 ps for both output pulses at a reverse bias of 2 V. Pulse widths remained unchanged up to high optical input power related to peak photocurrents of 10 mA. Owing to the highly symmetric characteristics of the balanced photodetector there is nearly perfect cancellation in case of vanishing phase delay between the exciting input pulses.

Utilizing a zero-biased Mach-Zehnder modulator in push-pull configuration and an optical delay line demodulator, initial experiments with a DPSK modulation format were performed at 40 Gbit/s in the balanced operation mode. The experimental setup is shown in Fig. 27.

The received eye pattern of a pseudo-random bit stream of length $2^{15}-1$ at an input power of 10 dBm is clearly opened (inset of Fig. 27). The receiver sensitivity for BER $= 10^{-9}$ is better than -29 dBm [32,33].

By integrating the load resistor on the detector chip, the bandwidth can be further broadened. Figure 28 shows the bandwidth of 70 GHz of a recently optimized InP-based balanced detector chip with integrated 50 Ω termination and controlled impedance layout of the pin-mesa-to-bondpad transition.

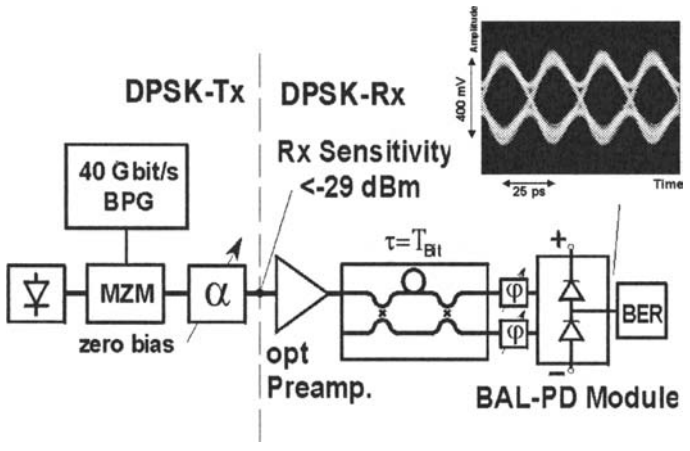

Fig. 27. Experimental setup for the 40-Gbit/s DPSK receiver sensitivity measurement with received eye diagram.

The experiments demonstrate high symmetry between both photodiodes up to signal frequencies of 70 GHz due to the compact monolithic integration scheme. This results in a broadband common-mode rejection ratio of more than 20 dB. Eye diagram and BER measurements reveal the suitability of these detector types for 40–80 Gbit/s DPSK transmission systems.

6. Photoreceivers

This section treats ultra-high speed photoreceiver concepts and some prototype realizations. As very high-speed data rates of 40 Gbit/s and beyond are discussed here, the main focus is laid on the receivers with integrated distributed amplifiers, other types of lower or medium speed receivers (sections 6.1.1–6.1.2) are mentioned only shortly for the completeness of the topic.

6.1. Circuit Types of Receiver Amplifiers

Various circuit concepts exist for photoreceivers, which have the common goal of achieving a high gain of electrical post amplification, a high bandwidth accompanied with a low minimum detectable optical power and a good receiving sensitivity. The gain characteristics have to be optimized for a low group delay scatter, oriented on the bit period, to provide low intersymbol distortions and jitter in the eye pattern. Depending on increasing bandwidth demands, the circuits types can be put into the order of the high impedance type, the transimpedance type and the distributed amplifier type. Because the first two circuit types are broadly discussed in the literature, see e.g., [52], the distributed amplifier or travelling wave amplifier will be treated here due to its superior broadband characteristics in, more detail and illustrated by receiver prototype examples.

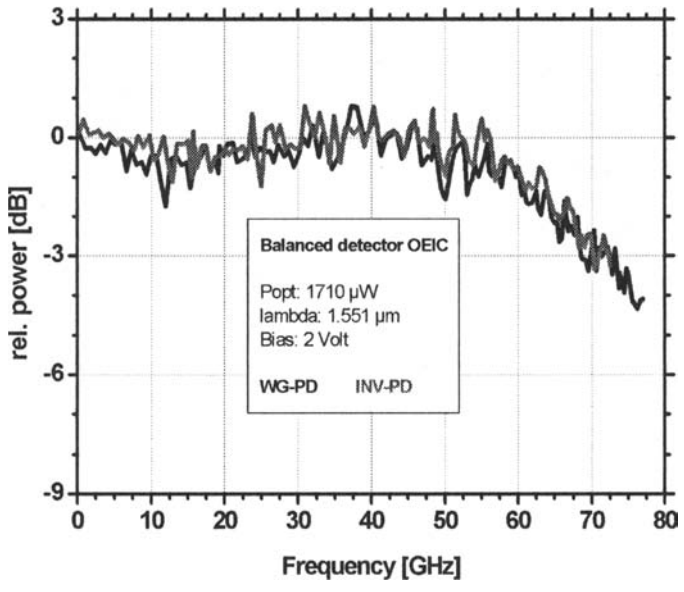

Fig. 28. Optimized InP-based balanced detector chip with integrated 50 Ω termination and controlled impedance layout of pin-mesa-to-bondpad transition, showing a bandwidth of 70 GHz.

6.1.1. High Impedance Type

The high impedance amplifier is a voltage amplifier, i.e., the photodiode's AC signal current develops an AC voltage at a parallel shunt load resistor. This resistor should be chosen as high as possible, within a given bandwidth and the resulting RC-limitation. The higher this input load resistance can be chosen, the lower is the resulting equivalent input noise current and the better the signal-to-noise ratio at the amplifier input of the voltage amplifier can be designed. Within this design scheme, demanding a high voltage gain at the load resistor already, the RC-limited bandwidth of the amplifier is relatively low (some 100 MHz–GHz), caused by the photodiode's and amplifier's input capacitances. Consequently a post equalizing circuit after the voltage amplifier, to increase again the total bandwidth of the receiver, is needed. The resulting bit rate capability is suitable for the lower speed range, but good sensitivities can be achieved at relatively low (Mbit/s–Gbit/s) data rates.

6.1.2. Transimpedance Type

The transimpedance amplifier is a current-to-voltage converting amplifier, i.e., the photodiode's AC signal current develops an AC voltage at the output of the amplifier. The load resistance of the photodiode is placed in the feed-back loop of the amplifier's output to its inverting input. Consequently the photodiode operates into a greatly

reduced effective input impedance, depending on the loop gain, compared to the direct feed-back resistance value, which helps considerably, to increase the RC-limited bandwidth of the input circuit. At the same time the thermal noise current from this feed-back resistor, which has to be summed up (quadratically) at the amplifiers input, together with the photodiode and amplifier input noise current, is much lower for the same given bandwidth, compared to the high impedance concept, especially at higher bit rates of 1–10 Gbit/s. Also the transimpedance amplifier type exhibits a clear advantage of improved dynamical range of the input current, to be linearly amplified. Consequently this amplifier type is most commonly used up to data rates of 10 Gbit/s and above. At 40 Gbit/s new problems arise, because the amplifier's loop gain exhibits an increasing phase shift at higher frequencies with respect to the ideal $-180°$ inverting case. This results into a gain peaking behavior of the transimpedance conversion characteristics. Also the time delay of signal propagation along the feed-back loop cannot be neglected any more, which causes additional instabilities. These problems can only be partially solved by miniaturizing the circuit topology by dense monolithic integration at the expense of the transimpedance gain, which often does not exceed 80–100 Ω, for obtaining a flat group delay response of the amplifier. Thus, at 40 Gbit/s and beyond, the distributed amplifier type gains much attraction.

6.1.3. Distributed Amplifier Type

The distributed or travelling wave amplifier (TWA) is a special type of ultra-broadband and high-speed amplifier [34]. In contrast to the amplifiers, discussed before, where the gain of subsequent transistor stages is multiplied, the gain of the distributed amplifier results from summing up the gain values of the single transistor stages additively. This results into lower amplifier gain values, if the same number of transistors are used as in other amplifier concepts. The advantage is the ultra-high bandwidth of the distributed amplifier, because the transistor input and output capacitances may be included into the distributed capacitances per unit length of the input and output lines of the amplifiers, which are designed to higher impedance values for this purpose. Thus the RC limitation effect is greatly reduced. Figure 29 shows the basic circuit of an FET (field-effect transistor)-based distributed amplifier, adapted to the application within a photoreceiver, where the left-sided input termination is omitted for achieving higher transimpedance values, thus the photodiode feeds its signal current directly into the gate input line. The distributed amplifier exploits well the transistor cut-off frequencies with respect to its bandwidth, i.e., often half of the cut-off frequencies can be achieved as the amplifiers bandwidth. The TWA has a good large signal behavior and can be designed for a very low group delay scatter up to very high frequencies (> 100 GHz).

Concerning the amplifier noise properties the distributed amplifier reduces the effects of the thermal noise of the gate line termination resistance. The noise of this resistor is counter-propagating to the signal, thus this noise is reduced over larger frequency ranges with respect to the equivalent input noise current of the amplifier, because the amplification of the TWA is optimized for the signal direction (from left to right), but not for the counter-propagating noise signal. Although this thermal noise contribution is frequency selective reduced, the noise of the transistors contribute to the equivalent input noise current, too.

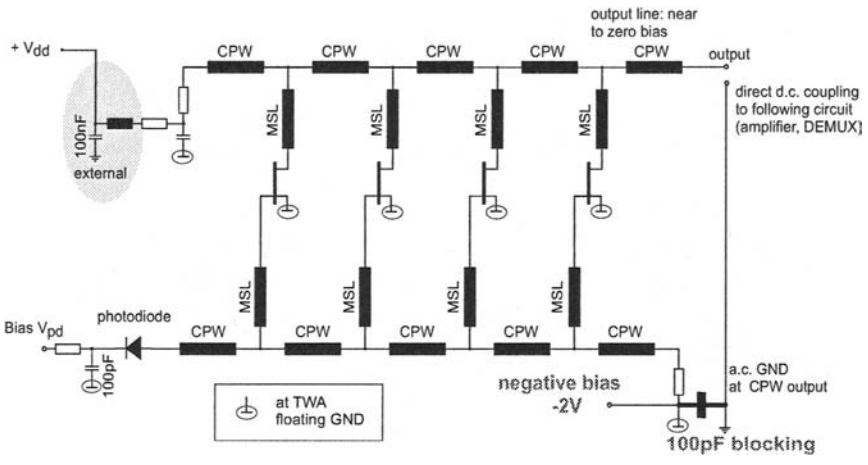

Fig. 29. Circuit diagram of a photoreceiver with negative bias and GND-isolated output port comprising a distributed amplifier.

6.2. Signal-to-Noise Ratio and Sensitivity of Photoreceivers

Equation (5), developed in section 2.6, gives the minimum detectable optical power at a given bitrate and a given bit error ratio. For this aim all noise sources of the photodiode and the amplifier have to be remapped to the input summation point and added, mostly linear with respect to their power contributions, because normally these sources are uncorrelated.

6.3. Hybrid Photoreceivers

Hybrid photoreceivers use separate photodiode and amplifier chips. This approach is less demanding on the integration of the single components and the good yield of single components can be exploited favorably. The drawback is less control on the parasitics. They affect the conversion gain curve and its group delay scatter increasingly serious, as the operating frequency is increased. Owing to the compactness of this section, this topic may be found in more depth elsewhere in the literature [35,36].

7. Monolithic Ultra-Broadband pinTWA Photoreceivers

Opto-electronic integrated receivers based on InP are the best promising candidates for high bit rate transmission system of 80 Gb/s and beyond (e.g., 100 Gbit/s Ethernet), operating at a wavelength of 1.55 μm. This section concentrates mainly on the recent achievements of monolithic integrated photoreceiver OEICs based on InP, which are fully packaged and capable of 80 Gbit/s NRZ modulation format transmission. The design, circuit scheme and fabrication of this DC-coupled high-speed receiver are presented as well as its characterization up to 110 GHz measurement frequencies and

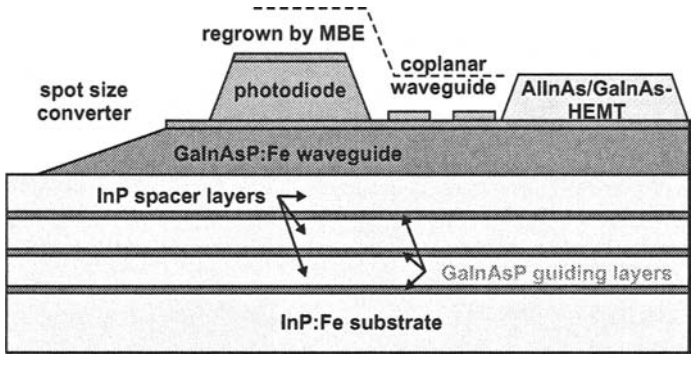

Fig. 30. Integration scheme of the PIN-HEMT/*pin*TWA photoreceiver.

its ultra-broadband NRZ format O/E conversion capability. Results on 40–60 Gbit/s receivers, following the integration and circuit concept discussed in the following can be found in [12,37–40,42,43].

7.1. A Versatile Ultra-High Speed pinTWA Photoreceiver Integration Concept

The integration scheme of the pinTWA photoreceiver is depicted in Fig. 30. It is composed of a waveguide-integrated photodiode with a spot-size converter and a special HEMT-based traveling wave amplifier. The process consists of an MOVPE growth of the photodetector and waveguide layers and an MBE regrowth of the HEMT layers. The two-step MOVPE/MBE epitaxial process preserves the properties of photodiode layers during the low-temperature MBE growth of the HEMT layers.The OEICs were fabricated employing a two-step MOVPE/MBE epitaxial approach for the WG-integrated PD/HEMT layer stacks, allowing an independent optimization of the single devices [41]. All devices are integrated on-top of a semi-insulating waveguide layer stack being composed of three quaternary optical guiding layers embedded within InP and an upper thicker waveguide layer. The evanescently coupled photodiode is grown on-top of this stack within a single MOVPE growth run.

After structuring the photodiode, MBE regrowth is applied for the AlInAs/GaInAs lattice-matched HEMT layer stack. All devices are well insulated from each other due to the good dielectric properties of the MOVPE grown Fe-doped layer stack.

The HEMT gate recess and the photodiode mesa are defined by dry chemical etching (RIE). The subsequent MMIC processing includes the formation of the NiCr resistors, MIM capacitors, and metallization for interconnections and airbridges. MIM capacitors and metal film resistors are used as passive devices, applied for the amplifier as well as for the biasing network of the photodiode. Coplanar waveguide interconnections employing air-bridges are formed by gold electroplating. The HEMTs are coupled to coplanar transmission lines by quasi microstrip lines, which are formed by airbridges over a groundplane.

The spot size converter is integrated by exploiting the additional diluted waveguide formed by the buried semi-insulating GaInAsP guiding layers beneath the more

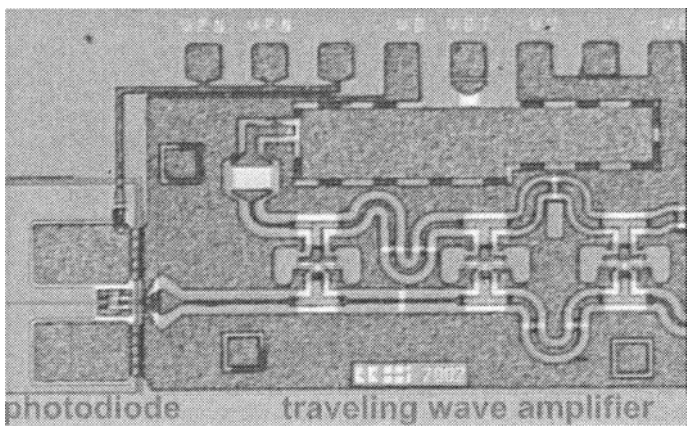

Fig. 31. Partial view of the integrated photoreceiver OEIC.

confining GaInAsP:Fe waveguide, which feeds the photodiode. The latter is vertically tapered with a ramp of less than 1 μm over a length of approximately 1 mm to provide a quasi-adiabatical conversion of the spot size. The spot size converter increases the fiber alignment tolerances by one order of magnitude and enables the use of a cleaved instead of a lensed fiber. For antireflection purposes, the optical input facet of the photoreceiver OEIC was covered by TiO_2/SiO_2.

7.2. A pinTWA Photoreceiver for 80/85 Gbit/s Detection: Photoreceiver Design

For the 80-Gbit/s system application a new circuit layout was developed, using HEMTs with modified layer structures and shorter gate lengths. The circuit was simulated using Agilent EEsof EDA (ADS). The biasing configuration is accomplished with a negative bias supply at the common source electrode with a MIM capacitor [44]. The circuit diagram of the photoreceiver with a negative bias and ground (GND)-isolated output port was already depicted in Fig. 29. The amplifier's DC current is fed into the terminal Vdd. The HEMTs (gate length $\sim$0.18 μm) exhibit maximum cut-off frequencies $f_T/f_{\max}$ of typically 129/260 GHz.

The simulated S_{21} and S_{22} of the amplifier (TWA) give 65 GHz and 8 dB, respectively. The reflection coefficient S_{22} is less than 10 dB over almost the whole frequency range.

7.3. Photoreceiver Fabrication

An enlarged partial view of the final chip is given in Fig. 31, which shows the photodiode at the left being connected to the input of the travelling wave amplifier via an air bridge.

7.4. Chip Measurement and Characterization

The on-wafer high-frequency measurements of the integrated distributed amplifier within the monolithic photoreceiver OEIC were performed with a network analyzer in

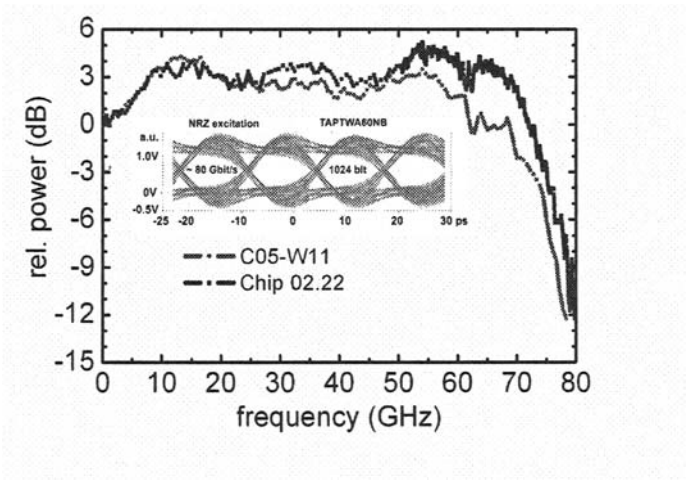

Fig. 32. Opto-electronic frequency response of the photoreceiver chip (upper line) and module (lower line), a synthesized eye pattern for the chip at 80 Gbit/s NRZ modulation format: see inset.

the frequency range of 0.45 to 110 GHz. The amplifier characteristics defined by the transimpedance (Z_T) is derived from the measured S-parameters. A transimpedance of 90 Ω (39 dBΩ) and a bandwidth of 72 GHz were deduced. The o/e conversion frequency characteristics of the photoreceiver was determined by an optical heterodyne measurement technique employing a fixed and a tuneable laser at 1.55 μm, covering a frequency range used up to 80 GHz, see Fig. 32. The measurement of the output power, up to the frequency range of 50 GHz was done with an electrical spectrum analyzer. For the measurements from 50 to 80 GHz, a power meter with a sensor head for the V-band was used. Owing to sufficient overlap of the two frequency ranges, we achieved continuous transitions between the two different measurements. The 3-dB bandwidth exceeds 70 GHz. The photodiode DC responsivity amounts to 0.64 A/W with a polarization dependent loss of 0.67 dB. The overall conversion gain of the photoreceiver chip is 45.4 V/W, which is high enough for 80 Gbit/s ETDM system applications as well as a component for developing measurement instrumentations.

Since an 80-Gbit/s eye pattern measurement equipment with NRZ modulation format was not at the moment to our disposal, we demonstrate it by synthesis [20]. The NRZ eye pattern with 1024 bit was deduced from the heterodyne measured frequency characteristics for a bit rate of 80 Gbit/s, given in the inset of Fig. 32. The phase is calculated from the magnitude of the output power assuming a minimum phase system and neglecting noise [20]. The minimum phase assumption was verified by circuit simulation and comparison of phase characteristics. The eye pattern is well opened demonstrating the handling capability of the data streams in 80 Gbit/s transmission systems.

7.5. Chip Packaging

Packaging of the photoreceiver chip was done into a module, according to Fig. 12. The optical coupling is done by fixing the butt fiber directly at the chip's waveguide facet by UV curable resin. The output of the chip is connected to a 1-mm coaxial connector via a short coplanar waveguide (CPW) on a quartz substrate to fit the geometry of the connector, which is used to operate up to 110 GHz. On the upper side of the module are the DC supply inputs.

The frequency characteristic of the module, which was determined by an optical heterodyne measurement technique at 1.55 μm is depicted in Fig. 32, too. The chip (upper curve) and the module (lower curve) measurements are plotted together, to compare their characteristics, since the packaging is not always simple as to have the chip performances. In both cases, the bandwidth is over 70 GHz, which shows that the high frequency packaging is of a good quality and can be applied up to the chip bandwidth. There was however a slight degradation in the photodiode responsivity from 0.64 to 0.59 A/W and polarization dependent loss, from 0.67 to 0.87 dB respectively.

For testing the time domain behavior of the opto-electronic conversion properties of the 80-Gbit/s receiver module, an 80-Gbit/s RZ-modulated (FWHM $\sim$ 1.7 ps) optical signal (PRBS 2^7-1) with a power of P_{opt}: +5 dBm was fed into the input fiber. The measurement was done with a 70-GHz Agilent 86100B scope with 86118A, jitter: 850 fs, 200 waveforms. The module biasing was V_{ss}: -2 V, V_{dt}: 2 V, I_{dt}: 40 mA, V_{pn}: 0 V (i.e., zero bias output). Figure 33 shows the converted electrical output signal of the module with $V_p \sim 160$ mV.

The eye is well opened, but shows effects of ringing and overshoot, which is attributed to the not yet optimized conversion curve in Fig. 32, which will be done within a circuit redesign. A further optimization offers the chance for designing the RZ to NRZ conversion property directly into the *pin*TWA receiver OEIC, without the need for further external ultra-broadband post filters. The output voltage is sufficient for driving a subsequent electrical 80 Gbit/s demultiplexing circuit.

8. Monolithic Balanced *pin*TWA-Based Photoreceivers

8.1. Introduction

Balanced photoreceivers gain growing attraction by system designers due to the potential of an improved receiver sensitivity in long haul fiber links utilizing DPSK modulation formats and balanced detection [33,47]. Previously, it has been shown that monolithically integrated balanced photodetectors provide a high common-mode rejection ratio, broad bandwidth and reduced packaging costs [32]. In order to achieve a low electrical output reflection these devices contain a 50-Ω matching resistance at the joined output of the two photodiodes at the expense of loosing 50% of the signal level, equivalent to 6 dB loss of the electrical power. In this section the first implementation of a monolithic integration of an amplified balanced photoreceiver OEIC, based on InP, comprising two waveguide integrated photodiodes and a broadband distributed amplifier is presented. The integration of the distributed amplifier provides about 12 dB of additional power gain and ensures a low output reflection, guaranteeing a good signal integrity in conjunction with subsequent electronics.

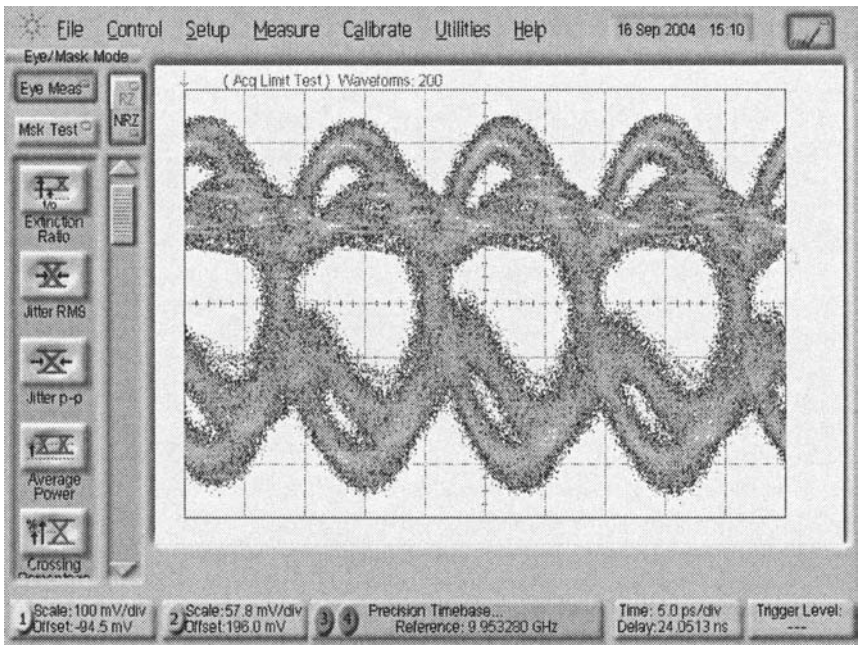

Fig. 33. *pin*TWA module output eye pattern of an o/e-converted 80-Gbit/s PRBS $2^7 - 1$ RZ optical input signal (+5 dBm), fed into the *pin*TWA module; $V_p \sim 160$ mV.

8.2. Balanced Receiver: Circuit Design and Fabrication

The InP-based balanced photoreceiver comprises the integration of two waveguide integrated photodiodes with spot size converters and a HEMT-based traveling wave amplifier (TWA). The circuit scheme of the OEIC is shown in Fig. 34. The *p-i-n* photodiodes PD1 and PD2 are connected electrically in an anti-parallel configuration and are biased by means of integrated bias circuits. The amplifier's DC current is fed into the terminal V_{dd}, which might be blocked additionally at the ceramic board in the packaged module with larger capacitors (100 nF) to GND, to provide a flat low-frequency gain down to 30 kHz. Concerning the circuit scheme at the output, the amplifier's RF output is still DC-coupled to the subsequent electronics, but the amplifier's source bias return path is DC-decoupled from the RF output GND employing an on-chip MIM capacitor of 100 pF. Owing to the applied negative bias at the source terminal the required reverse voltages for the photodiodes $V_{pd1,2}$ are 0 and -4 V, respectively. The supply voltages V_{dd} (+6.1 V) and V_{ss} (~ -2 V at the source terminal) can be fine adjusted to provide an arbitrary DC potential at the DC-coupled TWA output, in order to precisely fit the input specifications of the subsequent amplifier or DEMUX circuitry. By this OEIC design an external bias-T is omitted and the system costs of the photoreceiver operation are considerably reduced.

The OEICs were fabricated employing a two-step MOVPE/MBE epitaxial approach for the PD/HEMT layer stacks, allowing an independent optimization of the

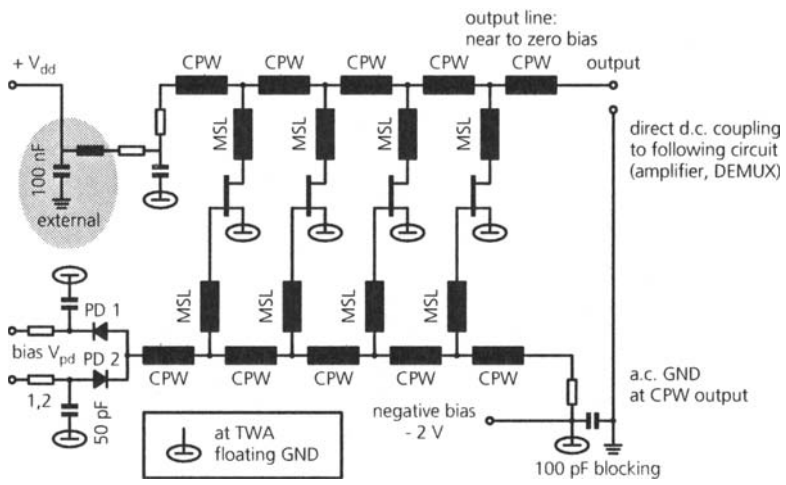

Fig. 34. Circuit scheme, the RF output is still DC coupled to subsequent electronics (post/limiting amplifier or DEMUX).

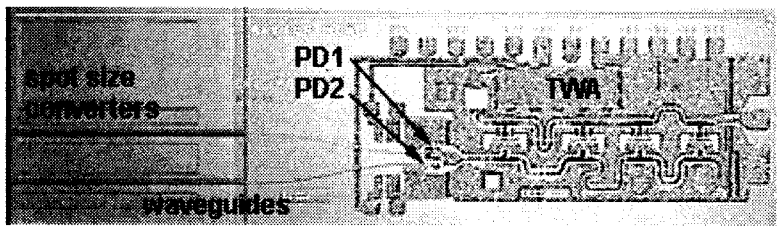

Fig. 35. Micrograph of the balanced photoreceiver chip.

single devices. All devices are integrated on-top of a semi-insulating waveguide layer stack being composed of three quaternary optical guiding layers embedded within InP and an upper thicker waveguide layer. The evanescently coupled photodiodes are grown on-top of this stack within a single MOVPE growth run. After structuring the photodiode, MBE regrowth is applied for the AlInAs/GaInAs lattice-matched HEMT layer stack. The HEMT gate recess and the photodiode mesas are defined by dry chemical etching (RIE). The subsequent MMIC processing includes the formation of the NiCr resistors, MIM capacitors, and metallization for interconnections (coplanar waveguides, microstrip lines) and airbridges. Further details on the processing are published in [12]. The finished OEIC with a chip area of $800 \times 3700\ \mu m^2$ is shown in Fig. 35.

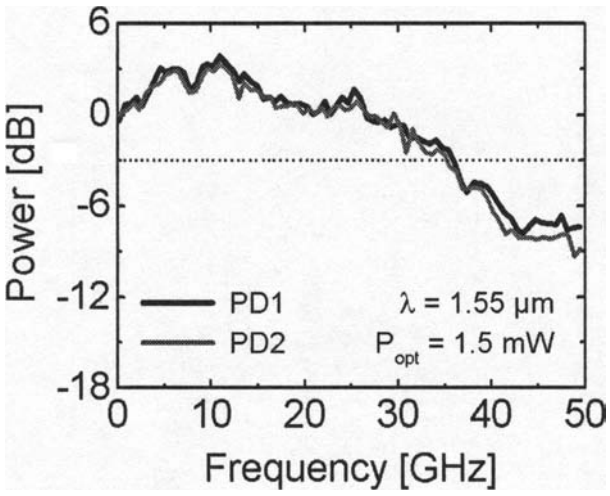

Fig. 36. Opto-electronic frequency response of the receiver, illuminating PD1 and PD2 separately.

8.3. Balanced Receiver OEIC Characterization

Using on-wafer probing techniques, network analyzer measurements of the integrated distributed amplifier within the monolithic balanced photoreceiver OEIC were performed up to 80 GHz. An averaged transimpedance of 40 dBΩ was derived from S-parameter measurements over a bandwidth of 50 GHz, which is somewhat higher than assumed in the circuit simulator before layout generation.

The electrical output reflection S_{22} was determined to be less than -10 dB over the entire bandwidth, assuring a good signal integrity in connection with subsequent electronics.

Figure 36 shows the relative opto-electronic frequency response of the OEIC, measured with a heterodyne setup at 1.55 μm wavelength. Illuminating only one PD at a time, a high symmetry of the o/e conversion capability is observed, which is essential for a high common-mode rejection ratio. The 3-dB cut-off frequency was determined to be 36 GHz. The DC responsivity amounts to 0.35 A/W per diode with a polarization dependent loss of less than 0.5 dB. The overall conversion gain of our balanced photoreceiver is greatly enhanced by the distributed amplifier. To elucidate the benefit of this new integration, the comparable value of the conversion gain of a simple balanced diode pair comprising a 50-Ω termination is calculated as 0.35 A/W $\times$ 25 Ω = 8.75 V/W. In the monolithic balanced receiver OEIC the conversion gain to be compared, amounts to 0.35 A/W $\times$ 100 Ω (averaged transimpedance over 36 GHz) = 35 V/W. This value is 4 times the value of a simple balanced detector, thus providing additional 12 dB of signal output power.

Figure 37 shows the pulse response, illuminating both photodiodes in the photoreceiver separately. In both cases we observe pulse widths of less than 14 ps at an amplitude of 0.8 V and negligible ringing (10%). To estimate the measured frequency

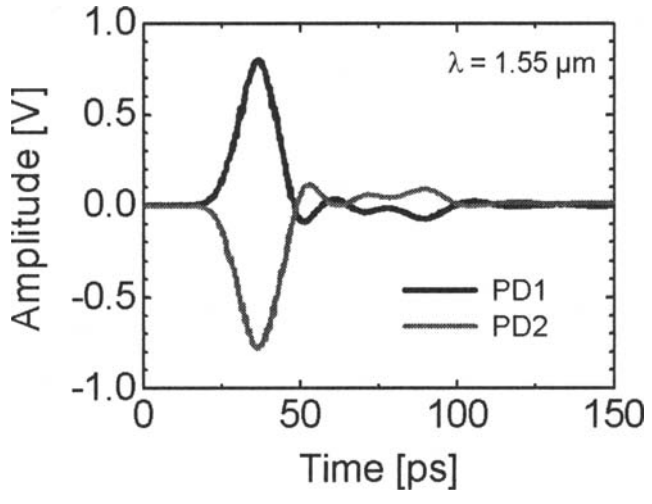

Fig. 37. Pulse response of the photoreceiver, measured with a 50-GHz sampling scope (FWHM of optical input pulses < 4 ps), illuminating PD1 and PD2 separately.

conversion behavior shown in Fig. 36 with respect to the eye pattern opening at 40 Gbit/s modulation format, the phase of the receiver was calculated by Hilbert's transform. With known magnitude from the heterodyne measurement and calculated phase an electrical output eye pattern of the balanced receiver at 40 Gbit/s NRZ modulation format was synthesized by applying established FFT/IFFT methods [20]. The eye pattern at 40 Gbit/s, applying 1024 bits of a PRBS NRZ data stream, is well opened, thus demonstrating a sufficient quality of the conversion gain behavior over a bandwidth of 40 GHz (Fig. 38).

Real NRZ-modulated eye pattern measurements, confirming very well these estimations, have been deduced from packaged balanced receiver OEICs and are published in [48], also the stable output eye quality and conversion gain characteristics vs. the dynamical input power range from -7 to $+7$ dBm is demonstrated in this reference.

9. Summary and Outlook

Ultra-wideband waveguide-integrated photodetector modules based on a waveguide-integrated *pin* photodiode with a responsivity of 0.63 A/W and 0.64 dB PDL were fabricated with 3 dB bandwidths of 85–100 GHz. The detected eye diagrams at 80 Gbit/s RZ data rates are well opened up to peak voltages of about 0.6 V. This value is twice as much as required by state-of-the-art demultiplexing electronics. At 160 Gbit/s a clearly opened eye pattern with an amplitude of 0.3 V was detected. These results demonstrate the potential of the *pin* photodetector module for the use in RF microwave links and ultra high-speed communication systems at 100 Gbit/s (e.g., 100 GE) and beyond.

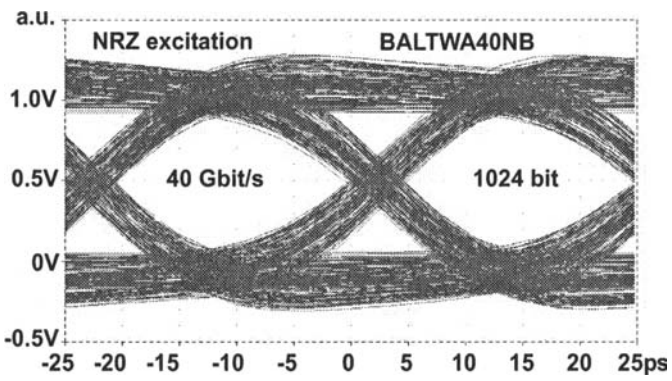

Fig. 38. Synthesized eye pattern at 40 Gbit/s NRZ ASK modulation format for the monolithic balanced photoreceiver OEIC (x: 5 ps/div, y: a.u.).

Narrowband photodetectors with internal gain values of 7 dB, provided by a passive impedance transforming CPW-based network, have been fabricated for a variety of applications with operating frequencies of 40/60/80/85 GHz. A high conversion efficiency up to 1 A/W and excellent high power linear behavior up to +14 dBm optical input power were demonstrated. A slight resonance tuneability with biasing voltage was shown, giving the possibility to adapt the resonant photodetector modules to specific applications. The resonant peak was proven to be stable with respect to the frequency position under variation of the optical input power up to +12 dBm. The output return loss was better than 10 dB under all optical input power operating conditions up to + 12 dBm.

Integrated differential photodetector modules with 35 GHz and 45 GHz electrical bandwidth were fabricated and characterized. The devices show total responsivities of 0.41 A/W and 0.31 A/W respectively and a PDL of less than 0.5 dB. The ratio of the photocurrents remains below 0.5 dB for different states of polarization demonstrating an excellent electrical and optical symmetry. The modules deliver high electrical output pulses of differential polarity in the 1-V regime to switch directly all known 40 Gbit/s demultiplexing electronics implemented in SiGe, GaAs or InP technology.

Fully packaged monolithically integrated balanced photodetectors were fabricated and characterized. The responsivities amount up to 0.5 A/W per PD. The modules show 3-dB cut-off frequencies in excess of 34 GHz and pulse widths of 15 ps. Recent balanced detector OEICs have been optimized up to 70 GHz bandwidth.

A novel *pin*TWA photoreceiver OEIC for 80/85 Gbit/s system applications was reported, which exhibits a bandwidth of 72 GHz and a conversion gain of 45.4 V/W. The photoreceiver OEIC was packaged into a module with 1 mm connector. The module exhibits o/e frequency characteristics comparable to the chip itself. Well opened eye diagrams were demonstrated at 80 Gbit/s NRZ and RZ modulation format. A monolithically integrated balanced *pin*TWA photoreceiver based on InP, comprising two waveguide integrated photodiodes with spot size converters and an integrated dis-

tributed amplifier was presented. The advantage of the broadband amplifier integration results in an additional 12 dB power gain and a low electrical output reflection. The OEIC exhibits a 3-dB bandwidth of 36 GHz and delivers electrical pulses with a differential pulse amplitude of $V_{pp} = 1.6$ V. A high symmetry of the o/e conversion capability and well opened eye pattern for 40 Gbit/s NRZ modulation format were demonstrated.

9.1. Outlook: 160 Gbit/s Data Rate O/E Front-Ends Using Photodiodes and Photoreceivers

Both active components, constituting an envisaged 160 Gbit/s data rate front-end, i.e., an evanescently coupled waveguide-integrated photodiode and a distributed amplifier, have a very promising broadband frequency potential clearly exceeding 100 GHz. Using the waveguide-integrated photodiodes of section 5.1, 160 Gbit/s data rates can already be o/e-converted. Corresponding electrically multiplexing and demultiplexing circuits for 80/85 Gbit/s are now realizable applying SiGe [62,63] or InP-based technology for digital circuits (HBT-based as well as HEMT-based [45]). For even higher bit rates (160 Gbit/s) the TWA concept will still be preserved [46], but now using further reduced HEMT gate lengths in the 80-nm range, for the photodiode the evanescent coupling may be complemented by a traveling wave design.

Acknowledgment

The author acknowledges contributions from his colleges A. Beling, W. Ebert, Th. Eckhardt, H. Ehlers, R. Gibis, G. Jacumeit, R. Kunkel, G.G. Mekonnen, W. Passenberg, G. Sahin, W. Schlaak, D. Schmidt, A. Seeger, R. Steingrüber, M. Stollberg, and P. Wolfram of the receiver team at FhI for telecommunications, Heinrich-Hertz-Institut, the assistance of students A. Becker, V. Eisner, R. Hesse, J. Jayasooriya, S. Jatta, and D. Tomecki for measurements, the measurement expertise of C. Schubert and S. Ferber of the OTDM group as well as contributions of former colleagues C. Schramm, A. Umbach, G. Unterbörsch and R. Ziegler (now with u2t Photonics AG, Berlin) and of Th. Engel (now with Siemens AG, Berlin). Special thanks are due to our industry partners B. Schmauß at Lucent Technologies, Nürnberg and B. Wedding, G. Veith, B. Franz at Alcatel SEL AG, Stuttgart and E. Gottwald and C.-J. Weiske at Siemens AG, ICN, Munich for valuable suggestions and system characterizations in TDM- and ETDM based test beds. This work was financed under the KomNet and MultiTeraNet programmes of the german BMBF and by the Senate of Berlin.

References

1. Kash N. Kashima, *Optical Transmission for the Subscriber Loop* (Artech House, Inc. Boston, London, 1993), pp. 57–65.
2. K. Kato, Ultrawide-Band/High-Frequency Photodetectors, IEEE Trans. MTT, **47** (7), 1265–1281 (1999).

3. J. Bowers and C. Burrus, Ultrawide-band long-wavelength p-i-n photodetectors, J. Lightwave Technol., **LT-5**, 1339–1350 (1987).
4. E.H. Böttcher, E. Dröge, D. Bimberg, A. Umbach, H. Engel, and M. Collischon, Polarization dependence of the response of micrometer and submicrometer InGaAs metal-semiconductor-metal photodetectors, IEEE Photon. Techn. Lett., **9**, 809–811 (1997).
5. K. Taguchi, InAlGaAs/InAlAs Quaternary Well Superlattice Avalanche Photodiodes (APDs), Proc. 22nd ECOC (1996), Vol. 1, Oslo, Norway, paper MoC.4.3.
6. J. Gowar, *Optical Communication Systems* (Prentice-Hall, New York, 1993), second edition, ISBN 0-13-638727-6.
7. A. R. Hawkins, Silicon-Indium-Gallium-Arsenide Avalanche Photodetectors, dissertation, UCSB, Dec. 1998.
8. H. Ito, T. Furuta, S. Kodama, and T. Ishibashi, InP/InGasAs uni-travelling-carrier photodiode with 310 GHz bandwidth, Electron. Lett., **36** (21), 1809–1810 (2000).
9. H. Fukano, Y. Muramoto, K. Takahata, and Y. Matsuoka, High efficiency edge-illuminated uni-travelling-carrier-structure refracting-facet photodiode, Electron. Lett., **35** (19), 1664–1665 (1999).
10. T. Furuta, T. Ito, Y. Muramoto, M. Tokumitsu, H. Ito and T. Ishibashi, D-band Rectangular-Waveguide-Output Uni-Traveling-Carrier Photodiode Modules, Proceedings 5, 30th Europ. Conf. on Optical Communications (ECOC 2004) Stockholm, Sweden, 5–9. Sept., paper Mo4.4.2 (2004), pp. 82–83.
11. C. Lenox, H. Nie, P. Yuan, G. Kinsey, A.L. Homles, Jr., B.G. Streetman, and J.C. Campbell, Resonant-Cavity InGaAs-InAlAs Avalanche Photodiodes with Gain-Bandwidth Product of 290 GHz, IEEE Photon. Lett., **11**, 1162–1164 (1999).
12. H.-G. Bach, A. Beling, G. G. Mekonnen, and W. Schlaak, Design and fabrication of 60-Gb/s InP-based monolithic photoreceiver OEICs and Modules, IEEE J. Select. Topics Quantum Electron., **8**, 1445–1450 (2002).
13. K. Kato, A. Kozen, Y Muramoto, Y. Itaya, T. Nagatsuma, and M. Yaita, 110-Ghz, 50% Efficiency Mushroom-Mesa Waveguide p-i-n Photodiode for a 1.55 μm Wavelength, IEEE Photon. Technol. Lett., **6** (6), 719–721 (1994).
14. Y. Muramoto, K. Yoshino, S. Kodama, Y. Hirota, H. Ito, and T. Ishibashi, 100 and 160 Gbit/s operation of uni-travelling carrier photodiode module, Electron. Lett., **40** (6), 378–380 (2004).
15. A. Umbach, D. Trommer, G.G. Mekonnen, W. Ebert and G. Unterbörsch, Waveguide Integrated 1.55 μm Photodetector with 45 GHz Bandwidth, Electron. Lett. **32**, 2143–2145 (1996).
16. G. Unterbörsch, D. Trommer, A. Umbach, R. Ludwig, and H.-G. Bach, High-Power Performance of a High-Speed Photodetector, Proc. 24th Europ. Conf. on Optical Communication (ECOC '98), (Madrid, Spain), Sept. 20–24, 1998, ISBN 84-89900-15-9, vol. 1, pp. 67–68.
17. A. Umbach, Th. Engel, H.-G. Bach, S.v. Waasen, E. Dröge, A. Strittmatter, W. Ebert, W. Passenberg, R. Steingrüber, W. Schlaak, G.G. Mekonnen, G. Unterbörsch, D. Bimberg, Technology of InP-Based 1.55 μm Ultrafast OEMMICs, 40 Gbit/s Broadband and 38/60 GHz Narrow-Band Photoreceivers, IEEE J. Quantum Electron., **35** (7), 1024–1031 (1999).

18. H.-G. Bach, A. Beling, G. G. Mekonnen, R. Kunkel, D. Schmidt, W. Ebert, A. Seeger, M. Stollberg, and W. Schlaak, InP-Based Waveguide-Integrated Photodetector with 100 GHz Bandwidth, invited paper in IEEE J. Select. Top. Quantum Electron. Photodetect. Imag., **10** (4), 668–672 (2004).

19. M. Achouche, V. Magnin, J. Harari, F. Lelarge, E. Derouin, C. Jany, D. Carpentier, F. Blache, and D. Decoster, High performance evanescent edge coupled waveguide unitraveling-carrier photodiodes for > 40-Gb/s optical receivers, IEEE Photon. Technol. Lett., **16**, 584–586 (2004).

20. H.-G. Bach, W. Schlaak, G. Unterbörsch, G.G. Mekonnen, G. Jacumeit, R. Ziegler, R. Steingrüber, A. Seeger, Th. Engel, A. Umbach, C. Schramm, W. Passenberg, 40 Gbit/s Photoreceiver Modules Comprising InP-OEICs for RZ and NRZ Coded TDM System Applications, Technical Digest, OFC'99/IOOC, Feb 21–26, 1999, San Diego, paper TuI5, pp. 108–110.

21. A. Beling, H.-G. Bach, G.G. Mekonnen, T. Eckhardt, R. Kunkel, G. Jacumeit, M. Kroh, and J. Berger, Fully Packaged InP-based Photodetector for 80/85 Gbit/s RZ Systems, Proceedings 29th European Conference on Optical Communication (ECOC 2003), September 21–25, 2003, Rimini, Italy, Vol. 6, pp. 82–83.

22. H. Ito, T. Nagatsuma, A. Hirata, T. Minotani, A. Sasaki, Y. Hirota, and T. Ishibashi, High-Power photonic millimetre wave generation at 100 GHz using matching-circuit-integrated uni-travelling-carrier photodiodes, IEE Proc.-Optoelectron., **150** (2), 138–142 (2000).

23. Th. Engel, E. Dröge, G. Unterbörsch, E.H. Böttcher, D. Bimberg, Reactive Matching of Millimeter-Wave Photodetectors Using Coplanar Waveguide Technology, IEE Electron. Lett., **34** (17), 1690–1691 (1998).

24. D. Trommer, R. Steingrüber, R. Löffler, A. Umbach, Ultrafast, High-Power Waveguide Fed Photodetector with Integrated Spot Size Converter, Proc. Of the 12th Int. Conf. On InP and Rel. Mat. (IPRM 2000), Williamsburg, VA, USA, 2000, paper WA2.

25. A. Umbach, G. Unterbörsch, D. Trommer, C. Schramm, G. G. Mekonnen, C.-J. Weiske, Integrated Differential Photoreceiver for 40 Gbit/s Systems, Proc. Of the 12th Int. Conf. On InP and Rel. Mat. (IPRM'00), Williamsburg, VA, USA, 2000

26. P. J. Winzer and S. Chandrasekhar, Influence of optical filtering on return-to-zero differential phase shift keying (RZ-DPSK), 28th European Conference on Optical Communication (ECOC 2002), paper 9.6.7, Copenhagen, Denmark, Sept. 8–12, 2002.

27. M. Rohde, C. Caspar, N. Heimes, M. Konitzer, E.-J. Bachus and N. Hanik, Robustness of DPSK direct detection transmission format in standard fiber WDM systems, Electron. Lett., **36** (17), 1483–1484 (2000).

28. M. S. Islam, T. Chau, S. Mathai, T. Itoh, M. C. Wu, D. L. Sivco, and A. Y. Cho, Distributed Balanced Photodetectors for Broad-Band Noise Suppression, IEEE Trans. Microwave Theory Tech., **47**, 1282–1287 (1999).

29. A. Beling, H.-G. Bach, G.G. Mekonnen, T. Eckhardt, R. Kunkel, D. Schmidt, and C. Schubert, Highly Efficient *pin* Photodetector Module for 80 Gbit/s and Beyond, to be published in Tech. Digest Optical Fiber Commun. (OFC 2005), Anaheim, CA, USA, paper OFM1, March 6–11, 2005.

30. H.-G. Bach, A. Beling, G. G. Mekonnen, D. Schmidt, W. Schlaak, R. Kunkel, A. Seeger, M. Stollberg, R. Steingrüber, W. Ebert, and Th. Eckhardt, Highly Efficient InP-Based Narrowband Photodetectors for 40 to 85 GHz Linear High Power Applications, Proc. of 16th Intern. Conf. on InP and Related Materials (IPRM 2004), May 31–June 6, 2004, Kagoshima, Japan, paper WA3-5, pp. 527–530.
31. A. Beling, D. Schmidt, H.-G. Bach, G. G. Mekonnen, R. Ziegler, V. Eisner, M. Stollberg, G. Jacumeit, E. Gottwald, C.-J. Weiske, A. Umbach, High power 1550 nm twin-photodetector modules with 45 GHz bandwidth based on InP, Tech. Digest Optical Fiber Commun. (OFC 2002) , March 17–22, 2002, Anaheim, CA, USA, paper WN4, pp. 274–275.
32. A. Beling, H.G. Bach, D. Schmidt, G.G. Mekonnen, M. Rohde, L. Molle, H. Ehlers, A. Umbach, High-Speed Balanced Photodetector Module with 20dB Broadband Common-Mode Rejection Ratio, Tech. Digest Optical Fiber Commun. (OFC 2003), Atlanta, GA, USA, vol. 1, pp. 339–340, paper WF4, March 23–28, 2003.
33. A. Beling, H.-G. Bach, D. Schmidt, G.G. Mekonnen, R. Ludwig, S. Ferber, C. Schubert, C. Boerner, B. Schmauss, J. Berger, C. Schmidt, U. Troppenz and H.G. Weber, Monolithically integrated balanced photodetector and its application in OTDM 160 Gbit/s DPSK transmission, Electron. Lett., **39** (16), 1204–1205 (2003).
34. Th.T.Y. Wong, *Fundamentals of Distributed Amplification* (Artech House, Boston, London, 1993), pp. 239–241.
35. Tran van Muoi, Receiver Design for High-Speed Optical-Fiber Systems, J. Lightwave Technol., **LT-2** (3), 243-265 (1984).
36. P.O. Haugsjaa, Packaging of Optoelectronic Components (Foster-Miller, Inc.), Short Course 133, 25th OFC, Optical Fiber Conference, March 5–10 (2000), Baltimore, USA.
37. H.-G. Bach, W. Schlaak, G.G. Mekonnen, A. Umbach, C. Schramm, G. Unterbörsch, and W. Passenberg, 40 GHz InP-based Photoreceiver OEICs, Application for 40 Gb/s TDM Systems and Beyond, Invited paper at the Integrated Photonics Research (IPR'2000), July 12–15, 2000, Technical Digest of IPR'2000, paper IThG6, pp. 141–143, Hilton Hotel, Quebec City, Canada.
38. H.-G. Bach, 40 Gbit/s Photoreceivers, Development of Rx-OEICs and Module Technology for Industry Partners within the KomNet Programme, Digest of the SODC 2002, Second Joint Symposium on Opto- and Microelectronic Devices and Circuits, March 10–16, 2002, Stuttgart, Germany, M. Berroth (Editor), pp. 42–46.
39. G.G. Mekonnen, H.-G. Bach, W. Schlaak, R. Steingrüber, A. Seeger, W. Passenberg, W. Ebert, G. Jacumeit, Th. Eckhardt, R. Ziegler, and A. Beling, 40 Gbit/s Photoreceiver with DC-Coupled Output and Operation without Bias-T, 14th Intern. Conf. on InP and Related Materials (IPRM 2002), May 12–16, 2002, Stockholm, Sweeden, paper A8-1.
40. H.-G. Bach, Monolithic Photoreceivers for 60 Gbit/s and Beyond, the 16th Annual Meeting of the IEEE Lasers & Electro-Optics Society "IEEE LEOS 2003", 26.10.–30.10. 2003 in Tucson, Arizona, USA, invited paper ThZ1, proceedings, pp. 991–992.

41. G.G. Mekonnen, W. Schlaak, H.-G. Bach, R. Steingrüber, A. Seeger, Th. Engel, W. Passenberg, A. Umbach, C. Schramm, G. Unterbörsch, S. van Waasen, 37-GHz Bandwidth InP-Based Photoreceiver OEIC Suitable for Data Rates up to 50 Gb/s, IEEE Photon. Technol. Lett., **11** (2), 257–259 (1999).

42. H.-G. Bach, A. Umbach, S. van Waasen, R.M. Bertenburg, G. Unterbörsch, Ultrafast monolithically integrated InP-based photoreceiver: OEIC-design, fabrication, and system application, Special Issue of IEEE J. Select. Top. Quantum Electron. Integrat. Opt. (JSTQE), **2** (2), 418–423 (1996).

43. W. Schlaak, G.G. Mekonnen, H.-G. Bach, C. Bornholdt, C. Schramm, A. Umbach, R. Steingrüber, A. Seeger, G. Unterbörsch, W. Passenberg, and P. Wolfram, "40 Gbit/s Eyepattern of a Photoreceiver OEIC with Monolithically Integrated Spot Size Converter", Technical Digest, OFC 2001, Mar 17–22, 2001, Anaheim, CA, USA, paper WQ4, pp. 1–3.

44. G.G. Mekonnen, H.-G. Bach, W. Schlaak, R. Steingrüber, A. Seeger, W. Passenberg, W. Ebert, G. Jacumeit, Th. Eckhardt, R. Ziegler, and A. Beling, 40 Gbit/s Photoreceiver with DC-Coupled Output and Operation without Bias-T, 14th Intern. Conf. on InP and Related Materials (IPRM 2002), May 12–16, 2002, Stockholm, Sweden, paper A8-1.

45. K. Murata, K. Sano, S. Sugitani, H. Sugahara, and T. Enoki, 100 Gbit/s multiplexing and demultiplexing IC operations in InP HEMT technology, Electron. Lett., **38** (24), (2002).

46. M. Rodwell, D. Mensa, Q. Lee, B. Agarwal, R. Pullela, J. Guthrie, S. Jaganathan, T. Mathew, High-Densitiy Mixed-Mode Microwave Integrated Circuits for Radar and Communication Systems, Final Report MICRO, University of California (www.ucop.edu/research/micro/96_97/96_080.pdf), 1996.

47. A.H. Gnauck, S. Chandrasekhar, J. Leuthold, and L. Stulz, Demonstration of 42.7 Gb/s DPSK receiver with 45 photons/bit sensitivity, IEEE Photon. Technol. Lett., **15** (1), 99–101 (2003).

48. C. Schramm, G. Unterbörsch, G. Jacumeit, R. Ziegler, H.-G. Bach, G.G. Mekonnen, A. Beling, 40 Gbit/s Balanced Photoreceiver Module, Proceedings 1, 30th Europ. Conf. on Optical Communications (ECOC 2004) Stockholm, Sweden, 5–9. Sept., paper Mo4.4.1 (2004), pp. 80–81.

49. I.V. Kaminow, Th.L. Koch (Editors), *Optical Fiber Telecommunications IIIB* (Academic Press, San Diego, London, 1997).

50. G.P. Agrawal, *Fiber-Optic Communication Systems, 2. Auflage* (John Wiley & Sons, Inc. New York, Toronto, 1997).

51. K.J. Ebeling, *Integrierte Optoelektronik* (Springer-Verlag Berlin, 1993).

52. J. Gowar, *Optical Communication Systems* (Prentice Hall, New York, 1993), zweite Auflage, ISBN 0-13-638727-6.

53. S.D. Personick, Receiver Design for Digital Fiber Optic Communication Systems, I, Bell Syst. Techn. J., **52** (6), 843–874 (1973).

54. S.D. Personick, Receiver Design for Digital Fiber Optic Communication Systems, II, Bell Syst. Techn. J., **52** (6), 875–886 (1973).

55. R.G. Smith and S.D. Personick, Receiver Design for Optical Fiber Communication Systems, Top. Appl. Phys. Bd. 39, **33**, 89–160 (1980).

56. Tran van Muoi, Receiver Design for High-Speed Optical-Fiber Systems, J. Lightwave Technol., **LT-2** (3), 243–265 (1984).

57. J. Franz, *Optische übertragungssysteme mit überlagerungsempfang* (Springer-Verlag, Berlin, 1988).

58. Th.T.Y. Wong, *Fundamentals of Distributed Amplification* (Artech House, Boston, London, 1993), pp. 239–241.

59. R. Müller, *Rauschen* (Springer-Verlag, Berlin, 1990), ISBN 3-540-51145-8, 2. Auflage.

60. G. Gronau, *Rauschparameter- und Streuparameter-Meßtechnik, Eine Einführung* (Verlagsbuchhandlung Nellissen-Wolff, Aachen, 1992).

61. D.P. Seraphim, R.C. Lasky, and Che-Yu Li (Eds), *Principles of Electronic Packaging* (McGraw-Hill, New York,Toronto, 1990).

62. M. Meghelli, A 108 Gbps 4:1 multiplexer in 0.13 mm SiGe-bipolar Technology, ISSCC Digest, Feb. 2004, Paper 13.3.

63. A. Joseph, D. Coolbaugh, D. Harame, G. Freeman, S. Subbanna, M. Doherty, J. Dunn, C. Dickey, D. Greenberg, R. Groves, M. Meghelli, A. Rylyakov, M. Sorna, O. Schreiber, D. Herman, T. Tanji, 0.13 mm 210 GHz fT SiGe HBTs—expanding the horizons of SiGe BiCMOS, ISSCC, 2002, pp. 180–181.

DOI: 10.1007/s10297-004-0027-8
Originally published in J. Opt. Fiber Commun. Rep. 2, 497–529 (2005)

Optical nonlinearities in semiconductor optical amplifier and electro-absorption modulator: their applications to all-optical regeneration

Masashi Usami and Kohsuke Nishimura
KDDI R&D Laboratories, Inc.
2-1-15 Ohara Fujimino-shi Saitama 356-8502, Japan
Email: usami@kddilabs.jp, nish@kddilabs.jp

Abstract. Semiconductors have large optical nonlinearity with response speed in the several tens of picosecond range, making them ideal use as all-optical regenerators and wavelength converters. We theoretically and experimentally investigated optical nonlinearities induced by carrier dynamics both in forward biased semiconductor waveguide (SOA) and in reverse biased semiconductor waveguide (EAM). We made a detailed theoretical study of carrier dynamics in semiconductor waveguides by using the newly developed time-dependent transfer matrix method. To confirm the simulation results, we propose utilizing a polarization discriminating delayed interferometer (PD-DI) configuration as a simple technique for measuring optical nonlinearities such as cross gain modulation (XGM), cross absorption modulation (XAM), and cross phase modulation (XPM). In the first part of the paper, we reviewed SOA-based regenerators. As expected from the simulation results, we confirmed that injection of the transparent assist light was very effective in reducing of the SOA gain recovery time of down to a few tens of picoseconds. We further demonstrated 40 Gbit/s regeneration using an SOA-one-arm MZI (so-called UNI) configuration. The superior regeneration capability of two-stage UNI was successfully confirmed by a recirculating loop experiment up to 30,000 km with 150 regenerations. In the latter part of the paper, we reviewed all-optical regenerators using EAM. A bit-synchronized rf-driven XAM 3R regenerator consisting of only one EAM for both gating and timing correction was demonstrated at 20 Gbit/s. An EAM in conjunction with delayed interferometer configuration, which utilizes XPM as well as XAM in the EAM, has structurral simplicity and fast regeneration operability up to 100 Gbit/s. The fast response of EAM allows the optical regeneration with a small pattern word effect.

1. Introduction

All-optical signal processing such as all-optical 3R (reamplification, reshaping, retiming) regeneration is a focus of great interest since it enhances the scalability and flexibility of future photonic networks. This is because all-optical regeneration is able to reset network impairments occurring due to channel interaction, noise accumulation of amplified spontaneous emission (ASE), chromatic dispersion, non-linearity of optical fibers and so forth. Unlike electrical 3R regenerators (Optical-Electrical-Optical conversion), all-optical regenerators (Optical-Optical conversion) are likely to be less complex and require fewer high-speed opto-electronic and electronic components since they use optical signal processing, which leads to a small footprint and low power consumption, even if they operate at high bit rate. So far, various types of all optical switching devices utilizing optical nonlinearity of fibers, semiconductor optical amplifiers (SOAs), and electro-absorption modulators (EAMs). All-optical regeneration performance depends on the physics of each optical nonlinearity, which has a respective trade-off between the switching speed and the required optical power for switching. A fiber-based regenerator utilizing the ultrafast third-order optical nonlinearity (Kerr effect) is operated at a high bit rate of 100 Gbit/s or more, but the optical power should be large due to the low efficiency. Optical nonlinearity in semiconductor waveguide induced by the carrier density variation on the other hand has much higher efficiency. The relaxation speed of the optical nonlinearity however is limited by the relatively long carrier life time (recombination time) of several tens of picoseconds. Two mechanisms to accelerate the recovery time of the optical nonlinearity are discussed for higher bit-rate operation and better performance. The first scheme is the injection of transparent assist light into a forward biased waveguide such as semiconductor optical amplifier (SOA), and the second scheme employs a reverse biased waveguide such as an electro-absorption modulator (EAM) in which the carriers are quickly swept out by the external electrical field. The injected light induces carrier density modulation in both types of semiconductor waveguides, with the result that both gain (XGM) [or absorption (XAM)] and phase (XPM) are modulated onto other light propagating in the waveguides. It is very important to qualitatively investigate those optical nonlinearities. However, there are few reports so far on the detailed physics on the optical nonlinearity in semiconductor waveguides. This paper will concentrate on the physics of the optical nonlinearity in SOAs and in EAMs and their applications to all-optical regeneration.

2. Cross Gain Modulation and Cross Phase Modulation in SOA

SOA-based all-optical regenerators have been most widely studied. A simple mechanism for achieving all-optical regeneration is using cross gain modulation (XGM) in a semiconductor optical amplifier (SOA). A CW (continuous wave) light at the desired output wavelength is modulated by the variation in gain, so it carries the same information as intensity modulated input signals. Although simple, the XGM-based regeneration scheme has some drawbacks, such as bit-inversion operation, limited extinction ratio, relatively large frequency chirping and a limited data rate up to 40 Gbit/s. To overcome those problems, SOA-based interferometric all-optical 2R or 3R regenerators were proposed. These regenerators utilize cross phase modulation (XPM)

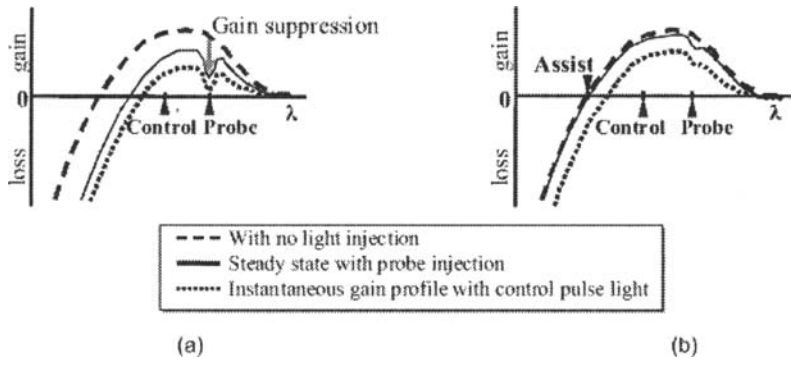

Fig. 1. Schematic viewgraph of gain profile in SOA. (a) Injection of strong probe light and control pulse. (b) Injection of moderate probe light, control pulse light and transparent assist light. Dashed lines show initial gain profile with no external light injection, solid line show gain profile with probe injection, and dotted lines show instantaneous gain profile at control pulse light injection.

induced by a control pulse light onto a probe light. When a control pulse light is injected into the active layer of the SOA, the phase of the probe light is modulated by a refractive index change via carrier depletion. This carrier depletion also induces XGM simultaneously. The carrier density (or gain) recovery time of the SOA which usually ranges over hundreds of picoseconds is a key parameter for the SOA-based switches because the operation speed of the SOA-based switch is limited by the gain recovery time. Therefore an optimum switching condition to obtain the highest extinction ratio and a minimal pattern effect will depend on the interplay of XPM (near π rad phase shift), XGM and the gain recovery time of the SOA. The gain recovery time can be shortened by increasing the injection current or by changing structural parameters of SOA, such as extending the device length or increasing the optical confinement factor. However, too large a current leads to heat dissipation problems as well as degrading the reliability. On the other hand, changing the structural parameter affects not only the gain recovery time but also gain efficiency, saturation power and so on, among which a complicated trade-off exists.

In this section, the carrier dynamics in an SOA is theoretically investigated, which governs XPM, XGM and the gain recovery time. The discussion in particular focuses on how to control and reduce the gain recovery time by injecting nearly transparent assist light. One effective way to reduce the gain recovery time is to increase the probe light intensity, which is called the holding beam effect. [1] However, the strong probe light clamps the gain of the SOA even at the steady state as schematically illustrated in Fig. 1 (a), resulting in lower cross-modulation efficiency. Another way to shorten the gain recovery time is to increase the optical power in the device either by an internal light such as a gain-clamped SOA [2] or by an external light. [3–7] In the latter case, one can set the external (assist) light conditions independently of the SOA conditions. Transparent assist light, which tends to clamp the transparent wavelength

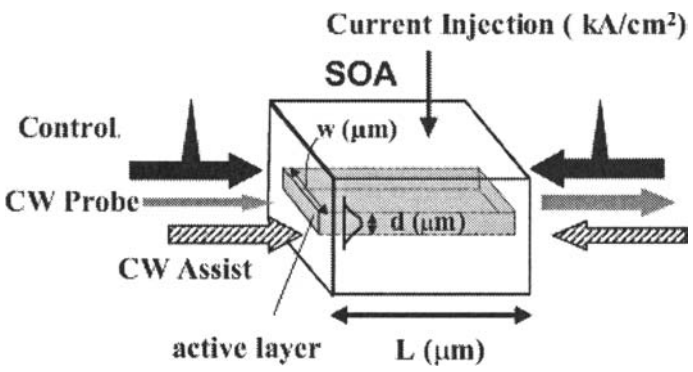

Fig. 2. Simulation model of carrier dynamics in SOA.

of the SOA to its wavelength at the steady state, serves to dynamically stabilize the gain characteristics of the SOA due to its absorption when an injected control pulse light instantaneously suppresses the SOA gain as shown in Fig. 1 (b). This results in the accelerating the gain recovery without suppressing the gain itself.

2.1. Theoretical Study of Carrier Dynamics in SOA Using Time-Dependent Transfer Matrix Method

2.1.1. Analysis Model and Algorithm

Although many theoretical studies have been made on carrier dynamics in SOA for wavelength converters, longitudinal variations in the carrier and photon densities in SOA using multi-section rate equations have rarely been considered. [8–10] The basis of the transfer matrix method (TMM) [11] is dividing a waveguide structure longitudinally into a number of sections where the structural and material parameters are assumed to be homogeneous throughout each section. The time-dependent TMM has been proposed for the purpose of characterizing the multi-electrode distributed feedback laser. [12] The TMM has been modified to be applied to an SOA by taking into account longitudinal variation in the carrier induced refractive index. [13] In order to expand this to handle additional external lights, we have further modified the time-dependent TMM, wherein the gain spectrum is recalculated according to the carrier statistics. A simulation model of carrier dynamics in the SOA is shown in Figs. 2 and 3. The conditions of three input lights of a CW probe (λ_p, P_p), a control pulse (λ_c, pulse energy E_c, pulse width Δt_c), and a CW assist (λ_a, P_a) are also defined. The injection direction of each light to the probe light direction is defined separately.

As a light wave is amplified by an optical gain along a traveling-wave-type SOA, the carrier density and the photon density in the SOA are changed along the longitudinal axis. Figure 3 shows the schematic of the modified time dependent TMM-based simulation model for evaluating the dynamics in the SOA. The SOA is divided into a

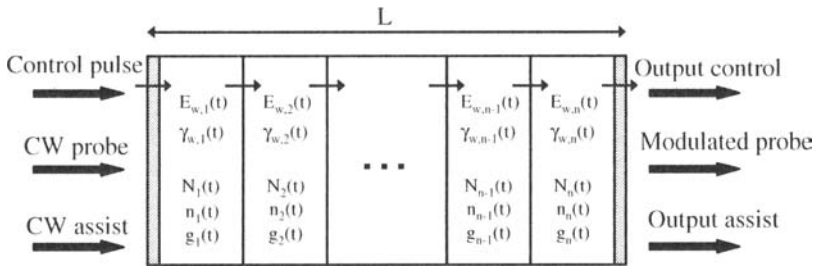

Fig. 3. Schematic of the modified TMM-based dynamic SOA model. The light amplitude E and the propagation constant in a time-space segment are deduced from local gain spectrum.

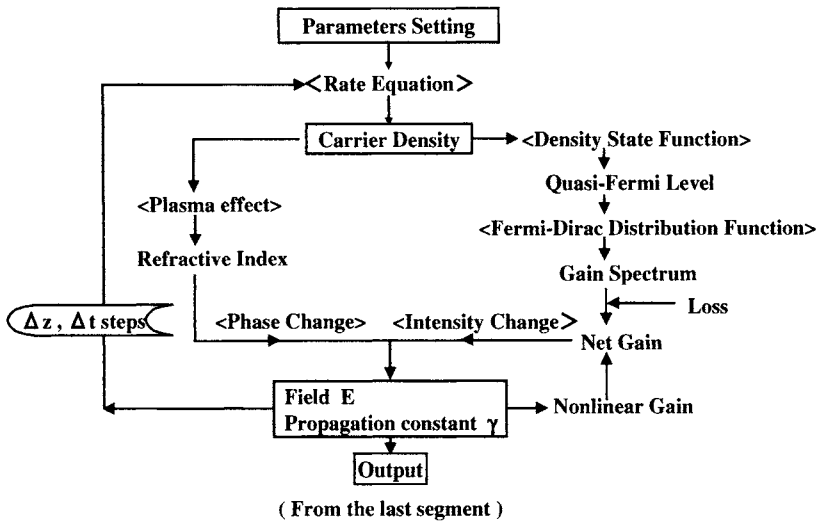

Fig. 4. Flow chart for simulating time and space dependent carrier dynamics in SOA.

series of longitudinal sections, in which a separate rate equations are solved to derive carrier density N through the interaction between carriers and photons. Multiple lights (control pulse, CW probe, and CW assist) are treated in this model, in which an index w refers to each light. Both the light amplitude E and the propagation constant γ in each section are calculated. The flow chart for simulating time and space dependent carrier dynamics in the SOA can be best explained by Fig. 4, which illustrates how the various mechanisms all relate to one another, where the rate equation, density of state function, Fermi-Dirac distribution function, linear and non-linear gain coefficient, refractive index change due to the Kramers-Krönig relation and the plasma effect are combined.

The rate equation is

$$\frac{\partial N}{\partial t} = \frac{I}{qV_a} - N(c_1 + c_2 N + c_3 N^2) - \sum_W \Gamma \nu_g g_w s_w / V_a, \tag{1}$$

where N is the carrier density, I is the injection current, V_a is the volume of active layer, v_g is the group velocity, g is the gain coefficient, s is the photon density, Γ is the optical confinement factor, c_1 is the leakage, c_2 is the radiative recombination, and c_3 is the Auger recombination.

The actual nonlinear gain coefficient calculated by using the dynamically changing quasi-Fermi levels and by also considering the spectral hole burning (SHB), is introduced into a static linear gain model in order to take the influence of fast nonlinear phenomena in an SOA into account. This is calculated by Eqs. (2)–(4).

The gain coefficient is expressed by

$$G_p = G_p^{(1)} - \sum_q G_{p,q}^{(3)} S_q, \tag{2}$$

where $G_p^{(1)}$ is the linear gain coefficient of the mode p, $G_{p,q}^{(3)}$ is the third-order nonlinear gain coefficient of the mode p generated by the other mode q, and S_q is the Photon number of the mode q.

The linear gain based on Fermi-Dirac distribution function is written by

$$G_p^{(1)} = \frac{\pi\omega_p}{n_{\mathrm{eq}}^2 \varepsilon_0} \int_{Eg}^{\infty} < R_{\mathrm{cv}}^2 > [f_c(E_{\mathrm{cv}}) - f_v(E_{\mathrm{cv}})]\, \rho(E_{\mathrm{cv}}) L(E_{\mathrm{cv}} - \hbar\omega_p) dE_{\mathrm{cv}}, \tag{3}$$

where E_{cv} is the transition energy,

$$L(E_{\mathrm{cv}} - \hbar\omega_p) = \frac{1}{\pi} \frac{\hbar/\tau_{\mathrm{in}}}{(E_{\mathrm{cv}} - \hbar\omega_p)^2 + (\hbar/\tau_{\mathrm{in}})^2}$$

is the Lorenzian function.

$\langle R_{\mathrm{cv}}^2 \rangle$ is the matrix element of the dipole moment, $\rho(E_{\mathrm{cv}})$ is the transition density of state, and τ_{in} is the intra-band relaxation time.

The third-order nonlinear gain coefficient is approximated by

$$G_{p,q}^{(3)} \approx \frac{3(2+\delta_{p,q})\xi^2 h\omega_p}{2(1+\delta_{p,q}) V_a n_{\mathrm{eq}}^2 \varepsilon_0} \left(\frac{\tau_{\mathrm{in}}}{\hbar}\right)^2 \frac{\langle R_{\mathrm{cv}}^2 \rangle G'(N - N_g)}{1 + (\tau_{\mathrm{in}}\omega_p/\lambda_q)^2 (\lambda_p - \lambda_q)^2}, \tag{4}$$

where $\delta_{p,q}$ is 1 if $p = q$, or 0 if $p \neq q$, G' is the differential gain, N_g is the carrier density at transparency, and ξ is the optical confinement factor.

The refractive index is also changed by the change in carrier density due to the plasma effect and by gain spectral change through the Kramars- Krönig relations, which determine the phase change of light in the segment. Consequently, a complete parameter set of the carrier density N, the light intensity I (photon density), the phase change of the light ϕ in one segment are obtained. These are the input parameters set in the next segment. A parameter set for the output signal are obtained when this procedure is repeated to the last segment of the SOA,. The probe light is modulated by a control light both in intensity (XGM) and in phase (XPM). Figure 5 (a) shows the schematic carrier density distributions in a segment when three lights are injected. SBH occurs at the instant of control light injection due to stimulated emission, which relaxes to equilibrium Fermi distribution in a few hundred femtoseconds. The assist light wavelength is set nearly at the transparent wavelength. Figures 5 (b) and (c), respectively, show the modal gain spectra and the refractive index spectra. The refractive index is mainly changed by the carrier plasma effect, while it is slightly modulated by the gain spectral change effect.

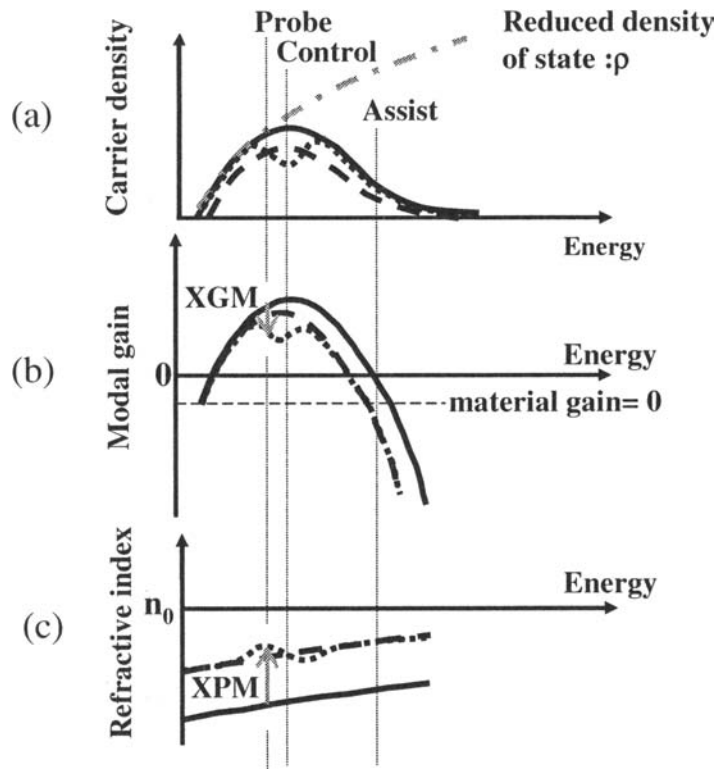

Fig. 5. Schematic spectra in a segment of SOA when the probe light, the control pulse light, and CW assist light are injected. (a) carrier density spectra, (b) modal gain spectra, (c) refractive index spectra. Solid lines show initial state, dashed lines show the condition under the control light injection without consideration of spectral hole burning (SHB), and dotted lines show the condition under the control light injection with SHB effect.

2.1.2. Simulation Results

The time-dependent TMM simulator that takes carrier spectrum distribution into account is a powerful tool for analyzing the dynamics of gain, carrier density, and photon density in SOA. It also can simultaneously handle any input light in either injection direction. In this section, several simulation results relating to accelerating gain recovery process are shown. Principle parameters of the cross modulations in the SOA are the initial amounts of XGM ($\Delta I_0/I_0$) and of XPM ($\Delta\phi_w$), and their recovery time constant (τ), which is defined as the time the XGM recovers to the amount of $1/e$ times the initial value, as shown in Fig. 6. Figure 7 (a) shows output waveforms (i.e., XGM waveforms) for respective SOA lengths of 700, 1000, and 2000 μm. In order to compare operating conditions of interest, the energy for each control pulse is set to a value to induce π phase shift $\Delta\phi$ by XPM. The XGM waveform shows that a longer SOA exhibits a faster recovery time as reported in [14,15]. Figure 7 (b) shows the modal gain in the 2-mm-long SOA at the respective traveling positions of 700,

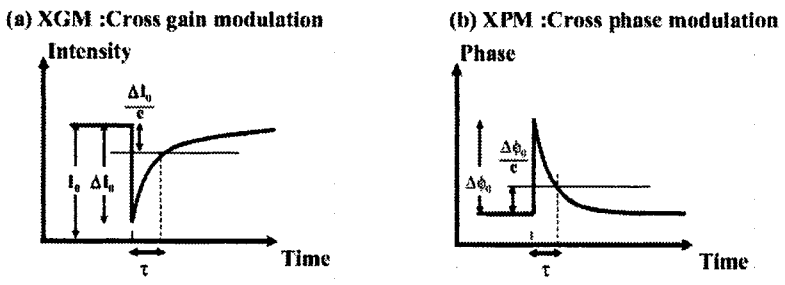

Fig. 6. Definitions of initial values of (a) XGM ($\Delta I_0/I_0$) and of (b) XPM ($\Delta\phi_0$), and their recovery time τ.

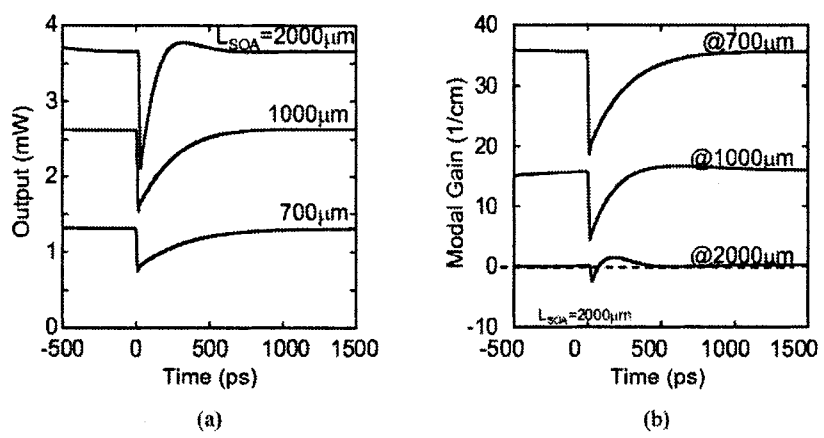

Fig. 7. (a) Output waveforms (i.e., XGM waveforms) for respective SOA lengths of 700, 1000, and 2000 μm; (b) modal gain in the 2-mm-long SOA at respective travel positions of 700, 1000, and 2000 μm.

1000, and 2000 μm (end segment). Gain is drastically suppressed due to the amplified control pulse light as increasing the traveling distance in the SOA. At the end segment of the 2-mm-long SOA, the net gain instantaneously turns to be negative and quickly recovers to become positive, resulting in an overshooting phenomena. This is a kind of relaxation oscillation due to the strong interaction between the large intensity fields and the carriers, and is the cause of the faster recovery time in longer SOA.

Figure 8 shows (a) the XGM waveform, and (b) the modal gain at the output segment of the 700-μm-long SOA with the transparent assist light injection at 13 dBm input power. Results show that the assist light accelerates the gain recovery process even in SOA shorter than 1000 μm, and especially in the counter-propagating configuration. This is explained by the following steps: (1) Gain is suppressed by the amplified control pulse and the suppression is getting larger as traveling length increase. (2) The assist light is absorbed and increase the carrier density in the gain suppressed region of the SOA. This is more efficient in the counter-propagating configuration. (3) The recovered

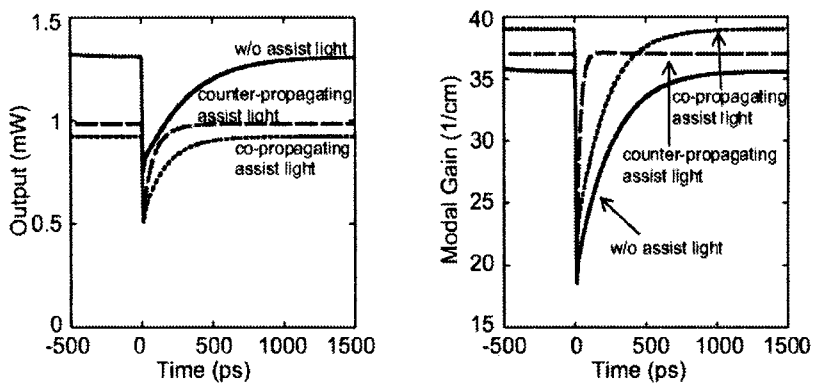

Fig. 8. (a) XGM waveform, and (b) modal gain at the output segment of the 700-μm-long SOA. Conditions are injection of transparent assist light and its direction.

local gain increases the photon density which shortens the effective carrier life time and accelerate the total recovery gain process.

2.2. Measurement of XGM, XPM and Gain Recovery Time in SOA

2.2.1. Measurement Procedure

In this section, experimental evaluations of XGM, XPM and gain recovery time in assist light injected SOA are discussed. [16,17] To evaluate XPM, a simple analysis technique utilizing a polarization discriminating delayed interferometer (PD-DI) was employed, which was originally proposed as a wavelength converter named "delayed interference signal-wavelength converter (DISC)" in [18]. Phase change by XPM and gain suppression by XGM can be individually estimated using this technique.

Figure 9 (a) illustrates the experimental setup, where PD-DI was deployed after the SOA and consists of a highly birefringent (HiBi) fiber and a polarizer. When a control pulse is injected into the SOA, the carrier density depletes instantaneously at $t = 0$, and both the intensity and the phase of the co-propagating CW probe light are modulated as mentioned in the previous section. For simplicity of analysis, both the intensity and the phase of the CW probe light were assumed to recover to the initial state according to a first order exponential decay with the same time constant τ. The evolution of amplified CW probe light power at the output of the SOA as a function of time, $I(t)$, namely the "theoretical XGM waveform," is expressed as

$$I(t) = I_0 \left\{ 1 - \Delta I_0 \exp\left(-\frac{t}{\tau}\right) \right\}, \tag{5}$$

where I_0 is the average power without control pulse, ΔI_0 is the ratio of initial gain suppression caused by the control pulse and τ is the gain recovery time. The XGM waveform measured at point A in Fig. 9 (a) is fit with Eq. (5) taking the least squares method to derive ΔI_0 and τ. In the same manner, the evolution of phase due to the XPM as a function of time, $\Delta\phi(t)$, can be expressed as

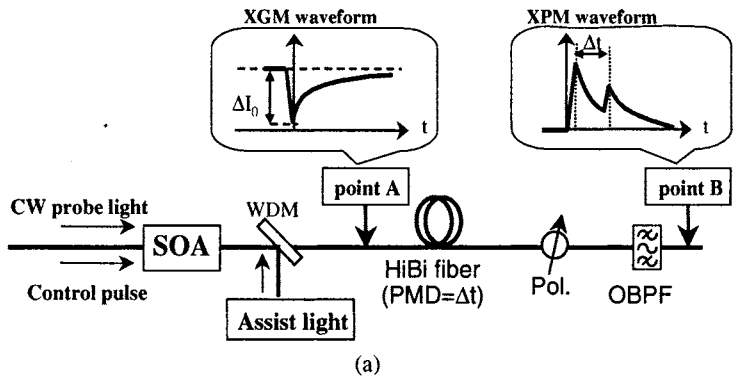

Fig. 9. (a) Measurement setup of XGM, XPM and gain recovery time in SOA; Pol. is the polarizer, and OBPF is the optical band-pass filter. (b) Polarization of CW probe light incident to HiBi fiber and the transparent axis of polarizer.

$$\Delta\phi(t) = \Delta\phi_0 \exp\left(-\frac{t}{\tau}\right), \tag{6}$$

where $\Delta\phi_0$ is the initial phase change of CW probe light caused by injecting the control pulse. ΔI_0 and $\Delta\phi_0$, respectively, represent XGM and XPM. The cross gain and the cross phase modulated probe signal is input to the HiBi fiber with a polarization direction of 45 degrees tilted from the fast axis of the HiBi fiber as shown in Fig. 9 (b). Consequently, the probe light is divided into two orthogonal polarization components with differential group delay (DGD), Δt. During the period of $0 \leq t \leq \Delta t$, only the fast polarization component is affected by both XGM and XPM. The electric field component of each polarization after passing through the HiBi fiber can then be expressed as

$$E_{\text{fast}}(t) = \frac{1}{\sqrt{2}}\sqrt{I(t)}\exp\left[j\Delta\phi\,(t)\right], \tag{7}$$

$$E_{\text{slow}}(t) = \frac{1}{\sqrt{2}}\sqrt{I_0}. \tag{8}$$

In the period $t \geq \Delta t$, the slow polarization component is also affected by both XGM and XPM with a relative time delay of Δt for the fast polarization component. In this period, the electric field of the fast component can also be expressed as Eq. (7). On the other hand, the slow component can be expressed as

$$E_{\text{slow}}(t) = \frac{1}{\sqrt{2}}\sqrt{I(t-\Delta t)}\exp\left[j\Delta\phi\,(t-\Delta t)\right]. \tag{9}$$

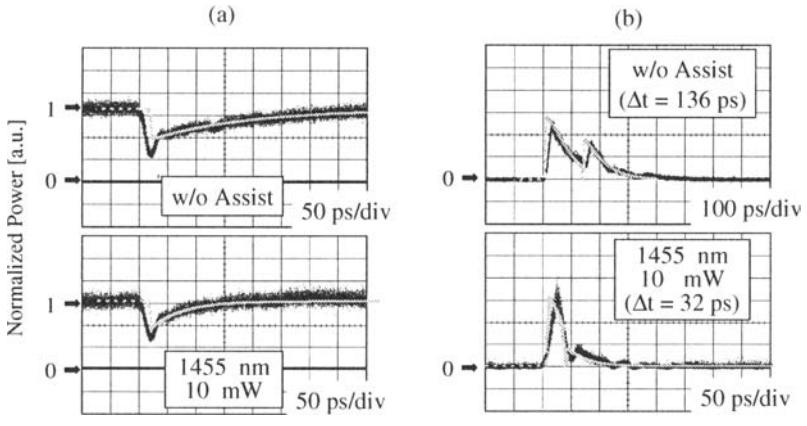

Fig. 10. (a) XGM waveform fitting, (b) XPM waveform fitting.

Consequently, the output signal monitored at point B in Fig. 9 (a), $I_{\text{out}}(t)$, namely "theoretical XPM waveform," is expressed as

$$I_{\text{out}}(t) = \frac{1}{2}\left|E_{\text{fast}}(t) + E_{\text{slow}}(t)\right|^2 . \tag{10}$$

The information of phase change is converted to the intensity change in twin-peaked XPM waveform. The theoretical XPM waveform, employing the values for ΔI_0 and τ that were already derived from the XGM fitting, is fit to the XPM waveform measured at point B. Finally, the initial phase change, $\Delta\phi_0$, is derived.

Figure 10 shows an example of the results of (a) the XGM waveform and (b) XPM waveform for an 800-μm-long InGaAsP/InP bulk type SOA with/without a nearly transparent CW assist light at 1455 nm. With optimized fitting parameters, the theoretical XGM waveforms corresponded well to the measured XGM waveforms. Estimated gain recovery times for respective cases were 174 and 58 ps. By fittings these parameters to the XPM waveform, the respective $\Delta\phi_0$s were estimated to be 0.84π and 0.70π. Consequently, a nearly transparent assist light injection was confirmed to shorten gain recovery time without significantly reducing the XPM efficiency. The accuracy of the phase of XPM in this measurement is less than 0.01 π rad.

2.2.2. Reduction of Gain Recovery Time in SOA by Injection of Transparent Assist Light

Gain recovery time in SOA under various conditions is discussed in this section. Figure 11 shows the gain recovery times of an InGaAsP/InP bulk type SOA. In this figure, the open circles represent the gain recovery time as a function of probe light power without assist light injection, and the closed circles represent it as a function of assist light power with a constant probe light power of -10 dBm. A transparent assist light at 1480 nm was injected from backside of the SOA via an optical circulator. The gain recovery times monotonically decreased with an increase in either the probe light power or the assist light power owing to increased photon density in the active layer. [19]

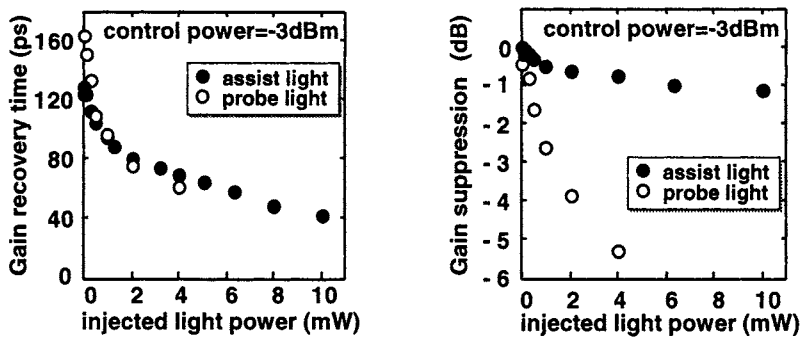

Fig. 11. (a) Gain recovery times as a function of probe light power and assist light power, (b) Gain suppressions as a function of probe light power and assist light power.

Figure 11(b) shows the gain suppression dependent on either the probe light power or the assist light power. The gain suppression was as small as 1 dB even when the assist light power was increased up to 10 mW because the assist light was almost transparent to the SOA, whereas the strong probe light depleted the gain substantially (e.g., 4 mW probe light suppressed the gain by 5.5 dB). As a result, a larger control pulse power is required to induce a refractive index change for a given switching (i.e., π-phase shift). The transparent assist light as a holding beam on the other hand achieves a reduced gain recovery time without increasing the switching power of the control light.

The actual reduction of the pattern effect of the SOA by injecting assist light was observed at 80 Gbit/s in Fig. 12. [20] Figure 12 (a) shows the eye diagram of 80 Gbit/s input data signal generated by 10 Gbit/s-based optical time-division multiplexing, which was captured by sampling oscilloscope equipped with 30 GHz bandwidth photodetector. Figure 12(b) shows the 80Gbit/s amplified output signal of the SOA without assist light injection under severely saturated condition (the input power of 0 dBm). A large pattern effect on the mark level was observed. On the other hand, the pattern effect was sufficiently suppressed by injecting an assist light of 10 mW, as shown in Fig. 12(c).

2.3. All-Optical Regeneration Utilizing SOA-Based Polarization-Discriminating Ultrafast Nonlinear Interferometer (UNI)

So far, various types of SOA-based optical 2R regenerators and 3R regenerators have been proposed and demonstrated with the goal of actual network applications. To achieve these functions operating at a high bit rate, all-optical switches utilizing XPM in SOAs employed in an interferometer have been widely studied. These include an SOA-Mach Zehnder interferometer (SOA-MZI, SMZ) [21–23], an SOA-delayed interferometer (SOA-DI) [10,24] and an SOA-one-arm MZI, which is the so called "ultrafast nonlinear interferometer (UNI)" or "polarization discriminated SMZ (PD-SMZ)". [25–28] Among these, the UNI which employs one SOA, has a simple structure yielding higher interferometer stability and lower power consumption.

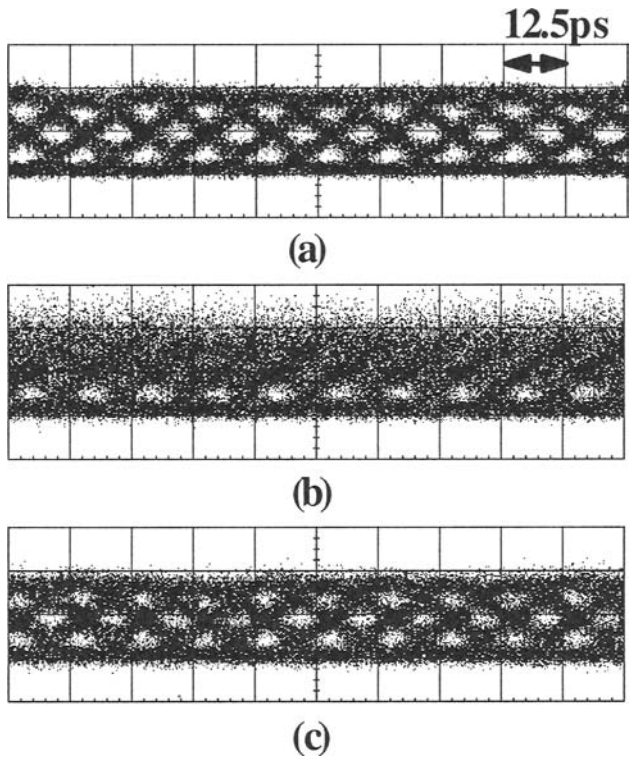

Fig. 12. (a) Eye diagrams of 80 Gbit/s input data signal, (b) output data signal without assist light injection and (c) output data signal with assist light injection.

2.3.1. Optical Regeneration at 40 Gbit/s Operation

Figure 13 shows the experimental setup for 40 Gbit/s optical regeneration using the UNI configuration. [29] The SOA-UNI consists of an SOA and two birefringent TiO_2 rutile crystals with PMD of 10ps as polarization discriminated interferometer. Both a 40-GHz clock pulse at 1555 nm and a 40-Gbit/s PRBS $2^{31} - 1$ data signal at 1545 nm were generated by fiber ring mode-locked lasers with a 10-GHz repetition rate and optical multiplexing. Power intensities of the clock and data pulses supplied to the SOA were -6 and -3 dBm, respectively. Assist light of +10 dBm at 1480 nm was supplied via an optical circulator from the back surface of the SOA. The Babinet-Soleil module was used for precise phase control.

The eye diagrams of the back-to-back signal at 1545 nm, the switched signal at 1555 nm without (case A) and with (case B) assist light injection are shown respectively in Fig. 14(a), (b), and (c). The switched signal without the assist light injection was impaired by the pattern effect on the mark level as observed in Fig. 14(b). As shown in Fig. 14(c), the pattern dependent impairment was suppressed due to the shorter recovery time owing to the assist light injection. The BER results are plotted in Fig. 15. The power penalty of 3.3 dB in case A (without assist light injection), which is

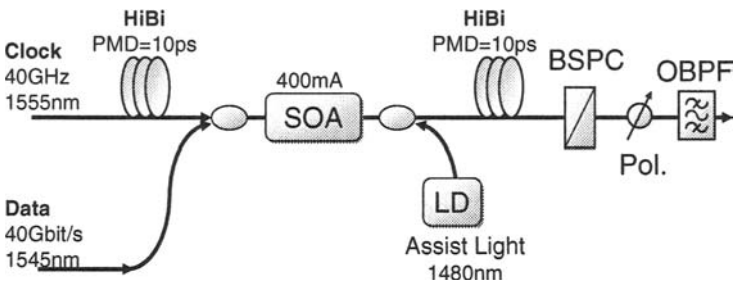

Fig. 13. 40 Gbit/s regeneration experimental setup of ultrafast nonlinear interferometer with assist light injection. HiBi: Highly birefringent medium, BSPC: Babinet Soleil phase compensator, Pol: Polarizer, BPF: Band-pass Filter.

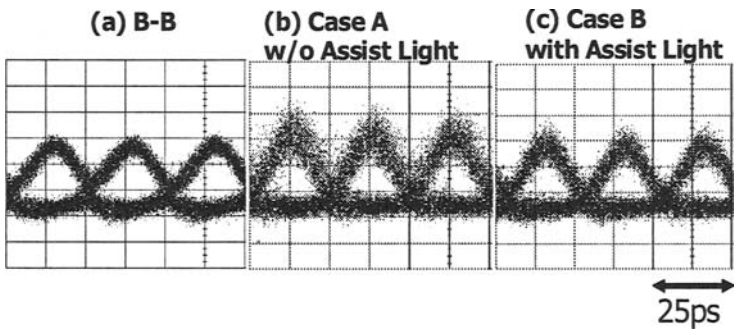

Fig. 14. (a) Eye diagrams of control signal as back-to-back, (b) Case A: regenerated signal without assist light, and (c) Case B: regenerated signal with assist light.

defined at BER = 10^{-9} with reference to the back-to-back, was improved to a level as small as 1.0 dB in case B (with assist light injection). In addition, no error floor was observed in the case of assist light injection, whereas a slight error floor (BER = 10^{-11}) was observed in case A.

2.3.2. Transmission Experiment By Recirculating Loop With 2-Stage UNI

In actual transmission line in the field, various kinds of impairment factors, such as ASE noise from concatenated EDFAs, chromatic dispersion, polarization mode dispersion (PMD) and nonlinear effects in fibers, distort the optical pulse waveform in amplitude, in pulse width and in phase of timing. As much progress has been made in developing all-optical regeneration technology in laboratories, it is now time that we verify their tolerances versus various transmission impairments by actual use in the field. Recently, several reports with this objective have been presented. [23,30] In [31], the transparent assist light injected UNI was confirmed to have relatively large tolerances against

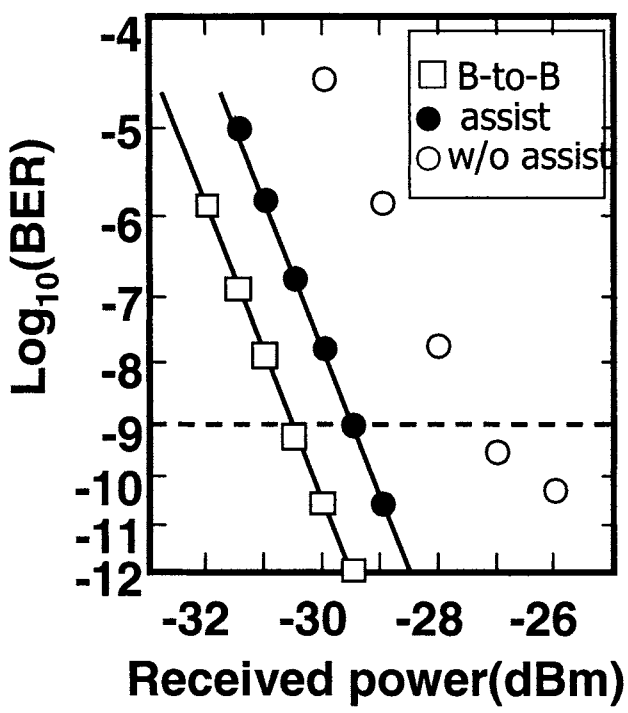

Fig. 15. Bit error rate characteristics of 40 Gbit/s optical regeneration using PRBS $2^{23} - 1$ data.

input power variations of 4.2 dB, timing jitter of 10 ps, and pulse width variations at 40 Gbit/s operation. These results prove that the UNI has the potential for an all-optical regenerator in the actual transmission systems and photonic networks. A recirculating loop transmission experiment was conducted to assess the cascadeability of UNI type all-optical 3R regenerator. [32] Figure 16 illustrates the experimental setup. The loop consists of 4×50 km dispersion shifted fibers (DSF) and 5 EDFAs, and the two-stage UNI-based 3R regenerator was set at the end of the loop. 40 Gbit/s PRBS of $2^{23} - 1$ data was generated by 10 GHz based optical time domain multiplexing. The wavelength of the data was set to 1555.6 nm, which is close to the zero dispersion wavelength of 1555.3 nm, so no dispersion compensation fiber was employed in the loop. In the 3R regenerator, the input data signal was wavelength-converted from 1555.6 nm to 1545.0 nm at the first-stage UNI, and regenerated back to 1555.6 nm at the second-stage UNI. The pattern length of the data signal was set to $2^{23} - 1$, which is limited by the loop length.

BER characteristics for different transmission distances in the recirculating loop experiment are shown in Fig. 17. Error free operation was confirmed for all transmission distances up to 30,000 km (150 hops) when a 3R regenerator was employed every 200 km. An error floor however appeared in 2000 km transmission when not using the 3R regenerator. Figure 18 depicts the estimated Q factor (i.e., Q^2) as a function of transmission distance. The Q^2 was estimated from the BER slope with changing the

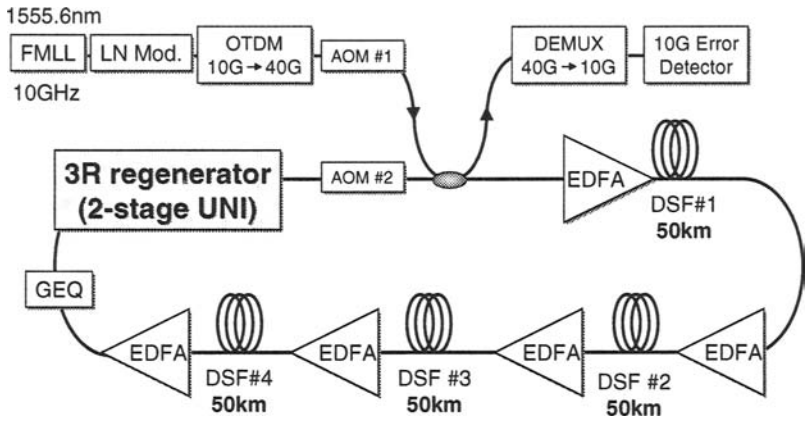

Fig. 16. Setup of recirculating loop experiment. FMLL: Fiber ring Mode-Locked Laser, LN Mod: $LiNbO_3$ Modulator, and GEQ: Gain Equalizer.

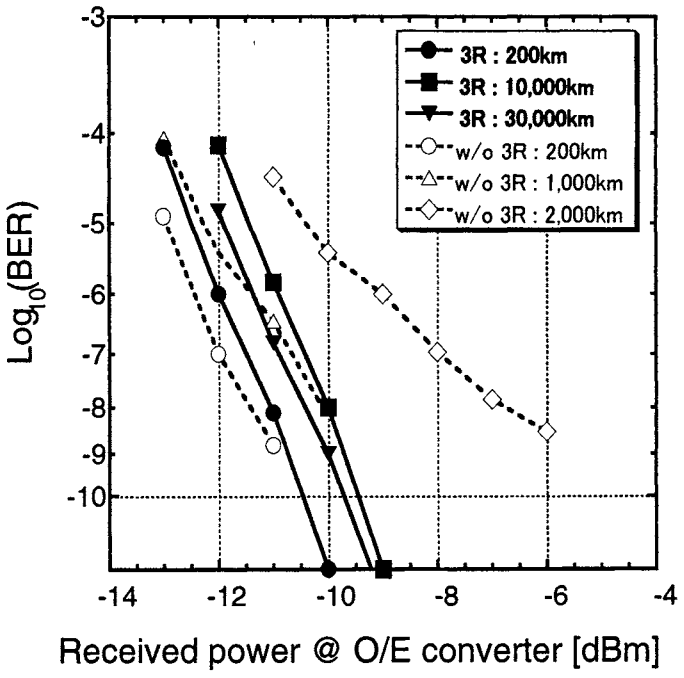

Fig. 17. BER for different number of hops with/without 3R regeneration in recirculating loop.

threshold voltage of the error detector with the received optical power of 0 dBm at the O/E converter, where the Gaussian noise distribution is assumed. [33] In the case without 3R regenerator, the Q^2 was rapidly degraded as the transmission distance increased. The Q^2 for example dropped to 9.2 dB (BER = 2.0×10^{-3}) after the 4000

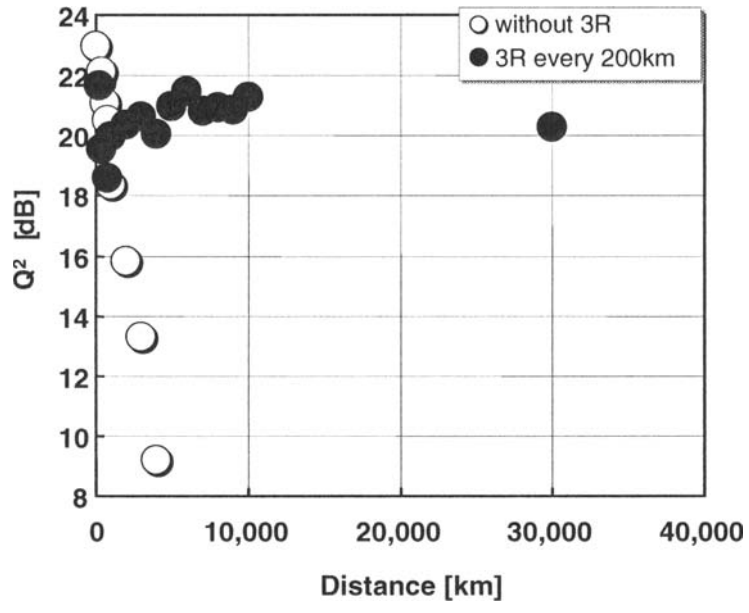

Fig. 18. Q^2 as a function of transmission distance.

km transmission. When we deployed the 3R regenerator in the recirculating loop, on the other hand, the estimated Q^2 remained almost constant over 20 dB even after a 30,000 km transmission, indicating a good transmission performance with the all-optical 3R regenerator employing a two-stage UNI. Strictly speaking, the Q^2 obtained by the method using BER vs. threshold voltage slope may have been slightly overestimated for non-Gaussian noise distributions transformed through the non-linear transfer function of the optical 3R regenerator. However, the error free operation was confirmed for all transmission distances up to 30,000 km and the difference in received power sensitivity at BER = 10^{-9} between 200 km transmission and 30,000 km transmission was less than 1 dB (as depicted in Fig. 17). This result suggests that the two-stage UNI with an electric clock recovery circuit should prove a likely candidate as a practical all-optical 3R regenerator.

2.3.3. Simultaneous Demultiplexing from 80 Gbit/s to 2 Channels of 40 Gbit/s Signals

An SOA-MZI with two output ports through a directional coupler can separately extract both the switched and the unswitched states. [34] The input signal can be fully utilized without any wasted power if both the output signals have high enough signal quality for further processing. Since the UNI has an assured balance in phase-shift because it consists of only one SOA, it can provide two output signals having equal signal quality with much less difficulty. This section discusses using a UNI for simultaneous demultiplexing into two channels with half bit-rates and with equal signal quality. The switched and the non-switched signals in the UNI are orthogonally polarized. It

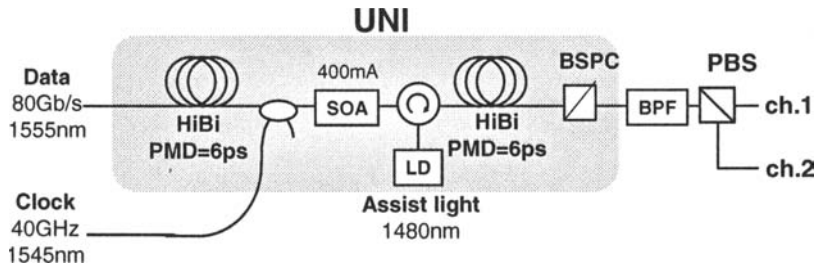

Fig. 19. Experimental setup for simultaneous demultiplexing using the UNI with the assist light.

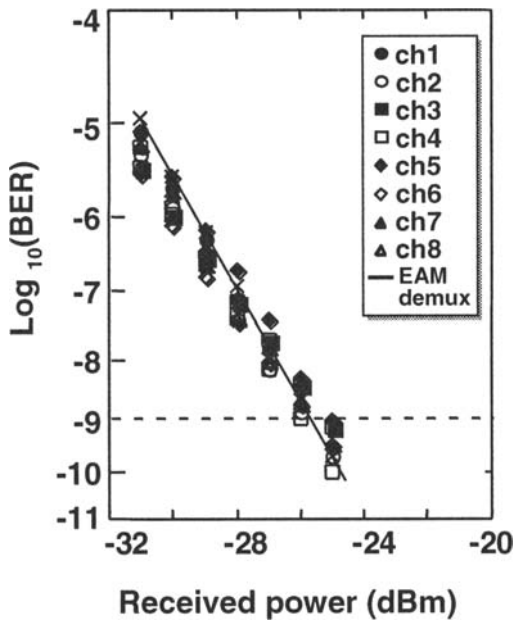

Fig. 20. BER measurement results for all eight channels. Solid line shows the characteristics of EAM-based demultiplexing as a reference.

is therefore possible to achieve simultaneous demultiplexing by extracting both the polarization-switched and non-switched outputs of the UNI through a polarization beam splitter (PBS) with no power sacrifice. [35,36] A large saving in power can be expected in this method compared to conventional switching gate demultiplexing such as with an electroabsorption modulator gate, because the switching gate demultiplexing method requires an intrinsic power splitting loss.

The experimental setup for a simultaneous optical demultiplexing using the UNI consisting of two polarization-maintaining fibers as a birefringent devices and an SOA is shown in Fig. 19. Both the 80-Gbit/s input data signal (2 ps pulse width) and 40 GHz

clock pulses (5 ps pulse width) were generated by 10-GHz-based optical time domain multiplexing. The optical powers of the 80-Gbit/s data stream and the 40-GHz clock pulses fed into the SOA were −5 dBm and +3 dBm, respectively. The transparent assist light of +10 dBm at 1480 nm was injected from the backside of the SOA. The PBS was utilized to simultaneously extract two orthogonally polarized signals, which are both polarization switched and non-switched signals in the UNI. The optical power of each extracted signal was about +1 dBm, which is lossless owing to the SOA gain.

Each output signal (ch.1 and 2) was demultiplexed from 40 to 10 Gbit/s by an EAM-based demultiplexer for BER measurement. The reference BER of the 80-Gbit/s input data signal was measured after being demultiplexed by two cascaded EAM-based demultiplexers (80 to 20 Gbit/s , 20 to 10 Gbit/s). An EDFA and an optical bandpass filter were set after each EAM in the EAM-based demultiplexer. Clear eye-openings were observed for all the channels. Figure 20 shows the BER measurement results for all channels demultiplexed by the UNI. The small differences within 1 dB in BER among all the demultiplexed channels indicate that orthogonal polarization was perfectly switched in terms of the switching balance. Note that this is comparable to the reference case of EAM-based demultiplexing, resulting that the power penalty for UNI-based demultiplexing from 80 Gbit/s into two channels of 40 Gbit/s was confirmed to be negligible.

3. Cross Absorption Modulation And Cross Phase Modulation in EAM

3.1. Mechanisms of XAM and XPM in EAM

The EAM was originally developed as an external light intensity modulator that could modulate an optical signal with small spectral chirping. The principles of light absorption using an external electric field in EAM are classified into two categories based on the structure of the absorption layer. The first principle is the Franz-Keldysh Effect (FK Effect) for a bulk absorption layer. The wave function smears into a forbidden band when a reverse voltage is applied to the device, resulting in the absorption spectrum moving to a longer wavelength. The other principle is for multiple quantum well (MQW) absorption layers and is called the Quantum Confined Stark Effect (QCSE). The quantum level in the conduction band and that in the valence band are moved closer to each other by applying a reverse bias voltage. The QCSE generally exhibits larger absorption change due to the change in electric field, compared to the FK effect. However, since the QCSE is sensitive to the polarized state of the light, this polarization dependency makes the MQW absorption layer more difficult to deal compared with the bulk absorption layer.

When the EAM is used as an all-optical wavelength converter, the CW probe light (λ_p, P_p) is modulated by the input optical data signal. The CW probe linght is simultaneously subjected to intensity modulation by cross absorption modulation (XAM) and phase modulation by cross phase modulation (XPM). As shown in Fig. 21, the input optical data signal is absorbed by the absorption layer in the EAM and generates electron-hole pairs (carriers). The optically generated carriers (1) screen the external electric field as well as (2) cause the so-called band filling. In addition, in the case of the MQW absorption layer, where the binding energy of an exciton is comparable to the thermal energy at room temperature ($kT \cong 25$ meV), (3) the effect

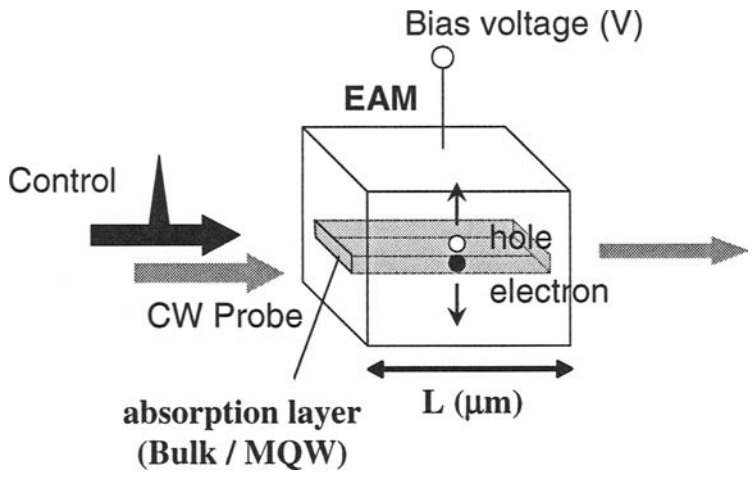

Fig. 21. Simulation model of optical nonlinearity in EAM.

of exciton bleaching is also taken into account. These three effects described above all work to shift the absorption spectrum edge to the shorter wavelength side, originating an intensity modulation of the CW probe light (XAM). On the other hand, the change in refractive index due to light absorption, which induce a phase modulation to the CW probe light (XPM), is governed by two physical mechanisms. The first one is based on the so-called Kramers-Krönig relation in which the refractive index (i.e., the imaginary part of the propagation coefficient) is changed according to the change in the absorption coefficient (i.e., the real part of the propagation coefficient). The second mechanism is the so-called plasma effect, wherein the refractive index of the semiconductor itself varies according to the variation in the carrier density. The principal mechanism of XPM in EAM is the refractive index spectrum change via the Kramers-Krönig relation. In SOA, the refraction index change is mainly caused by the plasma effect. The reason for the difference is that the absolute carrier density in an EAM is much smaller than that in an SOA. The optically generated carriers are extracted out by the external electric field in the EAM, which determines the absorption recovery time constant τ. Generally the absorption recovery time of EAM can be shorter than the gain recovery time of SOA in which the gain is recovered by injecting a current as described in section 2.2.1.

3.2. Measurement of XAM, XPM and Absorption Recovery Time in EAM

The XAM, XPM and the absorption recovery time in EAMs were measured by the polarization discriminating delayed interferometer (PD-DI) method precisely described in section 2.2.1. [37] InGaAsP-based 200-μm-long bulk type and 100-μm-long MQW type EAMs were measured. 3 dB bandwidths of electric-to-optical (EO) conversion are 16 GHz for the bulk type EAM and 33 GHz for the MQW type EAM, respectively. The static absorption characteristics of these EAMs are shown in Fig. 22. In order to reduce excessive insertion loss to the probe light for optical regeneration, the bandgap wavelength of the bulk-type and the MQW-type EAMs were respectively blueshifted

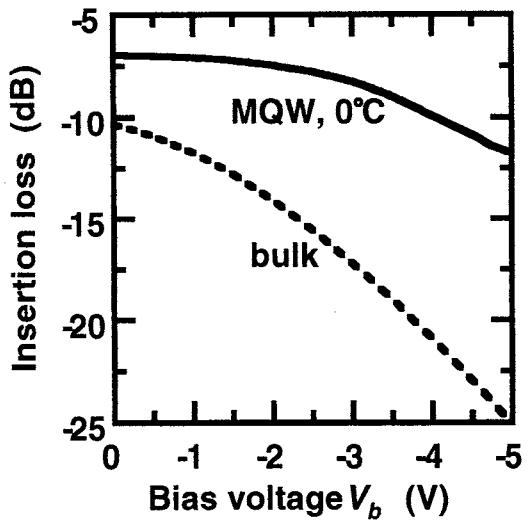

Fig. 22. Static absorption characteristics of MQW type (solid line) and bulk-type (dashed line) EAMs.

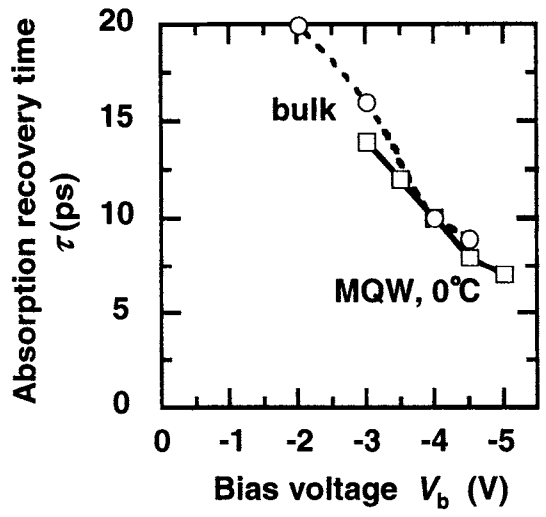

Fig. 23. Absorption recovery time as a function of bias voltage ; MQW type (solid line) and bulk-type (dashed line).

by ~40 nm and by ~30 nm, compared to a normal C-band intensity modulator. Figure 23 shows the measured absorption recovery time for a bulk-type EAM and a MQW EAM. The absorption recovery time was shortened by increasing the bias voltage due to accelerating the carrier sweep-out for the both EAM types. When the bias voltage of −4 V was applied, the absorption recovery times decreased down to about 10 ps.

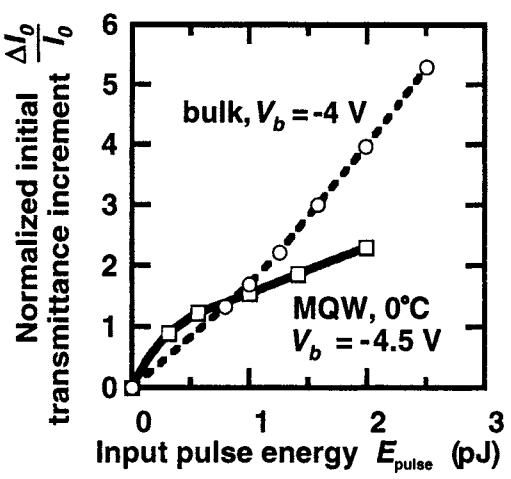

Fig. 24. Initial transmittance increment $\Delta I_0/I_0$ due to XAM as a function of input pulse energy; MQW type (solid line) and bulk-type (dashed line).

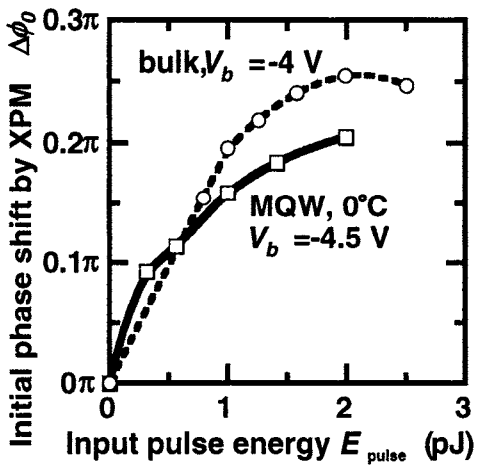

Fig. 25. Initial phase shift $\Delta\phi_0$ as a function of input pulse energy; MQW type (solid line) and bulk-type (dashed line).

XAM and XPM characteristics were evaluated as shown in Figs. 24 and 25. A normalized XAM ($\Delta I_0/I_0$) increases monotonically by increasing the input pulse energy. Using a 1.5-pJ input pulse, the normalized initial transmittance increment is, respectively, 2.8 for the bulk-type EAM and 1.9 for the MQW-type EAM. Referring to Fig. 22, the absorption loss of bulk-type EAM at -4.0 V is larger than that of MQW-type EAM at -4.5 V by about 10 dB, and the intensity of the probe light transmitting through the EAM at steady state, I_0, is about ten times larger for the MQW-type EAM than that for the bulk-type EAM. It should therefore be denoted that

the absolute value of the initial increment of transmitting intensity due to XAM, ΔI_0, is larger for the MQW-type EAM than for the bulk-type EAM, although the normalized initial increment of transmitting probe intensity $\Delta I_0/I_0$ is smaller for the MQW-type EAM, as shown in Fig. 24. On the other had, the XPM $\Delta\phi_0$ tends to saturate at the input pulse energy exceeding 1 pJ for the both EAM types. The XPM saturation might correlate with the peaks of the Kramers-Krönig induced refractive index variation in the wavelength spectrum domain, although further study is required for details. The initial phase shift with a 1.5-pJ input pulse was 0.18 π for the MQW-type EAM and 0.23 π for the bulk-type EAM, respectively.

In summary, the absorption recovery as well as the optical nonlinearity characteristics are similar and comparable for both bulk-type and MQW-type EAMs. Although the XAM and the XPM efficiencies are higher for the bulk-type EAM than the MQW-type, it is due to the larger insertion loss in the bulk-type EAM. In general, it is easier to achieve polarization insensitive structure by bulk-type than by MQW-type.

3.3. Optical Regeneration Using EAM

3.3.1. Optical 3R Regeneration Using XAM in Bit-Synchronized rf-Driven EAM

This section summarizes XAM-based optical regeneration. Continuous development of EAM for high-speed external intensity modulation has resulted in the 3-dB bandwidth of electric-to-optical (EO) conversion in the most advanced EAM to approach or exceed 40 GHz. [38–41] The ultrafast EO response of EAM is useful not only for conventional external modulation, but also for optical signal processing such as optical data regeneration that utilizes cross-absorption modulation (XAM) photoinduced in an EAM. [42–44] Figure 26(a) illustrates an optical 2R regenerator employing cross-absorption modulation (XAM) in an EAM (hereinafter referred to as "DC-XAM 2R"). A novel optical 3R regeneration technique, in which both gating and retiming functionality are achieved by just one EAM ("rf-XAM 3R"), was proposed as shown in Fig. 26(b). [45] XAM is induced in the EAM when a CW probe light and control data pulses are simultaneously fed into the EAM in both the of DC-XAM 2R and rf-XAM 3R schemes. However, in the rf-XAM 3R scheme, the EAM is driven by bit-synchronized rf-voltage superimposed on a deep DC bias. The optical gate opens due to the XAM induced by the incoming data pulse, and the gate is subsequently closed by the periodic rf-clock. Consequently, the timing jitter of the incoming data pulse is reset every bit-period.

This concept was verified at 20 Gbit/s in the experiment. Figure 27 (a) shows bit error rate (BER) measurement results. To emulate the timing jitter, the 20-Gbit/s control data pulse was intentionally FM-modulated with a 1-MHz modulation frequency and with a modulation index of 0.169, resulting in a timing jitter of ± 2.7 ps_{p-p}. The bias of the EAM was sinusoidally driven from -2.5 to -4.16 V in the rf-XAM scheme. Although error-free operation was confirmed for both optical regenerators, the power penalty at BER = 10^{-9} with the rf-XAM 3R regenerator was 3 dB smaller than that with the DC-XAM 2R regenerator. The remaining power penalty was caused by insertion loss of the used EAM of 10 dB at zero bias. This can be minimized by an optimum absorption layer design of in the EAM. Figure 27(b) shows eye-diagrams of the original data pulse with intentionally imposed with a timing jitter of ± 2.7 ps_{p-p},

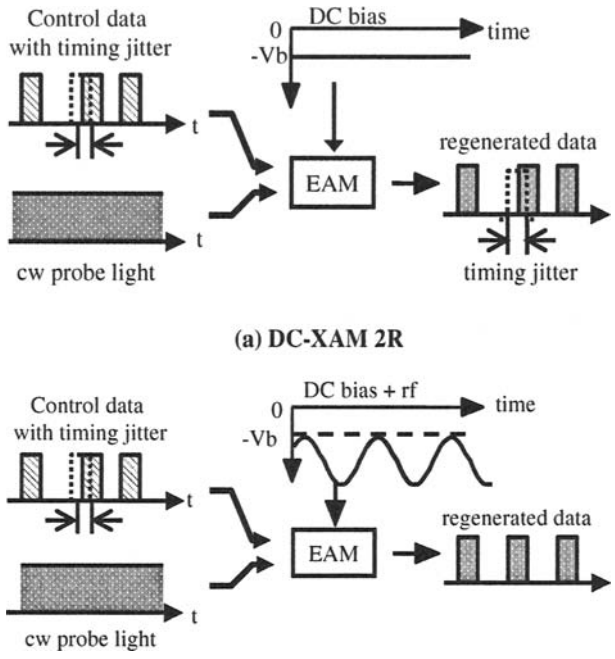

Fig. 26. Configurations of (a) DC-XAM 2R regenerator and (b) rf-XAM 3R regenerator.

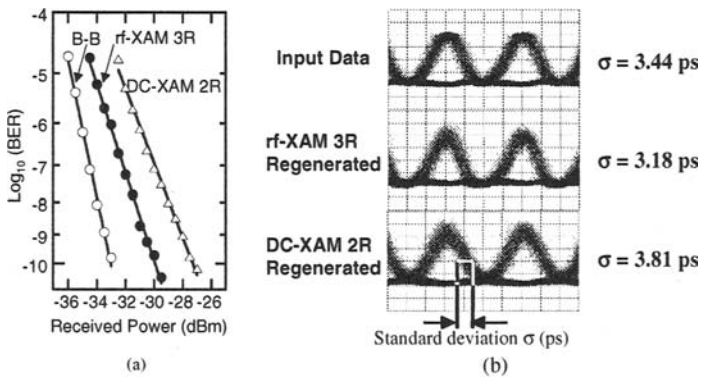

Fig. 27. (a) Results of bit error rate (BER) measurement, (b) Eye-diagrams of the original control with intentionally imposed timing jitter and corresponding regenerated data pulses.

and corresponding rf-XAM 3R or DC-XAM 2R regenerated data pulses. The standard deviation σ of the line width, which represents the timing jitter, was also improved from 3.44 to 3.18 ps. In addition to that, an inter-symbol interference is also suppressed by the rf-XAM 3R regeneration due to the periodic gate being closed by the rf clock

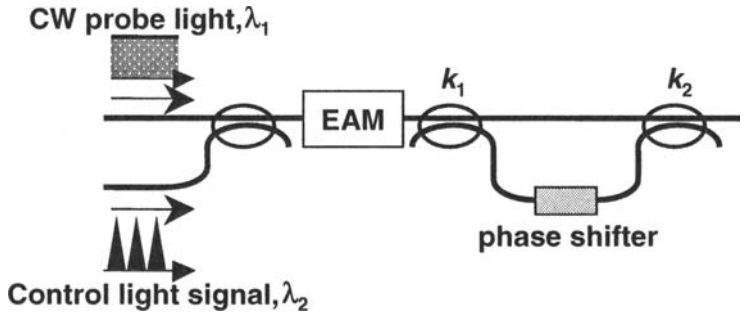

Fig. 28. Schematic illustration of EAM-DI wavelength converter.

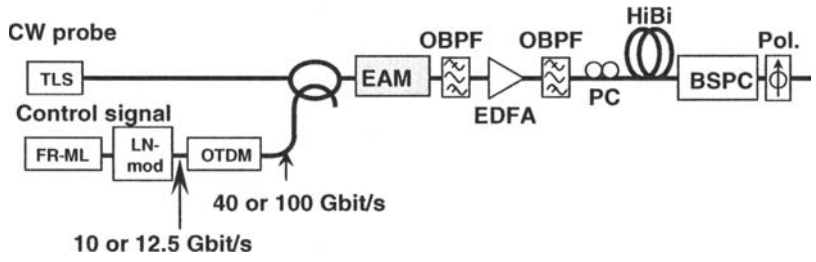

Fig. 29. Experimental setup of EAM-DI wavelength converter.

signal. The simple configuration of the proposed optical 3R regeneration with the timing correction function is expected to contribute not only to reduced size and power consumption but also high stability.

3.3.2. All-Optical Wavelength Conversion (2R) by EAM With Delayed-Interferometer

This section discusses all-optical wavelength conversion (2R) utilizing XPM in EAM operated up to 100 Gbit/s. The XPM in EAM can be utilized in an interferometic configuration such as a Mach-Zehnder interferometer (MZI) or a Michelson interferometer, as in SOA. The XPM-based interferometric wavelength converter generally has higher conversion efficiency than the XAM-based converter, because a high extinction ratio can easily be obtained by adjusting the destructive interferometoric condition. The delayed-interferometer (DI) configuration for the wavelength converter has a simple structure as well as the potential for high-speed operation. This configuration was employed to investigate the wavelength conversion by XPM in EAM. [46,47] Figure 28 schematically shows the EAM-DI wavelength converter. The probe light output from the EAM is fed into two arms of an asymmetric MZI, which is a delayed interferometer that gives a differential time delay of Δt between the two split components consisting of the leading component and trailing component. The initial phase offset between two components is adjusted by the phase shifter so that these components destructively interfere with each other. When the control light pulse is injected into the EAM,

both XAM and XPM are simultaneously induced. As the transmittance of the EAM increases due to XAM, the intensity of the leading component increases first, and this intensity increment turns the interference constructive due to the intensity imbalance. At the same time, the phase shift due to XPM also turns the interference constructive in addition due to the phase imbalance. After the differential time delay of Δt, the trailing component interferes destructively again with the leading component, which provides a high extinction ratio. A polarization-discriminated DI (PD-DI) wavelength converter (see Fig. 29) is more convenient in practice, because it is easy to precisely control the splitting ratios by just adjusting the polarizations of incident probe light to the highly birefringent device and to the polarizer in PD-DI configuration, while additional tunable couplers are required in the normal DI configuration.

The mechanism for wavelength conversion in this configuration is identical to that of SOA-DI configuration, although the EAM utilizes XAM (intensity increment) while SOA utilizes XGM (intensity decrement) to turn the interference constructive. The theoretical output waveform can be deduced in the same manner for SOA-DI as described in section 2.2.1. If we assume that the absorption of an EAM recovers exponentially with the single time constant of τ, then the time evolution of the intensity of transmitting probe light, $I(t)$, can be expressed as

$$I(t) = I_0 \left\{ 1 + \Delta I_0 \exp\left(-\frac{t}{\tau}\right) \right\}, \tag{11}$$

where I_0 is the transmittance at steady state and ΔI_0 is the ratio of the initial increment of transmitting intensity due to XAM. The time evolution of phase shift, $\Delta\phi(t)$, is also assumed to recover exponentially with the time constant of τ, and it is expressed as

$$\Delta\phi(t) = \Delta\phi_0 \exp\left(-\frac{t}{\tau}\right), \tag{12}$$

where $\Delta\phi_0$ is the initial phase shift due to XPM. When a control pulse is injected at $t = 0$, the electric fields of the leading and the trailing components are respectively expressed as

$$E_{\text{lead}}(t) = \sqrt{P_{\text{in}}}\sqrt{1-k_1}\sqrt{1-k_2}\sqrt{I(t)}\exp(j\Delta\phi(t)) \text{ for } 0 \le t \tag{13}$$

and

$$\begin{aligned} E_{\text{trail}}(t) &= \sqrt{P_{\text{in}}}\sqrt{k_1}\sqrt{k_2}\sqrt{I_0} \text{ for } 0 \le t \le \Delta t \\ E_{\text{trail}}(t) &= \sqrt{P_{\text{in}}}\sqrt{k_1}\sqrt{k_2}\sqrt{I(t-\Delta t)}\exp(j\Delta\phi(t)) \text{ for } \Delta t \le t \end{aligned} \tag{14}$$

where P_{in} is the power of the probe light input to the DI. The time evolution of the output power of the EAM-DI wavelength converter, $P(t)$, is expressed as

$$P_{\text{out}}(t) = |E_{\text{lead}}(t) + E_{\text{trail}}(t)|^2 . \tag{15}$$

These equations show that both XAM and XPM contribute to wavelength conversion in EAM-DI.

Figure 29 schematically depicts the experimental setup of an EAM-DI wavelength converter. Wavelength conversions at 40 Gbit/s ($V_b = -5.1$ V, 10°C) and at 100 Gbit/s ($V_b = -4.3$V, 0°C) were carried out using the MQW-type EAM. For 40 Gbit/s wavelength conversion, the input data signal, of which the launched power was +14.8

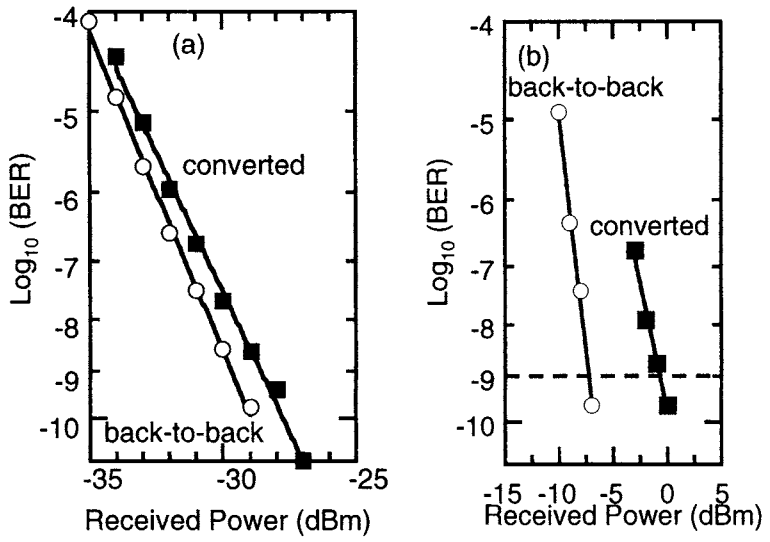

Fig. 30. BER measurement results of EAM-DI wavelength converters. (a) 40 Gbit/s results, and (b) 100 Gbit/s results. Open circles and closed squares correspond to back-to-back and wavelength converted signals, respectively.

dBm (1.51 pJ/pulse), was generated from 10 Gbit/s signal with $2^{31} - 1$ pattern length and 1544 nm in wavelength, and the probe signal was 1555 nm with launched power of +3.2 dBm. For 100 Gbit/s wavelength conversion, the input data signal, of which the launched power was +18.8 dBm (1.52 pJ/pulse), was generated from 12.5 Gbit/s signal with $2^7 - 1$ pattern length and 1545 nm in wavelength, and the probe signal was 1555 nm with launched power of +4.8 dBm. The relative time delay of the DI was 3.2 ps for both bit rates. The conditions for input optical signals are given in Table 1. The BER was measured after demultiplexing down to the respective base rates in electrical domain for 40 Gbit/s and in optical domain for 100 Gbit/s, and the results are shown respectively in Figs. 30 (a) for 40 Gbit/s and (b) for 100 Gbit/s. Error-free operations were confirmed for both bit rates. The power penalty at BER = 10^{-9} was as small as 1.5 dB for 40 Gbit/s wavelength conversion, while it was 6.6 dB for 100 Gbit/s wavelength conversion.

Table 1. Experimental conditions of optical input signals for wavelength conversion using EAM-DI at 40 and 100 Gbit/s.

		Probe Light	**Control Pulse Light**
Wavelength	40 Gbit/s	1532–1562 nm	1545–1562 nm
	100 Gbit/s	1555 nm	1545 nm
Power	40 Gbit/s	+1.2 dBm	+15.0 dBm (1.58 pJ/pulse)
	100 Gbit/s	+4.8 dBm	+18.8 dBm (1.52 pJ/pulse)
Pattern Length	40 Gbit/s	–	$2^{31} - 1$
	100 Gbit/s	–	$2^7 - 1$

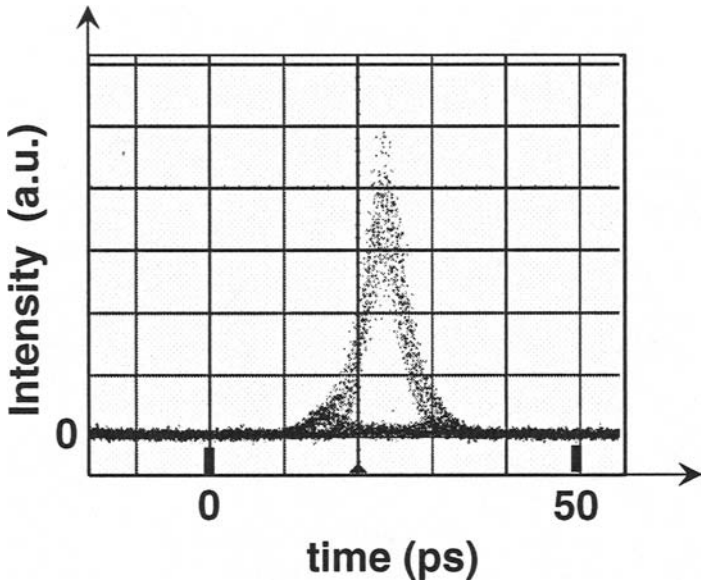

Fig. 31. Eye-diagram of 100 Gbit/s wavelength converted pulse after demultiplexing.

The eye-diagrams of the demultiplexed pulses that were wavelength converted at 100 Gbit/s are shown in Fig. 31. A slight patterning effect discernible on the mark level and the inter-symbol interference, which caused the power penalty, indicates that the absorption recovery of 7 ps was not fast enough for 100 Gbit/s operation. An improved MQW structure, such as graded SCH layer, [48] might prevent carrier pile-up phenomena and allow higher bit-rate operation exceeding 100 Gbit/s. The wide bandwidth operability of the EAM-DI wavelength converter was verified at 40 Gbit/s. The wavelength of the data signal was set at either 1545 or 1562 nm, and the probe wavelength was varied from 1532 to 1562 nm. The input powers of the data pulse and the cw probe light were fixed at +15.0 dBm and at +1.2 dBm, respectively.

In Fig. 32, the power penalty at BER = 10^{-9} that was averaged for all the four tributaries was plotted as a function of probe wavelength. For all the combinations of wavelengths, error-free operation was confirmed, and the power penalty was less than 2.5 dB for all the tributaries without changing input powers of data pulse and/or cw probe light. From these results, it is verified that the operable bandwidth of the EAM-DI wavelength converter covers full C-band.

4. Summary

We discussed optical nonlinearities both in forward biased semiconductor waveguide (SOA) and in reverse biased semiconductor waveguide (EAM) theoretically and experimentally. We also investigated in detail the modulation of the carrier density by

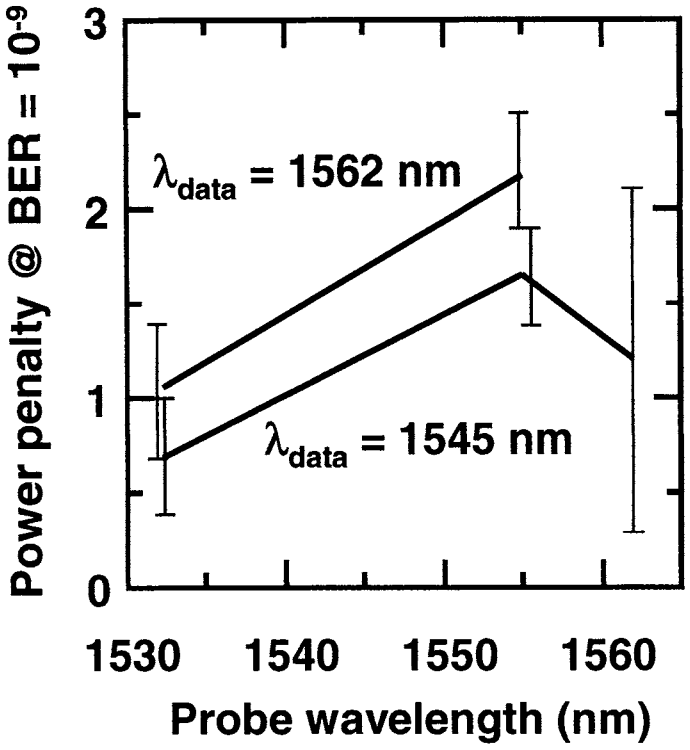

Fig. 32. Power penalty at BER = 10^{-9} for various combinations of data and probe wavelengths measured at 40 Gbit/s. The error bars show the variation among four tributaries.

light injection in both types of devices, since this determines the change in transmittance (XGM or XAM) and the change in the refractive index (XPM). Theoretical simulation based on the time-dependent transfer matrix method and the simple measurement technique for optical nonlinearities utilizing a polarization discriminating delayed interferometer (PD-DI) configuration were also discussed.

In the first part of this paper, we reviewed SOA-based regenerators operated with relatively small optical power owing to the SOA gain. The carrier life time, which is one bottleneck in ultra-high speed applications, was shortened down to a few tens of picoseconds by injecting transparent assist light. Also, 40Gbit/s regeneration was demonstrated using the so-called UNI configuration. The superior regeneration capability of two-stage UNI was confirmed by a recirculating loop experiment up to 30,000 km with 150 regenerations. These results prove that the SOA-based all-optical regenerator (UNI) injected with the assist light can be used in actual transmission systems and photonic networks.

In the latter part of the paper, we reviewed all-optical regenerators using EAM. Regeneration was performed with little pattern word effect owing to the fast EAM response. A rf-XAM 3R scheme regenerator, in which the EAM is driven by bit-synchronized rf-voltage, was demonstrated at 20Gbit/s signal. This regenerator con-

sists of only one EAM for both gating and timing correction. An EAM in conjunction with delayed interferometer configuration, which utilizes XAM as well as XPM in the EAM, has a simple structure. The demonstrations show fast regeneration capability up to 100Gbit/s as well as wide bandwidth operation covering full C-band. However, relatively large optical power is required for EAM-based regenerators due to the insertion loss. A blueshifting active layer might be one of the solutions.

Those all-optical regenerators offer many advantages in a practical sense for future large scale photonic network nodes. These advantages are not only due to their its high speed capability, but also to their simple configuration, compactness, low power consumption, and stability. Further studies on optimizing EAM as well as SOA, are expected to open the way to ultra-high speed all-optical regenerators capable of operation at 100 Gbit/s and higher.

References

1. R.J. Manning, A.D. Ellis, A.J. Pustie, and K.J. Blow, Semiconductor laser amplifier for ultrafast all-optical signal processing, J. Opt. Soc. Am. B, **14**, 3204 (1997).
2. M. Bachmann, P. Doussiere, J.U. Emery, R. N'Go, F. Pommereau, L. Goldstein, G. Soulage, and A. Jourdan, Polarization-insensitive clamped-gain SOA with integrated spot-size convertor and DBR gratings for WDM applications at 1.55 m wavelengh, Electron. Lett., **32**, 2076–2077 (1996).
3. R.J. Manning and D.A.O. Davies, Three-wavelength device for all-optical signal processing, Opt. Lett., **19**, 889–891 (1996).
4. M. Usami, M. Tsurusawa, and Y. Matsushima, Mechanism for reducing recovery time of optical nonlinearity in semiconductor laser amplifier, Appl. Phys. Lett., **72**, 2657–2659 (1998).
5. M. Tsurusawa, M. Usami, and Y. Matsushima, Demonstration of optical noise reduction using nonlinear absorption in semiconductor laser amplifier IEEE J. Selected Top. Quantum. Electron., **5**, 861 (1999).
6. A. Dupertuis, J.L. Pleumeekers, T.P. Hessler, P.E. Selbmann, B. Deveaud, B. Dagens, and J.Y. Emery, Extremely Fast High-Gain and Low-Current SOA by Optical Speed-Up at Transparency, IEEE Photon. Tech. Lett., **12**, 1453–1455 (2000).
7. J.L. Pleumeekers, M. Kauer, K. Dreyer, C. Burrus, A.G. Dentai, S. Shunk, J. Leuthold, and C.H. Joyner, Acceleration of Gain Recovery in Semiconductor Optical Amplifiers by Optical Injection Near Transparency Wavelength, IEEE Photon. Tech. Lett., **14**, 12–14 (2002).
8. T. Durhuus, B. Mikkelsen, and K.E. Stubkjaer, Detailed dynamic model for semiconductor optical amplifiers and their crosstalk and intermodulation distortion, J. Lightwave Technol., **10**, 1056–1065 (1992).
9. P.J. Annetts, M. Asghari, and I.H. White, The effect of carrier transport on the dynamic performance of gain-saturation wavelength conversion in MQW semiconductor optical amplifiers, IEEE J. Select. Topics Quantum Electron., **3**, 320–329 (1997).
10. M. Asghari, I.H. White, and R.V. Penty, Wavelength conversion using semiconductor optical amplifiers, J. Lightwave Technol., **15**, 1181–1190 (1997).
11. M.G. Davis and R.F. O'Dowd, A Transfer Matrix Method Based Large-Signal Dynamic Model for Mutilelectrode DFB Lasers, IEEE J. Quantum Electron., **30**, 2458–2466 (1994).

12. H. Lee, H. Yoon, Y. Kim, and J. Heong, Theoretical Study of Frequency Chirping and Exinction Ratio of Wavelength-Converted Optical Signals by XGM and XPM Using SOA, IEEE J. Quantum Electron., **35**, 1213–1219 (1999).

13. G. Björk and O. Nilsson, A new exact and efficient numerical matrix theory of complicated laser structures: Properties of asymmetric phase-shifted DFB lasers, J. Lightwave Technol., **LT-5**, 140–146 (1987).

14. T. Durhuus, B. Mikkelsen, C. Joergensen, S. Danielsen, and K.E. Stubkjaer, All-optical wavelength conversion by semiconductor optical amplifiers, J. Lightwave Technol., **14**, 942–954 (1996).

15. F. Girardin, G. Guekos, and A . Houbavlis, Gain recovery of bulk semiconductor optical amplifiers, IEEE Photon. Technol. Lett., **10**, 784–786 (1998).

16. M. Usami, R. Inohara, M. Tsurusawa, and K. Nishimura, Experimental analysys of cross gain modulation and cross phase modulation in SOA with assist light injection, Proc. IEEE LEOS Summer Topical Meetings, Mont Tremblant, Canada, paper TuK1, (2002)

17. R. Inohara, M. Tsurusawa, K. Nishimura, and M. Usami, Experimental Analysis of Cross Phase Modulation and Cross Gain Modulation in SOA Injecting CW Assist Light, IEEE Photon. Technol. Lett., **15**, 1192–1194 (2003).

18. Y. Ueno, S. Nakamura, K. Tajima and S. Kitamura, 3.8 THz Wavelength Conversion of Picosecond Pulses Using a Semiconductor Delayed-Interference Signal-Wavelength Converter (DISC), IEEE Photon. Tech. Lett., **10**, 346–348 (1998).

19. M. Tsurusawa, K. Nishimura, and M. Usami, First demonstration of pattern effect reduction in 40 Gbps semiconductor optical amplifier based all-optical switch utilizing transparent CW assist light, Electron. Lett. Jpn. J. Appl. Phys., **41**, 1199–1202 (2002).

20. M. Tsurusawa, R. Inohara, K. Nishimura, and M. Usami, 80 Gbit/s wavelength conversion using SOA-based all-optical polarization discriminated switch, Proc. OECC2002, Chiba Japan, 11c2-3, 466–467, (2002)

21. Y. Ueno, S. Nakamura, and K. Tajima, Penalty-Free Error-Free All-Optical Data Pulse Regeneration at 84 Gb/s by Using a Symmetric-Mach-Zehnder-Type Semiconductor Regenerator, Photon. Tech. Lett., **13**, 469–471 (2001).

22. S. Nakamura, Y. Ueno, and K. Tajima, 168-Gb/s All-Optical Wavelength Conversion with a Symmetric-Mach-Zehnder-Type Switch, Photon. Tech. Lett., **13**, 1091–1093 (2001).

23. B. Lavigne, E. Balmefrezol, P. Brindel, B. Dagens, L. Pierre, P. Pecci, R. Brenot, and O. Leclerc, Operation margins of 40 Gbit/s SOA-MZI used in differential scheme for optical 3R regeneration Proc. European Conference on Optical Communications ECOC2002, paper 7.3.5, 2002.

24. J. Leuthold, C.H. Joyner, B. Mikkelsen, G. Raybon, J.L. Pleumeekers, B.I. Miller, K. Dreyer, and C.A. Burrus, 100 Gbit/s all-optical wavelength conversion with integrated SOA delayed-interference configuration, Electron. Lett. **36**, 1129–1130 (2000).

25. K. Tajima, S. Nakamura, and Y. Sugimoto, Ultrafast polarization- discriminating Mach-Zehnder all optical switch, Appl. Phys. Lett., **67**, 3709–3711 (1995).

26. K.L. Hall and K.A. Rauschenbach, 100-Gbit/s bitwise logic, Optics Lett., **23**, 1271–1273 (1998).

27. A.E. Kelly, I.D. Phillips, R.J. Manning, A.D. Ellis, D. Nesset, D.G. Moodie, and R. Kashyap, 80 Gbit/s all-optical regenerative wavelength conversion using semiconductor optical amplifier based interferometer, Electron. Lett., **35**, 1477–1478 (1999).

28. H.J. Thiele, A.D. Ellis, and I.D. Phillips, Recirculating loop demonstration of 40Gbit/s all-optical 3R data regeneration using a semiconductor nonlinear interferometer, Electron. Lett., **35**, 230–231 (1999).

29. M. Tsurusawa, K. Nishimura, and M. Usami, Novel scheme for 40 Gbps SOA-based all-optical switch utilizing transparent CW assist light, Proc. Indium Phosphide and Related Materials IPRM2001, paper WP-12, 174, 2001.

30. J. Leuthold, M. Kauer, and M. Duelk, Power Equalization and Signal Regeneration with Delay Interferometer All-optical Wavelength Converters, Proc. European Conference on Optical Communications ECOC2002, paper 7.3.4, 2002.

31. M. Tsurusawa, K. Nishimura, R. Inohara, and M. Usami, Distinct regeneration capability of 40 Gbit/s signal impaired with amplitude noise and timing jitter using SOA-based all-optical polarization discriminated switch, Proc. Optical Fiber Communications OFC2002, paper TuN4, 2002.

32. R. Inohara, K. Nishimura, M. Tsurusawa, M. Usami, and S. Akiba, 40 Gbit/s transmission with all-optical 3R regeneration using two-stage SOA-based polarization discriminated switch with assist light injection, ICEIC, 2004.

33. N.S. Bergano, F.W. Kerfoot, and C.R. Davidson, Margin Measurements in Optical Amplifier Systems, IEEE Photon. Technol. Lett., **5**, 304–306 (1993).

34. R. Hess, M. Caraccua-Gross, W. Vogt, E. Gamper, P.A. Besse, M. Duelk, E. Gini, H. Melchior, B. Mikkelsen, M. Vaa, K.S. Jepsen, K.E. Stubkjaer, and S. Bouchoule, All-optical demultiplexing of 80 to 10 Gb/s signals with monolothic integrated high-performasnce Mach-Zehnder interferometer, IEEE Photon. Technol. Lett., **10**, 165–167 (1998).

35. M. Tsurusawa, K. Nishimura, and M. Usami, First demonstration of simultaneous demultiplexing from 40 Gbit/s into two channels of 20 Gbit/s by SOA-based all-optical polarization switch, Electron Lett., **37**, 1398–1399 (2001).

36. M. Tsurusawa, K. Nishimura, and M. Usami, First demonstration of simultaneous demultiplexing from 80Gb/s to 2×40 Gb/s by SOA-based all-optical polarization switch, Proc. European Conference on Optical Communications ECOC2001, Th.F-1-1, 500-501, 2001.

37. K. Nishimura, R. Inohara, M. Tsurusawa, and M. Usami, Delayed-Interferometric Wavelength Converter Using Electroabsorption Modulator with Optimized Bandgap Wavelength, Proc. European Conference on Optical Communications ECOC 2002, Paper 2.3.7, Copenhagen, Denmark, 2002.

38. A. Ougazzaden, C.W. Lentz, T.G.B. Mason, K.G. Glogovsky, C.L. Raynolds, G.J. Przybylek, R.E. Leibenguth, T.L. Kercher, J.W. Boardman, M.T. Rader, J.M. Geary, F.S. Walters, L.J. Peticolas, J.M. Freund, S.N.G. Chu, A. Sirenko, R.J. Jurchenko, M.S. Hybertsen, L.J.P. Ketelsen, and G. Raybon, 40 Gb/s tandem electro-absorption modulator, Proc. Optical Fiber Communications OFC2001, Anaheim, PD-14, 2001.

39. H. Takeuchi, Proc. Indium Phosphide and Related Materials IPRM2001, Nara, WA3-1, 2001.

40. R. Lewen, S. Irmscher, U. Westergren, and L. Thylen, Ultra high-speed segmented traveling-wave electroabsorption modulators, Proc. Optical Fiber Communications OFC2003, Georgia, PD38, 2003.

41. H. Fukano, M. Tamura, T. Yamanaka, H. Nakajima, Y. Akage, Y. Kondo, and T. Saitoh, Low Driving-Voltage (1.1 Vpp) Electroabsorption Modulators Operating at 40 Gbit/s, Proc. International Conference on Indium Phosphide and Related Materials IPRM2004, Paper ThA1-2, 573-576, Kagoshima, Japan, 2004.

42. N. Edagawa, M. Suzuki, and S. Yamamoto, Novel wavelength converter using an electroabsorption modulator, IEICE Trans. Electron., **E81-C**, 1251–1257 (1998).

43. N. Edagawa and M. Suzuki, Novel all optical limiter using electroabsorption modulators, Proc. Optical Fiber Communicaitons OFC2000, ThP1, 2000.

44. T. Otani, T. Miyazaki, and S. Yamamoto, Optical 3R Regenerator using wavelength converters based on electroabsorption modulator for all-optical network applications, IEEE Photon. Technol. Lett., **12**, 431–433 (2000).

45. Nishimura, R. Inohara, M. Tsurusawa, and M. Usami, Novel All-Optical 3R Regenerator Using Cross-Absorption Modulation in rf-Driven Electroabsorption Waveguide, Proc. European Conference on Optical Communications ECOC 2002, Paper 2.3.7, Copenhagen, Denmark, 2002.

46. K. Nishimura, M. Tsurusawa, and M. Usami, First demonstration of 40 Gbps wavelength conversion with no pattern effect utilizing cross-phase modulationon in an electroabsorption waveguide, Jpn. J. Appl. Phys., **41**, 1178–1181 (2002).

47. K. Nishimura, R. Inohara and M. Usami, 100 Gbit/s wavelength conversion using MQW-EAM with blueshifted absorption edge, Proc. Optical Fiber Communications OFC 2004, Los Angels, Paper FD2, 2004.

48. K. Morito, R. Sahara; K. Sato, Y. Kotaki, and H. Soda, High power modulator integrated DFB laser incorporating strain-compensated MQW and graded SCH modulator for 10 Gbit/s transmission, Electron. Lett. **31**, 975–976 (1995).

DOI: 10.1007/s10297-004-0024-y
Originally published in J. Opt. Fiber Commun. Rep. 2, 115–139 (2005)

Optical fibers and fiber dispersion compensators for high-speed optical communication

Masayuki Nishimura

Sumitomo Electric Industries, Ltd.
Optical Communications R&D Laboratories
Taya-cho 1, Sakae-ku, Yokohama, Japan 244-8588
Email: nishimura-masayuki@sei.co.jp

Abstract. In order to meet the requirements necessary for advanced optical fiber transmission schemes that enable larger transmission capacity, higher efficiency and/or lower transmission costs per bit, optical fiber technologies are still evolving toward ultimate performance. Recent developmental activities have realized a number of improved performance optical fibers, such as ultra-low loss or ultra-low nonlinearity fibers and various types of dispersion-modified fibers. Fiber-based dispersion compensators or dispersion compensating fibers have also become one of the most essential optical components that support high-speed large capacity optical transmission. Very recently, the dispersion compensating fibers have further evolved into dispersion-managed optical transmission lines, which are now being actually deployed in transoceanic submarine optical cable networks.

1. Introduction

Optical fibers are one of the most important key technologies that support the current optical communication networks. Especially, silica-glass-based optical fibers are exclusively used in long-distance, large-capacity optical transmission systems because of their high performance as transmission media, such as low losses and wide bandwidths.

Although it appears that the optical fiber technology is fully matured after more than 30 years of development and deployment since the first low-loss silica-based optical fiber was reported [1], there is still a significant amount of room for further improvement of the optical performance and development of novel optical fibers or optical transmission lines. For example, the very recent lowest transmission loss record of the silica-based fiber (0.1484 dB/km) [2] has finally broken the previous record of 0.154 dB/km [3] after an interval of 16 years. Some efforts have also recently been

devoted to development of optical fibers exhibiting low 'nonlinearity,' which is one of the optical parameters that were almost neglected in the optical fiber transmission systems 10 years ago. In the past several years, optical fiber manufacturers have developed and introduced various types of new optical fibers, most of which feature specific chromatic dispersion characteristics.

Those innovations in the optical fiber technology are closely related to evolution of the optical transmission technology, for example, the advent of the optical fiber amplifier (the erbium-doped fiber amplifier), the recent explosive development of the wavelength-division-multiplexed (WDM) transmission technology (increases in the number of optical signal channels for ultra-large capacity transmission) and the progress of the optical time-division-multiplexed (OTDM) transmission technology (ultra-high speed or ultra-high bit-rate signal transmission).

This paper describes the basics of the fundamental properties of optical fibers first, and then reviews the recent progress in optical fibers for transmission and the fiber-based dispersion compensating technology. Lastly, dispersion-managed optical transmission lines, which are one of the most advanced schemes of the dispersion compensation, are introduced.

2. Fundamental Properties of Optical Fibers

Optical fibers are classified into two major categories: multimode fibers and single mode fibers. Since multimode fibers are not suited for very high speed or high bit-rate transmission in principle because of their limited bandwidths, we concentrate only on single mode fibers throughout this paper.

As signal transmission media, single mode fibers have three fundamental properties: transmission loss, nonlinearity and dispersion. The dispersion is further classified into chromatic dispersion and polarization mode dispersion (PMD) in the case of the single mode fiber.

2.1. Transmission Loss

The transmission loss (or attenuation), which represents a decrease in optical power per unit length, is the most fundamental property of optical fibers. It is directly related to the power of optical signals that reach the end of optical fiber after transmission, and thus it basically determines the signal-to-noise ratio (SNR) of the signals in optical communication systems.

An example of typical transmission loss spectrum of a silica-glass-based optical fiber is shown in Fig. 1. The transmission loss of the optical fiber as a function of the wavelength, $\alpha(\lambda)$, is generally given

$$\alpha(\lambda) = A\lambda^{-4} + B + C(\lambda), \tag{1}$$

where λ is the wavelength of light and A, B and $C(\lambda)$ denote the Rayleigh scattering coefficient, the loss induced by structural imperfection and the wavelength-dependent loss induced by impurities and/or intrinsic absorption, respectively.

The first term in Eq. (1) is called Rayleigh scattering, which is caused by microscopic fluctuation of the density and/or the composition in glass, and it is one of the

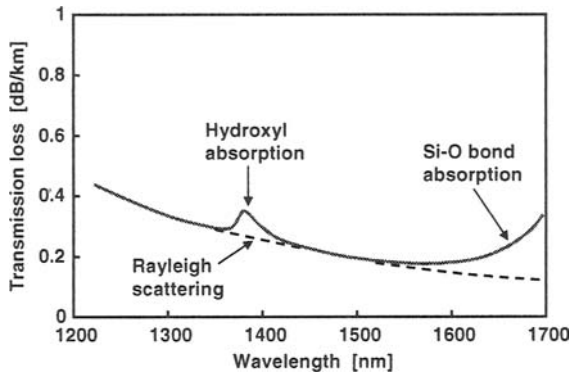

Fig. 1. Typical loss spectrum of silica-glass-based fiber.

fundamental losses of glass. The Rayleigh scattering loss is proportional to λ^{-4} and therefore it decreases quickly as the wavelength becomes longer. The Rayleigh scattering coefficient, A, is approximately 0.7 dB/km/μm^4 for pure silica, and it increases as the concentration of index-changing additives, such as GeO_2, is increased.

The second term (the structural-imperfection-induced loss) is related to longitudinal fluctuation of the core-cladding interface, for example, and it is generally independent of the wavelength. Improvement of the fabrication techniques has already reduced the structural-imperfection-induced loss to negligibly small levels.

One of the major contributions included in the third term of Eq. (1) is the intrinsic absorption induced by vibration of the Si-O bond in silica. A large absorption having a peak at 9.1 μm affects the transmission loss at wavelengths longer than 1.55 μm. Other important causes of absorption are hydroxyl bonds and transition-metal impurities, such as iron, copper, cobalt or nickel. In general, the concentration of the transition metal is so small that it does not affect the transmission loss of silica fibers manufactured properly. On the other hand, the hydroxyl bonds exhibit a peaky absorption loss spectrum around 1.39 μm. However, it is also possible to reduce the hydroxyl content to sufficiently small levels by using improved dehydration techniques in preform production [4]. Optical fibers with substantially no hydroxyl loss around 1.39 μm are now commercially available.

In the end, the fundamental loss causes in silica fibers are only Rayleigh scattering and the Si-O bond absorption. Since the Rayleigh scattering coefficient depends on the dopant concentration in the core, the lowest transmission loss can be achieved by a pure-silica-core fiber, which consists of a pure silica core with no additives and a cladding containing fluorine that lowers the refractive index.

2.2. *Nonlinearity*

In general, phenomena whereby the material properties of a given medium change when high intensity light is transmitted through it are called nonlinear effects [5]. The nonlinearity of silica is significantly small compared with other various glasses. It has, however, become important recently, because optical fiber amplifiers increase the optical signal power and the number of multiplexed optical signals in the optical fiber, resulting in noticeable levels of nonlinear effects even in silica fibers.

The nonlinear effects that are of most concern for optical fibers are nonlinear refractive index (optical Kerr effect) and stimulated scattering. The nonlinear refractive index is a small variation of the refractive index dependent upon the light intensity. This may cause various detrimental effects in the optical signal transmission, such as self-phase modulation, cross-phase modulation and four-wave mixing. Among the stimulated scattering phenomena are stimulated Raman scattering and stimulated Brillouin scattering. While nonlinear effects are generally harmful in the optical fiber communication, they are also useful in a variety of applications, such as fiber Raman amplifiers.

The nonlinear refractive index effect in the optical fiber is expressed by

$$n = N_0 + N_2 P/A_{\text{eff}} = N_0 + (N_2/A_{\text{eff}})P, \tag{2}$$

where N_0 and N_2 are the linear refractive index and the nonlinear refractive index of the fiber material, P denotes the optical power transmitted through the optical fiber and A_{eff} is called the effective core area, which is determined from the electromagnetic field distribution of the fundamental mode and represents how tightly the transmitted optical power is confined in the core. The larger the effective core area is, the lower the optical energy density is for the same total optical power P.

From Eq. (2), one of the important parameters representing the nonlinearity of the optical fiber is defined as (N_2/A_{eff}) and it is called the nonlinear coefficient. It is obvious from the definition that the nonlinear coefficient becomes small, when either the nonlinear refractive index is low, or the effective core area is large. The nonlinear refractive index depends upon the glass composition and it becomes higher when any dopant is added in silica glass. In other words, non-doped pure silica exhibits the lowest nonlinear refractive index among silica-based glasses. Differences in the nonlinear refractive index, however, are not significantly large for silica-glasses with slightly different levels of germanium concentration that are typical in various types of single mode fibers.

On the other hand, the effective core area depends strongly upon the optical fiber design or the refractive index profile of the core and it can be modified considerably by carefully designing the refractive index profile. This will be discussed in section 3.3.

2.3. Chromatic Dispersion

The dispersion represents variation in the group velocity of light transmitted through the optical fiber. In general, the dispersion determines deformation of the optical signal waveforms after transmission over the optical fiber, thus the transmission bandwidth of the optical fiber. The dispersion of the optical fiber is classified into three categories: multimode dispersion, chromatic dispersion and polarization mode dispersion.

There is no multimode dispersion in single mode fibers, since they have only one transmission mode. Therefore, single mode fibers, in principle, exhibit much larger transmission bandwidths than those of multimode fibers. The dispersion characteristics of single mode fibers are given by the chromatic dispersion and the polarization mode dispersion.

Figure 2 schematically shows the chromatic dispersion. The chromatic dispersion is the differential of the group delay of light transmitted through the optical fiber with

respect to the wavelength. The wavelength at which the chromatic dispersion is zero is called the zero-dispersion wavelength. The chromatic dispersion basically determines how much optical signals are deformed during transmission over the optical fiber, since any optical signals contain multiple light components with slightly different wavelengths or optical frequencies, which experience different group delays in the optical fiber, within some spectral bandwidths.

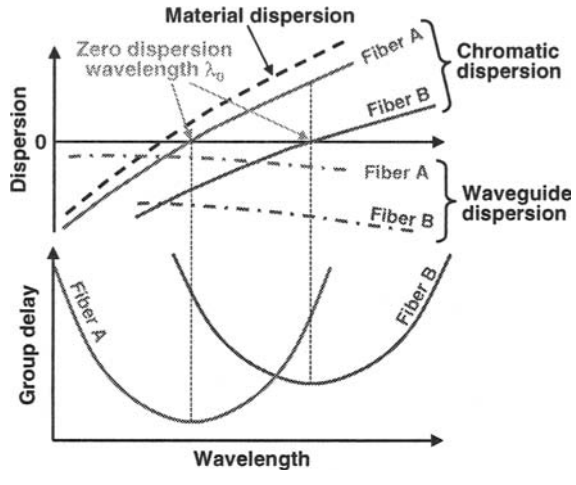

Fig. 2. Chromatic dispersion of optical fiber.

Since the signal spectral bandwidth depends fundamentally upon the signal bit rate (the higher the bit rate, the larger the signal spectral bandwidth, and the dependence is basically linear), the pulse spreading due to the chromatic dispersion is proportional to the bit rate. On the other hand, the time slot allocated for one bit optical pulse is inversely proportional to the bit rate. Therefore, the effects of the chromatic dispersion are substantially proportional to the square of the bit rate. This suggests that control of the chromatic dispersion becomes highly critical, when the signal bit rate is increased.

The chromatic dispersion can be divided further into two effects: material dispersion and waveguide dispersion. The material dispersion is the characteristic intrinsic to the material, silica in this case, and it varies depending upon the additives, such as germanium, but not very much. On the other hand, the waveguide dispersion is the dispersion induced by the fiber structure, and it strongly depends on the refractive index profile. By properly designing the refractive index profile, it is possible to some degree to tailor the waveguide dispersion, and thus the chromatic dispersion, as is illustrated in Fig. 2. This is the base of the various dispersion-modified fibers described in section 3.3.

Although it seems obvious that the chromatic dispersion of the optical fiber should be small enough or zero in order for high-speed or high-bit-rate optical signals to be transmitted over long distances, it has already been revealed that the requirements for the optical transmission line are somewhat more complicated, especially in the cases of advanced transmission systems, such as dense WDM transmission. When the chromatic dispersion of the optical fiber is close to zero in the signal wavelength band, optical signals with slightly different wavelengths traveling in the optical fiber tend to

fulfill the nearly 'matched phase' conditions, resulting in generation of the interactive nonlinear effects, such as four-wave-mixing (FWM).

In order to suppress such detrimental nonlinear effects, the chromatic dispersion of the optical fiber needs to be out of a certain range close to zero. This requirement apparently contradicts another requirement (zero or sufficiently low dispersion for signal transmission without waveform distortion). These contradictory conditions can be met by introducing dispersion compensation or dispersion management schemes, in which each of optical fibers for transmission exhibits non-zero chromatic dispersion locally and yet the overall (or average) dispersion is set close to zero in the signal wavelength band. Those are discussed in detail in sections 4 and 5.

2.4. Polarization Mode Dispersion

Actually, the single mode fiber has two transmission modes, both of which are basically the same but whose polarization axes are perpendicular to each other. The polarization mode dispersion (PMD) is the group delay difference between those two orthogonal polarization modes. If the optical fiber is perfectly circular, the two polarization modes have the same group velocity, but slight non-circularity of the fiber structure and/or asymmetric stress distribution applied to the fiber induces some birefringence, thus the PMD. Because optical power transfer between the two modes randomly occurs during transmission through the fiber, behavior of the PMD has a somewhat statistical nature.

The inter-mode group delay difference (optical pulse spreading) induced by the PMD is generally proportional to the square root of the fiber length, and it is expressed by

$$\Delta\tau_{\mathrm{total}} = \Delta\tau_{\mathrm{PMD}} \times L^{0.5} \tag{3}$$

where τ_{total} is the overall group delay difference or the total PMD (in ps), τ_{PMD} is the PMD coefficient of the fiber, which is normalized to the unit length (in ps/km$^{0.5}$), and L is the fiber length (in km).

In general, the PMD becomes more and more important, when the signal bit rate is higher and/or the transmission distance is longer. Although the requirements for the fiber PMD are dependent on the transmission schemes or the optical signal formats employed, it is a general understanding that the PMD-induced pulse spreading should be considerably smaller than the time slot allocated for one bit. Assuming the maximum allowable PMD-induced pulse spreading being one tenth of the one bit time slot, the maximum transmission distance limit posed by the fiber PMD is determined as shown in Fig. 3. It should be noted that as the signal bit rate is increased, the PMD becomes critical for long distance transmission. In order for 40 Gbit/s signals to be transmitted over 10,000 km, for example, the PMD coefficient must be around 0.02 ps/km$^{0.5}$ or lower.

Recent improvement of the production technologies has reduced the PMD to significantly low levels, such as 0.1 ps/km$^{0.5}$ or lower. Figure 4 shows an example of the PMD coefficient histogram observed for some of the latest fiber products (the extended bandwidth type NZ-DSF, PureGuide®, see section 3.3 for more details), which exhibit the average PMD coefficient less than 0.01 ps/km$^{0.5}$.

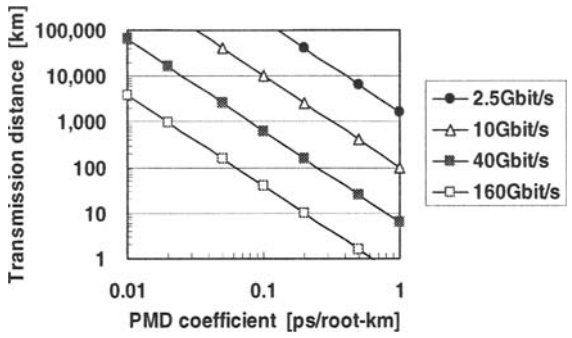

Fig. 3. Relationship between the maximum transmission distance and the fiber PMD coefficient for various bit rates.

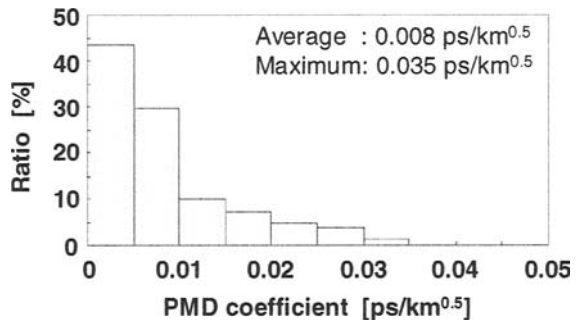

Fig. 4. An example of PMD coefficient distribution for optical fibers from recent mass production.

3. Advanced Optical Fibers for Transmission

Although it appears that optical fibers, which are now massively used in the telecommunication networks worldwide, have already reached the ultimate performance, a significant amount of efforts are still being made to improve further the optical performance or develop new types of optical fibers in order to meet the requirements necessary for advanced optical transmission. This section introduces some of the recent developmental activities in the field of advanced optical fibers for transmission.

3.1. Ultra-Low Loss Fibers

Since the advent of silica-based optical fibers, to reduce the transmission loss has been one of the biggest concerns for optical fiber manufacturers. As described in section 2, the transmission loss of the silica-based fiber is determined by the Rayleigh scattering and the Si-O bond absorption, both of which are fundamental in silica glass. Since the Rayleigh scattering coefficient becomes the lowest when no dopant is added in the silica glass, it is natural that pure-silica-core fibers (PSCF), which have no dopant in the core and contain fluorine in the cladding, exhibit the lowest transmission loss. In 1986, Sumitomo Electric Industries reported a pure-silica-core fiber having the then record

low loss of 0.154 dB/km [3], while typical transmission loss values of germanium-doped-core single mode fibers were around 0.2 dB/km in the 1.55-μm-wavelength band.

The lowest transmission loss record of the optical fiber has very recently been broken [2]. Figure 5 shows transmission loss spectra of the latest pure-silica-core fiber that has exhibited an ultra-low transmission loss less than 0.15 dB/km. This improvement has been realized through careful optimization of the production conditions. Figure 5(b) is an expanded view of the transmission loss spectrum. It is seen that the transmission loss is lower than 0.160 dB/km in a wavelength range wider than 100 nm and that the minimum loss of 0.1484 dB/km is observed at the wavelength of 1570 nm.

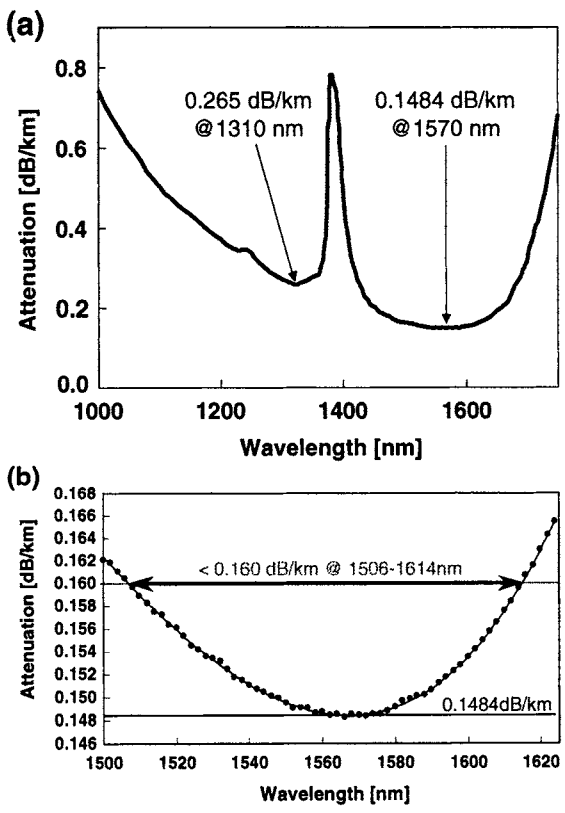

Fig. 5. Transmission loss spectrum of ultra-low loss pure-silica-core fiber (a) overall loss spectrum (b) an expanded view of the lowest loss region.

Further reduction in the transmission loss might be possible by further improvement of fabrication processes, but it is anticipated that the above loss value is very close to the theoretical limit determined by the fundamental loss causes in the silica-glass and that therefore much further improvement is almost impossible. Recent research has, however, indicated that photonic band-gap fibers may become a breakthrough in ultra-low loss optical fibers.

Figure 6 illustrates schematically the cross-section of the photonic band-gap fiber [6]. In the photonic band-gap fibers, the light is confined in the core by the photonic

band-gap that is produced by periodically arranged microscopic air holes. Unlike conventional optical fibers, in which the light is trapped in the core by the refractive index difference between the core and the cladding, in the photonic band-gap fibers, the refractive index of the core does not need to be higher than that of the cladding. The photonic band-gap fibers can transmit the light through hollow-cores or air-cores, which essentially exhibit no Rayleigh scattering and no absorption. Recent experimental results of the hollow-core photonic band-gap fibers have demonstrated the transmission loss of 13 dB/km [7], which is still significantly larger than those of the conventional fibers. This is possibly due to structural imperfections of the fibers and/or non-optimized fabrication conditions. It is anticipated that further reduction in the transmission loss may be possible in the future.

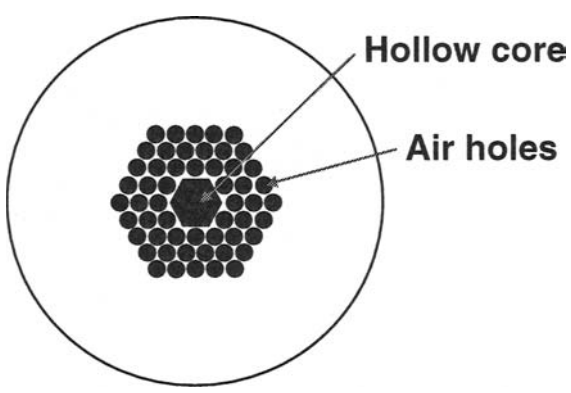

Fig. 6. Photonic band-gap fiber.

3.2. Ultra-Low Nonlinearity Fibers

The effective core area of the standard single mode fiber with a germanium-doped core is typically 80 μm^2, which is also typical with the pure-silica-core fiber. Some developmental efforts have recently been made to realize optical fibers exhibiting significantly larger effective core areas.

Figure 7 illustrates the optical fiber structure that has been investigated for this purpose [8]. The fiber design is based on the pure-silica-core fiber, which has the lowest nonlinear refractive index among various silica-based optical fibers because the core contains no additives. In general, the effective core area can be enlarged simply by lowering the refractive index difference between the core and the cladding, thus weakening confinement of the optical power into the core. It is well known, however, that this approach tends to deteriorate the bending loss performance of the fiber (increase in the transmission loss due to bending). The two-layer cladding configuration, which is called the depressed cladding structure, is effective for suppressing the bending-induced loss while enlarging the effective core area in this case.

By properly designing the structural parameters, such as the core diameter, the first cladding diameter, the refractive indexes of the core and the first and the second claddings, the pure-silica-core fiber that has a typical effective core area as large as 110 μm^2 and yet exhibits sufficiently good bending loss performance comparable to that of

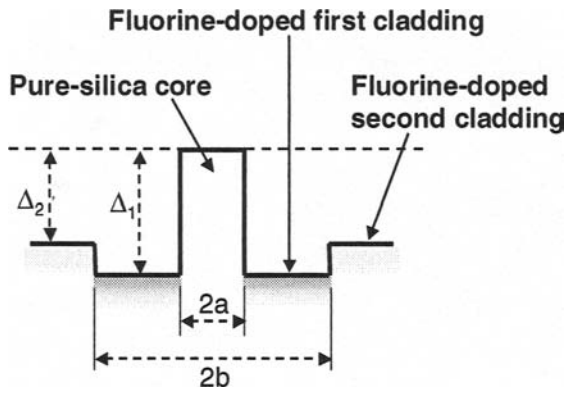

Fig. 7. Photonic band-gap fiber.

the conventional fiber has successfully been developed [8]. The nonlinear coefficient of the fiber is approximately 30% lower than that of the standard single mode fiber.

Even further reduction in the nonlinearity has also been explored by further enlarging the effective core area [9]. In general, the bending loss performance of the optical fiber has two aspects: the macro-bending loss and the micro-bending loss. The macro-bend is a type of bend with relatively large bend radii, such as several tens of millimeters, while the micro-bend is a sum of microscopic curvatures applied to the optical fiber. The micro-bending induced loss of the optical fiber is strongly dependent on the mode field diameter or the effective core area. As the effective core area is increased beyond 110 μm^2, in general, the micro-bending loss becomes so significant that the loss increase induced by just winding the optical fiber onto a spool is noticeable.

One of the possible ways of reducing the micro-bending loss in such situations is to suppress the micro-bend of the fiber itself. This can be realized by increasing the cladding diameter or the glass diameter of the fiber, thus enhancing stiffness of the fiber, which makes the fiber more resistant to the external force and suppresses the micro-bend itself. Figure 8 shows the micro-bending loss performance observed as a function of the effective core area for optical fibers having different fiber diameters. The micro-bending loss performance has been examined by measuring the loss increase after winding each of the optical fibers under test with a certain level of tension onto a spool whose surface is covered with wire mesh. It is clear from Fig. 8 that the micro-bending loss is increased as the effective core area is enlarged, but that it is suppressed significantly when the cladding diameter is increased from the standard value of 125 μm to 160 μm, for example.

Based on the above, pure-silica-core fibers having ultimately large effective core areas, as large as 211 μm^2, have successfully been fabricated [9]. These ultra-low nonlinearity fibers have the cladding diameters of 170 μm and exhibit no loss increase when they are wound on standard spools. These optical fibers have already been utilized in various optical transmission system experiments, and they have successfully proved their performance as ultra-low nonlinearity optical transmission media. Since they are off the current industrial standards of optical fibers, it might be difficult to deploy them very widely in the commercial optical transmission systems. It is, however, anticipated

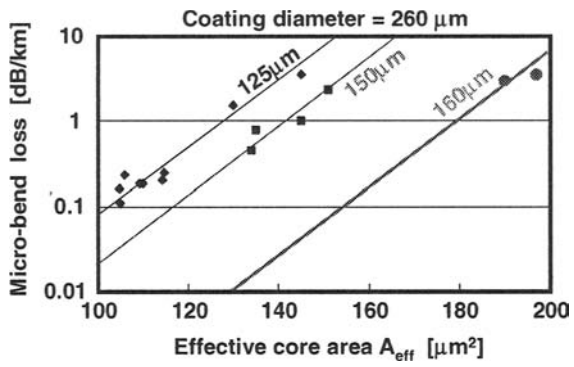

Fig. 8. Relationship between micro-bending-induced loss increase and the effective core area observed for optical fibers with different cladding diameters.

that they may find their applications in some limited areas where the nonlinearity is highly critical, such as ultra-long submarine transmission systems in the future.

Even further reduction in the nonlinearity might be possible by the hollow-core photonic band-gap fibers [6] for the same reason as the possibility of ultra-low losses. Since most of the optical power is transmitted through the air core, which is supposed to have substantially zero nonlinearity, and only a small portion of the light interacts the silica in the cladding, the hollow-core photonic band-gap fibers are expected to exhibit extremely low nonlinearity that the conventional solid-core fibers would never achieve. This would make sense, however, only when the transmission losses of such fibers are reduced to the levels of the conventional fibers, if they are to be used as long distance transmission media.

3.3. Dispersion-Modified Fibers

The standard single mode fiber (SMF) has the zero dispersion wavelengths around 1.3 μm as illustrated in Fig. 9. This is convenient when optical signals are transmitted using wavelengths around 1.3 μm, since the optical signal distortion due to the chromatic dispersion is minimized. Silica-based optical fibers, however, exhibit the lowest transmission loss around 1.55 μm. It is obvious that the 1.55-μm-wavelength band is more suited for long distance transmission, but the relatively large chromatic dispersion (approximately 17 ps/nm/km) of the standard single mode fiber tends to induce signal deterioration in this wavelength band, especially when the transmission distances are long and/or the signal bit rates are high.

In order to overcome this drawback of the standard single mode fiber, a significant amount of efforts have been made to modify the chromatic dispersion characteristics of the single mode fiber so that they are suited for advanced optical signal transmission in the 1.55-μm-wavelength band. Figure 9 shows some examples of such dispersion-modified single mode fibers.

In general, such modification of the chromatic dispersion of the single mode fiber tends to deteriorate the bending loss performance. One of the effective approaches of avoiding the bending performance degradation is to design the optical fiber so as to have relatively small mode field diameters or effective core areas with tighter confinement of

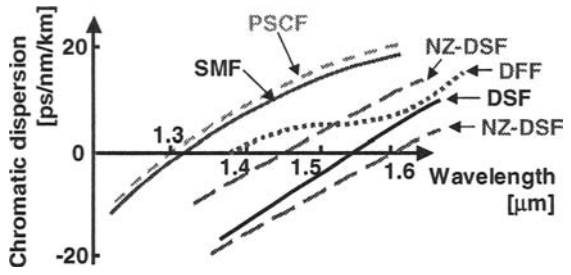

Fig. 9. Chromatic dispersion characteristics of various optical fibers.

the optical power into the core. In other words, dispersion-modified single mode fibers usually have smaller effective core areas than that of the standard single mode fiber, and thus exhibit higher nonlinearity, so long as good bending loss performance is to be maintained. Therefore, there is some fundamental constraint in designing single mode fibers having both large effective core areas and chromatic dispersion characteristics significantly different from that of the standard single mode fiber.

3.3.1. Dispersion-Shifted Fibers

The dispersion-shifted fiber (DSF) is the first generation of the dispersion-modified fiber, which has the zero-dispersion wavelength shifted from the 1.3-μm-wavelength band to the 1.55-μm-wavelength band [10,11]. The DSF is highly suited for long distance and high bit rate signal transmission in the 1.55-μm-wavelength band and has widely been deployed in the telecommunication networks. It has, however, been revealed that too small chromatic dispersion (close to zero) of the DSF in the signal wavelength band is not very preferable in the wavelength-division-multiplexed (WDM) transmission, especially when the wavelength spacing between adjacent WDM signals is relatively small, as described in section 2.3.

3.3.2. Non-Zero Dispersion-Shifted Fibers

In order to overcome the above-mentioned drawback of the DSF, non-zero dispersion-shifted fibers (NZ-DSF) have widely been developed. The NZ-DSF is the single mode fiber whose zero-dispersion wavelength is shifted from the 1.3-μm wavelength band to longer wavelengths but outside the signal wavelength bands (the 1.55-μm wavelength band, for example), and therefore it has small but not zero chromatic dispersion in the signal wavelength bands. It is relatively easy to simply adjust the zero-dispersion wavelength of the DSF to a certain point within appropriate wavelength ranges by properly choosing design parameters of the refractive index profiles.

The NZ-DSF has evolved in various ways from the first generation. Some of the important issues in designing advanced NZ-DSFs are to reduce the chromatic dispersion slope and to enlarge the effective core area. The former is intended for adjusting the chromatic dispersion to appropriate levels within a signal wavelength range as wide as possible and thus making the fiber suitable for use in wide wavelength bands. On the other hand, enlarging the effective core area is supposed to help suppress the nonlinear effects in the fiber. As described above, it generally requires some efforts

in the fiber design to achieve those targets, especially in the case of pursuing both. A number of refractive index profiles have been explored to improve the performance of the NZ-DSF [12–17], as illustrated in Fig. 10.

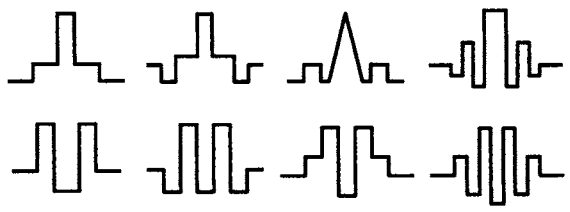

Fig. 10. Examples of refractive index profiles of NZ-DSFs that have been developed or explored.

Table 1 summarizes typical parameters of the major NZ-DSFs that are currently available in the market. Because of the constraint in the fiber design, there is a trade-off relationship between the dispersion slope and the effective core area. It should be noted that the NZ-DSF with a reduced dispersion slope (e.g., TrueWave-RS®) has a relatively small effective core area [18], while the large effective core area NZ-DSF (ex. LEAF®) exhibits a large dispersion slope [12]. The extended bandwidth type NZ-DSF (e.g., TeraLight®, PureGuide®), another class of NZ-DSF, has the zero-dispersion wavelength shorter than 1.45 μm [19,20], so that it would allow future extension of the signal wavelength bands used for the WDM transmission from the current C and L bands (1.53 $\sim$ 1.565 μm and 1.565 $\sim$ 1.625 μm) to the S band (1.46 $\sim$ 1.53 μm).

Table 1. Typical performance parameters of the major NZ-DSFs commercially available.

Parameter	Reduced-slope NZ-DSF	Large effective core NZ-DSF	Extended bandwidth NZ-DSF
Dispersion (ps/nm/km)	4	4	8
Dispersion slope (ps/nm^2/km)	0.045	0.085	0.058
Zero-dispersion wavelength (μm)	1.46	1.50	1.42
Effective core area (μm^2)	50	70	63

(Note: All parameters except zero-dispersion wavelength are values at 1.55 μm.)

3.3.3. Dispersion-Flattened Fibers

The DSFs or the NZ-DSFs whose dispersion slopes are very small and close to zero in the signal wavelength bands are specifically called dispersion-flattened fibers (DFF). The intent of the DFF is to maintain the chromatic dispersion within a certain narrow range in a signal wavelength band as wide as possible. The DFF may be useful for the ultra-large capacity WDM transmission utilizing very wide wavelength bands. The DFF may also be beneficial for transmission of very high speed or very high bit rate optical signals, which have wide spectral widths in themselves and therefore are prone to be affected by slight variations in the chromatic dispersion within the signal spectral widths.

Various types of DFFs have long been explored and developed. Recent efforts have been concentrated on the DFFs that exhibit sufficiently small dispersion slopes in the 1.55-μm wavelength band and also have reasonably large effective core areas

(low nonlinearity) [21–24]. In general, it is highly difficult to realize both nearly zero dispersion slopes and large effective core areas while maintaining the bending loss performance. In addition to that, the DFF has some fundamental difficulties in fabrication, since the chromatic dispersion characteristics of the DFF are highly sensitive to changes in the fiber structural parameters, such as the core diameter and the refractive index difference. It is anticipated that mass-production of such fibers requires high stability and controllability of the fabrication techniques. The DFFs have not yet been widely deployed in the telecommunication networks at this moment.

4. Fiber-Based Dispersion Compensators

When the 1.55-μm wavelength band of the standard single mode fiber is used for high bit rate transmission, its relatively large chromatic dispersion of approximately 17 ps/nm/km in the band limits the maximum distance over which the optical signals can be transmitted without significant waveform deformation. Table 2 summarizes typical values of the maximum transmission distances for different bit rates estimated assuming that 1.55 μm non-return-to-zero (NRZ) optical signals with no chirp are transmitted over the standard single mode fiber. As the bit rate is increased, the total dispersion that is allowed for the transmission fiber is decreased and thus the maximum transmission distance is reduced. The maximum allowable total dispersion and the maximum distance are inversely proportional to the square of the signal bit rate.

Table 2. Maximum dispersion-limited transmission distances vs. signal bit rates for 1.55 μm signal transmission over the standard single mode fiber.

Signal bit rate (bit/s)	Maximum total dispersion (ps/nm)	Maximum distance (km)
2.5 G	$\sim$ 16,000	$\sim$ 1,000
10 G	$\sim$ 1,000	$\sim$ 60
40 G	$\sim$ 60	$\sim$ 4

In order to expand the transmission distance beyond the maximum distance that is determined by the chromatic dispersion, the optical signal waveform deformation induced by the chromatic dispersion must be corrected in some way. One of the powerful techniques is to compensate for the chromatic dispersion itself of the transmission fiber. This is called dispersion compensation. Various types of technologies have already been developed to compensate for the chromatic dispersion. Fiber-based dispersion compensators are the most powerful and mature technique of the dispersion compensation, which is now widely used in the telecommunication networks.

4.1. Dispersion Compensating Fibers

Dispersion compensating fibers (DCF) are single mode fibers whose chromatic dispersions in the 1.55-μm wavelength band are negative with relatively large absolute values per unit length [25] (several tens ps/nm/km at least, typically 100 ps/nm/km or even more). As is illustrated in Fig. 11, the chromatic dispersion accumulated in the transmission fiber (the standard single mode fiber, in this case) is cancelled by inserting the DCF with an appropriate length that gives a negative total dispersion with

the absolute value matching to that of the transmission fiber. Since the DCF is used as a part of the optical transmission equipment and installed inside the transmission apparatus, the fiber is usually coiled and packaged into a small box (DCF module). An example of the DCF module is shown in Fig. 12.

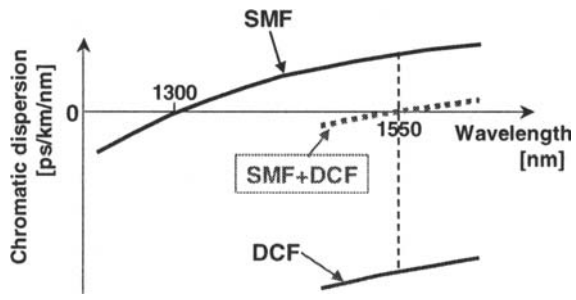

Fig. 11. Chromatic dispersion compensation by using dispersion compensating fiber (DCF).

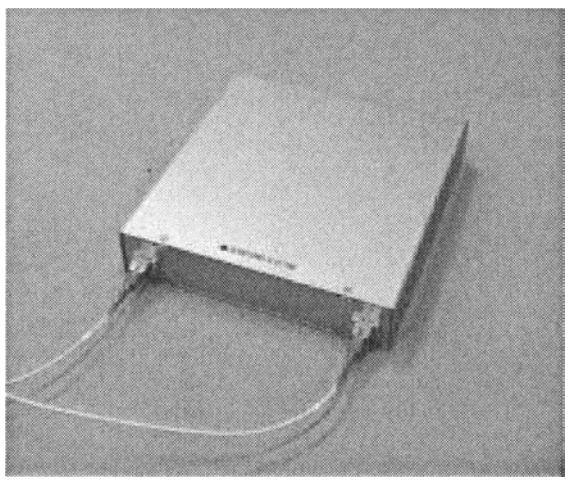

Fig. 12. Dispersion compensating fiber module.

As both the transmission distances and the signal bit rates are increased, the roll of the DCF becomes more and more important. Optical performance of the DCF has been improved dramatically since its early stage of development. A number of different types of DCFs and DCF modules have also been developed to satisfy the ever-increasing demand for more advanced optical transmission.

One of the important parameters representing the optical performance of the DCF is the figure of merit (FOM), which is defined by

$$\mathrm{FOM} = D/\alpha \quad (\mathrm{ps/nm/dB}), \tag{4}$$

where D is the chromatic dispersion at the operational wavelength and α is the transmission loss at the same wavelength. The FOM represents the dispersion per unit loss,

and it basically determines the insertion loss of the DCF module with a given dispersion value. Higher FOM can be realized either by increasing the absolute dispersion (ps/nm/km) or reducing the transmission loss (dB/km). High performance DCFs or DCF modules currently available in the market have typical FOM values of 200 to 300 ps/nm/dB [26]. More recent development has achieved advanced DCFs having both large absolute dispersion values around −300 ps/km/nm and high FOM more than 300ps/nm/dB, which have enabled ultra-compact DCF modules [27].

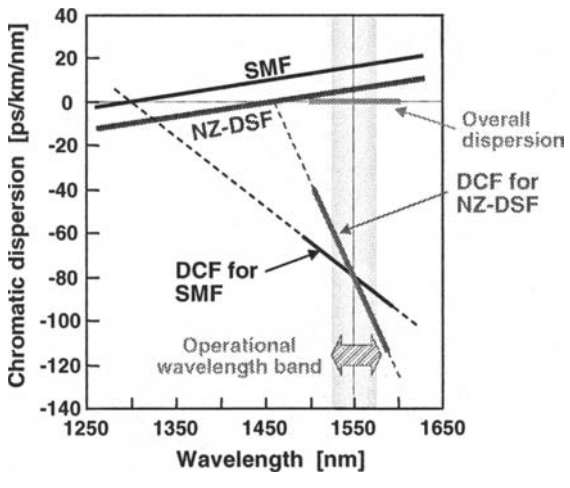

Fig. 13. Dispersion-slope compensating DCF.

Another issue of optical performance is how closely the DCF compensates for the dispersion of the transmission fiber within a wide signal wavelength range. As is illustrated in Fig. 13, when the DCF compensates for the dispersion slope as well as the dispersion of the transmission fiber at a certain wavelength, the residual dispersion after compensation becomes small enough within a certain wavelength band, not only at a single wavelength. This is highly preferable either in the wide-band WDM transmission or in the ultra-high-speed (high bit rate) signal transmission, where the dispersion needs to be sufficiently low in broad wavelength bands of the optical signals. The dispersion slope compensation is realized when the following condition is satisfied:

$$S_{\mathrm{DCF}}/D_{\mathrm{DCF}} = S_T/D_T \quad (\mathrm{nm}^{-1}), \tag{5}$$

where S_{DCF} and D_{DCF} denote the dispersion slope and the dispersion of the DCF and S_T and D_T are the same of the transmission fiber. The ratio of the dispersion slope to the dispersion (S/D) is called relative dispersion slope (RDS). Table 3 summarizes the RDS values of various types of transmission fibers.

When the RDS of the transmission fiber is relatively large, the RDS of the matching DCF must also be large. The DCFs for the NZ-DSFs need to have more negative dispersion slopes than those of the DCFs for the standard SMF or the pure-silica-core fiber. Therefore, it is generally more difficult to design and fabricate the DCFs for the NZ-DSFs while maintaining good bending loss performance. A considerable amount of efforts have been made to develop various types of DCFs so that they can cover most of the transmission fibers already installed in the fields and/or available in the

Table 3. Relative dispersion slopes (RDS) of various transmission fibers (all values are at 1.55 μm).

Fiber type	Dispersion (ps/nm/km)	Dispersion slope (ps/nm^2/km)	RDS (nm^{-1})
Standard SMF	16.5	0.058	0.0035
Pure-silica-core fiber	18.5	0.055	0.0030
Reduced-slope NZ-DSF	4	0.045	0.011
Large effective core area NZ-DSF	4	0.085	0.021
Extended-bandwidth NZ-DSF	8	0.058	0.007

market [28–30]. As a result, slope-compensating DCF modules are now commercially available for various transmission fibers including the NZ-DSFs.

Figure 14 shows an example of optical performance of the DCFs developed for the extended bandwidth type NZ-DSF (PureGuide®). It is clear that those DCFs are able to perfectly compensate for both the dispersion and the dispersion slope of the NZ-DSF either in the C band or the L band.

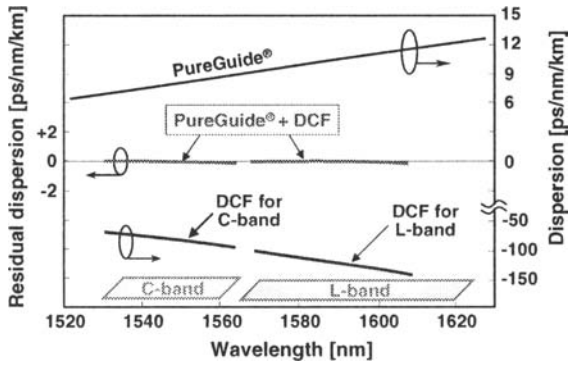

Fig. 14. Dispersion compensation performance of DCFs developed for NZ-DSF (PureGuide®).

4.2. Higher-Order Dispersion Compensation

As is shown in Fig. 14, the slope-compensating DCF compensates for the dispersion and the dispersion slope simultaneously in the signal wavelength band, however, there is some residual dispersion remaining after the compensation. Such residual dispersion is mainly caused by the slight curvature in the dispersion characteristics of both the transmission fiber and the DCF. This dispersion curvature is called higher-order dispersion (which is actually the forth-order dispersion, while the dispersion slope is the third-order dispersion).

When the bit rate of each channel is increased in the WDM transmission utilizing relatively wide signal wavelength bands, or ultra-high bit rate OTDM signals are transmitted over long-distances of transmission fibers with dispersion compensation, the residual higher-order dispersion might affect the transmission quality of the optical signals. Therefore, some efforts have also been made to develop the DCF module that can compensate the higher-order dispersion as well as the dispersion and the dispersion slope in the signal wavelength bands.

Because of some fundamental limitation of the dispersion characteristics attainable by modification of the refractive index profile, it is highly difficult to design and fabricate the DCF that perfectly compensates for the dispersion of the transmission fiber, including the higher-order dispersion, by itself. One of the promising approaches is to use two different types of DCF and cascade them so as to realize the dispersion profiles required by the transmission fiber. Figure 15(a) illustrates schematically the concept of such a hybrid DCF module [31]. The hybrid DCF module consists of a DCF having a slightly convex dispersion curve and another DCF having a slightly concave dispersion curve. By properly designing those two DCFs and adjusting the ratio of the fiber lengths to be cascaded, it is possible to achieve the dispersion spectrum that almost perfectly matches that of the transmission fiber including the higher-order dispersion.

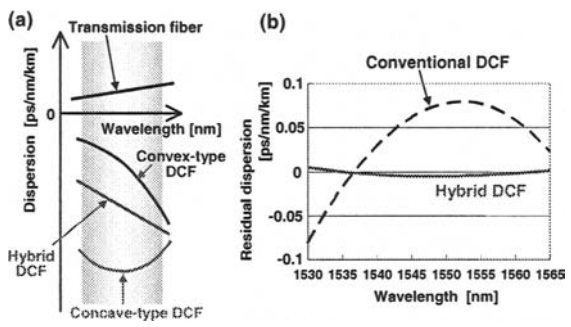

Fig. 15. Hybrid DCF module for higher-order dispersion compensation (a) Concept of the hybrid DCF module (b) Residual dispersion spectrum observed for NZ-DSF (PureGuide®) coupled with a matching hybrid DCF module.

Figure 15(b) demonstrates the dispersion characteristics observed when a higher-order dispersion compensating type hybrid DCF module is inserted after NZ-DSF (PureGuide®). A typical dispersion spectrum obtained by using a conventional slope-compensating type DCF is also plotted for comparison in the same figure. It is obvious that the newly developed hybrid DCF module can significantly reduce the residual dispersion down to nearly zero in a wide signal wavelength band.

5. Dispersion-Managed Optical Transmission Lines

Use of the DCF module is a powerful way of compensating for the dispersion of the transmission fiber and thus enabling the high-bit-rate optical signal transmission. The insertion loss of the DCF module is, however, not negligible, and therefore an additional optical amplifier is typically used in order to compensate for the loss of the DCF module in the actual transmission equipment. This may affect the signal-to-noise ratio performance of the optical transmission system.

This drawback can mostly be relieved by installing the DCF as a part of the optical transmission line, that is to say, by replacing part of the transmission fiber in the optical cable with the DCF. By properly adjusting the ratio of the transmission fiber length to the DCF length cascaded within each span or in the overall transmission distance,

the optical transmission line constructed in this way compensates for the dispersion by itself and exhibits low overall dispersions in the signal wavelength bands. This type of optical transmission line configuration is called the dispersion-managed optical transmission line.

5.1. Transmission Line Configurations

Figure 16 illustrates examples of the dispersion-managed transmission line configurations. The simplest configuration is a hybrid transmission line consisting of two fiber sections [32,33]. One of the two sections is a type of optical fiber that has a positive dispersion in the signal wavelength band, and the other is another type of fiber that has a negative dispersion. One of the variations derived from the simple hybrid configuration is a three-section configuration, in which a middle section consisting of one type of optical fiber is sandwiched between two sections consisting of another type fiber in each span [34]. In any case, in order to have the overall dispersion well under control (close to zero), it is necessary to precisely adjust lengths of the fiber sections depending upon dispersion values (per unit length) of the optical fibers to be concatenated.

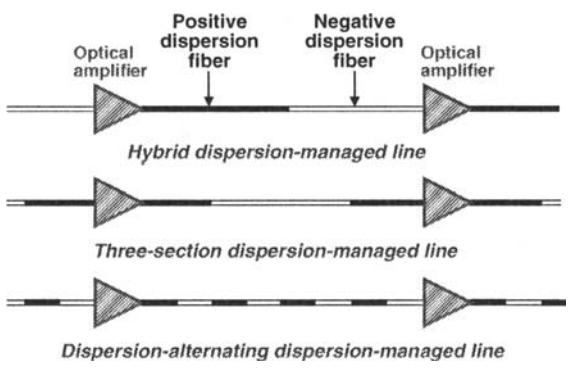

Fig. 16. Examples of dispersion managed optical transmission line configurations.

A more drastic type of dispersion-managed transmission line is the one that has the chromatic dispersion alternating (between positive values and negative values) frequently within each span. Since the number of fiber sections is large, it appears difficult to properly arrange the lengths and the dispersions of all fiber sections and thus to control the overall dispersion within a certain small range. It is, however, anticipated that some statistical nature of section-by-section variation in both the lengths and the dispersion values helps to have the overall dispersion converging to the average value in the end.

The dispersion-alternating type dispersion-managed transmission line can be realized, for example, by simply installing many pieces of optical fiber cables that contain both positive dispersion fibers and negative dispersion fibers and splicing the positive dispersion fiber to the negative dispersion fiber and vice versa at all cable joints. The dispersion-alternating fiber, which has its chromatic dispersion longitudinally alternating between a positive value and a negative value by itself within a single continuous fiber, has also been explored [35].

5.2. *Hybrid Transmission Lines*

The hybrid transmission line is one of the most promising schemes of the dispersion-managed transmission lines because of its simplicity. Actually, it has already been developed and installed as a part of submarine cable networks [36]. A typical configuration of the hybrid transmission line is illustrated in Fig. 17.

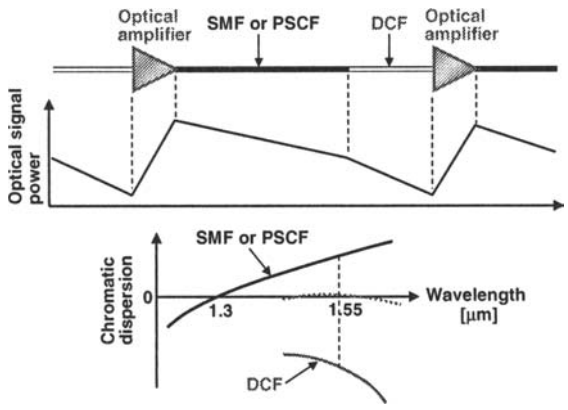

Fig. 17. Typical configuration of the hybrid optical transmission line.

The hybrid line usually consists of a positive dispersion (non-dispersion-shifted) fiber with a relatively large effective core area and negative dispersion fiber that compensates for the dispersion of the first fiber. The negative dispersion fiber (dispersion compensating fiber) tends to have a relatively small effective core area and thus to exhibit high nonlinearity. Therefore, in order to effectively suppress the overall nonlinearity of the hybrid line, it is reasonable to place the negative dispersion fiber after the positive dispersion fiber, where the optical signal power becomes relatively low after transmission over the first fiber.

The ratio of the two fiber lengths is determined by the dispersion values of the fibers. When the absolute dispersion values of the fibers are matched, the two fibers within each span are supposed to have the same lengths, assuming that the overall dispersion is set to zero (perfectly compensated). The length ratio may be different from one-to-one, depending upon the dispersion values of the fibers.

In addition to the perfect dispersion compensation, the hybrid transmission line is generally expected to have the overall dispersion slope also compensated in the signal wavelength band. This requirement is fulfilled similarly to the case of the DCF module, when the following equation is satisfied:

$$S_{\mathrm{PDF}}/D_{\mathrm{PDF}} = S_{\mathrm{NDF}}/D_{\mathrm{NDF}} \quad (\mathrm{nm}^{-1}), \tag{6}$$

where S_{PDF} and D_{PDF} denote the dispersion slope and the dispersion of the positive dispersion fiber and S_{NDF} and D_{NDF} are the same of the negative dispersion fiber.

5.3. *Design Optimization of Hybrid Transmission Lines*

There are a number of possible combinations of positive dispersion fibers and negative dispersion fibers that have different fiber structures and/or optical performance

parameters. In general, the fundamental performance of any optical transmission line is represented by the overall transmission loss and the overall nonlinearity, on condition that the chromatic dispersion is perfectly managed or compensated within the transmission line.

The overall transmission loss is simply a sum of losses of the optical fibers composing the transmission line and losses of splices made between the fibers. It is obvious that use of the low-loss pure-silica-core fiber (PSCF) as the positive dispersion fiber is beneficial for reducing the overall transmission loss [33].

The overall nonlinearity of the hybrid line can be quantitatively examined by utilizing the concept of the cumulative phase shift induced by the self phase modulation (one of the nonlinear effects) [37]. The cumulative phase shift is defined by

$$\Delta\phi = k \int_0^L \frac{N_2(z)}{A_{\text{eff}}(z)} P(z) dz, \tag{7}$$

where k is the wave number, $N_2(z)$, $A_{\text{eff}}(z)$ and $P(z)$ are the nonlinear refractive index, the effective core area and the optical signal power, respectively, at the longitudinal position z in the transmission line. The power $P(z)$ decreases as the light propagates because of the transmission loss of the optical fibers. The cumulative phase shift $\Delta\phi$ can be calculated, once the nonlinear refractive indexes, the effective core areas, the transmission losses and the lengths of the two fiber types are given.

By utilizing the cumulative SPM-induced phase shift as a measure, optimization of the hybrid transmission line configuration has been explored [37]. In this study, use of the pure-silica-core fiber with a large effective core area of 110 μm^2 has been assumed as the positive dispersion fiber, and various dispersion compensating fibers with different designs have been examined as the negative dispersion fiber. A series of calculations have revealed that there is an optimum range of the ratio between the two fiber lengths that minimizes the overall nonlinearity.

Figure 18 shows an example of such calculation results. The cumulative phase shifts calculated for various fiber designs are plotted as a function of the DCF length ratio, which is defined by the ratio of the DCF length to the span length. Four different cases, each of which gives a certain level of the average dispersion slope, are plotted in the same figure. It is found that pursuing zero dispersion slopes (perfect dispersion slope compensation) tend to slightly increase the overall nonlinearity and that the optimum DCF length ratio is around 30%. Further massive calculations have also indicated that this observation is somewhat universal and applicable to most of the cases with different fiber designs.

Another issue of the design optimization is to expand the signal wavelength band in which the overall dispersion is sufficiently small [38]. Figure 19 shows an example of dispersion characteristics of such wideband dispersion-compensated hybrid transmission lines. This specific case exhibits the maximum residual dispersion as low as 2 ps/nm/km for 100 km of the hybrid line within a broad wavelength band wider than 80 nm, which covers both C and L bands. The average transmission loss of the hybrid line (including a splice loss) is also as low as 0.202 dB/km at 1550 nm, which is almost equivalent to those of standard transmission fibers. This low average loss can definitely be attributed to use of a low loss pure-silica-core fiber.

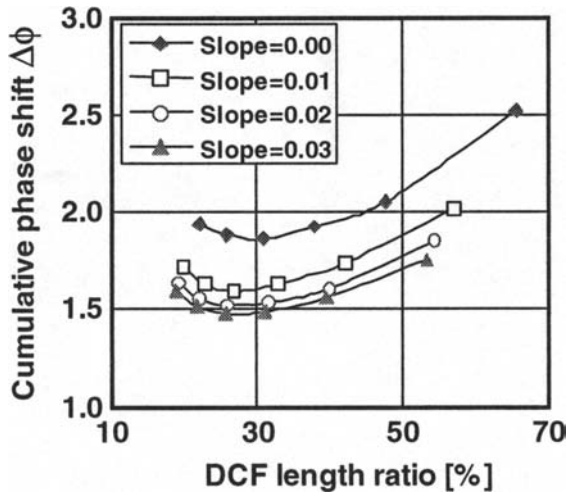

Fig. 18. Cumulative SPM-induced phase shift vs. DCF length ratio calculated for hybrid transmission lines consisting of A_{eff}-enlarged PSCF and various designs of DCF exhibiting different levels of average dispersion slopes (in ps/nm^2/km).

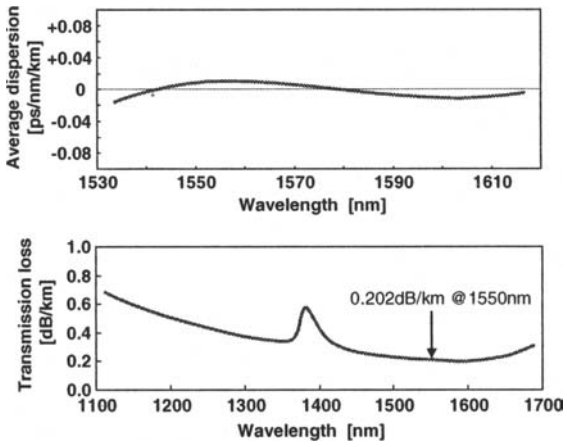

Fig. 19. Chromatic dispersion and transmission loss spectra of an ultra-wideband hybrid optical transmission line.

6. Summary

In parallel with the progress of the optical transmission technology, optical fibers and optical transmission lines have also evolved toward ultimate performance. Major directions of such evolutions in the optical fiber technology are reduction in attenuation, reduction in nonlinearity and precise control of dispersion. As for the attenuation and the nonlinearity, pure-silica-core fibers have recently achieved the record low attenuation of 1.484 dB/km and also the ultimately large effective core area of 211 μm^2.

For controlling the chromatic dispersion, various types of dispersion-modified fibers, such as non-zero dispersion-shifted fibers, have been developed and commercialized.

In order to cope with the chromatic dispersion of transmission fibers, fiber-based dispersion compensators or dispersion compensating fibers have also been developed and they are now employed very widely in actual optical transmission systems. Further improvements in optical performance of the fiber-based dispersion compensators, such as higher-order dispersion compensation, are being pursued. A more advanced scheme of the dispersion compensation, which is called the dispersion managed transmission line, has also been successfully developed and introduced into submarine cable networks.

Advancement of the optical transmission technology has been dependent strongly upon the performance of optical fibers or optical transmission lines. It is anticipated that the evolution of the optical fiber technology continues to support the progress of the optical transmission technology.

References

1. F. P. Kapron, D. B. Keck, R. D. Maurer, "Radiation losses in glass optical waveguides", in: Proceedings of Conference on Trunk Telecommunications by Guided Waves, pp. 148–153 (1970)
2. K. Nagayama, M. Kakui, M. Matsui, T. Saitoh, Y. Chigusa, "Ultra-low-loss (0.1484 dB/km) pure silica core fiber and extension of transmission distance", Electron. Lett., **38**, 1168–1169 (2002)
3. H. Kanamori, H. Yokota, G. Tanaka, M. Watanabe, Y. Ishiguro, I. Yoshida, T. Kakii, S. Itoh, Y. Asana, S. Tanaka, "Transmission characteristics and reliability of pure-silica-core single-mode fibers", J. Lightwave Technol., **LT-4**, 1144–1150 (1986)
4. F. Hanawa, S. Sudo, M. Kawachi, M. Nakahara, "Fabrication of completely OH-free VAD fiber", Electron. Lett., **16**, 669–700 (1981)
5. G. P. Agrawal, *Nonlinear Fiber Optics* (Academic Press, 1989)
6. T. Birks, P. J. Roberts, P. St. J. Russell, D. M. Atkin, T. J. Shepherd, "Full 2-D photonic bandgaps in silica/air structures", Electron. Lett., **31**, 1941–1942 (1995)
7. N. Venkataraman, M. T. Gallagher, C. M. Smith, D. Muller, J. A. West, K. W. Koch, J. C. Fajardo, S. Park, "Low loss (13 dB/km) air core photonic band-gap fibre", in: Proceedings of European Conference on Optical Communication (ECOC2002), Paper PD1.1 (2002)
8. T. Kato, M. Hirano, M. Onishi, M. Nishimura, "Ultra-low nonlinearity low-loss pure silica core fibre for long haul WDM transmission, Electron. Lett., **35**, 1615–1617 (1999)
9. M. Tsukitani, M. Matsui, K. Nagayama, E. Sasaoka, "Ultra low nonlinearity pure-silica-core fiber with an effective area of 211 μm^2 and transmission loss of 0.159 dB/km", in: Proceedings of European Conference on Optical Communication (ECOC2002), 2, Paper 3.2.2 (2002)
10. N. Kuwaki, M. Ohashi, C. Tanaka, N. Uesugi, "Dispersion-shifted convex-index single-mode fibres", Electron. Lett., **21**, 1186 (1985)
11. D. T. Croft, J. E. Ritter, "Low-loss dispersion-shifted single-mode fiber manufactured by the OVD process", in: Technical Digest of Optical Fiber Communication Conference (OFC'85), Paper WD2 (1985)

12. Y. Liu, A. J. Antos, V. A. Bhagavatula, M. A. Newhouse, Single-mode dispersion-shifted fibers with effective area larger than 80 μm^2 and good bending performance", in; Proceedings of European Conference on Optical Communication (ECOC'95), Paper TuL.2.4, pp. 333–336 (1995)

13. T. Kato, S. Ishikawa, E. Sasaoka, M. Nishimura, "Low nonlinearity dispersion-shifted fibers employing dual-shaped core profile with depressed cladding", in: Technical Digest of Optical Fiber Communication Conference (OFC'97), Paper TuN2, p. 66 (1997)

14. P. Nouchi, P. Sansonetti, J. von Wirth, C. Le Sergent, "New dispersion shifted fiber with effective area larger than 90 μm^2", in: Proceedings of European Conference on Optical Communication (ECOC'96), 1, Paper MoB.3.2, pp. 49–52 (1996)

15. Y. Liu, A. J. Antos, M. A. Newhouse, "Large effective area dispersion-shifted fibers with dual-ring index profiles", Technical Digest of Optical Fiber Communication Conference (OFC'96), Paper WK15, pp. 165-166 (1996)

16. M. Kato, K. Kurosawa, Y. Miyajima, "A new design for dispersion-shifted fiber with an effective core area larger than 100 μm^2 and good bending characteristics", in: Technical Digest of Optical Fiber Communication Conference (OFC'98), Paper ThK1, pp. 301–302 (1998)

17. M. Hirano, T. Kato, T. Ishihara, M. Nakamura, Y. Yokoyama, M. Onishi, E. Sasaoka, Y. Makio, M. Nishimura, "Novel ring core dispersion-shifted fiber with depressed cladding and its four-wave-mixing efficiency", in: Proceedings of European Conference on Optical Communication (ECOC'99), 2, pp. 278–279 (1999)

18. D. W. Peckham, A. F. Judy, R. B. Kummer, "Reduced dispersion slope non-zero dispersion fiber, Proceedings of European Conference on Optical Communication (ECOC'98)", 1, pp. 139–140 (1999)

19. S. Bigo, S. Gauchard, S. Borne, P. Bousselet, P. Poignant, L. Lorcy, A. Bertaina, J. -P. Thiery, S. Lanne, L. Pierre, D. Bayart, L. -A. De Montmorillon, R. Sauvageon, J. -F. Chariot, P. Nouchi, J. -P. Hamaide, J. -L. Beylatet, "1.5 Terabit/s WDM transmission of 150 channels at 10 Gbit/s over 4×100 km of TeraLight^{TM} fiber, in Proceedings of European Conference on Optical Communication (ECOC'99)", Paper PD2-9, pp. 40–41 (1999)

20. T. Ooishi, Y. Kubo, Y. Yokoyama, T. Kato, M. Yoshida, M. Onishi, Y. Makio, "Non-zero dispersion shifted fiber for wide band WDM transmission including S-band", in: Proceedings of Optoelectronics and Communications Conference (OECC2000), Paper 12B3-4, pp. 136-137 (2000)

21. Y. Liu, W. B. Mattingly, D. K. Smith, C. E. Lacy, J. A. Cline, E. M. DeLiso, "Design and fabrication of locally dispersion-flattened large effective area fibers", in: Proceedings of European Conference on Optical Communication (ECOC'98), 1, pp.37-38 (1998)

22. Y. Yokoyama, T. Kato, M. Hirano, M. Onishi, E. Sasaoka, Y. Makio, M. Nishimura, "Practically feasible dispersion flattened fibers produced by VAD technique, in Proceedings of European Conference on Optical Communication (ECOC'98), 1, pp. 131–132 (1998)

23. N. Kumano, K. Mukasa, M. Sakano, H. Moridaira, T. Yagi, K. Kokura, "Novel NZ-DSF with ultra-low dispersion slope lower than 0.020 ps/nm2/km, in Proceedings of European Conference on Optical Communication (ECOC2001)", 6, Paper PD.A.1.5, pp. 54–55 (2001)

24. S. Matsuo, Y. Takenaga, K. Himeno, K. Harada, "Ultra low dispersion-slope non-zero dispersion-shifted fiber with equivalent relative dispersion slope to conventional single-mode fiber", in: Proceedings of Optoelectronics and Communications Conference (OECC 2002), Paper 11D1-2 (2002)

25. J. M. Dugan, A. J. Price, M. Ramadan, D. L. Wolf, E. F. Murphy, A. J. Antos, D. K. Smith, D. W. Hall, "All-optical, fiber-based 1550 nm dispersion compensation in a 10 Gbit/s, 150

km transmission experiment over 1310 nm optimized fiber", in: Technical Digest of Optical Fiber Communication Conference (OFC'92), Paper PD14, pp. 367–370 (1992)

26. M. Onishi, Y. Koyano, M. Shigematsu, H. Kanamori, M. Nishimura, "Dispersion compensating fibre with a high figure of merit of 250 ps/nm/dB", Electron. Lett., **30**, 161–162 (1994)
27. T. Yokokawa, T. Kato, T. Fujii, Y. Yamamoto, N. Honma, A. Kataoka, M. Onishi, E. Sasaoka, K. Okamoto, "Dispersion compensating fiber with large negative dispersion around -300 ps/km/nm and its application to compact module for dispersion adjustment", in: Technical Digest of Optical Fiber Communication Conference (OFC2003), 2, Paper FK5, pp. 717–718 (2003)
28. M. Onishi, T. Kashiwada, Y. Koyano, Y. Ishiguro, M. Nishimura, H. Kanamori, "Third-order dispersion compensating fibres for non-zero dispersion shifted fibre links", Electron. Lett., **32**, 2344–2345 (1996)
29. T. Kato, M. Hirano, K. Fukuda, A. Tada, M. Onishi, M. Nishimura, "Design optimization of dispersion compensating fiber for NZ-DSF considering nonlinearity and packaging performance", in: Technical Digest of Optical Fiber Communication Conference (OFC2001), Paper TuS6 (2001)
30. H. Hatayama, M. Hirano, T. Yokokawa, T. Kato, M. Onishi, E. Sasaoka, "Dispersion compensating fiber for large-Aeff NZ-DSF with low residual dispersion by the technique of suppressing the micro-bending loss", in: Proceedings of European Conference on Optical Communication (ECOC2003), 3, Paper We4.P.32, pp. 620–621 (2003)
31. Y. Yamamoto, T. Fujii, T. Yokokawa, T. Kato, E. Sasaoka, M. Onishi, "Hybrid dispersion compensating fiber modules with ultra-low residual dispersion by canceling the dispersion curvature, to be presented in Optical Fiber Communication Conference (OFC2004) at Los Angeles, USA, February 2004
32. K. Mukasa, Y. Akasaka, Y. Suzuki, T. Kamiya, "Novel network fiber to manage dispersion at 1.55 m with combination of 1.55 m zero dispersion single mode fiber", in: Proceedings of European Conference on Optical Communication (ECOC'97), 1, pp. 127–130 (1997)
33. K. Kashiwada, M. Onishi, S. Ishikawa, T. Kato, T. Okuno, M. Nishimura, "Ultra-low chromatic and polarization mode dispersion hybrid fiber links for ultra-high speed transmission systems", in: Proceedings of Optoelectronics and Communications Conference (OECC'98), Paper 15C1-3, pp. 364-365 (1998)
34. R. Hainberger, J. Kumasako, K. Nakamura, T. Terahara, H. Onaka, "Optimum span configuration of Raman-amplified dispersion-managed fibers", in: Technical Digest of Optical Fiber Communication Conference (OFC2001), Paper MI5 (2001)
35. V. A. Bhagavatula, G. Berkey, D. Chowdhury, A. Evans, M. J. Li, "Novel fibers for dispersion-managed high-bit-rate systems", in: Technical Digest of Optical Fiber Communication Conference (OFC'98), Paper TuD2, pp. 21–22 (1998)
36. B. Bakhshi, D. Kovsh, G. Mohs, R. Lynch, M. Manna, E. Golovchenko, W. Patterson, M. Vaa, P. Corbett, M. Sanders, H. Li, G. Harvey, S. Abbott, "Terabit/s field trial over the first installed dispersion-flattened transpacific system", in: Technical Digest of Optical Fiber Communication Conference (OFC2003), Paper PD27 (2003)
37. M. Tsukitani, T. Kato, E. Yanada, M. Hirano, M. Nakamura, Y. Ohga, M. Onishi, E. Sasaoka, Y. Makio, M. Nishimura, "Low-loss dispersion-flattened lines consisting of low-nonlinearity pure silica core fibres and dispersion compensating fibres", Electron. Lett., **36**, 64–66 (2000)
38. M Tsukitani, E. Yanada, T. Kato, E. Sasaoka, Y. Makio, M. Nishimura, "Perfectly-dispersion-flattened hybrid optical transmission lines for ultra-large capacity WDM transmission", in: Proceedings of 4th International Topical Workshop on Contemporary Photonic Technologies (CPT2001), Paper P-01, pp. 81–82 (2001)

DOI: 10.1007/s10297-004-0026-9
Originally published in J. Opt. Fiber. Commun. Rep. 2, 256–278 (2005)

Fiber Bragg gratings for dispersion compensation in optical communication systems

M. Sumetsky[1] and B.J. Eggleton[2]

[1] OFS Laboratories, 19 Schoolhouse Rd.
Somerset, NJ 08873, USA
[2] CUDOS—Center for Ultra-high bandwidth Devices for Optical Systems
School of Physics, University of Sydney, NSW 2006, Australia

Abstract. This paper presents an overview of fiber Bragg gratings (FBGs) fabrication principles and applications with emphasis on the chirped FBG used for dispersion compensation in high-speed optical communication systems. We discuss the range of FBG parameters enabled by current fabrication methods, as well as the relation between the accuracy of FBG parameters and the performance of FBG-based dispersion compensators. We describe the theory of the group delay ripple (GDR) generated by apodized chirped fiber gratings using the analogy between noisy gratings and superstructure Bragg gratings. This analysis predicts the fundamental cutoff of the high frequency spatial noise of grating parameters in excellent agreement with the experimental data. We review the iterative GDR correction technique, which further improves the FBG quality and potentially enables consistent fabrication of FBG-based dispersion compensators and tunable dispersion compensators with unprecedented performance.

1. Introduction

Conventionally, compensation of the fiber dispersion is accomplished using dispersion compensation fiber (DCF), which is the main component of dispersion compensation modules (DCMs) employed in WDM and OTDM systems. Alternative solutions for dispersion compensation, other than DCF, have been suggested in order to reduce the insertion loss, spatial dimensions, nonlinearities, and costs. While transmission fibers and DCF has evolved to satisfy almost all of these demands [1], the new technologies have allowed important functions, such as dispersion tunability, as well as small size, cost, and loss for single channel applications. Currently, several types of dispersion compensation schemes are known and the fiber Bragg grating (FBG) dispersion compensator (DC) originally suggested in [2], is one of the most versatile

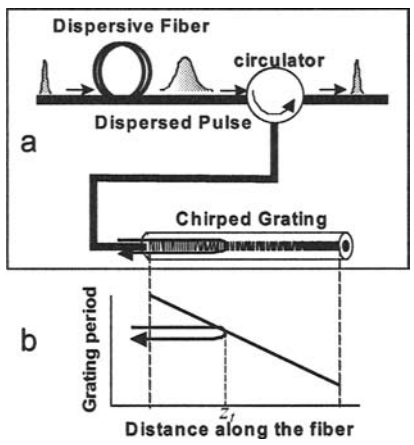

Fig. 1. (a) Schematic of DC device based on CFBG; (b) grating period variation along the fiber length.

and well developed techniques [3]. Generally, chirped FBG (CFBG) can serve as a single and a multi-channel DCM as well as provide additional feature of dynamic dispersion compensation [4], which are not possible with DCF and become critical for high-speed WDM and OTDM systems. In this paper we mostly concentrate on the fabrication principles, properties and applications of the single-channel CFBG, which find applications in both high-speed WDM and OTDM systems.

A schematic of CFBG based dispersion compensation is shown in Fig. 1. Depending on the wavelength of the light component, it is reflected from different locations within the FBG (Fig. 1) and therefore experiences different group delay, τ. The group delay is approximately proportional to the distance to the turning point, z_t, $\tau(\lambda) = z_t(\lambda)/c$, where c is the speed of light in the fiber and λ is the radiation wavelength. The distance z_t is determined by the local Bragg condition $\lambda = 2n_0\Lambda(z_t)$ where n_0 is the effective refractive index and $\Lambda(z)$ is the local FBG period. The device shown in Fig. 1 has negative dispersion enabling compensation of positive dispersion introduced by optical fiber. For WDM systems, in order to perform DC within a singe channel, the fiber grating should be linearly chirped, i.e., the change in FBG period Λ should be linear with the distance along the mask z, $\Lambda(z) = \Lambda_0 + Cz$, where the coefficient C determines the chirp of FBG. In the case of OTDM systems, the dependence $\Lambda(z)$ includes non-linear terms (see, e.g., [6]).

In practice, the requested dependence $\Lambda(z)$ cannot be achieved exactly because of systematic and random errors, which are introduced during the CFBGs fabrication. As the result, the spatial dependencies of realistic CFBG parameters are noisy. The latter introduces reflection amplitude ripple and group delay ripple (GDR) resulting in imperfect dispersion compensation and hence, optical signal-to-noise ratio (OSNR) penalty. Obviously, the performance of the FBG-based dispersion compensators is determined by the quality of CFBG fabrication.

This paper is structured as follows: In section 2 we review the principles of FBG fabrication. This discussion focuses on the methods utilizing high-quality chirped holographic and e-beam phase masks. Section 3 specifies the parameters of FBG and section 4 discusses the accuracy needed for fabrication of high-performance CFBG. In section 5 we review the theory of GDR for CFBGs and introduce the concept of GDR reduction through a correction technique. In section 6 we present detailed discussion on the CFBG correction methods. In section 7, we describe the 40-Gb/s tunable dispersion compensator, which was fabricated with the correction technique and discuss its performance. The paper is finalized by a short summary.

2. Fiber Bragg Grating Fabrication Principles

There are two principal problems to be solved in the field of FBG fabrication. The first one is related to the development of the advanced fiber grating fabrication techniques, which enables to create gratings having broad specifications of the period and amplitude variations (chirped, apodized, superstructure grating, etc). Solution of this problem is critical for development of the advanced FBG-based optical communication devices like multi-channel filters, dispersion compensators, and coders. The second equally important direction is the improvement of grating quality. Actually, the main impediment for several applications of FBG is the essential noise in their spectral characteristics. Reducing noise will enhance the desirability of FBGs against other optical communication devices, like dispersion compensating fibers, and significantly broaden the use of FBG.

One of the most accurate, reproducible, and convenient FBG fabrication technique utilizes the phase masks [6,3]. In the simplest FBG writing technique, the grating in fiber replicates the phase mask grating characteristics. In advanced fiber grating writing, the mask, the fiber, and the exposing laser beam may move with respect to each other. Then the FBG properties are governed by the mask parameters as well as the relative speeds of these movements. Once the phase mask is used in FBG writing, it is reasonable to look at the complete fiber grating production, which includes both the phase mask fabrication and FBG writing and is symbolically illustrated in Fig. 2. Below we consider only the holographic methods of phase mask and FBG manufacturing. The phase mask and FBG writing have much in common being similarly based on exposure with a spatially periodic pattern created by interference of coherent laser beams.

In general, holography is a method for creating images by means of interference between coherent beams and, also, for measuring the relation between the phases and amplitudes of the beams diffracted from the object under test and the physical properties of this object [7]. Consider the result of interference of coherent beams having spatial dependent amplitudes, $A_j(\mathbf{r})$, and phases, $j(\mathbf{r})$:

$$\Theta(\mathbf{r}) = \sum_j A_j(\mathbf{r}) \exp(i\phi_j(\mathbf{r})). \tag{1}$$

The interference pattern $\Theta(\mathbf{r})$ may be specially designed in order to create a predetermined image. Alternatively, if the pattern $\Theta(\mathbf{r})$ is a result of diffraction of several beams from the object under test, it may be used for measuring the geometrical and

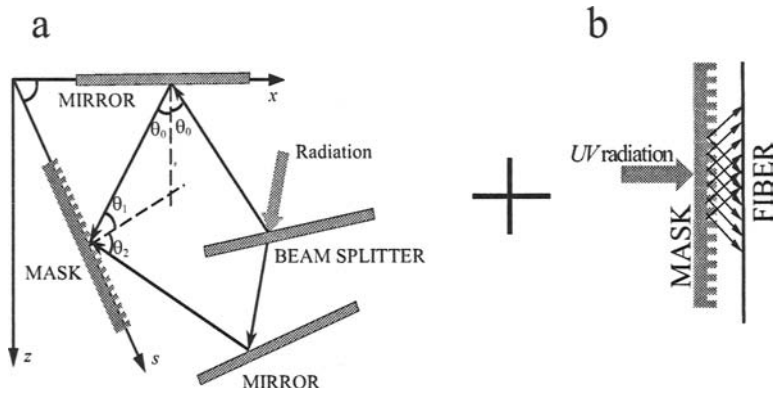

Fig. 2. Illustration of unified phase mask and fiber grating fabrication technique: (a) phase mask fabrication principle, (b) FBG fabrication principle.

physical properties of this object. In the particular applications reviewed in this paper, the first approach is used for holographic phase mask and fiber grating fabrication, while the second one allows to characterize these gratings.

The principles of holographic fabrication of phase masks and fiber gratings have much in common. Both utilize the laser beam transformed by the optomechanical system (OMS), which creates an interference pattern $\mid \Theta(x) \mid^2$ at the mask blank or at the fiber core, where $\Theta(x)$ is defined by Eq. (1), as illustrated in Fig. 2. The OMS splits the beam into two or more coherent beams and then directs them onto the surface of the mask or into the fiber core. Generally, this system performs spatial and temporal transformations of the beams. Figure 3 lists possible components of a grating writing holographic system. The spatial transformations are performed by mirrors, lenses, prisms, apertures, gratings, and beam splitters, while the temporal transformations are performed by beam modulators. The OMS realization depends on specific application and the technique one chooses to write a grating.

The output beams can be classified by the characteristic dimension of their cross-section along the mask or fiber. If the beam dimension is equal to the grating length then the beam translation is not needed and one deals with a "flood" exposure. If the grating to be written is longer than the size of interference pattern then the beams should be translated in order to fabricate the grating of a given length. The flood exposure is more stable and provides gratings of better quality than the moving beam exposure. However, for the flood exposure the grating modulation amplitude is replicating the local laser beam intensity and usually is not uniform. For a moving beam of width w, the grating amplitude can be made uniformly or predefined non-uniformly distributed by modulation of the beam power everywhere except for the vicinities of the edges of grating having the width of $w/2$. The simplest OMS utilizing the flood exposure is the Lloyd mirror configuration shown in Fig. 4(a) [3]. It consists of a beam expander and a mirror placed at normal direction to the exposing mask or fiber. The grating pattern is obtained by interference between the beam incident directly onto the mask and the beam reflected from the mirror. If the power density of the incident coherent beam

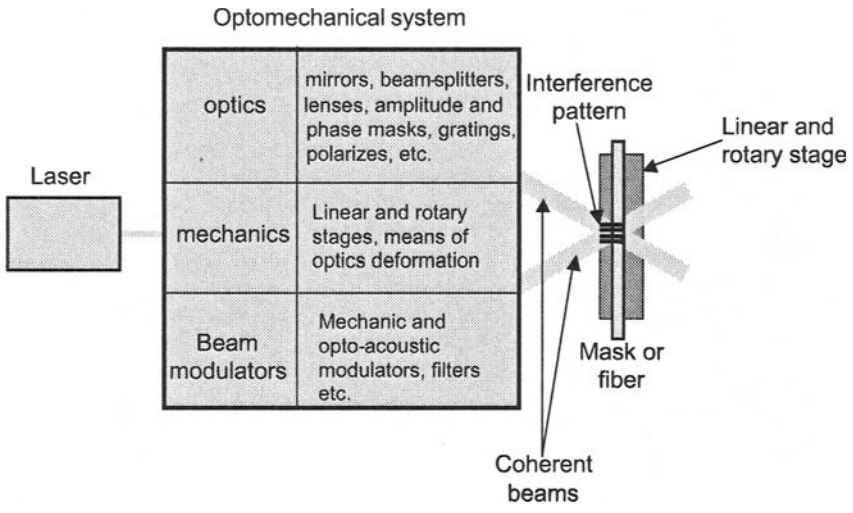

Fig. 3. Holographic system components for phase mask and FBG writing.

is not uniform then the resultant intensity of the fringe pattern introduced is also not uniform. For the Lloyd mirror system, the uniform fringe pattern can be achieved if the spatial power distribution of the incident beam is flattened by a beam homogenizer. Alternatively, the OMSs outlined in Fig. 4(b,c) [8] can be used for creating long grating patterns (limited by the mirror and beam splitter dimensions) by translation of relatively narrow interfering coherent beams along the mask or fiber. Both configurations, (b) and (c), are stable to first order in small deviations of the incident beam direction. The advantage of the system shown in Fig. 4(c) is that it can be adjusted to a zero path difference of the interfering beams and minimizes requirements on laser coherence length [8].

If the OMS creates and interferes the collimated beams it can fabricate the gratings with uniform period only. Several designs were suggested for manufacturing gratings having spatially dependent period (chirped gratings). In order to form a chirped interference pattern one has to ensure the non-planar wavefront of at least one of the interfering beams, which can be created using lenses and/or curved mirrors. The basic idea of writing a chirped grating using a curved mirror is illustrated in Fig. 5. The local grating period created by interference of two beams is defined by

$$\Lambda = \frac{\lambda_{uv}}{\sin\theta_1 + \sin\theta_2}, \tag{2}$$

where θ_1 and θ_2 are the incident angles of beams 1 and 2, respectively. As shown in Fig. 5(a), for a curved mirror the angle θ_1 is a function of coordinates along the mask or fiber.

The superstructure gratings can be created by periodic modulation of the laser beam while writing a mask or a FBG, as it was first demonstrated in [9]. For the same purpose one can use the long-period amplitude mask as shown in Fig. 5(b) [10]. The number of channels created, N, is inversely proportional to the duty cycle of the

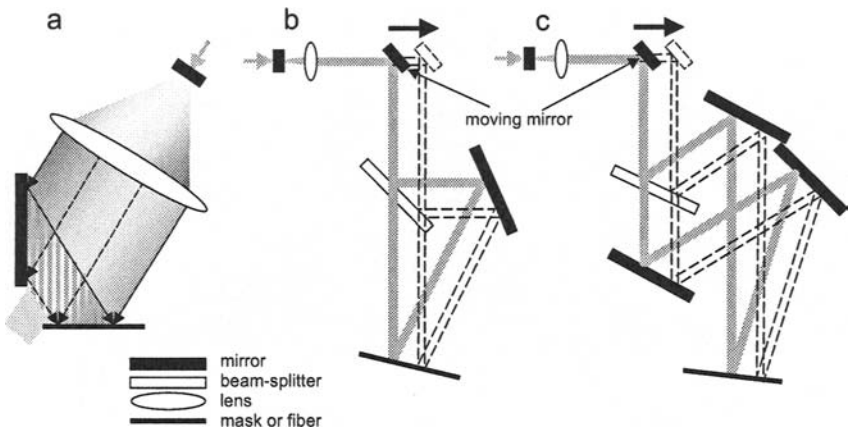

Fig. 4. (a) the Lloyd mirror grating writing system. (b) unbalanced grating writing system with a moving mirror. (c) balanced grating writing system with a moving mirror.

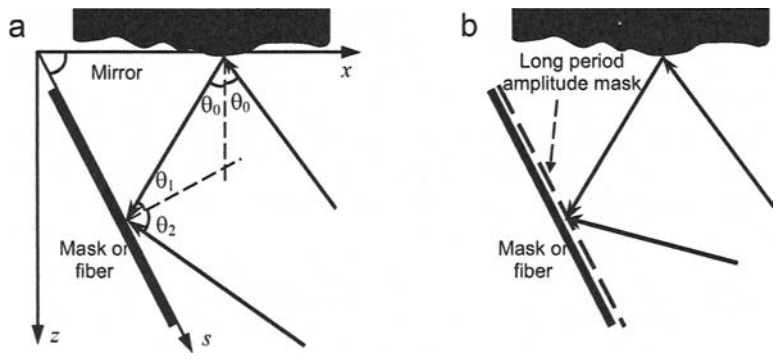

Fig. 5. (a) Creation of interference pattern by a curved mirror. (b)Superstructure grating writing.

amplitude mask and, for big N, much of the phase mask or fiber within a superstructure period remains empty. In order to use the space more effectively, the ideas of grating interleaving [11] and phase-only superstructure gratings [12–14] were proposed.

The OMSs described so far represent the most common attributes of the current conventional holographic phase mask and FBG writing systems. They allow fabrication of high quality phase masks and fiber gratings. The limitations of these systems are in grating length, which is bounded by the size of mirrors and a beam splitter, and in a

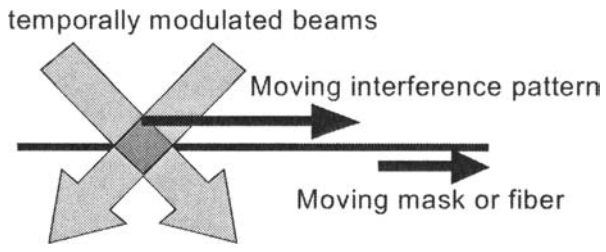

Fig. 6. Illustration of the point-by-point grating writing technique.

limited choice of grating chirp and amplitude dependences, which are defined by the curved mirror or lenses surface profile and the amplitude mask configuration. Also, the grating amplitude can be changed by the beam modulation with characteristic spatial resolution of the order of the beam size.

Going beyond these limitations the point-by-point grating writing technique was developed [16–18]. Similar to Doppler effect, if the interference pattern is moving with respect to the mask/fiber the inscribing grating experiences a shift in its period. The idea of point-by-point writing is to use this effect for chirping the grating period (see Fig. 6). It is necessary to use narrow interfering beams so that the moving pattern is not washed out during its displacement along the mask or fiber equal to the width of the beam. The width of such a "point" beam is usually of the order 100 μm. In order to write long gratings the beam modulator is used. It tunes the light off when the interference pattern is translated along the mask or a fiber by the integer number of grating periods.

To summarize, the current phase mask and FBG fabrication methods utilize a combination of different techniques based on the beam and OMS parts translation, rotation, and deformation, as well as spatial and temporal beam modulation. The characteristic spatial scales of the grating fabrication systems vary from meters, for FBG length, to fractions of nanometers, for phase mask and fiber positioning accuracy in advanced point-by-point fabrication. The characteristic time scales vary from hours, which are taken for long FBG writing, to fractions of milliseconds for the period of the beam temporal modulation.

3. FBG Specifications

The FBG used in optical communications may be classified by their bandwidth and separated into single-channel, multi-channel, and broadband gratings. The bandwidth of a single-channel grating is around 1 nm, while the bandwidth of a multi-channel and broadband grating is up to several tens of nm. Another kind of classification may be performed by featuring gratings by the type of variation of their period, amplitude, and other parameters. In this classification scheme, the gratings are separated into uniform, linearly or non-linearly chirped, phase- and amplitude-modulated, sampled, and others. The phase masks may be classified similarly to the corresponding FBG. Thus, there

exist single-channel, multi-channel, broadband, chirped, sampled, and other types of phase masks.

The principal property of FBG is the ability to reflect light at certain wavelengths. In many applications, the satisfactory performance of a grating assumes that its reflectivity, R, is not small,

$$R \sim 1. \tag{3}$$

This condition places a lower limit to the FBG length and index modulation amplitude and also the upper limit to its chirp.

For a uniform grating, the *maximum* reflectivity achieved at the Bragg condition is equal to

$$R = \tanh^2(\pi \Delta n_{AC} L/\lambda_0), \tag{4}$$

where n_{AC} is the effective index modulation amplitude, λ_0 is the wavelength of light, and L is the length of grating [3]. In this case Eq. (3) yields $\pi \Delta n_{AC} L/\lambda_0 \gtrsim 1$. Typically, n_{AC} is less or of order 10^{-3} and therefore the grating length should be greater or of order 1 mm.

For a chirped FBG, the maximum reflectivity achieved at the local Bragg condition is $R = -\exp(\pi^2 \Delta n_{AC}^2/2n_0^2 \mid C \mid)$, where n_0 is the effective refractive index and C is the chirp of grating period $\Lambda(x), C = d\Lambda(x)/dx$ [3]. Then Eq. (3) gives $\pi^2 \Delta n_{AC}^2 \mid C \mid \gtrsim 1$. For $n_{AC} \lesssim 1$ we have that the chirp of FBG should be less or of order 10 nm/cm. Typically, the chirp value of single-channel chirped gratings is of the order 0.1 nm/cm. For multi-channel and broadband gratings, the chirp may be of order 10 nm/cm.

For superstructure gratings the magnitude of reflectivity is "shared" between channels and, in order to achieve the reflectivity equal to similar single-channel grating, one has to increase the index modulation amplitude by a factor which is of order the number of channels for simple on-off sampled gratings and is of order square root of the number of channels for the phase-modulated superstructure FBG [12–14].

4. Accuracy Requirements for Chirped FBG

Roughly speaking, the optical signal-to-noise ratio (OSNR) penalty is the increase in OSNR required to overcome the unwanted residual signal distortions resulting from an optical component. The FBG performance is determined by the OSNR penalty it adds to the performance of the optical communication system (see, e.g., [4,19]). Indirectly, it can be characterized by the amplitude and phase ripple in reflection and transmission coefficients. "Ripple" is determined as the deviation of the actual dependence of a FBG characteristic, which are usually considered as a function of wavelength, from the desired value. Often, instead of the phase, a grating is characterized by the group delay time, which is proportional to the derivative of phase with respect to wavelength [3], and the group delay ripple (GDR). The GDR problem is especially important for a chirped FBG (CFBG).

The OSNR penalty introduced by the CFBG device depends on the bit rate and signal format of the system it is used in. It is found [4,19] that the relatively high as well as relatively low frequency GDR components introduce minor contribution to the OSNR. The principal contribution is made by the frequencies close to the bandwidth of a bit pulse. For example, for 10 Gbit/s systems it is around 0.1 nm, while for 40

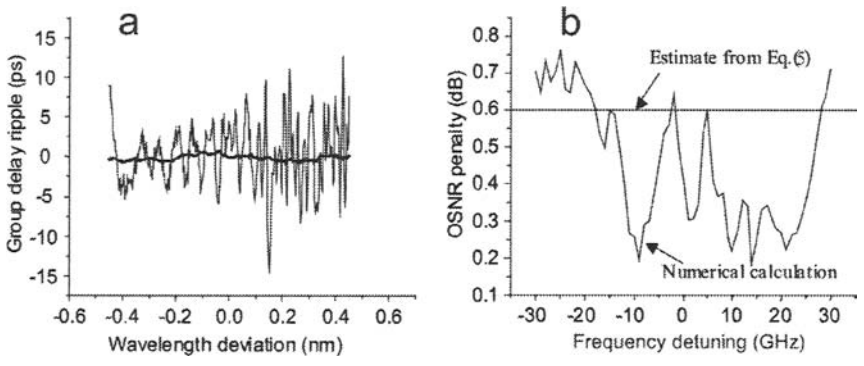

Fig. 7. (a) GDR for a grating with $\sim$ 750 ps/nm dispersion and $\sim$ 95% reflectivity (fine curve) and GDR averaged over 0.4 nm (bold curve). (b) OSNR penalty introduced by this grating in a 40-Gb/s system as a function of frequency detuning obtained by numerical simulation; the straight line is an estimate of the OSNR penalty from Eq. (5).

Gbit/s systems it is around 0.4 nm. For this reason, often the specification of CFBG system penalty employs GDR averaged over certain wavelength interval, typically of order of the bit rate of the system f_{bit}. The latter usually works well, however it should be mentioned that the OSNR value is the most adequate parameter determining the grating performance. Simple physical consideration following, e.g., from results of paper [20] shows that the order of OSNR penalty in decibels can be estimated by

$$\mathrm{ONSR} \sim 20\log(e) \mid \mathrm{GDR}_{f_{\mathrm{bit}}} \mid f_{\mathrm{bit}} \sim 10 \mid \mathrm{GDR}_{f_{\mathrm{bit}}} \mid f_{\mathrm{bit}}, \tag{5}$$

where $\mathrm{GDR}_{f_{\mathrm{bit}}}$ is the GDR averaged over the bit frequency bandwidth f_{bit} and it is assumed that $\mathrm{GDR}_{f_{\mathrm{bit}}} f_{\mathrm{bit}}$ is less than or around 1. Though Eq. (5) cannot give the accurate answer for the OSNR penalty, which depends on specific behavior of GDR and signal format, it correctly predicts the characteristic GDR values which one has to achieve in order to create a device with certain OSNR penalty. As an example, Fig. 7(a), fine curve, shows a typical GDR for a CFBG written at OFS Labs with chirp 0.045 nm/cm, corresponding to dispersion 750 ps/nm, and 95% reflectivity. The bold curve in this figure is the GDR averaged over the 40-GHz bandwidth having the peak-to-valley magnitude equal to $\mathrm{GDR}_{f_{\mathrm{bit}}} = 1.5$ ps. In Fig. 7(b), we compare the calculated OSNR penalty for this grating with a simple estimate from Eq. (5) yielding for this case OSNR $\sim$ 0.6 dB. The agreement is reasonable.

5. Relation Between GDR and Spatial Noise of CFBG Parameters

The GDR is the principal impediment restraining the practical implementation of CFBG. Analysis and calculations of GDR in CFBGs has been addressed in several publications [3,21–25]. In particular, the authors of [22–24] conducted the general study of random spatial variations of strength and period of gratings. They showed that these variations could have significant effect on group delay characteristics. In

[21] the effects of fiber diameter variation for the ultra-long fiber gratings, which have been proposed for broadband dispersion compensation, are studied. In this section we review a theory [25], which yields further understanding, predicts new effects, and establishes a simple relationship between the high-frequency spatial noise in grating parameters and the corresponding GDR. Typically, the length of a CFBG for the single-channel dispersion compensation $L \sim 10$ cm, its chirp $C \sim 0.1$ nm/cm, bandwidth ~ 1 nm, and the corresponding dispersion is ~ 1000 ps/nm. The GDR Fourier components having the characteristic periods of $\sim$ nm are referred to as low-frequency ripples, while the GDR components with smaller periods ~ 0.01 nm are the high-frequency ripples.

Without the loss of generality, it is assumed that there is no spatial ripple in the grating parameters other than in the period $\Lambda(z)$,

$$\begin{aligned} \Lambda(z) &= \Lambda_0 + C(z - z_0) + \Delta\Lambda(z) \\ \Delta\Lambda(z) &= \sum_{q>0} \Delta\Lambda_q \exp[iq(z - z_0)] + c.c., \end{aligned} \tag{6}$$

where, for convenience, we use the spectral representation of the grating period noise, $\Delta\Lambda(z)$. The spatial ripple of the other grating parameters, like the amplitude of index modulation, can be described similarly.

Let us consider first the description of the GDR based on the classical ray approximation, which, as it is shown below, is inadequate for the gratings of our concern. In this approximation, GDR appears only due to the ripple in the position of turning point z_t, and the grating period noise elsewhere does not matter (see Fig. 8). Simple calculation using Eq. (6) defines GDR in the form demonstrating its inverse proportionality to the chirp C:

$$\Delta\tau(\lambda) = \frac{2n_0}{c_0 C}\Delta\Lambda(z_t), \qquad z_t = z_0 + (\lambda - 2n_0\Lambda_0)/2n_0 C, \tag{7}$$

where n_0 is the effective refractive index and c_0 is the speed of light.

By contrast, for the GDR of gratings considered in this paper the contribution of the turning point ripple is irrelevant. Rather, the GDR is predominantly generated by the interference of the waves reflected from the weak non-homogeneities of grating parameters along the whole grating length traveled by the light. In terms of noise component with frequency q [see Eq. (7)] this reflection is nothing but the secondary Bragg reflection governed by the coupled wave equations [3] with $(2\pi/q)$-periodic coefficients.

A simple explanation of the properties of GDR is given in Fig. 9, which is a band diagram [26,27] of a CFBG with a weak long-period modulation representing a frequency component of the spatial noise $\Delta\Lambda(z)$ defined by Eq. (6). This modulation produces narrow and weak reflection sidebands, or photonic bandgaps, shaded in Fig. 9, spaced by interval $\Delta q \propto q$ (superstructure effect [27]). The GDR arises due to the interference of the light reflected from the main band and its sideband. There are two different wavelength regimes:

a.(*above cutoff*): If the light is reflected from the main reflection band only, without intersecting the sidebands then no GDR is observed.

b.(*below cutoff*): If the light also crosses the sideband then the interference of the wave reflected from the main band and the sideband causes GDR.

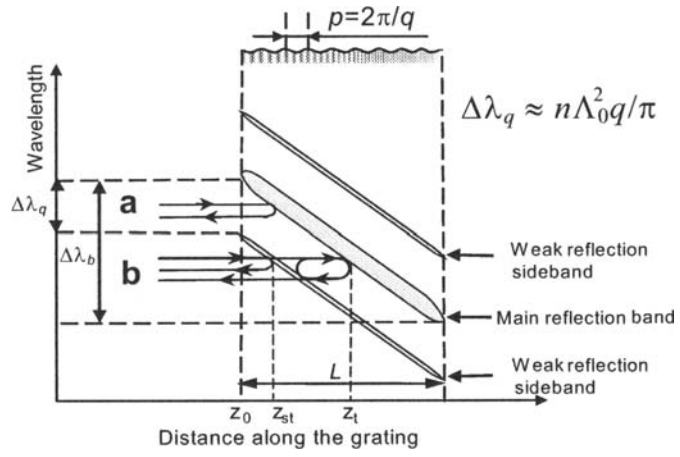

Fig. 8. Reflection of light from chirped Bragg fiber grating.

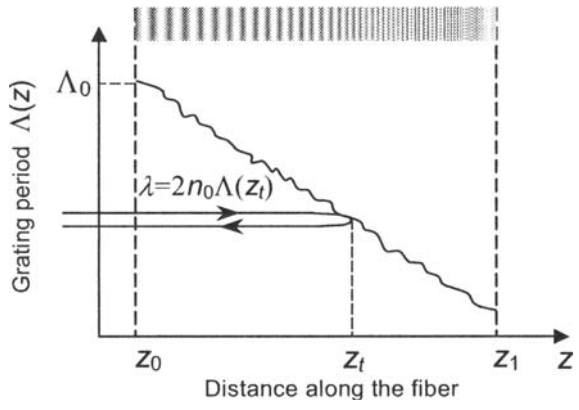

Fig. 9. Physical picture of the GDR cutoff effect.

Thus, the formation of sidebands is accompanied by GDR if the ripple period is below the cutoff magnitude. It is also clear from Fig. 9 that if the main band is partly transparent then, even in region *a*, the grating will exhibit GDR because of interference with the wave reflected from the upper sideband. Below we assume that the grating is strongly reflective and the GDR produced by this interference is negligible.

We calculate the GDR using the WKB approximation for the unperturbed solution of the coupled wave equations [26], and the first-order perturbation theory for the

noise. The secondary Bragg reflection point from the sideband, z_{st}, corresponding to the noise component with frequency q (see Fig. 9) is defined by

$$2k_{\text{eff}} = q, \qquad k_{\text{eff}}(z) = \frac{\pi}{2n_0\Lambda_0^2}\sqrt{[\Delta\lambda - 2n_0C(z-z_0)]^2 - \Lambda_0^2\Delta n^2(z)}. \quad (8)$$

Here k_{eff} is the effective (envelope) wavenumber, $\Delta\lambda$ is the detuning of wavelength of incident light, which is calculated from the high-wavelength edge of the reflection band, and $\Delta n(z)$ is the index modulation. It is seen from Fig. 9 that whenever z_{st} is outside the interval (z_0, z_t) the component with frequency q does not generate GDR. Equation (8) defines the cutoff spatial frequency, q_c, and the cutoff GDR frequency, ν_c, in the form

$$q_c = \frac{\pi\Delta\lambda}{n_0\Lambda_0^2}, \qquad \nu_c = \frac{\pi\Delta\lambda}{2Cn_0^2\Lambda_0^2}. \quad (9)$$

Equations (8) and (9) determine the frequency range, $q \sim \pi\Delta\lambda_b/(2n_0\Lambda_0^2)$, where the developed theory is valid. Here $\Delta\lambda_b$ is the reflection bandwidth, which can be expressed through the grating length L by the equation $\Delta\lambda_b = 2n_0CL$. For example, for the bandwidth $\Delta\lambda_b = 1$ our theory is valid for the spatial noise frequencies of the order 4 mm^{-1} and, respectively, for the periods of the order 1 mm. This frequency interval is, in fact, the interval of our interest where the following expression for the GDR is found:

$$\Delta\tau(\Delta\lambda) = \sum_{0<q<q_c} \Delta\tau_q \exp\left[\frac{iq\Delta\lambda}{2n_0C}\right] + c.c.,$$
$$\Delta\tau_q = \frac{\pi n_0\Delta n}{c_0(2C)^{3/2}} \exp\left(-\frac{iq^2\Delta\Lambda_0^2}{4n_0C}\right)\Delta\Lambda_q. \quad (10)$$

Figure 10(a) shows the comparison of the absolute value of GDR harmonic amplitude, $2 \mid \Delta\tau_q \mid$, given by this equation with numerical calculation for $L = 100$ mm, $\Lambda_0 = 540$ nm, $C = 0.05$ nm/cm, and $\Delta n = 2 \times 10^{-4}$. The agreement is very good in the interval of the spatial ripple period between the cut-off period equal to 0.8 mm and up to 1 cm. This figure also shows that the GDR value calculated from Eq. (7) is wrong. This approximation is, obviously, inadequate when the spatial frequency q and effective wavenumber k_{eff} are of the same order of magnitude. Interestingly, according to Eq. (10) a single harmonic of GDR depends on chirp as $\mid \Delta\tau_q \mid \sim C^{-3/2}$ but not as $\mid \Delta\tau_q \mid \sim C^{-1}$, which follows from Eq. (7). Figure 10(b) demonstrates that the $C^{-3/2}$ dependence is very accurate for the periods of spatial ripple up to 2 cm. The linear dependence on the index modulation, Δn, follows from Eq. (10) and can be understood from the linear dependence of the GDR on the amplitude of reflection coefficient from the sideband, which is proportional to Δn.

The predicted cutoff effect is confirmed by the numerical solution of the coupled wave equation for CFBG with the parameters indicated above. Figure 11(a,b) demonstrates the cutoff effect for GDR generated by spatial harmonic ripples having different periods. The sum of these harmonics [Fig. 11(c)] creates GDR, which has gradually disappearing high frequency components [Fig. 11(d)]. In this example the noise components with the periods less than 0.8 mm do not affect the GDR at all. Equation (9) defines the GDR-free bandwidth in the form $\Delta\lambda_q = n\Lambda_0^2 q/\pi$ in agreement with numerical simulations. Figure 11 explains the gradual suppression of the high-frequency

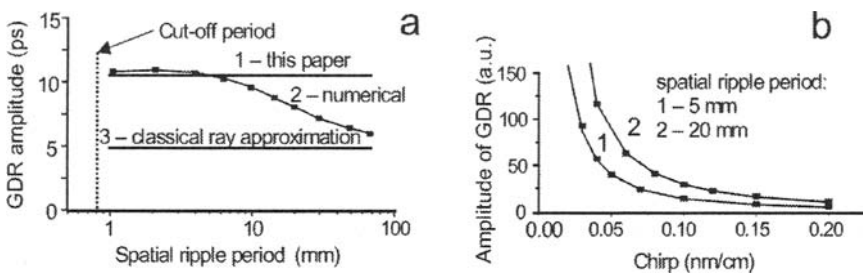

Fig. 10. (a) Comparison of the single-harmonic GDR amplitude calculated from Eq. (10) with numerical calculations and with classical ray approximation Eq. (7) for the amplitude of spatial ripple 0.0025 nm; (b) fitting the numerically calculated GDR amplitude vs. chirp dependence (squares) by power law (solid lines) for the spatial period ripple 5 and 20 mm.

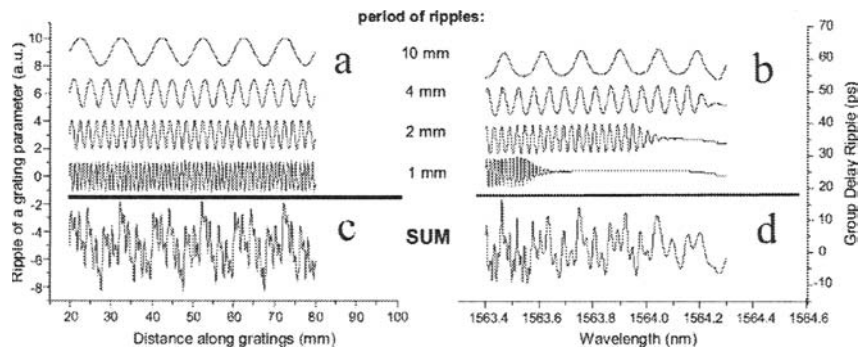

Fig. 11. Spatial ripple in grating parameters and corresponding GDR obtained by numerical solution of the coupled wave equations.

GDR, which is usually observed experimentally [2] and, in particular, is seen from Fig. 12. Figure 12(a) demonstrates typical group delay and GDR measurements for one of the gratings written from a phase mask fabricated at OFS Labs. Figure 12(b) shows the Fourier spectrums of this GDR calculated for different bandwidths $\Delta\lambda$ measured from the high-wavelength edge of the reflection band. It is seen that the experimental cutoff frequencies are in excellent agreement with the ones predicted by Eq. (9).

Equation (10) is convenient for investigating the statistical properties of grating noise. For example, assuming that are random statistically independent functions and ignoring the relatively small oscillatory components, we get for the standard deviation of the GDR, $\sqrt{\overline{\Delta\tau^2}} \propto \sqrt{\Delta\lambda}\Delta n/C^{3/2}$. This result, which is similar to the one obtained in [24], demonstrates the $C^{-3/2}$ dependence of the local standard deviation of GDR. In general, as follows from Eq. (10), the $C^{-3/2}$ dependence is valid for the single harmonic amplitude only and the arbitrary grating may not possess this property. However, Eq. (10) shows that the linear dependence of high-frequency GDR on the

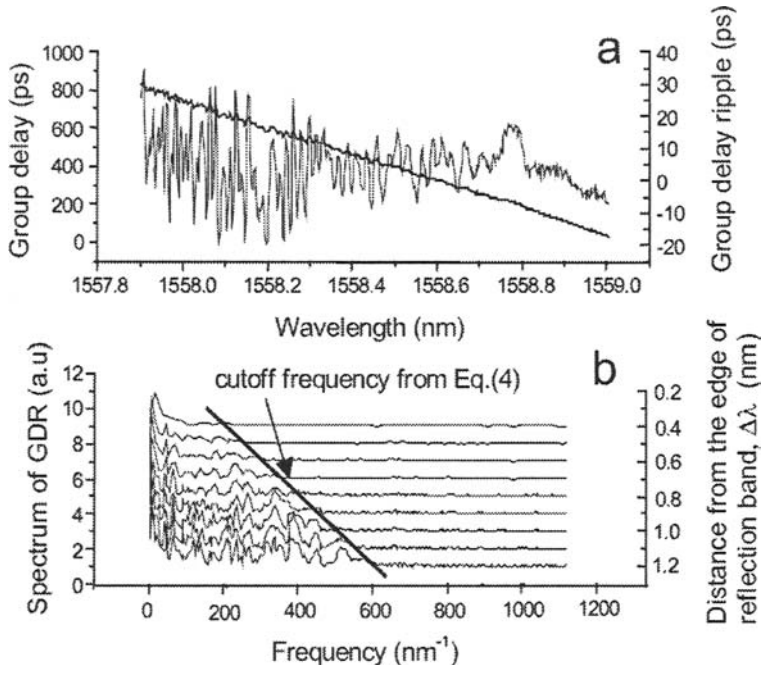

Fig. 12. (a) Group delay and GDR of a typical CFBG; (b) Fourier spectrum of this GDR calculated for different bandwidths $\Delta\lambda$ measured from the high-wavelength edge of the reflection band and demonstrating the cutoff frequencies coincident with the ones predicted by Eq. (9).

index modulation is valid for any particular grating. Notice that this result is not trivial and according to Eq. (7) fails for the low-frequency GDR. Interestingly, the $\Delta\lambda^{1/2}$ dependence of the GDR standard deviation is directly related to the cutoff effect. This dependence follows from Eq. (10) after statistical averaging and may not be valid for a specific grating. In summary, in this section we have investigated the effect of spatial noise of the apodized CFBGs on the GDR and found that the high frequency noise is cutting off. The cutoff effect is demonstrated here for the spatial noise in the grating period. It can be similarly shown that Eq. (9) holds for the spatial noise in any grating parameter. Generally, the results of this section demonstrate the link between the noisy gratings and the superstructure Bragg gratings. These results are important both for basic understanding and for the further improvement of the grating performance.

6. Correction of CFBG

GDR originates from random and systematic errors introduced during fiber grating fabrication. Several research groups have reported on modification of the fiber grating fabrication process to achieve reduced GDR [28–30]. The authors of [31] proposed a method for adjusting the grating profile to account for systematic grating imperfections by numerical solution of the inverse problem for the coupled wave equations.

Though these approaches allows for significant reduction of GDR, they do not deal with random errors introduced in fiber grating fabrication, which in typical fiber grating fabrication systems are larger than or comparable to systematic errors. Reference [32] demonstrates a technique for reducing the GDR in chirped fiber Bragg gratings by iteratively characterizing and subjecting the grating to additional UV corrective post-processing. This technique does not fully rely on the accuracy of the solution of the coupled wave equations using them as iterations only and, thus, equally well suited for correction of systematic as well as random deviations in CFBG parameters.

The idea of approach of [32] is illustrated in Fig. 13 and described further below in this section. After fabrication of CFBG using the conventional UV grating writing technique, e.g., with a phase mask the GDR ripple of grating is characterized [Fig. 13(a)]. The suggested grating correction is based on the fact that, it is only relatively low frequency GDR that affects the performance of CFBG devices [4,19]. For this reason, the correction of CFBGs can be performed in the adiabatic approximation when compensating slow varying index variation can be determined by simple rescaling of the low-frequency GDR component as schematically shown in Fig. 13(b,c) and described further below. In this section we consider strong gratings for which the numerical solution of coupled wave equations becomes unstable and its accuracy is questionable [33]. The corrective index variation is introduced by direct UV exposure to obtain the GDR having the reduced low frequency component of GDR [Fig. 13(d)]. The iterative steps ($b \to c \to d \to b$) are continued until the desired reduction of the GDR of the considered grating is achieved.

The correction algorithm of [32] is based on a simple solution of the inverse problem for coupled wave equation for CFBG. The GDR is usually relatively small and therefore the relation between the refractive index variation and corresponding GDR is linear. In the simplest adiabatic approximation, which is valid for slowly varying GDR, the "direct current" (DC) index variation, [3] (do not confuse this DC with DC corresponding to "dispersion compensation" introduced in the beginning of this paper), needed for compensation of the GDR, $\delta\tau(\lambda)$, is defined by

$$\delta n_{\mathrm{dc}} = \mathrm{const}\frac{cC}{\Lambda}\delta\tau(2n_{\mathrm{eff}}Cz), \tag{11}$$

where c is the speed of light in vacuum, n_{eff} is the effective index, $C = d\Lambda/dx$ is the chirp rate of the grating period, and const is of order 1. This constant is determined by experimental calibration. Equation (11) shows that in the adiabatic approximation the DC index needed to compensate the GDR is simply determined by rescaling the plot of GDR [see Fig. 13(b,c)]. It follows from Eq. (11) that $\delta n_{\mathrm{dc}}(x)$ which compensates 10 ps in GDR amplitude is $\sim 10^{-5}$. Note that if the grating is strong (as in the experiment considered below) the reflection amplitude is very close to unity and the reflection amplitude ripple introduced by $\delta n_{\mathrm{dc}}(x)$ is negligible. Interestingly, our simple inverse procedure is valid in the limit of strong gratings and is therefore suitable for strong gratings where layer-peeling algorithms are prone to errors [33].

If the characteristic frequency of the GDR becomes large enough Eq. (11) fails. In this case the local spatial peak in DC index no longer corresponds to a local peak in group delay but generates a complex GDR due to the interference of light reflected from this peak and from the Bragg reflection turning point as illustrated in Fig. 14(a,b). In order to enable local correction of the higher frequency ripple, it is necessary to determine a DC index profile, which corresponds to a narrow peak in GDR. Generally,

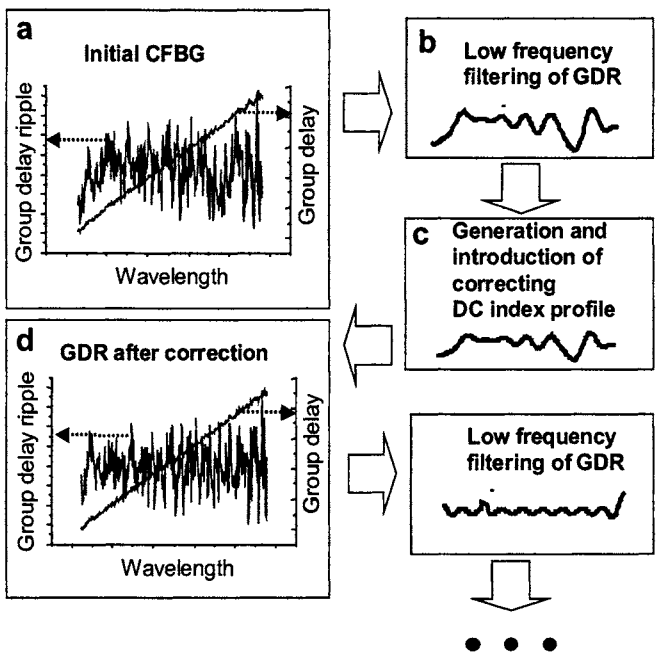

Fig. 13. Iterative CFBG correction. (a) Group delay and GDR of initial CFBG; (b) the result of low frequency filtering of the GDR shown in (a); (c) determination of corrective DC index and introduction it into CFBG by direct UV exposure; (d) group delay and GDR after first correction.

this can be done by solving the inverse problem for the coupled wave equation [33]. For practical purposes and also for general understanding it is desirable to have a simple relation, which determines the DC index profile corresponding to a local GDR peak. It was found in [32] that for the high frequency ripple, the relation between the spatial noise in DC index, $\delta n_{\rm dc}(z)$, and the GDR introduced by this noise is approximately defined by

$$\delta n_{\rm dc}(z) = \int_{-\infty}^{\infty} d\lambda \delta\tau(\lambda)\Phi(z,\lambda)$$
$$\Phi(z,\lambda) = {\rm const}\frac{c(C)^{1/2}}{2^{3/2}\pi^2\Lambda\Delta n_{\rm ac}}\int_0^{\infty} dq \cos\left[\left(z - \frac{\lambda}{2n_{\rm eff}C}\right)q + \frac{\Lambda^2}{4\pi C}q^2\right], \tag{12}$$

where $\Phi(x,\lambda)$ is a Fresnel-type integral, $n_{\rm ac}$ is the amplitude of "alternating current" (AC) index modulation [3], and const ~ 1. Equation (12) is derived by solving the coupled wave equations to the first order in the perturbation DC index profile $n_{\rm dc}$ and using the WKB approximation for the unperturbed solutions of these equations [26]. Similar to the result described in section 5, for the high-frequency GDR, the relation between spectral components of $\delta\tau$ and $n_{\rm dc}$ is defined by a Fourier transform which is inverted to arrive at Eq. (12). For simplicity, the high-frequency cut-off effect is

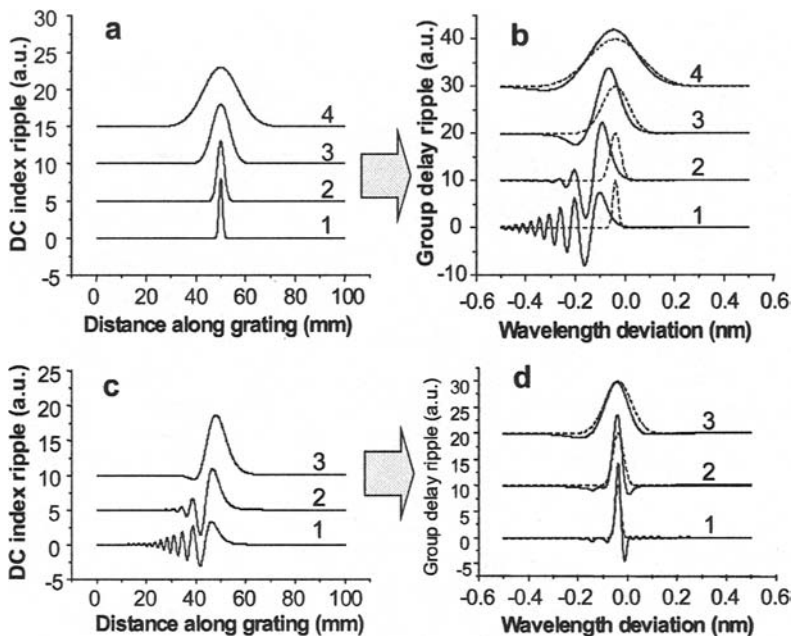

Fig. 14. (a) Gaussian peak DC index perturbations and (b) corresponding GDR obtained by numerical solution of the coupled wave equation for the peak widths equal to: 1 – 1 mm, 2 – 2 mm, 3 – 5 mm, and 4 – 10 mm (solid) compared to desired Gaussian GDR peaks obtained from Eq. (1) (dashed). (c) DC index perturbation profiles corresponding to Gaussian peaks in the GDR computed using Eq. (3). (d) GDR found by numerical solution of the coupled wave equation using the DC index perturbation profiles of (c) (solid). The peaks in (d) are close to the desired Gaussian GDR peaks (dashed).

ignored and, thus, Eq. (12) is valid for characteristic frequencies of the GDR, which are not exceeding the cut-off frequencies. According to Eq. (12), for large chirp, $C_{\rm gr}$, the function $\Phi(z,\lambda)$ is proportional to a δ-function, $\Phi(z,\lambda) \propto \delta[z - (\lambda/2n_{\rm eff}C)]$, and Eq. (12) coincides with Eq. (11) within a constant factor. Thus, within a constant factor of order 1, which is usually unknown and should be defined experimentally by calibration, Eq. (12) is valid for the low frequency GDR as well. However, this equation may loose its accuracy for intermediate frequencies. Assuming that the GDR has a Gaussian shape, $\delta\tau(\lambda) = \delta\tau_0 \exp[-(\lambda - \lambda_0)^2/\lambda_w^2]$, Eq. (12) yields [32]:

$$\delta n_{\rm dc}(z) = {\rm const}\frac{c(C_{\rm gr})^{1/2}\lambda_w \delta\tau_0}{2\pi^{3/2}\Delta n a c} \times \int_0^\infty dq \exp\left(-\frac{\lambda_w^2 q^2}{16 n_{\rm eff}^2 C^2}\right) \cos\left[\left(z - \frac{\lambda_0}{2n_{\rm eff}C}\right) q + \frac{\Lambda^2 q^2}{4\pi C}\right]. \quad (13)$$

Figure 14(c) shows the plot of determined by this equation for grating chirp $C_{\rm gr} =$ 0.05 nm/cm (corresponding to 750 ps/nm dispersion), $n_{\rm eff}$ = 1.5, $\Lambda_{\rm gr}$ =0.5 m, and peak widths of 0.015, 0.03, and 0.075 nm which, if the adiabatic approximation of

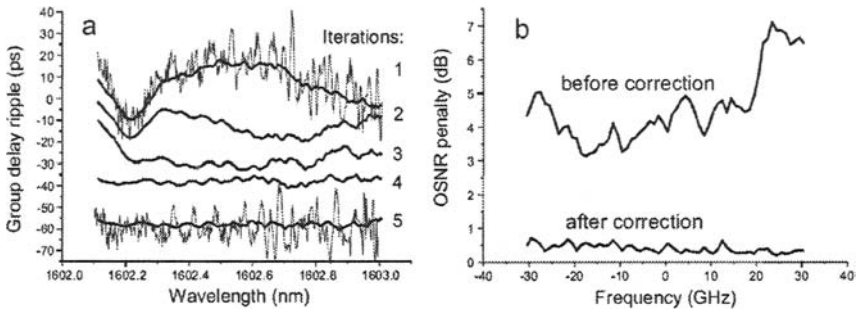

Fig. 15. (a) Iterative process of grating correction: GDR (fine) and GDR averaged over 0.1 nm (bold) after several correction steps, from 1 (initial) to 5 (final). For better visualization, the zero GDR of iterations has been arbitrary shifted along the GDR axis. (b) Computed OSNR penalties for initial (1) and final corrected (5) gratings.

Eq. (11) were correct, would correspond to spatial peaks of the widths 1, 2, and 5 mm. Figure 14(d) shows the result of accurate numerical solution of the coupled wave equations for DC index perturbations of Fig. 14(c) and demonstrates good accuracy for Eq. (13). Small deviation of the peaks from the Gaussian shape can be explained by the presence of intermediate, low frequency, and cut-off components in the Fourier expansion of the Gaussian peaks considered.

Reference [32] considers a CFBG written in hydrogen loaded single mode fiber, which has a grating period $\Lambda = 548$ nm, chirp $C = 0.048$ nm/cm, grating length 10 cm, and amplitude of index modulation $\sim 3 \times 10^{-4}$ corresponding to reflection coefficient 99.998%. The dispersion generated by this CFBG is around 780 ps/nm, bandwidth $\sim$ 1.2 nm, and the GDR observed is $\pm$ 25 ps peak-to-peak. For these grating parameters, Eq. (11) is reasonably accurate if the spatial resolution of index variation is $\geq$ 1 cm and, respectively, the characteristic wavelength of GDR variation is $\geq$ 0.1 nm. Fortunately, this range of wavelength variation corresponds to the low-frequency GDR, which introduces the major contribution into the OSNR penalty for the 40-Gb/s systems [4,19].

Figure 15(a) shows the original GDR of the grating considered (1, fine curve), and the result of its averaging over 0.1 nm (1, bold curve). The correction of the averaged GDR was performed in several iterations by successive elimination of individual ripples using the 5-mm-wide UV laser beam. The corresponding DC index variation was found using Eq. (1) with const determined by calibration of the beam power at each step of GDR trimming. Figure 15(a) 1–5, shows the actual results of several steps of correction. It demonstrates reduction of averaged GDR from 15 ps (curve 1) to $\pm$ 2 ps (curve 5). The OSNR penalty curves of Fig. 15(b) calculated for the un-smoothed GDR demonstrate the dramatic improvement obtained when the corrected device was implemented in a 40-Gb/sec CSRZ transmissions system simulation. The OSNR penalty is reduced from 7 dB to less than 1 dB in the $\pm$ 30 GHz bandwidth. Note that this comparison also highlights the dominant contribution of the low-frequency GDR, which can be improved through our procedure, relative to the small effect of high-frequency GDR component.

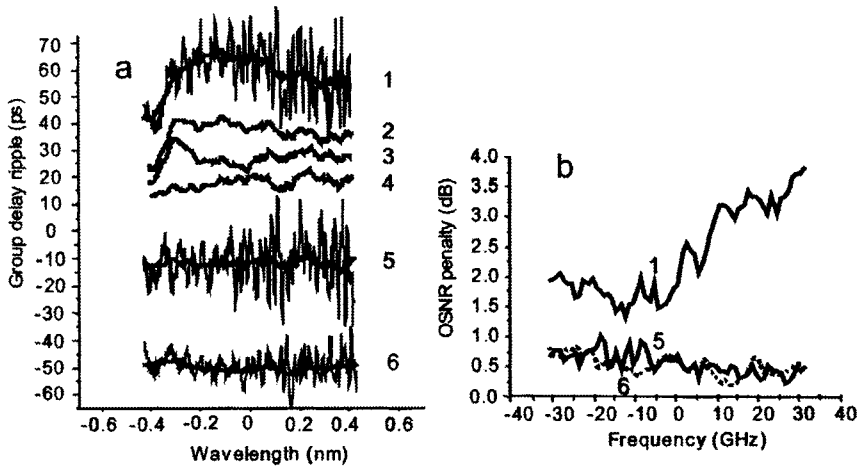

Fig. 16. (a) Iterative process of grating correction: GDR (thin line) and GDR averaged over 0.1 nm (bold line) after several correction steps, from 1 (initial) to 5 (final). Curves 6 show the GDR and averaged GDR of the grating after grating anneal. For better visualization, the zero GDR of iterations has been arbitrary shifted along the GDR axis. (b) Simulated OSNR penalties for original (1), corrected (5, solid curve) and annealed (6, dotted curve) gratings.

7. CFBG Tunable Dispersion Compensator

Reference [34] applied the GDR iterative correction method in fabrication of the high-performance tunable dispersion compensator (TDC). The original CFBG with a grating period $\Lambda = 548$ nm, chirp $C = 0.048$ nm/cm, grating length 10 cm, and amplitude of index modulation $\sim 3 \times 10^{-4}$ was fabricated. The dispersion of the CFBGs was around 780 ps/nm and the GDR is $\sim \pm 20$ ps. Figure 16(a) shows the original GDR of the grating considered (1, fine curve), and the result of its averaging over 0.1 nm (1, bold curve). The correction of the averaged GDR was performed in several iterations by successive elimination of individual ripples as described in the previous section. Figure 16(a) 1–5, shows the results of several steps of correction. It demonstrates reduction of averaged GDR from 10 ps (curve 1) to $\pm$ 2 ps (curve 5). Figure 16(b) demonstrates the corresponding improvement in CFBG performance obtained numerically when these devices are implemented in a 43-Gb/s CSRZ transmission simulation. The OSNR penalty is reduced from 4 dB (curve 1) to less than 1dB (curve 5) in a $\pm$ 30 GHz bandwidth of carrier frequencies.

After annealing of the corrected grating, (for thermal stabilization) its reflectivity was reduced from 99.995% to approximately 90%. The high frequency component of its GDR was also reduced by roughly a factor of 3, while the low-frequency GDR remained and the OSNR penalty was approximately unchanged [see Fig. 16(a,b) curve 6]. A TDC device was fabricated by integrating a resistive thin-film heater in close thermal contact with the fiber grating [4]. The dispersion of the TDC was tuned by the voltage applied to the film, which changed its temperature [4]. Figure 17 shows the results of OSNR penalty calculated for the fabricated TDC. These simulations show that the OSNR penalty was less than 0.8 dB for carrier frequency variation of $\pm$ 30

Fig. 17. (a) OSNR penalty calculated for the TDC device fabricated from annealed grating of Fig. 16(b), curve 6, as a function of voltage and carrier frequency for a 43-Gb/s CSRZ system. The insert shows the introduced dispersion as a function of applied voltage; (b) experimental setup for OSNR measurement (Att—attenuator, OF—optical filter, DCF—dispersion compensating fiber); (c) measured OSNR penalty for the same device for -10, 0, and 10 GHz carrier frequency shifts.

GHz and dispersion variation between 750 and 270 ps/nm. The OSNR penalty was also measured experimentally using the setup shown in Fig. 17(b). The 43-Gb/s CSRZ signal was controlled by adjusting the input power into an EDFA. The dispersion was varied by sending the signal through various lengths of DCF. The TDC was inserted in front of an ETDM receiver. Figure 17(c) shows the result of OSNR penalty measurement for carrier frequency shifts of -10, 0, and 10 GHz as a function of applied voltage. This carrier frequency deviation accounts for possible drift of the laser and grating central frequency. The measured OSNR penalties did not exceed 0.5 dB and were in reasonable agreement with numerical simulations.

8. Summary

In this paper we discussed the fabrication methods, theory, and applications of CFBG as dispersion compensators and tunable dispersion compensators. One of the most important options of CFBG, which is not provided by the conventional DCF, is the possibility of dispersion tuning. This option is critical for high-speed WDM and OTDM systems. Currently, the main impediment to broad application of the CFBGs for dispersion compensation is the GDR. Recent theoretical and experimental work on the GDR problem has shown that there exists a way to dramatic reduction of the GDR. It has been demonstrated, both theoretically and experimentally, that only relatively low-frequency components of spatial noise in CFBG parameters show up in its spectrum. For high bit rate systems, the low-frequency GDR can be significantly reduced by iterative correction. We believe that the further development of the CFBG fabrication technology will make it one of the most preferable, accurate, and low-loss way for tunable dispersion compensation in both WDM and OTDM communication systems.

References

1. L. Grüner-Nielsen and B. Edvold, "Status and future promises for dispersion compensating fibers," ECOC, paper 6.1.1 (2002).
2. F. Ouellette, "Dispersion cancellation using linearly chirped Bragg grating filters in optical waveguides," Opt. Lett., **12**, 847–849 (1987).
3. R. Kashyap, *Fiber Bragg Gratings* (Academic Press, 1999).
4. B.J. Eggleton, A. Ahuja, P.S. Westbrook, J.A. Rogers, P. Kuo, T.N. Nielsen, and B. Mikkelsen, "Integrated tunable fiber gratings for dispersion management in high-bit rate systems", J. Lightwave Technol., **18**, 1418–1432 (2000).
5. S.A. Hamilton, B.S. Robinson, T.E. Murphy, S.J. Savage, and E.P. Ippen, "100 Gb/s Optical Time-Division Multiplexed Networks", J. Lightwave Technol., **20**, 2086–2100 (2000).
6. K.O. Hill, B. Malo, F. Bilodeau, D.C. Johnson, and J. Albert, "Bragg gratings fabricated in monomode photosensitive optical fiber by UV exposure through a phase mask," Appl. Phys. Lett., **62**, 1035–1037 (1993).
7. T. Kreis, *Holographic interferometry: principles and methods* (John Wiley & Sons, Inc., 1996).
8. L.F. Mollenauer and W.J. Tomlinson, "Piecewise interferometric generation of precision gratings," Appl. Optics, **3**, 555–557 (1977).
9. B. Eggleton, P.A. Krug, L. Poladian, and F. Ouellette, "Long periodic superstructure Bragg gratings in optical fibres," Electr. Lett., **30**, 1620–1622 (1994).
10. M. Ibsen, B.J. Eggleton, M.G. Sceats, and F. Quellette, "Broadly tunable DBR fibre laser using sampled fibre Bragg gratings," Electr. Lett., **31**, 37–38 (1995).
11. W.H. Loh, F.Q. Zhou, and J.J. Pan , "Sampled fiber grating based-dispersion slope compensator," IEEE Photon.Technol. Lett., **11**, 1280–1282 (1999).
12. H. Ishii, Y. Tohmori, T. Tamamrua, and Y. Yoshikuni, "Super structure grating (SSG) lasers for broadly tunable DBR lasers," IEEE Photon. Technol. Lett., **4**, 393–395 (1993).
13. A.V. Buryak and D.Y. Stepanov, "Novel multi-channel grating devices," in *Bragg Gratings, Photosensitivity, and Poling in Glass Waveguides* (Washington, DC: OSA, 2001), vol. 61, paper BThB3.

14. J. E. Rothenberg, H. Li, Y. Li, J. Popelek, Y. Sheng, Y. Wang, R. B. Wilcox, and J.Zweiback, "Dammann Fiber Bragg Gratings and Phase-Only Sampling for High Channel Counts," IEEE Photon. Technol. Lett., **14**, 1309–1311 (2002).
15. M.J. Cole, W.H. Loh, R.I. Laming, M.N. Zervas, and S. Barcelos, "Moving fibre/phase mask-scanning beam technique for enhanced flexibility in producing fibre gratings with a uniform phase mask," Electron. Lett., **31**, 1483–1485 (1995).
16. R. Stubbe, B. Sahlgren, S. Sandgren, and A. Asseh, "Novel technique for writing long superstructured fiber Bragg gratings," in *Photosensitivity and quadratic nonlinearity in glass waveguides: Fundamentals and applications, 22*, (OSA, Washington D.C., 1995).
17. R. Kashyap, H.-G. Froehlich, A. Swanton, and D.J. Armes, "1.3 m long superstep-chirped fibre Bragg grating with a continuous delay of 13.5 ns and bandwidth 10 nm for broadband dispersion compensation," Electron. Lett. **32**, 1807–1809 (1996).
18. M. Ibsen, M.K. Durkin, R. Feced, M.J. Cole, M.N. Zervas, and R.I. Laming, "Dispersion compensating fibre Bragg gratings", in Active and Passive Optical Components for WDM Communication, Proceedings of SPIE, 4532, pp. 540–551, 2001.
19. K. Ennser, M. Ibsen, M. Durkin, M.N. Zervas, and R.I. Laming, IEEE Photon. Technol. Lett., **10**, 1476–1478 (1998).
20. C. Scheerer, C. Glingener, G. Fischer, M. Bohn, W. Rosenkranz, "Influence of filter group delay ripples on system performance," in Proc. ECOC 1999, pp. 1410–1411.
21. M. Ibsen, M.K. Durkin, R. Feced, M.J. Cole, M.N. Zervas, and R.I. Laming, "Dispersion compensating fibre Bragg gratings", in Active and Passive Optical Components for WDM Communication, Proceedings of SPIE, Vol. 4532, pp. 540–551, 2001.
22. F. Ouellette, "The effect of profile noise on the spectral response of fiber gratings" in Bragg Gratings, Photosensitivity, and Poling in Glass Fibers and Waveguides: Applications and Fundamentals, Paper BMG13-2, Williamsburg, 1997.
23. R. Feced and M.N. Zervas, "Effect of random phase and amplitude errors in optical fiber gratings", J. Lightwave Technol., **18**, 90–101 (2000).
24. R. Feced, J.A.J. Fells, S.E. Kanellopoulos, P.J. Bennett, and H.F.M. Priddle, "Impact of random phase errors on the performance of fiber grating dispersion compensators", Opcal Fiber Communication Conference (OFC), 2001, Anheim, CA, Paper WDD89, 2001.
25. M. Sumetsky, B.J. Eggleton, and C.M. de Sterke, "Theory of group delay ripple generated by chirped fiber gratings", Opt. Express, **10**, 332–340 (2002).
26. L. Poladian, "Graphical and WKB analysis of nonuniform Bragg gratings", Phys. Rev. E, **48**, 4758–4767 (1993).
27. N.G.R. Broderick and C.M. de Sterke, "Theory of grating superstructures", Phys. Rev. E, **55**, 3634–3646 (1997).
28. I. Riant, S. Gurib, J. Gourhant, P. Sansonetti, C. Bungarzeanu, and R. Kashyap, "Chirped fiber Bragg gratings for WDM chromatic dispersion compensation in multispan 10-Gb/s transmission," IEEE J. Select. Topics Quant. Electron., **5**, 1312–1324 (1999)
29. S.J. Mihailov, F. Bilodeau, K.O. Hill, D.C. Johnson, J. Albert, and A.S. Holmes, "Apodization technique for fiber grating fabrication with a halftone transmission amplitude mask," Appl. Opt., **39**, 3670–3677 (2000).
30. T. Komukai, T. Inui, and M. Nakazawa, " Very low group delay ripple characteristics of fibre Bragg grating with chirp induced by an S-curve bending technique," Electron. Lett., **37**, 449–451 (2001).
31. A.V. Buryak and D.Yu. Stepanov, "Correction of systematic errors in the fabrication of fiber Bragg gratings," Opt. Lett., **27**, 1099–1101 (2002).

32. M. Sumetsky, P.I. Reyes, P.S. Westbrook, N.M. Litchinitser, and B.J. Eggleton, "Group delay ripple correction in chirped fiber Bragg gratings," Opt. Lett. **28**, 777–779 (2003).

33. J. Skaar and R. Feced, "Reconstruction of gratings from noisy reflection data," J. Opt. Soc. Am. A, **19**, 2229–2237 (2002).

34. M. Sumetsky, N.M. Litchinitser, P.S. Westbrook, P.I. Reyes, B.J. Eggleton, Y. Li, R. Deshmukh, C. Soccolic, F. Rosca, J. Bennike, F. Liu, and S.Dey, "High performance 40 Gbit/s fibre Bragg grating tunable dispersion compensator fabricated using group delay ripple correction technique," Electron. Lett., **39**, 1196–1198 (2003).

DOI: 10.1007/s10297-004-0023-z
Originally published in J. Opt. Fiber. Commun. Rep. 3, 90–110 (2006)

Higher-order dispersion compensation using phase modulators

Mark D. Pelusi and Akira Suzuki

The Femtosecond Technology Research Association
5-5 Tokodai, Tsukuba, Japan 300-2635

Abstract. The use of electro-optic phase modulation of dispersed optical pulses is investigated for compensating higher-order chromatic dispersion effects. The capability and limitations of the technique are described for compensating third- and fourth-order dispersion terms.

Progress enabling data transmission rates beyond 1 Tb/s with a single laser source highlights the capability of OTDM to circumvent electrical bandwidth constraints in realizing high capacity fiber-optic communications with fewer wavelength channels (see "Ultrafast OTDM transmission using novel fiber devices for pulse compression, shaping, and demultiplexing" by T. Yamamoto and M. Nakazawa (DOI: 10.1007/s10297-005-0037-1). Although transmitter/receiver technology can accommodate an extremely short bit period, advancing to such high channel speeds in long haul transmission is challenged by the greater sensitivity to distortions such as polarization mode and chromatic dispersions of optical fiber that must be overcome. On the one hand, countering the reduced tolerance to signal dispersion within the shorter bit period for error free transmission demands tighter compensation precision. Furthermore, the significance of the broader signal bandwidth with respect to the inherent slope of the fiber chromatic dispersion against wavelength leads to a deviation from the linear group delay distortion of second-order dispersion (SOD) resulting in higher-order dispersion effects [1–3]. The most significant is third-order dispersion (TOD) caused by the linear slope of the fiber dispersion inducing a quadratic group delay distortion that impacts long haul pulse transmission at channel rates beyond $\sim$100 Gb/s. However, even if exactly compensated, system performance can still be degraded by the fourth-order dispersion (FOD) arising from a cubic group delay distortion induced by the slight parabolic curvature of the predominantly linear dispersion slope. While techniques for compensating SOD are well established, higher-order dispersion terms

require a dedicated solution. Section 2 overviews such techniques, however, the focus of this paper is on the use of a phase modulator which has been effective in the fastest OTDM fiber transmission experiments reported to date (see "Ultrafast OTDM transmission using novel fiber devices for pulse compression, shaping, and demultiplexing" by T. Yamamoto and M. Nakazawa (DOI: 10.1007/s10297-005-0037-1) in this publication). An overview of chromatic dispersion is given in Sec. 1 and the design principle for compensating both TOD and FOD is described in Sec. 3. The influence of key parameters on short pulse transmission is analyzed by numerical simulation in Sec. 4, and proof of concept laboratory results are presented in Sec. 5. Finally, a modified approach for potentially extending the application range of the technique is analyzed in Sec. 6.

1. Pulse Distortion Principle

Chromatic dispersion in optical fiber manifests from the various frequency components of the pulse spectrum propagating at different speeds given by $c/n(\omega)$ where n is the refractive index of the fiber, ω is the angular optical frequency and c is the speed of light [1]. The consequential frequency dependant phase shift is defined as the mode propagation constant, β, given by $\beta(\omega) = n(\omega)/c$. The distortion effect is expressed considering the input electric field of the pulse as $E_0(T) = A_0(T)\exp(j\omega_0 T)$ where $A_0(T)$ is the complex amplitude defined in polar coordinates with magnitude and phase, ϕ, as $A_0(T) = \mid A_0(T) \mid \exp[j\Phi(T)T]$, which is assumed slowly varying in time, T, with respect to the optical carrier of frequency, ω_0. The output after propagation in single mode fiber of length L is thus given by the inverse Fourier Transform of the function, $A(\omega) = A_0(\omega)\exp(j\beta L)$, where $A_0(\omega)$ is the Fourier Transform of $A_0(T)$.

The phase function required to compensate higher-order dispersion is apparent by expanding β in a Taylor series around the carrier frequency as [1]

$$\beta(\omega) = \beta_0 + (\omega-\omega_0)\beta_1 + (\omega-\omega_0)^2\beta_2/2 + (\omega-\omega_0)^3\beta_3/6 + (\omega-\omega_0)^4\beta_4/24 + \cdots + (\omega-\omega_0)^n\beta_n/n!. \quad (1)$$

The term $(\omega-\omega_0)^n\beta_n/n!$ is the average phase shift over L of nth order dispersion in units of radians/km, where β_n satisfies

$$\beta_n = [\delta\beta^n(\omega)\delta\omega^n]_{\omega=\omega_0}. \quad (2)$$

The pulse group delay, τ_g, and its linear distortion with frequency are determined by the coefficients β_1 and β_2, respectively, while higher-order terms correspond to $n \geq 3$. In practice, fiber dispersion is specified from the measured variation of group delay with wavelength, λ, as the parameter $D.L = \Delta\tau_g/\Delta\lambda$ in units of ps/nm, i.e., $D = \delta\beta_1/\delta\lambda$. Using Eq. (2) and noting $\omega = 2\pi c/\lambda$, the relation to the SOD coefficient is thus found as

$$D = \delta\beta_1/\delta\lambda = \beta_2(-2\pi c/\lambda^2). \quad (3)$$

Similarly, the fiber dispersion slope relates to the TOD coefficient as

$$D' = \delta D/\delta\lambda = [\beta_3(-2\pi c/\lambda^2)^2 - 2D/\lambda], \quad (4)$$

and its curvature relates to the FOD coefficient as

$$D'' = \delta^2 D/\delta\lambda^2 = [\beta_4(-2\pi c/\lambda^2)^3 - 6D'/\lambda - 6D/\lambda^2]. \quad (5)$$

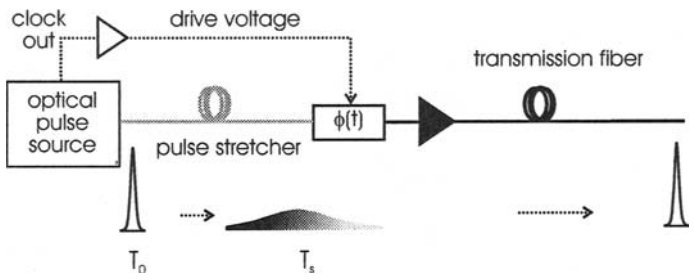

Fig. 1. Configuration for pre-compensating higher-order dispersion using a phase modulator $\phi(t)$.

2. Compensation Techniques

The impact of higher-order dispersion on ultra-short pulse transmission is evident considering that the fiber length whereby TOD and FOD doubles the width of a 1-ps pulse is typically on the order of 20 and 2000 km, respectively, and scales in inverse proportion to the third and fourth power of the pulse bandwidth, respectively. Consequently, high-speed OTDM transmission is constrained to very short distances [3] unless the nonlinear group delay distortion is countered over the optical bandwidth of the signal.

The broadband dispersion compensation technique widely employed in DWDM systems is negative slope dispersion compensating fiber (NS-DCF) having an opposite sign of dispersion and slope to standard single-mode fiber (SMF) enabling compensation of both at a specific wavelength ("Optical fibers and fiber dispersion compensators for high-speed optical communication" by Masayuki Nishimura (DOI: 10.1007/s10297-004-0024-y) in this publication). This technique has proven equally effective for compensating large TOD of broadband pulses [4], however, the shortcomings at higher bit rates are the tuning inflexibility impeding high compensation precision, and the unavoidable FOD. A unique solution is mid-span spectral inversion whereby a phase conjugating device is positioned along the fiber link such that SOD as well as FOD effects are cancelled by the matched dispersion of the remaining fiber. This method demonstrated both transmission of 600 fs pulses over 144 km [5] and 250 fs pulses over 66 km [23] using a periodically poled $LiNbO_3$ device.

Alternatively, devices such as optical fiber Bragg gratings, interferometer waveguide circuits, thin film filters, and phase modulators have experimentally demonstrated compensation of higher-order dispersion as summarized in Table 1. These devices can generally apply only limited phase change over a limited optical bandwidth and therefore cannot practically match NS-DCF for compensating a large dispersion slope. Phase modulation, however, features a broad optical bandwidth accommodating subpicosecond pulses, and is also programmable and capable of compensating FOD, which make it an attractive complement to NS-DCF especially at higher bit rates.

Two distinct methods of phase modulation are possible, whereby the pulse is dispersed either spatially or temporally before modulation. In the spatial approach, a grating disperses the pulse spectral energy across an array of liquid crystal pixels, which

Table 1. Techniques for compensating nth order pulse dispersion in fiber transmission.

Device	n	Pulse width in [ps]	Pulse width out [ps]	Distance [km]	Ref.	Constraints
NS-DCF	3	0.3	0.5	92	[4]	Precision
	3	0.25	0.5	139	[12]	control & FOD
Interferometer waveguide	3	2.6–4	~4	300	[6]	Max phase & bandwidth
Fiber grating	3	1.6	2.5	66	[7]	"
Thin-film filter	3	1.6	1.6	50	[8]	"
ϕ-conjugator	4	0.6	0.68	144[a]	[5]	Link dispersion
($LiNbO_3$)	4	0.25	0.3	66[a]	[23]	symmetry
ϕ-modulator	3, 4	0.4	0.4	10[a]	[9]	Frequency
(pixel array)	3, 4	0.2	0.49	85[a]	[10]	resolution
ϕ-modulator	3	0.25	0.32	0.6	[11]	V_π voltage &
($LiNbO_3$)	3	0.25	0.43	2.4	[24]	frequency
	4	0.25	0.39	139[a]	[12]	modulation
	3, 4	0.3	0.32	70[a]	[13]	

[a] Incorporates NS-DCF.

can be programmed to control the phase of the impinging slice of the pulse spectrum. By this method, transmission of 400 fs pulses over 10 km fiber without broadening [9], and 200 fs pulses over 80 km fiber for 490 fs output [10] have been reported. In general, performance is limited by the granularity of the spectral sampling resolution determined by the combination of parameters such as optical signal bandwidth, and pixel count, separation and phase step. On the other hand, the alternative approach of temporally dispersing the pulses before modulation avoids such issues and can be easily implemented all in-fiber without the need for a bulk optics setup using a conventional $LiNbO_3$ device. The remaining focus of this paper will be on the design performance of this technique in application to long distance fiber transmission of short pulses.

3. Phase Modulation Solution

The group delay distortion of an optical pulse is controllable using a $LiNbO_3$ electro-optic phase modulator configured as shown in Fig. 1. The technique requires a pulse stretcher to uniformly disperse the spectral energy so that the optical phase change induced by the following modulator device in response to a time varying drive voltage is translated directly to the frequency domain of the pulse, and therefore directly modifies

the group delay. This time domain approach for higher-order dispersion compensation [14,15] has also been applied to pulse shaping and compression [16–18].

The frequency–time translation is optimum when the pulse spectrum is widely dispersed satisfying $T_s \gg T_0$ where T_0 and T_s are the full width at half maximum power (FWHM) of the pulse before and after the pulse stretcher, respectively. In this condition, the pulse FWHM optical bandwidth, F_{BW}, is observed to be uniformly spread over a time interval approximately equal to T_s, as

$$f(t) \approx \pm F_{\mathrm{BW}}(t/T_s), \tag{6}$$

where f is the optical frequency relative to the carrier, and related to the angular frequency by $(\omega - \omega_0) = 2\pi f$. The parameter t is time relative to the total propagation delay of the pulse stretcher with sign determined by the dispersion. In an OTDM system, the technique can be implemented by pre-chirping the pulses before multiplexing to higher bit rates (see "Ultrafast OTDM transmission using novel fiber devices for pulse compression, shaping, and demultiplexing" by T. Yamamoto and M. Nakazawa (DOI: 10.1007/s10297-005-0037-1) in this publication), thus the phase modulation frequency, R, need only be as high as the repetition rate of the pulse source, which is typically on the order of 10 GHz. Since OTDM of many channels requires $T_0 \ll 1/R$, the phase modulation period is typically long compared to the pulse duration, and can therefore accommodate the broad T_s.

According to the configuration in Fig. 1, the higher-order dispersion terms corresponding to $n \geq 3$ in Eq. (1) are pre-compensated by applying the opposing phase with respect to the dispersed pulse described by Eq. (6). Thus the required voltage waveforms for driving the phase modulator to compensate TOD and FOD are cubic and quartic in time respectively. However, rather than synthesize such waveforms directly, the underlying principle of this compensation technique uses the basic function based upon the trigonometric series expansion in Eq. (7) to simplify the implementation:

$$\sin(x) = x - x^3/6 + \cdots, \tag{7a}$$

$$\cos(x) = 1 - x^2/2 + x^4/24 - \cdots. \tag{7b}$$

3.1. TOD Compensation Design

Comparing Eqs. (1) and (7a), the trigonometric series for a sinusoidal phase modulation defined as $\Phi_{\mathrm{PM}}(t) = \phi_p \sin(2\pi R t)$, includes a cubic term that can compensate TOD over the bandwidth satisfying $\Phi_{\mathrm{PM}}(f) \approx \Phi_D(f)$, where Φ_{PM} is the phase modulation translated to the frequency domain by Eq. (6) and Φ_D includes the relevant propagation terms from Eq. (1), defined as

$$\Phi_{\mathrm{PM}}(f) = \phi_p \sin[2\pi R T_s f / F_{\mathrm{BW}}], \tag{8}$$

$$\Phi_D(f) = \beta_1 L 2\pi f - \beta_3 L (2\pi f)^3/6. \tag{9}$$

The phase modulation parameters are designed to ensure the turning points of $\Phi_D(f)$ satisfying $\delta\Phi_D/\delta f = 0$ intersect the peak and trough of $\Phi_{\mathrm{PM}}(f)$ at the defined frequencies $\pm f_p$ as illustrated in Fig. 2(a). Since the point at $\delta\Phi_D/\delta f = 0$ satisfies $\Phi_D(f_p) = \phi_p$ for

$$f_p = (3\phi_p/\beta_3 L)^{1/3}/(2\pi), \tag{10}$$

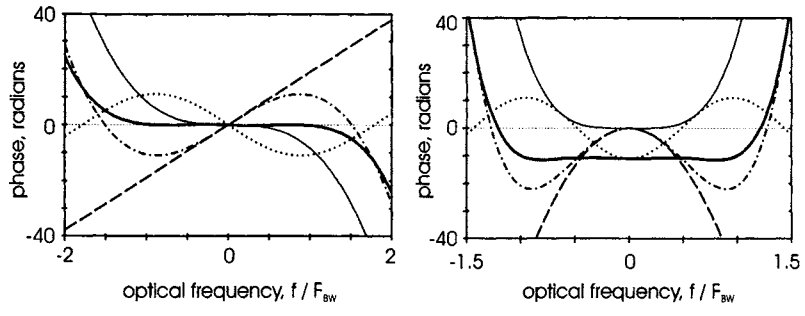

Fig. 2. Phase distortion of 250 fs pulse from (dash-dotted curve) Φ_D, (thin curve) higher-order component of Φ_D, (dashed curve) primary component of Φ_D, (dotted curve) $\Phi_{\rm PM}$ with $R = 5$ GHz, $\phi_p = 3.5\pi$, and (thick-solid curve) resultant $\Phi_D + \Phi_{\rm PM}$ for (a) TOD in 1 km link with $\beta_1 = 2.15$ ps/km, $\beta_2 = 0$, $\beta_3 = 0.1$ ps^3/km, $\beta_4 = 0$ and (b) FOD in 140 km link with $\beta_1 = 0$, $\beta_2 = -1.23 \times 10^{-2}$ ps^2/km, $\beta_3 = 0$, $\beta_4 = 1.46 \times 10^{-3}$ ps^4/km.

and $\Phi_{\rm PM}(f_p) = \phi_p$ for

$$f_p = F_{\rm BW}/(4RT_s), \tag{11}$$

the optimum pulse broadening for phase modulation is thus given by

$$T_s = \pi F_{\rm BW}/(2R)(\beta_3 L/3\phi_p)^{1/3}. \tag{12}$$

Also, substituting f_p from Eq. (10) into $\delta\Phi_D/\delta f = 0$ gives the induced time shift of the output pulse as

$$\tau_{\rm PM} = \beta_1 L = (\beta_3 L)^{1/3}(3\phi_p)^{2/3}/2. \tag{13}$$

3.2. FOD Compensation Design

Similarly, the trigonometric series for a cosine phase modulation defined as $\Phi_{\rm PM}(t) = \phi_p \cos(2\pi Rt)$, includes a quartic term that can compensate FOD over the bandwidth satisfying $\Phi_{\rm PM}(f) \approx \Phi_D(f)$, where $\Phi_{\rm PM}$ and Φ_D are now defined as

$$\Phi_{\rm PM}(f) = \phi_p \cos[2\pi RT_s f/F_{\rm BW}], \tag{14}$$

$$\Phi_D(f) = \beta_0 L - \beta_2 L(2\pi f)^2/2 + \beta_4 L(2\pi f)^4/24. \tag{15}$$

As for TOD, the phase modulation parameters are designed to ensure the turning points of $\Phi_D(f)$ satisfying $\delta\Phi_D/\delta f = 0$ intersect the peaks of $\Phi_{\rm PM}(f)$ at the defined frequencies $\pm f_p$. Since the amplitude of $\Phi_{\rm PM}(f)$ changes by $2\phi_p$ between $f = 0$ and f_p, the point at $\delta\Phi_D/\delta f = 0$ satisfies $\Phi_D(f_p) = 2\phi_p$ with $\beta_0 L = 0$ for

$$f_p = (-48\phi_p/\beta_4 L)^{1/4}/(2\pi), \tag{16}$$

and $\Phi_{\rm PM}(f_p) = \phi_p$ for

$$f_p = F_{\rm BW}/(2RT_s), \tag{17}$$

so the optimum pulse broadening for phase modulation can be expressed as

$$T_s = (\pi F_{\mathrm{BW}}/R)[\beta_4 L/(-48\phi_p)]^{1/4}. \tag{18}$$

Also, substituting f_p from Eq. (16) into $\delta\Phi_D/\delta f = 0$ gives the required residual SOD of the link, which unlike for Φ_{PM} in Eq. (13), must be accounted for in the design:

$$\beta_2 L = (\beta_4 L/6)[\pi F_{\mathrm{BW}}/(RT_s)]^2. \tag{19}$$

3.3. Phase Compensation Bandwidth

The performance of the technique is determined by the bandwidth of phase compensation with respect to the pulse. Since $\Phi_{\mathrm{PM}}(f)$ closely approximates $\Phi_D(f)$ primarily between the intersect points, the phase compensation bandwidth can be estimated as

$$F_\phi \sim 2f_p = F_{\mathrm{BW}}/(2RT_s) = (3\phi_p/\beta_3 L)^{1/3}/\pi \qquad \text{(TOD)}, \tag{20a}$$

$$F_\phi \sim 2f_p = F_{\mathrm{BW}}/(RT_s) = (-48\phi_p/\beta_4 L)^{1/4}/\pi \qquad \text{(FOD)}. \tag{20b}$$

The factor of two broader F_ϕ for FOD compensation with the same T_s is explained by the twice as large f_p for cosine. The actual phase compensation bandwidth ultimately depends on the tolerable phase deviation within the signal bandwidth and may extend beyond $2f_p$ as illustrated in the following examples. Figure 2(a) plots the phase functions for TOD compensation using 5 GHz phase modulation ($\phi_p = 3.5\pi$) in a 1-km fiber link with $\beta_3 = 0.1$ ps^3/km. The signal bandwidth shown corresponds to $T_0 = 250$ fs for a hyperbolic-secant pulse defined as $A(t) = 1/\cosh(1.763t/T_0)$ [1], whereby $F_{\mathrm{BW}} = 0.315/T_0 = 1.26$ THz. By observation, the sum of Eqs. (8) and (9) deviates within ± 0.5 radians over a bandwidth of 2.22 F_{BW} equal to 1.27 F_ϕ. Similarly, for FOD compensation using the same pulse and phase modulation in transmission over a 140-km fiber link with $\beta_4 = 1.46 \times 10^{-3}$ ps^4/km, the sum of Eqs. (14) and (15) in Fig. 2(b) deviates within ± 0.5 radians over 1.94 F_{BW} equal to 1.08 F_ϕ. Note, for TOD and FOD examples considered throughout this paper, the arguments of $\Phi_{\mathrm{PM}}(t)$ are multiplied by factors of 0.98 and 0.94, respectively, to slightly improve the phase flatness. The corresponding influence on output pulse quality will be addressed in the following sections.

3.4. Simultaneous TOD & FOD Compensation

So far, the design has treated TOD and FOD compensation independently using either sine or cosine phase modulation, respectively. It has been shown however, given that the sum of sine and cosine of the same frequency equals a sinusoid of the same frequency with different amplitude and phase, a single sinusoid function delayed appropriately with respect to the pulse can therefore simultaneously compensate both TOD and FOD [13]. For sine and cosine functions of frequency, R, and amplitude $-\phi_s$ and $-\phi_c$, respectively, the generalized phase modulation is

$$\Phi(t) = -\mathrm{sign}(\phi_c)\mathrm{sqrt}(\phi_c^2 + \phi_s^2)\cos[2\pi Rt - \arctan(\phi_s/\phi_c)]. \tag{21}$$

The delay parameter therefore offers an extra degree of tuning flexibility to compensate a residual TOD in addition to FOD. The effectiveness of this technique is highlighted in

"Ultrafast OTDM transmission using novel fiber devices for pulse compression, shaping, and demultiplexing" by T. Yamamoto and M. Nakazawa (DOI: 10.1007/s10297-005-0037-1) for transmission of 300 fs pulses in a 70-km fiber link with only 21 fs broadening [13].

4. Pulse Shaping Capability

Designing the phase modulation parameters to meet the desired performance improvement requires evaluating the pulse shape response. The numerical simulation model used for this purpose reflects the experimental hardware setup shown in Fig. 1, assuming both an ideal sinusoid phase modulation function and an ideal optical source of hyperbolic-secant shape pulses free of group delay distortion. The pulse stretcher is considered dispersion compensation fiber (DCF) with realistic SOD and TOD coefficients of $\beta_2 = 114.7$ ps^2/km, and $\beta_3 = 0.1$ ps^3/km, respectively, and length designed to appropriately disperse the pulse spectral energy for satisfying the required T_s. Since higher-order dispersion in the typical length pulse stretcher is relatively insignificant, the group delay distortion of the dispersed pulse remains predominantly linear according to Eq. (6).

The transmission fiber following phase modulation for TOD pre-compensation has the same TOD coefficient of $\beta_3 = 0.1$ ps^3/km and is designed so the total SOD for the link of combined length, L, is zero. On the other hand, the transmission fiber following FOD pre-compensation is designed so the combined link has zero total TOD and a residual SOD satisfying Eq. (19). Calculating the fiber propagation response follows Sec. 1 using algorithms for the discrete Fourier Transform and its inverse, with loss, and both polarization and nonlinear intensity-dependant effects ignored [1]. The FOD compensation analysis considers an opposite sign dispersion for the pulse stretcher and also includes a FOD coefficient of $\beta_4 = 1.1 \times 10^{-3}$ ps^4/km for both fibers, which is a realistic average for long distance fiber links incorporating NS-DCF.

The following examples consider parameters relevant to ultra-high speed OTDM for transmission of 250 fs pulses over a distance highlighting the influence of phase modulation with $R = 5$ GHz and a feasible peak amplitude of $\phi_p \sim 3\pi$. The numerical output waveform indicates severe TOD after only 1 km as shown in Fig. 3(a). However, applying phase modulation after broadening the pulse to 60 ps by a SOD of 7.58 ps^2 recovers a significantly improved pulse shape with compressed FWHM of 388 fs. For a fiber link with zero total dispersion-slope, FOD broadens the same pulse to 754 fs after a longer distance of 50 km as shown in Fig. 4(a). In this case, incorporating a residual SOD of -0.9 ps^2 and applying phase modulation with $\phi_p = 3.5\pi$ after broadening the pulses to 80 ps by a SOD of -10 ps^2 recovers an improved pulse shape with FWHM of 343 fs.

4.1. Bandwidth Effects

The output pulse quality is influenced by the residual phase distortion of optical frequencies falling outside the phase compensation bandwidth, which from Eq. (20) equals 1.7 and 2.5 F_{BW} for the above TOD and FOD examples, respectively. The band-edge sensitivity is evident considering that truncating the power spectrum of an

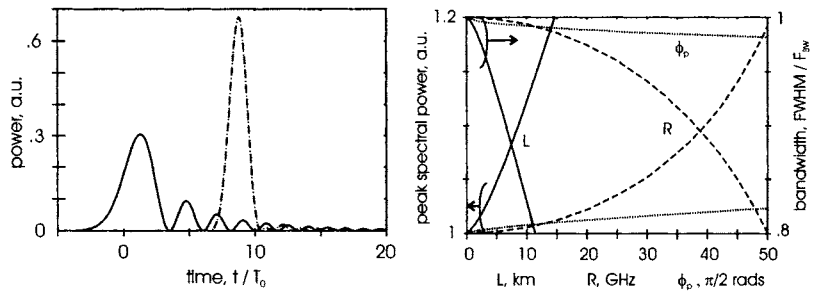

Fig. 3. Numerical output (a) $\mid A(t) \mid^2$ waveform from 1 km link for (solid curve) TOD of 250 fs pulse with $\beta_3 = 0.1$ ps^3/km and compensation with $\phi_p = 3\pi$, and $R =$ (dashed curve) 5 GHz (dotted curve) 10 GHz and (b) $\mid A(f) \mid^2$ optical spectrum distortion for (solid curve) increasing L with $\phi_p = 3\pi$, $R = 10$ GHz, (dashed curve) increasing R with $\phi_p = 3\pi$, $L = 1$ km, and (dotted curve) increasing ϕ_p with $L = 1$ km, $R = 10$ GHz, while maintaining optimal T_s for satisfying the design equations in each case.

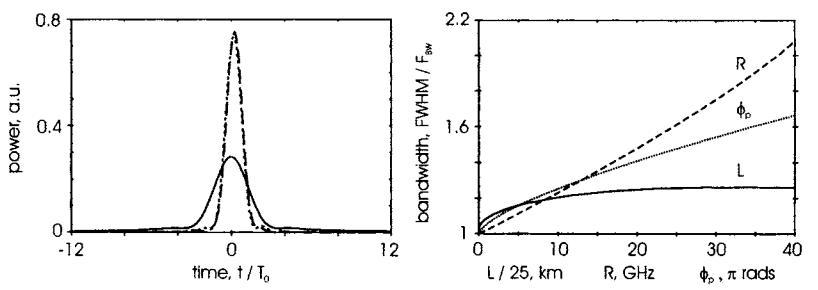

Fig. 4. Numerical output (a) $\mid A(t) \mid^2$ waveform for (solid curve) FOD of 250 fs pulse with $\beta_4 = 1.1 \times 10^{-3}$ ps^4/km and compensation in 50 km link with R, $\phi_p =$ (dashed curve) 5 GHz, 3.5π, (dotted curve) 10 GHz, 2.5π and (b) $\mid A(f) \mid^2$ optical spectrum distortion for (solid curve) increasing L with $\phi_p = 3\pi$, $R = 5$ GHz, (dashed curve) increasing R with $\phi_p = 3\pi$, $L = 50$ km, and (dotted curve) increasing ϕ_p with $L = 50$ km, $R = 5$ GHz, while maintaining optimal $\beta_2 L$ and T_s (via pulse stretcher with negative SOD coefficient).

ideal hyper-secant pulse to within an optical bandwidth of $2F_{\mathrm{BW}}$ broadens an ideal hyperbolic-secant pulse by a factor of 1.7 while removing only 6% of the energy. Thus, higher-order dispersion compensation in general would benefit from filtering to produce a more spectrally compact pulse shape.

Nevertheless, given F_ϕ in Eq. (20) scales in proportion to $(\phi_p/L)^{1/3}$ and $(\phi_p/L)^{1/4}$ for TOD and FOD compensation, respectively, the output pulse degrades only gradually with either increasing link length or decreasing ϕ_p. Figure 5(a) shows doubling the link length to 2 km broadens the TOD compensated output from 388 to 458 fs for the same phase modulation. Also, the FOD compensated output broadens from 343 to 383 fs for doubling of the link length to 100 km as shown in Fig. 5(b) with negligible change in pulse shape [15]. In these TOD and FOD examples, F_ϕ is

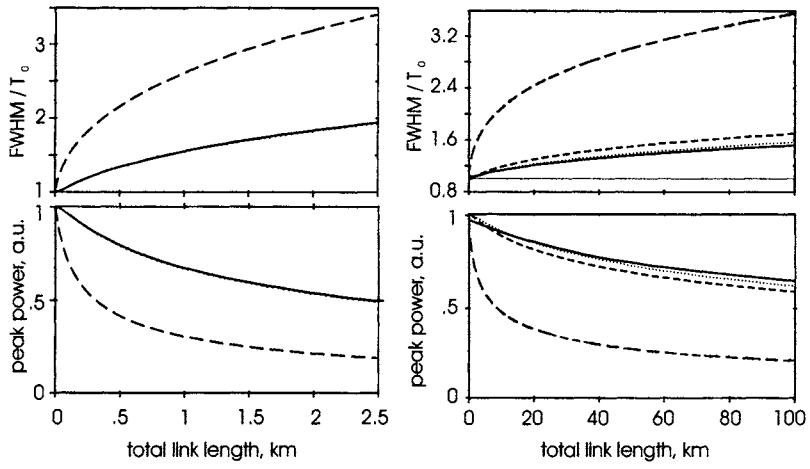

Fig. 5. Link length effect on 250 fs pulse transmission after (a) (dashed curve) TOD with $\beta_3 = 0.1$ ps^3/km and compensation for $\phi_p = 3\pi$ and $R =$ (solid curve) 5 GHz, (dotted curve) 10 GHz, and (b) (dashed curve) FOD with $\beta_4 = 1.1 \times 10^{-3}$ ps^4/km and compensation for R, $\phi_p =$ (solid curve) 5 GHz, 3.5π (dashed curve) 10 GHz, 2.5π, (dotted curve) 10 GHz, 1.5π. Optimal T_s and $\beta_2 L$ are maintained throughout to satisfy design equations .

narrowed by 21% and 16%, respectively. Similarly, reducing ϕ_p by a factor of 3 to 1.2π narrows F_ϕ (FOD) by 24%, which further broadens the output after 100 km to 431 fs without significant change in shape [15].

4.2. *Frequency Modulation Effects*

On the other hand, significantly increasing either R, ϕ_p, or L has the undesirable tradeoff of increased frequency modulation inherent to phase modulation as described by Eq. (22), which distorts the pulse depending upon the relation to the predominant uniform dispersion given in Eq. (6):

$$f_{\mathrm{PM}} = (2\pi)^{-1}\delta\Phi_{\mathrm{PM}}/\delta t = \phi_p R\cos(2\pi Rt) \qquad (\mathrm{TOD}), \qquad (22)$$
$$= \phi_p R\sin(2\pi Rt) \qquad (\mathrm{FOD}).$$

Insight into the basic distortion of the pulse power spectrum, $|\ A(f)\ |^2$, can be inferred from the frequency translated function, $|\ A(f - f_{\mathrm{PM}})\ |^2$, where f_{PM} is Eq. (22) with time mapped to frequency by Eq.(6). It suggests TOD compensation of hyperbolic-secant pulses will frequency shift the spectral peak from $f = 0$ according to the amplitude of frequency modulation and with sign determined by Eq. (6). Also, the output spectrum will acquire an asymmetric shape and narrower FWHM. On the other hand, FOD compensation symmetrically distorts the spectrum without frequency shifting the peak, and either broadens or narrows the bandwidth depending on the sign of Eq. (6). In general, the degree of distortion is determined by the variation of the induced frequency shift over the signal band-width, and thus increases for

frequency modulation of either larger amplitude or shorter period ($T_{\rm PM}$) with respect to T_s. Although the amplitude is proportional to both ϕ_p and R, the distortion is less sensitive to increasing ϕ_p since the ratio $T_{\rm PM} : T_s$ is simultaneously increased by the corresponding shorter T_s, but remains constant for increasing R. Similarly, increasing the link length also enhances distortion since the corresponding broader T_s reduces the ratio $T_{\rm PM} : T_s$.

The impact of frequency modulation on output pulse quality is evident from numerical simulation. In the example of Fig. 3(a), the TOD compensated output from the 1-km link shows negligible difference for increasing R from 5 to 10 GHz, and the corresponding output spectrum remains close to original. However, the distortion increases sharply for frequencies beyond 10 GHz. This is highlighted in Sec. 6 for the case of $R = 40$ GHz, in demonstrating a solution for mitigating the effect. Figure 3(b) compares the spectral distortion dependence on the parameters R, L and ϕ_p and shows the distortion evident at $R = 40$ GHz is roughly comparable in effect to increasing the link length to 8 km, whereby $T_{\rm PM} : T_s$ is halved. In contrast, the apparent smaller sensitivity to larger ϕ_p is due to the combined increase in $T_{\rm PM} : T_s$ and the slow amplitude roll off of cosine frequency modulation causing less variable frequency shift across $F_{\rm BW}$. However, observation of the output spectrum reveals large asymmetric distortion outside the bandwidth $F_{\rm BW}$, along with frequency shifting of the peak, which significantly degrades the output pulse shape. Nevertheless, the FWHM narrows to a minimum of ~339 fs for $\phi_p \sim 9\pi$, and equals 390 fs for $\phi_p = 25\pi$.

The effect of frequency modulation in FOD compensation differs considerably. Reversing the sign of β_2 in the pulse stretcher from positive to negative causes the phase modulation to spectrally broaden rather than narrow the pulse, and produce a slightly shorter output. In the example of Fig. 4(a), the original 1.26-THz bandwidth is broadened to 1.43 THz after 50 km for $R = 5$ GHz, $\phi_p = 3.5\pi$. Increasing R to 10 GHz with $\phi_p = 2.5\pi$ produced comparable output with a FWHM of 348 fs and bandwidth of 1.52 THz. The distortion dependence on the various parameters in Fig. 4(b) shows the signal bandwidth remains narrower than 1.59 THz for link lengths up to 1000 km, but is more dramatically influenced by R and ϕ_p. Raising R from 5 to 20 GHz in a 50-km link with $\phi_p = 3\pi$ broadens the bandwidth from 1.40 to 1.86 THz. Although the corresponding output pulse shortens from 349 to 328 fs, the waveform shape is distorted. Similarly, increasing ϕ_p to 8π with $R = 5$ GHz broadens the bandwidth to 1.53 THz, and produces 323 fs pulses with significant pedestal.

4.3. Normalization Limits

Frequency modulation distortion impedes applying the technique to OTDM at lower bit rates. The relation is evident from normalizing the parameters with respect to pulse bandwidth. From Eq. (1), pulse distortion due to TOD and FOD scales with link length as $L \propto F_{\rm BW}^{-3}$, and $L \propto F_{\rm BW}^{-4}$, respectively. Also, maintaining the same F_ϕ normalized to $F_{\rm BW}$ for the same ϕ_p satisfying T_s requires $R \propto F_{\rm BW}$, and therefore $T_s \propto 1/R$. Thus Figures 3(a) and (b) for 5–10 GHz phase modulation equivalently correspond to TOD compensation of 1 ps pulses in a 64-km fiber link with 1.25–2.5 GHz phase modulation, and FOD compensation of 500 fs pulses in a 800-km link with 2.5–5 GHz phase modulation respectively. In both cases, increasing R to 10 GHz to maintain compatibility for OTDM of OC-192 rate channels raises the same

frequency modulation distortion tradeoff described above, which limits the broadest suitable pulse width, and thus, the lowest OTDM bit rate.

5. Pulse Transmission Experiments

The phase modulation technique has proven practically viable in application to ultra-high speed OTDM fiber optic communications, and capable of delivering the improved transmission performance expected from analysis. The fastest single wavelength channel system reported to date demonstrated simultaneous compensation of both TOD and FOD in a 70-km fiber link by applying phase modulation to each 10 Gb/s channel before multiplexing to an aggregate data rate of 1.28 Tb/s (see "Ultrafast OTDM transmission using novel fiber devices for pulse compression, shaping, and demultiplexing" by T. Yamamoto and M. Nakazawa (DOI: 10.1007/s10297-005-0037-1) in this publication). Single channel transmission experiments have also shown effective TOD and FOD compensation of 250 fs pulses over various links with 5∼6 GHz phase modulation applied in accordance with the design scheme presented in Sec. 3 [11,12,24]. Table 2 summarizes the link designs of length 0.6 km and 2.33 km, and a longer 139-km link incorporating NS-DCF for complete dispersion slope compensation. The set-ups for compensating TOD and FOD are shown in Figs. 1 and 6, respectively. Both include the same source of 250 fs optical pulses generated from an external cavity semiconductor laser using an electro-absorption modulator and higher-order soliton compression in a 3.8-km SMF and 630-m dispersion-decreasing fiber [19]. The source allows the pulse center wavelength to be tuned to coincide with the minimum dispersion wavelength of each link, which differ slightly around 1550 nm as shown by the group delay measurements in Fig. 7. The desired features of a hyperbolic-secant pulse shape and negligible group delay distortion are apparent in Fig. 8 from both the autocorrelation trace and the optical spectrum showing a close fit to a sech^2 function of FWHM bandwidth equal to 10 nm, giving a time-bandwidth product near the ideal value of 0.315. The broad low intensity pedestal accompanying each pulse evident from the intense spike in the optical spectrum has little influence on the results.

The link includes a $LiNbO_3$ phase modulator driven by a sinusoidal voltage derived either from a rf oscillator, or, for better synchronization, from the incoming pulses using a simple detector and band-pass filter circuit as depicted in Figs. 1 and 6, respectively. The amplitude of the synchronous phase modulation is tunable up to a maximum of $\phi_p \sim 3.8\pi$, limited by the modulator V_π of 3.7 V and saturation power of the driving amplifier. Optimum performance requiring alignment between the phase modulation period and incoming pulse to within $\pm 1 \sim 2$ ps is met using an optical delay line. Optical amplifiers overcome the link losses while maintaining a maximum average power below several tens of mW to avoid intensity dependant nonlinear effects in fiber arising from cross phase modulation and four wave mixing between the widely dispersed pulses [20,21]. The extreme sensitivity of ultra-short pulse propagation to polarization mode dispersion is countered by periodically adjusting the state of polarization at various points along the link to manipulate the delay between the propagation along the fast and slow polarization axis for overall cancellation at the output.

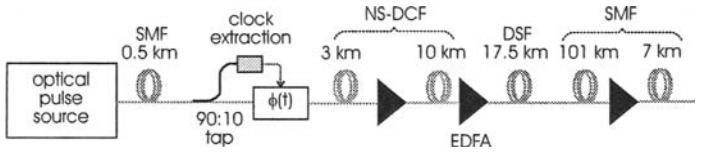

Fig. 6. Hardware configuration of higher-order dispersion compensation in 139 km fiber link.

Table 2. Fiber link design for compensating nth-order dispersion of 250 fs pulses using 5–6 GHz phase modulation.

n	Pulse stretcher			Transmission fiber	Combined link	
	Length [km]	Total D /ps nm^{-1}	T_s /ps	length [km]	$D(\lambda)L$ /ps nm^{-1}	L [km]
3	~0.05 (DCF)	−4.5	47	0.3 (SMF) + 0.25 (DSF)	0.046 (λ− 1551.4)	0.6
3	~0.08 (DCF)	−7.5	76	0.5 (SMF) + 1.75 (DSF)	0.174 (λ− 1549.5)	2.33
4	0.5 (SMF)	8.25	87	13 (NS-DCF) + 108 (SMF) + 17.5 (DSF)	0.5− 0.049 (λ− 1552.3)^2	139

$D(\lambda)L$ approximate fit to the measured dispersion plotted in Fig. 7, DSF dispersion shifted fiber. Typical values of (D, D') for NS-DCF, SMF and DSF at $\lambda = 1550$ nm are (−137, −0.6), (16.5, 0.06), and (0, 0.06), respectively.

5.1. *TOD Link Measurements*

The dispersion measurement in Fig. 7 fitted by $D(\lambda)$ in Table 2 indicates zero dispersion for the 600-m link near the 1550-nm wavelength with a slope corresponding to an average TOD coefficient of 0.125 ps^3/km, by calculation from Eq. (4). The DCF has a total dispersion of −4.5 ps/nm that broadens the 250-fs pulses to 47 ps as required for optimum TOD compensation using 5 GHz modulation with maximum $\phi_p = 3.8\pi$. Similarly, the 2.33-km link has zero dispersion near the 1550-nm wavelength with a slope corresponding to $\beta_3 \sim 0.12$ ps^3/km. The longer DCF with total dispersion of −7.5 ps/nm broadens the 250-fs pulses to 76 ps, enabling the same phase modulation to apply a larger phase-shift within F_{BW} to account for the larger total TOD.

TOD distorts the output after 600 m as shown in Fig. 8, however, applying phase modulation recovers a significantly improved pulse shape with shorter FWHM of 321 fs[1]. The output autocorrelation shows good agreement with numerical simulation for $R = 5$ GHz and $\phi_p = 3.8\pi$ as shown in Fig. 9, and predicts a pulse width of 300 fs compared to 338 fs for the direct output waveform. The technique is similarly effective for countering severe pulse distortion from the quadruple TOD in the 2.33-km link. Figure 10 shows the drastically improved output pulse shape with FWHM of 425 fs recovered by applying the same phase modulation. The broader output FWHM is explained by the narrower phase compensation bandwidth according to the inverse dependence of F_ϕ on T_s in Eq. (20) equaling a ~0.6 scale factor. As discussed in

[1] In this paper, pulse width inferred from the autocorrelation trace assumes a hyperbolic-secant pulse shape, and thus equals 0.648 times the measured FWHM from the autocorrelation definition $G(\tau) = \int A(t)A(t-\tau)\delta t$ with $A(t) = 1/\cosh(1.763t/T_0)$.

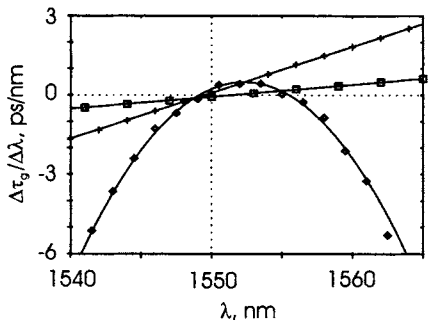

Fig. 7. Measured group delay variation with wavelength ($\Delta\tau_g/\delta\lambda$) for (box-points) 600 m, (cross-points) 2.33 km and (diamond points) 139 km fiber links. Solid curves are approximate function fits, $D(\lambda)L$, defined in Table 2.

Sec. 4, the output FWHM sensitivity to the limited phase compensation bandwidth is emphasized by the use of an unfiltered pulse source in the experiments.

Although the fiber links in these measurements were designed to satisfy the optimum T_s, significant variation of the parameters T_0, T_s, R, and ϕ_p is tolerable in practice for maintaining comparable output quality [11]. For example, lowering ϕ_p from 3.8π to 1.75π broadens the measured output FWHM of the 600 m link from $\sim$320 fs to 450 fs respectively without significantly changing the pulse shape. Also, a similar quality pulse shape with FWHM between 320–350 fs is observed from the same link for arbitrary modulation frequency between 4–6 GHz after optimizing ϕ_p accordingly.

5.2. FOD Link Measurements

The measured dispersion in Fig. 7 fitted by $D(\lambda)$ in Table 2 indicates an average FOD coefficient for the 139-km link of $\beta_4 = 1.46 \times 10^{-3}$ ps^4/km, as calculated from Eq. (5). Numerical simulation predicts such FOD will broaden the 250-fs pulse to 1.06 ps as shown in Fig. 12. In practice, a shorter FWHM of 503 fs is measured after optimizing the length of the last SMF spool in 5 m increments. The difference is explained by the excess dispersion of 0.5 ps/nm evident in Fig. 7 at the pulse carrier wavelength, corresponding to $\beta_2 L = -0.64$ ps^2. From Eq. (15), the corresponding induced quadratic phase has an appropriate sign to counter the FOD phase distortion over the signal bandwidth and thereby shorten the output pulse width even without phase modulation. Numerical simulation confirms including an excess SOD of -0.42 ps^2 equivalent to 20 m SMF produces a similarly shorter FWHM of 590 fs, albeit with significant pedestal due to the residual phase distortion. Laboratory measurements show more effective FOD compensation by applying 6 GHz phase modulation with $\phi_p = 3.7\pi$ after broadening the 250-fs pulses to 87 ps and inserting an extra 50-m SMF to the link output for a total residual SOD of -1.69 ps^2, close to the expected -1.72 ps^2. The significantly improved output pulse in Fig. 11 has a shorter FWHM of

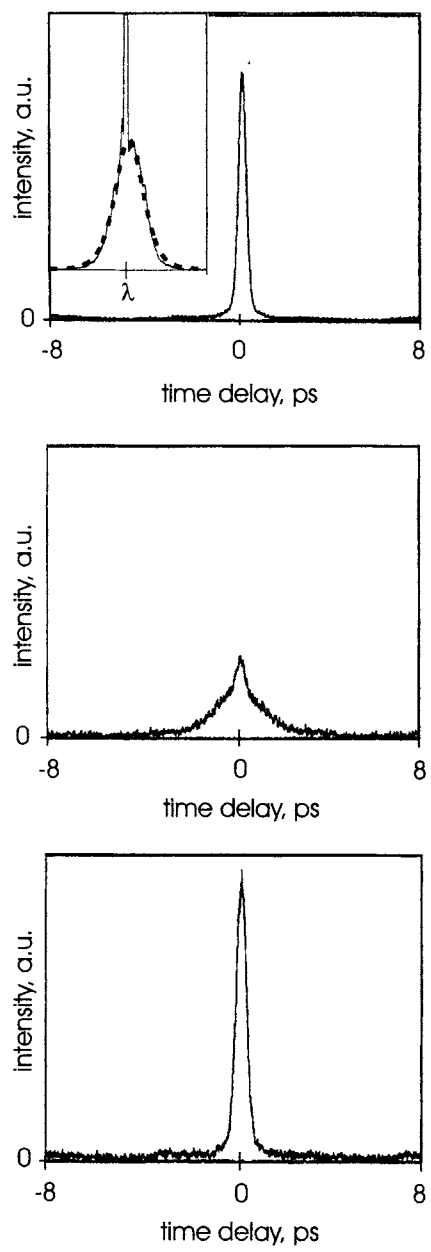

Fig. 8. Measured autocorrelation of 250 fs pulse at (a) input and output of 600 m link with (b) $\phi_p = 0$ and (c) $\phi_p = 3.8\pi$ in TOD compensation by 5 GHz phase modulation. Inset: optical spectrum on 50 nm span centered at 1550 nm with (dashed curve) sech^2 fit of FWHM = 10 nm.

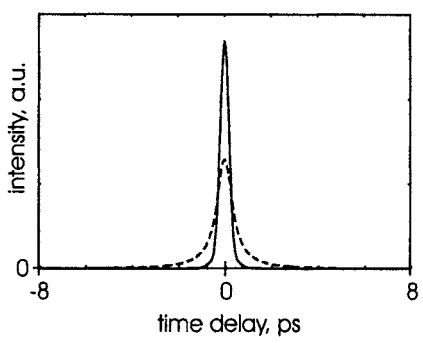

Fig. 9. Numerical autocorrelation of 250 fs pulse at output of 600 m link with $\beta_3 = 0.1$ ps^3/km and (dashed curve) $\phi_p = 0$ and (solid curve) $\phi_p = 3.8\pi$ in TOD compensation by 5 GHz phase modulation.

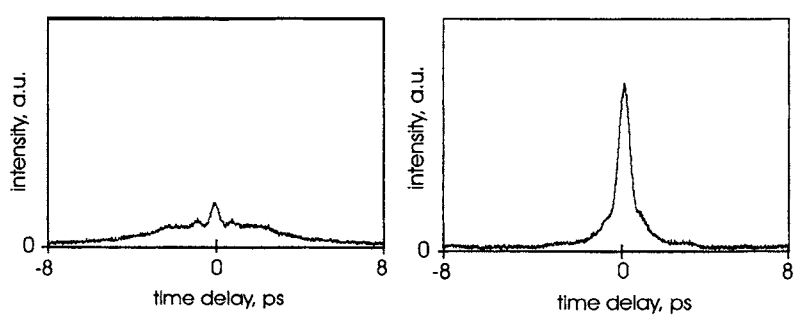

Fig. 10. Measured autocorrelation of 250 fs pulse at output of 2.33 km link with (a) $\phi_p = 0$ and (b) $\phi_p = 3.8\pi$ in TOD compensation by 5 GHz phase modulation.

390 fs and shows good agreement with the numerical generated waveform having an identical FWHM.

6. Performance Enhancing Schemes

Extending the application range of the phase modulation technique towards higher quality output, higher modulation frequency or longer reach is constrained by frequency modulation distortion inherent to phase modulation as described in Sec. 4. A potential solution applicable to both TOD and FOD compensation is the cascaded configuration presented in Fig. 13 whereby phase modulation is applied in two stages [22]. The overall distortion is mitigated at the second stage by reversing the sign of the uniform dispersion for the incoming pulse using another pulse stretcher with total SOD of opposite sign and twice the magnitude to the first. Applying the same sign phase shift with respect to signal frequency therefore induces a counter sign frequency modulation enabling partial cancellation of the distortion. As for the single stage approach,

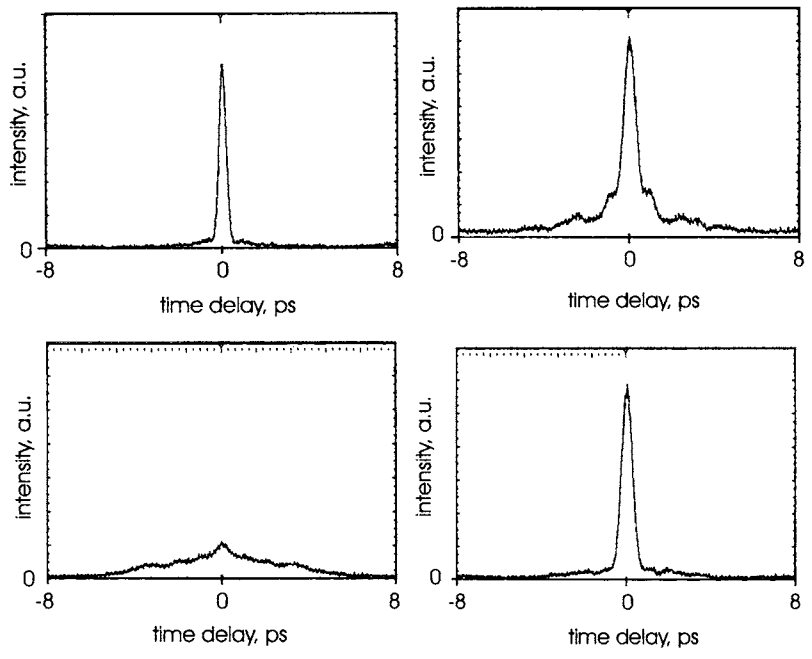

Fig. 11. Measured autocorrelation of 250 fs pulse at (a) input and output of 139 km link with (b) optimum residual dispersion of 0.5 ps/nm ($\beta_2 L = -0.64$ ps^2) for minimum FWHM, and (c) residual dispersion of 1.32 ps/nm ($\beta_2 L = -1.69$ ps^2) (d) combined with 6 GHz phase modulation ($\phi_p = 3.7\pi$) for FOD compensation.

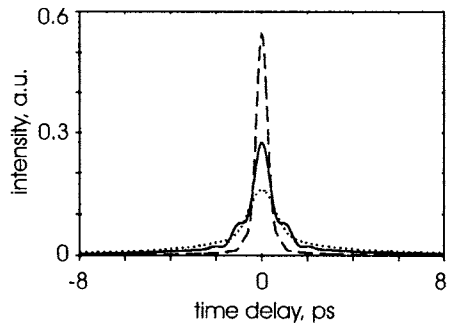

Fig. 12. Numerical autocorrelation of 250 fs pulse at output of 139 km link with $\beta_4 = 1.46 \times 10^{-3}$ ps^4/km and (dotted curve) $\beta_2 = \beta_3 = 0$ (solid curve) optimum $\beta_2 L = -0.42$ ps^2 for minimum FWHM and (dashed curve) FOD compensation by combined $\beta_2 L = -1.72$ ps^2 and 6 GHz phase modulation ($\phi_p = 3.5\pi$).

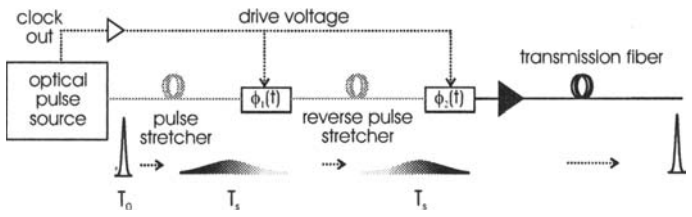

Fig. 13. Cascaded phase modulation configuration for suppressed frequency modulation distortion.

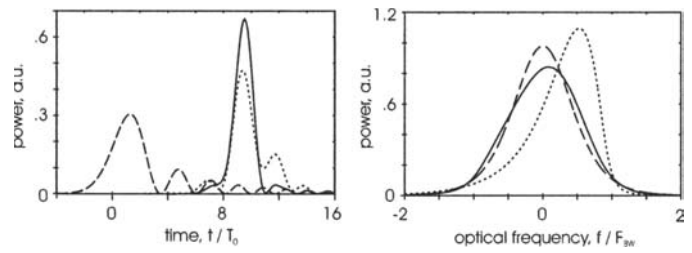

Fig. 14. Numerical output waveform and optical spectrum from 1 km fiber link for (dashed curve) TOD of 250 fs pulse with $\beta_3 = 0.1$ ps^3/km and (dotted curve) compensation by single and (solid curve) cascaded stage 40 GHz phase modulation with $\phi_p = 3.5\pi$.

the transmission fiber following the second stage is designed so that the combined link of length, L, satisfies either zero total SOD or TOD in the case of TOD and FOD compensation respectively. The other parameters are designed to satisfy the same equations presented in Sec. 3 with ϕ_p now representing the combined magnitude of both stages, which are considered equal, and in the case of TOD compensation of opposite sign.

The advantage of the technique is highlighted in the following examples for TOD compensation assuming $\beta_3 = 0.1$ ps^3/km throughout the link. The effect of applying phase modulation at a higher frequency of 40 GHz with $\phi_p = 3.5\pi$ for 250 fs pulse transmission in a 1-km fiber link is shown in Fig. 14. As described in Sec. 4, the power spectrum for single stage phase modulation is asymmetrically distorted by the induced frequency modulation with respect to the temporally dispersed pulse. Thus reversing the sign of dispersion in the pulse stretcher induces an opposite sign frequency shift which inverts the asymmetrically distorted spectrum in frequency, so the net counter effect for the two-stage configuration is a more symmetric output spectrum and improved temporal pulse shape with FWHM of 1.46 T_0. By the normalization discussed in Sec. 4.3, the result with the same ϕ_p is identical for either transmission of 1 ps pulses over 64 km with $R = 10$ GHz, or 4 ps pulses over 4096 km with $R = 2.5$ GHz, and is thus applicable to OTDM of OC-192 or OC-48 channels respectively for aggregate data rates in the lower range of ~100–400 Gb/s.

The two-stage configuration is similarly advantageous for extending the transmission distance and using larger ϕ_p. Figure 15 highlights the output pulse improvement

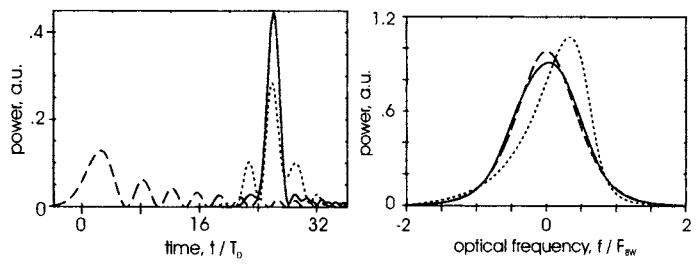

Fig. 15. Numerical output waveform and optical spectrum from 5 km fiber link for (dashed curve) TOD of 250 fs pulse with $\beta_3 = 0.1$ ps^3/km and (dotted curve) compensation by single and (solid curve) cascaded stage 10 GHz phase modulation with $\phi_p = 7\pi$.

for compensating severe TOD of 250 fs pulses in a 5-km fiber link using phase modulation at 10 GHz frequency with $\phi_p = 7\pi$. In this case, (ϕ_p/L) is around half that of the 1-km example in Fig. 3(a). The corresponding narrower phase compensation bandwidth expected from Eq. (20) explains the broader output FWHM of 1.9 T_0, which is compressed to $\sim$1.25 T_0 for a 600-m link using the same magnitude phase modulation.

Acknowledgments

This work was supported by the Femtosecond Technology Research Association (FESTA) and New Energy and Industrial Technology Development Organisation (NEDO).

References

1. G.P. Agrawal, *Nonlinear Fiber Optics*, 2nd ed. (Academic Press, 1989)
2. D. Marcuse, "Pulse distortion in single-mode fibers. 3: Chirped pulses", Appl. Optics **20**, 3573 (1981)
3. M. Amemiya, "Pulse broadening due to higher-order dispersion and its transmission limit", J. Lightwave Technol. **20**, 591 (2002)
4. T. Yamamoto, E. Yoshida, K. R. Tamura, K. Yonenaga, M. Nakazawa, "640-Gbit/s optical TDM transmission over 92 km through a dispersion-managed fiber consisting of single-mode fiber and reverse dispersion fiber", IEEE Photon. Technol. Lett. **12**, 353 (2000)
5. D. Kunimatsu, C.Q. Xu, M.D. Pelusi, X. Wang, K. Kikuchi, H. Ito, A. Suzuki, "Subpicosecond pulse transmission over 144 km using midway optical phase conjugation via a cascaded second-order process in a $LiNbO_3$ waveguide", IEEE Photon. Technol. Lett. **12**, 1621 (2000)
6. K. Takiguchi, S. Kawanishi, H. Takara, A. Himeno, K. Hattori, "Dispersion slope equalizer for dispersion shifted fiber using a lattice-form programmable optical filter on a planar lightwave circuit", J. Lightwave Technol. **16**, 1647 (1998)

7. T. Imai, T. Komukai, M. Nakazawa, "Second- and third-order dispersion compensation of picosecond pulses achieved by combining two nonlinearly chirped fibre Bragg gratings", Electron. Lett. **34**, 2422 (1998)

8. M. Jablonski, Y. Takushima, K. Kikuchi, Y. Tanaka, K. Furuki, K. Sato, N. Higashi, "Layered optical thin-film allpass dispersion equaliser for compensation of dispersion slope of optical fibres", Electron. Lett. **36**, 1139 (2000)

9. S. Shen, A.M. Weiner, "Complete dispersion compensation for 400 fs pulse transmission over 10-km fiber link using dispersion compensating fiber and spectral phase equalizer", IEEE Photon. Technol. Lett. **11**, 827 (1999)

10. F. Futami, K. Taira, K. Kikuchi, A. Suzuki, "Wideband fibre dispersion equalisation up to fourth-order for long-distance subpicosecond optical pulse transmission", Electron. Lett. **35**, 2221 (1999)

11. M.D. Pelusi, Y. Matsui, A. Suzuki, "Electro-optic phase modulation of stretched 250 fs pulses for suppression of third-order fiber dispersion in transmission", IEEE Photon. Technol. Lett. **11**, 1461 (1999)

12. M.D. Pelusi, X. Wang, F. Futami, K. Kikuchi, A. Suzuki, "Fourth-order dispersion compensation for 250-fs pulse transmission over 139-km optical fiber", IEEE Photon. Technol. Lett. **12**, 795 (2000)

13. T. Yamamoto, M. Nakazawa, "Third- and fourth-order active dispersion compensation with a phase modulator in a terabit-per-second optical time-division multiplexed transmission", Opt. Lett. **26**, 647 (2001)

14. M.D. Pelusi, Y. Matsui, A. Suzuki, "Phase modulation of stretched optical pulses for suppression of third-order dispersion effects in fibre transmission", Electron. Lett. **34**, 1675 (1998)

15. M.D. Pelusi, Y. Matsui, A. Suzuki, "Fourth-order dispersion suppression of ultra-short optical pulses using second-order dispersion and cosine phase modulation", Opt. Lett. **25**, 296 (2000)

16. M. Haner, W.S. Warren, "Synthesis of crafted optical pulses by time domain modulation in a fiber-grating compressor", Appl. Phys. Lett. **52**, 1458 (1988)

17. B.H. Kolner, "Active pulse compression using an integrated electro-optic phase modulator", Appl. Phys. Lett. **52**, 1123 (1988)

18. A.A. Godil, B.A. Auld, D.M. Bloom, "Time-lens producing 1.9 ps optical pulses", Appl. Phys. Lett. **10**, 1047 (1993)

19. M.D. Pelusi, Y. Matsui, A. Suzuki, "Frequency tunable femtosecond pulse generation from an electro-absorption modulator by enhanced higher-order soliton compression in dispersion decreasing fibre", Electron. Lett. **35**, 734 (1999)

20. I. Shake, H. Takara, K. Mori, S. Kawanishi, Y. Yamabayashi, "Influence of interbit four-wave mixing in optical TDM transmission", Electron. Lett. **34**, 1600 (1999)

21. P.V. Mamyshev, N.A. Mamysheva, "Pulse-overlapped dispersion-managed data transmission and intrachannel four-wave mixing", Opt. Lett. **24**, 1454 (1999)

22. M.D. Pelusi, A. Suzuki, "Cascaded phase modulation of reverse-stretched optical pulses for improved higher-order fibre dispersion compensation", Electron. Lett. **37**, 907 (2001)

23. D. Kunimatsu, C.Q. Xu, M.D. Pelusi, X. Wang, K. Kikuchi, H. Itoh, A. Suzuki, "Fourth-order dispersion compensation using a periodically polled LiNbO3 optical phase conjugator", in Proc. 4th Pacific Rim Conf. on Lasers and Electro-Optics, Chiba, Japan, July 2001, (CLEO-Pacific Rim 2001), vol. 1, pp. 452–453

24. M.D. Pelusi, Y. Matsui, A. Suzuki, "Fiber transmission of 250 fs optical pulses with suppressed third-order dispersion by electro-optic phase modulation", in Proc. IEEE 12th Annual meeting of Lasers and Electro-Optics Society, San Francisco, CA, USA, November 1999 (LEOS '99), vol. 2, pp. 541–542

DOI: 10.1007/s10297-005-0035-3
Originally published in J. Opt. Fiber Commun. Rep. 2, 32–55 (2005)

PMD-compensation techniques

Harald Rosenfeldt and Ernst Brinkmeyer

[1] adaptif PHOTONICS GmbH, Harburger Schloßstr. 6-12, 21079 Hamburg, Germany
[2] Technische Universität Hamburg-Harburg, Eißendorfer Str. 40, 21073 Hamburg, Germany

Abstract. PMD has become a serious limitation for the advent of 40G optical transmission systems. Commercial operators still avoid the utilization of optical PMD compensators since crucial questions such as expected performance and reliability are still subject to research and are not yet satisfactory answered for all relevant cases. The common solutions of tackling PMD, e.g., limiting transmission distance or selecting low-PMD fibers, does not necessarily apply for optical OTDM systems with bit rates beyond 160 Gbit/s. This article describes current approaches for PMD compensators with special focus on the requirements of optical OTDM systems.

Although Polarization Mode Dispersion (PMD) in optical fibers has been investigated since the late 70s, it became a matter of increasing importance since approximately 1997 due to the commercial advent of 10 Gbit/s optical transmission systems. After having removed limitations caused by chromatic dispersion and non-linear effects in optical WDM systems, the problems caused by PMD still pose an ultimate limit for optical high-speed transmission and have not yet been satisfactory solved.

The main reason for the difficulties in compensating PMD-induced distortions probably is that PMD changes statistically with time at different time scales. Therefore, unlike chromatic dispersion, PMD has to be compensated dynamically, e.g., by an active control circuitry. Therefore, the main goal of compensating PMD is not only to find the compensator's optimum settings to combat the PMD-induced distortions but also to keep track of the temporal fluctuations of the transmission link and to maintain the quality of compensation. This gives rise to numerous questions regarding response time, reliability, complexity and cost of such a solution.

If the differential group delay (DGD) of a fiber stays well below the duration of a single bit, the PMD-induced impairments can be neglected. However, particularly OTDM systems with bit rates of 160 Gbit/s and bit durations of less than 6.25 ps will be severely disturbed by the DGD levels of common deployed fibers. At these bit rates

it will thus be unavoidable to actively counteract PMD-induced impairments since the common approach, namely selecting a low-PMD fiber, will not always be an option.

PMD is a consequence of fiber birefringence mainly caused by mechanical stress and elliptical core profile of the waveguide. Owing to the cabling and deploying process the orientation of the waveguide as well as the mechanical stress varies randomly along the fiber link. In order to describe this stochastic behavior the so-called *waveplate model* is commonly used to investigate the properties of real fiber links. The main approach of the waveplate model is to divide the fiber into several randomly concatenated linearly birefringent elements (i.e., waveplates).

Considering a single waveplate, a polarized signal propagating through such a (linearly birefringent) element is split into its two components coinciding with the element's birefringent axes. These two components are traveling at different propagating speeds. Thus a single waveplate can cause two-path propagation and therefore may induce inter-symbol interference if the time delay between the two signal components (i.e., the DGD) is large enough. In the waveplate model these two components pass the second waveplate, which has a different orientation than the first. Thus the two components decompose into four signals. These four signals, again, are divided into eight signals when passing the third waveplate and so forth. Having this model in mind, PMD can be interpreted as a problem of multi-path propagation. As explained in the next paragraphs, the complex model of concatenated waveplates can be simplified by modeling a fiber as a (single) birefringent element whose DGD and birefringent axes (the so-called Principal States of Polarization, PSP) are wavelength-dependent.

The following sections show how the PSP-concept helps to understand the principles of optical PMD compensation and its limitations.

1. Concepts of PMD Compensation

The concepts of PMD compensators (PMDCs) can be classified in many different ways such as the operating domain (electrical/optical), the control structure (feed-back or feed-forward), the operating principle of the control elements (e.g. electro-optical/magneto-optical) and the detection scheme (RF tones, degree of polarization—DOP, state of polarization—SOP, etc.).

1.1. Feed-Back and Feed-Forward Structures

The most popular concepts of optical PMD compensation use a feed-back loop comprising an equalizer part to manipulate the optical signal, a detection part to derive an error signal and an algorithm that adaptively optimizes the parameter settings of the equalizer. The parameter settings of the equalizer are typically dithered around the current operating point and the gradient of the error signal is used to find the way of the steepest descent [2]. The number of parameter settings widely varies from three degrees of freedom (polarization controller + DGD) in [11, 15] to 246 voltages in [8] depending on the complexity of the equalizing element. Since the feed-back signal often is a scalar value (such as the RF power after an electrical bandpass filter, the degree of polarization or eye opening) it is not trivial to find the optimum equalizer settings if the number of control parameters is high. Furthermore, the number of control

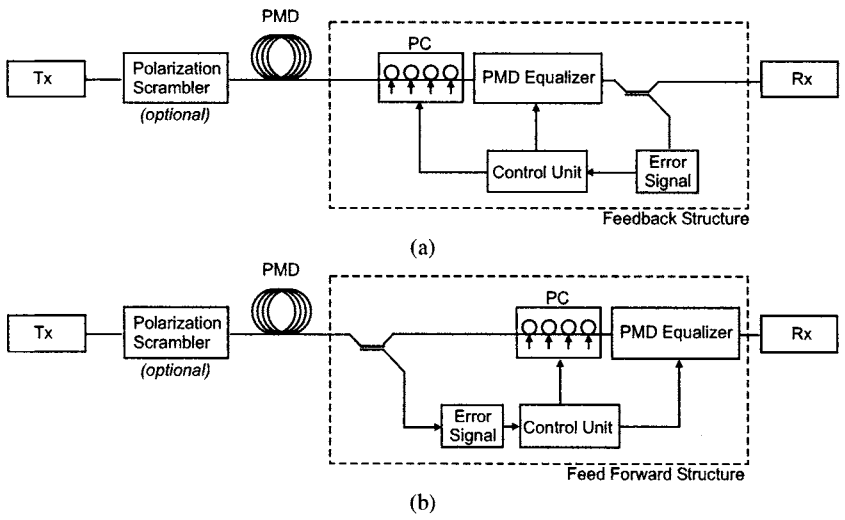

Fig. 1. (a) Feed-back structure (b) Feed-forward structure.

steps that are needed to find the optimum settings strongly influences the compensator speed since the equalizer response time is usually limited. Recent developments have shown that feed-forward approaches can avoid some of the aforementioned problems [19, 15]. In a feed-forward structure, error signals are derived before the signal passes the equalizer and the equalizer settings are directly set by the control algorithm without the need for dithering. This improves speed and can prevent the compensator from being trapped in local optima.

1.2. PMD Equalizers

The equalizing elements of optical PMD compensators typically introduce a tunable amount of birefringence into the system. The preferred way of counteracting the accumulated PMD is to compensate for the time delays at the output of the fiber (i.e., in front of the receiver). Often a cascade of polarization controllers and birefringent elements [11] is used to provide tunable birefringence. An elegant way to combine birefringent elements, polarization controllers and speed advantages has been presented in [8] by using the intrinsic birefringence and the electro-optical properties of a $LiNbO_3$ waveguide chip. Low-speed, but potentially low-cost, devices using silica-on-silicon technology have been presented in [20]. A hybrid approach using electro-optical polarization controllers and tunable Faraday rotators in combination with birefringent crystals is given in [21]. The combination of so-called fiber squeezers as polarization controllers and polarization maintaining fiber as birefringent elements can be advantageous in terms of insertion loss and also in terms of speed. However, reliability of this piezo-based technology has to be carefully considered. Although the optical performance is limited, a tendency to simple one- or two-stage equalizers can be observed which is the current tradeoff between cost and complexity.

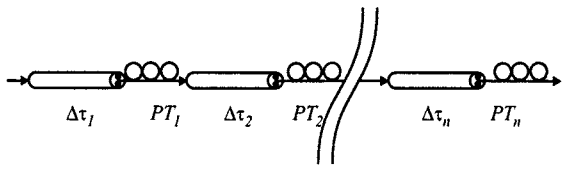

Fig. 2. Waveplate model: A real fiber can be modeled as cascade of birefringent elements ($\Delta\tau_i$) connected by polarization transformers (PT_i).

1.3. PMD Detection

The early approaches of PMD compensation utilized the fact that PMD-induced distortion causes changes in the RF spectrum of the detected signal [2, 8]. This indirect way of measuring PMD-induced distortion is still an attractive solution since the photodiode of the receiver can be used and the detection only requires simple electrical bandpass filters. However, the dependence on the modulation format as well as the need to introduce an additional high-speed receiver for building a stand-alone PMDC is considered to be a disadvantage. Electrical eye-monitors have been presented for example in [12] that assess a readout directly related to the bit error rate. Alternatively, PMD can be detected indirectly by monitoring optical properties of the received signal such as wavelength dependent SOP (State of Polarizaton) and DOP (Degree of Polarizaton). Since only low-speed electronics is used in these concepts, they are suitable for OTDM systems with bit rates as high as 160 Gbit/s where direct detection is expensive or even impossible [15, 21]. However, the relationship between the readout (e.g., the DOP) and the resulting bit error rate differs for different pulse shapes and modulation formats. For a given noise level, this relationship determines whether a readout is sensitive enough to detect small BER (bit error rate) changes or not. Some recent concepts involve polarization scrambling at the beginning of the fiber and therefore enable better detection schemes as well as feed-forward structures. It is obvious that in this case, the link PDL (polarization dependent loss) has to be kept at a minimum since otherwise the OSNR (optical signal-to-noise ratio) or the power levels are fluctuating with the scrambling rate. However, the fact that polarization scrambling is frequently used in long-haul submarine systems confirms the practicability of the solution.

2. Modeling the PMD of Optical Fibers: The Waveplate Model

The next sections describe some selected aspects of PMD-induced signal impairments. The widely used waveplate model for distributed PMD is briefly introduced and the PMD tolerance of current telecommunication systems is discussed.

2.1. First- and Second-Order PMD

A waveplate, i.e., a linearly birefringent medium, is the simplest example of a device exhibiting polarization dependent group delays. It is characterized by two fixed main axes, say x and y, along which and only along which SOPs are maintained for any wavelength. The respective propagation constants β_x and β_y differ from each other

and x- and y-polarized pulses have different group delays[3] $\tau_x = L \cdot d\beta_x/d\omega$ and $\tau_y = L \cdot d\beta_y/d\omega$. The difference $\Delta\tau = \tau_x - \tau_y$ is referred to as differential group delay. A general birefringent medium like a fiber will behave similarly in any given narrow wavelength range: there are two particular—in general elliptical—input SOPs yielding output SOPs which to first order do not depend on wavelength. These states are called principal states of polarization (PSP). The associated group delays differ by an amount called again differential group delay DGD. In a waveplate the PSPs and the DGD are independent of wavelength. If that holds for a fiber it is said to show first-order PMD only. In general, in a fiber both the PSPs and the DGD change with wavelength, in other words they exhibit higher-order PMD. With first-order PMD any arbitrarily polarized input signal will decompose into two components traveling at different group velocities. The ratio of the power in one principal state and the total power is referred to as power splitting ratio. The consequences of second-order PMD can be summarized as follows: with a wavelength dependence of the DGD the two PSP-components will see different chromatic dispersions while a wavelength dependence of the PSPs will yield a depolarization at the output even in the case of PSP pulse launching. As mentioned earlier, the so-called waveplate model is a widely accepted tool for modelling PMD of single mode fibers. In that model the whole fiber is considered to be a concatenation of short linearly birefringent sections, i.e., waveplates, with random orientation of their main axes. A fixed configuration of the numerous waveplates, referred to as one implementation of the fiber, is a transmission medium with first and higher-order PMD. In particular, its DGD value will depend on wavelength. Another implementation may be regarded as representing the fiber at another time so that different properties of different implementations will reflect the statistical behavior with time to be anticipated. The mean value of the DGD, i.e., the average over wavelength and time, is called PMD value of a fiber. Owing to the random orientation of the fiber sections in the waveplate model the PMD value does not increase linearly with fiber length but only scales with the square root of the fiber length. This consequence from the model is in good agreement with experimental results. A given fiber therefore is characterized by its PMD coefficient in $\mathrm{ps}/\sqrt{\mathrm{km}}$.

2.2. *Numerical Simulations*

The numerical model of PDL-free randomly coupled birefringent elements (Fig. 2) is given by its unitary Jones matrix:

$$\underline{\mathbf{J}}(\omega) = \prod_{i=1..n} \begin{bmatrix} \underline{u}_{1i} & \underline{u}_{2i} \\ -\underline{u}_{2i}^* & \underline{u}_{1i}^* \end{bmatrix} \cdot \begin{bmatrix} e^{+j\frac{1}{2}\Delta\tau_i\omega} & 0 \\ 0 & e^{-j\frac{1}{2}\Delta\tau_i\omega} \end{bmatrix} \qquad |\underline{u}_{1i}| + |\underline{u}_{2i}| = 1. \tag{1}$$

The randomly chosen parameters $\underline{u}_{1i}, \underline{u}_{2i}$ correspond to a polarization transformer, $\Delta\tau_i$ describes the DGD of a single birefringent element. Typically, $\underline{u}_{1i}$ and $\underline{u}_{2i}$ are uniformly distributed whereas $\Delta\tau_i$ is normally distributed. With all of these parameters being a random process the number of elements needed for reproducing realistic statistical properties is well below 100. Figure 3 shows results of a Monte-Carlo simulation with 100000 simulated implementations according to the introduced waveplate

[3] ω denotes the optical angular frequency $2\pi\nu$

model. The expectation value of a single element's DGD can be calculated from the desired PMD $\overline{\Delta\tau}$ (i.e., mean DGD):

$$\overline{\Delta\tau_i} = \frac{\overline{\Delta\tau}}{\sqrt{n}}. \tag{2}$$

The instantaneous DGD of a particular sample at a certain optical frequency ω is Maxwellian distributed which is fully determined by the mean DGD $\overline{\Delta\tau}$:

$$\mathrm{pdf}_{\Delta\tau}(\Delta\tau) = \sqrt{\frac{2}{\pi}}\frac{\Delta\tau^2}{\alpha^3}\exp\left(-\frac{\Delta\tau^2}{2\alpha^2}\right) \qquad \alpha = \overline{\Delta\tau}\sqrt{\frac{\pi}{8}}. \tag{3}$$

Owing to the statistical orientation of the birefringent elements the expectation value of the DGD grows with the square root of fiber length. Older fibers may have a PMD coefficient up to 2 ps/$\sqrt{\mathrm{km}}$ while modern fibers can have a PMD coefficient as low as 0.01 ps/$\sqrt{\mathrm{km}}$.

As explained before, PMD can be described by wavelength-dependent DGD and PSP. Both parameters are often expressed by the PMD vector $\boldsymbol{\Omega}$ that points into the direction of the fast PSP $\boldsymbol{s}_+$ (in Stokes space) and whose length is given by the DGD $\Delta\tau$:

$$\boldsymbol{\Omega}(\omega) = \Delta\tau \cdot \boldsymbol{s}_+. \tag{4}$$

Second-order PMD is usually described by the frequency dependence of $\boldsymbol{\Omega}$, i.e., the derivative of the PMD vector $\boldsymbol{\Omega}$ with respect to ω. This derivative comprises two components [10]:

$$\boldsymbol{\Omega}'(\omega) = \underbrace{\Delta\tau'\boldsymbol{s}_+}_{PCD} + \underbrace{\Delta\tau\,\boldsymbol{s}'_+}_{\text{depolarization}}. \tag{5}$$

The first component is parallel to the PMD vector and thus changes its length. It is associated with a polarization dependent chromatic dispersion (PCD). The second component is orthogonal to $\boldsymbol{\Omega}$ and thus changes its direction. If the direction of the PSPs changes with frequency, a modulated (broadband) signal cannot match the PSPs for all frequency components. In that case, a DOP reduction will occur for all possible signal polarizations. Therefore, this term is often referred to as depolarization component [1, 10]. The absolute value is distributed according to the following probability density function:

$$\mathrm{pdf}_{\Omega'}\left(\left|\boldsymbol{\Omega}'\right|\right) = \frac{2}{\pi}\frac{|\boldsymbol{\Omega}'|}{\sigma}\frac{\tanh\left(|\boldsymbol{\Omega}'|/\sigma\right)}{\cosh\left(|\boldsymbol{\Omega}'|/\sigma\right)} \qquad \sigma = \frac{1}{4}\overline{\Delta\tau}^2. \tag{6}$$

The distribution is also fully determined by the mean DGD value of the fiber [10]. Figure 3(b) shows the good agreement of simulation and theory.

The aforementioned statistical properties of a fiber are only valid for randomly mode-coupled fibers. If this assumption is not given (e.g., for polarization maintaining fibers, PMF) the observed DGD values may differ from the predicted values. Also the DGD of components (such as EDFAs) distributed along a fiber link may disturb the predicted properties. If the DGD of one ore more components dominate the PMD of the fiber, the DGD distribution may be shifted to higher values.

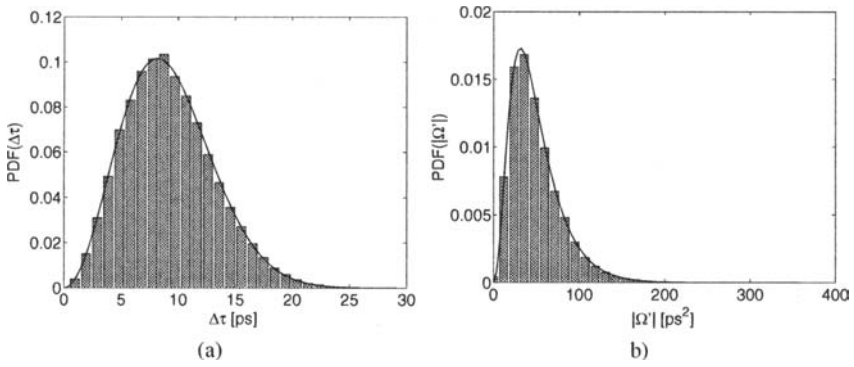

Fig. 3. Simulation results of a set of 100000 implementations ($\overline{\Delta\tau} = 10$ ps). Each fiber comprises 120 elements. (a) The distribution of the instantaneous DGD meets the Maxwellian distribution very well. (b) The absolute value of the derivative of the PMD vector $|\boldsymbol{\Omega}'|$ also meets the analytical prediction.

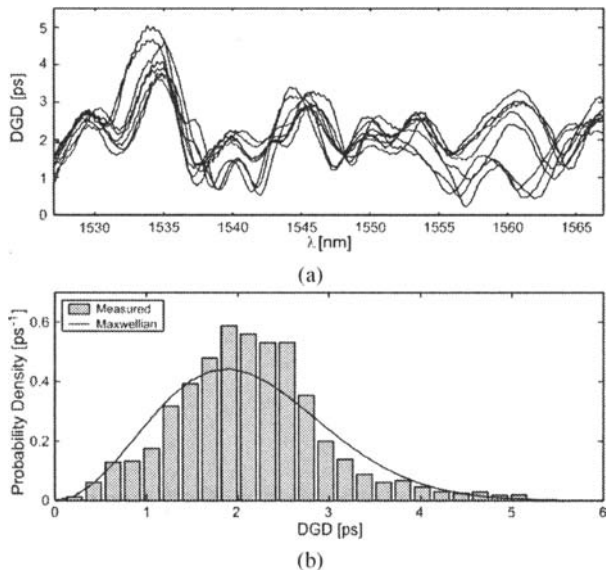

Fig. 4. DGD statistics of an installed fiber, measured over several days. (a) DGD spectra at different points in time. (b) Probability density function of measured DGD values including Maxwellian fit.

3. PMD-Induced Impairments

PMD-induced impairments are a consequence of the (polarization dependent) multiple path propagation inside the optical fiber. Thus the distortions tend to have the nature of inter-symbol interferences that, as opposed to OSNR reduction, can be compensated by applying an inverse system to recover the original signal. In an optical transmission system PMD-induced distortions can cause spontaneous changes of the bit error rate

(BER). This BER-fading is typically caused by the infrequent events in the tail of the Maxwellian distribution where the instantaneous DGD is high. The rareness of these events makes it sometimes hard to determine if the fading events are caused by PMD or other failures. It is important to understand that the actual vulnerability of a transmission system to PMD strongly depends on the transmitter and receiver structure. The following section shows that there can be huge differences between direct-detection NRZ/RZ systems and OTDM systems that demultiplex the received signal by means of a high-speed optical switch.

3.1. Eye Opening Penalty for First-order PMD

In this section, the tolerance of an optical communication system against first-order PMD, i.e., DGD, is analyzed using the (vertical) eye-opening penalty (EOP). All simulations are performed with the worst input polarization, i.e., both PSPs are equally excited. This case is often expressed by the power splitting ratio γ:

$$\gamma \stackrel{def}{=} \frac{\text{power in the fast PSP}}{\text{total power}}. \tag{7}$$

Thus the worst input polarization corresponds to $\gamma = 0.5$.

Calculating the vertical eye-openings in case of NRZ modulation is straight forward. We define the EOP as vertical eye-closure in dB compared to the undistorted eye-opening. Figure 5 shows simulated eye diagrams for distortions caused by first-order PMD ($\gamma = 0.5$). In this example, rising and falling edge of the signal occupy 40% of the bit slot. Consequently, first BER penalties occur for DGD values beyond 60% of the bit period if the decision time is at a discrete position in the middle of the bit slot. Typically, the DGD tolerance of an NRZ system will be lower since receiver properties such as low-pass characteristic and timing jitter have been neglected, here.

It is extremely important to consider the optical *and* electrical properties of the receiver to quantify the over-all PMD tolerance of a transmission system. This becomes clear in case of RZ modulation. Particularly the low-pass characteristic of the receiver dramatically influences the PMD tolerance of an RZ receiver. Figures 6(a)–(c) show simulated eye diagrams for an RZ signal distorted by first-order PMD ($\gamma = 0.5$). The RZ pulses have a Gaussian shape with a FWHM pulse width of $0.3 \cdot T_{\text{bit}}$. The receiver is assumed to have an unlimited bandwidth (i.e., no low-pass function). It is clearly visible that the signal splits up into two components separated by the DGD. Interestingly, the decision time can be set either onto the first pulse or onto the second pulse since there are now two eye-openings inside one bit slot.

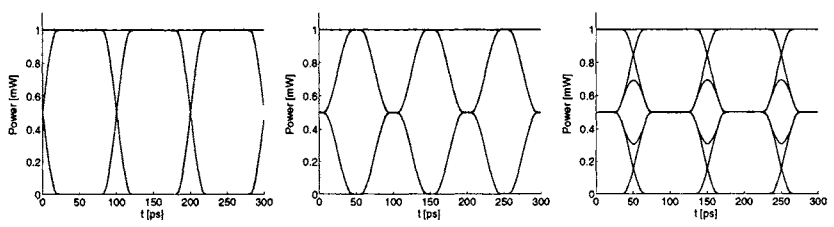

Fig. 5. NRZ eye-openings at 10 Gbit/s.

Although both eyes are completely opened, there is a penalty caused by the reduced power levels. Unlike expected for PMD, this penalty is not caused by inter-symbol interference (ISI), it is caused by the reduced OSNR. In other words, the pulse energy is spread over the bit slot and the detector sees a reduced peak power.

This behavior makes the receiver very sensitive to PMD since even for small DGD values a significant EOP occurs (Fig. 6b). A straight-forward approach could be to compensate the distortion simply by reamplifying the signal or allocating some power margin for the PMD-induced distortion and to select one of the peaks by the appropriate decision time. However, this does not solve the problems occurring when the power splitting factor γ changes. In that case, all power can move from one peak to the other which makes it necessary to switch the decision time from one peak to the other. During this switching process the signal will be lost.

An example for such a system without low-pass behavior at the receiver is given in [5, 14] where a fast non-linear optical switch is used to demultiplex the received OTDM signal. Without further measures this system has a much lower PMD tolerance than expected for direct-detection RZ systems. For $\gamma = 0.5$, Fig. 7(a) shows simulated EOP values as a function of DGD $\Delta\tau_n$ (normalized to the bit duration). If the DGD is increased, the eye closes until the two pulses are fully separated. The EOP stays at 3 dB until the pulse energy of the adjacent pulse leaks into the observed bit slot that then produces ISI. The fast optical sampling scheme behaves like a non-bandwidth-limited receiver. In combination with the short pulse width the system shows reduced performance even for low PMD values.

As opposed to the latter system, direct-detection receivers are operated at their bandwidth limit and the photodiode acts like an electrical low-pass filter. This behavior reduces the aforementioned effect because, to some extent, the detector accumulates

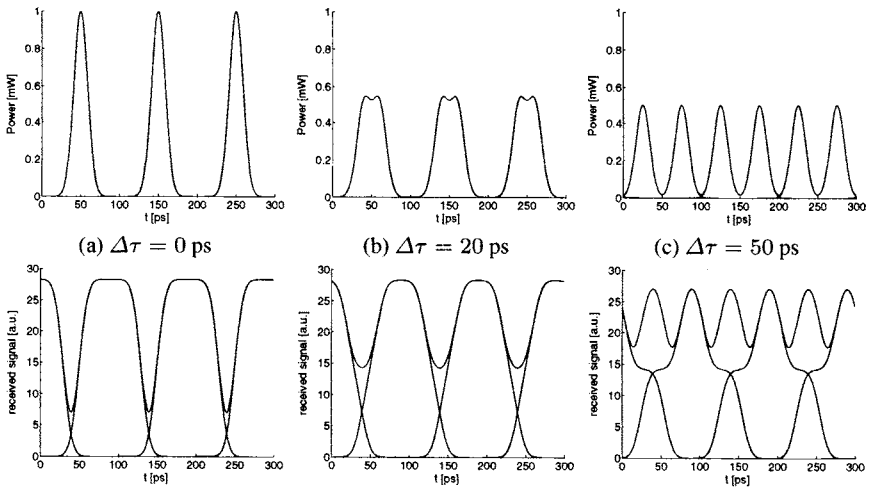

(a) $\Delta\tau = 0$ ps (b) $\Delta\tau = 20$ ps (c) $\Delta\tau = 50$ ps

(d) $\Delta\tau = 0$ ps, LP filtered (e) $\Delta\tau = 20$ ps, LP filtered (f) $\Delta\tau = 50$ ps, LP filtered

Fig. 6. RZ eye-openings at 10 Gbit/s for different DGD values ($\gamma = 0.5$). The bottom row shows that a low-pass filter can concentrate the signal power in the center of a bit slot and reopens the eye of the eye diagram.

the power inside a bit slot and the two separated pulses are recombined in the electrical signal.

We thus model the receiver by an ideal, not bandwidth limited photodiode with a subsequent low-pass filter. The decision is performed after the low-pass filter that has a rectangular impulse response with a length of $0.8T_{bit}$. It thus integrates over 80% of the bit slot. Figures 6(d)–(e) show the eye diagrams after the low-pass filter for the RZ case.

In case of NRZ modulation, the low-pass characteristic of the receiver can produce ISI. This is mainly because signal power is not as concentrated in the middle of the bit slot as it is in the RZ case. Thus pulse power is leaking earlier into the adjacent bit slot if the receiver is limited in bandwidth. Figure 7 depicts simulated EOP values for first order PMD distortion ($\gamma = 0.5$).

In this model, the maximum tolerable DGD corresponding to a maximum tolerable EOP of 1 dB is approximately 60% of the bit period for the RZ case. For NRZ modulation, the tolerance is approximately 48% of the bit slot. In real systems, effects like clock regeneration and timing jitter can further reduce the DGD tolerance. Also, the pulse shape of the signals has great impact on the DGD tolerance.

Commercial systems are often specified to have a DGD tolerance of approximately 30% to 35% of the bit period. Together with the Maxwellian probability density function of the DGD and the requirement to have 99.999% availability, this leads to a handy rule of thumb: *The fiber PMD (without PMDC) should be below one third of the system's DGD tolerance.* In case of a 10 Gbit/s system this corresponds to approximately 10 ps. A 160 Gbit/s system would tolerate a maximum fiber PMD of 0.63 ps that strongly limits the number of usable fiber links. Note that this rule only applies to Maxwellian distributed fibers. It does not apply anymore if the DGD distribution is manipulated, e.g., by a high-PMD span or even by a PMDC.

It should be noted that in this simple approach the advantages of RZ transmission reported in the literature [17, 18, 3] cannot be fully reproduced since non-linear effects like soliton self-trapping are not included in the model.

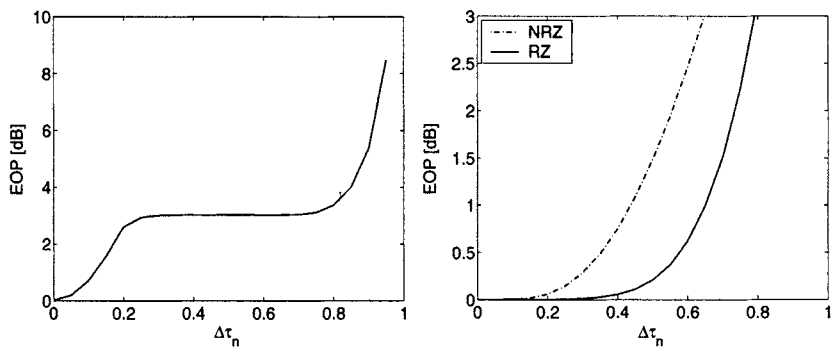

Fig. 7. (a) EOP for an RZ signal at different DGD values (normalized to the bit duration). The receiver has an unlimited bandwidth. The first EOP increase is caused by the pulse energy being spread over the bit slot. The second EOP increase is caused by ISI. (b) Tolerance of simulated NRZ and RZ signals to first-order PMD including low-pass behavior of the receiver.

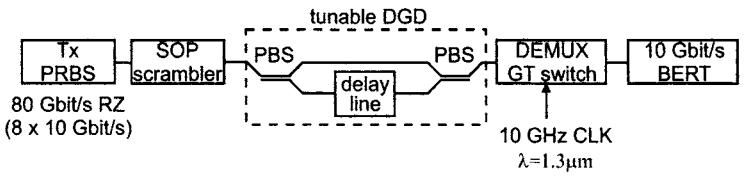

Fig. 8. Experimental setup for determining PMD tolerance of an 80 Gbit/s OTDM system.

3.2. PMD Tolerance of an 80 Gbit/s RZ OTDM System

In the following, we discuss the experimentally measured PMD tolerance of an 80 Gbit/s RZ system. The system used for these experiments is shown in Fig. 8 and uses the OTDM technology developed at the Fraunhofer Institut für Nachrichtentechnik, Heinrich-Hertz-Institut. The OTDM multiplexer was operated at a bit rate of 80 Gbit/s. We measured the RZ pulse width to be approximately 1.2 ps by means of an autocorrelator. The receiver comprises a gain transparent optical switch (GT switch) as OTDM demultiplexer [16] and a 10 Gbit/s bit error rate tester. To provide polarization independence, the demultiplexer was operated in a polarization diversity scheme. The input polarization was scrambled so that the measured BER averages over all possible input polarization states. Figures 9(a) and (b) show the results of BER measurements performed at different power levels and DGD settings. The BER measurements shown in Fig. 9(a) show that the system performance decreases severely for DGD values beyond 2 ps (i.e., 16% of the bit duration). This indicates that this system is not optimum with respect to PMD tolerance since we would expect a tolerance in the order of 60% of the bit duration.

As explained in the last section, the poor PMD tolerance is caused by the short pulses (10% of the bit duration) in combination with the ultra-fast optical demultiplexer. The receiver comprising the optical GT switch and the detector acts similar to a direct-detection receiver with extremely high bandwidth. Owing to the missing low-pass behavior the short RZ pulses split-up into two parts separated in time by the amount of the DGD. Polarization scrambling at the input causes the power to fluctuate between the two pulses and the eye diagram will be closed even for low DGD values.

Without scrambling, we found two decision times with a receiver power penalty of 3 dB that corresponds to an EOP of 3 dB ($\Delta\tau_n$=0.5, $\gamma = 0.5$) indicating that the performance degradation for $\Delta\tau_n < 0.5$ is not caused by ISI.

4. Error Signals for PMD Compensation

A crucial question when implementing an optical PMD compensator relates to the error signal that is used to properly adjust the equalizing elements. This error signal does not necessarily have to derive the link's PMD value quantitatively. When used in a feed-back scheme, it is enough if the error signal correlates to the current distortion level of the signal. The compensation algorithm will iteratively try to optimize the error signal by changing the equalizer settings. The following aspects play a role when selecting an error signal:

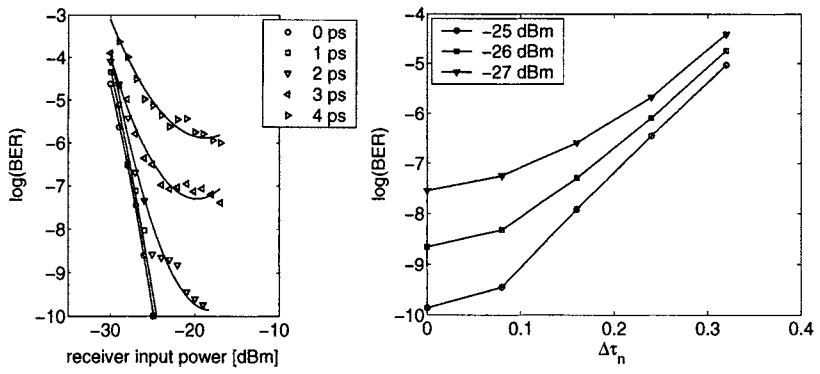

Fig. 9. PMD-tolerance of an 80 Gbit/s OTDM system (scrambled input polarization) (a) Measured BER performance for different DGD settings. (b) Measured and simulated BER as a function of DGD for different power levels.

- *Correlation to Signal Distortion*
  Most error signals do not directly reflect the BER of the signal since they are just derived from physical properties of the optical or electrical signal. A suitable error signal should reflect the actual distortion of the received signal even for low distortion levels.
- *Local Optima*
  An iterative minimum-search algorithm can be trapped in local optima. It is therefore desirable to use an error signal with only a single optimum that coincides with the optimum BER.
- *Response Time*
  A PMD compensator operated in a feed-back loop needs several control steps to find the optimum setting. To achieve an over-all response time of milliseconds, the error signal should be derived within sub-milliseconds.
- *Maximum Speed of Electronics*
  Since OTDM bit rates can be much higher than the maximum available speed of electronics, some error signals (such as RF tone detection) may not be suited. Error signals measuring optical properties can overcome this limitation since only low-speed electronics is needed.
- *Manipulation of Input Polarization State*
  Some error signals can only be derived if the input polarization is manipulated. This is typically implemented by means of a polarization scrambler at the input of a fiber link. Although reducing the tolerable PDL level, the ability of measuring the orientation of the link's PSP and the link's DGD make scrambling-based solutions attractive and enable feed-forward schemes.

The next paragraphs describe different error signals that can be derived by means of a Stokes polarimeter.

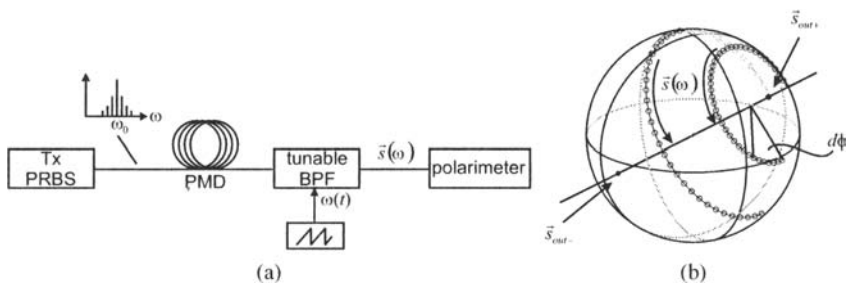

Fig. 10. (a) Utilizing the broad spectrum of a modulated signal as stimulus for PMD analysis of a fiber. (b) Trajectories of the output SOP for two different power splitting ratios γ.

4.1. Spectrally Resolved SOP Measurement

An established method for measuring the PMD of a fiber is the so-called *Poincaré arc Method.* Usually a swept laser source is used at the input of the fiber sweeping the operating wavelength while a polarimeter observes the output SOP trajectory. One way to adapt this method to a fiber that is in service is to filter the received signal by a scanning optical bandpass filter (see Fig. 10). In this way the modulated broadband signal is used as stimulus and the SOP of the filtered signal can be used to derive an SOP trajectory that can be evaluated similarly to the SOP trajectory of the Poincaré arc Method.

For a given input polarization the output SOP changes according to

$$\frac{d\boldsymbol{s}}{d\omega} = \boldsymbol{\Omega} \times \boldsymbol{s} = (\Delta\tau \cdot \boldsymbol{s}_{\,\mathrm{out}+}) \times \boldsymbol{s} \qquad \left|\frac{d\boldsymbol{s}}{d\omega}\right| = 2\sqrt{\gamma(1-\gamma)}\Delta\tau. \tag{8}$$

The input polarization is expressed by means of the power splitting ratio γ. The output SOP rotates around an axis determined by the output PSPs. Thus the trajectory is a part of a circle the diameter of which depends on the power splitting ratio. The angular rotation rate of the SOP depends on the fiber DGD:

$$\frac{d\phi}{d\omega} = \Delta\tau. \tag{9}$$

During a measurement cycle the bandpass filter is swept across the signal spectrum and the corresponding SOP trajectory is recorded. Let $\boldsymbol{s}_i$ be the recorded SOPs. For low enough second-order PMD, the PSPs can be found using three SOPs of the measured trajectory with maximum distance:

$$\Delta\boldsymbol{s}_1 \stackrel{def}{=} \boldsymbol{s}_q - \boldsymbol{s}_p \qquad \Delta\boldsymbol{s}_2 \stackrel{def}{=} \boldsymbol{s}_r - \boldsymbol{s}_q \qquad p < q < r, \tag{10}$$

$$\boldsymbol{s}_{\,\mathrm{out}+} = \frac{\Delta\boldsymbol{s}_1 \times \Delta\boldsymbol{s}_2}{|\Delta\boldsymbol{s}_1 \times \Delta\boldsymbol{s}_2|}. \tag{11}$$

The power splitting ratio can be calculated using the following relationship:

$$\gamma = \frac{1}{2} + \frac{1}{2}\boldsymbol{s}_i \cdot \boldsymbol{s}_{\,\mathrm{out}+}. \tag{12}$$

Now that γ and $\left|\frac{d\boldsymbol{s}}{d\omega}\right|$ are known, the DGD can be calculated using Eq. (8).

Measuring the DGD in this way only works if γ is not close to zero or one. This drawback can be accepted since these are the cases where the signal is traveling in one of the principal states and is not disturbed by the fiber PMD. In other words, the error signal only provides usable readouts if the signal is in fact disturbed by PMD. Simulations show that if γ is close to zero or one, measurement accuracy is reduced dramatically due to the limited accuracy of the polarimeter.

In the feed-back configuration, it is not necessary to measure the fiber DGD quantitatively. It is thus more convenient to derive an error signal that just correlates to the distortion level of the signal. This can be done, for example, by using the frequency-stability of the output SOP as error signal. A robust scalar value is the standard deviation of the measured SOPs from the mean SOP:

$$\sigma_{\mathrm{SOP}} \stackrel{def}{=} \left[\frac{1}{\omega_B}\int_{-\omega_B/2}^{\omega_B/2} |\boldsymbol{s}_{\mathrm{out}}(\omega) - \overline{\boldsymbol{s}_{\mathrm{out}}}|^2\, d\omega\right]^{1/2} \tag{13}$$

If the signal is not distorted by PMD, the SOP does not change with frequency and σ_{SOP} is zero. In all other cases σ_{SOP} will more or less differ from zero. This error signal is closely related to the Poincaré arc method that evaluates only the first and the last measured SOP of an acquired trajectory. In practice σ_{SOP} is more robust against noisy measurement data since the whole trajectory is used for calculating the standard deviation.

The main drawbacks turned out to be the low power level after the bandpass filter together with the limitation of measurement speed caused by the maximum scanning frequency of the filter. The correlation of the error signal to the BER was quite good and allowed completely automatic operation of the PMDC.

4.2. *DOP as Distortion Monitor*

As investigated in [4] the response time of a PMD compensator should be in the order of milliseconds. This requirement is difficult to achieve using the spectrally resolved SOP measurement since the scanning speed of tunable optical filters is usually also in the order of milliseconds (e.g. piezo-driven Fabry-Perot filters). With respect to acquisition time, the DOP of the received data signal is an attractive error signal that can be used for PMD compensation [7]. The DOP is an optical property that is influenced by PMD and that can be acquired within less than one microsecond. This is fast enough to provide millisecond response time for the total compensator system.

The DOP can be calculated from an SOP trajectory (over frequency) by taking the length of the average normalized SOP vector (weighted with the power spectral density). If the trajectory describes a large arc in Stokes space, the average SOP vector will be shorter than unity indicating a reduced DOP. Considering the SOP trajectories of the preceding section, the DOP will be reduced at high DGD levels *and* γ values differing from 0 and 1. The DOP will not be reduced if the DGD is zero *or* γ is 0 or 1.

Instead of considering the SOP spectrum, the temporal change of the SOP in presence of DGD can be visualized to understand the DOP reduction (see Fig. 11). The time delay between the two principal states causes the SOP of the signal to fluctuate at the speed of the bit rate. This behavior can be visualized by trajectories on the Poincaré sphere (over time). Typical polarimeters integrate over a time much longer than a bit

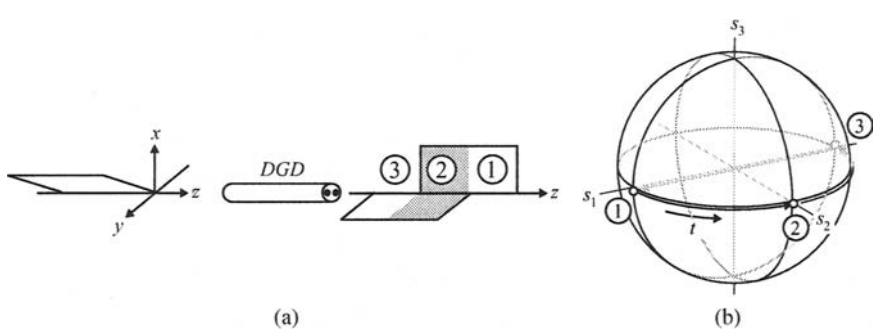

Fig. 11. An optical pulse distorted by PMD shows a time variant SOP. (a) shows an ideal rectangular pulse distorted by first-order PMD. The output SOP moves sequentially from linear vertical (1) to 45° linear (2) and finally to horizontal linear (3). State (2) was arbitrarily chosen to be 45°. It depends on the phase delay between the PSP and could be circular or elliptical as well. (b) shows the SOP trajectory on the Poincaré sphere. A polarimeter averages over many pulses and thus over many cycles of the trajectory shown in (b). The DGD determines how long each of the three SOPs is present. In this way the DGD influences the resulting DOP reduction.

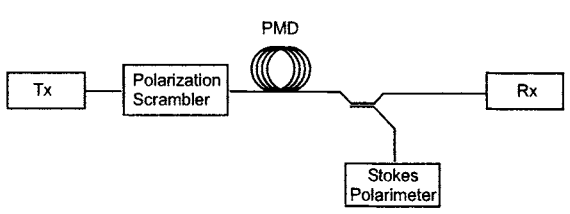

Fig. 12. DOP measurement in combination with polarization scrambling at the link input can be used to eliminate dependencies on input polarization. The instantaneous DGD of the fiber link can be measured at any time.

duration. Therefore, these polarimeters observe a mean SOP averaged over the whole trajectory (weighted by the instantaneous pulse power and the retention period of each SOP) that leads to a DOP smaller than unity. In [6, 7, 13] the DOP criterion has been successfully applied assuming that an increased DOP leads to a reduced BER.

Similar to the error signal described in the last section, the DOP also suffers from the fact that the link's DGD cannot be observed if γ is close to 0 or 1 (because there is no signal distortion at all). In that case, a compensator is "blind" for any PMD on the fiber link and should move into a neutral state waiting for γ to change. If γ changes, it may be necessary to quickly set the compensator DGD to the fiber DGD level. The next section describes how to overcome this limitation by using a polarization scrambler at the fiber input. This allows not only to determine the link DGD at any time but also to determine the orientation of the link's PSPs [15, 14].

4.3. DOP Measurement with Input Polarization Scrambling

As described in the last section, the DOP of a modulated signal is reduced in the presence of PMD. The amount of reduction depends on the amount of first and higher-order PMD, the spectral bandwidth of the signal and the input polarization. Particularly

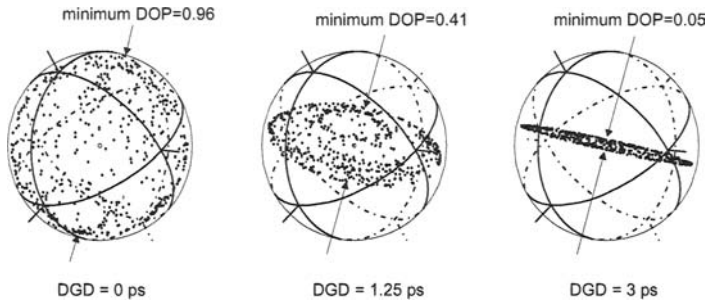

Fig. 13. Measured output SOPs with polarization scrambling at the link input (40 Gbit/s, RZ). The signal was distorted by means of a tunable DGD element. The short axis of the ellipsoid changes as a function of DGD while the length of the long axis is maintained.

the dependence on input polarization causes problems because a compensator based on simple DOP measurement is "blind" for the fiber PMD if the input SOP matches the fiber PSP. Polarization scrambling at the fiber input can overcome this limitation.

In [14] we used a pair of piezo-driven fiber squeezers causing the input polarization to cover the whole Poincaré sphere within 18 ms. At the fiber output a Stokes polarimeter monitors the variation of the SOP including the DOP (see Fig. 12). This polarimeter acquires 140 SOPs in 18 ms and displays the measured SOPs on the Poincaré sphere, where the DOP determines the length of a (normalized) Stokes vector. The measured SOPs form an ellipsoid whose shape reveals information about the system's PMD and PSP. In a first-order PMD-disturbed system the DOP is equal to unity for input polarizations matching the PSP. The more the input SOPs differ from the PSP, the more the DOP is reduced.

Thus the measured output SOPs form an ellipsoid, the long axis of which has unity length and points into the direction of the PSPs, as demonstrated by the experimental data depicted in Fig. 13. The length of the short axis (denoted *minimum DOP*) depends on the amount of fiber DGD. The relationship between minimum DOP and (first-order) DGD derived from our experiment is shown in Fig. 14 for different bit rates and modulation formats. These curves give an estimate on how sensitively a PMD compensator could track the PMD of the fiber link. It is obvious that the sensitivity depends strongly on the pulse shape. The sensitivity for the RZ signals used in our experiments is in the sub-picosecond range due to the short pulse width of 1.2 ps for 10, 40 and 160 Gbit/s. For the 10 Gbit/s NRZ system, the sensitivity is much lower due to the larger pulse width. This illustrates the beneficial fact that sensitivity of the error signal scales with decreasing pulse width.

The main advantage of this measurement approach is that the data shown in Fig. 14 can be used as calibration curve for deriving the fiber DGD from the measured minimum DOP at any time. This is particularly useful for feed-forward approaches, since the appropriate equalizer DGD can be set in a single step.

Figure 14 also shows that the noise (Amplified Spontaneous Emission, ASE) of fiber amplifiers causes a partial depolarization even if no PMD is present. A compensator using a maximum-search algorithm is not affected. However, ASE complicates a quantitative estimation of the system's PMD if the intensity of the ASE is unknown.

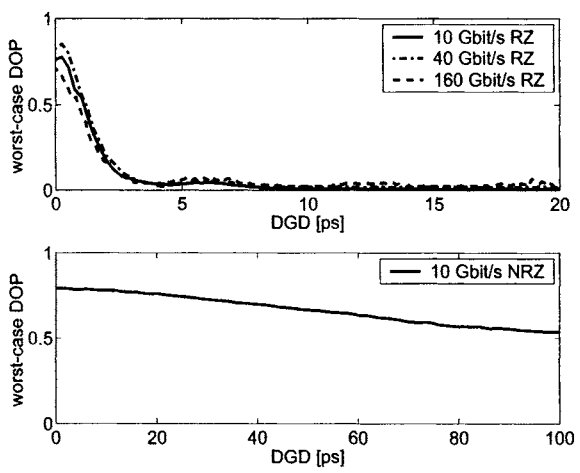

Fig. 14. Measured response function of the minimum DOP at different bit rates with polarization scrambling at the link input. The response function depends mainly on the signal's pulse shape. Since all RZ signals have been derived from the same base signal the shape of the RZ pulses and thus the response function is the same for all investigated bit rates. For NRZ signals the DOP criterion is significantly less sensitive.

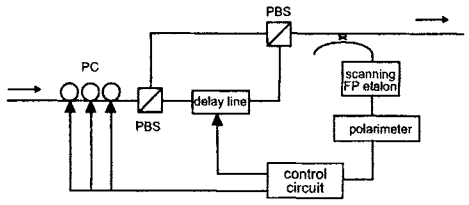

Fig. 15. PMDC with spectrally resolved SOP measurement as feed-back signal.

5. Compensation Experiments

The described concepts of deriving error signals and equalizing PMD can be combined in various ways to build a PMD-compensating system. The next sections summarize results of experiments conducted mainly using the OTDM system of the Fraunhofer Institut für Nachrichtentechnik, Heinrich-Hertz-Institut.

5.1. PMDC with Spectrally Resolved Error Signal

To evaluate the applicability of spectrally resolved SOP measurement (see section 4.1) for PMD compensation, we used the compensating setup shown in Fig. 15. The equalizing part consists of a motorized polarization controller and a motorized tunable DGD element that is able to generate a maximum DGD of 140 ps. A scanning Fabry-Perot filter and a fast Stokes-polarimeter is used for monitoring the change of the SOP with the optical frequency. The Fabry-Perot etalon allowed to sweep across the signal bandwidth within 20 ms with a spectral resolution of 1.25 GHz.

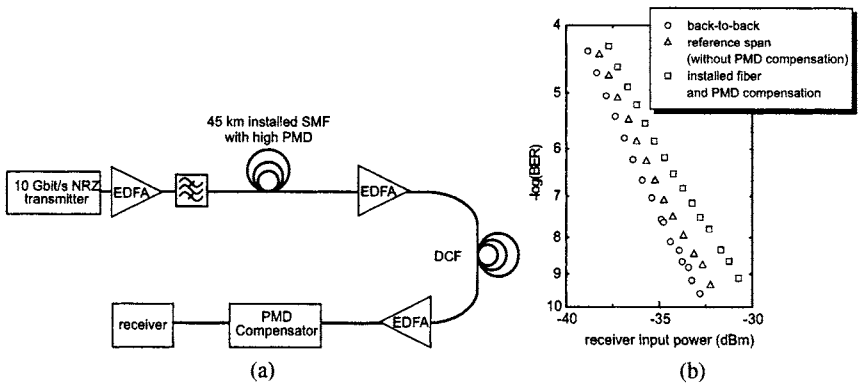

Fig. 16. (a) Experimental setup. (b) BER performance for the compensated case. In the uncompensated case, the signal distortions were too high to make a BER measurement.

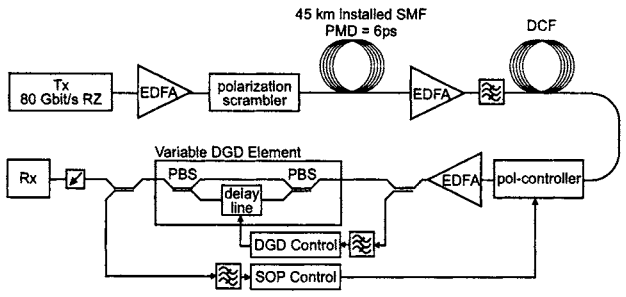

Fig. 17. Experimental setup for DOP-based PMD compensation with input polarization scrambling.

The adaptive compensation algorithm minimizes the standard deviation of the SOP with respect to the average SOP over the central bandwidth of the data signal. This turned out to be a very robust feed-back signal with good correlation to the bit error rate. Successful operation could be demonstrated at 10 Gbit/s NRZ modulation over an installed fiber [9] that showed an instantaneous DGD of 60 ps ($0.6 \cdot T_{\mathrm{bit}}$) at the operating wavelength.

Figure 16(b) shows the resulting BER performance after compensation. Because of the high instantaneous DGD level, it was not possible to take a BER measurement for the uncompensated case. After compensation, however, a residual penalty of 2 dB remained with respect to the back-to-back measurement.

5.2. PMDC with Input Polarization Scrambling

Previous investigations have shown that a response time in the millisecond range is desirable for PMD-compensation. If the parameters of the equalizing unit have to be dithered to find the optimum settings, this implies that the response time of the equalizing elements has to be shorter by an order of magnitude. We reduced this requirement for the differential group delay (DGD) element of the compensator by applying feed-forward control in an open loop.

In our experiment, the link DGD is continuously measured and fed forward to a variable DGD element in order to set the appropriate DGD of the compensator in a single step. Continuous DGD monitoring is realized by a polarization-resolved evaluation of the degree of polarization (DOP) combined with a polarization scrambler at the fiber input (see section 4.3). Using this PMD compensator, we achieved error-free transmission of an 80 Gbit/s RZ data signal over a PMD-compensated installed fiber link of 45 km length with an average DGD of 6 ps.

The scrambler causes the input polarization to cover the whole Poincaré-sphere within 18 ms, the minimum DOP occurring within that time interval belongs to a power-splitting ratio of 0.5 and allows to derive the link DGD from a lookup table. This lookup table has to be measured once for the transmission system [see Fig. 18(b)]. As we used short pulses in the experiment, the DOP was very sensitive to DGD variations and decreased to zero for a DGD larger than 2 ps. This would make DGD measurements beyond this value impossible. The DOP response function can be flattened by means of an optical bandpass filter in front of the polarimeter. We, therefore, used a filter with a bandwidth of 1.2 nm to extend the response curve and thus the measurement range to about 7 ps [see Fig. 18(b)].

Figure 17 shows the setup of the field experiment. We used an 80 Gbit/s OTDM transmission system operating at 1550 nm with 1.2 ps RZ pulses. The transmission link comprised 45 km standard single-mode fiber installed in the city of Berlin. At the output of the link, the dispersion was compensated by means of a slope compensating DCF module. The mean DGD of the fiber link was about 6 ps and the instantaneous values varied between 3 ps and 12 ps. The PMD-compensator comprised two controllers, one for the motor-driven variable DGD element and one for the polarization controller that was based on piezo-driven fiber squeezers. The variable DGD element was controlled by continuously measuring the minimum DOP at the input of the delay line. A lookup table was used to derive the link DGD. This value directly controls the DGD of the compensator in a feed-forward structure.

Although it would be desirable to also control the polarization controller in feed-forward mode, the second controller is operated in feed-back mode. The settings of the polarization controller were dithered to increase the minimum DOP measured within intervals of 18 ms. Operating the polarization controller in feed-forward mode would require deterministic behavior that was not given for that type of polarization controller. However, the PSPs can be determined by monitoring the SOP with the largest DOP within a time interval of 18 ms.

Figure 18a depicts the bit-error rate performance of the system (pattern length: $2^7 - 1$). At the operating wavelength the instantaneous DGD was about 3.7 ps. Without PMD-compensation, an error floor occurs at a BER of 10^{-6} and error-free transmission was not possible. With PMD-compensation, we obtained error free transmission with a penalty of less than 1 dB as compared to the back-to-back measurements.

5.3. PMDC with Scrambling/Descrambling Scheme and Magneto-Optically Tuned DGD Element

The experiments of the preceding sections all used a motorized tunable DGD element. If a tunable DGD element is required, fast tuning mechanisms will be needed to achieve the desired response time. In the following experiment, we investigated the performance and applicability of tunable Faraday rotators for building adjustable DGD

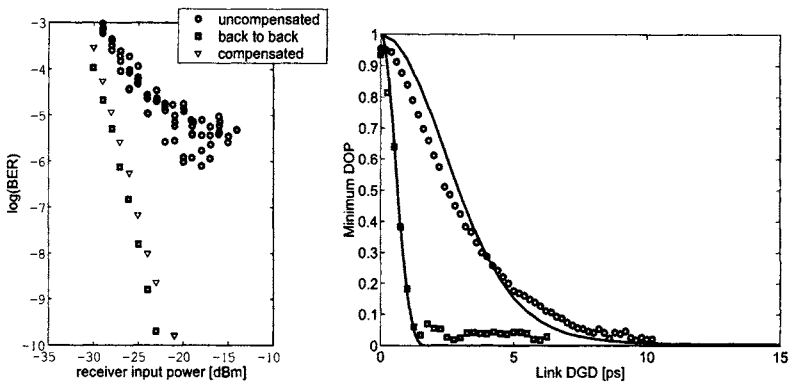

(a) (b)

Fig. 18. (a) BER performance for the compensated and the uncompensated case. (b) Minimum DOP as a function of link DGD. A bandpass filter can extend the response curve to about 7 ps. This response curve can be used to generate a lookup table for the PMDC to calculate the required compensator DGD from the measured DOP.

equalizers. We used birefringent crystals (YVO_4) of different thickness with Faraday rotators between them to manipulate the overall birefringence (see Fig. 19). Although the equalizer can be set to states where higher-order PMD is generated, we are using only the first-order states. Higher-order PMD is only generated during the switching process and is kept at a small level (see below).

The equalizer is designed to cover a DGD range from 0.31 ps to 4.70 ps in steps of 0.63 ps. The magneto-optical polarization rotators have a response time of less than 1 ms and are used to couple light from one main axis of a crystal to one of the main axes of the next crystal, requiring driving currents of less than 100 mA each, consuming less than 250 mW. The crystal thickness (and thus the DGD of the birefringent elements) varies in powers of two, allowing for a sufficiently small step size, that is important for minimizing second-order PMD as well as frequency independent changes of the principal states of polarization (PSPs) of the PMDC during switching. Neglecting small wavelength dependencies of the Faraday rotators, there will be no polarization-dependent chromatic dispersion and the depolarization rate can be kept low due to the small step size. The insertion loss of the equalizer is 5 dB and its polarization dependent loss (PDL) is less than 0.5 dB.

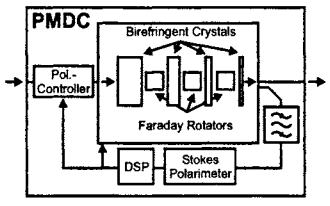

Fig. 19. First-order PMDC, based on birefringent crystals, magneto-optical polarization rotators, $LiNbO_3$-polarization controller and Stokes polarimeter

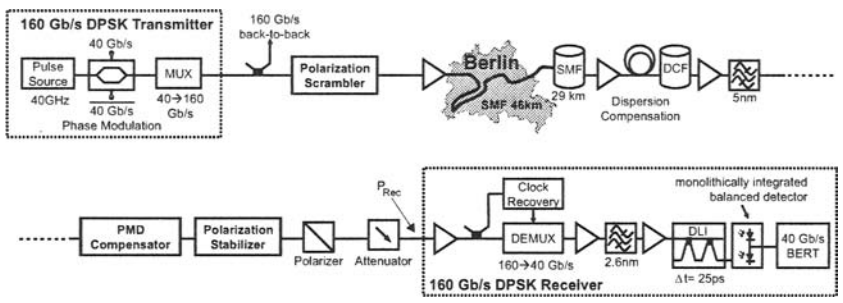

Fig. 20. Experimental setup for 160 Gbit/s transmission including polarization scrambler, PMD compensator and polarization stabilizer.

Using only the first-order states of the equalizer allows only two settings for each of the three Faraday rotators. The total number of states is thus $2^3 = 8$. It can be shown that the resulting DGD can be adjusted in equidistant steps if the birefringence of the crystals is chosen in powers of two. Special attention has to be paid to the switching process since intermediate states will occur with higher-order PMD. Therefore, it is only allowed to switch one rotator at a time. Thus it takes in fact 8 switching cycles to change the birefringence from the smallest to the highest value. Furthermore there is a preferred direction of propagation through the equalizer. It turns out that the PSPs at one port (i.e., the slow and the fast eigenstate) are stable during the switching process while the PSPs at the other port (the port with the short crystal) are rotating by 180° on the Poincaré. It is therefore preferable to use the port with the stable PSPs on the link side. In that case, the polarization controller does not have to follow the quick switching process to maintain compensation. However the output polarization is rotated during the switching process that has no effect when using a polarization insensitive receiver such as a PIN diode. In our experiment we used a polarization sensitive DPSK demodulator. Therefore, the polarization was stabilized, even during the switching process.

The complete experimental setup is shown in Fig. 20. A $LiNbO_3$ polarization controller was used at the input of the transmission link to scramble the polarization. This ensures that changes of the instantaneous DGD will be detected independently from the input polarization. The maximum-search control algorithm adjusts the polarization controller and the DGD of the equalizer to maximize the mean DOP. The maximum detectable DGD was increased by placing an optical bandpass filter with 2.6 nm bandwidth in front of the polarimeter. Since the delay line interferometer in the DPSK receiver is slightly polarization sensitive, a polarizer was placed in front of the receiver and the state of polarization at the PMDC output was kept constant using an automatic polarization stabilizer comprising an additional polarization controller and a polarimeter.

The 160 Gbit/s DPSK transmitter comprised a 40 GHz optical pulse source, including a semiconductor laser and a phase-stabilized multiplexer, a phase modulator driven by a pattern generator, and a fiber delay line multiplexer providing a single polarization 160 Gbit/s PRBS signal (word length $2^7 - 1$ bit). The polarization-scrambled signal (pulse width 1.4 ps, transform-limited sech^2 pulses) was transmitted over a 75 km fiber span including 46 km of buried fiber in the network of the Deutsche Telekom.

The PMD of the fiber link, including the dispersion compensating fiber (DCF) modules and three erbium-doped fiber amplifiers (EDFA), was measured at several days, showing a mean DGD of 2.1 ps. The wavelength of the laser was set to 1547 nm, where the instantaneous DGD was approximately 2.2 ps, with a steep slope over the spectral range of the signal. All measurements were also confirmed at 1550 nm. The overall span attenuation was increased to almost 23 dB due to connectors, splices etc. The power at the span input was about 9 dBm and the input power to the DCF was 0 dBm. The demultiplexer comprised an optical gate, based on an electro-absorption modulator (EAM) and an EAM-based clock recovery with a prescaled PLL feed-back. After optical preamplification and optical filtering with 2.6 nm bandwidth, a balanced detection scheme with a delay line interferometer (DLI) and a balanced detector was used before the bit error ratio tester (BERT).

Figure 21 shows the measured BER performance. To estimate the performance without PMD compensation the input polarization was adjusted manually according to the best (one fiber PSP excited) and worst case (both fiber PSPs excited equally). For the best-case input polarization (triangles), we obtained a penalty of about 0.6 dB, compared to back-to-back performance (circles). For the worst-case input polarization, the pulses are broadened due to the DGD. Crosstalk from the neighboring 160 GHz pulses, i.e., crosstalk from other channels, then causes a large penalty in the general case as well as a strong channel deviation due to coherent effects, prohibiting an error-free transmission (filled and open diamonds, representing best and worst channel). Activating the polarization scrambling and the adaptive PMDC (stars) results in a penalty improvement of at least 8 dB compared to the worst case situation, leaving a residual penalty of only 1.3 dB compared to the back-to-back-performance. We assume the remaining penalty to be caused by PDL, the scrambling/stabilizing scheme and second-order PMD effects. Now, an error-free transmission for all four 40 Gbit/s channels and thus the 160 Gbit/s signal is possible. The performance of the 40 Gbit/s channels (with respect to the received power for a BER of 10^{-9}) varies within less than 2 dB after the transmission, similar to the transmission with manually adjusted, best-case input polarization.

6. Conclusion

The preceding sections have given an introduction to the fundamentals of optical PMD compensation. It has been shown that different concepts of equalizing and detecting PMD are capable to mitigate PMD-induced distortions and to extend the reach of high-speed OTDM systems over installed fiber links. Particularly at bit rates of 160 Gbit/s and above, optical PMD compensation turns out to be an attractive way to overcome PMD-induced limitations since the speed of the electronics can be smaller by orders of magnitude than the operating bit rate.

It has also been shown that questions regarding the expected performance of a PMDC concept (e.g., in terms of maximum tolerable link PMD) are difficult to answer since the performance depends not only on the link properties but also on the transmitter/receiver properties, the modulation format and on the bit rate. Particularly the bit rate dependence reduces the benefit of a PMDC when migrating to higher bit rates: Doubling the bit rate will reduce the maximum tolerable link PMD by a factor of two

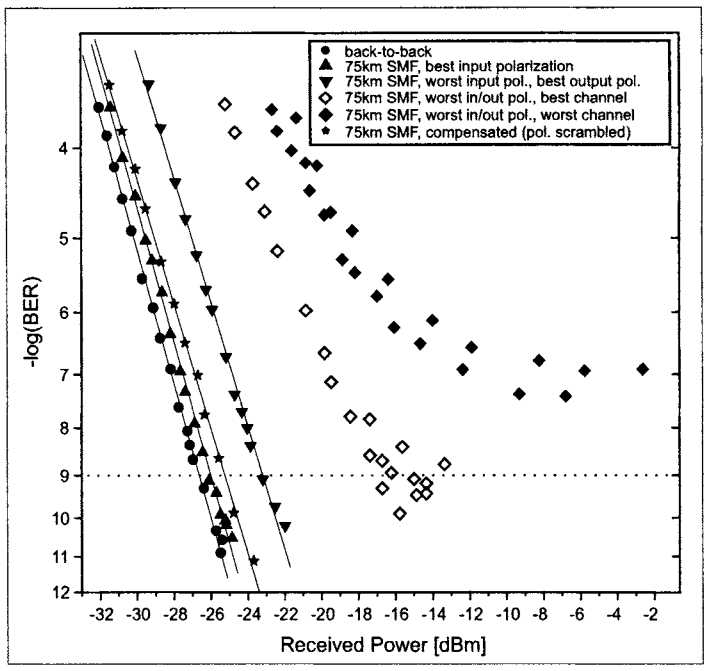

Fig. 21. BER performance of the 160 Gbit/s compensation experiment.

(for the same PMDC). Therefore, further investigations will have to show if higher-order optical equalizers with more degrees of freedom can remove the limits of simple first-order PMDCs without sacrificing speed and stability of the control algorithm.

References

1. F. Bruyére, "Impact of First- and Second-order PMD in Optical Digital Transmission Systems", *Opt. Fiber Technol.*, **2**, 269 (1996).
2. F. Heismann, D. A. Fishman, and D. L. Wilson, "Automatic Compensation of First-Order Polarization Mode Dispersion in a 10 Gb/s Transmission System", Proc. ECOC, Madrid, Spain, volume I, pp. 529–530, 1998.
3. H. Taga, M. Suzuki, and Y. Namihira, "Polarization Mode Dispersion Tolerance of 10 Gbit/s NRZ and RZ Optical Signals", *Electron. Lett.*, **34** (22), 2098–2100 (1998).
4. H. Bülow, W. Baumert, H. Schmuck, F. Mohr, T. Schulz, F. Küppers, and W. Weiershausen, "Measurement of the Maximum Speed of PMD Fluctuation in Installed Field Fiber", Proc. OFC, San Diego, CA, USA, paper WE4, pp. 83–85, 1999.
5. U. Feiste, R. Ludwig, S. Diez, C. Schmidt, H. J. Ehrke, H. G. Weber, and F. Küppers, "Unrepeatered 80 Gbit/s RZ single channel transmission over 160 km of standard fiber at 1.55 μm with a large wavelength tolerance", Proc. OFC, San Diego, CA, USA, paper FI1, 1999.
6. C. Francia, F. Bruyère, J.-P. Thiéry, and D. Penninckx, "Simple Dynamic Polarisation Mode Dispersion Compensator", *Electron. Lett.*, **35** (5), 414–415 (1999).

7. N. Kikuchi and S. Sasaki, "Polarization-Mode Dispersion (PMD) Detection Sensitivity of Degree of Polarization Method for PMD Compensation", Proc. ECOC, Nice, France, volume II, paper WeA1.3, pp. 8–9, 1999.
8. R. Noé, D. Sandel, S. Hinz, M. Yoshida-Dierolf, V. Mirvoda, G. Feise, H. Herrmann, R. Ricken, W. Sohler, F. Wehrmann, C. Glingener, A. Schöpflin, A. Färbert, and G. Fischer, "Integrated Optical LiNbO3 Distributed Polarisation Mode Dispersion Compensator in 20 Gbit/s Transmission System", *Electron. Lett.*, **35** (8), 652–954 (1999).
9. H. Rosenfeldt, R. Ulrich, U. Feiste, R. Ludwig, H. G. Weber, and A. Ehrhardt, "First Order PMD-Compensation in a 10 Gbit/s NRZ Field Experiment Using a Polarimetric Feedback-Signal", Proc. ECOC, Nice, France, volume II, paper WeC3.2, pp. 134–135, 1999.
10. G. J. Foschini, L. E. Nelson, R. M. Jopson, and H. Kogelnik, "Probability Densities of Second-Order Polarization Mode Dispersion Including Polarization Dependent Chromatic-Fiber Dispersion", *IEEE Photon. Techn. Lett.*, **12** (3), 293–295 (2000).
11. M. Karlsson, H. Sunnerud, and P. A. Andrekson, "A comparison of different PMD-compensation techniques", Proc. ECOC, Munich, Germany, volume II, paper 4.2.2, pp. 33–35, 2000.
12. F. Buchali, S. Lanne, J.-P. Thiéry, W. Baumert, and H. Bülow, "Fast Eye Monitor for 10 Gbit/s and its Application for Optical PMD Compensation", Proc. OFC, Anaheim, CA, USA, paper TuP5, 2001.
13. N. Kikuchi, "Analysis of Signal Degree of Polarization Degradation Used as Control Signal for Optical Polarization Mode Dispersion Compensation", *J. Lightwave Technol.*, **19** (4), 480–486 (2001).
14. H. Rosenfeldt, Ch. Knothe, R. Ulrich, E. Brinkmeyer, U. Feiste, C. Schubert, J. Berger, R. Ludwig, H. G. Weber, and A. Ehrhardt, "Automatic PMD Compensation at 40 Gbit/s and 80 Gbit/s Using a 3-Dimensional DOP Evaluation for Feedback", Proc. OFC, Anaheim, CA, USA, paper Postdeadline Paper PD27, 2001.
15. H. Rosenfeldt, R. Ulrich, E. Brinkmeyer, U. Feiste, C. Schubert, J. Berger, R. Ludwig, H. G. Weber, and A. Ehrhardt, "Feed-Forward Approach for Automatic PMD-Compensation at 80 Gbit/s over 45 km Installed Single Mode Fiber", Proc. ECOC, Amsterdam, The Netherlands, paper postdeadline paper PD.4.8, 2001.
16. C. Schubert, J. Berger, U. Feiste, R. Ludwig, C. Schmidt, and H. G. Weber, "160 Gb/s Polarization Insensitive All-Optical Demultiplexing using a Gain-Transparent Ultrafast-Nonlinear Interferometer (GT-UNI)", Proc. OAA, Stresa, Italy, paper OWA4, 2001.
17. H. Sunnerud, M. Karlsson, and P. A. Andrekson, "A Comparison Between NRZ and RZ Data Formats with Respect to PMD-induced System Degradation", Proc. OFC, Anaheim, CA, USA, paper WT3, 2001.
18. H. Sunnerud, M. Karlsson, and P. A. Andrekson, "A Comparison Between NRZ and RZ Data Formats with Respect to PMD-Induced System Degradation", *IEEE Photon. Techn. Lett.*, **13** (5), 448–450 (2001).
19. P. C. Chou, J. M. Fini, and H. A. Haus, "Demonstration of a feed-forward PMD compensation technique", *IEEE Photon. Techn. Lett.*, **14** (2), 161–163 (2002).
20. T. Saida, K. Takiguchi, S. Kuwahara, Y. Kisaka, Y. Miyamoto, Y. Hashizume, T. Shibata, and K. Okamoto, "Planar Lightwave Circuit Polarization Mode Dispersion Compensator", *IEEE Photon. Techn. Lett.*, **14** (4), 507–509 (2002).
21. S. Kieckbusch, S. Ferber, H. Rosenfeldt, R. Ludwig, C. Boerner, A. Ehrhardt, E. Brinkmeyer, and H. G. Weber, "Adaptive PMD compensator in 160Gb/s DPSK transmission over installed fiber", Proc. OFC, Los Angeles, CA, USA, paper PDP31, 2004.

DOI: 10.1007/s10297-005-0032-6
Originally published in J. Opt. Fiber. Commun. Rep. 2, 140–270 (2005)

Application of electroabsorption modulators for high-speed transmission systems

Eugen Lach, Karsten Schuh and Michael Schmidt

Alcatel Research and Innovation
Holderaeckerstrasse 35, D-70499 Stuttgart, Germany
Email: Eugen.Lach@alcatel.de
Karsten.Schuh@alcatel.de
Mi.Schmidt@alcatel.de

Abstract. To achieve ultra-high bit rate signal beyond existing ETDM technology optical time division multiplexing (OTDM) is been used. In this paper the various applications of electroabsorption modulators in transmitters and receivers in ultra-high speed OTDM-based transmission systems is reviewed. Results of single channel and DWDM fiber transmission experiments are presented.

1. Introduction

To increase the capacity of optical fiber links according to the bandwidth demand of a carrier, the network operator can either lighten further dark fibers in a cable, increase the TDM bit rate of a single optical channel or apply wavelength division multiplexing (WDM) technology by using further wavelengths in the same fiber. The overall costs of the investment and installation, the costs of operation and maintainance and later the costs for further extension of the capacity are strongly related on that choice.

Dense wavelength division multiplexing (DWDM) is an attractive technique to increase the capacity of a fiber link in a cost-effective and flexible way. The DWDM approach allows to share the transmission medium, expensive equipment like optical amplifiers and dispersion compensation fibers of long distant links. To keep costs low an optimum choice of the bit rate of the DWDM channels has to be taken for a given capacity.

At low channel bit rates a large number of optical channels on a narrow wavelength grid are applied. Such systems comprise of a very large number of optical and opto-electronic components and need a high wavelength stability of the transmitters, and

optical devices like add-and-drop demultiplexers and optical channel selection filters. For very narrow channel spacing non-linear crosstalk due to four-wave mixing (FWM) is one of the main limiting effects for achieving larger transmission reach. A larger number of channels is furthermore associated with a high complexity of the terminal equipment, higher installation costs, larger space and power consumption and higher effort for the DWDM channel management.

In contrast, higher DWDM channel bit rates, i.e., a lower number of optical channels with a larger channel spacing, potentially reduce many of these costs. On the other hand additional effort and investment are needed for fiber transmission of higher bit rate DWDM channels. Owing to shorter bit periode and broader optical spectrum a much more careful compensation of the fiber impairments, e.g., chromatic dispersion (CD) and polarization mode dispersion (PMD) has do be applied. High speed 40/42.7 Gbit/s ETDM technology was the key for achieving ultra-high fiber transmission capacity of several Terabit/s and recently more than 10 Tbit/s transmisson capacity has been demonstrated in the lab by Alcatel using 256 DWDM wavelength channels in 2 transmission windows, e.g., in the C+L band [1], and by NEC by using 273 DWDM channels in 3 transmission windows, e.g., in the C+L+S band [2].

Systems with even higher TDM bit rates from 80 Gbit/s up to 1.28 Tbit/s have been developed in research labs [3–10]. Owing to the speed bottleneck of electronic and opto-electronic components OTDM technology was usually applied with an OTDM base rate of 10 Gbit/s up to 40 Gbit/s. For picosecond pulse generation mode-locked lasers and fiber based pulse compressors are mainly used for single channel experiments. Optical pulse sources and supercontinuum fibers together with spectral slicing is the main aproach for DWDM signal generation [11–13].

Picosecond OTDM pulse sources and optical gates which base on optical modulators are an attractive solution for single channels [3,8,14] as well as for DWDM application [8,14]. Owing to the highly nonlinear characteristics of their extinction curves EA-modulators can be applied by appropriate sinusoidal driving and biasing for short pulse generation for transmitters and optical gating for demultiplexing in receivers.

Wavelength channel selection of modulator based systems can simply be achieved by selecting a appropriate DFB laser in the transmitter on the ITU grid. DWDM experiments benefit from simultaneous modulation of several wavelength signals. This paper reviews recent achievements of 160 Gbit/s single channel and $N\times$ 160 Gbit/s DWDM transmission systems which base on EA-modulators.

2. EA Modulator Based Subsystems For High-Speed Transmission Systems

For generation of digital ultra-high speed optical data signals electronic time division multiplexing (ETDM) is applied. Presently digital electronic circuits and broadband amplifier are widely commercially available for TDM bit rates up to 42.7 Gbit/s, e.g., 40 Gbit/s + 7% overhead for forward error correction (FEC).

The electrical output signal of the multiplexer is amplified by a high bandwidth amplifier which drives an optical intensity modulators for optical on-off keying. At highest data rates direct modulation of a DFB laser is usually not applied due limitation by the modulation bandwidth of the laser structure, high transient laser chirp and relaxation oscillations which lead to signal overshoots.

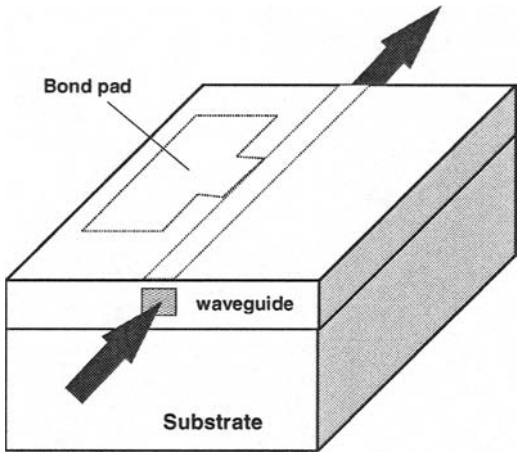

Fig. 1. Scheme of an electroabsorption modulator with a waveguide consisting of a bulk semiconductor or a quantum well structure.

2.1. Principles of Electro-Absorption Modulation

Two types of optical modulators are usually applied for intensity-modulation. Optical data modulators which are based on an electrically switched Mach-Zehnder (MZ) interferometer are fabricated mainly from $LiNbO_3$, which is a mature, but on the other hand an expensive technology due to the large size of the devices of several cm. Recently MZ-modulatores (MZM) are developed which are fabricated from polymers targeting for low-cost fabrication.

Owing to the optical transparency in a wide wavelength range and the interferometric principle of the modulation MZ-modulators can be applied in a very wide wavelength range of serveral 100 nm. $LiNbO_3$ MZ modulators are normally packaged using polarization maintaining fibers because the modulation characteristics exhibit a strong dependency on the polarization of the input light.

Electroabsorption modulators are very attractive components for ultra-high speed modulation due to their small size and low modulation voltage. Furthermore EA-modulators offer the possibility for monolithic intergration with opto-electronic devices like lasers and semiconductor optical amplifiers. In Fig. 1 a scheme of an electroabsorption modulator is shown which consists of a single waveguide which contains a doped p-i-n structure. The lateral optical confinement is usually achieved by etching a deep-ridge waveguide which is planarized either by regrowth of InP or using polyimide. fibers are coupled to the optical input and optical output of the EA-modulator (EAM) chip which has a typical length between 80 to 350 μm.

The optical modulation arises from a change of the loss in the linear waveguide in the presence of an electrical field. Electroabsorption modulators can be fabricated either from bulk III-V semiconductor material, e.g., quaternary GaInAsP for 1.55μm wavelength, or from quantum well structures which consist on alternating layers on quaternary or ternary III-V semiconductor layers.

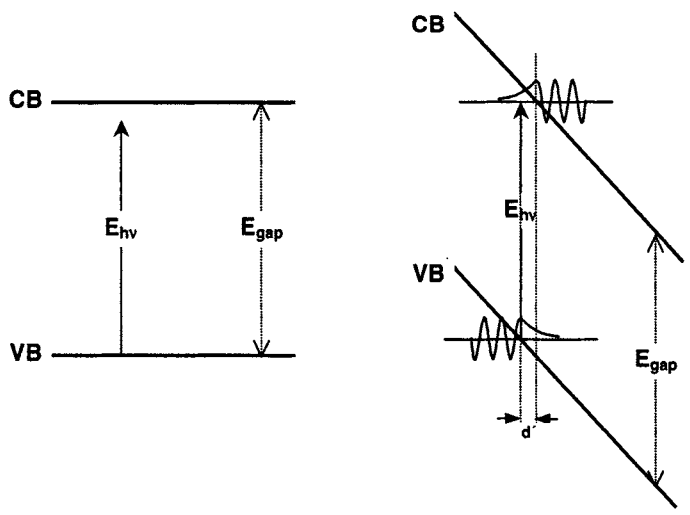

Fig. 2. Band diagram of a transparent bulk semiconductor and optical absorption due to Franz-Keldysh effect in the presence of an electrical field.

In bulk semiconductor the optical loss below the band-edge energy between conduction band (CB) and valence band (VB) of a direct semiconductor in the presence of an electrical field is called Franz-Keldysh effect. The physical effect for the change of the optical loss is field induced optical absorption. In Fig. 2 the band diagram illustrates band gap and the optical transition without and with electrical field. Without electrical field the absorption of a photon with an energy $h\nu < E_{\mathrm{gap}}$ is impossible. By tilting the band structure by an electrical field a photon induced tunnelling between the valence band (VB) and the conduction band (CB) due to partial overlap of the wavefunctions gives rise to absorption below the band gap energy of the bulk semiconductor. The probability of the transition, and thus the absorption, of the semiconductor is increased with a increase of the electrical field.

In quantum well structures, which consist of an alternating sequence of thin semiconductors with alternating lower and larger bandgap energies, electrons and holes are confined in the potential structure to two dimensions (2D) leading to a splitting and shift of the energy states of the semiconductor. A scheme of the band characteristics of the quantum-well structure is illustrated in the left part of Fig. 3. In 2D structures the density of states is modified from a square-root function of bulk semiconductors to a constant function for each confined state in CB and VB. The energy shift of the ground state and the energy difference between the confined states depend mainly on the quantum well width and the effective mass of electrons in the conduction band (CB) and holes in the valence band (VB). The quantum well thickness is typically between 5 to 10 nm. Different effective mass of the heavy holes (hh) and light holes (lh) leads to an energy splitting of their confined states.

Selection rules for optical transitions allow only optical transitions and thus absorption between subbands in the VB and CB of equal subband index. If several states in VB and CB are existing the effective density of states and thus the absorption charac-

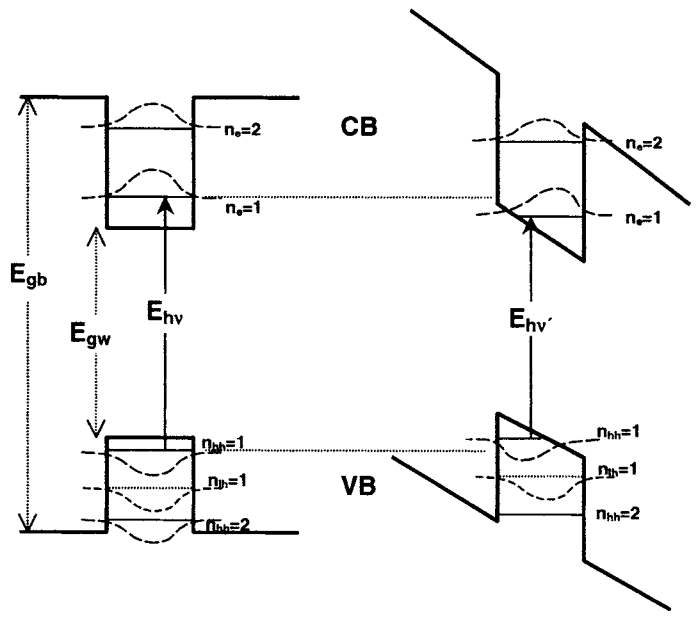

Fig. 3. Band diagram of a quantum-well structure and optical absorption below the effective bandgap energy due to Quantum-Confined Stark effect in the presence of an electrical field. The wave function of the different subbands are schematically shown.

teristics vs. the energy of a quantum-well structure corresponds to a step-like function due to the energy splitting of the levels in the VB and CB. Additionally below the band edge of each subband transition an absorption peak is seen which is associated to the excitons of the quantum well structure.

If an electrical field is applied to quantum-well structures the energy bands are tilted leading to a deviation from the square-like potential wells. Especially at the bottom of the quantum-wells a triangle-shaped potential is achieved and the effective band gap energy shrinks. The energy shift and the change of the wavefunctions of electrons and holes by the applied electrical field is schematically shown in Fig. 3.

Owing to the electrical field electrons and holes are spatially separated which leads to a reduced optical absorption of the exciton related to the band edge. The shrinkage of the effective band gap energy of the quantum well structure leads to a change of the transmission at energies below the bandgap with increasing electrical field. This effect which is called quantum confined Stark effect (QCSE) is applied in quantum well based EA-modulatores for the optical modulation.

For all types of EA-modulation the optical intensity modulation is associated with optical phase modulation leading to a wavelength chirp

Wavelength Dependency of Operation: In contrast to interferometric MZ-modulators, electro-absorption due to Franz-Keldish effect in bulk semiconductor structures and due to quantum-confined Stark effects in quantum well structures shows a strong variation with the wavelength. In Fig. 4 as an example the extinction curve vs. the reverse

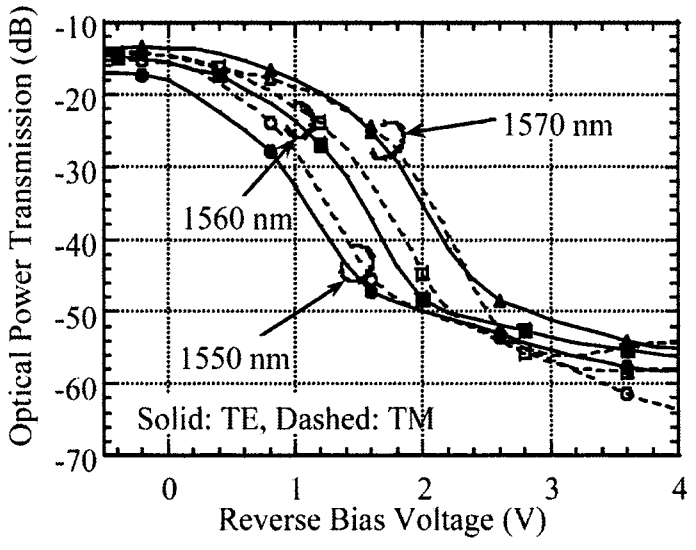

Fig. 4. Measured extinction characteristics of an EA-modulator as a function of the reverse bias voltage for wavelengths between 1550 and 1570 nm for TE and TM polarization [from 15].

bias voltage of an EA-modulator based on Quantum Confined Stark Effect in Quantum Well structures is depicted [from 15]. The minimum insertion loss as well as the total extinction ratio only show a small variation for different wavelengths. But the whole extinction curve and thus the optimum reverse bias voltage exhibits a large shift for the different wavelengths. As consequence optimization of the bias voltage is mandatory for the different wavelengths. Alternatively the device temperature can be optimized which shifts the bandgap corresponding to a wavelength shift of about 2 nm/K at room temperature.

Polarization Dependency: The Franz-Keldysh effect in a bulk semiconductor allows for fabricating EA-modulators which are insensitive to the input polarization of the light. A small deviation might occur due to a polarization dependent confinement of the optical wave to the waveguide due to a mismatch of the waveguide geometry from the ideal square-like shape.

In quantum-well based EA-modulators polarization independent operation needs a careful design of the waveguide. In the quantum well structure polarization dependency is associated mainly with the different absorption in 1hh-1e and 1lh-1e transitions. Tensile strain in the quantum wells together with compressive strained barriers can be applied to shift the states of the 1hh and 1lh-holes in the valence band to the same energy. This allows to achieve a polarization independent modulator design.

Higher Speed EAM: Classically EA-modulators comprise of a waveguide with a single electrode for applying the reverse bias voltage. For this lumped modulator design the modulator length is a compromise between modulation bandwidth and optical extinction ratio. More than 50 GHz modulation bandwidth has been reported for an

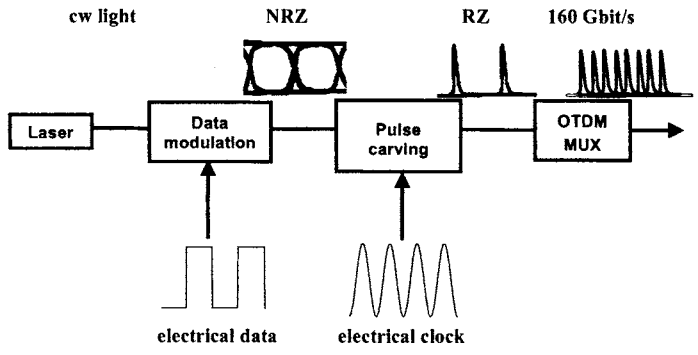

Fig. 5. Principal setup of an EAM based 160 Gbit/s OTDM transmitter.

EA-modulator with a modulator section length of 100 μm [16]. As for MZ modulators the traveling-wave approach has been applied to EA modulators to overcome the RC limitation of lumped EA modulators allowing the realization of longer devices with high bandwidth and with increased extinction ratio [15].

2.2. *Data Modulation and Pulse Carving Using EA Modulators*

An EAM based OTDM transmitter consists of four logical building blocks: a light source, a data modulation unit, a pulse carving or NRZ to RZ conversion unit and an OTDM multiplexer. Of course the functionality of several building blocks can be combined, e.g., a simultaneous RZ data modulation, or the succession of units can be exchanged, e.g., pulse carving and data modulation. In this subsection the building blocks are described in detail with a focus on EAM application.

Data Modulation: EAMs are attractive devices for data modulation and/or pulse carving. The reasons for this are that EAMs can be potentially cheaper than $LiNbO_3$-modulators and offer various possibilities of integration together with lasers, SOAs, as Tandem EAMs or even complete subsystems. Furthermore EAMs require a lower driving voltage for data modulation and have already been demonstrated with a measured electro-optic bandwidth exceeding 50 GHz. The data modulation performance of the latest EAMs can well compete with the up to now more common MZ-modulators. But the potential cost advantage of EAMs could shrink with the release of better Polymer-MZ-modulators. A comparison of EAM and $LiNbO_3$-MZM is given in Table 1.

The different ways for data modulation are the conventional NRZ data modulation with NRZ to RZ conversion, direct RZ data modulation and inverse RZ (or dark pulse) data modulation.

The Conventional NRZ Data Modulation With NRZ to RZ Conversion: The most common way for realizing NRZ data modulation is the use of $LiNbO_3$ MZMs. This is the technology EAMs have to compete with in this field. An example for realization is given in Fig. 6. An extensive study of data modulation using EAMs can be found in [20].

Table 1. Comparison of EAM and $LiNbO_3$-MZM

	$LiNbO_3$ MZM	**EAM**
Cost	High (production process)	Potentially low
Power consumption	High drive voltage	Half drive voltage of $LiNbO_3$ MZM for same extinction ratio
Insertion loss	5–6 dB wavelength transparent	6–15 dB increase to low wavelength
Polarization dependency	yes	can be independent
Optical input power	High damage level	Max. ~10-12 dBm mean
Chirp	Different chirp for raising and falling part Zero chirp available	Low chirp available
Extinction ratio	Typically ~15 dB	High, >30 dB reported [e.g., 17] decrease to long wavelength
Bandwidth	~45 GHz	>50 GHz [18]
Pulse carving	33, 50 or 66% duty cycle [19] not suitable for OTDM	10-20% possible with high dynamic extinction ratio

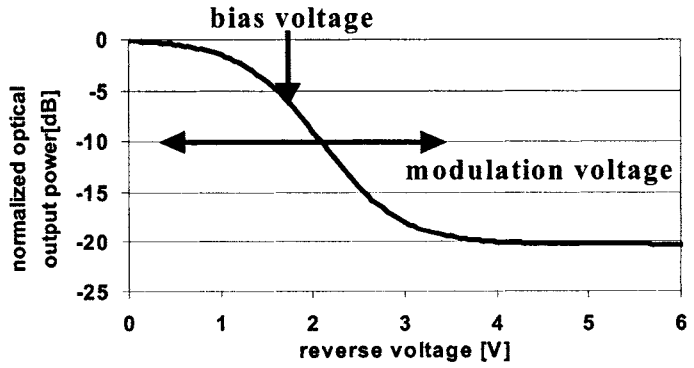

Fig. 6. EAM driving scheme for high extinction ratio NRZ modulation.

To achieve an RZ signal a pulse carver, usually an EAM, is applied in series to the data modulator. A comparison of the performance of discrete transmitters and an integrated EAM-SOA-EAM data modulation and pulse carving module was examined in [21].

Direct RZ Data Modulation: Choosing an appropriate EAM bias voltage and applying a superimposed electrical signal of clock and data an EAM allows to generate an optical output signal which is RZ data modulated using a single component. The application of EAMs for simultaneous data and RZ modulation was shown by Mohs et al. [22]. They combined a 10 Gbit/s data stream and the 10 GHz clock signal as input for the EAM resulting in an RZ data modulated signal having an extinction ratio of 12 dB, this is illustrated in Fig. 7. Compared to an NRZ signal of a $LiNbO_3$ MZM only a slight penalty of ~0.5 dB was observed.

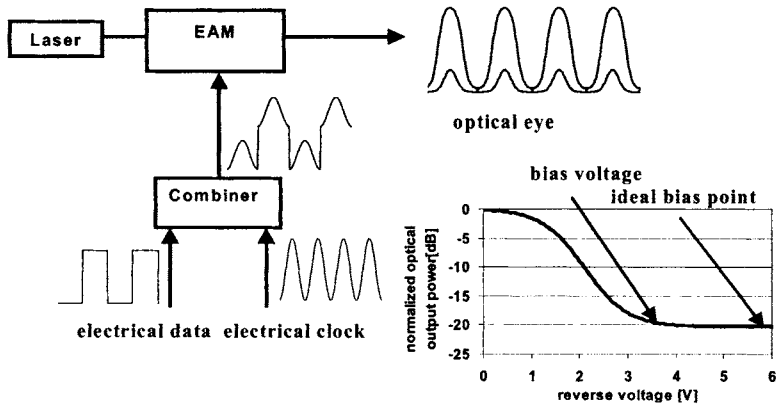

Fig. 7. EAM for direct RZ data modulation.

The disadvantage of this modulation scheme is that with today's generation of EAMs the zeros will be represented by small pulses (see optical eye), which lowers the possible extinction ratio and does not allow for OTDM multiplexing because the pulses are relatively broad. For selection of the reverse bias voltage the destruction limits of the EAM have to be taken into account, e.g., electrical limitations of the structure due to limited break-through voltage. Instead of the ideally large reverse bias point a reduced bias voltage has to be used as illustrated in Fig 7. Using the ideal bias point would highly improve the extinction ratio and also the FWHM pulse width. This can only be achieved, without destroying the EAM, by using some kind of nonlinear electrical limiting technique which suppresses the negative half-wave of the clock. In consequence of this the voltage applied to the EAM cannot exceed the bias voltage protecting the device from damage.

Pulse Carving: Pulse carving with EA-modulators can be achieved by applying a sinusoidal clock signal with a high voltage swing to the electrical input of the modulator, which is biased highly negative. Owing to the nonlinear characteristic of the EAM this results in a train of short optical pulses. One possibility is to modulate from a highly negative bias voltage with a high modulation voltage swing into the steep part of the EAM characteristic which results in short optical pulses. The other possibility is to fully modulate through the EAM characteristic having broader optical pulses but with a higher extinction ratio.

Figure 8 illustrates both operation modes of the EAM. On the left part typical bias voltages and modulation voltage swings are indicated for short pulse generation (solid arrows) and for the generation of longer pulses with higher extinction ratio (dotted arrows). On the right an example for the short pulse (solid line) and the high extinction ratio pulse (dotted line) regime is given. The characteristics of the resulting optical pulse train depends mainly on the EAM, the chosen bias voltage and the spectral purity and amplitude of the applied clock signal. A big advantage of pulse carving by EAMs is the stability and the low jitter, which mainly depends on the local oscillator and quality of the used electrical components.

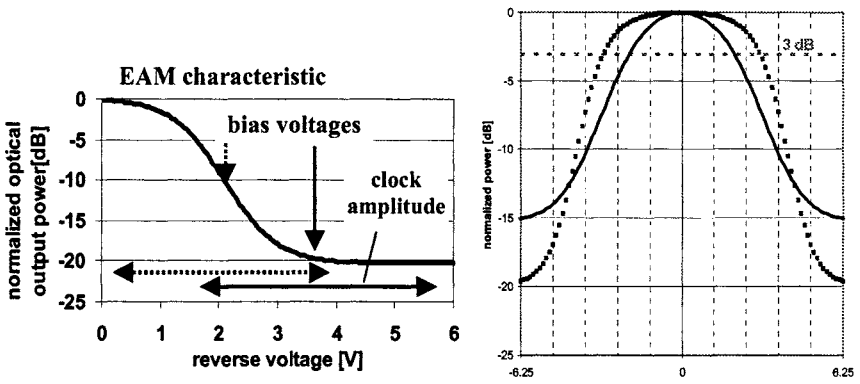

Fig. 8. left: EAM characteristic for pulse carving with typical bias voltages and clock amplitudes for short pulse generation and high extinction pulse generation, right: resulting short pulse (solid line) and high extinction ratio pulse (dotted line).

For OTDM multiplexing to higher bit rates short pulses with a high pulse tail extinction ratio (PTER) are necessary, where the PTER is defined as the power ratio of the pulse peak power to the power level at the next bit position after OTDM multiplexing. In simulations the 1 dB penalty for 4 × 40 Gbit/s OTDM multiplexing with parallel polarization was found to be 29 dB PTER for a duty cycle of 50% [23]. The requirements for the PTER are relaxing with shorter pulses. For the 1 dB penalty at a duty cycle of 40% the PTER is 27 dB. The requirements on FWHM pulse width and PTER for OTDM multiplexing to 160 Gbit/s are thus very demanding and cannot be fulfilled by pulse carving with a single EAM, where an FWHM pulse width of ∼3.5 ps and a PTER of 25 dB can be achieved. Therefor in several experiments a cascade of EAMs was used to achieve the necessary FWHM pulse width and PTER. In some experiments two discrete EAMs were cascaded [3,8,24–25] and, e.g., FWHM pulse width of 2.8 ps and a PTER of ∼30 dB were achieved using a clock frequency of 40 GHz. Also integration of two EAMs [26] and with an SOA between them [27] was shown.

Another often used configuration is pulse carving by a single EAM followed by supercontinuum generation using a nonlinear fiber and subsequent spectral filtering [5,12,28]. This configuration was also used for OTDM experiments at bit rates of 320 Gbit/s or more [29–30].

Pure EAM pulse carving is especially useful when the highest possible clock frequency is used, because short pulse generation means high optical loss and the noise of the following EDFA will have major impact on the whole transmitter OSNR. Today's commercially available EAMs are limited to 43 GHz, but with EAMs having travelling wave electrodes very high electro-optical bandwidth exceeding 50 GHz were already demonstrated [18].

For optimum performance a compensation of the EAM's chirp is also necessary. Using a short piece of DCF will usually be sufficient to remove the chirp and result in a ∼10% FWHM pulse width improvement and transform limited pulses.

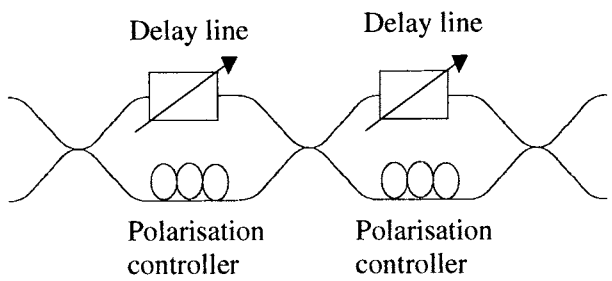

Fig. 9. Fiber based OTDM multiplexer.

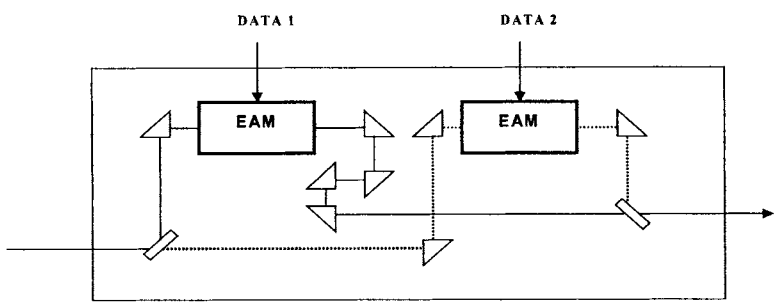

Fig. 10. Free space 40:80 Gbit/s EAM OTDM module using EAMs for data modulation of the OTDM channels.

OTDM Multiplexers: For OTDM multiplexing of the optical signal to the aggregated OTDM data rate three different setups are commonly used. The fiber based OTDM multiplexer as shown in Fig. 9 consists of Mach-Zehnder-like interleavers each multiplexing the signal with a copy of itself typically delayed by half the PRBS word length duration, e.g., for $2^7 - 1$ a delay of $(2^7 - 1) \times$ bit duration/2 is used. For stability improvements fiber based multiplexers are commonly realized with polarization maintaining components.

By replacing the last coupler by a polarizing beam combiner the popular bit interleaved alternating polarization format can be achieved. The adjacent OTDM channels are then orthogonally polarized to reduce coherent crosstalk between the OTDM channels.

A complete EAM OTDM module for 40:80 Gbit/s multiplexing was presented by Oki [31–33]. It is made by free space optics as shown in Fig. 10 and in each path an EAM is used for data modulation at the ETDM base rate. An improved version of the module allows for multiplexing a 40 Gbit/s signal to 80 and 160 Gbit/s with several outputs one for the RZ and one for the CS-RZ format at both data rates [34–36]. The disadvantage of this setup is the high insertion loss of 23 dB.

This module allows for optical phase control so that the phase between the OTDM tributaries of the multiplexed signal can be adjusted to achieve the desired modulation

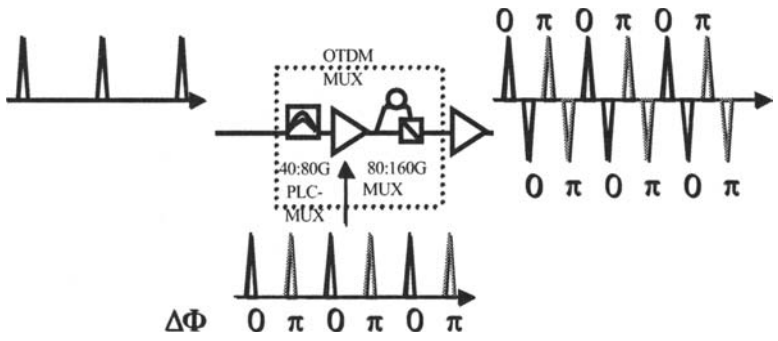

Fig. 11. Two stage 40:160 Gbit/s OTDM multiplexer.

format, e.g., RZ or CS-RZ. The optical phase control was demonstrated also for four WDM channels.

To study OTDM transmission in conjunction with DWDM and the same modulation format for all wavelength channels a PLC-based multiplexer can be used [37]. When temperature stabilized the PLC-multiplexer allows for simultaneous phase control of all DWDM channels. A two stage multiplexer consisting of a PLC for 40:80 Gbit/s multiplexing in combination with a fiber based 80:160 Gbit/s multiplexer stage with a polarizing beam combiner at the output is an attractive combination (see Fig. 11). With this combination the optical phase can be adjusted at 80 Gbit/s and is not altered by the subsequent bit interleaved alternating polarization multiplexing.

The advantage of phase stabilization in conjunction with bit interleaved alternating polarization is that an increased tolerance to the FWHM pulse width and the PTER of RZ pulses can be observed. Also the interferometric beat-noise is reduced. Under appropriate driving conditions it was possible to use a single EAM for RZ pulse generation and still achieving error free operation.

2.3. EAM-Based Wavelength-Transparent DWDM Transmitters for High-Channel Bit Rates

Two different wavelength transparent OTDM DWDM transmitter types incorporating EAMs in wavelength transparent operation were used within the recent years. Cascaded EAMs for pulse carving and single EAM for pulse carving based transmitters were applied. All used transmitter setups incorporated the latest available ETDM technology having ETDM base rates of 40 or 42.7 Gbit/s. An interesting issue is that when EAMs are used for simultaneous pulse carving of the used wavelength channels mostly the bit interleaved alternating polarization format was used. This format works very well with EAM based WDM transmitters as the pulse requirements are relaxed and a higher spectral efficiency can be obtained.

In two 4×160 Gbit/s WDM experiments cascaded EAMs for pulse carving have been applied using a 400 GHz channel spacing thus obtaining a spectral efficiency of 0.4 bit/s/Hz. The WDM wavelength transparency of these transmitters, see Fig. 12 for typical configuration, was demonstrated over $\sim$20 nm.

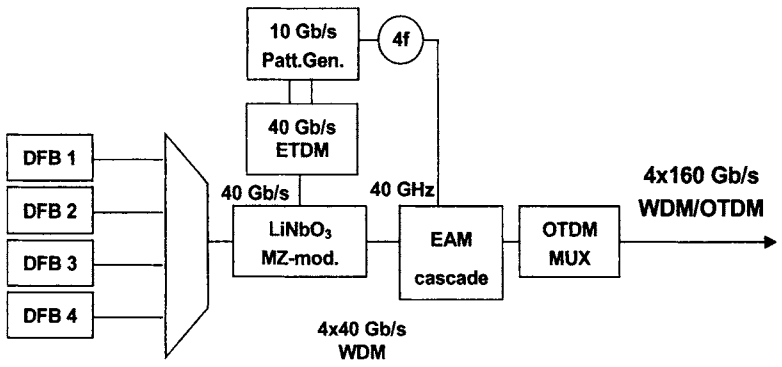

Fig. 12. Transmitter setup for 4 × 160 Gbit/s with cascaded EAMs.

In [14] FWHM pulse width of 5.5 ps and a PRBS word length of $2^{15}-1$ were reported forcing polarization demultiplexing at the receiver, whereas in [38] a PRBS word length of $2^{7}-1$ and FWHM pulse width of 2.75 to 3.05 ps was used with only optical TDM demultiplexing.

In [36] an EAM cascade in conjunction with the above described 40:160 Gbit/s EAM OTDM module was used with a channel spacing of 320 GHz resulting in a spectral efficiency of 0.5 bit/s/Hz. The FWHM pulse width varied from 2.8 ps for the channel with the shortest wavelength to 3.3 ps for the channel with the longest wavelength. The observed Q-factor variations occurring in back-to-back configuration illustrate the problems using EAMs in wavelength transparent transmitters.

The use of more channels is difficult because of the EAM characteristics. Using additional channels at shorter wavelength leads to problems with OSNR, due to the increasing insertion loss for shorter wavelength. For additional channels at longer wavelength it will be very difficult to fulfill the PTER and FWHM pulse width conditions for 160 Gbit/s OTDM. In general also achieving a uniform WDM spectrum with low power and FWHM pulse width variations between the wavelength channels is getting more challenging with increased channel count. In the WDM experiments using this transmitter type all WDM channels were modulated with the same data signal. For decorrelation of the adjacent WDM channels a second data modulator would be necessary to have different data for the neighboring WDM channels and thus a more realistic impact of the interchannel effects during fiber transmission.

Taking advantage of the relaxed pulse requirements due to simultaneous phase stabilization for all WDM channels in a PLC-based optical multiplexer the pulses carved with only a single EAM were used for the latest high capacity OTDM DWDM experiments with an overall capacity exceeding 1 Tbit/s [39]. The eight channels with 300 GHz spacing were divided into even and odd channels according to their ITU channel number and single EAM pulse carving was done for each subgroup. After modulation by Mach-Zehnder modulators of one group with DATA and the other with $\underline{\text{DATA}}$ having a PRBS word length of $2^{7}-1$ both WDM channel groups were combined by an interleaver with a periodic filter function. The 8 × 40 Gbit/s WDM channels were then simultaneously multiplexed up to 8 × 80 Gbit/s CS-RZ by a PLC multiplexer

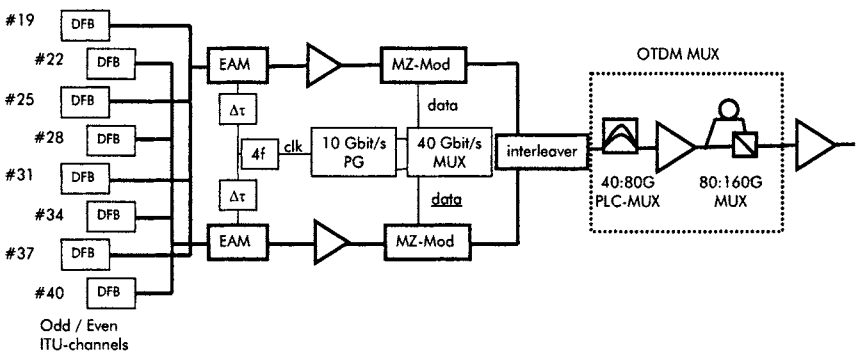

Fig. 13. Transmitter setup for 8 × 160 Gbit/s OTDM DWDM.

and up to 8 × 160 Gbit/s with alternating polarization by a fiber based multiplexer. A scheme of the setup is shown in Fig. 13.

In this experiment a spectral efficiency of 0.53 bit/s/Hz was achieved. Broad pulses in the range of 5 to 5.5 ps were used forcing a polarization demultiplexing at the receiver.

2.4. Optical Demultiplexing Using Electro-Absorption Modulators

Ultra-high speed optical transmission systems with channel bit rates beyond the speed limits of electronics rely on ultrafast electro-optical or all-optical gates for demultiplexing the tributary channels from the aggregated OTDM signal.

To achieve error-free optical demultiplexing the optical gate must fulfill demanding requirements for the temporal width and extinction ratio of the switching window in order to suppress the cross-talk from neighboring channels. Furthermore it is desirable to provide the optical gating function at the repetition rate of the fastest available ETDM technology. A broad optical bandwidth is required to apply optical gates in ultra-high speed hybrid DWDM/OTDM transmission systems.

Early electro-absorption modulators have been identified as key devices to meet the challenges of ultra-high bit rate optical demultiplexing. Their characteristics such as low driving voltage requirements, high modulation efficiency and polarization insensitivity are attractive in order to generate switching windows in the pico-second region with high extinction ratios. In its basic mode of operation only narrowband sinusoidal drive electronics are required, so electro-absorption based optical demultiplexers are attractive, easy-to-implement and potentially cost-effective subsystems for ultra-high speed OTDM transmission systems.

A number of different designs of the optical demultiplexer have been reported in the literature. The most simple and cost-effective approach is a single-stage setup of the optical demultiplexer, which consists of one electro-absorption modulator driven sinusoidally at the base rate of the OTDM tributary channel. In [41] Marcenac et al. reported on error-free 8:1 optical demultiplexing in a 80 Gbit/s OTDM system and in [8] Lach et al. have demonstrated feasibility of error-free 4:1 demultiplexing in a 160 Gbit/s OTDM system using a commercially available electro-absorption modulator.

One solution to achieve demultiplexing ratios higher than 8:1 is to cascade electro-absorption modulators. The basic idea is simply to use single-stage optical demultiplexers in series, effectively narrowing the switching window and improving the extinction ratio. In particular, double-stage optical demultiplexing subsystems are widely used in ultra-high bit rate transmission systems.

In [42] Ellis et al. reported on error-free 10:1 demultiplexing in a 100 Gbit/s OTDM system with a double-stage EAM based optical demultiplexer. Mikkelsen et al. demonstrated feasibility of error-free 16:1 demultiplexing in a 160 Gbit/s OTDM system [43], which has been extended to bit rate of 320 Gbit/s with additional polarization demultiplexing [44].

To overcome bandwidth limitations of the electro-absorption modulator imposed by the driver amplifiers and the electrical interconnections, Kodama et al. have proposed a monolithical optical gate comprising a uni-travelling-carrier photodiode and a travelling wave electro-absorption modulator (TW-EAM), in which the output signal of the photodiode directly drives the TW-EAM [45]. In a number of experiments Kodama et al. have reported on error-free demultiplexing from 160 Gbit/s [46], 320 Gbit/s [47] and recently demonstrated optical demultiplexing from 500 Gbit/s [48].

To date, electro-absorption modulators are being used in numerous 160 Gbit/s OTDM transmission experiments, highlighting their advantageous properties to build stable, compact OTDM receiver subsystems. A overview of transmission experiments in which EA-modulators are applied in the receiver is given in section 3.

Apart from optical demultiplexing, the receiver must be able to recover the tributary clock from the aggregated bit rate. In particular, clock recovery circuits based on phase-locked loops require an ultrafast nonlinear optical device acting as an optical phase comparator. Electro-absorption modulators have been successfully applied to build pre-scaled PLL-based clock recovery subsystems for 80 Gbit/s [49] and 160 Gbit/s [50–51] OTDM signals.

In a number of ultra-high bit rate experiments an opto-electronic regenerative circuit proposed by Yoa et al. [52] and Cisternio et al. [53] has been used for clock recovery from 160 Gbit/s [8,43] and 320 Gbit/s [29,44]. It consists of an opto-electronic oscillator comprising an electro-absorption modulator and a narrow-band filtered feedback loop. The electro-absorption modulator is applied to mix the incoming optical signal with the tributary clock line and its harmonics due to its nonlinear transmission characteristics. The resulting beat signal at the subharmonic clock rate of the tributary channel is now synchronized to the incoming data signal and can be used to drive the optical demultiplexer after narrowband filtering.

2.5. Wavelength Transparent High-Speed OTDM Receiver

For the first time Mikkelsen et al. [12] applied electro-absorption modulators in a hybrid DWDM/OTDM receiver. Using a double-stage approach, error-free 16:1 demultiplexing of six 160 Gbit/s wavelength channels has been achieved, which highlights the potential of electro-absorption modulators to build wavelength transparent DWDM subsystems.

The implementation of the latest 40 Gbit/s ETDM technology simplified the design of 160 Gbit/s OTDM receivers considerably. In [8] Lach et al. introduced a 160 Gbit/s OTDM transmission system entirely based on 40 Gbit/s ETDM technology requiring only a single stage optical demultiplexer. With minor changes the receiver subsystem

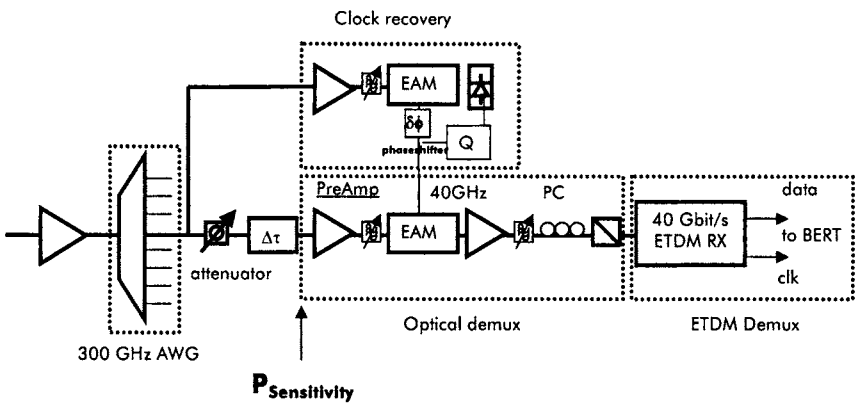

Fig. 14. Setup of an electro-absorption modulator based $N \times 160$ Gbit/s DWDM/OTDM receiver using 40 Gbit/s ETDM subsystems[39].

has been used in a 4×160 Gbit/s DWDM transmission experiment by Schuh et al. [38].

In a recent experiment Schmidt et al. have reported on a 8×160 Gbit/s DWDM/OTDM transmission experiment with 1.28 Tbit/s capacity using only single-stage optical transmitters and demultiplexer based on electro-absorption modulators [39]. Error-free optical demultiplexing has been achieved for all eight DWDM channels covering an optical bandwidth of 17 nm. The experimental setup of the hybrid 160 Gbit/s DWDM/OTDM receiver is shown in Fig. 14. Two interleaved arrayed waveguide gratings form a DWDM channel selector with 300 GHz channel spacing. A part of the optical signal is tapped to the clock recovery circuit, which consists of an injection-locked opto-electronic circuit as described in the preceding paragraph. The recovered 40 GHz clock line is used to drive the single stage electro-absorption modulator based optical demultiplexer. A switching window with a temporal width of around 4 ps at FWHM has been used for error-free demultiplexing from 160 Gbit/s. For all DWDM channels the same driving voltage, bias voltage and temperature of the electro-absorption modulators were maintained.

By using 160 Gbit/s OTDM signals with alternating polarization residual polarization demultiplexing could be performed in front of the 40 Gbit/s ETDM receiver, which in turn enabled to use the broad pulse-widths necessary for achieving a spectral efficiency of 0.53 bit/s/Hz. Figure 15 shows the measured bit-error rate curves of all DWDM channels labelled according to its ITU channel number along with the corresponding optical spectrum. Error-free (BER $< 10^{-9}$) system performance with no signs of an error-floor is achieved for all eight 160 Gbit/s DWDM channels.

The receiver shown in Fig. 14 is not fully equipped as the four 40 Gbit/s tributary channels are not demultiplexed in parallel. In contrast, an optical delay line in front of the demultiplexer is used to sequentially assess the system performance of all tributary channels.

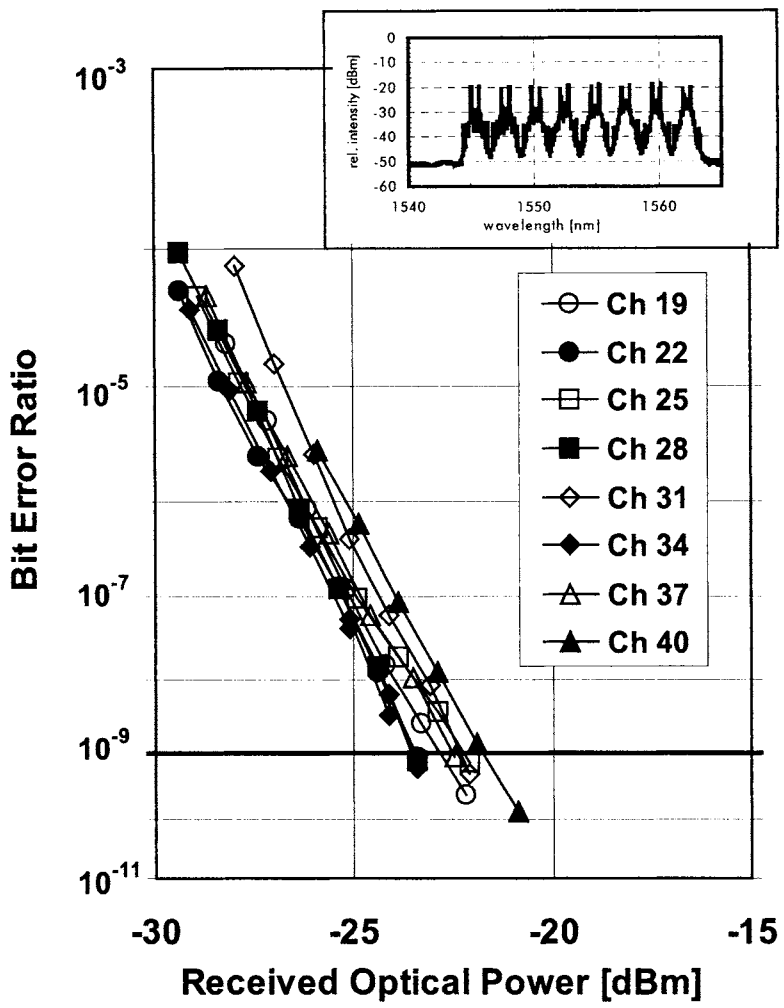

Fig. 15. System performance of an electro-absorption modulator based receiver for an 8 × 160 Gbit/s DWDM signal with a spectral efficiency of 0.53 bit/s/Hz [39].

3. High-Channel Bit Rate DWDM Transmission

Transmission experiments of ultra-high bit rates using subsystems which are based on EA-modulators for data generation, RZ pulse carving, optical demultiplexing or clock recovery have been reported. This demonstrates the wide field of application of EA-modulation for high-speed system application.

3.1. Single Channel Transmission Experiments

Raybon et al. have demonstrated 100 Gbit/s single channel transmission over 200 km of Non-zero Dispersion-shifted fiber (NZDSF) and 160 km of standard fiber [5]. In the transmitter an EA-modulator is applied for RZ pulse carving at 20 GHz followed by a pulse compression to 3 ps pulse width by non-linear fiber compressor proposed by Mamyshev [54]. In the receiver two cascaded EA-modulators which operate at 10 GHz are used to reduce the switching window for 100:10 Gbit/s demultiplexing and optical clock recovery, respectively.

With the same transmitter concept Mikkelsen achieved 160 Gbit/s by reducing the pulse width in the 8 $\times$ 20 Gbit/s OTDM transmitter to 1.8 ps and demonstated feasibility of 160 Gbit/s transmission over 3 $\times$ 100 km of NZDSF [43]. In the receiver EA-modulators are used in a modified two-stage configuration for optical 160:20:10 Gbit/s demultiplexing and 10 GHz clock recovery.

The transmitter has been extended to achieve a single channel bit rate of 320 Gbit/s by using the same pulse width of 1.8 ps and applying polarization time-interleaved multiplexing. In the receiver a polarization demultiplexing was added. Transmission of 320 Gbit/s data over 2 $\times$ 100 km NZDSF in a pseudo-linear transmission regime has been reported by Raybon et al. [30] and Mikkelsen et al. [44]. The dispersion of the two spans are post-compensated by slope-compensating DCF and a hybride EDFA and Raman amplification scheme is applied.

With the advent of 40 Gbit/s ETDM components and ETDM subsystems $N\times$ 40 Gbit/s based OTDM has widely been applied which makes OTDM an easier approach to upgrade latest ETDM system technology.

Mikkelsen et al. reported on a 160 Gbit/s transmission experiment over 4 $\times$ 100 km NZDSF using only Raman amplification for the link and post-compensation of the whole dispersion by DCF [24]. In the transmitter 40 Gbit/s ETDM technology with EA-modulators for 40 Gbit/s data modulation and 40 GHz pulse generation followed by a fiber based pulse compression is utilized. The receiver comprises a EAM based two-stage optical 160:40:10 Gbit/s demultiplexer and clock recovery, respectively.

In [55] Augé et al. reported on a 160 Gbit/s transmission experiment. A monolithic semiconductor based 40 GHz mode-locked laser and 40 Gbit/s ETDM technology is used in the OTDM transmitter. The receiver consists of a two stage optical 160:10 Gbit/s demultiplexer in which both EA-modulators are driven with a mixed electrical 10 + 40 GHz signal to achieve short switching window with high extinction ratio. The 6 $\times$ 80 km standard fiber link was equipped with EDFA and pre-compensation and inline dispersion compensation is applied. The launched optical power in each span was +4 dBm and error-free transmission was shown.

Murai et al. [34] have demonstrated 160 Gbit/s transmission over 3 $\times$ 100 km standard fiber using an external-cavity mode-locked laser and 40 Gbit/s EA-modulator in the transmitter which emits 160 Gbit/s data signals with alternating polarization. In the receiver first polarization demultiplexing is applied which is followed by optical demultiplexing from 80:20:10 Gbit/s using two cascaded EA modulators. In [58] a modified setup with EAM for 40 Gbit/s data modulation and 40 GHz pulse carving is used to generate single polarization 160 Gbit/s to compare fiber transmission performance of RZ and CS-RZ modulation format. fiber transmission has been performed in a loop configuration with a hybride EDFA & Raman amplification scheme. Superior

performance has been measured for CS-RZ format which allows transmission over 8 $\times$ 80 km SMF with BER $< 10^{-9}$ whereas RZ was limited to 7 $\times$ 80 km.

Berger et al. reported on a 160 Gbit/s transmission experiment which is based on 40 Gbit/s ETDM technology in the transmitter and in the receiver [56]. In the transmitter a 40 GHz pulse source comprising of a 10 GHz mode-locked laser and a passive multiplexer is used. An optical 10 GHz clock is transmitted on a separate wavelength. In the receiver optical 160:40 Gbit/s demultiplexing is performed by a 40 GHz driven self-cascading electro-absorption modulator [57]. 160 Gbit/s transmission performance over dispersion managed 3 $\times$ 80 km links of standard SMF and of super large area (SLA) fiber is compared. The standard fiber spans are post-compensated by slope-compensating fiber whereas the other type is a fully compensated link consisting of SLA fiber and inverse dispersion fiber (IDF). The SLA-IDF based links exhibits superior performance at high optical input power.

In [8] Lach et al. have reported on a 160 Gbit/s system which is based fully on 40 Gbit/s ETDM technology for the first time in the transmitter as well as in the receiver. In the transmitter 40 GHz pulse carving is performed by two cascaded EA-modulators resulting in a pulse width of around 3 ps and alternating polarization time-interleaved OTDM multiplexing is used. In the receiver a single polarization insensitive EA-modulator is applied for optical 160:40 Gbit/s demultiplexing with a gating window of $\sim$4 ps and 40 GHz clock recovery in an opto-electronic PLL-based clock recovery. In system experiments error-free transmission over 2 $\times$ 100 km TeraLight is achieved [8].

Based on an entire $N\times$ 40 Gbit/s OTDM approach Schmidt reported on a 320 Gbit/s transmitter which used a tandem-EAM 40 GHz pulse source followed by pulse compression based on Dispersion Decreasing fiber and a dispersion imbalanced NOLM to suppress pulse pedestals after compression. In the transmitter time-interleaved multiplexing with alternating polarization is applied.

The receiver comprises a single EAM with subsequent polarization demultiplexing for simultaneous optical 320:40 Gbit/s demultiplexing and a pre-scaled 40 GHz electro-optic clock recovery. Error-free unrepeatered 320 Gbit/s (8 $\times$ 40 Gbit/s) transmission over a fully dispersion compensated 80 km fiber link of TeraLight / Reverse-TeraLight is demonstrated [29].

3.2. High-Capacity DWDM Transmission

Generation of supercontinuum pulses and spectral slicing was the first technique for achieving $N\times$ 160 Gbit/s DWDM signals. Mikkelsen et al. [24] have used a highly nonlinear dispersion shifted fiber (HN-DSF) to generate a supercontinuum from 20 Gbit/s RZ data. Two AWG's with 300 GHz channel spacing are applied for spectral slicing leading to a pulse width of 3 ps. OTDM multiplexing is performed to achieve othogonal polarization of adjacent OTDM tributaries of all 6 $\times$ 160 Gbit/s RZ DWDM signals respectively. In front of the receiver a tunable filter is applied for DWDM demultiplexing. Errorfree $N\times$ 160 Gbit/s DWDM transmission is shown over 80 km of NZDSF.

This setup has been modified for 40 Gbit/s ETDM data modulation and 40 GHz pulse carving by EA-modulators, respectively. A scheme of the 6 $\times$ 160 Gbit/s DWDM transmission experiment over 400 km NSDSF is depicted in Fig. 16 [12]. The loss of the link comprising 4 $\times$ 100 km NZDSF is compensated by applying only distributed

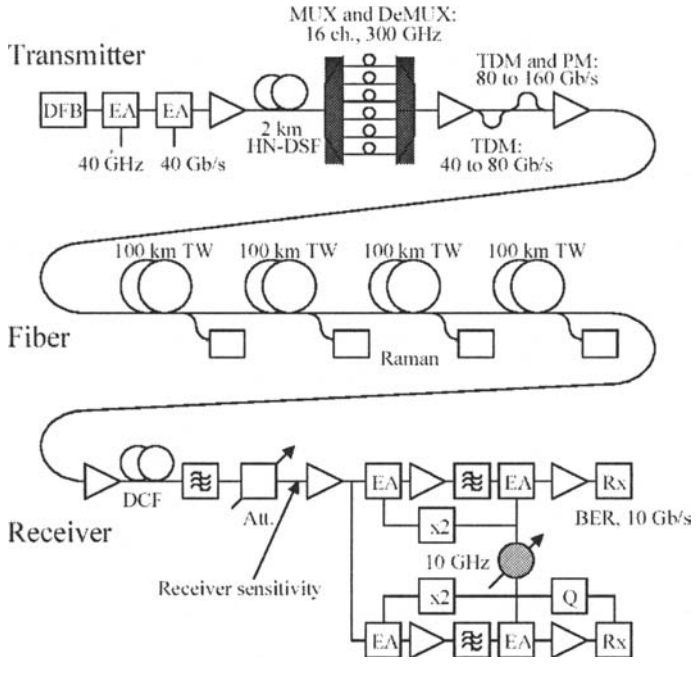

Fig. 16. Setup of a 6 × 160 Gbit/s DWDM transmission experiment with all EA-modulator based subsystems [from 12].

Raman amplification. In the 6 × 160 Gbit/s DWDM transmission experiment, which is performed in a pseudo-linear transmission regime with 100% post-compensation by DCF, error-free transmission and demultiplexing is achieved with a spectral efficiency of 0.53 bit/s/Hz.

The use of wavelength transparent optical modulators in OTDM subsystems allows for extension of a single channel OTDM system to an ultra-high channel bit rate DWDM by simply adding new DFB laser wavelength in the transmitter [8]. This approach was applied to $N\times$ 160 Gbit/s DWDM transmission experiments [36,38]

Schuh et al. [38] reported on a 4 × 160 Gbit/s DWDM system which is based fully on 40 Gbit/s ETDM technology in the transmitter as well as in the receiver. In the transmitter a $LiNbO_3$-MZ-modulator is used for 40 Gbit/s data modulation and two cascaded EA-modulators for 40 GHz pulse carving. An AWG with a channel spacing of 400 GHz is used for DWDM channel selection. In the receiver optical 160:40 Gbit/s demultiplexing is achieved by a single EA-modulator. All four DWDM channel carry the same 160 Gbit/s data, therefore a large channel spacing of 400 GHz which corresponds to spectral efficiency of 0.4 bit/s/Hz is chosen to reduce DWDM channel crosstalk. 4 × 160 Gbit/s DWDM transmission is achieved over 3 × 80 km TeraLight/Reverse-TeraLight fiber with a channel input power of +7 dBm.

Daikoku et al. reported on a 4 × 160 Gbit/s DWDM transmission experiment with 400 GHz channel spacing using a similar transmitter emitting OTDM signal with

alternating polarization [14]. In contrast to [8,38] first a polarization demultiplex is performed at the input of the receiver [58] followed by a two-stage optical 80:40:10 Gbit/s demultiplex by cascaded EA-modulators. Error-free 4 × 160 Gbit/s transmission over 3 × 75 km NZDSF are achieved.

Higher spectral efficiency, e.g., a reduction of the DWDM channel spacing can be achieved by reducing their spectral width. Schmidt et al. applied a temperature stabilized PLC-based OTDM interleaver for 40:80 Gbit/s OTDM multiplexing [39]. A constant optical phase between the two interleaved OTDM tributaries can be achieved, which minimizes interferometric crosstalk between 80 Gbit/s signals. The optical phase was adjusted to get CS-RZ spectrum of the 80 Gbit/s tributares. This allows for using only a single EA-modulator for pulse carving with larger pulse width and lower extinction ratio. Alternating polarization OTDM format is chosen to enhance dispersion tolerance of the 160 Gbit/s channels. Owing to the narrower channel spacing of 300 GHz which corresponds to a spectral efficiency of 0.53 bit/s/Hz adjacent DWDM channels have been decorrelated by using two different groups of modulator for odd and even channel numbers (see Fig. 13). 8 × 160 Gbit/s DWDM transmission with a spectral efficiency of 0.53 bit/s/Hz and decorrelated DWDM channels is achieved over 85 km TeraLight-Ultra fiber.

In contrast Murai et al. [36] realized 4 × 160 Gbit/s DWDM transmitter with EAM-based pulse carver and with an OTDM module which uses EAM data modulation. The transmitter emits 160 Gbit/s channels with single polarization and allows to generate RZ or CS-RZ format. In the receiver two cascaded EA-modulators are applied for optical 160:40:10 Gbit/s demultiplexing. A 4 × 160 Gbit/s DWDM transmission experiment with a channel spacing of 320 GHz which corresponds to a spectral efficiency of 0.5 bit/s/Hz has been performed. In the transmission experiments over 80 km of standard fiber a superior transmission performance is measured for 4 × 160 Gbit/s CR-RZ as compared to RZ format.

Application of FEC in OTDM Transmission: Forward Error Correction is widely used in transmission systems to extend the fiber transmission reach. For concatenated FEC a BER of 10^{-13} (error free) after FEC decoding is achieved for an initial BER of 2×10^{-3} [60].

To achieve large transmission reach the $N\times$ 160 Gbit/s system [39] is upgraded for operation with a FEC overhead of 7% leading to 170 Gbit/s channel rate. For this increase of the bit rate specific components, e.g., the PLC-based multiplexer, and the clock recovery (see Figs. 13 and 14) have been replaced, whereas the channel spacing of 300 GHz and thus the spectral information density is kept. The orthogonal polarization bit interleaving OTDM scheme supports transmission over larger distance due to enhanced tolerance for chromatic dispersion and PMD as compared to parallel polarization.

The investigation of fiber transmission over several hundred km is usually performed in a recirculating fiber loop. The fiber loop used consists of three 100 km spans of standard SMF compensated by slope-compensating DCF. An EDFA is used at the input of each span and distributed Raman amplification is applied in SMF and DCF (see Fig. 17). Details of the loop experiment are given in [40].

An optical 42.7 GHz clock has been transmitted on a separate wavelength which allows for measurement of each of the four 42.7 Gbit/s OTDM tributaries in loop

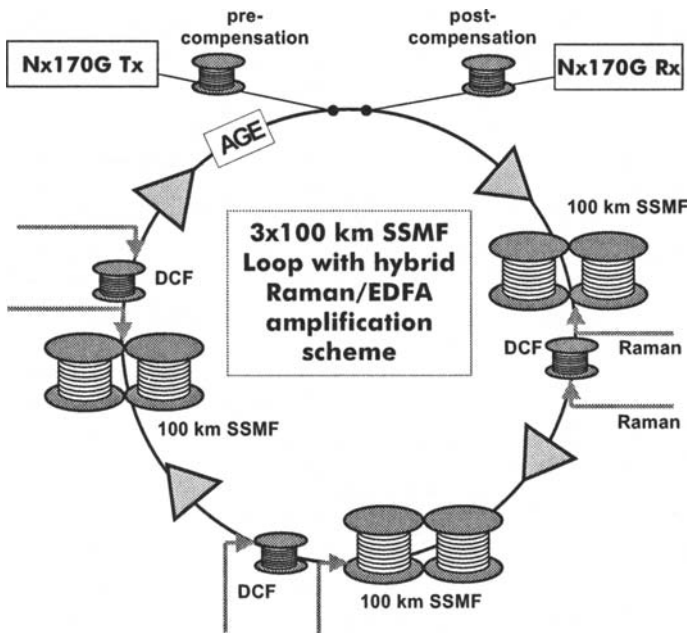

Fig. 17. Scheme of the fiber loop consisting of 3 × 100 km of standard SMF.

experiments. In all measurements a PRBS length of $2^{23} - 1$ PRBS is used for the 42.7 Gbit/s tributaries.

First transmission performance at 170 Gbit/s has been tested in a single channel loop experiment. The Q-factor is calculated from BER measurement after each circulation. In Fig. 18 the evolution of Q-factor vs. the transmission distance for all four 42.7 Gbit/s tributaries is shown.

Error-free condition, e.g., a BER of 2×10^{-3} corresponds to a Q-factor limit of 9.2 dB which is indicated in Fig. 18. From these measurements the limit of error-free transmission distance of a single 170 Gbit/s channel can be estimated to be to 1200 km. The limitation of the 170 Gbit/s transmission reach is attributed mainly to PMD.

7×170 Gbit/s DWDM transmission has been performed using a channel spacing of 300 GHz (0.53 bit/s/Hz spectral efficiency). In Fig. 19 the optical spectrum of the 7×170 Gbit/s DWDM channels and the optical 42.7 GHz clock after 600 km transmission over SMF is depicted. A channel power uniformity of $\sim$2 dB is achieved.

The Q-factor is extracted from BER measurements after 7×170 Gbit/s DWDM transmission over 600 km of standard SMF. For all 42.7 Gbit/s tributaries of all DWDM channels the Q-factor is above the FEC limit (see Fig. 20) indicating error free transmission.

Transmission of >1 Terabit/s information capacity has been demonstrated over terrestrial distances of standard SMF by using only 7 DWDM channels.

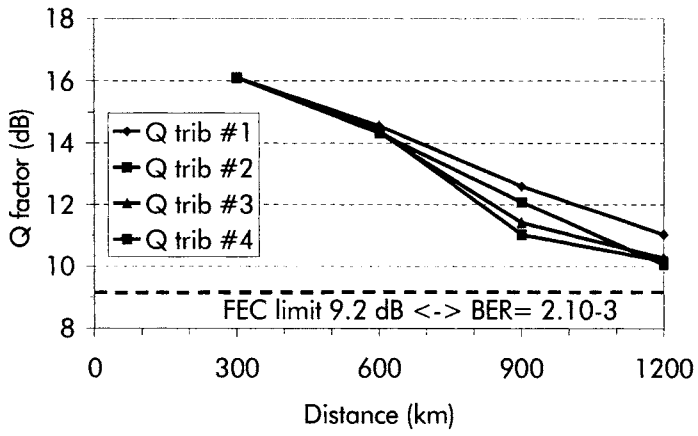

Fig. 18. Q-factor for single channel 170 Gbit/s transmission over SMF vs. distance.

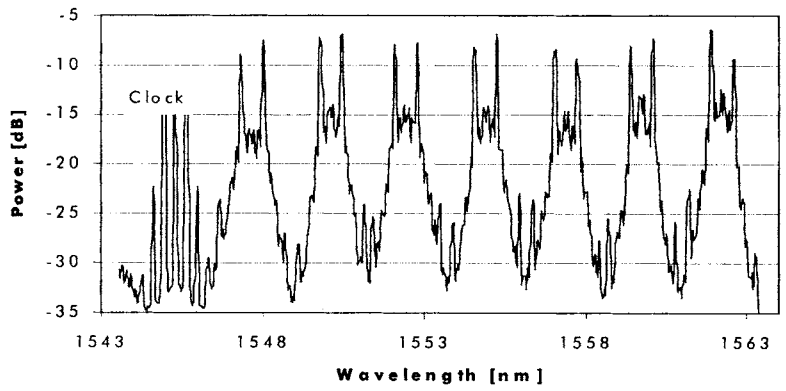

Fig. 19. Optical spectrum of the 7 × 170 Gbit/s DWDM and 42.7 GHz clock after 600 km transmission over SMF.

Application of DPSK in 160 Gbit/s OTDM Transmission: Differential phase-shift keying (DPSK) has been used at 40 Gbit/s DWDM transmission to improve receiver sensitivity to extend transmission system margin or achieve larger transmission reach. For bit rates beyond 40/43 Gbit DPSK is also applied together with OTDM to achieve 160 Gbit/s [61] and 170 Gbit/s [62]. Theoretically 3 dB improvement of the receiver sensitivity is expected which gives additional system margin.

Ludwig et al. demonstrated an increase of transmission reach for 160 Gbit/s single channel and single polarization transmission and reported on a 410 km transmission experiment [63]. The experimental setup of the transmission experiment is shown in Fig. 21. In this experiment EA-modulators are applied in the 160 Gbit/s receiver for clock recovery in a bi-directional configuration [64] and for optical 160:40 Gbit/s demultiplexing in a self cascading configuration [57].

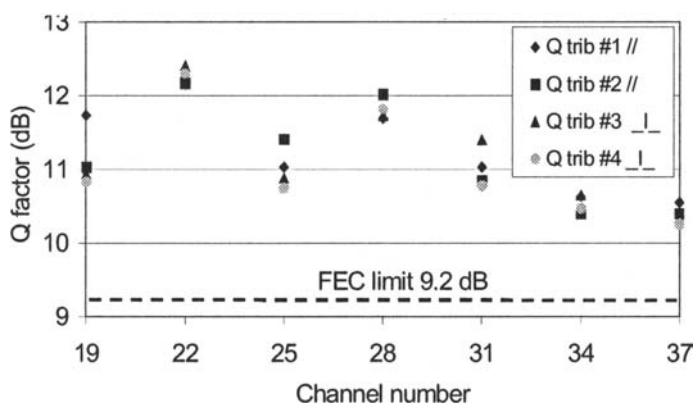

Fig. 20. Q-factor for 7 × 170 Gbit/s DWDM transmission over 600 km SMF for all 42.7 Gbit/s tributaries.

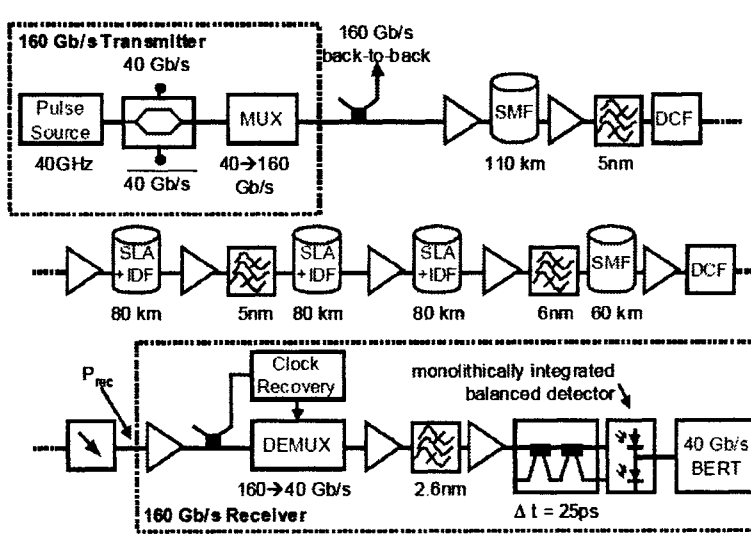

Fig. 21. Setup of a 160 Gbit/s RZ-DPSK transmission experiment [from 63].

In Fig. 22 results of BER measurement without and after transmission are compared for standard RZ-On-Off.Keying (OOK) and RZ-DPSK. Without transmission RZ-DPSK has an improved receiver sensitivity by about 2.5 dB compared to RZ-OOK. After transmission over 410 km fiber link consisting of five spans of different fiber types error-free OTDM-demultiplexing and DPSK-demodulation is achieved using a monolithically intergrated balanced detector.

Gnauck et al. applied DPSK for 4 × 42.7 Gbit/s OTDM and transmitted a 6 × 170 Gbit/s DWDM data signal, with 7% FEC overhead and OTDM format with alternating

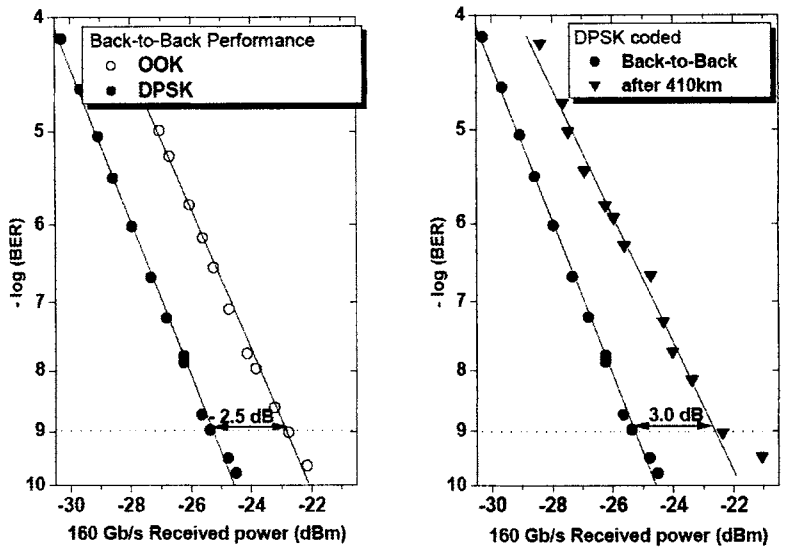

Fig. 22. BER performance at 160 Gbit/s comparing DPSK- and OOK-coding format (left) and after 410 km transmission distance (right) [from 62].

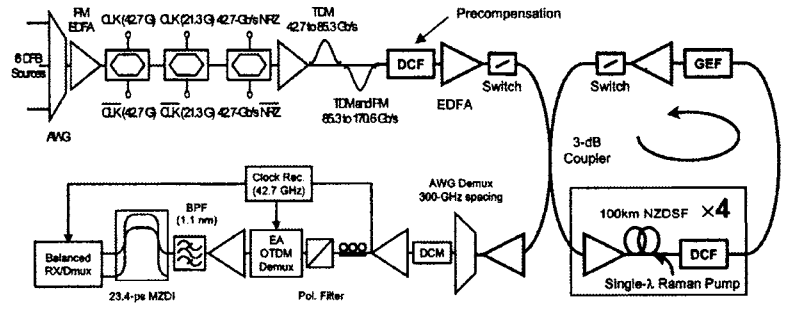

Fig. 23. Experimental setup of the 6 × 170 Gbit/s DWDM transmission experiment over $N \times$ 100 km NZDSF in a loop configuration [from 62].

polarization over NZDSF fibers in a loop experiment using hybride EDFA + Raman amplification scheme [62]. The experimental setup is shown in Fig. 23. Polarization demultiplex is performed in front of the EA-modulators based optical 170:42.7 Gbit/s demultiplexer. In the OTDM multiplexer the 42.7 Gbit/s tributaries have 10% power difference leading to a residual 42.7 GHz clock tone which is recovered and used for optical demultiplexing in the receiver.

In this 6 × 170 Gbit/s DWDM transmission experiment with 300 GHz spacing a total information capacity of nearly 1 Tbit/s and a transmission length of 2000 km is achieved with BER better than 4×10^{-6} which is correctable by applying a FEC to less than 10^{-12}.

4. Summary/Outlook

In this article an overview on various applications of EA-modulators for ultra-high bit rate single channel and DWDM transmission is given.

OTDM is presently applied to achieve data rates of optical transmission systems beyond the speed of electronics and opto-electronic devices. EA-modulators are widely used in OTDM based single channel and DWDM transmission systems operating at channel rates of 160 Gbit/s and 170 Gbit/s corresponding to 160 Gbit/s + 7% FEC overhead. They are well suited for data modulation and pulse carving in OTDM transmitters and for optical demultiplexing and clock recovery in receivers. The focus of most of the work reviewed is to study transmission beyond the speed of electronic circuits and opto-electronic components in an early stage to evaluate the potential and the impact of ultra-high bit rates in optical networks.

In the future, EA-modulators may enable ultra-high bit rates by direct data-modulation once ultra-high high bit rate electronics will be available. Single channel and DWDM transmission systems at ultra-high bit rates of 80 Gbit/s to 160 Gbit/s might then offer a cost-effective solution for high capacity fiber transmission over short reach up to long-haul distances.

Acknowledgment

This work has partly been supported by the European Commission within the IST project IST-2000-28657 TOPRATE.

References

1. S. Bigo, Y. Frignac, G. Charlet, W. Idler, S. Borne, H. Gross, R. Dischler, W. Poehlmann, P. Tran, C. Simonneau, D. Bayard, G. Veith, A. Jourdan, J. P. Hamaide, "10.2 Tbit/s (256 × 42.7 Gbit/s PDM/WDM) transmission over 100 km TeraLight fiber with 1.28 bit/s/Hz spectral efficiency", OFC 2001 Anaheim, post deadline paper PD25
2. Kiyoshi Fukuchi, Tadashi Kasamatsu, Masao Morie, Risato Ohhira, Toshiharu Ito, Kayato Sekiya, Daisaku Ogasahara, Takashi Ono, "10.92-Tb/s (273 × 40-Gb/s) triple-band/ultra-dense WDM optical-repeatered transmission experiment", OFC 2001 Anaheim, post deadline paper PD24
3. D.D. Marcenac, A.D. Ellis, D.G. Moodie,"80 Gbit/s OTDM using electroabsorption modulators over 100 km", ECOC 1999 Munich, paper WeC4.1
4. T. Yamamoto, E. Yoshida, K.R. Tamura, M. Nakazawa, "Single Channel 640 Gbit/s TDM Transmission over 100 km", ECOC 1999 Munich, paper WeC4.1
5. G. Raybon, B. Mikkelsen, R.-J. Essiambre, J.E. Johnson, K. Dreyer, L.E. Nelson,"100 Gbit/s single-channel transmission over 200 km TrueWave and 160 km conventional fiber with EAM source and demultiplexer", ECOC'99, Nice, paper WeC2.5

6. U. Feiste, R. Ludwig, C. Schubert, J. Berger, C. Schmidt, H.G. Weber, B. Schmauss, A. Munk, B. Buchold, D. Briggmann, F. Kueppers, F. Rumpf, "160 Gbit/s Transmission over 116 km Field-Installed Fiber Using 160 Gbit/s OTDM and 40 Gbit/s ETDM", Proc. OFC 2001, paper ThF3
7. J. Li, J. Hansryd, P.O. Hedekvist, P.A. Andrekson, S.N. Knudsen, "300-Gb/s Eye-Diagram Measurement by Optical Sampling Using Fiber-Based Parametric Amplification", IEEE PTL 13, pp. 987–989, 2001
8. E. Lach, M. Schmidt, K. Schuh B. Junginger, G. Veith, P. Nouchi,"Advanced 160 Gb/s OTDM system based on wavelength transparent 4 × 40 Gb/s ETDM transmitters and receivers", OFC 2002 Anaheim, paper TuA2
9. M. Heid, S. L. Jansen, S. Spälter, E. Meissner, W. Vogt, H. Melchior,"160-Gbit/s demultiplexing to base rates of 10 and 40 Gbit/s with amonolithically integrated SOA-Mach-Zehnder interferometer", ECOC 2002, paper 8.4.3, Copenhagen 2002
10. W.S. Lee, Yanjun Zhu, B. Shaw, D. Watley, C. Scahill, J. Homan, C. Fludger, M. Jones and A. Hadjifotiou, "2.56 Tb/s capacity, 0.8 b/Hz/s DWDM transmission over 120 km NDSF using polarization-bit-interleaved 80 Gb/s OTDM signal, OFC 2001, paper TuU1
11. S. Kawanishi, H. Takara, K. Uchiyama, I. Shake, K. Mori, "3 Tbit/s (160 Gbit/s × 19 ch.) OTDM/WDM Transmission Experiment", Proc. OFC 1999, paper PD1
12. B. Mikkelsen, G. Raybon, B. Zhu, R.-J. Essiambre, P.G. Bernasconi, K. Dreyer, L.W. Stulz, S.N. Knudsen,"High spectral efficiency (0.53 bit/s/Hz) WDM transmission of 160 Gb/s per wavelength over 400 km of fiber", OFC 2001, paper ThF2-1, Anaheim
13. A. Suzuki, X. Wang, T. Hasegawa, Y. Ogawa, S. Arahira, K. Tajima, S. Nakamura, "8 × 160 Gb/s (1.28 Tb/s) DWDM/OTDM unrepeatered transmission over 140 km standard fiber by semiconductor-based devices", ECOC 2003, Rimini, paper Mo3.6.1
14. M. Daikoku, T. Otani, M. Suzuki, "160 Gbit/s 4 WDM dispersion managed soliton transmission over 225 km NZ-DSF", Proc. OECC 2002, paper PD-1-5
15. Y.-J. Chiu, S.Z. Zhang, V. Kaman, J. Piprek, J.E. Bowers, "High-Speed Traveling-Wave Electroabsorption Modulators", Symposium on Radio Frequency Photonic Devices and Systems II, 46th SPIE Annual Meeting, Aug. 2001, San Diego
16. N. Mineo, K. Yamada, K. Nakamura, Y. Shibuya, K. Nagai,"More than 50 GHz Bandwidth Electroabsorption Modulator Module", OECC 2000, paper PD2-7
17. Y.-J. Chiu, H.-F. Chou, V. Kaman, P. Abraham, J. E. Bowers, "High extinction ratio and saturation power travelling wave electroabsorption modulator", IEEE Photon. Technol. Lett., **14**, 792–794 (2002)
18. T. Yamanaka, "Ultrafast electroabsorption modulators with travelling-wave electrodes", Proc. ECOC 2001, pp. 328-331
19. W. Idler, A. Klekamp, R. Dischler, J. Lazaro, A. Konczykowska, "System performance and tolerances of 43 Gb/s ASK and DPSK modulation formats," Proc. ECOC 2003 paper Th2.6.3

20. D.G. Moodie, A.D. Ellis, P.J. Cannard, C.W. Ford, A.H. Barrell, R.T. Moore, S.D. Perrin, R.I. McLaughlin, F. Garcia, "40 Gbit/s modulator with low drive voltage and high optical output power", Proc. ECOC 2001 paper 332
21. J.-L. Augé, M. Cavallari, T. Hadjifotiou, P. Kean, D. Watley, "Comparison between an integrated and discrete transmitter for high line rate OTDM systems", Proc. OFC 2002 paper WF6
22. G. Mohs, C. Fürst, H. Geiger, G. Fischer,"Data encoded pulse source using a single electro-absorption modulator", Proc. ECOC 2000 paper 9.4.7
23. A.T. Clausen, H.N. Poulsen, L.K. Oxenløwe, A.I. Siahlo, J. Seoane, P. Jeppesen, "Pulse source requirements for OTDM systems", Technical Digest IEEE Laser and Electro-Optics Society Annual Meeting, LEOS'03, paper TuY2, 2003
24. B. Mikkelsen, G. Raybon, R.-J. Essiambre, "160 Gb/s transmission systems", Proc. Ecoc 2000, Inv. Paper 6.1.1
25. J. Yu, K. Kojima, N. Chand, M.C. Fischer, R. Espindola, T.G.B. Mason, "160Gb/s single-channel unrepeatured transmission over 200 km of non-zero dispersion shifted fiber", Proc. ECOC 2001 paper PD M.1.10
26. B. Mason, A.Ougazzaden, C.W. Lentz, K.G. Glogovsky, C.L. Reynolds, G.J. Przybylek, R.E. Leibenguth, T.L. Kercher, J.W. Boardman, M.T. Radar, J.M. Geary, F.S. Walters, L.J. Peticolas, J.M. Freund, S.N.G. Chu, A. Sirenko, R.J. Jurchenko, M.S. Hybertsen, L.J.P. Ketelsen, G. Raybon,"40-Gb/s tandem electroabsorption modulator", IEEE Photon. Technol. Lett., **14**, 27–29 (2002)
27. R. Lewén, S. Irmscher, U. Westergren, L. Tylén, U. Eriksson,"Ultra high-speed segmented travelling-wave electroabsortion modulators", Proc. OFC 2003, PD38-1
28. M. J. Guy, S. V. Chernikov, J. R. Taylor, D. G. Moodie and R. Kashyap,"200 fs soliton pulse generation at 10 GHz through the nonlinear compression of transform-limited pulses from an electroabsorption modulator", Electron. Lett., **31**, 740–741 (1995)
29. M. Schmidt, E. Lach, K. Schuh, M. Schilling, P. Sillard and G. Veith, "Unrepeatered 320 Gbit/s (8×40 Gbit/s) OTDM transmission over 80 km TeraLight^{TM}-reverse TeraLight^{TM} fiber link", ECOC 2003, We.4.P.117, Rimini
30. G. Raybon, B. Mikkelsen, R.-J. Essiambre, A.J. Stentz, T.N. Nielsen, D.W. Peckham, L. Hsu, L. Gruner-Nielsen, K. Dreyer, J.E. Johnson,"320 Gbit/s single-channel pseudo-linear transmission over 200 km of nonzero-dispersion fiber", Proc. OFC 2000, paper PD29-1
31. H. Murai, H.T. Yamada, K. Fujii, Y. Ozeki, I. Ogura, T. Ono, H. Yokoyama,"$3 \times$ 80 Gbit/s WDM-transmission over 600 km using mode-locked laser diodes with an 80 Gbit/s OTDM module", Proc. ECOC 2001, Tu.L.2.1
32. H.T. Yamada, H. Murai, K. Fujii,"80-Gbit/s Authentic OTDM MUX Transmitter using Reflective EAMs," Proc. OEC/IOOC 2001 Conference Incorporating ACOFT, pp. 309–310
33. H. Murai, H. T. Yamada, K. Fujii and Y. Ozeki,"Carrier-suppressed Dispersion-managed RZ transmission using novel OTDM techniques with phase alternation", 2001 IEEE/LEOS Summer Topical Meetings, TuC3.2, pp.29–30

34. H. Murai, M. Kagawa, H. Tsuji, K. Fujii, Y. Hashimoto, H. Yokoyama,"Single Channel 160 Gbit/s (40 Gbit/s × 4) 300 km—Transmission Using EA Modulator based—OTDM Module and 40 GHz External—Cavity Mode-locked LD", ECOC 2002, paper 2.1.4, Copenhagen

35. M. Kagawa, H. Murai, H. Tsuji, K. Fujii,"Single Channel 40 Gbit/s-based 160 Gbit/s OTDM Transmission over 180 km of SMF", Proc. OECC 2002, 9B1-2, pp. 20–21

36. H. Murai, M. Kagawa, H. Tsuji, K. Fujii,"Ultra fast optical transmission with EAM-based OTDM techniques", Proc. 10th international workshop on femtosecond technology 2003 paper WC-2

37. M. Schilling, O. Blume, L-H. Nguyen, M. Schmidt, E. Lach,"OTDM Planar Lightwave Components (PLCs) for multiplexing from 40 Gb/s to 80–640 Gb/s", Proc. LEOS 2002 paper ThBB5

38. K. Schuh, M. Schmidt, E. Lach, B. Junginger, A. Klekamp, G. Veith, P. Sillard,"4 × 160 Gbit/s DWDM/OTDM transmission over 3 × 80 km TeraLight™-Reverse TeraLight™-fibre", ECOC 2002, paper 2.1.2, Copenhagen

39. M. Schmidt, K. Schuh, E. Lach, M. Schilling and G. Veith, "8 × 160 Gbit/s (1.28 Tbit/s DWDM transmission with 0.53 bit/s/Hz spectral efficiency using single EA-modulator based RZ pulse source and demux", ECOC 2003, paper Mo3.6.5, Rimini

40. E. Lach, K. Schuh, M. Schmidt, B. Junginger, G. Charlet, P. Pecci, G. Veith,"7 × 170 Gbit/s (160 Gbit/s + FEC overhead) DWDM transmission with 0.53 bit/s/Hz spectral efficiency over long haul distance of Standard SMF", Proc. ECOC 2003 paper PD Th4.3.5

41. D.D. Marcenac, A.D. Ellis and D.G. Moodie,"80 Gbit/s OTDM using electroabsorption modulators", Electron. Lett. **34** (1), 101–103 (1998)

42. A.D. Ellis, J.K. Lucek, D. Pitcher, D.G. Moodie and D. Cotter ,"Full 10 × 10 Gbit/s OTDM data generation and demultiplexing using electroabsorption modulators", Electron. Lett. **34** (18), 1766–1767 (1998)

43. B. Mikkelsen, G. Raybon, R.-J. Essiambre, K. Dreyer, Y. Su, L.E. Nelson, J.E. Johnson, G. Shtengel, A. Bond, D.G. Moodie and A.D. Ellis, "160 Gbit/s single-channel transmission over 300 km nonzero-dispersion fiber with semiconductor based transmitter and demultiplexer", ECOC 1999, postdeadline paper 2-3, Nice

44. B. Mikkelsen, G. Raybon, R.-J. Essiambre, A.J. Stentz, T.N. Nielsen, D.W. Peckham, L. Hsu, L. Gruner-Nielsen, K. Dreyer and J.E. Johnson,"320 Gbit/s single-channel pseudolinear transmission over 200 km nonzero-dispersion fiber", IEEE Photon. Technol. Lett., **12** (10), 1400–1402 (2000)

45. S. Kodama, T. Ito, N. Watanabe, S. Kondo, H. Takeuchi, H. Ito, and T. Ishibashi, "2.3 picoseconds optical gate monolithically integrating photodiode and electroabsorption modulator", Electron. Lett. **37**, 1580–1581 (2001)

46. S. Kodama, T. Yoshimatsu, T. Ito, H. Ito and T. Ishibashi,"160 Gbit/s error-free demultiplexing by ultrafast optical gate monolithically integrating photodiode and electroabsorption modulator", Electron. Lett. **38** (24), 1575–1576 (2002)

47. S. Kodama, T. Yoshimatsu and H. Ito, "320 Gbit/s error-free demultiplexing using ultrafast optical gate monolithically integrating a photodiode and electroabsorption modulator", Electron. Lett. **39** (17), 1269–1270 (2003)

48. S. Kodama, T. Yoshimatsu and H. Ito,"500-Gbit/s demultiplexing operationof monolithic PD-EAM gate", postdeadline paper Th4.2.8, ECOC 2003, Rimini

49. D.T.K. Tong, B. Mikkelsen, G. Raybon, T.N. Nielsen, K.F. Dreyer and J.E. Johnson,"Optoelectronic phase-locked loop with photodetection for clock recovery in high speed optical time-division multiplexed systems" IEEE Photon. Technol. Lett., **12** (8), 1064–1066 (2000)

50. D.T.K. Tong, K.-L. Deng, B. Mikkelsen, G. Raybon, K.F. Dreyer and J.E.Johnson, "160 Gbit/s clock recovery using electroabsorption modulator based phase-locked loop", Electron. Lett., **36** (23), 1951–1952 (2000)

51. C. Boerner, C. Schubert, C. Schmidt, E. Hilliger, V. Marembert, J. Berger, S. Ferber, E. Dietrich, R. Ludwig, B. Schmauss, H.G. Weber, "160 Gbit/s Clock recovery with electro-optical PLL using a bidirectionally operated electroabsorption modulator as phase comparator", Electron. Lett. **39** (14), 1071–1073 (2003)

52. X.S. Yao, L. Maleki,"Optoelectronic Oscillator for Photonic Systems", IEEE J. Quant. Electron., **32** (7), 1141 (July 1996)

53. F. Cisternino, R. Girardi, S. Römisch, R. Calvani, E.Riccardi, P. Garino,"Novel approach to pre-scaled clock recovery in OTDM systems", ECOC 1998, Madrid

54. P.V. Mamyshev, "All-optical data regeneration based on self-phase modulation effect; Proc. ECOC 1998, Madrid, p. 475

55. J-L. Augé, M. Cavallari, M. Jones, P. Kean, D. Watley and A. Hadjifotiou, "Single channel 160 GB/s OTDM propagation over 480 km of standard fiber using a 40 GHz semiconductor mode-locked laser pulse source", OFC 2002, paper TuA3, Anaheim

56. J. Berger, Q. Le, A. Wietfeld, S. Ferber, L. Grüner-Nielsen, B. Schmauss, H.G. Weber, "160 Gbit/s Transmission over Dispersion Managed Fibre Set", ECOC 2003, paper Mo3.6.6, Rimini 2003

57. E. Hilliger, V. Marembert, S. Ferber, M. Kroh, J. Berger, H.G. Weber, B. Schmauss, "AM with Improved Switching Performance by Self Cascading", OFC 2003 paper TuP2, Atlanta 2003

58. H. Murai, K. Masatoshi, H. Tsuji, and K. Fujii,"Single Channel 160 Gbit/s Carrier-Suppressed RZ Transmission over 640 km with EA Modulator based OTDM Module", ECOC 2003, paper Mo.3.6.4, Rimini

59. M. Daikoku, T. Otani and M. Suzuki, "160 Gb/s Four WDM Quasi-linear transmission over 225 km NZ-DSF with 75 km spacing", IEEE Photon. Technol. Lett., **15** (8), 1165–1167 (2003)

60. G. Charlet, S. Lanne, L. Pierre, C. Simonneau, P. Tran, H. Mardoyan, P. Brindel, M. Gorlier, J.-C. Antona, M. Molina, P. Sillard, J. Godin, W. Idler, S. Bigo, "Cost-optimized 6.3 Tbit/s-capacity terrestrial link over 17 × 100 km using Phase-Shaped Binary Transmission in a conventional all-EDFA SMF-based system", OFC 2003, Atlanta, post-deadline paper PD25

61. S. Ferber, R. Ludwig, C. Boerner, A. Wietfeld, B. Schmauss, J. Berger, C. Schubert, G. Unterboersch, H.G. Weber,"Comparison of DPSK and OOK modulation format in 160 Gbit/s transmission system", Electron. Lett., **39** (20), 1458–1459 (2003)

62. A. H. Gnauck, G. Raybon, P.G. Bernasconi, J. Leuthold, C.R. Doerr, L.W. Stulz, "1 Tb/s 6 × 170.6 Gb/s) transmission over 200 km NZDF using OTDM and RZ-DPSK", IEEE Photon. Technol. Lett., **15** (11), 1618–1620 (2003)

63. R. Ludwig, S. Ferber, C. Schubert, C. Boerner, A. Beling, H.-G. Bach, B. Schmauss, A. Wietfeld, J. Berger, C. Schmidt, H.G. Weber, "160 Gbit/s DPSK Transmission over 410 km Dispersion-Managed Fiber", Proc. 8th European Conference on Networks & Optical Communications NOC 2003, Vienna, ISBN: 3-905084-69-4 (AKM-AG Basel)

64. C. Boerner, C. Schubert, C. Schmidt, E. Hilliger, V. Marembert, J. Berger, S. Ferber, E. Dietrich, R. Ludwig, H.G. Weber, B. Schmauss, "160 Gbit/s Clock recovery with electro-optical PLL using a bidirectionally operated electroabsorption modulator as phase comparator", Proc. OFC 2003, Paper FF3

DOI: 10.1007/s10297-005-0037-1
Originally published in J. Opt. Fiber. Commun. Rep. 2, 209–225 (2005)

Ultrafast OTDM transmission using novel fiber devices for pulse compression, shaping, and demultiplexing

T. Yamamoto[1] and M. Nakazawa[2]

[1] NTT Network Innovation Laboratories, NTT Corporation
1-1 Hikari-no-oka, Yokosuka, Kanagawa, 239-0847 Japan
Email: yamamoto.takashi@lab.ntt.co.jp
[2] Research Institute of Electrical Communication, Tohoku University
2-1-1 Katahira, Aoba-ku, Sendai, Miyagi, 980-8577 Japan
Email: nakazawa@riec.tohoku.ac.jp

Abstract. This paper describes key fiber devices that were used to generate and handle femtosecond optical pulses in the 1.28-Tbit/s OTDM transmission experiment.

1. Introduction

Many researchers in the field of photonics technology have devoted themselves to increasing the speed of OTDM signal transmission [1–3]. Femtosecond optical pulses must be used to realize OTDM transmission speeds above 1 terabit/s, because the width of one OTDM signal time slot is less than 1 ps. The highest OTDM transmission speed ever reported is 1.28 Tbit/s [4], where 400 fs signal pulses were transmitted through a 70-km fiber.

This paper describes key fiber devices that were used to generate and handle femtosecond optical pulses in the 1.28-Tbit/s OTDM transmission experiment. Section 2 describes an adiabatic soliton compression technique that employs dispersion-flattened dispersion-decreasing fiber (DF-DDF). The pulse width of an optical signal generated with a mode-locked fiber laser was compressed from 3 ps to 200 fs. The compressed optical pulses usually have unwanted dispersive waves (pedestal components). Section 3 describes a pedestal elimination technique that uses a dispersion-imbalanced nonlinear optical loop mirror (DI-NOLM). An all-optical demultiplexing technique is required in ultrafast OTDM transmission because of the limitation imposed by the speed of electronics. Section 4 describes ultrafast demultiplexing with a nonlinear optical loop mirror (NOLM), where the precise dispersion control of the NOLM fiber is

essential. Section 5 discusses the details of the 1.28-Tbit/s OTDM experiment, which employed a simultaneous third- and fourth-order dispersion compensation technique.

2. Optical Pulse Compression Using Dispersion Decreasing Fiber (DDF)

It is difficult to obtain femtosecond optical pulses with a repetition rate of 10–40 GHz directly from a pulse laser, and so an optical pulse compression technique is indispensable for Tbit/s OTDM transmission. Adiabatic soliton compression in the anomalous dispersion region realized using a dispersion decreasing fiber (DDF) is currently one of the most practical ways of compressing high repetition rate picosecond pulses to femtosecond durations [5,6]. The generated short pulse trains can be applied not only to OTDM signal pulses, but also to all-optical sampling and all-optical switching.

The principle of adiabatic soliton compression can be understood from the following formula, which gives the soliton order parameter N:

$$N^2 = \frac{\gamma P_0 T_0^2}{\mid \beta_2 \mid} = \gamma (P_0 T_0) \frac{T_0}{\mid \beta_2 \mid}, \tag{1}$$

where $\gamma (= n_2 \omega / (c A_{\text{eff}}))$ is a nonlinear parameter, P_0 and T_0 are the peak power and the pulse width of the soliton, and β_2 is the group velocity dispersion. T_0 is related to the full-width at half-maximum (FWHM) $\Delta\tau$ by $\Delta\tau = 1.76 T_0$. We consider the injection of a fundamental soliton pulse with $N = 1$ into a DDF. As the soliton energy is preserved in the DDF, $(P_0 T_0)$ in Eq. (1) is constant. The soliton order N is preserved when the pulse width T_0 decreases as $\mid \beta_2 \mid$ decreases.

One problem with a conventional DDF constructed from step-index fibers is that third-order dispersion can shift the pulse spectrum toward a wavelength regime different from that of the input pulse. Another problem is that the compressed pulse spectrum varies significantly with the input wavelength. Both of these problems are substantially reduced when a dispersion-flattened DDF is used, because it has low third-order dispersion.

Below is a specific description of a pulse compression experiment that used dispersion-flattened DDF [7]. The DDF had a W-shaped core and a length of 1106 m. The measured dispersion of the DDF is shown in Fig. 1. D_{total} is the total dispersion, and D_{out} is the dispersion of a 100-m segment cut from the output end. D_{out} had the most important effect on the compressed pulse, and for the dispersion-flattened DDF, D_{out} had a slope that changed from 1.4×10^{-2} to 2×10^{-3} ps/nm^2/km over a wavelength range of 1530–1565 nm. The changing slope indicates that the fourth-order dispersion is -3.6×10^{-4} ps/nm^3/km. The DDF had a mode field diameter of approximately 6 μm. The seed pulses were generated from a 10-GHz regeneratively mode-locked fiber laser emitting transform-limited pulses with a pulse width of 3.0–3.6 ps over a wavelength range of 1533–1565 nm. The detail of the regeneratively mode-locked fiber laser is certainly described in "Ultrafast mode-locked fiber laser for high-speed OTDM transmission and related topics" by M. Nakazawa (DOI: 10.1007/s10297-004-0029-6) in this publication. The pulses were amplified to an average power of more than 140 mW using an erbium-doped fiber amplifier (EDFA) and were launched into the DDF. Figure 2 shows the output spectra from the dispersion-flattened DDF as the input wavelength λ_i was varied from 1533 to 1565 nm. The output

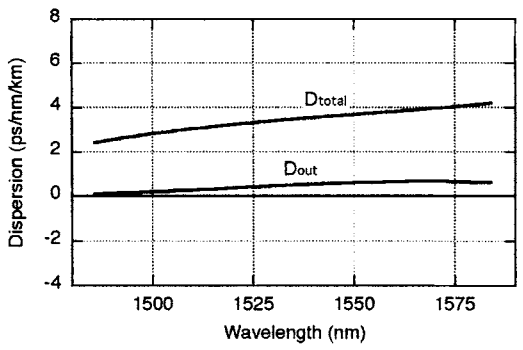

Fig. 1. Dispersion characteristics of dispersion-flattened DDF.

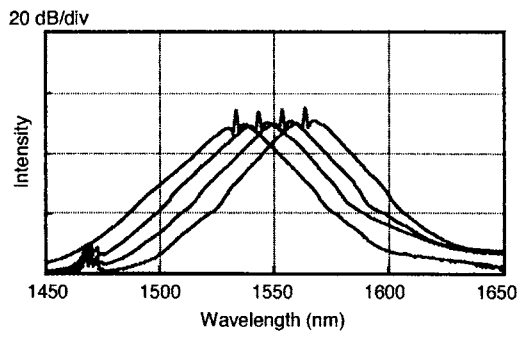

Fig. 2. Optical spectra of the pulse train at the output of the dispersion-flattened DDF for different wavelength settings of the pulse train.

power was between 51 and 55 mW. In contrast to results obtained for conventional DDF, similar and symmetrically broadened spectra are obtained over the entire input wavelength range as the result of the small third-order dispersion. Figure 3 shows the compressed pulse width as a function of output power for an input wavelength of 1553.5 nm. The pulse narrowing was ceased at approximately 100 fs. The higher order dispersion of the DDF is expected to be the main limit to further compression. As a dispersion-flattened DDF has lower third-order dispersion than a conventional DDF, it can realize a smaller pulse width. The inset in Fig. 3 shows an autocorrelation waveform of an optical pulse compressed by using the dispersion-flattened DDF. The peak-to-pedestal ratio (PPR) was greater than 20 dB.

3. Optical Pulse Shaping Using Dispersion Imbalanced Nonlinear Optical Loop Mirror (DI-NOLM)

A problem with optical pulse compression using DDF is that non-ideal adiabatic compression in the DDF causes the compressed pulse to have a broad pedestal [8]. The

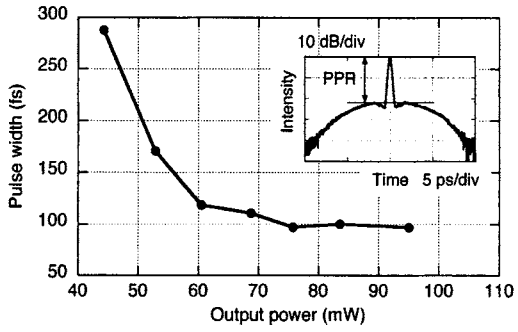

Fig. 3. Compressed pulse width as a function of output power. The inset shows an autocorrelation waveform of a compressed pulse.

pedestal of the optical signal pulse causes crosstalk in OTDM systems. Here we describe a dispersion-imbalanced nonlinear optical loop mirror (DI-NOLM), which is a nonlinear optical device for removing the pedestal of a broad bandwidth pulse train [9].

Figure 4 shows the configuration of a nonlinear optical loop mirror (NOLM). A NOLM is an all-fiber Sagnac interferometer constructed by connecting a long fiber to the two output ports of a fiber coupler to form a loop [10]. An optical wave coupled into the NOLM is divided into two waves at the coupler. The two optical waves counter-propagate in the fiber loop and recombine at the coupler. Both optical waves have a nonlinear phase shift in the fiber loop. The transmittance T of the NOLM is determined by the phase shift difference between the two counter-propagating optical waves and it is given by

$$T \equiv P_{\mathrm{trs}}/P_{\mathrm{in}} = 1 - 4\alpha(1-\alpha)\cos^2[(1-2\alpha)\gamma P_{\mathrm{in}} L/2], \tag{2}$$

where P_{in} and P_{trs} are the input power and transmitted power, respectively, L is the fiber loop length, and α is the splitting ratio of the coupler. When $\alpha = 1/2$, the phase shift between the two optical waves is balanced and T becomes zero. In this case, the optical signal launched into the coupler is totally reflected for any input power. The imbalance between the phase shifts of the two optical waves is realized by setting α so that it does not equal 1/2. In this case, the power difference between the two counter-propagating optical waves leads to a phase shift difference, and part of the injected optical wave is transmitted through the NOLM. Equation (2) shows that the transmittance of the NOLM is a function of the input power, that is, the NOLM acts as a nonlinear optical switch. Self-switching to the transmission port of the coupler is realized for a high-power optical signal while reflection to the input port occurs at low power levels. The minimum input power for 100% transmission is $P_{\mathrm{in}} = \pi/\{\mid 1-2\alpha \mid \gamma L\}$. From Eq. (2), the transmittance at $P_{\mathrm{in}} \to 0$ is given by

$$T_{P_{\mathrm{in}}\to 0} = 4(\alpha - 1/2)^2. \tag{3}$$

Equation (3) shows that the transmittance at a low input power increases for a large deviation of α from 1/2, which leads to degradation of the extinction ratio during

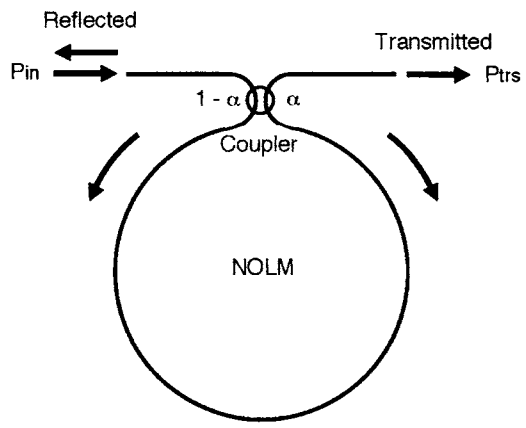

Fig. 4. Configuration of NOLM.

switching. Although the extinction ratio is improved by setting α close to 1/2, in this case, switching requires a large input power.

Figure 5 shows the configuration of a DI-NOLM. The NOLM shown in Fig. 4 uses the splitting ratio of the fiber coupler to generate an imbalance in the phase shift between the clockwise and counterclockwise optical waves, while the DI-NOLM generates an imbalance with the dispersion in the fiber loop. The DI-NOLM consists of a 50/50 fiber coupler, an optical fiber loop, and dispersion compensation fiber (DCF). A fiber with a large dispersion is inserted at an asymmetrical position in the optical fiber loop with a low dispersion. An optical pulse injected into a port of the fiber coupler is divided into two equal pulse components, which are transmitted through the optical loop. One of the pulses, which is first transmitted through the large dispersion fiber, is broadened and the peak power becomes low. In contrast, the other pulse is transmitted through a large proportion of the loop with its peak power intact because the pulse width is not broadened. This causes an imbalance in the phase shift at the pulse center between the two counter-propagating pulse components. When the phase shift difference after a round trip becomes π, the center part of the pulse transmits through the DI-NOLM. The dispersion induced pulse broadening in the loop is compensated for by the DCF placed at the loop output. On the other hand, the pedestal power of the optical pulse in the loop remains largely unaffected by the dispersion of the loop fiber and the pedestal is reflected by the DI-NOLM. By using these characteristics of the DI-NOLM, we can eliminate the optical pulse pedestal generated after the pulse compression. Thus the DI-NOLM realizes a high quality optical pulse with a high extinction ratio, which is vital for OTDM signal pulse applications.

An experimental result for pedestal reduction using a DI-NOLM [11] is described below. In this experiment, the fiber loop of the DI-NOLM consisted of a 1-m-long single-mode fiber (SMF) with a dispersion of 17.3 ps/nm/km and a 100-m-long dispersion-flattened fiber (DFF). Large dispersion was provided by the SMF and a nonlinear phase shift was provided by the DFF. The 50/50 coupler was constructed from dispersion-shifted fibers (DSF). A 110-cm-long segment of DCF with a disper-

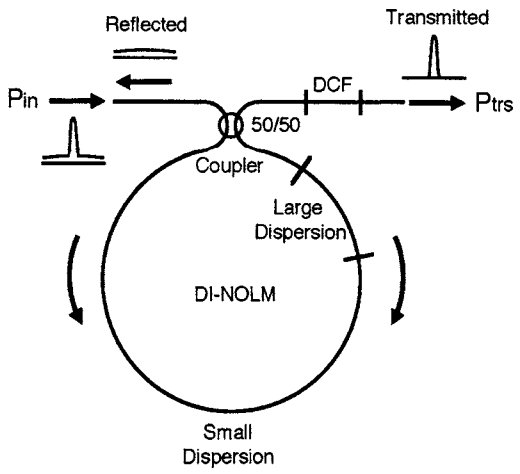

Fig. 5. Configuration of DI-NOLM.

sion of approximately −50 ps/nm/km was placed at the output of the loop for chirp compensation. An optical pulse train with a repetition rate of 10 GHz was generated using a regeneratively mode-locked fiber laser and a dispersion decreasing fiber as described in section 2. Figure 6 shows the autocorrelation waveforms of 10 GHz optical pulses before and after the DI-NOLM. The optical pulse before the DI-NOLM had a broad pedestal, which existed at 22 dB down from the peak. The extinction ratio of the optical pulse was improved after the DI-NOLM by reducing the pedestal by more than 15 dB. The optical spectra measured before and after the DI-NOLM are shown in the inset in Fig. 6. By reducing the pedestal, the large spike observed at the center of the spectrum was almost completely removed. As the loop fiber mainly consists of DFF, the DI-NOLM operates effectively over a broad input wavelength range of over 32 nm.

4. Demultiplexing Ultrafast OTDM signals Using a Nonlinear Optical Loop Mirror (NOLM)

The demultiplexing of individual channels from an OTDM signal after transmission is an indispensable procedure for an OTDM system. When the OTDM signal speed is greater than the maximum speed of the electronic circuit, an all-optical demultiplexing technique must be employed. The nonlinearity of optical fibers is widely utilized in all-optical demultiplexing techniques. An optical pulse train, which is synchronized with a specific channel of the OTDM signal, is injected into the optical fiber with the OTDM signal. The phase or wavelength of the channel is changed by the nonlinear interaction in the fiber, and the channel is distinguished from the others. The demultiplexing of a 500 Gbit/s OTDM signal using fiber four-wave mixing has been reported [12]. A nonlinear optical loop mirror (NOLM) controlled by an ultra short pulse is another promising demultiplexing technique [13–16]. As described in section 3, the NOLM acts

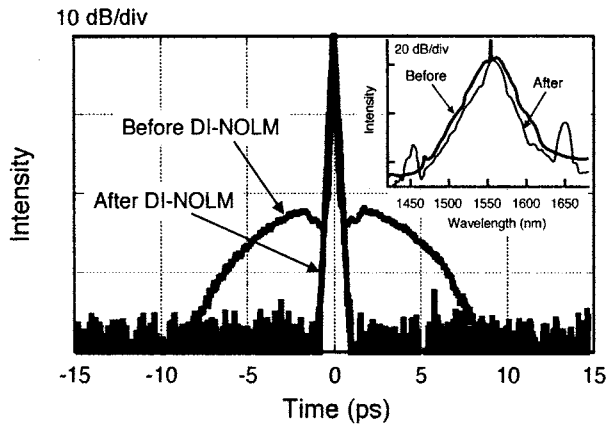

Fig. 6. Autocorrelation waveforms of a 10 GHz optical pulse before and after the DI-NOLM. The inset shows corresponding optical spectra.

as a nonlinear optical switch, which transmits only the high intensity part of an optical pulse. The transmittance is determined by the phase difference between the two lights transmitting through the loop fiber in clockwise and counter-clockwise directions. The phase difference is generated by the self phase modulation (SPM) in the loop fiber. The NOLM can be applied as a demultiplexer by utilizing the cross phase modulation (XPM) effect in the loop fiber. Figure 7 is a schematic diagram of the NOLM that acts as a demultiplexer. The NOLM consists of a 50/50 fiber coupler and an optical fiber loop. A fiber coupler is inserted in the fiber loop to couple a control pulse, which is synchronized with one channel of the OTDM signal. The control pulse has a different wavelength from the OTDM signal. The phase of the signal pulse propagating in the loop together with the control pulse is changed by cross phase modulation. When the phase difference between the clockwise and counter-clockwise signal reaches π, the channel transmits through the NOLM, while the other channels are reflected. The control pulse is removed at an optical filter. Thus, the OTDM signal is demultiplexed.

The maximum bit-rate for demultiplexing using a NOLM is determined by the pulse width of the control pulse and the walk-off between the signal and control pulses in the NOLM fiber. The walk-off is caused by the chromatic dispersion of the loop fiber. Even when the control pulse width is sufficiently shorter than one time slot of the OTDM signal, the walk-off causes a serious unwanted overlap between the signal and the control pulses, which makes it difficult to extract only one channel of the OTDM signal. The walk-off can be reduced by shortening the length of the NOLM. However, in this case, the power for NOLM switching, which generates a nonlinear phase change of π, has to be increased. Therefore, in order to realize efficient switching with a large extinction ratio, we must prepare a loop of sufficient length that can also reduce the switching power. Figure 8 is a schematic diagram of a NOLM demultiplexer that meets the requirements for reduced walk-off and sufficient loop length. The fiber loop is constructed by connecting multiple short fiber sections so that the sign of the

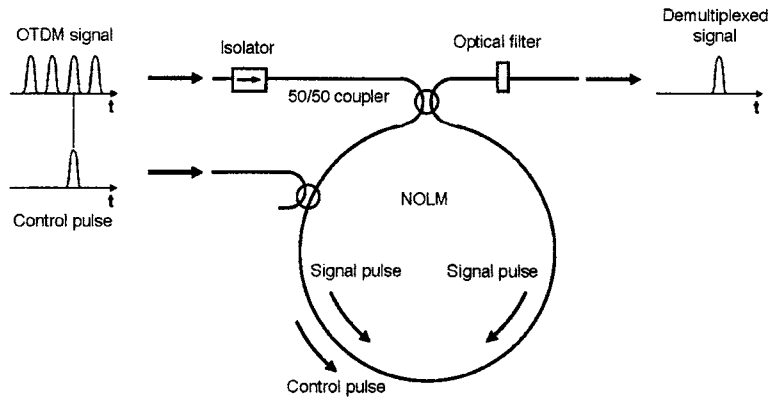

Fig. 7. Demultiplexing of an OTDM signal using a NOLM.

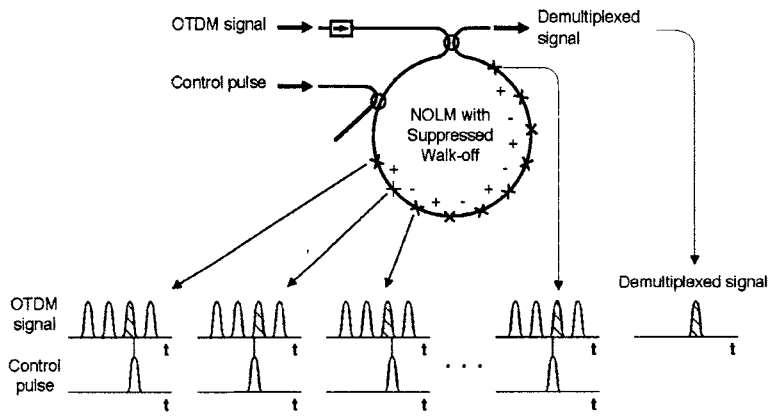

Fig. 8. Configuration of a NOLM with suppressed walk-off.

walk-off alternates along the NOLM. With this arrangement, the control pulse does not interact with the adjacent channels of the OTDM signals.

The following describes a demultiplexing experiment [17], where a 640-Gbit/s OTDM signal was demultiplexed down to 10 Gbit/s using a walk-off reduced NOLM. The NOLM had a loop length of 450 m consisting of nine 50-m-long sections of DFF. The group delay characteristics of many 50 m DFFs were measured and nine fibers whose walk-offs were within $\pm$ 400 fs were selected. The nine DFFs were connected so that the sign of the walk-off alternated (from $-$ to $+$, from $+$ to $-$) along the NOLM within approximately $\pm$ 400 fs. Figure 9 shows the group delay characteristics of the nine DFFs (thin lines) and the 450-m NOLM (thick line). The group delay is plotted to zero at the control pulse wavelength. Although the group delay of each DFF ranged from -330 to $+280$ fs, the absolute value of the total walk-off of the NOLM was suppressed to much less than 100 fs. As the pulse separation of the 640-Gbit/s OTDM

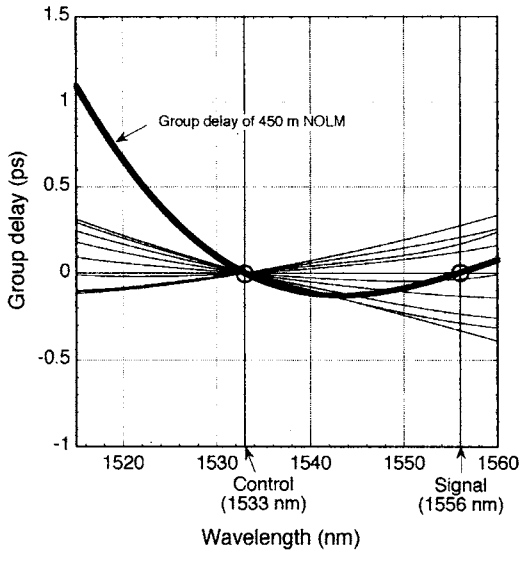

Fig. 9. Group delay characteristics of nine DFFs (thin lines) and the whole 450-m-long NOLM (thick line).

signal was 1.56 ps, the walk-off in this NOLM was negligible. The chromatic dispersion of the whole NOLM fiber at the signal ($\lambda = 1556$ nm) and control pulse ($\lambda = 1533$ nm) wavelengths was as small as $+0.017$ and -0.028 ps/km/nm, respectively. This means that the pulse broadening of the signal and control pulses caused by the dispersion over the 450-m loop length was also negligible. Figures 10(a),(b) show the experimentally obtained pulse waveforms of a 640 Gbit/s OTDM signal and a demultiplexed 10-Gbit/s signal, respectively. The pulse widths of the 640-Gbit/s OTDM signal and the 10-GHz control pulses were 400 fs and 1.1 ps, respectively. The pulse width of the demultiplexed signal was broadened to approximately 600 fs due to optical filtering. By using the walk-off reduced NOLM, the power of the adjacent channels was almost completely suppressed and demultiplexing with a high extinction ratio was realized.

5. Terabit/s OTDM Transmission Experiment

A 1.28 Tbit/s–70 km OTDM signal transmission experiment [4] was successfully performed by adopting the femtosecond pulse generation technique and the ultrafast demultiplexing technique described in the previous sections. This section provides the details of this experiment including higher order dispersion compensation technique.

In this experiment, a 380-fs signal pulse was transmitted through a 70-km transmission line consisting of a 40-km SMF, a 5-km DSF, and a 25-km reverse dispersion fiber (RDF) [18]. The dispersion and dispersion slope of the RDF had opposite signs and nearly the same magnitudes as those of the SMF. As the pulse waveform distortions caused by the third- and fourth-order dispersion are inversely proportional

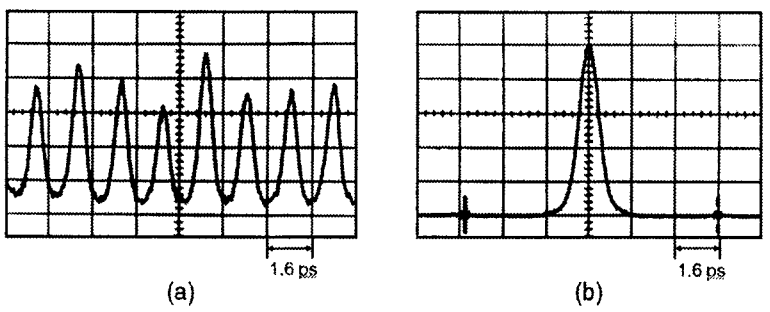

Fig. 10. Pulse waveforms. (a) Pseudorandom 640 Gbit/s OTDM signal (crosscorrelation). (b) Demultiplexed 10 Gbit/s signal (autocorrelation).

to the third- and fourth- power of the pulse width, a higher order dispersion compensation technique is essential for femtosecond pulse transmission. The second- and third-order dispersion can be compensated for simultaneously by using a combination of SMF, DSF, and RDF. However, this method cannot be used to compensate simultaneously for second-, third-, and fourth-order dispersion because the fourth-order dispersion ($d^2D/d\lambda^2$) of these fibers has the same sign. Pelusi et al. demonstrated that the fourth-order dispersion of the transmission fiber could be compensated for by applying excess second-order dispersion and cosine phase modulation to the pulses [19]. The detail of the higher-order dispersion compensation technique is certainly described in "Higher-order dispersion compensation using phase modulators" by M. D. Pelusi and A. Suzuki (DOI:10.1007/s10297-004-0023-z) in this publication. In the 1.28 Tbit/s–70 km transmission experiment, the simultaneous compensation of third- and fourth-order dispersion was realized by using the phase modulation technique [20]. We describe this technique in detail below.

The distortion of pulse waveforms by dispersion results from the phase shift that affects each spectral component of the pulse. The frequency dependence of the phase shift (in radians) is expressed in a Taylor series as

$$\beta L = \beta_0 L + \beta_1 L(\omega - \omega_0) + \frac{\beta_2 L}{2}(\omega - \omega_0)^2 + \frac{\beta_3 L}{6}(\omega - \omega_0)^3 + \frac{\beta_4 L}{24}(\omega - \omega_0)^4 + \cdots, \tag{4}$$

where L is the fiber length and ω_0 is the center frequency. Second-, third-, and fourth-order dispersion arise from terms including β_2, β_3, and β_4, respectively. Figure 11 shows the calculated phase shift and pulse waveform distortion caused by third- and fourth-order dispersion. The parameters $\beta_3 (= 4.0 \times 10^{-4}$ ps^3/km) and $\beta_4 (= 8.6 \times 10^{-4}$ ps^4/km) used in the calculation are the same values as those for the entire transmission line of the 1.28-Tbit/s OTDM transmission experiment, which includes a 70-km transmission fiber, three EDFAs, and fibers applying excess second-order dispersion for higher-order dispersion compensation. The cubic curve shown in Fig. 11(a) is the angular frequency dependence of the phase shift caused by the third-order dispersion. This phase shift affects each spectral component of the 380-fs signal pulse, and distorts the waveform as shown in Fig. 11(b). The pulse waveform is distorted asymmetrically by the third-order dispersion, an oscillating tail is generated,

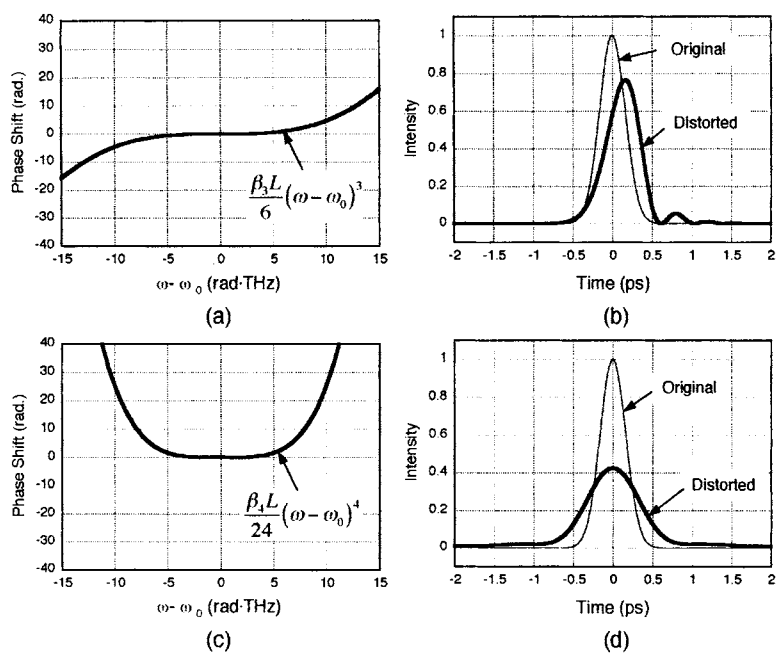

Fig. 11. Phase shift and waveform distortion caused by higher order dispersion. (a) Phase shift caused by third-order dispersion. (b) Waveform distortion caused by third-order dispersion. (c) Phase shift caused by fourth-order dispersion. (d) Waveform distortion caused by fourth-order dispersion.

and the pulse width is broadened to 490 fs. The quartic curve shown in Fig. 11(c) is the phase shift caused by the fourth-order dispersion. As shown in Fig. 11(d), the fourth-order dispersion broadens the pulse waveform symmetrically, generates a long pedestal on both sides, and broadens the pulse width to 760 fs. These pulse distortions leads to crosstalk in the OTDM transmission.

Figure 12 shows the principle of the simultaneous compensation of third- and fourth-order dispersion using phase modulation. The vertical axis shows the phase. The thin solid line shows the sum of the phase shifts caused by second-, third-, and fourth-order dispersion. When we add an appropriate sinusoidal phase modulation (dotted line) to the phase shift curve, an approximately linear region appears (thick solid line). In this case, we intentionally applied the second-order dispersion so that the sum of these phase shifts becomes linear. As the linear phase shift does not affect the pulse waveform, we can compensate for the distortion caused by the second-, third-, and fourth-order dispersion. Figure 13 shows the compensated pulse waveform. The oscillating tail and the long pedestal are significantly reduced, and there is less pulse broadening (the pulse width is 410 fs). The key to this compensation technique is to apply a sinusoidal phase modulation in the spectral domain for each signal pulse.

Figure 14 shows the method for realizing the spectral-domain modulation. The unit used to achieve this consisted of an SMF, a $LiNbO_3$ phase modulator, and an RDF.

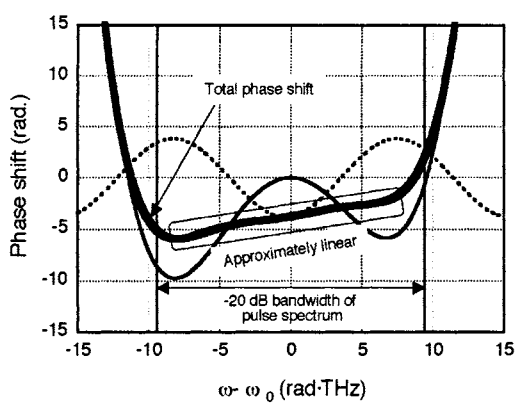

Fig. 12. Phase shift caused by the sum of the second-, third-, and fourth-order dispersion (thin solid line), the optimized sinusoidal phase modulation (dotted line), and the sum of these phase shifts (thick solid line).

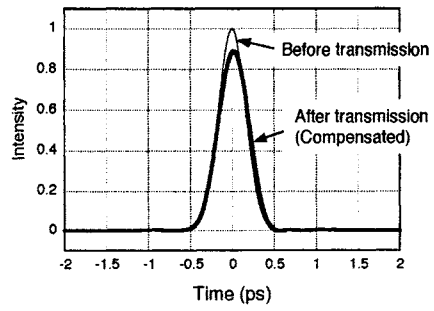

Fig. 13. Calculated pulse waveform before and after transmission with higher order dispersion compensation.

The 276-m SMF broadened the pulse width of the injected 10-Gbit/s signal pulse from 380 fs to 46 ps, which resulted in a linear chirp. This linear chirp meant that the angular frequency of the pulse spectrum became a linear function of time at the input of the phase modulator. Then a 10-GHz sinusoidal phase modulation was applied to the broadened pulse using a phase modulator. As the signal pulse was linearly chirped, a sinusoidal phase modulation applied in the time domain also became a sinusoidal phase modulation in the spectral domain. The modulation index was set at 1.21π. A 139-m-long RDF was installed after the phase modulator to adjust the second-order dispersion of the entire transmission line. This set up enabled us to pre-chirp the signal pulse to compensate for the third- and fourth-order dispersion of the transmission line.

Figure 15 shows the entire experimental setup for the 1.28 Tbit/s–70 km OTDM transmission experiment. The setup consisted of a 10-Gbit/s femtosecond signal pulse generator, a pre-chirping unit for higher order dispersion compensation, a 10-Gbit/s

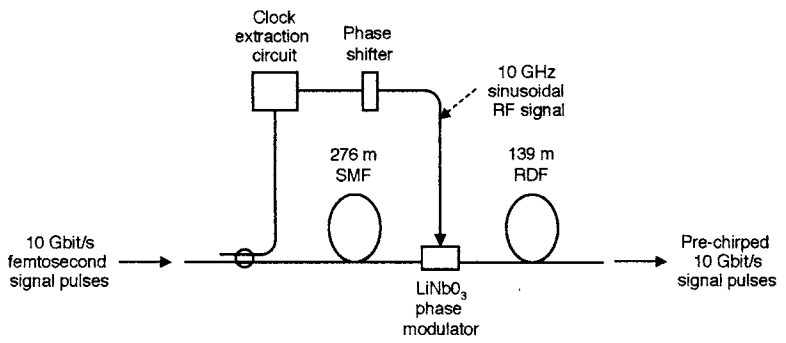

Fig. 14. Experimental setup for the third- and fourth-order dispersion-compensation scheme.

to 1.28-Tbit/s multiplexer, a 70-km transmission line, and a 1.28-Tbit/s to 10-Gbit/s demultiplexer. In the signal pulse generator, a 3-ps, 10-GHz signal pulse train was generated by using a regeneratively modelocked fiber laser operating at 1544 nm. The optical pulse train was modulated at 10 Gbit/s with a PRBS of $2^{15} - 1$ by a $LiNbO_3$ intensity modulator. Then the signal pulses were amplified using an EDFA and coupled into the 1100-m-long dispersion-flattened dispersion-decreasing fiber (DF-DDF) described in section 2. After the pulse was compressed to less than 200 fs, the signal was coupled into the dispersion imbalanced nonlinear optical loop mirror (DI-NOLM) described in section 3 to reduce the pedestal of the signal pulse. The pulse width at the DI-NOLM output was 200 fs and the peak-to-pedestal ratio was larger than 30 dB. For the 1.28-Tbit/s OTDM transmission, the signal pulse width was broadened to an optimized value of 380 fs by using an optical filter with a bandwidth of 15 nm.

A pre-chirping unit for higher order dispersion compensation was installed in front of the time division multiplexer. The pre-chirped 10 Gbit/s signal was optically multiplexed up to 640 Gbit/s in the time division using a PLC. Then the signal was polarization multiplexed up to 1.28 Tbit/s using two polarization beam splitters and an optical delay. After amplification by an EDFA, the 1.28-Tbit/s signal was coupled into the 70-km transmission line. Figure 15(b) shows the experimental set up we used for demultiplexing. First, a transmitted 1.28-Tbit/s signal was polarization demultiplexed to 640 Gbit/s using a polarization beam splitter. Then, the signal was demultiplexed to 10-Gbit/s using the walk-off reduced NOLM described in section 4. A 10-GHz control pulse train was generated using a phase-locked loop (PLL) operated mode-locked fiber laser. The oscillation wavelength and the pulse width of the control pulse were 1533 nm and 1.1 ps, respectively. To obtain a 10-GHz clock to drive the PLL fiber laser, a 10-GHz clock light, which was synchronized with the original 10 Gbit/s signal, was transmitted through the 70 km fiber with the 1.28-Tbit/s signal. The clock light was generated by intensity modulating a 1542-nm CW light with the same 10-GHz clock that was used for the pre-chirping unit. After the transmission, the clock light was optically separated from the signal light using optical filters and was injected into the clock extraction circuit.

The bit error rate (BER) was measured for 128 channel signals after the demultiplexing. A BER of 1×10^{-9} was achieved for all of the channels at a received

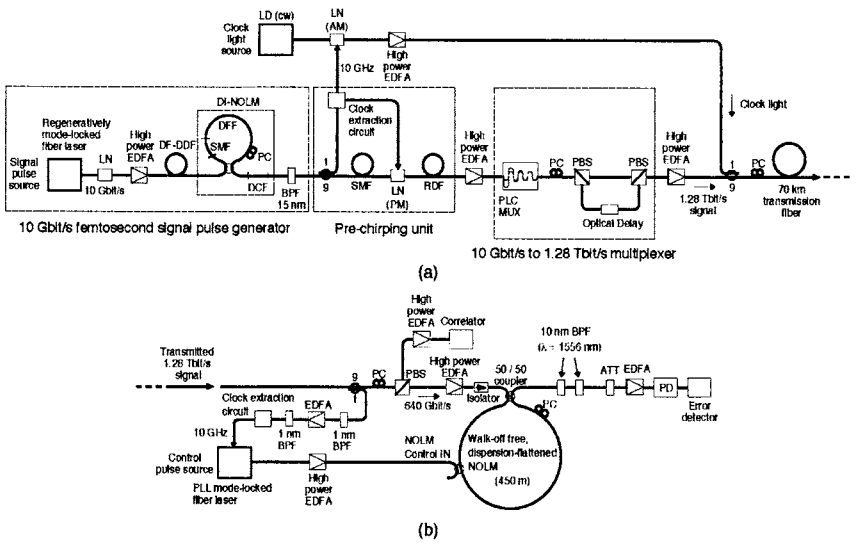

Fig. 15. Experimental setup for 1.28 Tbit/s–70 km OTDM transmission. (a) Configuration for the generation of 1.28 Tbit/s OTDM signals, for pre-chirping, and a 70 km transmission line. (b) Configuration for the demultiplexing of 1.28 Tbit/s signals to 10 Gbit/s.

power of more than −21 dBm. Figures 16 (a),(b) show the measured autocorrelation waveforms of a single optical pulse before pre-chirping and after a 70-km transmission, respectively. The pulse width after transmission was 400 fs, that is, the pulse waveform distortion caused by the dispersion and higher order dispersion of the transmission fiber was sufficiently suppressed and the broadening was as small as 20 fs. Figures 17(a)–(d) show the input and output data patterns. Figure 17(a) shows the signal waveform of the 1.28-Tbit/s OTDM signal before transmission. The signal waveform was distorted due to the pre-chirping that was used to compensate for the higher order dispersion. A clear 1.28-Tbit/s signal waveform was obtained after the transmission as shown in Fig. 17(b). Figures 17(c),(d) show the two 640-Gbit/s OTDM signals separated using a polarization beam splitter.

Summary

This paper described key technologies that have enabled us to realize the first terabit/s OTDM transmission utilizing femtosecond optical pulses, namely the generation of pedestal-free femtosecond pulses, the compensation of higher-order dispersion up to fourth-order dispersion, and ultrafast demultiplexing using a nonlinear optical loop mirror. These technologies are expected to play an important role in the handling of ultrashort pulse trains for high-speed signal processing and in enabling us to realize a high-speed optical network.

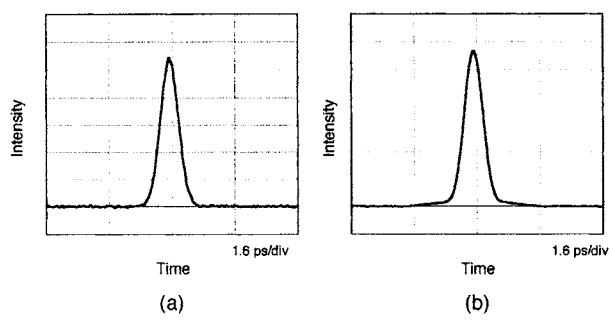

Fig. 16. Autocorrelation pulse waveforms of the signal pulse. (a) Before transmission (before pre-chirping). (b) After 70 km transmission.

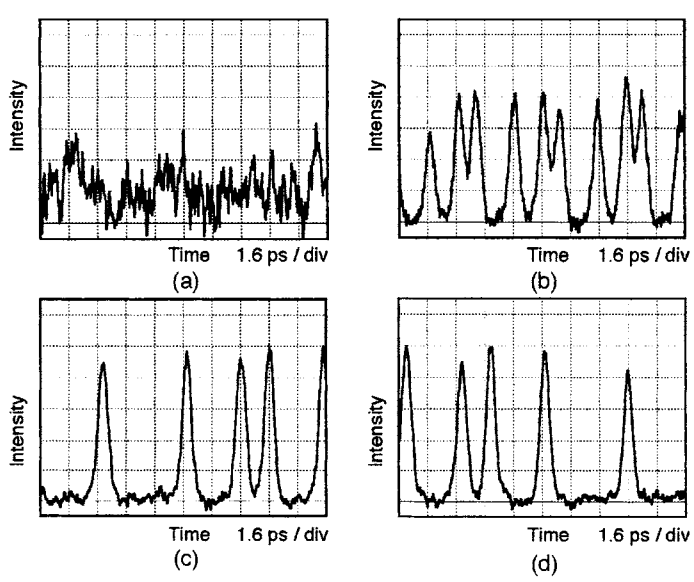

Fig. 17. Cross correlation pulse waveforms of the signal pulse for a fixed pattern. (a) Pulse waveform of 1.28 Tbit/s signal before transmission (after pre-chirping). (b) Pulse waveform of 1.28 Tbit/s signal after 70 km transmission. (c) and (d) Pulse waveforms of 640 Gbit/s signal after polarization demultiplexing.

References

1. S. Kawanishi, H. Takara, T. Morioka, O. Kamatani, K. Takiguchi, T, Kitoh, and M. Saruwatari, "Single channel 400 Gbit/s time-division-multiplexed transmission of 0.98 ps pulses over 40 km employing dispersion slope compensation", Electron. Lett., **32**, 916 (1996).
2. S. Diez, R. Ludwig and H. G. Weber, "All-optical switch for TDM and WDM/TDM systems demonstrated in a 640 Gbit/s demultiplexing experiment", Electron. Lett., **34**, 803 (1998).

3. B. Mikkelsen, G. Raybon, R.-J. Essiambre, A. J. Stentz, T. N. Nielsen, D. W. Peckham, L. Hsu, L. Gruner-Nielsen, K. Dreyer, and J. E. Johnson, "320-Gb/s Single-Channel Pseudo-linear Transmission over 200 km of Nonzero-Dispersion Fiber", IEEE Photon. Tech. Lett., **12**, 1400 (2000).
4. M. Nakazawa, T. Yamamoto and K. R. Tamura, "1.28 Tbit/s–70 km OTDM transmission using third-and fourth-order simultaneous dispersion compensation with a phase modulator", Electron. Lett., **36**, 2027 (2000).
5. S. V. Chernikov and P. V. Mamyshev, "Femtosecond soliton propagation in fibers with slowly decreasing dispersion," J. Opt. Soc. Amer. B, **8**, 1633 (1991).
6. M. Nakazawa, E. Yoshida, K. Kubota, and Y. Kimura, Generation of a 170 fs, 10 GHz transform-limited pulse train at 1.55 m using a dispersion-decreasing, erbium-doped active soliton compressor", Electron. Lett., **30**, 2038 (1994).
7. K. R. Tamura and M. Nakazawa, "Femtosecond Soliton Generation over a 32-nm Wavelength Range Using a Dispersion-Flattened Dispersion-Decreasing Fiber", IEEE Photon. Tech. Lett., **11**, 319 (1999).
8. K. Tamura, E. Yoshida, E. Yamada, and M. Nakazawa,: "Generation of a 0.5 W average power train of femtosecond pulses at 10 GHz in the 1.55 m region", Electron. Lett., **32**, 835 (1996).
9. W. S. Wong, S. Namiki, M. Margalit, H. A. Haus, and E. P. Ippen, "Self-switching of optical pulses in dispersion-imbalanced nonlinear loop mirrors, Opt. Lett., **22**, 1150 (1997).
10. N. J. Doran and D. Wood, "Nonlinear-optical loop mirror", Opt. Lett., **13**, 56 (1988).
11. K. R. Tamura and M. Nakazawa, "Spectral-smoothing and pedestal reduction of wavelength tunable quasi-adiabatically compressed femtosecond solitons using a dispersion-flattened dispersion-imbalanced loop mirror", IEEE Photon. Tech. Lett., **11**, 230 (1999).
12. T. Morioka, H. Takara, S. Kawanishi, T. Kitoh, and M. Saruwatari, "Error-free 500 Gbit/s all-optical demultiplexing using low-noise, low-jitter supercontinuum short pulses", Electron. Lett., **32**, 833 (1996).
13. K. J. Blow, N. J. Doran and B. P. Nelson, "Demonstration of the nonlinear fibre loop mirror as an ultrafast all-optical demultiplexer", Electron. Lett., **26**, 962 (1990).
14. P. A. Andrekson, N. A. Olsson, J. R. Simpson, D. J. Digiovanni, P. A. Morton, T. Tanbun-Ek, R. A. Logan and K. W. Wecht, "64 Gb/s all-optical demultiplexing with the nonlinear optical-loop mirror", IEEE Photon. Tech. Lett., **4**, 644 (1992).
15. E. Yamada, K. Suzuki and M. Nakazawa, "Subpicosecond optical demultiplexing at 10 GHz with zero-dispersion, dispersion-flatted, nonlinear fibre loop mirror controlled by 500 fs gain-switched laser diode", Electron. Lett., **30**, 1966 (1994).
16. K. Uchiyama, H. Takara. T. Morioka, S. Kawanishi and M. Saruwatari, "100 Gbit/s multiple-channel output all-optical demultiplexing based on TDM-WDM conversion in a nonlinear optical loop mirror", Electron. Lett., **32**, 1989 (1996).
17. T. Yamamoto, E. Yoshida, and M. Nakazawa, "Ultrafast nonlinear optical loop mirror for demultiplexing 640 Gbit/s TDM signals, Electron. Lett., **34**, 1013 (1998).
18. K. Mukasa, Y. Akasaka, Y. Suzuki, and T. Kamiya, "Novel network fiber to manage dispersion at 1.55 m with combination of 1.3 m zero dispersion Single-Mode fiber", Proc. 23rd European Conference on Optical Communication, UK, Sept. 1997, p. 127.
19. M. D. Pelusi, X. Wang, F. Futami, K. Kikuchi, and A. Suzuki, "Fourth-order dispersion compensation for 250-fs pulse transmission over 139-km optical fiber", IEEE Photon. Tech. Lett., **12**, 795 (2000).

20. T. Yamamoto and M. Nakazawa, "Third- and fourth-order active dispersion compensation with a phase modulator in a terabit-per-second optical time-division multiplexed transmission", Opt. Lett., **26**, 647 (2001).

DOI: 10.1007/s10297-005-0051-3
Originally published in J. Opt. Fiber. Commun. Rep. 4, 14–40 (2007)

Ultrafast optical technologies for large-capacity TDM/WDM photonic networks

Toshio Morioka

NTT Network Innovation Laboratories, NTT Corporation
1-1 Hikari-no-oka, Yokosuka, Kanagawa, 239-0847, Japan
Email: morioka.toshio@lab.ntt.co.jp; tmorioka@nict.go.jp

Abstract. As the Internet data traffic increases explosively, the optical networks will evolve into "photonic networks", in which "wavelength" label is used to route large-capacity optical signals at optical path cross connect (OPXCs) nodes. [34] Further development of ultrafast all-optical processing technologies enables us to further upgrade the photonic networks into those with much more flexibility and higher transparency, where ultrafast optical signals of any bit rates (2.5, 10, 40, 100, 160 G/ch) and frame/modulation formats (GbE, 10 GbE, SDH, OTN/ NRZ, RZ, CS-RZ, RZ-DPSK, etc.) are processed and transmitted all-optically without optical-electrical-optical (O-E-O) conversion from end-to-end.

1. Introduction

There have been basically four research and development directions in TDM/WDM technologies which have been conducted for the past decade as shown in Fig. 1, namely, 10-Gbit/s-based WDM for as many as 1000 ch systems [74], 40-Gbit/s-based ETDM/WDM for >10 Tbit/s systems, 160-Gbit/s-based OTDM/WDM, and single-channel OTDM for Tbit/s TDM systems. The last two directions reside in the so-called all-optical processing region. Regarding the 40-Gbit/s-based ETDM/WDM efforts, a total capacity of 10 Tbit/s was demonstrated in the year of 2001 by a couple of organizations.

As for OTDM/WDM demonstrations, a 1-Tbit/s (100 Gbit/s × 10) [48] and 3-Tbit/s (160 Gbit/s × 19) [31] transmission experiment were demonstrated in 1996 and 1999, respectively, followed by many laboratories/ field experiments, and more recently, 3.2 Tbit/s (320 Gbit/s × 10) transmission was reported in 2004 [85]. For

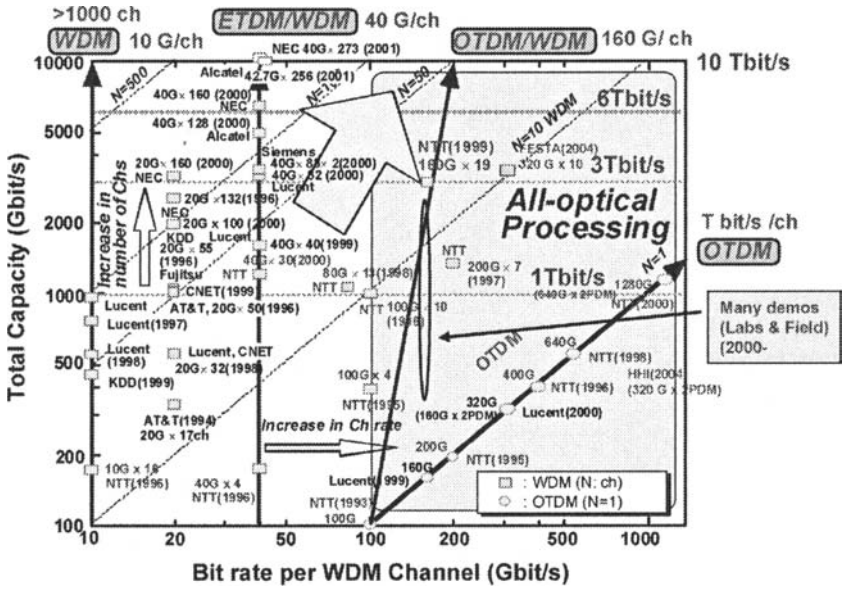

Fig. 1. Research directions in TDM/WDM technologies.

single-channel OTDM demonstrations, 1.28 Tbit/s [640 Gbit/s × 2 PDM (polarization-division multiplexing)] was demonstrated in 2000 [56], and more recently, 640 Gbit/s (320 Gbit/s × 2 PDM) transmission in RZ-DPSK format was reported in 2004 [86]. This paper briefly describes various enabling technologies both in ultrafast TDM handling more than 100 Gbit/s per wavelength channel in order to realize transparent and highly flexible next-generation photonic networks.

2. Ultrafast OTDM Technologies

The key elements of ultrafast OTDM systems [30,79] are depicted in Fig. 2. They consist of optical short pulse generation, optical multiplexing (MUX), optical demultiplexing (DEMUX), add-drop multiplexing (ADM), clock recovery, 2R (regeneration, reshaping) /3R (2R + retiming), signal quality (waveform) monitoring, and adaptive dispersion equalizing. These elements will be described along with large-capacity transmission schemes in more detail in the next sections.

2.1. Optical Short Pulse Generation

For TDM bit rates over 100 Gbit/s per wavelength channel, it is essential to generate stable, low-noise optical pulses with high-repetition rate, low-jitter, and picosecond (ps) to sub-picosecond pulse width. The pulse width for 160 Gbit/s OTDM transmission, for example, can be estimated to be less than 2.5 ps assuming a maximum width of 40%

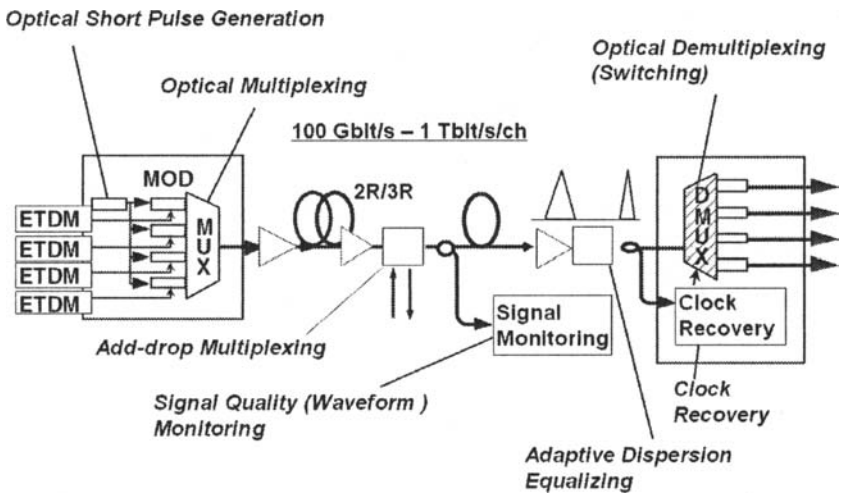

Fig. 2. Basic functions for ultrafast OTDM systems.

of the time slot as shown in Table 1, with less than 310 fs for 1.28 Tbit/s TDM. Various methods for high-repetition rate (more than 10 GHz) optical pulse generation have intensively been studied and developed to date utilizing mode-locked, [4,63,70,84] gain-switched [39] laser diodes, fiber ring lasers, [11,72] and electroabsorption modulator (EAM)-based pulse generation [69] producing optical pulses having a width of a few ps either directly or with some additional pulse compression. For bit rates over 640 Gbit/s, however, further nonlinear pulse compression should be needed to obtain 300–600 fs pulses with timing jitter of around 100 fs as shown in Table 1. Soliton adiabatic compression based on dispersion-flattened fiber (DFF) and nonlinear loop mirror (NOLM) can produce such pedestal-free femtosecond pulses. [76] Approximate channel spacing and number of WDM channels are shown in Table 1 assuming 25 THz total bandwidth and 40% spectrum utilization efficiency.

Table 1. Optical short pulse generation required for ultrafast OTDM.

	160 G/ch	**640 G/ch**	**1.28 T/ch**
Time slot	6.25 ps	1.56 ps	0.78 ps
Pulse width (40% time slot)	<2.5 ps	<630 fs	<310 fs
Timing jitter (1/8 time slot)	<780 fs	<200 fs	<100 fs
Bandwidth (Gaussian)	180 GHz	700 GHz	1400 GHz
Ch spacing	>400 GHz	>1600 GHz	>3200 GHz
Number of Ch for S+C+L bands	64	16	8

Supercontinuum (SC) generation [40,45] is another powerful method to obtain ultra-wide-band flat-top spectral broadening over the 200-nm range at 1.55 μm so as to generate ultrashort pulses. By filtering out the desired spectral components from the

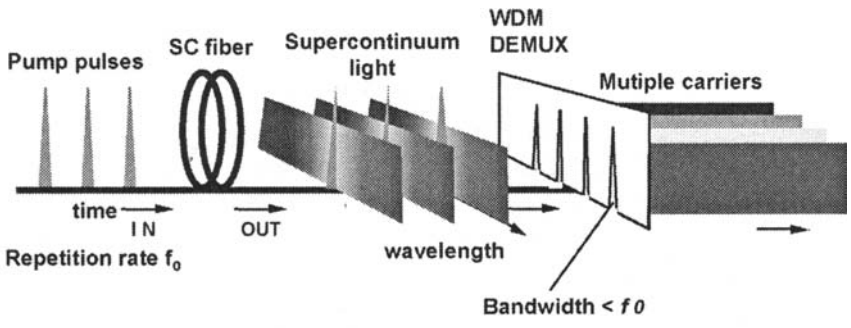

Fig. 3. Principle of SC (supercontinuum) generation.

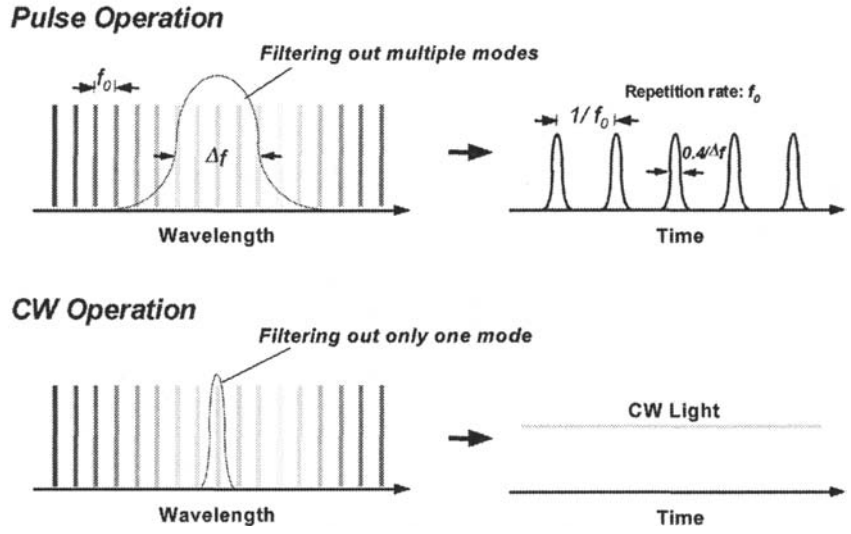

Fig. 4. Two operation modes for utilizing SC spectrum.

SC spectra, pulse-width-tunable, wavelength-tunable [47] or even multi-wavelength [42] ultrashort optical pulses can easily be obtained. The principle of SC generation is depicted in Fig. 3. The spectrum of the pump pulses (a few ps with about 1 nm bandwidth) broadens by $\times 100$ in the SC fiber [40] as a combined effect of nonlinear phenomena (SPM, XPM, FWM). The channel spacing of the SC spectra (longitudinal modes) is precisely equal to the repetition frequency f_0 of the pump pulses arising from the Fourier transform relations.

Also from the Fourier transform relations, two modes of operation can be achieved as explained in Fig. 4, i.e., a multi-color pulse operation with multiple center wavelengths, and a multiple CW operation. Firstly, by filtering out multiple longitudinal

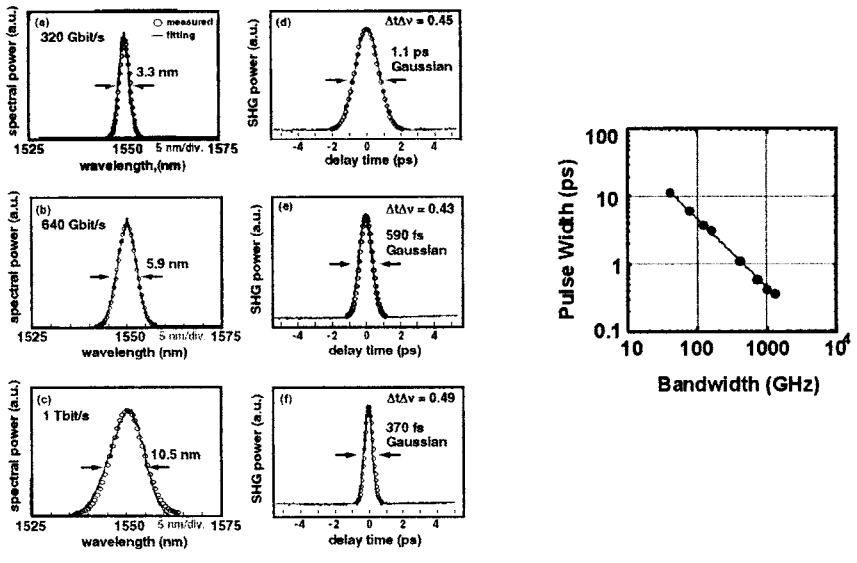

Fig. 5. Supercontinuum ultrashort pulses with pulse-width tunability controlled by the filter bandwidth.

modes of the SC spectra, transform-limited short optical pulses can be obtained with a repetition frequency f_0 and a pulse width determined by the filtered bandwidth Δf. In the Gaussian case, the pulse width equals $0.44/\Delta f$; it is 440 fs for a $\Delta f = 1$ THz. If only one longitudinal mode is filtered out, one can obtain a CW light and the frequency spacing equals the pump source repetition frequency f_0, which is controlled by the radio frequency (RF) oscillator driving the pump pulse source. If a 25-GHz pump pulse source is used, 25-GHz-spaced, 1000 channels are obtained over the 200-nm (25-THz) range at 1.55 μm with a potential total bit rate of 10 Tbit/s (10 Gbit/s $\times$ 1000 ch).

SC pulses of different bandwidths generated by filtering out with Gaussian filters are displayed in Fig. 5, which could be applicable to 320 Gbit/s, 640 Gbit/s, and Tbit/s TDM transmission with corresponding pulse widths of 1.1 ps, 590 fs, 370 fs, respectively. Both the spectral and temporal pulse shapes agree well with Gaussian fitting with the time-bandwidth product $\Delta t \Delta v$ of 0.45, 0.43, and 0.49, respectively. The relationship between the bandwidths and the measured pulse widths are plotted in the lower part of Fig. 5 for eight bandwidths from 0.32 (40 GHz) to 10.5 nm (1310 GHz), which indicate the pulse width tunability of picosecond to subpicosecond (0.37–11.3 ps). [47]

The pulse (spectral) shape selectivity is one of the great features of SC generation where a flat-top, chirp-less spectrum is obtained over a wide range of 100 nm or more. By using optical bandpass filters of different shapes, different pulse shapes can be obtained. This is demonstrated in Fig. 6 where the SC spectrum was sliced by two conventional optical filters with different shapes but of about the same 3-dB bandwidth of 5 nm. The upper two figures (a) correspond to Lorentzian square shape with a time-bandwidth product of 0.155, which is very close to the theoretical value of 0.142 with

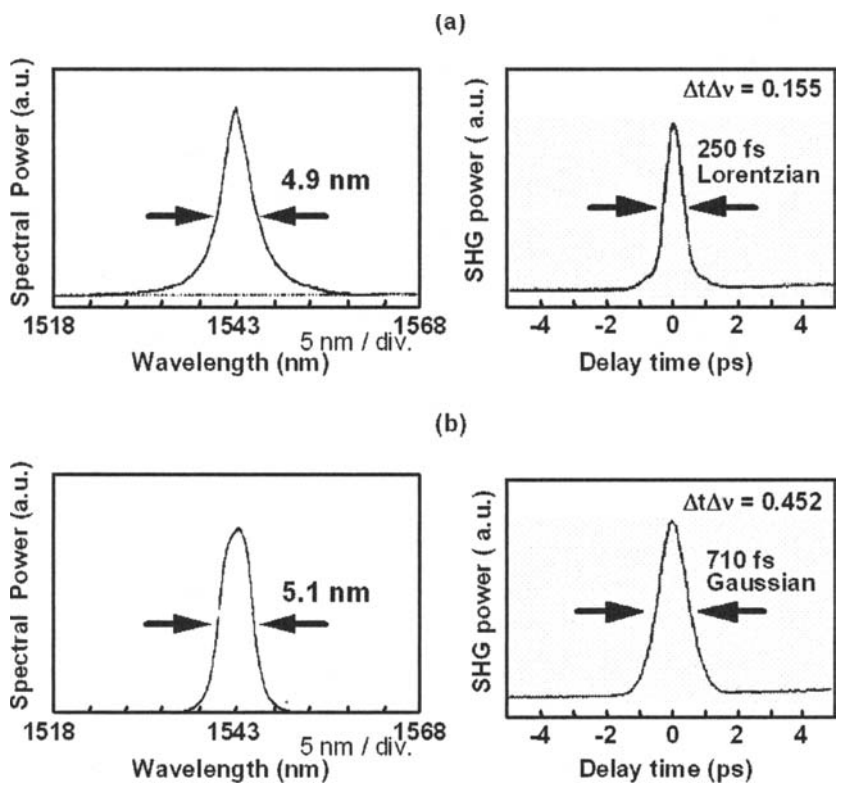

Fig. 6. Supercontinuum ultrashort pulses with pulse-shape tunability.

a deconvolved pulse width of 250 fs. The lower figures (b) correspond to Gaussian shape with a time-bandwidth product of 0.452 and a pulse width of 710 fs. This SC source was successfully used as an OTDM/WDM transmitter in a 1 Tbit/s (100 Gbit/s $\times$ 10 ch) [48] and 3 Tbit/s (160 Gbit/s $\times$ 19 ch) [31] transmission experiment where the Gaussian filters were used. [31]

2.2. *Optical TDM MUX/DEMUX With Clock Recovery*

OTDM multiplexers/ demultiplexers (MUXs/DEMUXs) play a vital role in constructing ultrafast OTDM/WDM photonic networks. Passive delay lines could be used for MUXs, where TDM channels are multiplexed passively after each channel is modulated at lower electrical line rates (10–40 Gbit/s). [10] DEMUXs or add-drop MUXs, [7,22,64] however, require ultrafast active switching controlled by an extracted optical clock pulse. Various ultrafast all-optical switches proposed to date are summarized in Fig. 7, which are based either on the real part or on the imaginary part of nonlinear susceptibility. Switches based on the real nonlinear susceptibility have two types, namely nonlinear phase-shift or frequency shift type. Nonlinear phase-shift switches include

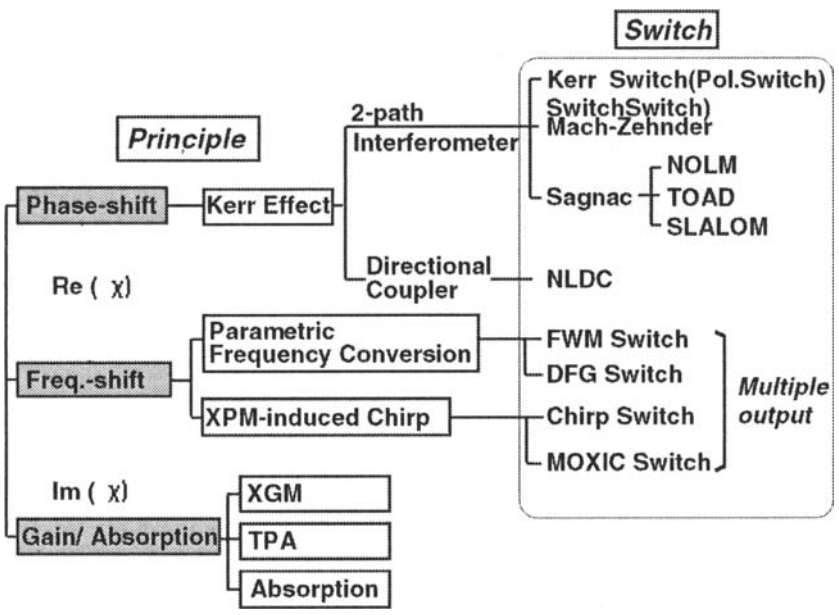

Fig. 7. Classification of all-optical switching technologies.

the optical Kerr switch, [41] Mach-Zehnder switch, [55] and Sagnac interferometer switch [21] while frequency-shift switches include four wave mixing (FWM) switch [2,3], difference frequency generation (DFG) switch, [14] and chirp (MOXIC) switch. Switches based on the imaginary nonlinear susceptibility utilize ultrafast cross gain modulation (XGM), two photon absorption (TPA), and absorption saturation [1,71] mainly in semiconductors. Frequency-shift-type switches can perform wavelength conversion and are capable of having multiple channel (multiple wavelength) outputs as opposed to phase-shift-type switches where only two outputs are obtained as a result of their interferometer nature.

For TDM bit-rates exceeding 100 Gbit/s, integration of MUXs/DEMUXs will be necessary for N:1 or 1:N operations because the required timing precision between adjacent TDM channels becomes less than 1 ps (200 μm in fibers). Figure 8 shows a recently demonstrated integrated OTDM MUX (20 Gbit/s $\times$ 8 ch) on a planar lightwave circuit (PLC) waveguide where each channel was modulated all-optically based on the cascaded second-order nonlinearity in periodically poled lithium niobate (PPLN). [57] The fabrication precision of a PLC-based OTDM MUX is less than 0.1 ps, which would be sufficient even for 1 Tbit/s OTDM multiplexing.

Figure 9 shows an example of an integrated DEMUX on PLCs (160 Gbit/s to 8 ch $\times$ 20 Gbit/s) where switching was done all-optically based on the FWM effect in semiconductor optical amplifiers (SOAs). [68] Using the integrated MUX and the DEMUX in Figs. 8 and 9, successful 160 Gbit/s OTDM transmission has been demonstrated. [58]

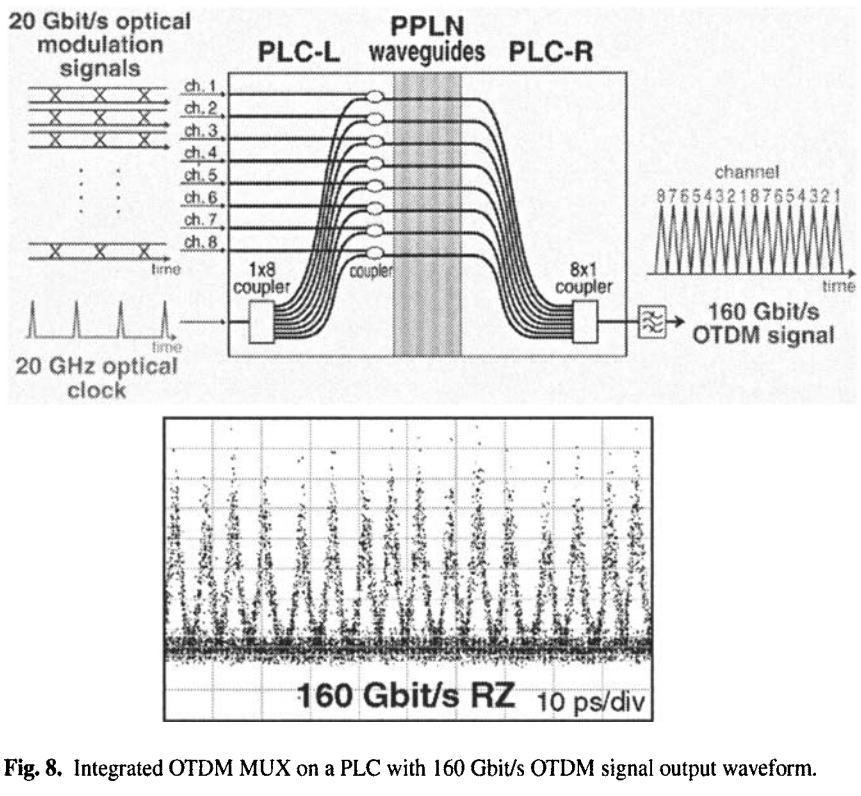

Fig. 8. Integrated OTDM MUX on a PLC with 160 Gbit/s OTDM signal output waveform.

Because the DEMUXs are placed at the end of the transmission line, ultrafast TDM DEMUXs require polarization-independent operation in addition to ultrafast multiple channel output (1:N) operation exceeding 100 Gbit/s. Polarization-independent operation can be achieved either by using polarization-independent effects such as absorption saturation or utilizing a polarization diversity configuration. [51] Regarding the ultrafast operation speeds, up to 640 Gbit/s error-free DEMUX operation has been achieved with a fiber-based nonlinear optical loop mirror (NOLM) DEMUXs, [83] 500 Gbit/s with a fiber-based FWM DEMUXs, [49] 200 Gbit/s with SOA-based FWM DEMUXs, [50] 336 Gbit/s with Mach-Zehnder interferometer (MZI)-SOA DEMUXs, [55] 500 Gbit/s with photodiode-electroabsorption modulator (PD-EAM) DEMUXs, [33] and 80 Gbit/s with optically-controlled electroabsorption modulators (EAMs). [62]

Multiple channel output operation can be achieved by the serial-parallel configuration described above or by utilizing the frequency-shift type switches. Figure 10 shows an example of a multiple channel output demultiplexer called MOXIC (Multiple-channel Output all-optical OTDM Demultiplexer using XPM-induced Chirp Compensation), which utilizes XPM-assisted chirp compensation in an optical fiber. [78] The 100 Gbit/s demultiplexing to 10 ch $\times$ 10 Gbit/s is shown in Fig. 10.

Figure 11 shows another example of multiple channel output DEMUX based on the FWM effect pumped by a chirped square pump pulse. [43] In the FWM nonlinear

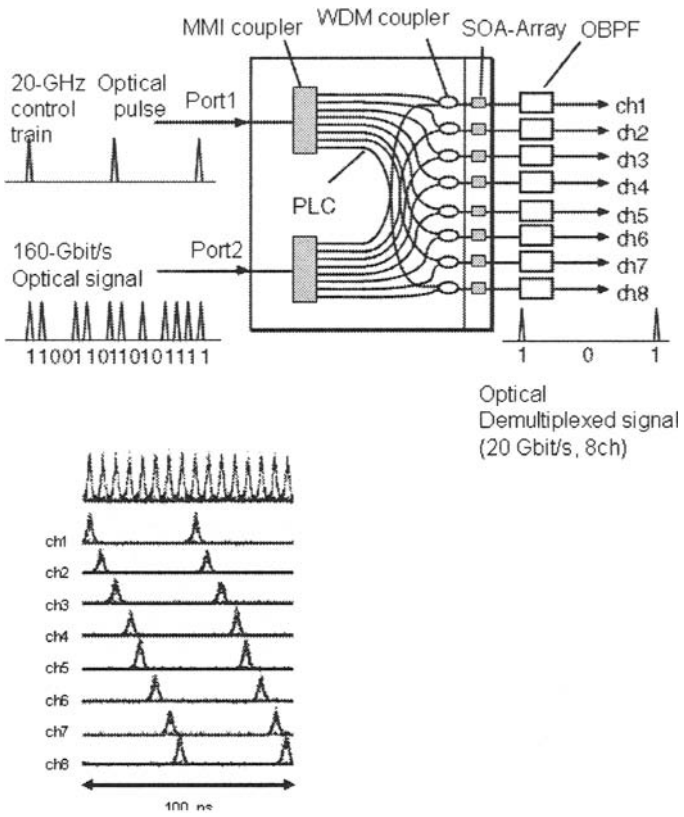

Fig. 9. Integrated OTDM DEMUX on PLC with the 8 ch × 20 Gbit/s demultiplexed signals.

medium, ultrafast (>100 Gbit/s) signal pulses (optical frequency ν_s) and linearly-chirped square pump pulses (ν_p) generate four different frequency components corresponding to independent TDM channels (channel 1 to channel 4) as shown in Fig. 11. All four channels can therefore, simultaneously be separated using a $1 \times N$ WDM DEMUX (AWG, for example).

Other important issues associated with ultrafast TDM DEMUXs are clock recovery to drive optical DEMUXs and optical 3R regenerators, as well as bit synchronization between the incoming TDM signal and the optical clock. To date, many high-speed clock recovery methods have been proposed such as injection locking, [36] hybrid phase-locked loop (PLL) using semiconductor optical amplifiers (SOAs) or electroabsorption modulators (EAMs) as comparators in the optical domain, [5,23] and photonic down conversion (PDC)-PLL [17] where modulation sidebands are used to sense the signal phase as shown in Fig. 12. In both PLL methods, a prescaled clock can be obtained. The hybrid-PLL was tested at up to 400 Gbit/s in high-speed transmission experiment. [23]

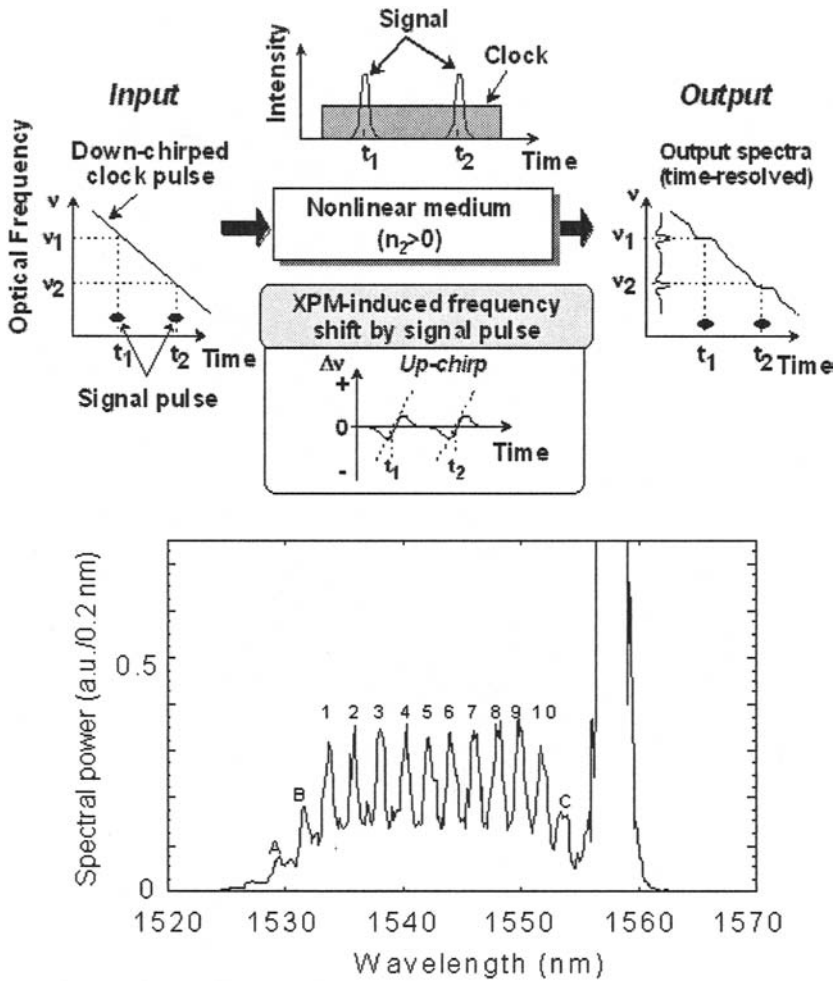

Fig. 10. MOXIC: 100 Gbit/s to 10 ch × 10 Gbit/s demultiplexing.

Bit synchronization becomes vital when the local optical clock pulse to drive an optical DEMUX traverses a long optical fiber for further pulse compression, and moves relative to the incoming signal. A synchronization scheme based on photonic down-conversion has recently demonstrated in MOXIC DEMUX as shown in Fig. 13. [78] The PLL operates such that the relative phase between the signal and the control pulses is locked at the WDM coupler, meaning that the control pulse endlessly tracks the signal stream regardless of the thermally induced fluctuations in the optical fibers such as the SC fiber. The locally generated clock pulse achieved an rms timing jitter of 0.12 ps and one-hour stability in terms of relative timing displacement of better than 0.7 ps.

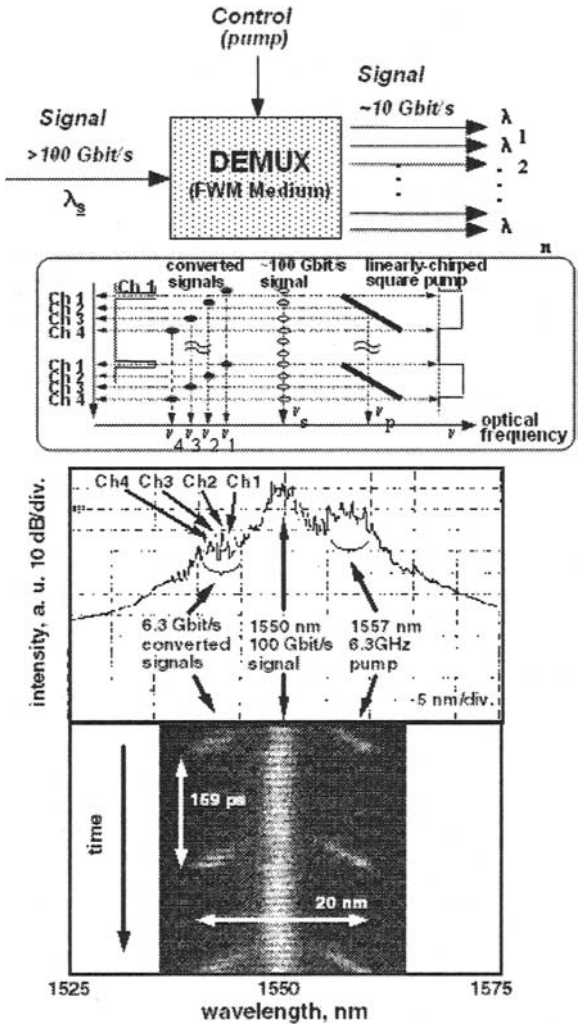

Fig. 11. Multiple channel output DEMUX based on FWM with chirped square pump pulses.

2.3. Optical 2R/3R

Optical 2R/ 3R operation will be essential to increase the transmission distance by restoring the ultrafast optical signals degraded by dispersion and nonlinear effects in transmission fibers. Most optical 2R regenerators operate in the "self-switching" mode where self-phase modulation (SPM) [37,38,59] and absorption saturation are utilized with no external optical clock. In optical 3R regeneration, on the other hand, extracted clock optical pulses are switched (modulated) by the incoming data signals. [81] Wavelength conversion is normally accompanied because external clocks of different wavelengths are normally used.

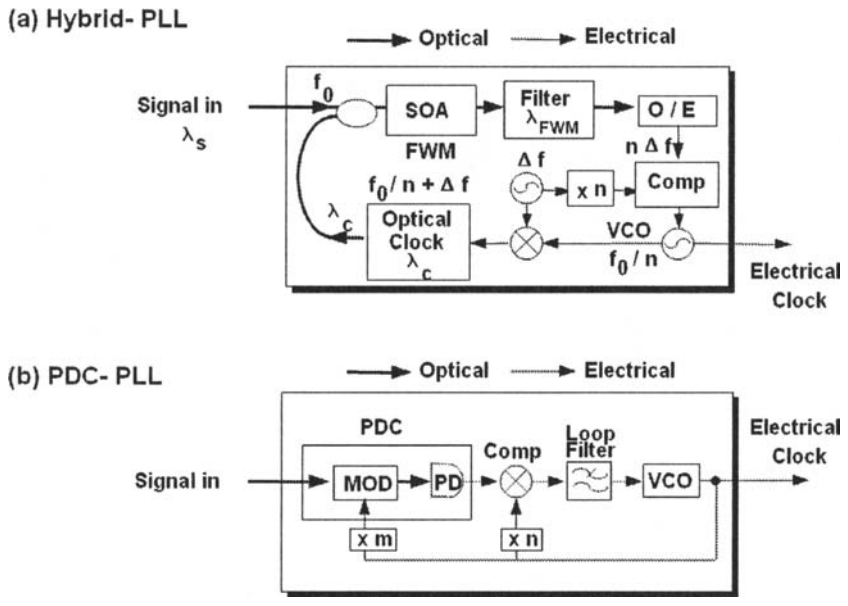

PDC: Photonic down conversion

Fig. 12. Ultrafast clock recovery schemes.

Figure 14 depicts the principle of operation of a WDM optical limiter to suppress the mark level noise. [61] In this limiter, intensity fluctuations of each WDM signals are converted to spectral fluctuations through soliton spectral broadening in a nonlinear optical fiber, which can be eliminated by filtering out the fluctuated wings by an optical filter. If WDM DEMUX/DEMUXs are used, multi-channel limiting operations can be achieved as shown in Fig. 14. When the center frequency of the optical filter is shifted with respect to that of the signal, optical 2R operation for both mark and space level noise suppression is obtained. [37,38] 3R regenerators based on cross absorption modulation (XAM) in EAMs [18,53,61] have actively been studied to achieve 3R functions and wavelength conversion simultaneously where up to 80 Gbit/s optical 3R operation has been reported.

2.4. Optical Signal Quality Monitoring

Ultrafast and flexible optical waveform/optical signal quality monitoring plays an important role in transparent OTDM/WDM photonic networks. A recently developed optical waveform measurement (monitoring) system based on ultrafast optical sampling technique using sum frequency generation (SFG) is shown in Fig. 15, which is capable of displaying eye-diagrams of 400–500 Gbit/s signals. [73]

Recently, in order to achieve bit-rate flexibility, an asynchronous optical signal quality monitoring system based on optical sampling has also been proposed. [65] The

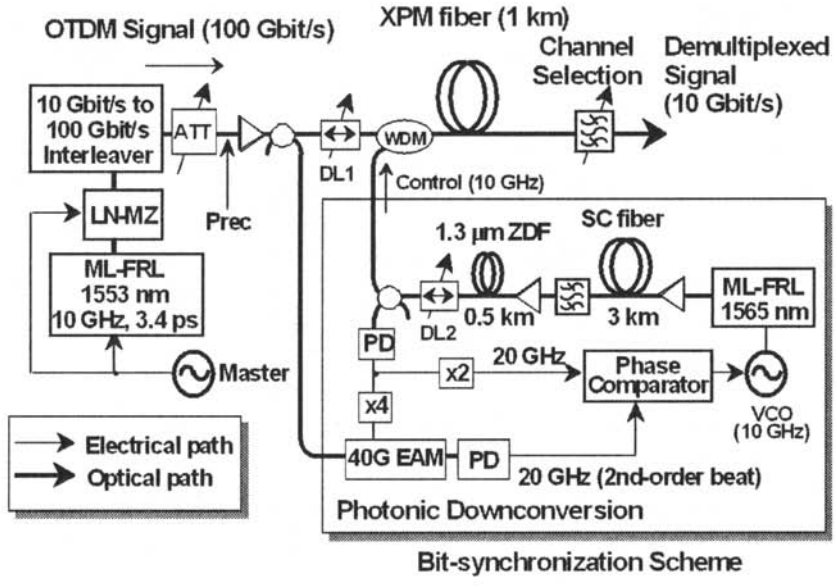

Fig. 13. OTDM DEMUX bit-synchronization scheme.

principle of operation is shown in Fig. 16 where the asynchronous eye-diagram and its measured amplitude histogram are shown. By defining the average quality factor

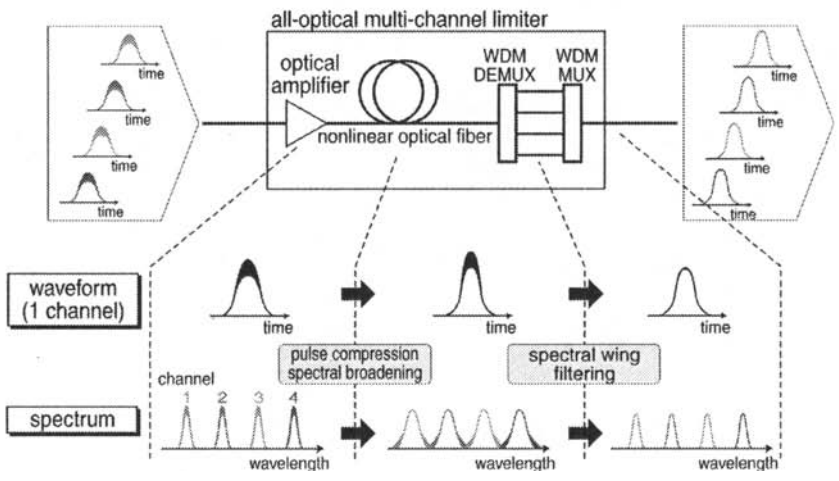

Fig. 14. Principle of operation of WDM optical limiter.

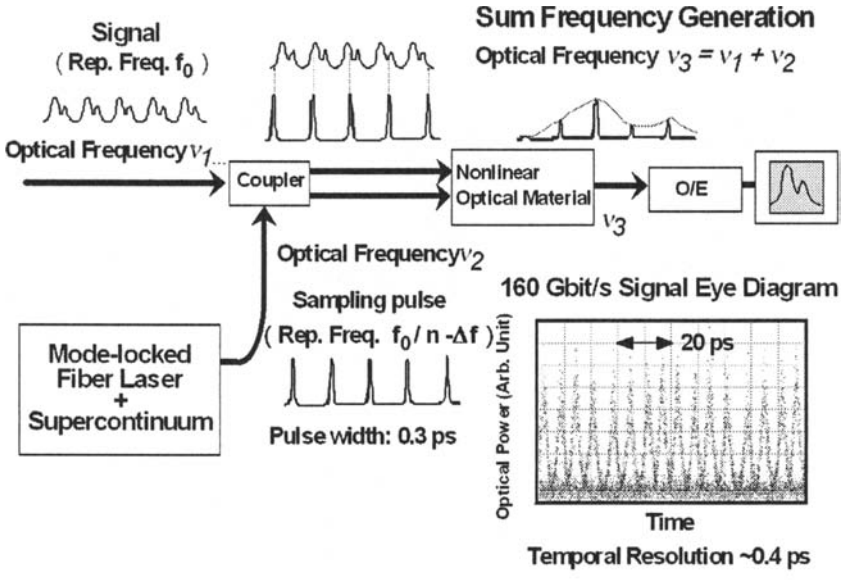

Fig. 15. Optical waveform monitoring system based on ultrafast optical sampling.

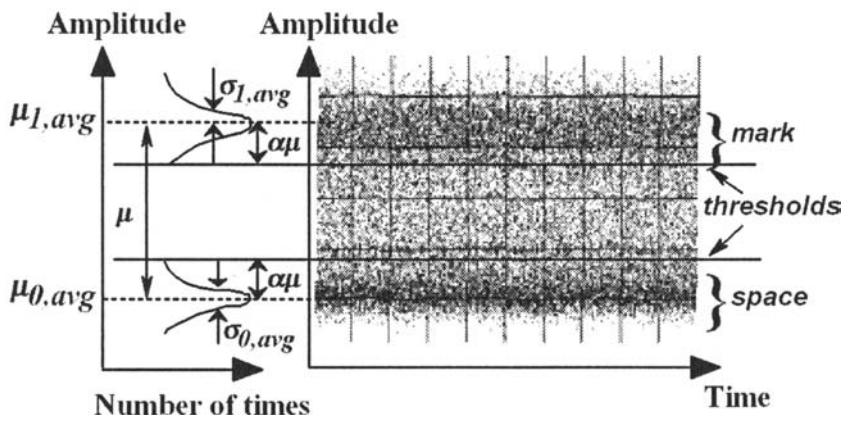

Fig. 16. Asynchronous optical signal quality monitoring system: principle.

(Q-factor), Q_{av} as below which has a strong correlation with the normal Q-factor, the actual Q-factor can be deduced:

$$Q_{\mathrm{av}} = | \nu_{1,\mathrm{av}} - \nu_{0,\mathrm{av}} | / \sigma_{1,\mathrm{av}} + \sigma_{0,\mathrm{av}}. \tag{1}$$

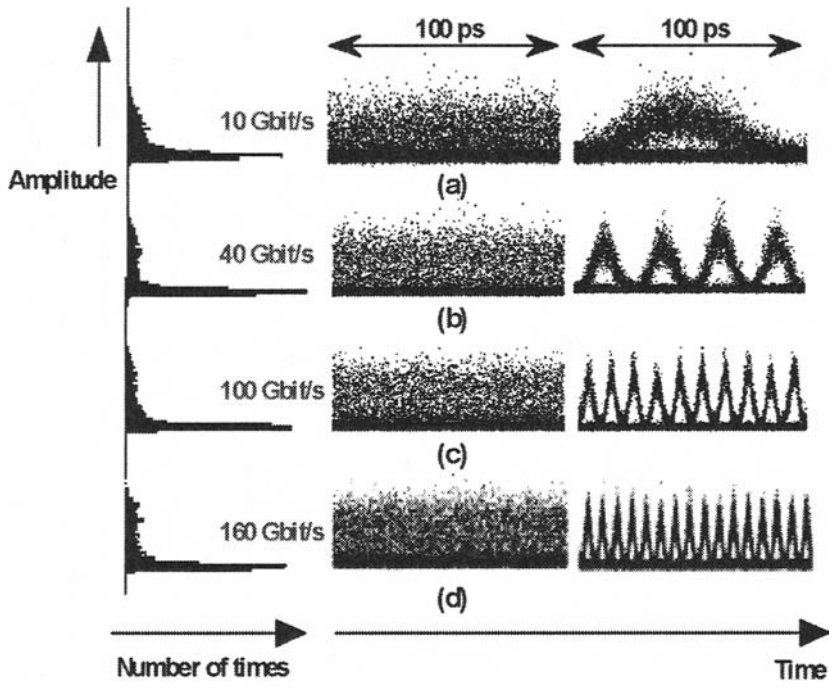

Fig. 17. Asynchronous optical signal quality monitoring system: results.

Here, $\nu_{i,\mathrm{av}}$ and $\sigma_{i,\mathrm{av}}$ are the mean and standard deviation of the mark $(i = 1)$ and space $(i = 0)$ levels of all sampled data, respectively. The unwanted cross-points data in the eye diagram are removed by setting certain threshold levels. Because the method is asynchronous, it features bit-rate and format independency. Up to 160 Gbit/s bit-rate flexible operation has been demonstrated as shown in Fig. 17 (right: synchronous sampling, middle: asynchronous sampling). [66] In addition, a simple asynchronous Q-factor monitoring method based on open eye diagrams has recently been proposed and demonstrated by using high-speed (around GHz) electro-optical sampling. [67]

2.5. Adaptive Dispersion Compensation

For the signal bit rates exceeding 100 Gbit/s, effects of temperature and stress change on the dispersions have to be controlled to achieve stable transmission. For example, the tolerance of wavelength dispersion and differential group delay (DGD) are approximately 2 ps/nm and less than 1 ps, respectively, for 160 Gbit/s transmission. Considering the temperature change of 40 degrees, it would change the chromatic dispersion of 80 km fibers by 6–7 ps/nm, and make adaptive dispersion as well as dispersion slope compensation [19,75,77,80] indispensable.

The schematic diagram of an adaptive dispersion equalizer is shown in Fig. 18, which is composed of a tunable dispersion equalizer and a novel chirp monitor which

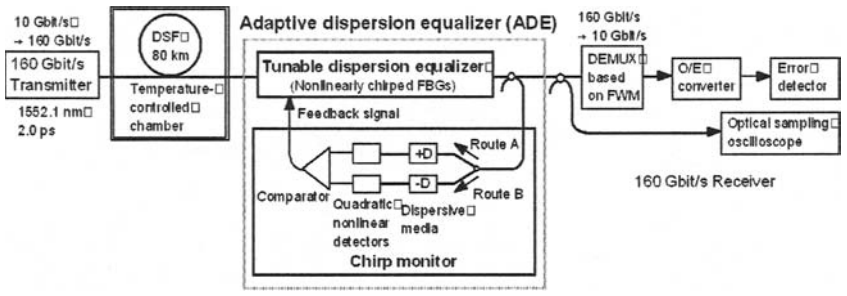

Fig. 18. Adaptive dispersion equalizer.

detects the signal peak intensity reflecting the signal chirp experienced in the dispersive transmission line and feeds back this information to the equalizer to achieve adaptive equalization. The first 160-Gbit/s adaptive dispersion equalizer has recently been demonstrated in an 80-km dispersion-shifted fiber (DSF) [20] using a nonlinear chirped fiber grating (FBG) as a tunable dispersion equalizer and a two-path chirp detector as a chirp monitor which is capable of detecting the sign of the chirp. Other tunable equalizers have actively been investigated. Regarding the adaptive PMD equalization, there have been many demonstrations at 160 Gbit/s even in an installed fiber line. [6,32,60,82]

2.6. Wavelength Conversion

Wavelength conversion is an essential function in photonic networks to accommodate optical paths and to avoid wavelength blocking as depicted in Fig. 19. Some of the requirements for wavelength conversion at intermediate nodes are conversion of arbitrary input wavelength to arbitrary output wavelength with polarization independent capability.

Many proposals and demonstrations of wavelength conversion have been made based on various all-optical switching schemes listed in Fig. 7 [9,54] as part of the optical 3 R. Supercontinuum generation can also be used as a powerful wavelength converter when data signals are used as pump pulses as displayed in Fig. 20, where multicast or broadcast wavelength conversion can be achieved. [15,44] This so-called self-frequency conversion of ultrashort optical pulses into arbitrary multiwavelength components without the use of a pump consists of an Er-doped fiber amplifier (EDFA), an SC fiber, an optical fiber for chirp compensation, and optical filters. Randomly-modulated high-speed optical signal pulses at 6.3 Gbit/s are input into the self-frequency converter (SFC) where they are amplified to a peak power of 2 W and coupled into the SC fiber, the output of which is a super-broadened SC spectrum spanning over 200 nm for the input signal wavelengths of 1535∼1560 nm. The generated SC is then filtered by a periodical optical filter, producing duplicates of the input signal pulses at many different wavelength channels.

The streak camera images of the frequency-converted signals at each wavelength exhibit no pedestal components as shown in the lower left of Fig. 20. From the auto-

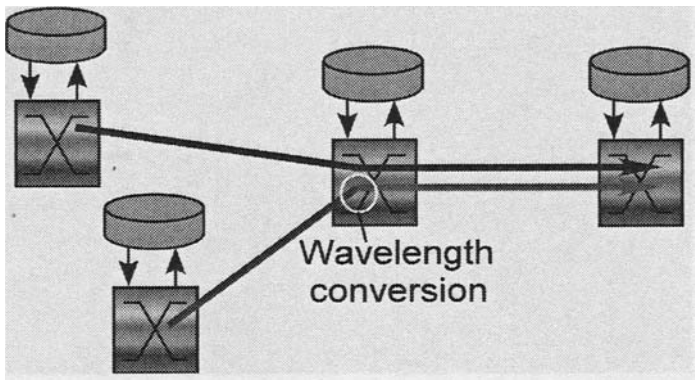

Fig. 19. Wavelength conversion in Photonic Networks.

correlation measurements, the actual pulse widths were estimated to be 1.0 ps. Figure 20 also shows the bit-error rate (BER) curves of the 6.3-Gbit/s frequency-converted signals at 1440, 1550, 1560, and 1600 nm for the input signal wavelength of 1542 nm. This simultaneous multi-wavelength frequency conversion can be used for arbitrary channel selection in WDM distribution networks.

2.7. *Large-Capacity OTDM/WDM Transmission*

Large-capacity OTDM/WDM transmission experiments (>100 Gbit/s per channel) combining the ultrafast OTDM and ultra-wideband WDM technologies have been demonstrated since 1995 [29,31,46,48] where 100 Gbit/s × 4 ch OTDM/WDM signals was first transmitted over a 100 km DSF using a SC source. The experiment was soon followed by the first 1 Tbit/s (100 Gbit/s × 10ch) transmission experiment in 1996, the experimental setup of which is shown in Fig. 21. [48]

The 100 Gbit/s × 10 channel (1 Tbit/s) OTDM/WDM signals were generated from a low-noise single SC WDM source combined with an arrayed-waveguide grating demultiplexer/multiplexer of 140 GHz channel bandwidth and 400 GHz channel spacing, and were transmitted over a 40-km dispersion-shifted fiber. The low-noise SC pulse source (generator) consisted of a stabilized actively mode-locked Er^{3+}-doped fiber ring laser (ML-EDFRL) outputting 10 GHz, 1572 nm, 3.5 ps pump pulses, an Er^{3+}-doped fiber amplifier (EDFA) that amplifies the pump pulses to a peak power of 1.5 W, and a 3-km SC fiber for SC generation. The WDM SC spectra filtered with the AWG DEMUX/MUX have more than 80 nm bandwidth as shown in Fig. 21. The adjacent channel crosstalk was less than −25 dB for all-channels ranging from 1533.6 to 1562.0 nm. The average output power per channel from the DEMUX/MUX was around −10 dBm. The 10 WDM channels from the DEMUX/MUX were modulated by a common $LiNbO_3$ intensity modulator ($2^{15}-1$, PRBS) and time-division multiplexed to 100 Gbit/s × 10 channel OTDM/WDM signals by using a 10 × planar lightwave circuit OTDM multiplexer. The pulse width of each channel was about 3 ps. The OTDM-WDM signals were then amplified to average power of 5 dBm per channel by a fluoride-based broadband EDFA with a gain flatness of less than 1.5 dB within

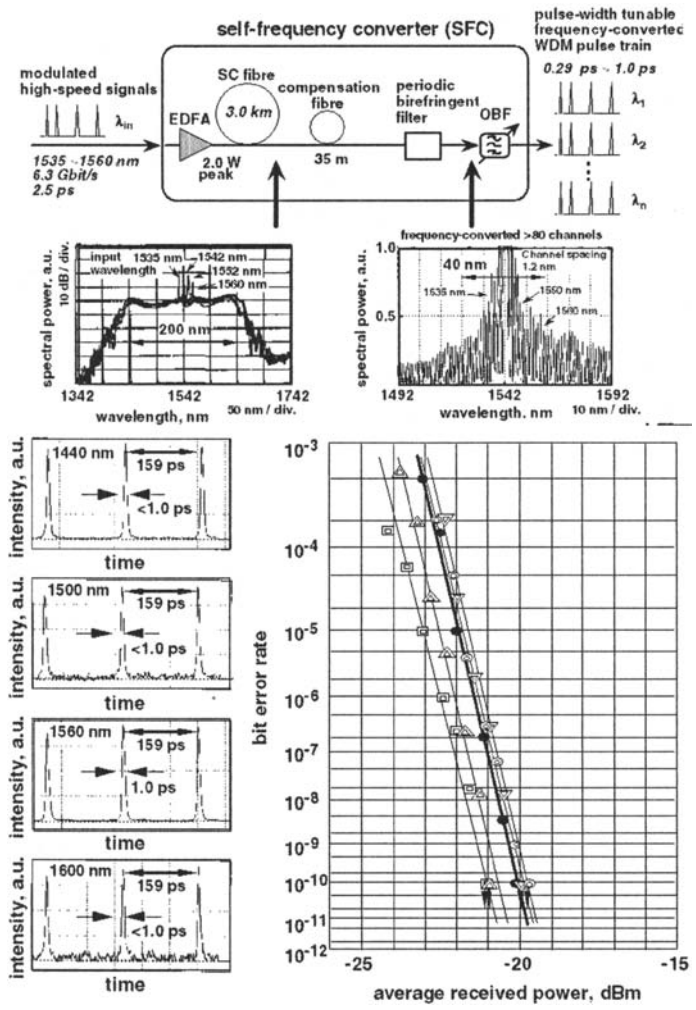

Fig. 20. Wavelength conversion based on supercontinuum.

the 30-nm bandwidth. They were transmitted over a 40-km dispersion-shifted fiber of zero dispersion wavelength of 1561.3 nm. The output signals were filtered by three 3 nm OBFs in series having a net bandwidth of 2.4 nm and an adjacent channel rejection ratio of more than 30 dB. Compensation single-mode (SM) fibers (CF) were used to compensate for the transmission fiber dispersion of up to 74 ps/nm. By the dispersion compensation, the output pulse waveform recovered its original pulse shape and the 100-Gbit/s signals were input into a prescaled PLL timing extraction circuit and an all-optical time-domain demultiplexer (DEMUX) based on fiber four-wave mixing (FWM) . The extracted electrical clock was supplied to the FWM-DEMUX with low rms timing jitter of less than 0.2 ps. The demultiplexed 10-Gbit/s signal was detected

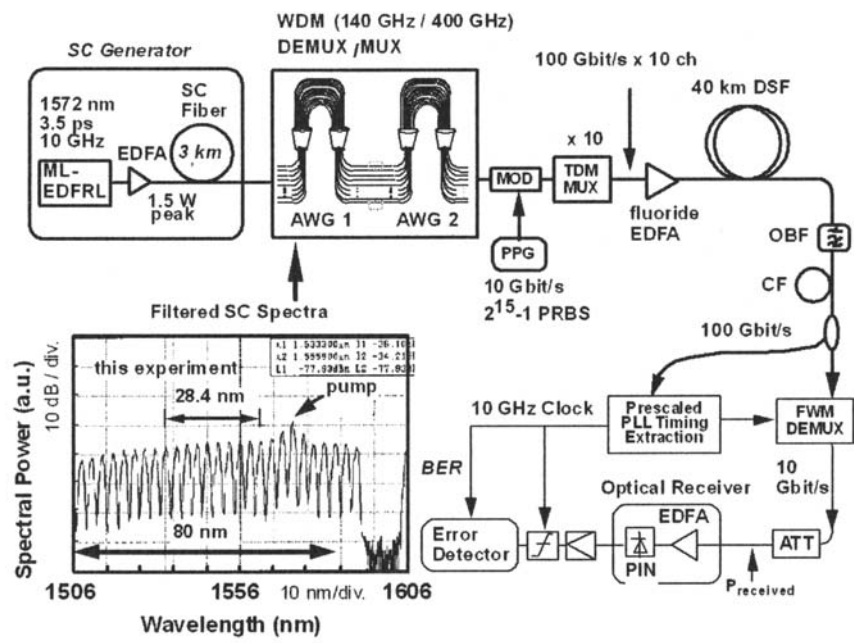

Fig. 21. Schematic setup of the first 1-Tbit/s OTDM/WDM transmission experiment.

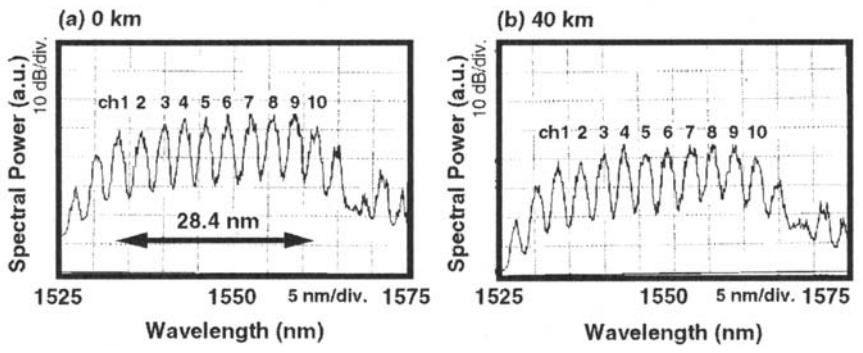

Fig. 22. The 1-Tbit/s WDM spectra (a) before and (b) after 40 km DSF transmission.

by an optical receiver and bit-error rate (BER) performance was measured. Figure 22 shows the input and output spectra of the 100 Gbit/s × 10 channel OTDM-WDM signals. No noticeable SPM spectral broadening nor FWM components were observed. Figure 23 shows the BER curves of all the 10 channels. The rather large departure from the 10-GHz baseline especially at channel 10 (1533.6 nm) is partly attributed to the wavelength conversion characteristics associated with the FWM demultiplexing.

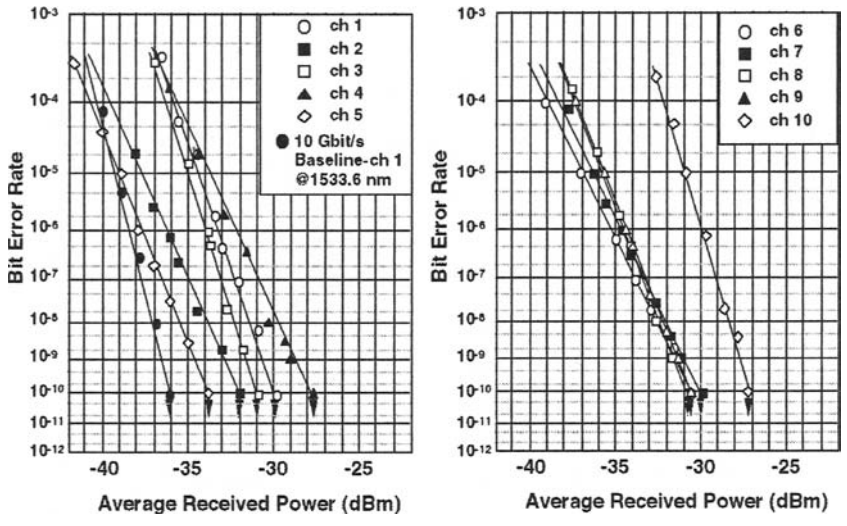

Fig. 23. Bit-error rate performance of 100 Gbit/s × 10 ch, 40 km transmission. (a) ch 1∼ch 5, and (b) ch 6∼ch 10.

This experiment was further upgraded to 3 Tbit/s (160 Gbit/s × 19 ch) transmission in 1999, [31] the schematic setup of which is shown in Fig. 24. The 19 wavelength channels ranged from 1540 to 1609 nm with a channel spacing of 480 GHz. The 3 Tbit/s signal generator consisted of two independent OTDM/WDM signal generators both for the short wavelength (1540–1566 nm) and the long wavelength region (1570–1609 nm). Each OTDM/WDM generator consisted of a 10-GHz mode-locked Er^{3+}-doped fiber ring laser, an optical modulator, an optical amplifier, and an SC fiber. The SC fibers were dispersion-decreasing fiber with a convex dispersion profile producing a flat SC spectrum over the 200-nm spectral region [40]. The generated 10-Gbit/s SC signal pulses were time-division multiplexed by 16 times and multiplexed by AWG filters to produce the 3-Tbit/s WDM signal. The total optical power launched into the 40-km transmission DSF was 20.2 dBm. The zero dispersion wavelength of the transmission fiber was 1535 nm, such that all WDM channels were in the anomalous dispersion region. Demultiplexing of the 160-Gbit/s signal into a 10-Gbit/s signal was performed again by an all-optical fiber FWM-DEMUX driven by a 10-GHz clock extracted from the 160-Gbit/s signal channel and error free operation was confirmed for all 19 channels.

For the past years, many OTDM/WDM transmission experiments have been performed using such new formats as carrier-suppressed return-to-zero (CS-RZ) and differential phase shift keying (DPSK) in addition to the conventional return-to-zero (RZ) formats. [8,13,16,35,52] The major issue here is clearly the bandwidth of the optical amplifiers. More research effort is required to extend the bandwidth of the optical amplifiers to fully utilize the entire 200-nm range, which the SC sources offer.

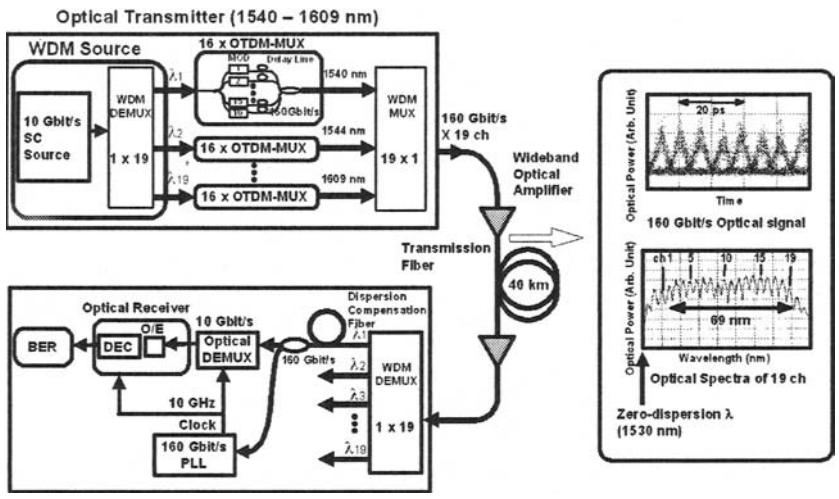

Fig. 24. Schematic setup of 3 Tbit/s OTDM/WDM transmission experiment.

Single channel OTDM transmission experiments over 100 Gbit/s have been demonstrated since 1993 when 100 Gbit/s (50 Gbit/s OTDM $\times$ 2PDM) signals were first transmitted over a 50-km DSF, [24] followed by 100 Gbit/s, 200–500 km transmission, [25, 26] 200 Gbit/s, 100 km transmission, [27] 400 Gbit/s, 40 km transmission. [28] The year 2000 was an epoch-making one when a single-channel 1.28-Tbit/s transmission over 72 km was achieved by combining the ultrafast optical technologies and a highly sophisticated dispersion compensation technique. [56] Field demonstration of 160 Gbit/s transmission has also been demonstrated testing the system stability, monitoring and adaptive dispersion compensation schemes. [12]

3. Conclusion

Various enabling technologies in ultrafast TDM handling more than 100 Gbit/s per wavelength channel is briefly described in order to realize transparent and highly flexible next-generation photonic networks. Based on the many demonstrations, the next step would be to construct the real systems combining the ETDM/WDM technologies, making full use of the optical integration technologies.

References

1. Akiyama T, Georgiev N, Mozume T, Yoshida H, Gopal AV, Wada O, 1.55-μm picosecond all-optical switching by using intersubband absorption in InGaAs-AlAs-AlAsSb coupled quantum wells, IEEE Photon. Technol. Lett., **14**, 495–497 (2002)
2. Andrekson PA, Olsson NA, Simpson JR, Tanbun-Ek T, Logan RA, Haner M, 16 Gbit/s all-optical demultiplexing using four-wave mixing, Electron. Lett., **27**, 922–924 (1991)

3. Arahira S, Ogawa Y, 160-Gb/s All-Optical Encoding Experiments by Four-Wave Mixing in a Gain-Clamped SOA With Assist-Light Injection, IEEE Photon. Technol. Lett., **16**, 653–655 (2002)
4. Arahira S, Mineo N, Tachibana K, Ogawa Y, 40 GHz hybrid modelocked laser diode module operated at ultra-low RF power with impedance-matching circuit, Electron. Lett., **39**, 287–289 (2003)
5. Boerner C, Schubert C, Schmidt C, Hilliger E, Marembert V, Berger J, Ferber S, Dietrich E, Ludwig R, Schmauss B, Weber HG, 160 Gbit/s clock recovery with electro-optical PLL using bidirectionally operated electroabsorption modulator as phase comparator, Electron. Lett., **39**, 1071–1073 (2003)
6. Buchali F, Baumert W, Schmidt M, Bulow H, Dynamic distortion compensation in a 160 Gb/s RZ OTDM system: adaptive 2 stage PMD compensation. Optical Fiber Communication Conf., pp. 589–590, 2003
7. Chou HF, Bowers JE, Blumenthal DJ, Compact 160-Gb/s Add-Drop Multiplexing with a 40-Gb/s Base-Rate, Optical Fiber Communication Conf., 2004, Paper PD28, 2004
8. Daikoku M, Otani T, Suzuki M, 160-Gb/s four WDM quasi-linear transmission over 225-km NZ-DSF with 75-km spacing, IEEE Photon. Technol. Lett., **15**, 1165–1167 (2003)
9. Edagawa N, Suzuki M, Yamamoto S, Novel Wavelength Converter Using an Electroabsorption Modulator, IEICE Trans. Electron., **E81-C**, 1251–1257 (1998)
10. Ellis AD, Lucek JK, Pitcher D, Moodie DG, Cotter D, Full 10 × 10 Gbit/s OTDM data generation and demultiplexing using electroabsorption modulators, Electron. Lett., **34**, 1766–1767 (1998)
11. Ellis AD, Manning RJ, Phillips ID, Nesset D, 1.6 ps pulse generation at 40 GHz in phase-locked ring laser incorporating highly nonlinear fibre for application to 160 Gbit/s OTDM networks, Electron. Lett., **35**, 645–646 (1999)
12. Feiste U, Ludwig R, Schubert C, Berger J, Schmidt C, Weber H.G, Schmauss B, Munk A, Buchold B, Briggmann, D Kueppers, F Rumpf, F, 160 Gbit/s transmission over 116 km field-installed fibre using 160 Gbit/s OTDM and 40 Gbit/s ETDM, Electron. Lett., **37**, 443–445 (2001)
13. Ferber S, Ludwig R, Boerner C, Wietfeld A, Schmauss B, Berger J, Schubert C, Unterboersch G, Weber HG, Comparison of DPSK and OOK modulation format in 160 Gbit/s transmission system, Electron. Lett., **39**, 1458–1459 (2003)
14. Fukuchi Y, Sakamoto T, Taira K, Kikuchi K, All-optical time-division demultiplexing of 160 Gbit/s signal using cascaded second-order nonlinear effect in quasi-phase matched $LiNbO_3$ waveguide device, Electron. Lett., **39**, 789–790 (2003)
15. Futami F, Okabe R, Takita Y, Watanabe S, Transparent wavelength conversion at up to 160 Gbit/s by using supercontinuum generation in a nonlinear fiber. Optical Amplifiers and their Applications, Paper MD07, 2003
16. Gnauck AH, Raybon G, Bernasconi PG, Leuthold J, Doerr CR, Stulz LW, 1-Tb/s (6 × 170.6 Gb/s) transmission over 2000-km NZDF using OTDM and RZ-DPSK format, IEEE Photon. Technol. Lett., **15**, 1618–1620 (2003)
17. Hashimoto E, Takada A, Katagiri Y, Clock source-limited low jitter, subterahertz signal generation from mode-locked semiconductor laser controlled by phase locked loop (PLL) with photonic downconversion. Microwave Photonics, pp. 169–172, 1998
18. Hayashi M, Otani T, Tanaka H, Suzuki M, Analysis on jitter tolerance of optical 3R regenerator, IEEE Photon. Technol. Lett., **15**, 1609–1611 (2003)

19. Inui T, Komukai T, Nakazawa M, Suzuki K, Tamura KR, Uchiyama K, Morioka T, Adaptive dispersion slope equalizer using a nonlinearly chirped fiber Bragg grating pair with a novel dispersion detection technique, IEEE Photon. Technol. Lett., **14**, 549–551 (2002)

20. Inui T, Mori K, Ohara T, Takara H, Komukai T, Morioka T, 160 Gbit/s adaptive dispersion equalizer using a chirp monitor with a balanced dispersion configuration, 29th European Conf. Optical Communications, Paper Tu3.6.3, 2003

21. Jinno M, Matsumoto T, Nonlinear Sagnac interferometer switch and its applications, IEEE J. Quantum Electron., **28**, 875–882 (1992)

22. Kamatani O, Kawanishi S, Add/drop operation for 100 Gbit/s optical signal based on optical wavelength conversion by four-wave mixing, Electron. Lett., **32**, 911–913 (1996)

23. Kamatani O, Kawanishi S, Prescaled Timing extraction from 400 Gbit/s optical signal using a phase lock loop based on four-wave mixing, IEEE Photon. Technol. Lett., **8**, 1094–1096 (1996)

24. Kawanishi S, Takara H, Uchiyama K, Kitoh T, Saruwatari M, 100 Gbit/s, 50 km, and non-repeated optical transmission employing all-optical multi/demultiplexing and PLL timing extraction, Electron. Lett., **29**, 1075–1077 (1993)

25. Kawanishi S, Morioka T, Kamatani O, Takara H, Saruwatari M, 100 Gbit/s, 200 km optical transmission experiment using extremely low jitter PLL timing extraction and all-optical demultiplexing based on polarisation insensitive four-wave mixing, Electron. Lett., **30**, 800–801 (1994)

26. Kawanishi S, Takara H, Kamatani O, Morioka T, 100 Gbit/s, 500 km optical transmission experiment, Electron. Lett., **31**, 737–738 (1995)

27. Kawanishi S, Takara H, Morioka T, Kamatani O, Saruwatari M, 200 Gbit/s, 100 km time-division-multiplexed optical transmission using supercontinuum pulses with prescaled PLL timing extraction and all-optical demultiplexing, Electron. Lett., **31**, 816–817 (1995)

28. Kawanishi S, Takara H, Morioka T, Kamatani O, Takiguchi K, Kitoh T, Saruwatari M, Single channel 400 Gbit/s time-division-multiplexed transmission of 0.98 ps pulses over 40 km employing dispersion slope compensation, Electron. Lett., **32**, 916–918 (1996)

29. Kawanishi S, Takara H, Uchiyama K, Shake I, Kamatani O, Takahashi H, 1.4 Tbit/s (200 Gbit/s $\times$ 7 ch) 50 km optical transmission experiment, Electron. Lett., **33**, 1716–1717 (1997)

30. Kawanishi S, Ultrahigh-speed optical time-division-multiplexed transmission technology based on optical signal processing, IEEE J. Quantum Electron. **34**, 2064–2079 (1998)

31. Kawanishi S, Takara H, Uchiyama K, Shake I, Mori K, 3 Tbit/s (160 Gbit/s $\times$ 19 channel) optical TDM and WDM transmission experiment, Electron. Lett., **35**, 826–827 (1999)

32. Kieckbusch S, Ferber S, Rosenfeldt H, Ludwig R, Boerner C, Ehrhardt A, Brinkmeyer E, Weber HG, Adaptive PMD compensator in 160Gb/s DPSK transmission over installed fiber, Optical Fiber Communication Conf., Paper PD31, 2004

33. Kodama S, Yoshimatsu T, Ito H, 500-Gbit/s Demultiplexing Operation of Monolithic PD-EAM Optical Gate, 29th European Conf. Optical Communication, 2003, Paper Th4.2.8, 2003

34. Koga M, Morioka T, Miyamoto Y, Next Generation optical communication technologies for Realizing Bandwidth Abundant Networking Capability, Opt. Rev., **11**, 87–97 (2004)

35. Lach E, Schuh K, Schmidt M, Junginger B, Charlet G, Pecci P, Veith G, 7 $\times$ 170 Gbit/s (160 Gbit/s + FEC overhead) DWDM transmission with 0.53 bit/s/Hz spectral efficiency over long haul distance of Standard SMF, 29th European Conf. Optical Communications, Paper Th4.3.5, 2003

36. Ludwig R, Ehrhardt RA, Pieper W, Jahn E, Agrawal N, Ehrke HJ, Kuller L, Weber HG, 40 Gbit/s demultiplexing experiment with 10 GHz all-optical clock recovery using a modelocked semiconductor laser, Electron. Lett., **32**, 327–329 (1996)

37. Mamyshev PV, All-optical data regeneration based on self-phase modulation effect, 24th European Conf. Optical Communication, vol. 1, pp. 475–476, 1998

38. Matsumoto M, Performance comparison of all-optical signal regenerators utilizing self-phase modulation in fibers, Optical Fiber Communication Conf., pp. 108–109, 2003

39. Miyamoto M, Tsuchiya M, Liu H-F, Kamiya T, Generation of ultrafast (65 fs) pulses from 1.55 mm gain-switched distributed feedback (DFB) laser with soliton compression by dispersion arrangements, Jpn. J. Appl. Phys., **35**, 1330–1332 (1996)

40. Mori K, Takara H, Kawanishi S, Sàruwatari M, Morioka T, Flatly broadened supercontinuum spectrum generated in a dispersion decreasing fibre with convex dispersion profile, Electron. Lett., **33**, 1806–1808 (1997)

41. Morioka T, Saruwatari M, Ultrafast all-optical switching utilizing the optical Kerr effect in polarization-maintaining single-mode fibers, IEEE J. Select. Areas Commun., **6**, 1186–1198 (1988)

42. Morioka T, Kawanishi S, Mori K, Saruwatari M, Transform-limited, femtosecond WDM pulse generation by spectral filtering of gigahertz Supercontinuum, Electron. Lett., **30**, 1166–1168 (1994)

43. Morioka T, Kawanishi S, Takara H, Saruwatari M, Multiple-output, 100 Gbit/s all-optical demultiplexer based on multichannel four-wave mixing pumped by a linearly-chirped square pulse, Electron. Lett., **30**, 1959–1960 (1994)

44. Morioka T, Mori K, Kawanishi S, Saruwatari M, Pulse-width tunable, self-frequency conversion of short optical pulses over 200 nm based on supercontinuum generation, Electron. Lett., **30**, 1960–1962 (1994)

45. Morioka T, Supercontinuum lightwave optical sources for large capacity transmission. Proc. 21st European Conf. Optical Communication, Paper Th.A.1.2, pp.821–828, 1995

46. Morioka T, Kawanishi S, Takara H, Kamatani O, Yamada M, Kanamori T, Uchiyama K, Saruwatari M, 100 Gbit/s $\times$ 4 ch, 100 km repeaterless TDM-WDM transmission using a single supercontinuum source, Electron. Lett., **32**, 468–470 (1996)

47. Morioka T, Okamoto K, Ishii M, Saruwatari M,) Low-noise, pulsewidth tunable picosecond to femtosecond pulse generation by spectral filtering of wideband Supercontinuum with variable bandwidth arrayed-waveguide grating filters, Electron. Lett., **32**, 836–837 (1996)

48. Morioka T, Takara H, Kawanishi S, Kamatani O, Takiguchi K, Uchiyama K, Saruwatari M, Takahashi H, Yamada M, Kanamori T, Ono H, 1 Tbit/s (100 Gbit/s $\times$ 10 channel) OTDM/WDM transmission using a single supercontinuum WDM source, Electron. Lett., **32**, 906–907 (1996)

49. Morioka T, Takara H, Kawanishi S, Kitoh T, Saruwatari M, Error-free 500 Gbit/s all-optical demultiplexing using low-noise, low-jitter supercontinuum short pulses, Electron. Lett., **32**, 833–834 (1996)

50. Morioka T, Takara H, Kawanishi S, Uchiyama K, Saruwatari M, Polarisation-independent all-optical demultiplexing up to 200 Gbit/s using four-wave mixing in a semiconductor laser amplifier, Electron. Lett., **32**, 840–842 (1996)

51. Morioka T, Kawanishi S, Uchiyama K, Takara H, Saruwatari M, Polarisation-independent 100 Gbit/s all-optical demultiplexer using four-wave mixing in a polarisation-maintaining fibre loop, Electron. Lett., **30**, 591–592 (1994)

52. Murai H, Kagawa M, Tsuji H, Fujii K, Single Channel 160 Gbit/s Carrier-Suppressed RZ Transmission over 640 km with EA Modulator based OTDM Module. 29th European Conf. Optical Communications, Paper Mo3.6.4, 2003

53. Murai M, Kagawa M, Tsuji H, Fujii K, All-optical 3R-signal regeneration at 80 Gbit/s using high-speed electro-absorption modulator. Optical Amplifiers and their Applications, Paper MD11, 2003

54. Nakamura S, Ueno Y, Tajima K, 168-Gb/s all-optical wavelength conversion with a symmetric-Mach-Zehnder-type switch, IEEE Photon. Technol. Lett., **13**, 1091–1093 (2001)

55. Nakamura S, Ueno Y, Tajima K, Error-free all-optical demultiplexing at 336 Gb/s with a hybrid-integrated symmetric-Mach-Zehnder switch. Optical Fiber Communication Conf., Paper FD1, 2002

56. Nakazawa M, Yamamoto T, Tamura KR, 1.28 Tbit/s-70 km OTDM transmission using third- and fourth-order simultaneous dispersion compensation with a phase modulator, Electron. Lett., **36**, 2027–2029 (2000)

57. Ohara T, Takara H, Shake I, Mori K, Kawanishi S, Mino S, Yamada T, Ishii M, Kitoh T. Kitagawa T, Parameswaran KR, Fejer MM, 160 Gbit/s optical-time-division multiplexing with PPLN hybrid integrated planar lightwave circuit, IEEE Photon. Technol. Lett., **15**, 302–304 (2003)

58. Ohara T, Takara H, Shake I, Mori K, Sato K, Kawanishi S, Mino S, Yamada T, Ishii M, Ogawa I, Kitoh T, Magari K, Okamoto M, Roussev RV, Kurz JR, Parameswaran KR, Fejer MM, 160-Gb/s OTDM Transmission Using Integrated All-Optical MUX/DEMUX With All-Channel Modulation and Demultiplexing, IEEE Photon. Technol. Lett., **16**, 650–652 (2004)

59. Ohara T, Takara H, Kawanishi S, Yamada T, Fejer MM, 160 Gbit/s all-optical limiter based on spectrally filtered optical solitons, Optical Fiber Communication Conf., Paper WN3, 2004

60. Ooi H, Akiyama Y, Ishikawa G, Automatic polarization-mode dispersion compensation in 40 Gbit/s transmission, Optical Fiber Communication Conf. /International Conf. Integrated Optics and Optical Fiber Communication, vol.2, pp. 86–88, 1999

61. Otani T, Miyazaki T, Yamamoto S, 40-Gb/s optical 3R regenerator using electroabsorption modulators for optical networks, IEEE Lightwave Technol., **20**, 195–200 (2002)

62. Oxenlowe LK, Hilliger E, Tersigni A, Nik AM, Hojfeldt S, Romstad F, Yvind K, Skovgaard PMW, Hoppe K, Hanberg J, All-optical demultiplexing and wavelength conversion in an electroabsorption modulator, 27th European Conf. Optical Communication, 604-605, vol.4, 2001

63. Sato K, Hirano A, Ishii H, Chirp-compensated 40-GHz mode-locked lasers integrated with electroabsorption modulators and chirped gratings, IEEE J. Select. Top. Quantum Electron., **5**, 590–595 (1999)

64. Schubert C, Schmidt C, Ferber S, Ludwig R, Weber HG, Error-free all-optical add-drop multiplexing at 160 Gbit/s, Electron. Lett., **39**, 1074–1076 (2003)

65. Shake I, Takara H, Kawanishi S, Yamabayashi Y, Optical signal quality monitoring method based on optical sampling, Electron. Lett., **34**, 2152–2154 (1998)

66. Shake I, Otani E, Takara H, Uchiyama K, Yamabayashi Y, Morioka T, Bit rate flexible quality monitoring of 10 to 160 Gbit/s optical signals based on optical sampling technique, Electron. Lett., **36** , 2087–2088 (2000)

67. Shake I, Takara H, Kawanishi S, Simple Q factor monitoring for BER estimation using opened eye diagrams captured by high-speed asynchronous electrooptical sampling, IEEE Photon. Technol. Lett., **15**, 620–622 (2003)

68. Shake I, Takara H, Uchiyama K, Ogawa I, Kitoh T, Kitagawa T, Okamoto M, Magari M, Suzuki Y, Morioka T, 160 Gbit/s full optical time-division demultiplexing using FWM of SOA-array integrated on PLC, Electron. Lett., **38**, 37–38 (2002)

69. Suzuki M, Tanaka H, Edagawa N, Utaka K, Matsushima Y, Transform-limited optical pulse generation up to 20-GHz repetition rate by a sinusoidally driven InGaAsP electroabsorption modulator, IEEE J. Lightwave Technol. **11**, 468–473 (1993)

70. Takada A, Sato K, Saruwatari M, Yamamoto M, Pulse width tunable subpicosecond pulse generation from an actively modelocked monolithic MQW laser/MQW electroabsorption modulator, Electron. Lett., **30**, 898–899 (1994)

71. Takahashi R, Low-temperature-grown surface-reflection all-optical switch (LOTOS), Opt. Quantum Electron., **33**, 999–1017 (2001)

72. Takara H, Kawanishi S, Saruwatari M, Stabilization of a mode locked Er-doped fibre laser by suppressing the relaxation oscillation frequency component, Electron. Lett., **31**, 292–293 (1995)

73. Takara H, Kawanishi S, Saruwatari M, Optical signal eye diagram measurement with sub-picosecond resolution using optical sampling, Electron. Lett., **32**, 1399–1400 (1996)

74. Takara H, Ohara T, Mori K, Sato K, Yamada E, Inoue Y, Shibata T, Abe M, Morioka T, Sato K-I, More than 1000 channel optical frequency chain generation from single supercontinuum source with 12.5 GHz channel spacing, Electron. Lett., **36**, 2089–2090 (2000)

75. Takiguchi K, Kawanishi S, Takara H, Himeno A, Hattori K, Dispersion slope equalizer for dispersion shifted fiber using a lattice-form programmable optical filter on a planar lightwave circuit, IEEE J. Lightwave Technol. **16**, 1647–1656 (1998)

76. Tamura KR, Nakazawa M, A polarization-maintaining pedestal-free femtosecond pulse compressor incorporating an ultrafast dispersion-imbalanced nonlinear optical loop mirror, IEEE Photon. Technol. Lett., **13**, 526–528 (2001)

77. Tsuda H, Okamoto K, Ishii T, Naganuma K, Inoue Y, Takenouchi H, Kurokawa T, Second- and third-order dispersion compensator using a high-resolution arrayed-waveguide grating, IEEE Photon. Technol. Lett., 11, 569–571 (1999)

78. Uchiyama K, Hashimoto E, Yamabalashi Y, Highly precise bit-phase synchronization technique for an optically controlled time-division demultiplexer, IEEE Photon. Technol. Lett., **12**, 915–917 (2000)

79. Wada O, Femtosecond all-optical devices for Tera-bit/sec optical networks, Electro Devices Meeting, IEDM Technical Digest, 589–592, 2000

80. Wakabayashi S, Baba A, Moriya H, Wang X, Hasegawa T, Suzuki A, Tunable dispersion slope compensator based on chirped FBGs with temperature distribution for 160 Gbit/s, Optical Fiber Communication Conf., pp. 30–31, 2003

81. Watanabe S, Futami F, Okabe R, Takita Y, Ferber S, Ludwig R, Schubert C, Schmidt C, Weber HG, 160 Gbit/s optical 3R-regenerator in a fiber transmission experiment, Optical Fiber Communication Conf., Paper PD16, 2003

82. Westlund M, Sunnerud H, Li J, Hansryd J, Karlsson M, Hedekvist PO, Andrekson PA, Long-term automatic PMD compensation for 160 Gbit/s RZ transmission, Electron. Lett., **38**, 982–983 (2002)

83. Yamamoto T, Yoshida E, Nakazawa M, Ultrafast nonlinear optical loop mirror for demultiplexing 640 Gbit/s TDM signals, Electron. Lett., **34**, 1013–1014 (1998)

84. Yokoyama H, Highly reliable mode-locked semiconductor lasers, IEICE Trans. Electron., **E85-C**, 27–36 (2002)

85. Suzuki A, Wang X , Ogawa Y, and Nakamura S, 10 × 320 Gb/s (3.2 Tb/s) DWDM/OTDM transmission in C-band by semiconductor-based devices, Proc. ECOC 2004, Th4.1.7, 2004

86. Marembert V, Schubert C, Ferber S, Schulze K, Schmidt-Langhorst C, Boemer C, Kroh M, Ludwig R, Watanabe S, Futami F, Okabe R, and Weber HG, Single-channel 640 Gbit/s DPSK Transmission over a 160 km Fibre Link, Proc. ECOC 2004 Post-Deadline, Th4.4.2, 42–43, 2004

DOI: 10.1007/s10297-005-0050-4
Originally published in J. Opt. Fiber. Commun. Rep. 2, 530–557 (2005)

New optical device technologies for ultrafast OTDM systems

T. Sakurai[1] and N. Kobayashi[2]

[1] Photonics Research Institute (PRI)
National Institute of Advanced Industrial Science and Technology (AIST)
1-1-1 Umezono, Tsukuba, Ibaraki 305-8568 Japan
Email: teruo-sakurai@aist.go.jp
[2] National Institute of Advanced Industrial Science and Yechnology (AIST)
1-1-1 Umezono, Tsukuba, Ibaraki 305-8568 Japan
Email: naoto.kobayashi@aist.go.jp

Abstract. Optoelectronic devices handling high bit-rate signals of picosecond or sub-picosecond pulse repetitions are necessary for the OTDM or OTDM/WDM-mixed systems. The bit-rate is 1st or 2nd order higher than the operation speed of conventional devices. To meet the higher speed requirement, we have to develop ultrafast optoelectronic device technologies in new device principles and materials.

1. Introduction

A national project of the Femtosecond Technology (FST project) in Japan that is sponsored by NEDO (New Energy and Industrial Technology Development Organization) develops ultrafast optoelectronic devices in order to make OTDM/WDM-mixed Tb/s-class photonic networks possible. The project was started in 1995 and will reach its goal in 2004. FESTA (The Femtosecond Technology Research Association) and AIST (National Institute of Advanced Industrial Science and Technology) execute the project in cooperative works.

Most of the optoelectronic devices are based on the semiconductor device and material technology in the project. We also develop organic dye aggregates as new materials for the ultrafast optical switch. The reason why we challenge these devices and materials instead of fiber-based technologies is the stable operation and the possibility of device integration in future.

One of the key issues is the generation and the formation of ultrashort light-pulses in the signal transmission. Mode-locked semiconductor laser diodes are suitable for

oscillators of light pulses and/or standard signal pulses in OTDM light sources due to their low jitter characteristics (see section 2). The group-velocity-dispersion compensation is one of big issues in the ultrashort-pulse laser and in the OTDM transmission. We developed a semiconductor pulse compressing device and a pulse shaping device respectively for the dispersion compensation [1]. Pulse compressing devices are composed of the semiconductor coupled-waveguide structure and will be used to make the chirped laser-pulse width short in transmitters. Fiber Bragg gratings will be applied to adaptive pulse forming devices for compensating pulse form fluctuations by the environmental temperature in the long haul transmission [2].

Optical switches as optical node devices in the OTDM/WDM-mixed system will be operated above 160 Gb/s. Speed limits of current electronic technologies are believed to be about 100 Gb/s and the optical switches must be operated by some other control pulses than electronic ones. Light pulses are used for the purpose. These devices are called as all-optical switches.

Ultrafast optical switches developed in the project are based on new phenomena and/or new materials. SMZ (Symmetric Mach-Zehnder) switches composed of PLC (Planar Lightwave Circuit) Mach-Zehnder interferometer and SOAs for phase modulation were used in the Demux and logic operations (see section 3). The PLC will be replaced with photonic crystal waveguides in future. The photonic crystal SMZ device partially embedded with quantum dots as optical nonlinear materials, i.e., PC-SMZ, is expected to have abilities of small size and device integration. The ISBT (Inter Subband Transition) switch uses high-speed recovery characteristics of the absorption saturation in the quantum wells (see section 4). Ultrafast optical gates and Demux are its promising applications. The two-photon resonance multi-layer device utilizing the Kerr effect enhanced by the optical field confinement will be used as an ultrafast optical gate [3].

FESLAP (Femtosecond Large Area Parallel Processor) switches using the saturation absorption in organic dye aggregates convert the time serial signals to space parallel signals (see section 5). This switch is suited for header recognition in photonic nodes because of dividing the frequency for lower-frequency circuit operations. The high-speed wavelength conversion at the node is required in the OTDM/WDM-mixed system. Four-wave mixing in semiconductor gain medium is employed in wavelength conversion devices (see section 6).

Precise characterization of light pulses is inevitable for the development of optical devices. Timing jitter measurements were developed using time domain methods of both the time domain demodulation and the time interval analysis. For high repetition rate OTDM pulses, new technologies of the double-balanced mixing and the optoelectronic harmonic mixing were combined to these time domain methods (see section 7). The ultrashort light-pulses are extremely chirped and broadened under chromatic dispersion in optical fibers because of their broadband spectrum. Time-dependent variation of the pulse waveform is significant in long-distance propagation due to variation of chromatic dispersion under temperature drift. We have developed a frequency-resolved optical gating method using two-photon absorption, which enables high-sensitivity real-time characterisation in time-spectral domain of the pulses [4].

In this paper, we will introduce several ultrafast optical devices developed in the Femtosecond Technology Project.

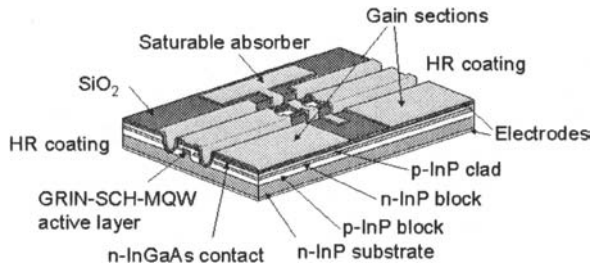

Fig. 1. Schematic structure of CPM-LD.

2. Mode-Locked Laser Diodes

Ultrafast optical pulse generation is of great interests for many applications, such as optical time division multiplexing systems, soliton transmission systems, optical measurement systems, and so on. Mode-locked laser diodes (MLLD) are very attractive for such applications because of its small size, high reliability, and high stability. Furthermore, a passively mode-locked laser diode (PML-LD) has the fascinating feature of generating ultrafast optical pulses beyond limit of electrical speed, because it needs no external modulation source for pulse generation [5]. In practical use, the most important technical problems of PML-LD are synchronization of such high repetition pulses to an external clock signal and reduction of the comparably large timing jitter. Hybrid mode-locking [6] and optical synchronous mode-locking are well-known methods for stabilization of PML-LD. These methods, however, require an electrical/optical signal with a repetition frequency almost equal to that of the PML-LD. In this section, the generation of ultrafast optical pulse train with a mode-locked laser diode and its control techniques are described.

Figure 1 shows a schematic structure of a colliding-pulse mode-locked laser diode (CPM-LD) [7]. The CPM-LD is a kind of PML-LDs in which the saturable absorber is placed at the center of the laser cavity. Both the gain and the absorber sections consist of eight compressively strained InGaAsP quantum wells separated by In-GaAsP barriers, with the GRIN-SCH for avoiding the electrical screening effect by trapped photo-carriers at hetero-interface. The mode-locking frequency can be basically increased as the cavity length is shortened. However the mode-locking frequency is restricted by the carrier dynamics in the saturable absorber. When the repetition time is close to or beyond the recovery time of the saturable absorber, the modulation depth at the saturable absorber become shallow. And then, the pulse width becomes broader and the mode-locking operation itself is impeded in the worst case. This is because the GRIN-SCH structure is introduced to the high repetition MLLD. When the currents were injected to the two gain sections and the absorber section was reverse biased suitably, passive mode-locking occurred. Figure 2 shows (a) SHG correlation trace and (b) optical spectrum of the output of the CPM-LD. The saturable absorber section was 17 μm and the total cavity length was about 174 μm. The repetition frequency was about 480 GHz, which coincided with twice the round-trip frequency estimated

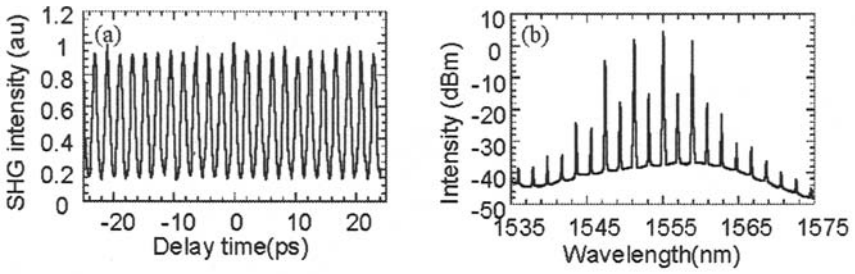

Fig. 2. (a) Correlation trace and (b) optical spectrum of CPM-LD with the cavity length of 174 μm.

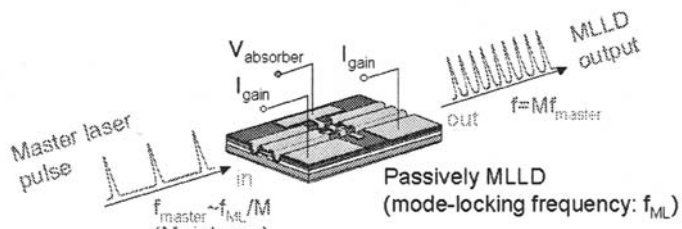

Fig. 3. SSML method.

from the cavity length. The pulse width was estimated to be 0.58 ps, assuming the sech^2 waveform. The center wavelength and the spectral width were 1555 nm and 8 nm, respectively. The time-bandwidth product was 0.58, close to the transform limited value of sech^2 pulses.

When the mode-locking frequency is extremely high, subharmonic optical synchronous mode-locking (SSML) [8,9] by a subharmonic frequency optical pulse injection (Fig. 3) is the most promising way for synchronization with an external signal because this can be achieved with low-frequency master laser pulses and the application is not limited by bandwidth of the drive electronics. The 480-GHz CPM-LD has been stabilized by the SSML, using the hybrid mode-locked laser diode as a master laser. The repetition frequency of the master laser (f_{master}) was 9.954 GHz, corresponding to 48th subharmonics of the slave laser's repetition frequency (f_{ML}). The center wavelength and the pulse width were about 1558 nm and 1.6 ps, respectively. In the SSML experiment, no significant degradations were observed in both of the pulse shape and the optical spectrum when the injected power was below -10 dBm.

Figure 4 shows an experimental setup for the jitter measurement of ultrafast optical pulses [10]. Ultrafast optical pulses with frequency of f_{ML} and reference pulses with frequency of f_{ref} were injected in a semiconductor optical amplifier (SOA) simultaneously. Beat signal was generated due to nonlinear coupling for cross gain modulation

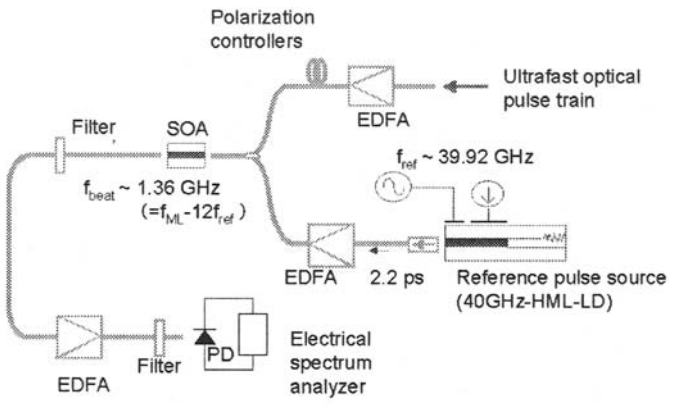

Fig. 4. Experimental setup for the timing jitter measurements of 480 GHz CPM-LD.

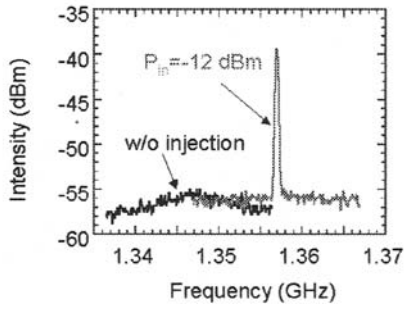

Fig. 5. Changes in electrical power spectra of beat signals in the SSML of 480 GHz CPM-LD.

between those pulses. We can estimate the timing jitter of the ultrafast optical pulse train from the SSB noise of the beat signal, because the squared timing jitter of the beat signal is given by the summation of those of the signal and the reference pulse trains. In this experiment, the reference pulse source was a hybrid mode-locked laser diode. The repetition frequency of the reference pulse train was 39.919 GHz. The pulse width, the center wavelength, and the timing jitter were 2.25 ps, 1539.5 nm, and 0.23 ps, respectively. Figure 5 shows the changes in the beat power spectra with and without the master laser pulse injection. Without master laser pulse injection, the spectrum was broadened and no discrete frequency component was observed. This indicates that the mode-locking frequency fluctuated under the passive mode-locking operation. In contrast, a discrete frequency component corresponding to $f_{\mathrm{ML}} - 12 f_{\mathrm{ref}}$ appeared and the side band noise level decreased with master laser pulse injection at the average power of -12 dBm. This implies that the mode-locking frequency of the CPM-LD was exactly locked to 48th harmonics of the master laser's repetition frequency and

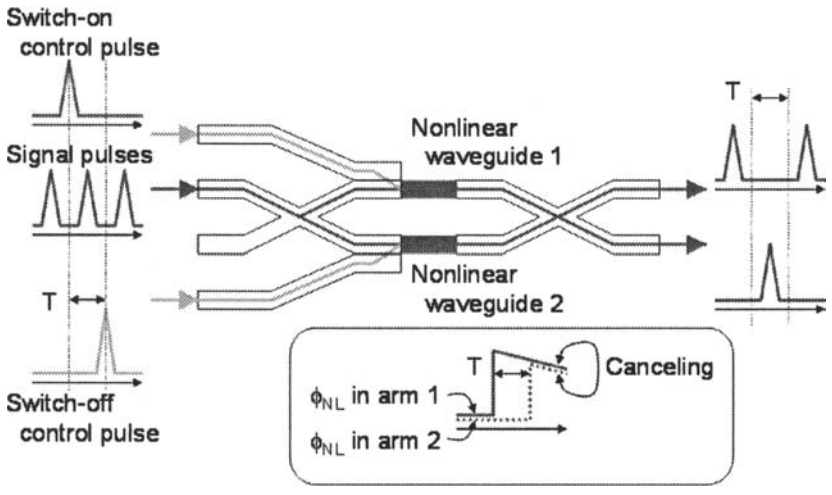

Fig. 6. Schematic representation of a symmetric Mach-Zehnder all-optical switch. Differential phase modulation is also illustrated in the inset.

that the timing jitter was also reduced. The timing jitter was estimated to be about 0.14 ps, less than that of the master laser. Stable ultrafast optical pulse generation by SSML is very promising as a compact and reliable pulse source for future advanced applications.

3. Symmetric Mach-Zehnder Type All-Optical Switches and Ultrafast All-Optical Signal Processing

3.1. Symmetric Mach-Zehnder (SMZ) Type All-Optical Switches

A symmetric Mach-Zehnder (SMZ)-type ultra-fast all-optical switch has been developed for a key device in an optical-time-division-multiplexing (OTDM) system [11,12]. From practical application point of view, one of the requirements for all-optical switches is that a control-light-pulse energy must be much less than 1 pJ, otherwise the control light power is too high even at a few tens of Gb/s. To satisfy this requirement, the SMZ switch uses semiconductor optical amplifiers (SOAs) for nonlinear elements to enhance the band-filling non-linearity in semiconductors by stimulated emission. This enables true femto-joule switching, but the relaxation time of SOAs limits the operating speed to less than a few tens of Gb/s. A promising way to mitigate this problem is to use a differential phase modulation (DPM) scheme [11]. In this way, the difference in nonlinear phase shifts (ϕ_{NL}) optically induced in the two nonlinear elements defines the state of the switch, so the effect of slow relaxation is circumvented, as illustrated in Fig. 6. The DPM scheme also realizes a rectangle-like switching window, which is highly desirable in many applications. There are two

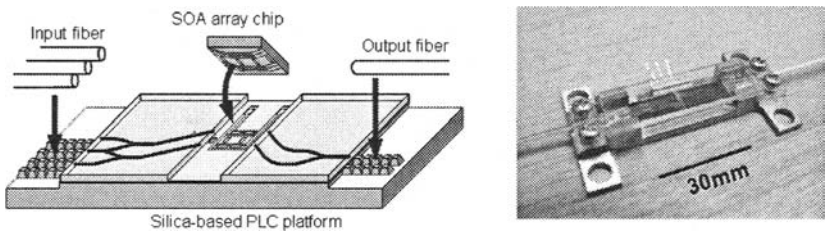

Fig. 7. Structure and photograph of a hybrid-integrated symmetric Mach-Zehnder all-optical switch.

variants of the SMZ switch: a polarization-discriminating SMZ [13] (PD-SMZ, often called UNI) and a delayed-interference signal-wavelength converter (DISC) [14]. These devices can be configured in inherently stable forms suitable for bulk optics implementation. The original SMZ switch, on the other hand, can be unstable unless integrated. Hybrid-integrated [15,16] (Fig. 7) and monolithic [17] SMZ-type switches have been reported.

3.2. Ultra-Fast All-Optical Signal Processing With the SMZ All-Optical Switches

As an example of ultra-fast all-optical signal processing, a de-multiplexing experiment is explained here, in which the original 42-Gb/s signal is retrieved (de-multiplexed) from a 336-Gb/s signal that is made by optically time-division-multiplexing 8–42 Gb/s signal channels. Figure 8 shows an experimental setup. A HI (hybrid integrated)-SMZ all-optical switch is driven by a 42-GHz control pulse train to retrieve 42 Gb/s signal pulses from 336 Gb/s signal pulses. Control pulses were generated by multiplexing the output of a mode-locked fiber laser (MLFL, 10.5 GHz) twice by two-stage optical delay lines. The 336 Gb/s signal was generated from the same MLFL. Here the output of the MLFL was compressed, wavelength converted, and modulated with a pseudo-random bit sequence (PRBS) of 2^7-1 before being multiplexed to 336 Gb/s by optical delay lines. The low noise compression and wavelength conversion were achieved by first generating super-continuum in an optical fiber, spectrally slicing it by a filter, and applying a dispersion compensating technique. In this experiment, the control pulse width was set relatively wide (1.5 ps), compared with the interval (3.0 ps) and the width (0.9 ps) of the 336 Gb/s signal pulses, to minimize the degradation in switching characteristics due to the intra-band effects in the SOA type nonlinear phase shifters. If the control pulse width approaches or exceeds 1 ps, the switching energy increases and the differential phase modulation becomes less complete, because of the hole burning and the subsequent carrier heating effects in SOAs [18]. Of course, wider control pulses allow a higher level of crosstalk between adjacent bits, but it is a weak function of the control pulse width, because of the sinusoidal transfer function characteristic of a Mach-Zehnder interferometer. Thus, the degradation in switching characteristics and the cross-talk are compromised at 1.5 ps. Figure 9(a) shows an eye-diagram of the 336 Gb/s input signal measured by an optical sampling oscilloscope, indicating uniformity

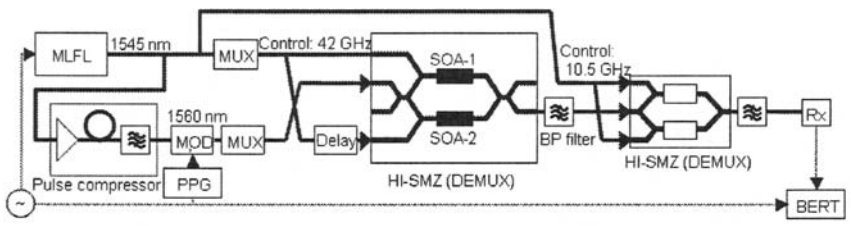

Fig. 8. Setup for 336→42 de-multiplexing experiment. MOD: EO optical modulator, PPG: Pulse-pattern generator, Rx: Receiver system, BERT: Bit-error-rate tester.

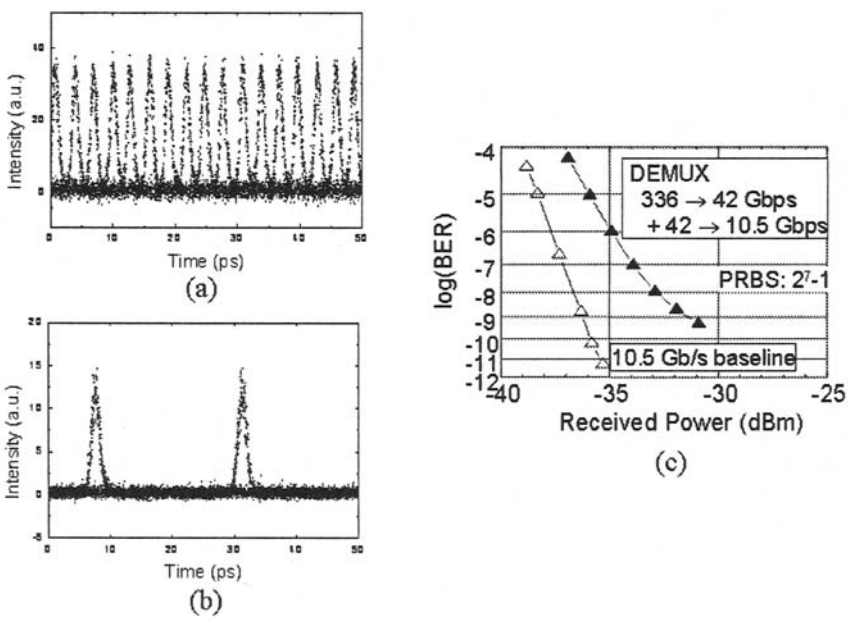

Fig. 9. (a) Eye-diagram of the 336-Gb/s input signal. (b) Eye-diagram of the 42-Gb/s signal de-multiplexed from the 336-Gb/s input signal. (c) Result of bit-error-rate measurements of 336→42 Gb/s de-multiplexing (42→10.5 Gb/s optical de-multiplexing).

in multiplexing from 10.5 to 336 Gb/s, while Fig. 9(b) shows an eye-diagram of the de-multiplexed 10.5 Gb/s signal. The extinction ratio between de-multiplexed and rejected pulses was approximately 17 dB. A bit-error-rate (BER) was assessed at 10.5 Gb/s after further de-multiplexing the output 42 Gb/s pulses down to 10.5 Gb/s signal by using another HI-SMZ. As can be see from Fig. 9(c), error free operation (BER $< 10^{-9}$) was achieved.

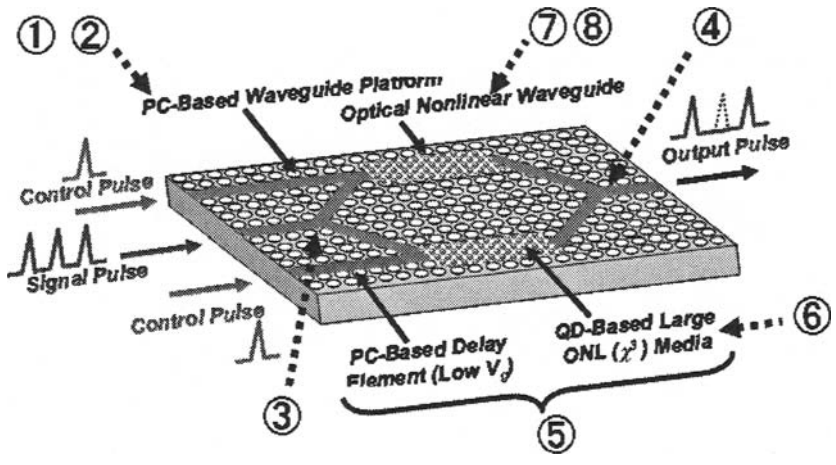

Fig. 10. Schematic diagram of a 2DPC slab waveguide-based all-optical switch (PC-SMZ).

3.3. Challenging Photonic Crystal-Based Ultra-Small All-Optical Switches

A GaAs two-dimensional photonic crystal (2DPC)-based ultra-small symmetrical Mach-Zehnder (SMZ) all-optical switch (hereafter referred to as PC-SMZ) was proposed [19]. 2DPC straight- [20], bent- [21], Y-branch- [22], directional coupler- [23], quantum dot (QD)-embedded nonlinear-waveguides [24] and a PC-SMZ chip including these waveguides [25] have been fabricated using a GaAs air-bridge membrane with triangular-lattice line-defect waveguides. Figure 10 shows a schematic picture of the PC-SMZ. Technical key issues are indicated by numbers 1–8. InAs quantum dots (QDs) as optical nonliear (ONL) mateials are embedded only in the straight ONL phase-shift arms between the Y-branch splitter (3) and Y-junction coupler (4). The device is expected to exhibit optical switching at a speed of over 40 Gb/s on a principle of the conventional SMZ switch, while optical switching energy can be dramatically reduced by using a low group velocity (V_g), appearing in the vicinity of a photonic bandgap [24,26].

So far, single chip of the PC-SMZ was integrated in the area of about 500 $\times$ 500 μm^2 [25], while an extremely low propagation loss, less than 1 dB/mm, obtained recently [27,28] allows us to integrate many chips in the area up to 1 cm in length. For the Y-junction (4), use of a directional coupler [23] instead of a three-fold symmetry Y-branch enables exhibiting a desired SMZ interference, otherwise an undesirable ring resonance mode is generated in the SMZ loop. In the QD-embedded ONL arm, on the other hand, a phase shift $\Delta\phi$ of $\pi/2$, which is necessary for operation of the SMZ switching, was verified experimentally [29], while enhancement of the ONL effect by use of the low V_g was predicted theoretically [24].

Typical SEM (canning electron microscope) photographs and transmittance spectra of the PC-SMZ membrane are shown in Fig. 11 [25]. Figure 11(a)–(c) show a total

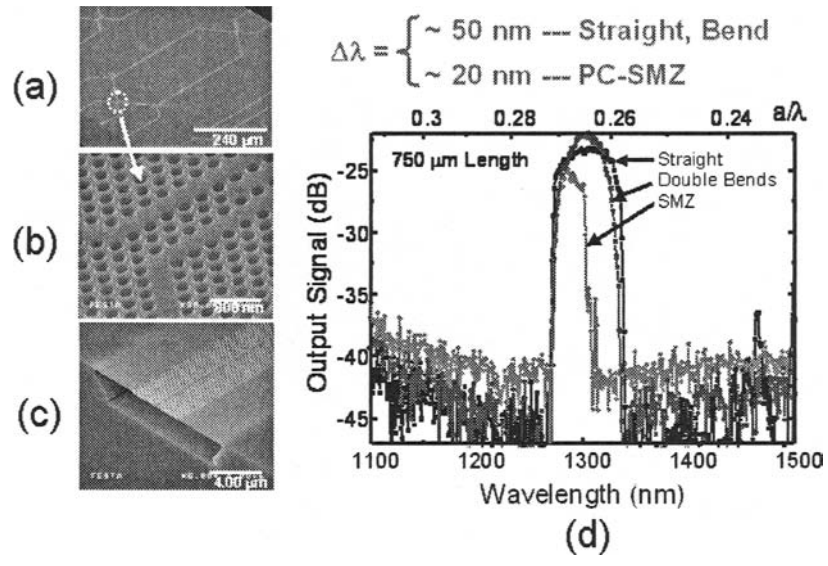

Fig. 11. (a)–(c): SEM photographs of an air-bridge type 2DPC slab waveguide sample including PC-SMZ patterns. (d) Transmittance spectra of the PC-SMZ membrane.

PC-SMZ pattern, expanded part of the directional coupler and cleaved edge of the air-bridge, respectively, while Figure 11(d) shows transmission spectra of straight, double bend and PC-SMZ-waveguides. A bandwidth of the PC-SMZ is narrower (~20 nm) than those of the straight and bend waveguides (~50 nm). Nevertheless, it should be noted that the transmittance of the PC-SMZ is not so degraded as that of the straight waveguide, taking into account that the PC-SMZ involves eight bends between the input and output ports.

3.4. Conclusion

A symmetric Mach-Zehnder (SMZ) all-optical switch achieves ultra-fast, low-power switching by differential phase modulation. So far, ultra-fast de-multiplexing from 336 to 10.5 Gb/s was performed. The application of this device is not limited to de-multiplexing alone. Error-free all-optical regeneration at 84 Gb/s [30] and error-free wavelength conversion at 168 Gb/s [31] have also been reported, indicating the high repetition capability of SMZ type all-optical switches. On the other hand, a 2DPC-based GaAs ultra-small SMZ all-optical switch was also developed. Air-bridge membranes including the PC-SMZ pattern as well as straight, bend, Y-branch and directional coupler waveguides were fabricated and characterized in the 1.1–1.55 μm wavelength region. 2DPC technologies developed here is promising not only for the PC-SMZ but also for wide applications to other ultra-small photonic integrated circuits.

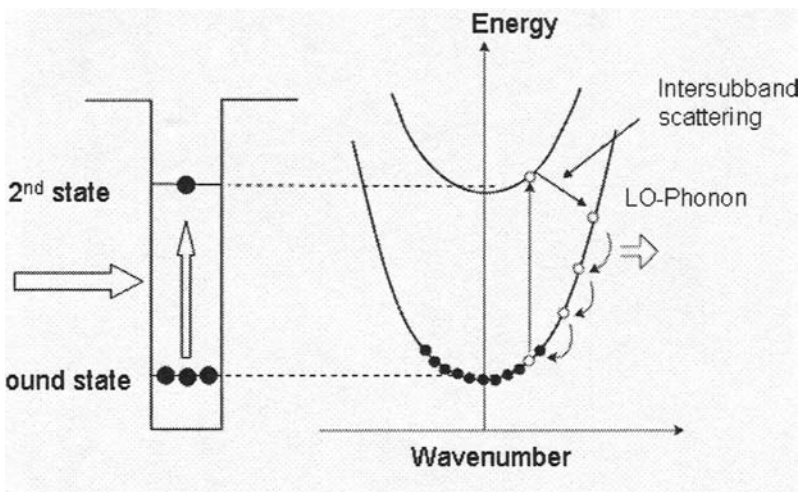

Fig. 12. Schematic potential lineup and subband structure of quantum well.

4. Ultrafast All-Optical Switch Using Intersubband Transition in Quantum Well

4.1. Introduction

Absorption saturation effect in the intersubband transition (ISBT) of a quantum well is very attractive for ultrafast all-optical switches because of its very fast absorption recovery [32]. Since it is necessary to use deep potential well to obtain 1.55 μm-intersubband transitions, we are investigating three types of material systems. The investigation will also provide us deeper understanding of ISBT leading to the development of better performance switches. Here, we first review the principle of the ISBT switch and show the-state-of-the-art development.

4.2. Principle of the ISBT Switch

Figure 12 shows the potential lineup and the corresponding band diagram of a quantum well. The well layer is heavily doped and then the ground state is occupied by electrons. If we illuminate the quantum well with an intense p-polarized optical pulse (gate pulse) whose wavelength corresponds to the transition wavelength between the ground state and the second state, the carriers in the ground state is excited to the second state. When the carrier number in the ground state and the upper sate becomes equal, the quantum well is transparent. Therefore a small intensity signal pulse can transmit through the quantum well; it means that the switch is in the "on" state. After the excitation pulse, carriers in the second state relax to the ground sate and then the quantum well is absorptive again, i.e., the switch is in the "off" sate. The most attractive feature of the ISBT is that the excited carriers relax to the ground state with a time constant of a few

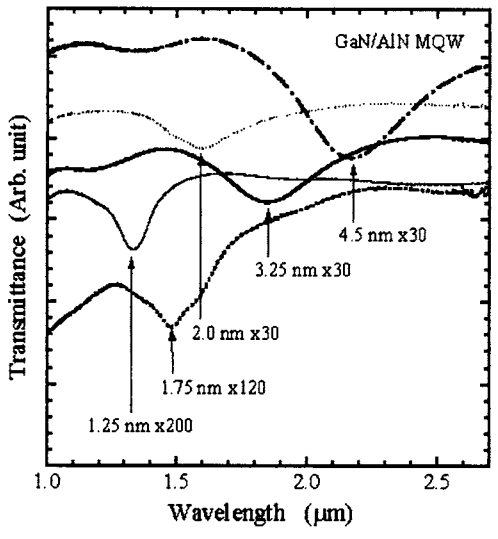

Fig. 13. Transmittance of GaN/AlN quantum well for various well layer thicknesses and layer numbers.

100 fs to a few ps. Because of this very fast relaxation time, we can make use of ISBT for ultrafast all-optical switches.

To realize intersubband transition at the communication wavelength of 1.55 μm, we need a very deep potential well. Three material systems are being developed. They are GaN/AlGaN system [33–37] (well depth; 2 eV), InGaAs/AlAsSb system [38–40] (1.6–1.7 eV), and CdS/ZnSe/BeTe system [41,42] (2.3 eV). Even with these materials we need a very thin quantum well of a thickness of a few mono-layers to obtain the transition wavelength of 1.55 μm.

The absorption recovery time is mainly limited by intersubband scattering time. The scattering time depends on electron effective mass, dielectric constant, and LO-phonon energy [43]. The calculated scattering times are 90 fs in GaN, 2500 fs in InGaAs, and 180 fs in CdS. The scattering time is the shortest in GaN and the longest in InGaAs.

4.3. Quantum Wells for ISBT

4.3.1. GaN/AlGaN Quantum Well

The fastest response speed can be expected with this material because of the shortest intersubband scattering time. We started the growth of GaN/AlGaN quantum well using MOCVD and attained very fast response speed of 150 fs at the wavelength of 4.5 μm [34]. However, it was difficult to obtain the absorption peak at shorter wavelengths of below 2.9 μm. We therefore changed the growth method to MBE and changed the barrier layer to AlN [35]. Figure 13 shows the absorption spectrum for various well layer thicknesses and numbers. Barrier thickness was 4.5 nm. A high density doping of

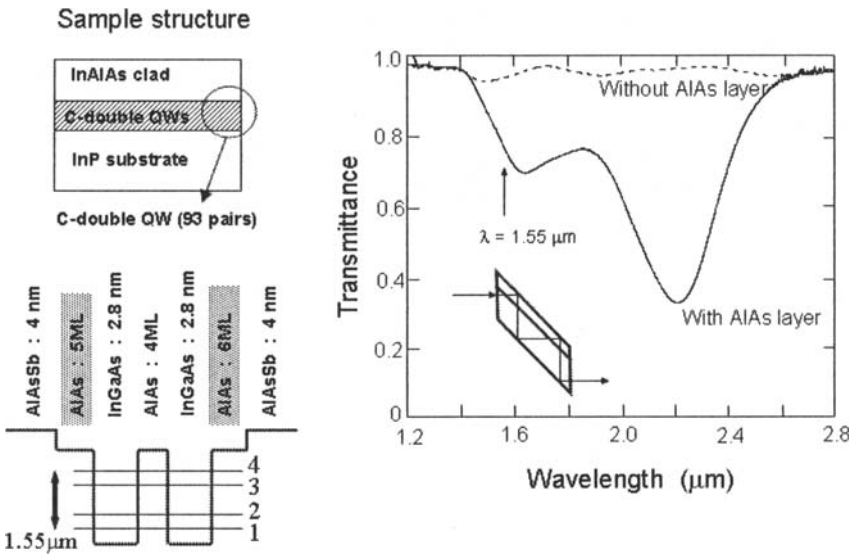

Fig. 14. (a) Sample structure and the potential lineup. (b) Transmittance of the coupled-double quantum well. Light was introduced at the 45 degrees lapped wafer end. Multiple reflections were used.

8×10^{19} cm^{-3} was performed to the well layer. In the measurement p-polarized light was injected to the grown quantum well in Brewster angle. The shortest absorption wavelength was 1.33 μm. The saturation energy, which is pulse energy to give half of the initial absorption coefficient, was measured to be 500 fJ/μm^2 at 1.55 μm. The response speed at this wavelength was estimated to be 400 fs.

4.3.2. InGaAs/AlAsSb Quantum Well

The potential well depth of this system is rather shallow than that of GaN/AlN and CdS/ZnSe/BeTe systems. It was then difficult to obtain the transition wavelength of 1.55 μm with InGaAs/AlAsSb single-quantum well due to the inter-diffusion of composite atoms between well and barrier layer. To suppress the inter-diffusion, we inserted a few mono-layers of AlAs between the InGaAs well layer and AlAsSb barrier layer [38]. Further we introduced a coupled-quantum well structure. Figure 14 shows the coupled-quantum well structure and the absorption spectrum [40]. The coupled-quantum well structure splits the ground state and upper state. We can obtain the transition wavelength of 1.55 μm between sublevels 1 and 4. The insertion of a few mono-layers of AlAs at the interface increased the absorption coefficient largely. Absorption spectrum without insertion of AlAs layer is also shown for comparison. It was also confirmed that the coupled quantum well gives faster response than the single quantum well [41]. This is because of the second sublevel serving as a carrier reservoir, which rapidly supplies carriers to the depleted ground state. We obtained absorption recovery time of 600fs in the coupled quantum well, while the time was 1.5–2.0 ps in

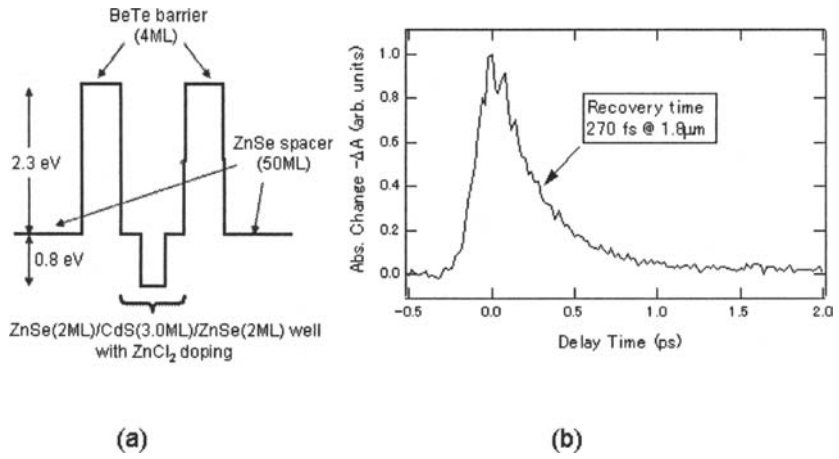

Fig. 15. (a) A schematic potential lineup of CdS/ZnSe/BeTe quantum well. (b) Absorption recovery under short pulse excitation.

the single quantum well. The absorption saturation of the quantum well was evaluated with the same measurement configuration as shown in the inset of Fig. 14. The value ranged 40 fJ/μm^2 to a several hundred fJ/μm^2.

4.3.3. CdS/ZnSe/BeTe Quantum Well

Figure 15(a) shows the structure of the quantum well. The well layer consists of very thin CdS layer and ZnSe layers [42]. The CdS layer was introduced to eliminate the effect of X-band in the BeTe cladding layer. The thin CdS layer lowers the energy levels so that the second level is lower than the X-band of the BeTe layer. This eliminates the carrier relaxation via X-band in BeTe layer, and enables us to obtain very fast response. Figure 15(b) shows the response for a sample whose absorption peak is 1.8 μm. We can confirm a very fast recovery of 270fs. The saturation powers ranging 100–600 fJ/μm^2 were obtained for the samples with absorption peak wavelength of 1.6–1.8 μm. The shortest absorption wavelength so far achieved with this quantum well was 1.58 μm.

4.4. ISBT Switching Device

Waveguide-type switching device is under development for these three types of material systems. Figure 16 shows an example of the device structure realized using InGaAs/AlAs/AlAsSb coupled-quantum well [39]. A ridge type waveguide is used and the ridge is tilted by about 7 degrees to reduce the reflection at the facet. Figure 16 shows the input pulse energy versus transmittance characteristics of the device for a pulse width of 150 fs. In this case 40 pairs of coupled-quantum well were used. Transmission increased by 3 dB for input-pulse energy of 20 pJ. The problem in this specific device is that the two-photon absorption is large as evidence in the steep reduction in

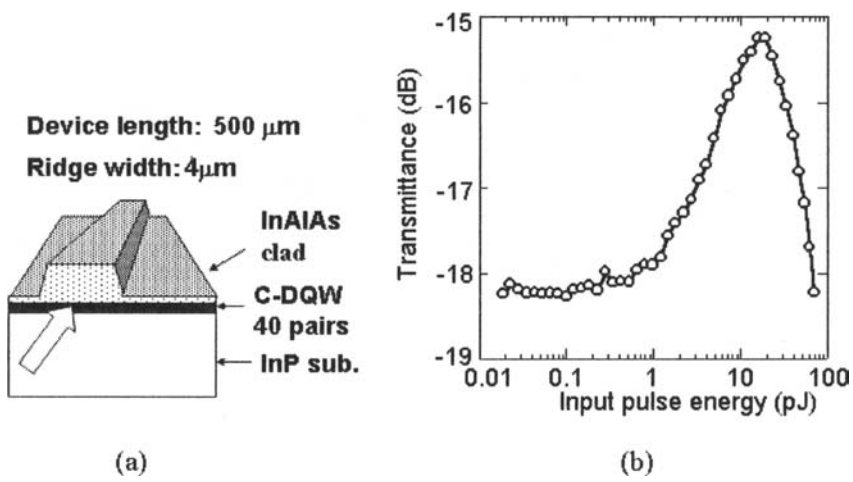

Fig. 16. (a) Schematic structure of ridge-waveguide type ISBT switch. (b) Transmittance of the ISBT switch for 150-fs gate pulse.

transmittance at high pulse energy. This two-photon absorption comes mainly from the InP substrate. The reduction of the field penetration to the substrate would improve this situation largely and the improved structure is under development.

4.5. Summary

Because of material parameters, the GaN, and CdS/ZnSe well layer gives very fast response while the InGaAs quantum well gives slower response. It is a general principle that higher energy is needed for faster response. Therefore it will be necessary to select material systems depending on the applications considering required switching speed and energy. One of the promising applications of the ISBT switch is ultrafast switching in OTDM systems. At present, the switching energy and the extinction of InGaAs/AlAsSb device are yet unsatisfactory. We can further improve the performances by employing the structure to reduce the two-photon absorption, and further reduction of the switching energy by the improvement of the quantum well. Devices using GaN/AlN, and CdS/ZnSe/BeTe quantum well are also under development to realize ultrafast switches.

5. All-Optical Spatial Switch Using Ultrafast Nonlinear-Optical Response of Organic Films

5.1. Introduction

In the field of optical switching materials, compound semiconductors such as InGaAs and dielectric materials such as silica optical fibers have been commonly used.

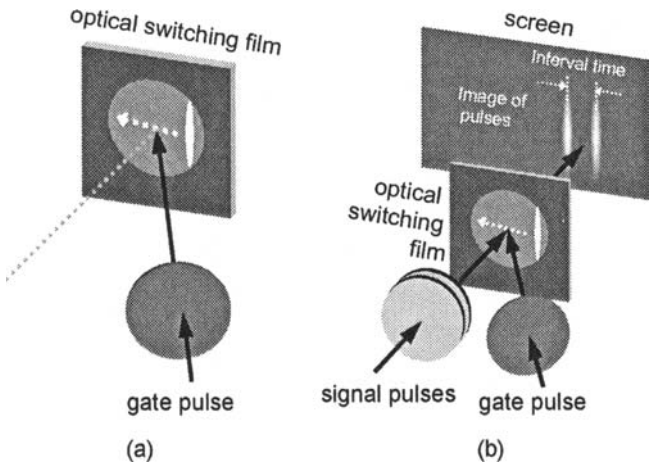

Fig. 17. Principle of ultrafast moving slit (a) and serial to parallel conversion of signal pulses (b) activated by irradiation of a gate pulse from horizontally oblique angle.

Semiconductors exhibit high nonlinear-optical susceptibility, however speeds of their responses are relatively slow. For silica fibers, ultrafast switching can be achieved while requires long interaction length because of lower susceptibility. To fabricate ultrafast all-optical switches using such materials, device structures should be designed to utilize their characteristics effectively. In case of organic dye molecules, strong absorption at resonant wavelength of $\pi - \pi^*$ transition reflects in exhibition of high nonlinear susceptibility. Furthermore, when highly ordered molecular arrangement called J-aggregates are formed, ultrafast decay of response can be achieved [44,45]. Characteristics of organic materials lie on strong interaction with the light at resonant wavelength and should be used in a form of thin film. In order to make full use of these ultrafast organic films, unique concepts of optical switches would be desired.

5.2. Principle of the FESLAP

Femtosecond laser pulses are characterized by short duration, strong peak intensity and thinness in propagation direction. A laser pulse of 100 fs duration has thinness of only 30 μm. A train of femtosecond laser pulses at 1 Tbit/s aligns with distance of 0.3 mm to each other. When keeping eyes on this thinness of the femtosecond pulses and an organic thin film exhibiting ultrafast response, we can observe a cross-sectional intensity distribution of pulses in space domain by using the film as an ultrafast shutter. As shown in Fig. 17(a), when activation gate pulse of a switching film irradiated in a horizontally oblique angle, only narrow intersection area of the film and the gate pulse turned to be transparent like a slit at a certain instant. The slit moves with propagation of the gate pulse, which acts as an ultrafast shutter. If we irradiate other signal pulses from normal direction to the film, a spatial patten of the signal pulses will be projected on a screen behind the film as shown in Fig. 17(b). The spatial distance between the

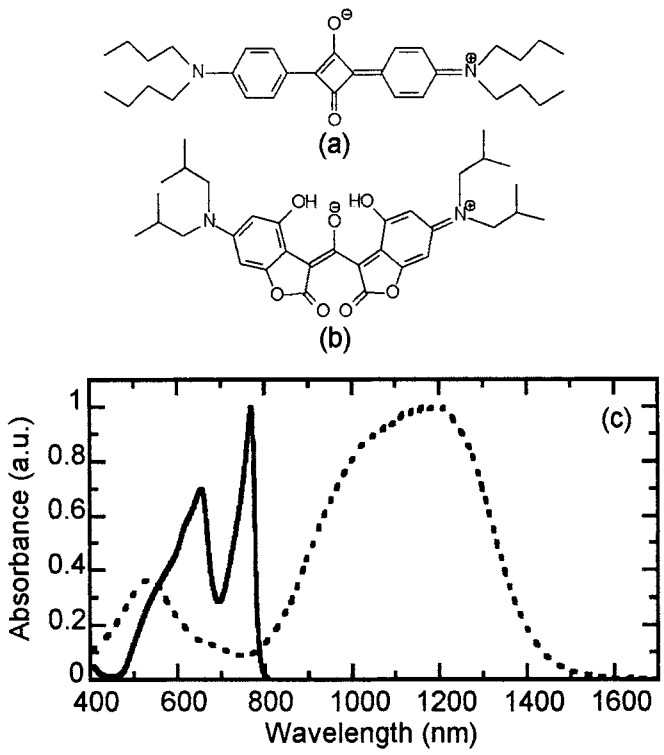

Fig. 18. Chemical formulas and absorption spectra of organic dye molecules for ultrafast optical switching; SQ (a) and solid line, BM (b) and broken line.

observed narrow lines on the screen indicates the interval time between the signal pulses. Using an ultrafast switching film, train of serial pulses in Tbit/s repetition rate can be converted into parallel pulses in space domain of mm size, which corresponding the light velocity. We named this principle to be FESLAP: femtosecond large-area parallel processor [46]. Although similar method for measuring time profiles of short pulses using converted spatial patterns of them have been proposed using second harmonic generation from a nonlinear crystal [47] and optical Kerr gate of quartz plate [48], our proposed principle has advantage in simplicity of the configuration, wider dynamic range and lower driving energy.

5.3. Verification of the Principle of FESLAP

For the materials of the ultrafast optical switching films, we have been studying on formation and characterization of squarylium-dye J-aggregates (SQ-J) film and reported that the SQ-J film exhibit ultrafast and efficient absorption saturation [49, 50]. We also succeeded synthesis of a new type of infrared absorbing dye molecules (BM dye), which exhibit ultrafast switching around telecommunication wavelength range [51]. Chemical formulas and absorption spectra of these dye molecules and films are shown

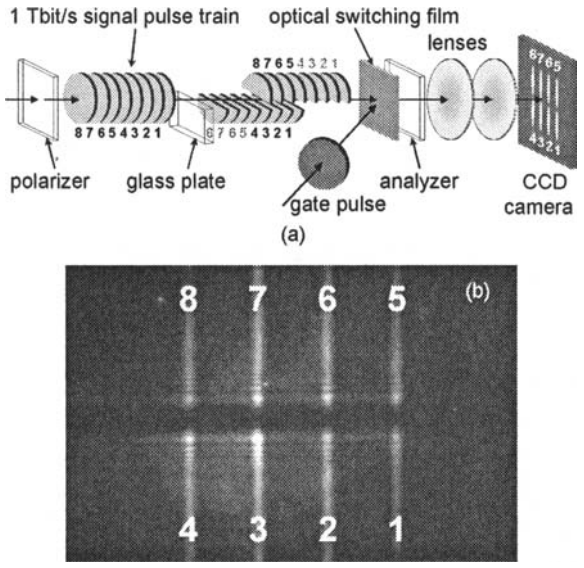

Fig. 19. Experimental set up for serial-to-parallel conversion of a 1-Tbit/s signal pulse train into two-dimensionally aligned pulses (a) and a typical image of converted signal pulses observed by a CCD camera (b).

in Fig. 18. In order to verify the principle of FESLAP, we used the SQ-J film for a switching film [52]. As shown in Fig. 19(a), we applied optical Kerr gate configuration to achieve enough on/off ratio. A train of 8 signal pulses with time interval of 1 ps is formed by splitting and joining fs laser pulses at 773 nm using half mirrors and retro-reflectors. Time delay of 4 ps is added to lower half of the signal pulse train passed though a polarizer using transparent glass plate. A single gate pulse at 810 nm with polarization 45 degrees tilted to the polarizer irradiates the SQ-J film in horizontally oblique angle with the signal pulses. Part of each pulse in the signal pulse train, which irradiate an area on the SQ-J film where the gate pulse irradiates in the same timing changes to tilted elliptically polarization because of instantaneously induced dichroism and birefringence by the gate pulse. Finally, different part of each pulse in the signal pulse train passes thorough cross-polarized analyzer. As the result, an image of two-dimensionally arranged signal pulses was observed on a charge coupled device (CCD) camera as shown in Fig. 19(b). Switching on/off ratios more than 5 were observed under gate pulse energy density of 2 pJ/ μm^2.

5.4. Future Prospects

We also think on the required efficiency of the switching for practical applications. Such open-air configuration requires irradiation of the gate pulse in large area on the film where switching of signal pulses occur only a small restricted area (or a spot). In order to reduce switching energy, it is effective that focusing signal and gate pulses to

the same small spots on the film. We can achieve the same driving energy densities with much lower total energy through tight focusing and reducing the size of switching spots. Further progress in configuration of this optical switch using focusing lenses and enlarging number of output channels through modularizations of optical components is now in progress.

6. Sub-Picosecond Wavelength Conversion by Four-Wave Mixing in Distributed-Feedback Laser and Semiconductor Optical Amplifiers

6.1. Introduction

High-speed wavelength conversion is strongly required in the future OTDM/WDM all optical network. In order to operate this network smoothly, the wavelength conversion occurs at every node.

The idea introduced here is to construct the simple wavelength conversion devices. We utilize the four wave mixing process (FWM). We try using two devices of the distributed feedback (DFB) laser and the semiconductor optical amplifiers (SOA). In the following the performance of these two types of wavelength conversion is introduced.

6.2. FWM With DFB Lasers

The FWM using lasers has been first proposed and demonstrated by H. Nakajima et al. [53]. In this report, the lasing light working as the pump is a conventional Fabry-Perot lasers. FWM using DFB lasers have been demonstrated in highly nondegenerate case [54] and in nearly degenerate case [55]. Wavelength conversion for input signals with continuous wavelengths has been demonstrated using a $\lambda/4$ phase shifted DFB laser [56].

To realize the wavelength conversion of short pulses with a pulsewidth of less than several pico-seconds, there are two subjects to be overcome; the suppression of a slow component of the 3rd order nonlinear effect and the avoidance of the cavity mode of a laser cavity.

$\lambda/4$ phase shifted DFB lasers are suitable for the overcome of these subjects [57]. The carrier density pulsation effect can be suppressed due to the stopband of the grating. In usual case, the carrier density effect strongly occurs in the small detuning of less than 100 GHz from the pump frequency and generates a long tail in converted pulses. In a $\lambda/4$ phase shifted DFB laser, the small detuning components in signal pulses and converted pulses are blocked by the stop-band. The cavity mode effect can be also avoided. A $\lambda/4$ phase shifted DFB laser has anti-reflection coatings in both facets. The laser works as the traveling wave semiconductor optical amplifier for the signal pulse and the converted pulse.

The structure of a $\lambda/4$ phase-shifted DFB laser used in the experiment of short pulse wavelength conversion is shown in Fig. 20. The auto-correlation traces of an input signal pulse of a wavelength of 1558 nm and an output converted pulse of a wavelength of 1548 nm are shown in Fig. 21. The pulsewidths are estimated to be 1.4 ps for input and 2.5 ps for output under the assumption of the hyperbolic cosine pulse shape. The result shows that a long tail of several 10 ps due to the carrier density pulsation effect is suppressed.

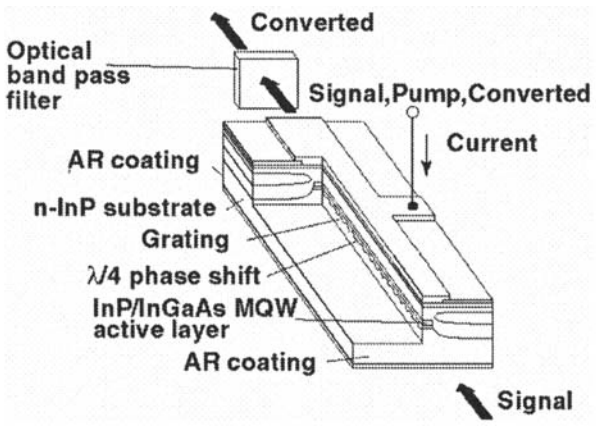

Fig. 20. The arrangement of wavelength conversion using FWM in a $\lambda/4$ phase shifted DFB laser. The signal pulse is input from one side of facets of the laser. The converted pulse is obtained from another side of the facets.

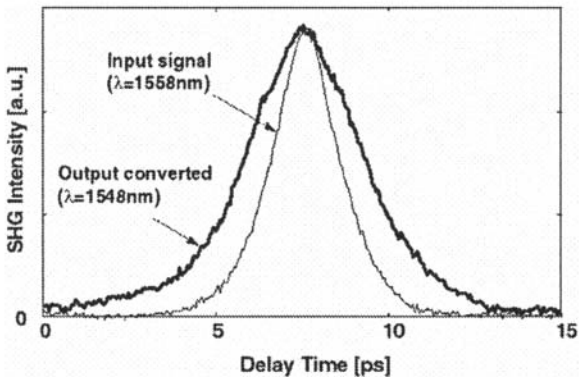

Fig. 21. The auto-correlation trace of a pulse after wavelength conversion. The peak wavelength of the pulse is converted to 10 nm shorter than that of the input signal pulse.

6.3. FWM With SOA

Conventional SOAs with the bulk or quantum-well active region have a drawback that the efficiency of the conversion to longer wavelengths is too small [58,59]. The application of quantum-dot SOAs to this scheme is attractive, because of the possibilities of eliminating destructive interference and obtaining symmetric, i.e., direction-independent, and large conversion efficiency by their small linewidth enhancement factor as well as their intense spectral hole burning [60]. The conversion efficiency is proportional to the absolute value of the third-order susceptibility given as

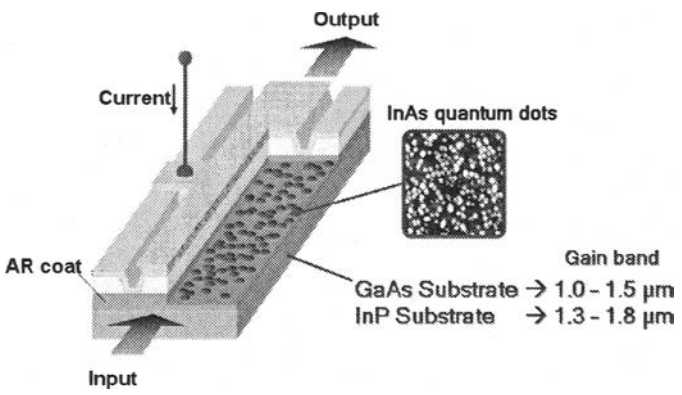

Fig. 22. Structure of the quantum-dot SOA, with self-assembled InAs quantum dots in the active region.

$$\chi^{(3)} = A_p \frac{\beta_p \Delta T_{\text{in}}}{\Gamma_{\text{cv}}[\Delta\omega^2 + T_{\text{in}}^2]} + \frac{\alpha\Delta\omega + (R_{\text{rec}} + R_{\text{stim}})}{[\Delta\omega^2 + (R_{\text{rec}} + R_{\text{stim}})^2]}, \tag{1}$$

where the first term on the right-hand side represents the contribution of the spectral hole burning, the second term is that of the carrier density pulsation, A_p is the differential gain, T_{in} is the intraband relaxation rate, $\beta_p \Delta$ is the constant inversely proportional to the differential gain, Γ_{cv} is the polarization dephasing rate, α is the alpha parameter, R_{rec} is the carrier recombination rate, R_{stim} is the stimulated emission rate, and $\Delta\omega = \omega_p - \omega_s$ is the detuning. Equation (1) tells us that the zero alpha parameter enables symmetric conversion and that the slower relaxation rate of $T_{\text{in}} = 200$–300 fs in quantum dots than that of $T_{\text{in}} = 10$–50 fs in conventional semiconductors improves efficiency.

Figure 22 shows the structure of the quantum-dot SOA, with self-assembled InAs quantum dots in the active region. With the inputs of both the pump at the frequency of ω_p and the signal lights at ω_s, we obtain the converted signal at $\omega_c = 2\omega_p - \omega_s$.

Figure 23 shows the conversion efficiency for positive (closed circles) and negative (open circles) detuning [61]. Remarkable differences were observed in comparison with those in a bulk SOA (taken from [58]); The efficiency for both the positive and negative detuning in the quantum-dot SOA has become almost same (symmetric). The detuning dependence is much flatter due to the spectral-hole burning. These results are indicative of the advantages of quantum-dot SOAs as devices for FWM wavelength conversion.

6.4. Summary

The FWM has the merit of fast wavelength conversion. We introduced two promising types. The introduced devices have merits and demerits in the present stage. We need the much improvement keeping each merit. These devices are key devices in the future all optical networks.

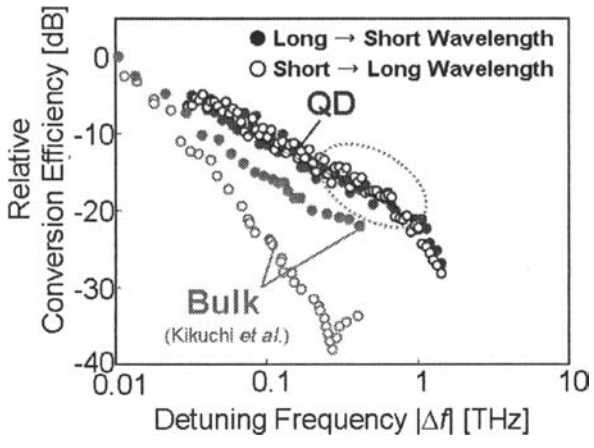

Fig. 23. Conversion efficiency for positive (closed circles) and negative (open circles) detunings in the quantum-dot and bulk SOAs

7. Precise Measurement of Timing Jitters of Repetitive Laser Pulses

Generation of highly repetitive laser pulses is an important issue for such applications as optical time-division multiplexed (OTDM) communication [62], high-resolution photonic analog-to-digital conversion [63,64], and high-speed optical sampling measurement [65]. Since these applications require stringent performances on pulse timing jitter as well as on pulse width, it has become a matter of great concern to precisely evaluate the magnitude of timing jitter in repetitive laser pulses. For example, to ensure the bit error rate below 10^{-12} in OTDM transmission systems, timing jitter should be less than 1/14.1 of the bit period [66], which corresponds to 443 fs in a 160-Gbit/s transmission.

A commonly employed method for timing jitter measurement is the so-called single sideband (SSB) phase noise measurement proposed by von der Linde [67], which performs noise measurement in a frequency domain and is based on the standard technique used for microwave and millimeter-wave phase noise measurements. If we detect the intensity of repetitive laser pulses with a fast photodiode, the first harmonic component of the electrical output signal is given by

$$I(t) = I_0\{1 + \epsilon(t)\}\sin\{2\pi f_{\mathrm{rep}}t + \phi(t)\}, \tag{2}$$

where I_0 and f_{rep} are the nominal amplitude and repetition frequency, respectively, and $\epsilon(t)$ and $\phi(t)$ represent the amplitude and phase noise, respectively. Timing noise $J(t)$ is related to phase noise $\phi(t)$ by

$$J(t) = \phi(t)/2\pi f_{\mathrm{rep}}. \tag{3}$$

The most fundamental measure of the timing noise is a phase power spectral density (PN-PSD) $S_\phi(f)$ of $\phi(t)$, where f represents the Fourier frequency, and a root-mean-square (RMS) timing jitter σ_J is calculated from $S_\phi(f)$ using the relation

$$\sigma_J(f_h, f_l) = \frac{1}{2\pi f_{\text{rep}}} \sqrt{\int_{f_l}^{f_h} S_\phi(f) df}, \tag{4}$$

where f_l and f_h denote the lower and upper limits of integration, respectively.

In SSB phase noise measurement, the quantity $L(f)$, which is the ratio of the noise power in one sideband to the total signal power, is used as a measure of timing noise. This quantity corresponds to the power spectral density of the first harmonic $I(t)$ and contains information on both the amplitude and phase noise. When the RMS phase deviation is much smaller than 1 radian, $L(f)$ is related to the phase noise power spectral density (PSD) $S_\phi(f)$ by an approximated relation $S_\phi(f) \approx 2L(f)$. Although SSB phase noise measurement is quit easy to implement, it is accompanied by inherent limitations, such as limited frequency span and dynamic range, difficulty in discriminating amplitude and phase noise, and inaccuracy when applied to a non-stationary process such as passively mode-locked laser pulses [68].

In order to overcome the above difficulties, the time domain demodulation (TDD) [69] and the time interval analysis (TIA) [70] techniques were developed, both of which perform measurements in a time domain. The TDD technique directly measures the phase noise $\phi(t)$ of a sinusoidal signal from the in- and quadrature-phase amplitudes, while the TIA technique measures the period $\Delta T = 2\pi\{d\phi(t)/dt\}^{-1}$ using zero-dead-time counters. The former technique offers a high sensitivity but is not suitable for measuring signals exhibiting a timing drift. In contrast, although the sensitivity is limited, the latter technique is effective for the measurement of drifting signals. These two techniques are complementary with each other and are used properly or combined depending on the properties of timing noise.

Since the time domain measurement equipment cannot directly handle highly repetitive signals beyond 10 GHz, electrical and/or optical frequency down conversion is required before signal processing. A double-balanced mixer (DBM) can be employed to down-convert an electrical signal at f_{rep} into a lower frequency IF signal at $f_{\text{IF}} = f_{\text{rep}} - f_{\text{LO}}$, where f_{LO} represents the frequency of an electrical local oscillator (LO). This method is applicable to pulses with the repetition frequency up to 50 GHz [71] as limited by the response time of photodetectors. To down-convert pulses beyond 50 GHz, an optoelectronic harmonic mixer (OEHM) were developed [72] which produces an IF signal at $f_{\text{IF}} = f_{\text{rep}} - nf_{\text{LO}}$ with the help an electro-optic intensity modulator, where n is the integer. The modulator driven by an LO signal generates modulation sidebands located at $\pm nf_{\text{LO}}$ from each longitudinal mode and produces beat signals between the nth sidebands and the adjacent longitudinal modes.

Figure 24 shows the results of timing noise measurement for various repetitive laser pulses, where curves A–E represent the PN-PSD $S_\phi(f)$ and curves F–J represent RMS jitter σ_J. The value of σ_J is calculated for $f_h = 18$ MHz and is plotted as a function of f_l. Curves B and G represent the noise of 19.444 GHz pulses emitted by a hybrid mode-locked laser diode [73] and were evaluated by the combination of TDD and DBM. For comparison, noise of the frequency synthesizer is plotted by curves A and F. Curves A and B almost overlap below 100 kHz Fourier frequency, which suggest that the laser is accurately synchronized with the RF signal. However, the existence of a white noise component above 100 kHz indicates the incomplete synchronization caused by the spontaneous emission coupled into the lasing modes. The RMS jitter for the laser pulses amounts to 3.4 ps (2.5 mHz–18 MHz).

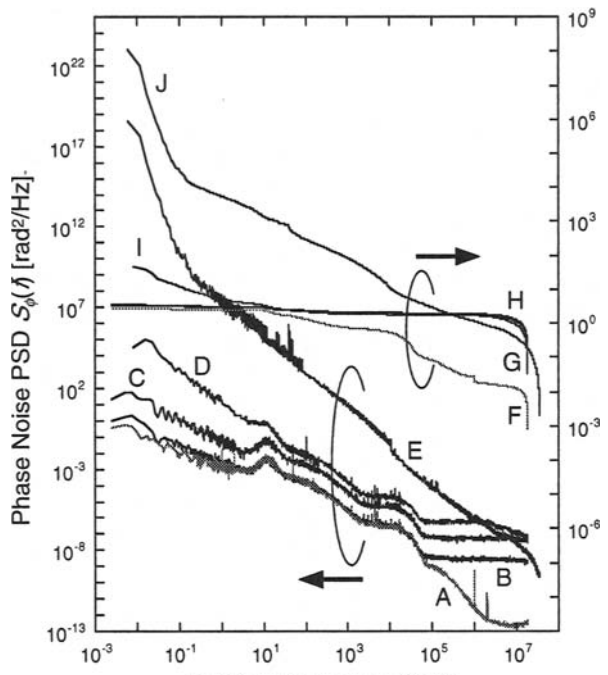

Fig. 24. PN-PSD $S_\phi(f)$ (curves A– E) and RMS timing jitter σ_J. (curves F–J) for various repetitive laser pulses. A, F: frequency synthesizer that drives the 19.444-GHz hybrid mode-locked laser; B, G: 19.444 GHz pulses emitted by hybrid mode-locked laser; C, H: 77.776 GHz OTDM pulses generated from the hybrid mode-locked laser diode; D, I: 155.552 GHz OTDM pulses generated from the hybrid mode-locked laser diode; E, J: 160.64 GHz pulses emitted by the colliding-pulse mode-locked laser diode.

Curves C and H correspond to 77.776 GHz OTDM pulses and were evaluated by the combination of TDD and OEHM. These pulses were generated from the 19.444-GHz mode-locked laser diode by the use of fiber-optic multiplexers. Frequency down-conversion was achieved with the second order modulation sidebands produced by a 40-GHz intensity modulator. The values of $S_\phi(f)$ for curve C are approximately 16 times as large as those on curve B, which is consistent with the increased repetition frequency. Moreover, the shapes of curves B and C are almost identical indicating that the excess noise added during the multiplexing process is small and that the timing noise of the original laser pulses is dominant. The RMS jitter for the OTDM pulses amounts to 3.7 ps, which is almost equal to that of the original laser pulses.

Curves D and I correspond to 155.552 GHz OTDM pulses evaluated by the combination of TDD and OEHM. Although the values of $S_\phi(f)$ on curve D are nearly 64 times as large as those on curve B between 10 Hz and 1 MHz, they increase rapidly below 10 Hz. The observed increase in the low frequency noise is attributed to the thermal drift of the OTDM multiplexer. A slight decrease of $S_\phi(f)$ on curve D above 1

MHz is due to the incoherent addition of the pulse intensity at the output of the OTDM multiplexer [74]. The RMS jitter amounts to 4.5 ps (7.8 mHz–18 MHz).

Curves E and J represent the noise of 160.64 GHz pulses emitted directly by a colliding-pulse mode-locked laser diode [75]. Since the laser exhibits large timing variation under passively mode-locked operation, TIA technique combined with OEHM was employed. The values of $S_\phi(f)$ on curve E are inversely proportional to f^2 above 1 Hz, which is characteristic of random walk noise. However, it rapidly increases below 1 Hz due to the slow drift caused mainly by the temperature variation. The RMS jitter amounts to 0.11 ms (5.8 mHz–34 MHz).

From the above results it can be seen that TDD and TIA techniques have enabled the timing noise evaluation of repetitive laser pulses up to 160 GHz over nine decades of Fourier frequency (2.5 mHz–34 MHz) with 300-dB dynamic range. To handle higher repetitive pulses, nonlinear frequency conversion technique [75] will be promising although it requires a stable reference pulses instead of an electrical LO source.

8. Summary

It is remarkable that many leading research results on the ultrafast optical devices and related technology have been produced in the systematic and long-term R&D of FST project. A novel technology platform of optical devices will be formed by the development of devices in the project.

Using a mode-locked semiconductor laser and SMZ switches developed in the FST project, we successfully accomplished an unrepeated 140 km transmission of 8 $\times$ 160 Gb/s OTDM/DWDM signals [76]. It is also expected that the application of the OTDM technology will be realistically promoted by taking advantage of these advanced devices.

This direction of the R&D will, moreover, open the possibility of the future ultrafast optical signal processing. Ubiquitous information networking system based on such ultrafast optical signal processing and communication technology will play an important role to meet the demands in the business, social security and human life as a flexible and reliable communication system in the future.

Acknowledgments

The authors would like to express their thanks to Profs. and Drs. Masahiro Okabe (section 1), Yoh Ogawa (2), Kiyoshi Asakawa (3), Kazuhito Tajima (3), Ryoichi Akimoto (4), Hiroshi Ishikawa(4), Nobuo Suzuki (4), Makoto Furuki (5), Hajime Imai (6), Hidemi Tsuchida (7), Toshifumi Hasama (8) and Masanobu Watanabe (8) for their contribution of the discussion and paper manuscript.

References

1. Y. Lee, Appl. Phys. Lett., **73**, 2715 (1998).
2. S. Wakabayashi, A. Baba, and H. Moriya, OFC2003, MF27, **1**, 30 (2003).

3. K. Akiyama, N. Tomita, T. Nishimura, Y. Nomura, and T. Isu, 10th Intern. Workshop on Femtosecond Technology, WD-2, 41 (2003).
4. K. Ogawa and M.D. Pelusi, Opt. Comm., 198, 83 (2001).
5. S. Arahira, Y. Matsui, and Y. Ogawa, IEEE J. Quantum Electron., **32**, 1211 (1996).
6. S. Arahira and Y. Ogawa, Electron. Lett., **31**, 808 (1995).
7. Y. K. Chen and M. C. Wu, IEEE J. Quantum Electron., **28**, 2176 (1992).
8. S. Arahira and Y. Ogawa, IEEE Photon. Technol. Lett., **8**, 191 (1996).
9. X. Wang, H. Yokoyama, and T. Shimizu, IEEE Photon. Technol. Lett., **8**, 617 (1996).
10. S. Arahira, Y. Katoh, D. Kunimatsu, and Y. Ogawa, IEICE Trans. Electron., E83-C, 966 (2000).
11. K. Tajima: Jpn. J. Appl. Phys., **32**, L1746 (1993).
12. S. Nakamura, K. Tajima, and Y. Sugimoto, Appl. Phys. Lett., **65**, 283 (1994).
13. K. Tajima, S. Nakamura, and Y. Sugimoto, Appl. Phys. Lett., **67**, 3709 (1995).
14. Y. Ueno, S. Nakamura, K. Tajima, and S. Kitamura, IEEE Photonics Technol. Lett., **10**, 346 (1998).
15. K. Tajima, S. Nakamura, Y. Ueno, J. Sasaki, T. Sugimoto, T. Kato, T. Shimoda, M. Itoh, H. Hatakeyama, T. Tamanuki, and T. Sasaki, IEE Electron. Lett., **35**, 2030 (1999).
16. S. Nakamura, Y. Ueno, K. Tajima, J. Sasaki, T. Sugimoto, T. Kato, T. Shimoda, M. Itoh, H. Hatakeyama, T. Tamanuki, and T. Sasaki, IEEE Photon. Technol. Lett., **12**, 425 (2000).
17. R. Hess, M. Caraccia-Gross, W. Vogt, E. Gamper, P. A. Besse, M. Duelk, E. Gini, H. Melchior, B. Mikkelsen, M. Vaa, K. S. Jepsen, K. E. Stubkjaer, and S. Bouchoule,: IEEE Photon. Technol. Lett., **10**, 165 (1998).
18. S. Nakamura, Y. Ueno, and K. Tajima, Appl. Phys. Lett., **78**, 3929 (2001).
19. Y. Sugimoto, N. Ikeda , N. Carlsson, K. Asakawa, N. Kawai, and K. Inoue, J. App. Phys., **91**, 992 (2002).
20. Y. Sugimoto, N. Ikeda , N. Carlsson, K. Asakawa, N. Kawai, and K. Inoue, Appl. Phys. Lett., **79**, 4286 (2001).
21. Y. Sugimoto, N. Ikeda , N. Carlsson, K. Asakawa, N. Kawai, and K. Inoue, J. Appl. Phys., **91**, 3477 (2002).
22. K. Inoue, T. Maruyama, K. Miyashita, K. Ishida, Y. Sugimoto, N. Ikeda, Y. Tanaka and K. Asakawa: accepted for Jpn. J. Appl. Phys.
23. Y. Sugimoto, Y. Tanaka, N. Ikeda, T. Yang, H. Nakamura, K. Asakawa, K. Inoue, T. Maruyama, K. Miyashita, and K. Ishida, Appl. Phys. Lett., **83**, 3236 (2003).
24. H. Nakamura, S. Nishikawa, S. Kohmoto and K. Asakawa, Proceedings of LEOS2001, San Diego, Wu2 (2001).
25. Y. Sugimoto, Y. Tanaka, N. Ikeda, H. Nakamura, K. Asakawa, and K. Inoue, to be published in the Proceedings of PECS-V, Kyoto, 2004.
26. K. Inoue, N. Kawai, Y. Sugimoto, N. Carlsson, N. Ikeda, and K. Asakawa, Phys. Rev. B, **65**, 121308 (2002).
27. Y. Tanaka, Y. Sugimoto, N. Ikeda, H. Tanaka, K. Asakawa, K. Inoue, and S. Johnson, accepted for Electron. Lett.
28. Y. Sugimoto, Y. Tanaka, N. Ikeda, Y. Nakamura, K. Asakawa, submitted to Opt. Express.

29. K. Kanamoto, H. Nakamura, Y. Nakamura, Y. Sugimoto, N. Ikeda, Y. Tanaka, S. Ohkouchi, H. Ishikawa and K. Asakawa, 2003 IEEE LEOS Annual Meeting Conference Proceedings, 2, 561 (2993).
30. Y. Ueno, S. Nakamura, and K. Tajima, IEEE Photon. Technol. Lett., **13**, 469 (2001).
31. S. Nakamura, Y. Ueno, and K. Tajima, IEEE Photon. Technol. Lett., **13**, 1091 (2001).
32. S. Noda, T. Yamamoto, M. Ohya, Y. Muramoto, and A. Sasaki, IEEE J. Quantum Electron., **29**, 1640 (1993).
33. N. Suzuki, and N. Iizuka, Jpn. J. Appl. Phys., **36**, Pt.2, L1006 (1997).
34. N. Iizuka, K. Kaneko, N. Suzuki, T. Asano, S. Noda, and O. Wada, Appl. Phys. Lett., **77**, 648 (2000).
35. N. Iizuka, K. Kaneko, and N. Suzuki, Appl. Phys. Lett., **81**, 1803 (2002).
36. C. Gmachl, H. M. Ng, and Y. Cho, Appl. Phys. Lett., **79**, 1590 (2001).
37. K. Kishino, A. Kikuchi, H. Kanazawa, and T. Tachibana, Appl. Phys. Lett., **81**, 1234 (2002).
38. T. Mozume, N. Georgiev, T. Simoyama, A. V. Gopal, and H. Yoshida, 14th Indium Phosphide and Related Materials Conf. Stockholm, 2002, Post Deadline Paper.
39. T. Simoyama, H. Yoshida, J. Kasai, T. Mozume, A. V. Gopal., and H. Ishikawa, IEEE Photonic Technol. Lett., **15**, 1363 (2003).
40. H. Yoshida, T. Mozume, A. Neogi, and O. Wada, Electron. Lett., **35**, 1103 (1999).
41. R. Akimoto, Y. Kinpara, K. Akita, F. Sasaki, and S. Kobayashi, Appl. Phys. Lett., **78**, 580 (2001).
42. R. Akimoto, K. Akita, F. Sasaki, and T. Hazama, Appl. Phys. Lett., **81**, 2998 (2002).
43. K. Ridley, Phys. Rev. B, **39**, 5282 (1989)
44. S. Kobayashi and F. Sasaki, J. Lumin. **58**, 113 (1994).
45. K. Minoshima, M. Taiji, K. Misawa, and T. Kobayashi, Chem. Phys. Lett. **218**, 67 (1994).
46. M. Furuki, M. Tian, Y. Sato, L. S. Pu, S. Tatsuura, and O. Wada, Appl. Pys. Lett. **77**, 472 (2000).
47. F. Salin, P. Georeges, G. Roger, and A. Brun, Appl. Opt. **26**, 4528 (1987).
48. D. J. Kane and R. Trebino, Opt. Lett. **18**, 823 (1993).
49. S. Tatsuura, M. Tian, M. Furuki, Y. Sato, L. S. Pu, and O. Wada, Jpn. J. Appl. Phys. **39**, part 1, 4782 (2000).
50. M. Furuki, M. Tian, Y. Sato, L. S. Pu, H. Kawashima, S. Tastuura, and O. Wada, Appl. Phys. Lett. **78**, 2634 (2001).
51. M. Tian, S. Tatsuura, M. Furuki, Y. Sato, I. Iwasa, and L. S. Pu, J. Am. Chem. Soc. **125**, 348 (2003).
52. Y. Sato, M. Furuki, M. Tian, L. S. Pu, and S. Tatsuura, Appl. Phys. Lett. **80**, 2254 (2002).
53. H. Nakajima and R. Fery, Appl. Phys. Lett., **47**, 769(1985).
54. S. Murata, A. Tomita, J. Shimizu, M. Kitamura, and A. Suzuki, Appl. Phys. Lett., **58**, 1458(1991).
55. R. Hui, S. Benedetto, and I. Montrosset, J. Lightwave Technol., **11**, 2026 (1993).
56. H. Kuwatsuka, H. Shoji, M. Matsuda, and H. Ishikawa, Electron. Lett., **31**, 2108 (1995).
57. H. Kuwatsuka, T. Akiyama, B. E. Little, T. Simoyama, and H. Ishikawa, Tech. Digest of 26th European Conference on Optical Communication (ECOC 2000), Vol.3, 65, 2000, Munich.

58. K. Kikuchi, M. Kakui, C-E Zah, and T-P Lee, IEEE Journal of Quantum Electron., **28**, 151 (1992).
59. G. P. Agrawal and N. Andes Olsson, IEEE Journal of Quantum Electron., **25**, 2297 (1989).
60. M. Sugawara, T. Akiyama, N. Hatori, Y. Nakata, K, Otsubo, and H. Ebe, APOC 02, Materials and Devices for Optical and Wireless Communications, Shanghai, in Proceedings of SPIE Vol. 4905, (2002), p. 259.
61. T. Akiyama, H. Kuwatsuka, N. Hatori, Y. Nakata, H. Ebe, and M. Sugawara, IEEE Photon. Tech. Lett., **14**, 1133 (2002).
62. M. Nakazawa, T. Yamamoto, and K. R. Tamura, Electron. Lett., **36**, 2027 (2000).
63. C. M. DePriest, T. Yilmaz, A. Braun, J. Abeles, and P. J. Delfyett, Jr., IEEE J. Quantum Electron., **38**, 380 (2002).
64. A. S. Bhushan, P. V. Kelkar, B. Jalali, O. Boyraz, and M. Islam, IEEE Photon. Technol. Lett., **14**, 684 (2002).
65. M. Shirane, Y. Hashimoto, H. Yamada, and H. Yokoyama, IEEE Photon. Technol. Lett., **12**, 1537 (2000).
66. M. Jinno, IEEE J. Quantum Electron., **30**, 2842 (1994).
67. D. von der Linde, Appl. Phys. B, **39**, 201 (1986).
68. H. A. Haus and A. Mecozzi, IEEE J. Quantum Electron., **29**, 983 (1993).
69. H. Tsuchida, Opt. Lett., **23**, 286 (1998).
70. H. Tsuchida, Opt. Lett., **24**, 1434 (1999).
71. H. Tsuchida, IEEE Photon. Technol. Lett., **14**, 535 (2002).
72. H. Tsuchida, Opt. Lett., **27**, 2040 (2002).
73. S. Arahira, Y. Katoh, and Y. Ogawa, Electron. Lett., **36**, 454 (2000).
74. H. Tsuchida, IEEE J. Sell. Top. Quantum Electron., **9**, 535 (2003).
75. S. Arahira, Y. Katoh, D. Kunimatsu, and Y. Ogawa, IEICE Trans. Electron., **83-C**, 966 (2000).
76. A. Suzuki, X. Wang, T. Hasegawa, Y. Ogawa, S. Arahira, K. Tajima, and S. Nakamura, ECOC 2003, Mo3.6.1, 1, 44 (2003).

DOI: 10.1007/s10297-005-0034-4
Originally published in J. Opt. Fiber. Commun. Rep. 2, 86–114 (2005)

Optical sampling techniques

Carsten Schmidt-Langhorst and Hans-Georg Weber

Fraunhofer Institute for Telecommunications, Heinrich Hertz Institut
Einsteinufer 37, 10587 Berlin, Germany

Abstract. The optical sampling technique is a novel method to perform time-resolved measurements of optical data signals at high bit rates with a bandwidth that cannot be reached by conventional photodetectors and oscilloscopes. The chapter reviews the techniques that are used in optical sampling systems to perform the ultrafast sampling of the signal under investigation. In addition to the various nonlinear materials and effects used for the optical sampling gates and pulse sources, the realized optical sampling systems also differ in the way, in which the system is synchronized to the data signal. Systems have been reported using synchronous, random and software synchronized configurations. Applications of optical sampling systems include high bit rate waveform and eye diagram measurements, measurements of constellation diagrams of phase modulated data signals, time-resolved measurements of the state-of-polarization as well as investigations of fiber transmission impairments.

1. Introduction

The commonly used method to characterize an optical data signal is the detection by a photodetector and the measurement of the temporal variation of the generated photocurrent versus the time using an oscilloscope. The shortest pulse width which can be measured using this technique is determined by the response time of the photodetector and the bandwidth of the oscilloscope. Using an electrical sampling oscilloscope and the fastest photodetectors available today, the overall bandwidth of such a measurement system is about 65-70 GHz (e.g. [1–3]). This bandwidth allows the measurement of data signals with optical pulses having a pulse width as low as about 7 ps.

The bandwidth of this "conventional" sampling technique (photodetector + electrical sampling) can be extended by shifting the sampling process from the electrical to the optical domain. This technique is called "optical sampling". In an optical sampling system, the optical signal is sampled in the optical domain by an optical sampling gate.

Only then, the resulting samples are converted to an electrical signal and detected. In this case the need for high bandwidth electronics is circumvented and the bandwidth of the measurement instrument is only limited by the optical sampling gate.

In the literature, the term optical sampling is used for a variety of experiments, where optical signals are sampled by means of optical or even opto-electrical gates. This paper, however, covers only optical sampling systems that enable the measurement of eye diagrams. Early scientific publications in this field date back to the mid 1990s, when the first optically sampled eye diagrams of 10 Gbit/s optical data signals were published. Since then, there has been growing interest in the optical sampling technique, mainly driven by the increase of bit rates in the past 10 years. During the last decade, about 50 publications have appeared with a variety of experimental configurations for high resolution optical sampling. Today, optical sampling systems enable measurements of eye diagrams of data signals with bit rates up to 640 Gbit/s [4, 5].

2. Principle of Optical Sampling

Figure 1 explains the principle of optical sampling. The upper part of the figure shows an optical data signal with RZ modulation format as example. The data signal is a concatenation of optical data bits, each within a bit slot of 6.25 ps corresponding to a bit rate of 160 Gbit/s.

This optical data signal is passed through an optical gate. The gate is closed by default, i.e. it does not transmit the data signal for most of the time except for ultra short periods of time. The period of time for which the gate transmits the data signal is called "gating window". If the width of the gating window is shorter than the bit duration, as shown in Fig. 1, only a fraction of the optical data bit is sliced out. This fraction is called "optical sample". The optical sample is determined by the instantaneous amplitude of the data bit at the sampling time. Ideally, the sampling gate should exhibit a linear

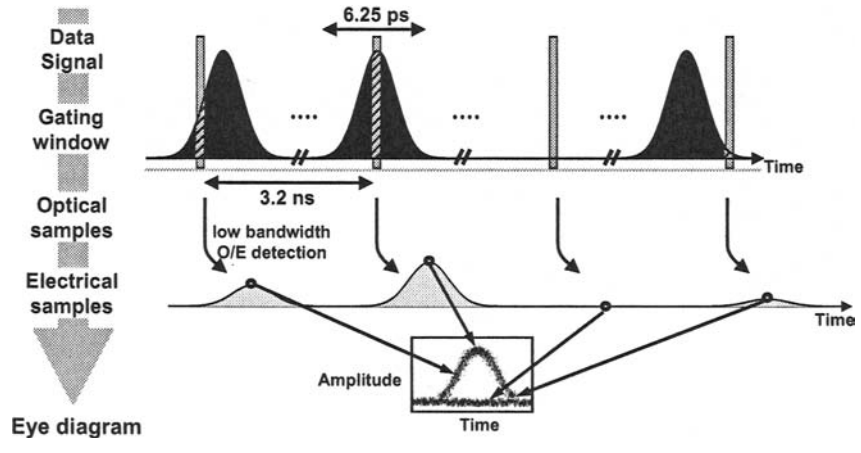

Fig. 1. Principle of optical sampling.

transfer function making the amplitude of the optical sample directly proportional to the instantaneous power of the data signal at the sampling time.

In order to avoid high-speed electronic signal processing for the detection of the optical samples, it is useful to operate the sampling gate with a modest repetition frequency. In Fig. 1, the time between two sampling instants was chosen to be 3.2 ns, which corresponds to a sampling frequency of roughly 310 MHz. This frequency is significantly lower (by a factor of 512) than the bit rate and thus the sampling process occurs only for every 512th optical data bit (as indicated in Fig. 1 by the interceptions of the time axis of the data signal). This allows to detect the optical samples with a low bandwidth opto/electrical (O/E) detector. At the output of the detector, the "electrical sample" appears broadened in time due to the low bandwidth of the detector, but still generates a photocurrent that is proportional to the instantaneous optical power of the optical data bit at the sampling time. After a transimpedance amplifier, the peak voltage V_p of each electrical sample is measured by an analog/digital converter.

The eye diagram of the optical data signal is obtained from the measured V_p-values if the corresponding sampling times are known. A number of techniques have been proposed to obtain this timing information. The description of these techniques is the subject of Sec. 3.

The optical sampling technique described in Figure 1 allows to visualize the eye diagram of any data signal that has been encoded by an amplitude modulation format. In the case of a phase modulation format, this sampling technique will not distinguish between logical mark and space levels in the eye diagram. Up to now, only few work has been reported on the monitoring of phase modulated optical data signals. In a simple approach, a phase demodulator was incorporated in an optical sampling system [6]. The demodulator converted the phase modulated data signal into an amplitude modulated data signal before the sampling operation. Thus it enabled the measurement of a conventional eye diagram even for phase-modulated data signals up to a bit rate of 320 Gbit/s. Another approach is the measurement of constellation diagrams of a phase modulated data signal [7]. Such diagrams represent the amplitude and phase information of the data signal in the complex plane. This approach will be described in more detail in Sec. 7.2.

3. Technical Realizations

Figure 2 shows the block diagrams of two configurations of an optical sampling system. In both configurations, the data signal is input into the optical sampling gate, which is controlled by short optical pulses from the sampling pulse source. The optical samples are detected by the opto/electrical (O/E) detector. A clock recovery provides the timing information. However, different techniques have been demonstrated to use the timing information for the reconstruction of the eye diagram from the detected optical samples.

Synchronous Sampling

In the synchronous sampling configuration, the sampling gate is opened synchronous to the optical data signal but with a fixed frequency offset in order to scan over the complete bit slot. Thus a technique is needed for the synchronization of the sampling gate to the optical data signal under investigation. This function is performed by an

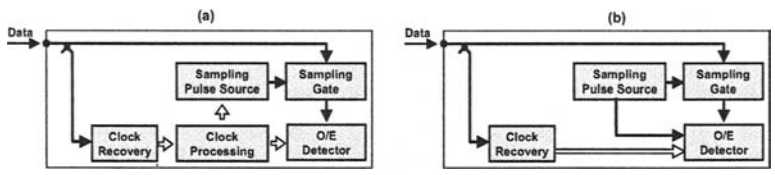

Fig. 2. Different configurations of optical sampling systems. Solid symbols indicate the optical path, hollow symbols indicate the electrical path. (a) Synchronous sampling, (b) random sampling.

optical clock recovery (Fig. 2a). The clock recovery generates an electrical clock signal, which is synchronous to the optical data signal and which is a subharmonic of the bit rate of the input data signal. Typically, the frequency of the extracted clock signal is around 10 GHz. In a clock processing circuitry the required frequency offset for the gating window is generated. The clock processing also provides the timing information for the O/E detector and thus enables the reconstruction of the eye diagram. The synchronous configuration has been widely used in optical sampling systems, for example in [8,9]. Synchronous sampling systems in which the electrical clock signal was taken directly from the transmitter were reported for example in [4,5].

Random Sampling

In the random sampling configuration, the clock processing is omitted and the sampling process is performed at random times [10]. The sampling times are derived from an arrival time measurement of the sampling pulses themselves. As compared to the synchronous sampling configuration, the random sampling configuration requires less components as there is no need for a clock processing circuitry (see Fig. 2b). However, it requires the use of a special O/E-detector, which performs the arrival time measurement of the sampling pulses with high temporal accuracy, as an error in the arrival time measurement directly translates into timing jitter of the sampling system.

In order to synchronize the random sampling system to the data signal under investigation, a clock recovery is needed in the random sampling configuration as well. A random sampling system including clock recovery has been shown in [6] for example.

Software Synchronized Sampling

In this configuration, the clock processing unit as well as the clock recovery unit are both omitted and the timing information of the individual optical samples is reconstructed from the measured sampling data using a special software algorithm [11, 12]. This configuration requires the least amount of hardware components. On the other hand, the update rate of the sampled eye diagrams depends on the computation speed involved in sorting and positioning the sampled V_p values on the time axis. A special feature of this technique is the possibility to synchronize the sampling system not only to the bit slot but also to the word frame in the case of a PRBS sequence for example. This allows not only to measure the eye diagram of the data signal but also to visualize any data pattern that might be present in the data signal [12].

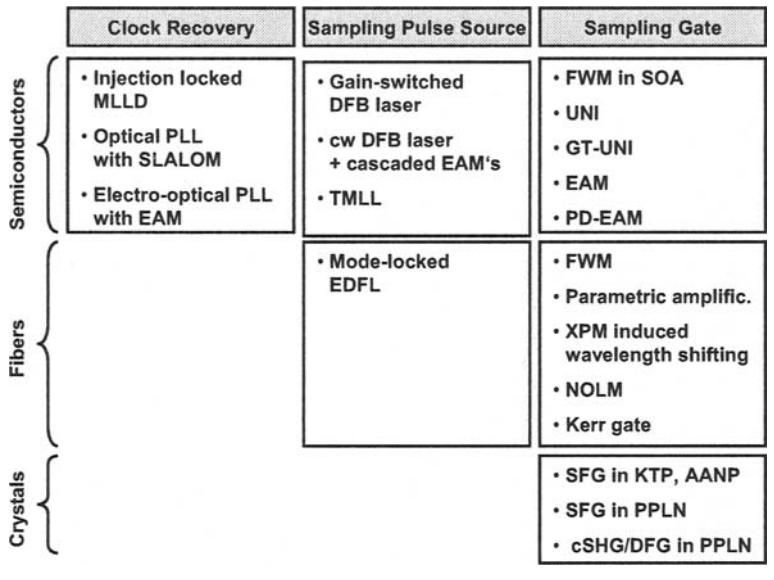

Fig. 3. Different techniques used for the realization of an optical sampling system. The abbreviations are explained in the text.

4. Components Used for Optical Sampling

Different techniques have been reported for the realization of the subsystems of an optical sampling system. They are summarized in Fig. 3. The O/E detector subsystem is omitted in this overview, since it was almost identical in all reported experiments.

4.1. Clock Recovery

Although a complete optical sampling system requires a clock recovery to synchronize the sampling operation to the optical data signal under investigation, only few realizations of optical clock recoveries have been reported up to now as Fig. 3 shows. In most experiments the synchronization signal was directly tapped at the transmitter.

In the clock recovery, the most important parameters are the timing jitter and the stability of the recovered clock signal. The jitter of the recovered clock signal should be as low as possible to achieve an overall low jitter sampling system.

All reported clock recovery configurations are based on semiconductor components. Injection locking of a semiconductor mode-locked laser diode (MLLD) was reported at the bit rates of 80 Gbit/s and 160 Gbit/s [13–15]. This configuration, however, has stability problems, since the injection locking is performed at a subharmonic of the repetition frequency of the MLLD. This leads to the well known "channel hopping" of the recovered clock signal.

A more stable clock recovery is achieved with the use of a feedback loop. One example is the optical clock recovery based on an all-optical phase-locked loop (PLL)

where the optical phase comparator comprises a semiconductor optical amplifier (SOA) in a Sagnac fiber loop (SLALOM) [8]. (For more details see "High-speed optical signal processing using semiconductor optical amplifiers" by Schubert, Ludwig and Weber in this publication [DOI:10.1007/s10297-005-0036-2].) This clock recovery was operated at a bit rate of 160 Gbit/s and showed stable operation with low timing jitter.

In another clock recovery the PLL comprised an electro-optical phase comparator based on a bidirectionally operated electroabsorption modulator [6]. This clock recovery is very compact and was operated up to a bit rate of 320 Gbit/s. An electroabsorption modulator was also used in another PLL configuration to measure eye diagrams at a bit rate of 160 Gbit/s [16].

4.2. Sampling Pulse Source

The most important parameters of the sampling pulse source are the timing jitter and the pulse width. The timing jitter of the pulse source determines the timing jitter of the whole sampling system, whereas the pulse width limits the temporal resolution of the sampling system. As a rough estimate, a timing jitter of less than 300 fs and a pulse width of about 1 ps are necessary to measure a 160 Gbit/s optical eye diagram. Another important parameter is the repetition frequency of the pulse source. The required sampling rate is typically a few hundred MHz, since the O/E detection frequency in the optical sampling systems is limited to a few hundred MHz. Therefore, either pulse sources with low repetition frequency must be used, or the repetition frequency must be reduced externally, for instance by gating the pulse train.

Early sampling systems used directly modulated, gain-switched laser diodes (distributed feedback lasers, DFB) in order to generate short pulses at a MHz-repetition rate [17–21]. These pulse sources, however, produced a rather large timing jitter, which could be reduced by an additional stabilization circuitry using optical holding beams. Moreover, the generated pulses had a rather broad pulse width (5-10 ps). Therefore, an additional pulse compression stage was necessary for applying these pulses as sampling pulses.

The jitter issue was relieved by operating the DFB lasers in continuous wave mode (cw) and using cascaded electroabsorption modulators (EAM) to carve sampling pulses out of this cw signal with the desired repetition frequency [22]. However, the width of the generated pulses was broad (12 ps) due to the limited bandwidth of the available EAM's. Therefore, the pulses had to be compressed in special dispersion decreasing fibers for the application as sampling pulses.

Another semiconductor based pulse source for optical sampling systems is the hybrid mode-locked semiconductor laser diode (TMLL) operating at a fundamental resonator mode repetition frequency of 10 GHz [8,23–25]. Besides being a compact device, this pulse source offers the potential of monolithic integration. For the application as sampling pulse source, the pulse repetition frequency of the TMLL was externally reduced to 311 MHz by the use of a Lithiumniobate ($LiNbO_3$) amplitude modulator. A similar type of mode-locked semiconductor laser was also used in [9, 13, 15, 26]. This pulse source, however, had a fundamental repetition rate of 620 MHz and was operated without further reduction of the repetition frequency.

Despite the efforts of using semiconductor based pulse sources for optical sampling, mode-locked Erbium doped fiber lasers (EDFL) became the most widely used

sampling pulse sources. They had been developed as pulse sources for 10 Gbit/s optical transmitters and exhibit very low jitter. However, for the application as sampling pulse sources, the pulse repetition frequency has to be externally reduced to a few hundred MHz by gating the pulse train with a $LiNbO_3$ modulator. Such a setup has been used for example in [27–30]. These lasers however suffered from a low long term stability as they were operated at a high harmonic of the fundamental resonator mode. Since a low repetition frequency was required anyhow, it was therefore reasonable to operate such lasers directly in their fundamental resonator mode. A mode-locked Erbium doped fiber laser with 50 MHz repetition rate was used in [4, 31–33]. However, it is difficult to synchronize a pulse source operating at a low repetition frequency to a reference clock signal operating at a high frequency with femtosecond timing jitter. This issue is circumvented in the random sampling configuration. For instance, this sampling configuration was demonstrated with use of a passively mode-locked Erbium doped fiber laser (EDFL) operating at a repetition frequency of 48 MHz in [6, 10].

4.3. Sampling Gate

The sampling gate is the central subsystem of the optical sampling system. Its gating window determines the temporal resolution of the optical sampling system. Almost all optical sampling experiments reported so far applied nonlinear optical effects for optical gating. It should be mentioned though that lately also linear optical signal processing was applied in an optical sampling system [34]. This technique relies on coherent signal detection and is thus rather wavelength selective since the wavelength of the sampling pulse source has to match the wavelength of the data signal under investigation.

The nonlinear optical gates can be classified by the type of process that is used. Among the processes that are caused by the second-order susceptibility $\chi^{(2)}$ are sum frequency generation (SFG) and difference frequency generation (DFG). Examples of processes that result from the third-order susceptibility $\chi^{(3)}$ are four-wave mixing (FWM), cross-phase modulation (XPM), and parametric amplification.

A second classification of the optical gates can be done by the nonlinear optical material that is used. This approach was taken in Fig. 3.

The most commonly used technique for optical gating in sampling experiments is sum frequency generation (SFG) in the nonlinear crystals KTP [22,27,33], periodically poled Lithiumniobate (PPLN) [4, 19, 21, 31] or the organic crystal AANP [28]. While these gates provide very short optical gating windows (<1 ps), their main drawback is the required high peak power, which is necessary to generate a sufficient amplitude of the frequency converted signal. In general, the use of periodically poled material reduces the power requirements as long interaction lengths without loss of phase matching can be achieved. Moreover, if the SFG process is performed with sampling pulses at about 780 nm, the generated light has a wavelength of about 520 nm and can be easily separated from the sampling pulse light as was shown in [10]. In addition to the SFG process, the cascaded $\chi^{(2)}$ processes of second harmonic generation and difference frequency generation (cSHG/DFG) have been used as well [35].

The resonant nonlinearity of a semiconductor optical amplifier (SOA) requires less optical power for the gating pulses. Narrow gating windows were obtained comparable to those of the crystal based gates with use of FWM in a SOA [9, 26]. However, the FWM conversion efficiency was rather low and limited together with the amplified

spontaneous emission (ASE) of the SOA the performance of this gate. A higher switching efficiency is obtained by XPM in an SOA in combination with an interferometric configuration as gate. (For more details see "High-speed optical signal processing using semiconductor optical amplifiers" by Schubert, Ludwig and Weber in this publication [DOI:10.1007/s10297-005-0036-2].) A promising gate of this kind is the so called "ultrafast nonlinear interferometer" (UNI), which was used in [36]. However, this gate suffered from the amplified spontaneous emission (ASE) of the SOA. An electroabsorption modulator (EAM) with sophisticated synchronization and driving electronics was additionally needed to suppress the ASE after the UNI gate.

In a more advanced scheme, the superior gating performance of interferometric optical gates was combined with the so called gain-transparent operation of an SOA (see Schubert, Ludwig, and Weber in this publication). In this operation of the SOA, the wavelength of the data signal is outside the gain spectrum of the SOA. Therefore it does not suffer from ASE degradation. Moreover, the gain-transparent SOA gate exhibits a linear transfer function for the data signal. This is in contrast to the conventional SOA gates, which show a strong saturation. Finally, the gain-transparent operation enables a wide wavelength acceptance range of the gate. These properties of the gain-transparent operation of an SOA are in particular favorable for optical sampling. The gain-transparent configuration was used in the "gain-transparent ultrafast-nonlinear interferometer" (GT-UNI) sampling gate in [23–25].

For the sake of completeness it should be mentioned also that even electroabsorption modulators (EAM) have been used recently as sampling gates in optical sampling experiments. Since the width of the gating window, which can be achieved with an EAM, is rather large (about 5 ps), these gates could be applied only to bit rates up to 40 Gbit/s [37–39]. Recently though, eye diagrams even at a bit rate of 160 Gbit/s were measured using a double-pass EAM configuration [40]. In another experiment, an EAM was monolithically integrated with a fast photodetector (PD-EAM). In this device, optical sampling pulses were converted to short electrical pulses by the photodetector which in turn were used to drive the EAM. 80 Gbit/s eye diagrams have been measured using such a setup [41].

The third class of nonlinear optical materials is the optical fiber. The ultra-fast Kerr nonlinearity of the fiber provides short gating windows comparable to those of the crystal based gates. Recent progress in fiber manufacturing technology allows to produce "highly nonlinear fibers" (HNLF), which have an enhanced nonlinearity coefficient. The high nonlinearity reduces the required fiber length for optical switching by more than a factor 10 as compared to the required length of conventional fibers. This makes highly nonlinear fibers very attractive for switching applications. The exploited nonlinear processes included FWM [15], parametric amplification [29] and XPM induced wavelength shifting [30]. As the efficiency of these processes is rather small, high peak powers were needed for switching.

Interferometric gates based on highly nonlinear fibers need less peak power of the sampling pulses to achieve gating windows with high on-off contrast. Examples include the nonlinear optical loop mirror (NOLM) [8] and the so-called "Kerr gate" [6]. The latter was recently combined with the effect of parametric amplification in [5].

4.4. *Opto/Electrical Detection*

With respect to the subsystem of opto/electrical (O/E) detection, more or less the same setup was used in all experiments reported. The optical samples after the sampling gate were either amplified by an EDFA and detected by a low speed (few hundred MHz bandwidth) PIN photo diode or were directly detected by a low speed avalanche photo diode (APD). Depending on the nonlinear effect that had been used for gating, the detectors were sensitive at about 1550 nm, 780 nm or 520 nm. Finally, the signal was processed by either an A/D conversion board in a personal computer or by a digital oscilloscope. The resulting eye diagram was finally plotted on the personal computer or directly shown on the oscilloscope.

5. Characterization of Sampling Systems

The overall performance of an optical sampling system can be characterized by a number of parameters. These parameters are summarized in Table 1. The table also shows which parameter is related with which particular subsystem of the optical sampling system. In this section, the various parameters are discussed.

Temporal resolution

The temporal resolution is the most prominent figure of merit of an optical sampling system. It is typically specified by the full-width at half maximum (FWHM) τ_{GW} of the gating window of the sampling system. The temporal resolution is equivalent to the bandwidth of the sampling system. Under the assumption of a Gaussian shaped gating window, the relation between the width of the gating window and the bandwidth B can be calculated using the Fourier-transform with the following result:

$$B = \frac{0.44}{\tau_{\mathrm{GW}}}. \tag{1}$$

Table 1. Matrix showing the parameters which determine the performance of the optical sampling system with respect to the subsystems.

	Clock Recovery	Sampling Pulse Source	Sampling Gate	O/E Detector
Temporal resolution		X	X	
Timing jitter	X	X		
Wavelength range	X		X	
Sensitivity	X	X	X	X
Dynamic range	X		X	X
Polarization sensitivity	X		X	
Applicable bit rate	X	X	X	

Thus a gating window with a width of 1.5 ps corresponds to an optical sampling system having a bandwidth of 300 GHz. As the width of the gating window depends on the width of the sampling pulses in most configurations, the temporal resolution depends on the pulse source as well as on the sampling gate.

Timing jitter

The timing jitter of a sampling system is a figure of merit, which is as important as the temporal resolution. In order to visualize the eye diagrams of high bit rate data signals, the sampling system must provide high temporal resolution and low timing jitter simultaneously. For an optimum system, the timing jitter should be as low as possible. The timing jitter is typically specified as root-mean-square (RMS) jitter in units of femtoseconds. The internal timing jitter of a sampling system (typically less than a few hundred femtoseconds) is derived either from single sideband phase noise measurements [42] or from measured eye diagrams of signals with known jitter.

If the timing jitter of the sampling system is derived from measurements of a signal with known jitter $\Delta\tau_{\mathrm{signal}}$, it is usually assumed that both jitter statistics are independent of each other and Gaussian. In this case, the jitter $\Delta\tau$ of the sampling system can be calculated from the measured combined jitter $\Delta\tau_{\mathrm{meas}}$ by

$$\Delta\tau = \sqrt{\Delta\tau_{\mathrm{meas}}^2 - \Delta\tau_{\mathrm{signal}}^2}. \tag{2}$$

The components which determine the timing jitter of the sampling system depend on the particular configuration of the sampling system. In the synchronous sampling configuration for example, the timing jitter is determined by the timing jitter of the sampling pulse source. In the random sampling configuration the accuracy of the arrival time measurement of the sampling pulses by the O/E converter determines the timing jitter of the sampling system. In general, the timing jitter of the clock recovery (if present) has a direct influence on the timing jitter of the sampling system.

Wavelength range

The wavelength (acceptance) range of the optical sampling system is usually specified as 3 dB bandwidth (in nanometers) and defines the range of wavelengths, which a data signal can have to be accepted by the sampling system. In general, the wavelength range is limited by the sampling gate and the clock recovery since both subsystems have to accept the wavelength of the signal under investigation. Ideally, the wavelength range should be as large as possible. It should cover at least one communication band (C-,L-, or S-band) without tuning the subsystems of the optical sampling system.

Sensitivity

Although the sensitivity is an important figure of merit for any measurement instrument, there is no common definition of this parameter with respect to optical sampling systems. Some authors (e.g. [43]) use the product of the average sampling pulse power and the peak signal power in units of W^2 as definition of the sensitivity. This is a common definition for instruments like autocorrelators, but it is not useful as a general

figure of merit to compare different sampling techniques. Another definition of the sensitivity uses the peak power of the signal pulses, which is required to achieve a certain displayed signal-to-noise ratio (SNR), for example SNR = 20 dB [29, 44]. Therefore it is very difficult to compare the different sampling systems with respect to the sensitivity. Most authors define the sensitivity by specifying the peak powers of the sampling and the signal pulses required to measure a somehow open and clean eye diagram. This however allows only a very rough comparison among the different techniques.

It can be seen from Fig. 1 that the sensitivity depends on all subsystems of the optical sampling system. Primarily, it depends on the effectiveness, by which the samples of the signal are generated by the sampling gate, and on the amount of noise, which is present in the O/E detector. In addition, the effectiveness of the sampling gate is typically related to the power of the sampling pulses. Finally, also the clock recovery must work properly even for low powers of the input signal. Therefore, the sensitivity is also determined by the clock recovery.

Dynamic range

The dynamic range of a measurement instrument is usually specified in decibel and describes the power range, in which the signal under investigation must fall. Usually, the high power limit of the sampling systems is either determined by the loss of the linearity of the system or by the damage of the sampling gate due to the signal power. The low power limit is hard to determine, since there exists no common definition of the limit where an eye diagram is still measurable. The choice is usually taken based on the intuition of the particular author. Therefore, most authors do not specify a dynamic range at all. The dynamic range is determined by almost all subsystems of the optical sampling system.

Polarization sensitivity

The polarization sensitivity describes the amount by which the amplitude of the generated samples varies, when the polarization of the signal under investigation changes. The polarization sensitivity is usually specified in percent or in decibel. It should be as low as possible in order to measure eye diagrams for example after fiber transmission links, where the polarization of the data signal varies slowly with time. On the other hand, a strong polarization sensitivity can be used to select a certain polarization of the signal under investigation. This allows to visualize effects like polarization mode dispersion (PMD) or the state of polarization (see Sec. 7.3).

The polarization sensitivity is determined by the sampling gate and the clock recovery.

Applicable bit rate

This figure of merit is also not consistently used in the literature. Most authors specify the maximum bit rate, at which a particular sampling system was able to display an open eye diagram. In this case, the value is equivalent to the specification of the temporal resolution or bandwidth of the sampling system.

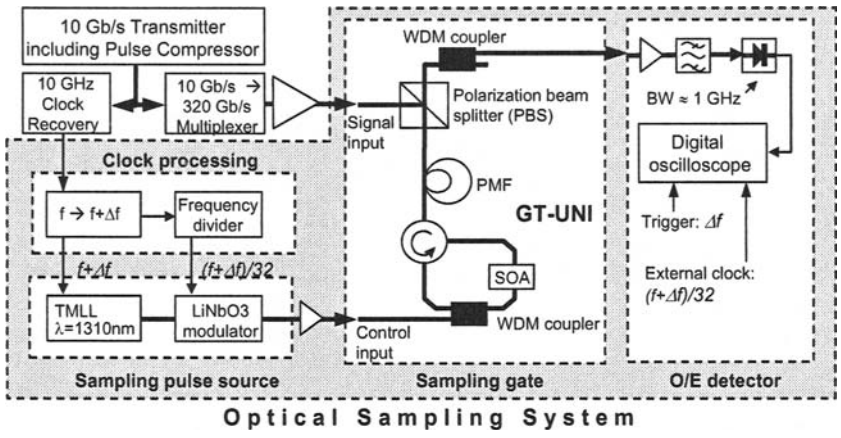

Fig. 4. Setup of a synchronous optical sampling system based on semiconductor components. It was applied to measure 320 Gbit/s optical eye diagrams.

In a complete system on the other hand, the maximum applicable bit rate depends also on the type of synchronization used, since the clock recovery must be able to handle the bit rate under investigation. Therefore, the applicable bit rate depends in general on the sampling gate, the sampling pulse source and the clock recovery.

6. Examples of Optical Sampling Systems

In the following subsections, two examples of optical sampling systems will be discussed in more detail. The first example is a synchronous optical sampling system, which is based on semiconductor components for the sampling pulse source and the sampling gate. The second example is a random optical sampling system, in which fiber components were used for the sampling pulse source and the sampling gate.

6.1. Synchronous Optical Sampling System

The setup is depicted in Fig. 4. The optical sampling system was applied to measure the eye diagram of a 320 Gbit/s optical data signal. This data signal was generated by a 10 Gbit/s PRBS-RZ transmitter followed by a passive fibre delay line multiplexer. The 10 Gbit/s transmitter (output wavelength 1550 nm) comprised a tunable mode-locked semiconductor laser (TMLL, 1.2 ps sech^2 pulses, 0.2 ps timing jitter), an external modulator and a pulse-compressor using supercontinuum generation in a highly nonlinear fiber. The pulse width of the data pulses at the input of the sampling system was 0.6 ps as determined by an autocorrelation measurement.

The sampling system comprised four main parts: the clock processing, the sampling pulse source, the sampling gate (GT-UNI) and the opto/electrical (O/E) detector.

Since there was no fiber transmission involved in this experiment, the optical clock recovery was replaced by a simple RF clock extraction unit providing the clock frequency $f = 10$ GHz from the 10 Gbit/s optical data signal of the transmitter.

The sampling pulse source was a semiconductor mode-locked laser with an external cavity (tunable mode-locked laser, TMLL). It generated 1.5 ps sech^2 pulses with 0.2 ps RMS timing jitter at a wavelength of 1310 nm. The laser was driven at the frequency $f + \Delta f$ with Δf =50 kHz. Owing to the limited clock speed of the digital oscilloscope in the O/E detector, the sampling pulse rate was reduced by a factor of 32 to 310 MHz by a $LiNbO_3$-Mach-Zehnder modulator.

The sampling gate was an interferometric gate based on cross-phase modulation in a semiconductor optical amplifier (SOA). The gate is called GT-UNI, where UNI stands for "ultrafast nonlinear interferometer" and GT stands for the gain-transparent operation of the SOA. The operation principle of the GT-UNI is described in [45]. (For more details see "High-speed optical signal processing using semiconductor optical amplifiers" by Schubert, Ludwig and Weber in this publication [DOI:10.1007/s10297-005-0036-2].) The sampling pulses were fed into the control port of the GT-UNI and opened the gating window. As the sampling pulses had a wavelength near 1300 nm, the optical samples of the data signal with a wavelength near 1550 nm were easily separated from the sampling pulses by a 1550 nm/1300 nm WDM coupler. This particular sampling gate was polarization dependent. However, a polarization insensitive operation of this gate has been shown in [46] by using a polarization diversity configuration. One drawback of this sampling gate was its poor sensitivity. A data pulse energy of about 2.5 pJ was needed at the input of the sampling gate. This was due to the gain-transparent operation of the SOA in the interferometer. On the other hand, the gain-transparent operation had a number of advantages. It added only negligible low noise to the signal, yielded a linear transfer function for the signal (over an input power range of 50 dB) and provided a large wavelength acceptance range of the sampling gate.

Finally, the peak powers of the optical samples were detected and displayed in the O/E detector using a photodiode (1 GHz bandwidth) and a digital oscilloscope with external clock input. The oscilloscope was triggered by the frequency offset Δf, and allowed recording of eye diagrams with arbitrary persistence time.

Figure 5 shows the result of a pump-probe measurement of the gating window of the GT-UNI sampling gate. The full width at half maximum (FWHM) of the measured curve was 1.8 ps. The actual width of the gating window was calculated from this value by deconvolution with the pulse width of the probe pulses used in the pump-probe measurement. Under the assumption of a Gaussian shaped gating window and probe pulses with a FWHM of 0.6 ps the calculation yielded a width of the gating window of

$$\tau_{\mathrm{GW}} = \sqrt{\tau^2_{\mathrm{meas}} - \tau^2_{\mathrm{probe}}} = 1.7 \text{ ps}. \tag{3}$$

This width of the gating window represents the temporal resolution of this particular optical sampling system. Following Eq. (1), the corresponding bandwidth for this particular sampling system is about 260 GHz. It should be noted that the determination of the bandwidth from the measurement of the gating window is only very roughly accurate (about $\pm 5\%$), since the shape of the actual gating window is not Gaussian for most systems and the error in the measurements of the pulse widths is also on the order of 5%.

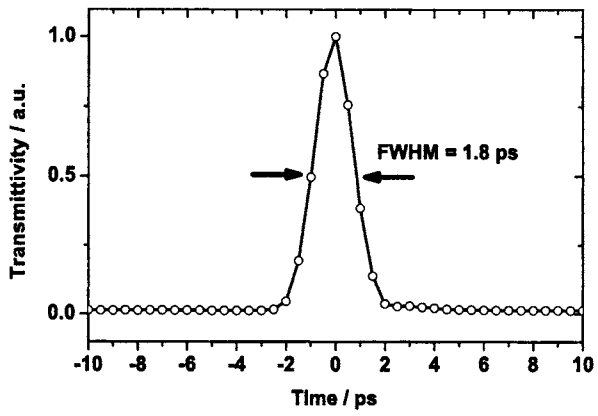

Fig. 5. Measured gating window of the GT-UNI sampling gate.

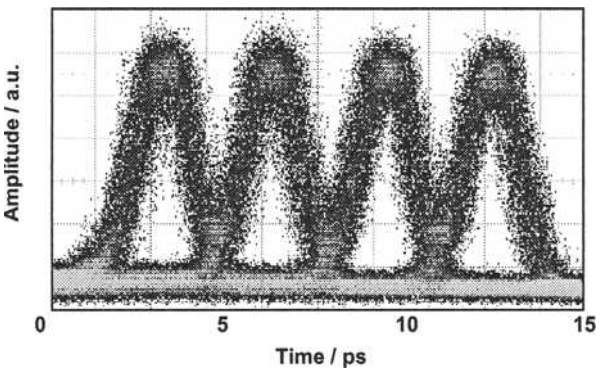

Fig. 6. Eye diagram of a quasi 320 Gbit/s data signal in which only four subsequent OTDM channels are present. The measurement was done with the synchronous sampling system based on semiconductor components.

The bandwidth of the sampling system was appropriate for the measurement of waveforms and eye diagrams of a signal at a bit rate of 320 Gbit/s. An example of an eye diagram is shown in Fig. 6. The average powers of the data signal and sampling pulses were 23 dBm and 4 dBm, respectively, at the input of the GT-UNI sampling gate. The eyes exhibit a clear opening and equal shape at a persistence of 120 traces, i.e., after superposition of 120 measured traces. Owing to the large bandwidth of the sampling system, no ringing occurs.

The eye diagrams show a width (FWHM) of the eyes of about 2.0 ps. The evaluation of a horizontal histogram on the flanks of the eyes yielded a timing jitter of about 650 fs. It should be noted however, that such a horizontal histogram is influenced also by the amplitude noise on the flanks, which cannot be separated from the phase noise. This

effect is similar to the situation described in Sec. 7.4 for the evaluation of Q-factors from vertical histograms.

6.2. *Random Sampling System*

Figure 7 shows the setup of a particular sampling system based on the random sampling configuration. The system includes an optical clock recovery, which enabled measurements of optical eye diagrams with large persistence times of a 320 Gbit/s data signal after transmission over a 160 km long fiber link [6]. In contrast to the sampling experiment described in Sec. 6.1, a data signal was used having the differential phase shift keying (DPSK) modulation format.

The setup comprised a 40 Gbit/s DPSK transmitter, a 40 to 320 Gbit/s OTDM-multiplexer, a fiber transmission link with a length of 160 km (2 spans of 80 km SLA-IDF) and the optical sampling system.

The sampling system was based on the random sampling principle reported in [10], but the actual setup was different from the setup in [10]. The first stage of the sampling system was an automatic polarization controller (APC), which provided a fixed polarization into the phase demodulator (DLI). After the APC, the data signal was split into two signal components by a 3 dB coupler. One signal component was directed to the clock recovery and the other to the DPSK demodulator. The clock recovery was an electro-optical PLL using a bidirectionally operated electroabsorption modulator as phase comparator [47]. The extracted 10 GHz clock signal was fed into the precision time base of the Agilent Infinium DCA86100.

The DPSK demodulator was a hybrid fiber delay line (asymmetric Mach-Zehnder) interferometer (DLI) with a differential delay of 25 ps corresponding to the DPSK base rate (40 Gbit/s). Such a phase demodulator is independent of the multiplexed rate of the OTDM data signal. The DLI has two optical outputs, which are logically inverse. Here, only one output was used. The DLI was biased such that an input pulse train with constant phase of consecutive 40 GHz pulses was completely transmitted to this port. In this arrangement, a DPSK modulated input signal was converted to an amplitude modulated data signal. In order to monitor OOK modulated data signals using the same setup, the demodulator could be bypassed. In this case, the data signal may also have a different base rate, e.g., an FEC bit rate.

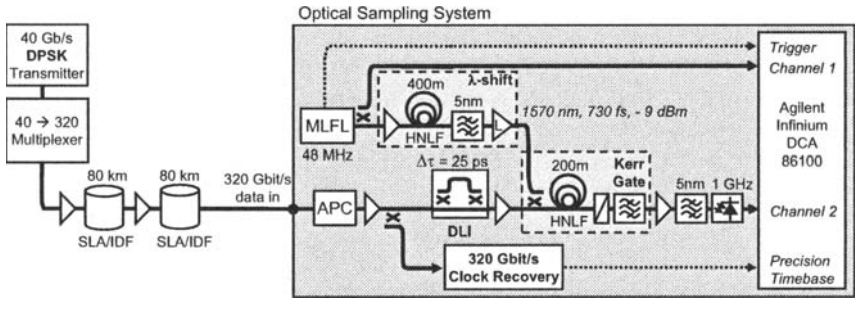

Fig. 7. Setup for 320 Gbit/s sampling of DPSK and OOK using a random sampling system.

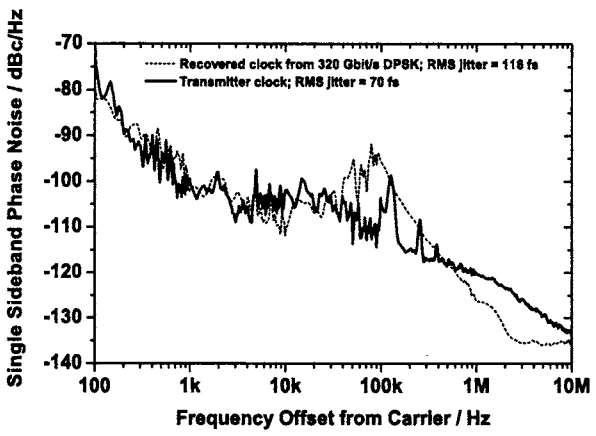

Fig. 8. Single sideband phase noise measurement of the transmitter clock and of the recovered clock from the 320 Gbit/s DPSK data signal.

The output of the DLI was fed into the sampling gate, which was a Kerr gate based on 200 m of highly nonlinear fiber (HNLF) [48]. The control pulses for the sampling gate were generated by a passive mode-locked fiber laser (MLFL, 48 MHz repetition rate). Via a 3 dB coupler, these pulses were fed into channel 1 of the DCA86100 (which was also triggered by the MLFL pulses) and into a wavelength shifter. The wavelength shifter provided a shift of the control pulses from 1560 nm to 1570 nm using supercontinuum generation in 400 m of HNLF and subsequent carving of the spectrum by a bandpass filter (3dB bandwidth 5 nm). This enabled a wavelength acceptance range of the sampling system from 1535 nm (limited by the EDFAs) up to 1560 nm. The resulting control pulses were finally amplified by an L-band EDFA and fed into the Kerr gate with an average input power of 9 dBm and a pulse width of 730 fs.

At the output of the Kerr gate, the sampled data signal was optically re-amplified and detected by a photodetector with 1 GHz bandwidth. This signal was connected to channel 2 of the DCA86100.

Figure 8 gives an example of measurements of the timing jitter of the sampling system. This figure shows the measurements of the single sideband (SSB) phase noise of the recovered electrical clock signal at the output of the clock recovery. Also shown in this figure is the SSB noise curve of the electrical 10 GHz reference clock from the DPSK transmitter. From these measurements (integration from 100 Hz to 10 MHz), the RMS jitter values of 70 fs for the transmitter clock signal and of 116 fs for the recovered clock signal were obtained. Please note that the jitter of the precision timebase module used in the O/E detector was specified by the manufacturer to 200 fs, which is larger than the value measured for the recovered clock signal. Since the recovered clock signal was used as input signal for the precision timebase of the oscilloscope, the overall timing jitter of the sampling system was thus limited by the timebase module.

The temporal resolution and the applicable bit rate (bandwidth) of this random sampling system are illustrated in Fig. 9. The figure shows the eye diagram of a

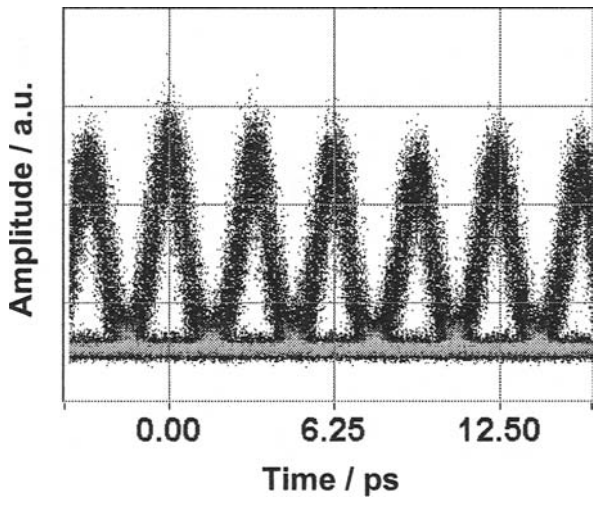

Fig. 9. Eye diagram of a 320 Gbit/s DPSK signal after 160 km of fiber transmission (measured with the random sampling system).

320 Gbit/s DPSK data signal which was recorded with a persistence of 200 sweeps (about 6.7 sec). The average timing jitter in these measurements was 240±30 fs as calculated from horizontal histograms on the flanks of the eyes. The width (FWHM) of the measured eye diagrams was 1.5 ps. Considering the pulse width of 1.1 ps of the data pulses at the input of the optical sampling system (measured by autocorrelation) and the jitter of 0.24 ps, this yields a temporal resolution of the sampling system of 1.0 ps corresponding to a bandwidth of 440 GHz.

7. Applications of Optical Sampling

The most prominent feature of optical sampling systems is their high temporal resolution. This enables a number of measurements on optical data signals at bit rates above 40 Gbit/s where conventional electric measurement techniques fail due to their limited bandwidth. Examples are: waveform and eye diagram measurements of amplitude modulated data signals, constellation diagrams of phase modulated data signals, time resolved monitoring of the state of polarization (SOP) as well as the investigation of fiber transmission impairments at high bit rates. These applications are discussed in the following subsections.

7.1. High Bit Rate Waveform and Eye Diagram Measurements

A number of groups have demonstrated the measurement of optical waveforms at bit rates above 100 Gbit/s. In simple setups, the signal under investigation was generated by interleaving (multiplexing) sufficiently short optical pulses to a periodic train of

pulses with a pulse separation that corresponds to the desired bit rate. Using such a setup, a 160 Gbit/s pulse train was sampled for example using a sampling system with cSHG/DFG in periodically poled Lithiumniobate (see Sec. 4.3) as sampling gate [35]. The temporal resolution of this system was 3.6 ps. In another experiment, a repetitive 160 Gbit/s data pattern consisting of 16 bits was measured using an optical sampling setup which used four-wave mixing in a gain-transparent operated semiconductor optical amplifier as sampling gate [49]. The temporal resolution of this sampling system was approximately 1.7 ps.

In contrast to these experiments, in which short repetitive pulse sequences were used as signal under investigation, more advanced optical sampling systems enabled the measurement of longer data patterns like for example pseudo-random bit sequences (PRBS) that are frequently used for testing optical communication systems. The key to visualize such bit sequences either lies in the generation of the required hardware for trigger signals or in special software for processing of the sampled data (finding the correct pattern periodicity). One example of an optical sampling system with an advanced trigger technique was presented in [50]. The reported system had a temporal resolution of 1 ps and was used to measure waveforms of data pattern of return-to-zero (RZ) and non-return-to-zero (NRZ) PRBS sequences with a word length $2^7 - 1$. However, the pattern length had to be known in advance in order to set the correct trigger parameters in this setup. In another experiment, a software synchronized sampling system was used to visualize the waveform of a multiplexed PRBS sequence at a bit rate of 160 Gbit/s [12]. The temporal resolution of this sampling system was 1.6 ps. In contrast to the previous example, a software algorithm was used in this experiment to retrieve the information on pattern length from the measured data. It was shown that this sampling system could be operated independently of the pattern length up to pattern lengths of at least $2^{11} - 1$.

Finally, most optical sampling systems were used to measure eye diagrams with high temporal resolution at ultra-high bit rates. The highest bit rate, at which an optical eye diagram was measured, is 640 Gbit/s presently. This was reported for the first time in [4]. In this experiment, a synchronous sampling system was used. The sampling

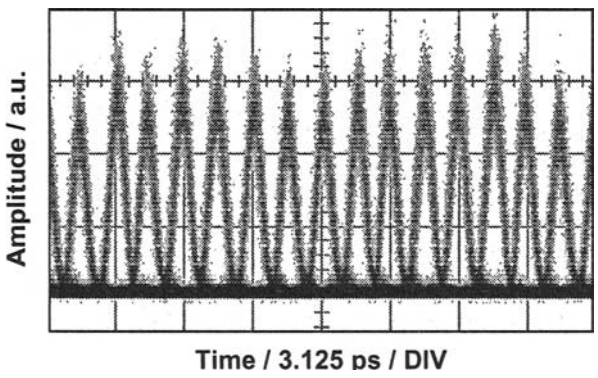

Fig. 10. Eye diagram of a 640 Gbit/s data signal measured with a synchronous sampling system based on fiber components.

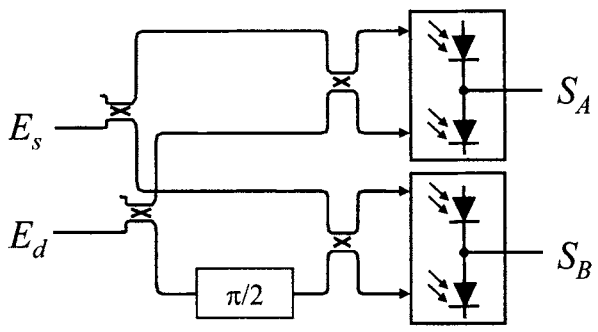

Fig. 11. Schematic diagram of the coherent homodyne linear optical sampling technique.

gate used sum frequency generation in a periodically poled Lithiumniobate crystal and the sampling pulse source was a synchronized mode-locked fiber laser. The temporal resolution of the system was 280 fs while the timing jitter was estimated to be 80 fs. Another measurement of an eye diagram of a data signal at 640 Gbit/s was reported in [5]. This result is shown in Fig. 10. The sampling system was based on the synchronous sampling configuration and used fiber components for the optical sampling pulse source and the sampling gate. The sampling gate in particular was a modified optical Kerr-gate based on 20 m of highly nonlinear fiber, in which parametric amplification was exploited to increase the sampling efficiency.

7.2. Constellation Diagrams of Phase-Modulated Data Signals

Recent transmission experiments revealed an advantage of the modulation format differential phase-shift keying (DPSK) in comparison to on-off keying (OOK) for high speed data transmission. Up to now, only few work has been reported on the characterization of high speed phase modulated data signals. The monitoring of the 320 Gbit/s DPSK data signal reported in Sec. 6.2 was only possible with use of a phase demodulator in the input stage of the sampling system. The sampling system measured the squared electrical field of the demodulated data signal. The system did not provide phase sensitive optical sampling.

One approach to monitor the phase of an optical data signal directly is the measurement of constellation diagrams [7] by means of coherent homodyne linear optical sampling [51]. In this sampling technique, samples of the electric field (i.e. amplitude and phase) of a signal under test are collected. Moreover, since the sampling process is a coherent homodyne process, the linear sampling technique offers a higher sensitivity as compared to the sampling technique using optical gates based on nonlinear optical signal processing.

Figure 11 shows a schematic diagram of the coherent homodyne detector used in the linear optical sampling technique. At the inputs, both the data signal $E_d(t)$ and sampling pulses $E_s(t)$ are split each by a 3 dB coupler into an upper component and a lower component. The upper components of $E_d(t)$ and $E_s(t)$ interfere at the upper balanced detector and generate the signal $S_A = Re\{E_s(t)^* E_d(t)\}$. The lower

components of $E_d(t)$ and $E_s(t)$ interfere at the lower balanced detector and generate the signal $S_B = Im\{E_s(t)^* E_d(t)\}$, which differs from S_A due to the additional phase shift $\pi/2$ in the lower component of $E_d(t)$. Together both signals give the complex quantity $E_s(t)^* E_d(t)$ completely up to a proportionality constant. Such quadrature detection has been implemented using either a free space setup [51] or a waveguide structure [7].

It should be pointed out that unless one of the modes of the sampling pulse source is locked to the optical carrier of the data signal, additional software correction methods are required to gain the correct phase angle from the measured data. This was done in [7] by assuming a constant phase difference between consecutive sampling pulses. With this setup, constellation diagrams of DPSK modulated data signals up to 40 Gbit/s were measured.

7.3. Time Resolved State-of-Polarization Monitoring

The high temporal resolution of the optical sampling technique can also be applied to realize a time resolved monitoring of the state of polarization of optical data signals. This is useful as the design of fiber optical communication systems requires careful control of the polarization effects in the transmission fiber as well as in the system components. Two realizations have been reported up to now, in which a time-resolved measurement of the state of polarization of an optical signal was performed by measurement of the Stokes parameters.

In one experiment, the signal under investigation was passed through a combination of polarization filters and the transmitted light was then input into an optical sampling system. In this case, a random optical sampling system based on nonlinear sampling in a periodically poled Lithiumniobate crystal was used with a temporal resolution of about 650 fs [52]. By setting appropriate polarization filters to four predefined states, the four Stokes parameters could be measured. This technique enables measurements of the time-resolved polarization evolution of picosecond pulses affected by polarization mode dispersion. One drawback of the proposed technique is, however, that sequential measurements are needed. This requires that the signal under investigation is repetitive and has a high stability, as the measurement time for one intensity trace was about one minute in the reported experiments.

In another approach, a software synchronized sampling system based on four-wave mixing in a highly nonlinear fiber was used for time-resolved state-of-polarization measurements [53] with a temporal resolution of 1.6 ps. In this experiment, the polarization sensitivity of the four-wave mixing process acted as polarization filter. The virtual rotation of the polarization filter was achieved by rotating the polarization of the sampling pulses. In contrast to [52], the polarization of the sampling pulses was continuously rotated in this experiment by driving a fast polarization controller with two sinusoidal RF signals at 3 kHz and 5 kHz. By using the software synchronization method and by performing a proper calibration of the system, the authors were able to measure the time-resolved evolution of the state of polarization (SOP) of picosecond pulses in a single measurement. This was demonstrated by the measurement of the Stokes parameters of a 2.3 ps pulse affected by a predefined amount of differential group delay. Moreover, as an extension of the capability of the software synchronization method, this sampling system also allowed to visualize the SOP evolution of a polarization multiplexed 160 Gbit/s PRBS data signal.

7.4. Investigation of Fiber Transmission Impairments

In high speed fiber optical transmission systems, the main distortions of the transmitted optical data signal arise from fiber nonlinearity, chromatic dispersion and polarization mode dispersion as well as from the degradation of the optical signal-to-noise ratio (OSNR) due to amplified spontaneous emission (ASE) of the fiber amplifiers along the transmission link. Eye diagrams measured with optical sampling systems provide the temporal resolution to evaluate such distortions at bit rates above 100 Gbit/s. Some of the results obtained are summarized in this section.

Fiber Nonlinearity

In high-speed fiber-optic transmission systems (40 Gbit/s and above), the maximum power into the fiber is limited mainly due to signal degradations by intra-channel perturbations caused by the nonlinearity of the fiber. The nonlinearity gives rise to mainly two nonlinear effects known as intra-channel cross-phase modulation (IXPM) and intra-channel four-wave mixing (IFWM) [54, 55]. While IXPM results in an increase of the timing jitter of the data signal, IFWM is responsible for the generation of so-called ghost pulses. In [25] a synchronous optical sampling system was used to investigate the generation of ghost pulses due to IFWM at a bit rate of 160 Gbit/s. The setup of the experiment is shown in Fig. 12.

The 160 Gbit/s transmitter generated a particular 160 Gbit/s RZ, OOK data signal, in which only two adjacent OTDM channels were present. This was done to clearly identify the nonlinear interaction of two adjacent pulses. The data signal (pulse width 1.6 ps) was launched into 80 km of non-zero dispersion shifted fiber (NZDSF). At the output of the fiber link, the signal was fed into a dispersion compensating fiber (DCF), which fully compensated the dispersion of the transmission fiber. Finally the signal was fed into the optical sampling system. The sampling system was based on a semiconductor mode-locked laser as sampling pulse source and on a gain-transparent ultrafast-nonlinear interferometer as sampling gate. The temporal resolution of the system was 2.1 ps.

Figure 13 shows measurements of the 160 Gbit/s eye diagrams at the output of the transmission link for various peak powers P_{in} of the data pulses at the input of the link. As the peak power at the input of the fiber link increased, part of the signal power at the output was transferred to new positions in time due to intra-channel four-wave-mixing. The newly generated signal components generated so called ghost-pulses, which appeared before and after the actual data channels. Increasing the peak

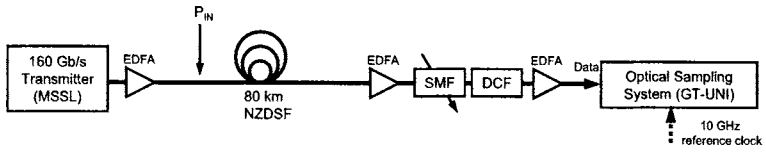

Fig. 12. Experimental setup for the investigation of intra-channel four-wave mixing using a synchronous optical sampling system.

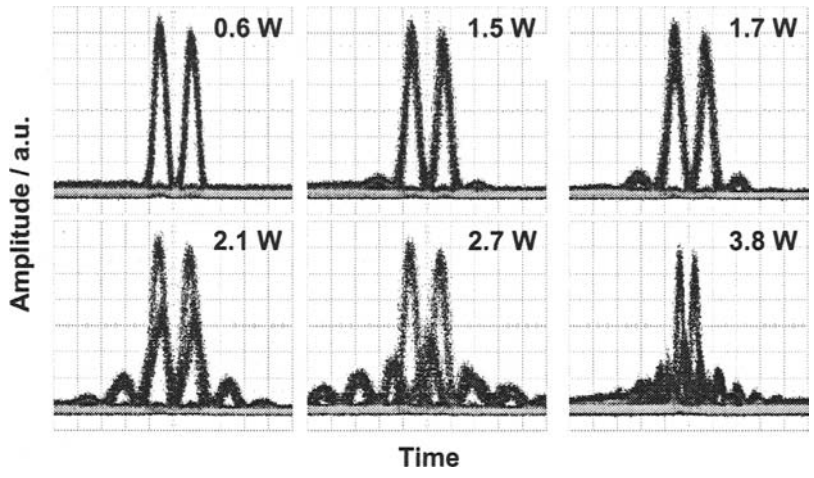

Fig. 13. Eye diagrams of a 2 channel data signal for different input peak powers. Each diagram shows a time segment of 49 ps, with the exception of the diagram for 3.8 W, which shows 98 ps.

power of the input pulses to more than 2 W generated even higher order ghost-pulses. The measured eye diagrams were evaluated with respect to amplitudes and temporal positions of the identified peaks in the eye diagram. It was found that the "ghost-pulses" appeared for $P_{\mathrm{in}} > 1.2\ W$ and that their amplitudes increased with the input peak power. Simultaneously, the central double peaks decreased, as energy was transferred from these central peaks to the ghost-pulses. An asymmetry was found for example between the intensities and temporal positions of the left and right ghost-pulses. It could be shown that this asymmetry was caused by the relative optical phase of the adjacent pulses in the OTDM data signal.

Chromatic Dispersion

If optical data signals with high bit rates are transmitted over fiber links, in which the second order chromatic dispersion is fully compensated, the residual third order chromatic dispersion (TOD) becomes a limiting factor. It results in characteristic oscillating pulse tails. The oscillation period is of the same order of magnitude as the pulse width itself. Therefore, the tails are hardly visible using conventional electric measurement equipment. In [56] an optical sampling system with 1.6 ps temporal resolution was used to measure the shapes of 2.0 ps pulses after transmission over 626 km of standard single mode fiber. The transmission link included dispersion compensating fiber modules to compensate for the second order chromatic dispersion. The optical sampling system allowed to visualize the oscillating tails of the transmitted pulses due to TOD. The investigations showed also that a TOD compensator was able to reduce the oscillating tails almost completely. In a second experiment, the effect of TOD was also studied in 160 Gbit/s data transmission using the same sampling system. It was found that without TOD compensation, the eye diagram is partially closed already

after 300 km, while the use of a TOD compensator produced open eyes even after the full transmission distance of 626 km.

OSNR degradation

Another important impairment for high-speed optical data signals is degradation of the optical signal-to-noise ratio due to accumulated noise of the in-line fiber amplifiers in a fiber transmission link. A common way to characterize such distortions quantitatively is the so-called Q-factor method. By this method, the eye diagram of the data signal is evaluated as follows: A vertical histogram is taken at the center of the eye diagram (see Fig. 14a for example). The histogram contains two distinct distributions originating from the marks and spaces of the data signal. Using the means $\mu_{0,1}$ and standard deviations $\sigma_{0,1}$ of the two distributions, the Q-factor is calculated as

$$Q = \frac{\mu_1 - \mu_0}{\sigma_1 + \sigma_0}. \tag{4}$$

Optical sampling systems enable such Q-factor evaluation even at high bit rates as they measure optical eye diagrams with the required temporal resolution. In early work, the Q-factor of optical data signals was measured using asynchronous optical sampling setups [57–60]. These setups are similar to the software synchronized configuration of optical sampling systems, but they are not synchronized to the data signal. Thus they do not allow to evaluate a synchronous vertical histogram in the center of the eye. Instead, they yield asynchronous histograms, which contain samples from the whole bit period. Therefore, a calibration of the Q-factors is required, which is dependent on parameters like the modulation format and the duty cycle of the data signal for example.

The evaluation of synchronous vertical histograms for the measurement of Q-values was reported in [61, 62]. The experiments in [61] were performed at a bit rate of 10 Gbit/s and with RZ (pulse width 30 ps) and NRZ modulation formats. The optical Q-values determined from the optically sampled eye diagrams were compared to electrical Q-values that were determined from electrically sampled eye diagrams. A good correlation was found between the measured optical and electrical Q-values. However, the optical Q-values were always lower than the electrical Q-values. This was attributed to the higher bandwidth of the optical sampling system as compared to the electrical measurement equipment. The higher bandwidth resulted in a larger amount of noise present in the sampled signal and thus reduced the measured optical Q-values.

In [62], eye diagrams at a bit rate of 160 Gbit/s were measured after transmission over 80 km of standard single mode fiber. Optical Q-values were derived from the measured 160 Gbit/s eye diagrams by evaluating synchronous vertical histograms in the center of the bit-slot. In order to compare the optical Q-values to electrical Q-values, the data signal under investigation was also fed into a 160 Gbit/s receiver, which allowed to measure simultaneously the bit-error ratio of the data signal. Then an electrical Q-factor was calculated from the measured bit-error ratio. The experiments showed a good correlation between the optical and electrical Q-values. However, for Q-values larger than five, the optical Q-values from the optically sampled eye diagrams saturated. This was attributed to timing jitter.

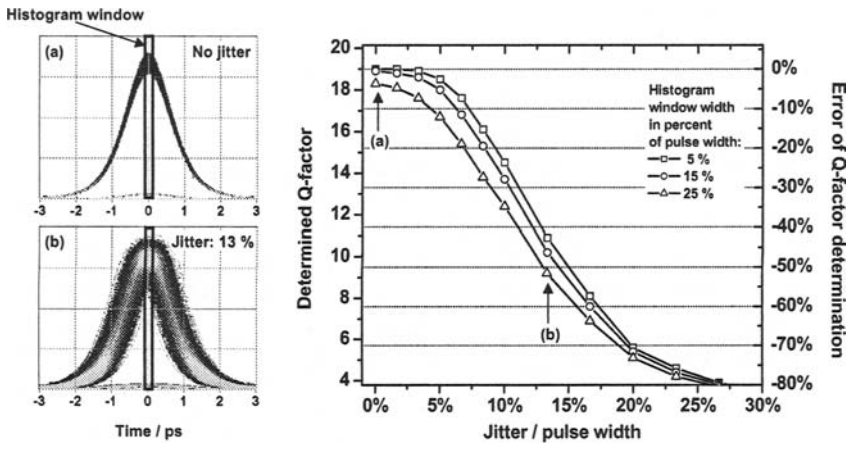

Fig. 14. Q-factor (determined by the evaluation of synchronous vertical histograms) as a function of the jitter in the eye diagram measurement. The different traces show different histogram window widths. As example two eye diagrams are shown for the case of no jitter (a) and 13% jitter (b).

Figure 14 shows the result of numerical simulations using an optical RZ data signal at a bit rate of 160 Gbit/s (1.5 ps sech^2 pulses). The intensity noise of the data signal was chosen such that the Q-factor became 19 in the example. Then timing jitter was added to the data signal and the Q-factor was determined (using vertical histograms in the center of the eye) as a function of the added timing jitter of the data signal. Please note that the addition of timing jitter to the data signal is equivalent to the presence of jitter in the sampling process of the optical sampling system. The eye diagram (Fig. 14b) clearly shows that the jitter influences the vertical histogram as samples from the flanks of the data signal leak into the histogram window. This leads to an error in the determination of the correct Q-factor as shown in the plot. The error already becomes about 45% for a timing jitter of 13% of the data pulse width. In the example (pulse width 1.5 ps) this corresponds to a jitter of only 200 fs, which is a typical value for optical sampling systems.

Figure 14 shows also that the temporal width of the window for the vertical histogram has only a minor effect on the determination of the Q-factor when jitter is present. Changing the window width from 5% of the data pulse width (i.e., 75 fs in the example) to 25% (375 fs), adds an error of less than 10%.

The effect described above imposes severe limitations on the evaluation of synchronous Q-factors from eye diagrams of data signals with short duty cycles, like for example high bit rate RZ signals. In order to keep the error in the Q-factor determination below 5%, the jitter of the sampling system should be below 5% of the pulse width of the signal and the window width of the histogram should be chosen to be 5% of the pulse width of the signal.

8. Conclusions

The optical sampling technique is a novel method to perform time-resolved measurements of optical data signals at high bit rates with a bandwidth that cannot be reached by conventional photodetectors and oscilloscopes. Various optical sampling systems have been realized so far using a number of nonlinear optical processes to perform the ultrafast gating needed to sample the signal under investigation. The realized optical sampling systems differ not only by the optical sampling gates and pulse sources but also by the technologies that are used to synchronize the systems to the data signal under investigation. Systems have been reported using synchronous, random and software synchronized configurations.

Applications of optical sampling systems include high bit rate waveform and eye diagram measurements, measurements of constellation diagrams of phase modulated data signals, time-resolved measurements of the state of polarization as well as investigations of fiber transmission impairments.

Presently, the measurement of optical eye diagrams at a bit rate of 640 Gbit/s represents the maximum applicable bit rate of all reported systems. This has been achieved using nonlinear processes in periodically poled Lithiumniobate [4] and in highly nonlinear fibers [5].

Most optical sampling systems rely on nonlinear processes to sample the signal under investigation. Most of the nonlinear processes used are however insensitive to the optical phase of the signal under investigation. On the other hand, with the increasing use of phase-modulated data signals for long haul high-speed optical communications, a demand has emerged for techniques, which allow to measure the amplitude and phase of the electrical field of optical data signals with high temporal resolution. The use of the linear optical sampling technique as reported in [7] is one approach and the development of phase sensitive optical sampling systems is expected to become more and more important in the future.

References

1. Datasheet of 86116B 65 GHz Optical / 80 GHz Electrical Plug-In Module, Agilent Technologies, Inc., 2002.
2. Datasheet of 80E06 70+ GHz Sampling Head, Tektronix, Inc., 2003.
3. Datasheet of XPDV2020R Photodetector, U2T Photonics AG, 2003.
4. N. Yamada, S. Nogiwa, and H. Ohta, "640 Gb/s OTDM signal measurement with high-resolution optical sampling system using wavelength-tunable soliton pulses," IEEE Photon. Technol. Lett., **16** (4), 1125–1127, April 2004.
5. S. Watanabe, R. Okabe, F. Futami, R. Hainberger, C. Schmidt-Langhorst, C. Schubert, and H.G. Weber, "Novel fiber kerr-switch with parametric gain: Demonstration of optical demultiplexing and sampling up to 640 Gb/s," in Proc. 30th Eur. Conf. on Opt. Comm. (ECOC'04), Stockholm, Sweden, 2004, postdeadline paper Th4.1.6.
6. C. Schmidt-Langhorst, C. Schubert, C. Boerner, V. Marembert, S. Ferber, R. Ludwig, and H.G. Weber, "Optical sampling system including clock recovery for 320 Gbit/s DPSK and OOK data signals," in *Proc. 30th Opt. Fiber Commun. Conf. (OFC 2005).* Washington, DC: Optical Society of America, March 2005, paper OWJ6.

7. C. Dorrer, J. Leuthold, and C. Doerr, "Direct measurement of constellation diagrams of optical sources," in Proc. 29th Opt. Fiber Commun. Conf. (OFC 2004), Los Angeles, CA (USA), 22-27 February 2004, postdeadline paper PDP33.
8. C. Schmidt, F. Futami, S. Watanabe, T. Yamamoto, C. Schubert, J. Berger, M. Kroh, H.-J. Ehrke, E. Dietrich, C. Börner, R. Ludwig, and H.G. Weber, "Complete optical sampling system with broad gap-free spectral range for 160 Gbit/s and 320 Gbit/s and its application in a transmission system," in Opt. Fiber Commun. Conf. Techn. Dig., Anaheim, USA, March 2002, pp. 528–530, paper ThU1.
9. M. Shirane, Y. Hashimoto, H. Yamada, and H. Yokoyama, "Optical sampling system using compact and stable external-cavity mode-locked laser diode modules," IEICE Trans. Electron., **E87-C** (7), 1173–1180, July 2004.
10. R.L.Jungerman, G. Lee, O. Baccafusca, Y. Yaneko, N. Itagaki, R. Shioda, A. Harada, Y. Nihei, and G. Sucha, "1-THz bandwidth C- and L-Band optical sampling with a bit rate agile timebase," IEEE Photon. Technol. Lett., **14** (8), 1148–1150, August 2002.
11. M. Westlund, H. Sunnerud, M. Karlsson, and P. Andrekson, "Software-synchronized all-optical sampling," in *OSA Trends in Optics and Photonics (TOPS) Vol. 86, Optical Fiber Commun. Conf., Technical Digest, Postconference Edition*, Atlanta, Georgia (USA), March 23-28 2003, pp. 409–410, paper WP6.
12. ——, "160 Gb/s optical data pattern monitoring using a software-synchronized all-optical sampling system," in Proc. 29th Eur. Conf. on Opt. Comm. (ECOC'03), Rimini (Italy), September 21-25 2003, pp. 48–49, paper Mo3.6.2.
13. T. Miyazaki, H. Sotobayashi, and W. Chujo, "Optical sampling and demultiplexing of 80 Gb/s OTDM signals with optically recovered clock by injection mode-locked laser diode," in Proc. 28th Eur. Conf. on Opt. Comm. (ECOC'02), Copenhagen, Denmark, 2002, paper 2.1.6.
14. M. Shirane, Y. Hashimoto, H. Kurita, H. Yamada, and H. Yokoyama, "Optical sampling measurement with all-optical clock recovery using mode-locked diode lasers," in *OSA Trends in Optics and Photonics (TOPS) Vol. 54, Optical Fiber Commun. Conf., Technical Digest, Postconference Edition*. Washington DC: Optical Society of America, 2001, p. MG2.
15. T. Miyazaki and F. Kubota, "Simultaneous demultiplexing and clock recovery for 160 Gb/s OTDM signal using a symmetric Mach-Zehnder switch in electrooptic feedback loop," IEEE Photon. Technol. Lett., **15** (7), 1008–1010, July 2003.
16. I. Kang and M. Yan, "Simple setup for simultaneous optical clock recovery and ultra-short sampling pulse generation," Electron. Lett., **38** (20), 1199–1200, 26th September 2002.
17. H. Otha, S. Nogiwa, N. Oda, and H. Chiba, "Highly sensitive optical sampling system using timing-jitter-reduced gain-switched optical pulse," Electron. Lett., **33** (25), 2142–2144, December 1997.
18. H. Ohta, S. Nogiwa, and H. Chiba, "Highly sensitive optical sampling system with 100 GHz bandwidth," in Proc. 24th Europ. Conf. Opt. Commun., Madrid (Spain), September 20-24 1998, pp. 503–504.
19. S. Nogiwa, H. Otha, K. Kawaguchi, and Y. Endo, "Improvement of sensitivity in optical sampling system," Electron. Lett.,**35** (11), 917–918, 27th May 1999.
20. H. Ohta, S. Nogiwa, Y. Kawaguchi, and Y. Endo, "Measurement of 200 Gbit/s optical eye diagram by optical sampling with gain-switched optical pulse," Electron. Lett., **36** (8), 737–739, 13th April 2000.
21. S. Nogiwa, Y. Kawaguchi, H. Ohta, and Y. Endo, "Highly sensitive and time-resolving optical sampling system using thin PPLN crystal," Electron. Lett., **36** (20), 1727–1728, 28th September 2000.

22. A. Otani, T. Otsubo, and H. Watanabe, "A turn-key-ready optical sampling oscilloscope by using electro-absorption modulators," in Proc. 25th Europ. Conf. Opt. Commun., 1999, pp. 374–375, paper P3.2.

23. C. Schubert, C. Schmidt, C. Börner, E. Dietrich, S. Ferber, R. Ludwig, and H.G. Weber, "A gain-transparent ultrafast-nonlinear interferometer (GT-UNI) in a 160 Gb/s optical sampling system," in Techn. Dig. of Optical Amplifiers and their Applications, OAA, 2002, paper OTuD5.

24. C. Schmidt, C. Schubert, S. Watanabe, F. Futami, R. Ludwig, and H.G. Weber, "320 Gb/s all-optical eye diagram sampling using gain-transparent ultrafast nonlinear interferometer (GT-UNI)," in Proc. 28th Eur. Conf. on Opt. Comm. (ECOC'02), Copenhagen, Denmark, 2002, paper 2.1.3.

25. C. Schmidt, C. Schubert, C. Börner, C. M. Weinert, H. Bülow, E. Lach, and H.G. Weber, "Investigation of intra-channel four-wave mixing at 160 Gb/s using an optical sampling system," in *Proc. 29th Eur. Conf. on Opt. Comm. (ECOC'03)*, Rimini, Italy, September 21-25 2003, pp. 990–991, paper Th2.5.2.

26. M. Shirane, Y. Hashimoto, H. Yamada, and H. Yokoyama, "A compact optical sampling measurement system using mode-locked laser-diode modules," IEEE Photon. Technol. Lett., **12** (11), 1537–1539, November 2000.

27. H. Takara, S. Kawanishi, and M. Saruwatari, "Optical signal eye diagram measurement with subpicosecond resolution using optical sampling," Electron. Lett., **32** (15), 1399–1400, 18 July 1996.

28. H. Takara, S. Kawanishi, A. Yokoo, S. Tomaru, T. Kitoh, and M. Saruwatari, "100 Gbit/s optical signal eye-diagram measurement with optical sampling using organic nonlinear optical crystal," Electron. Lett., **32** (24), 2256–2258, 21 November 1996.

29. J. Li, J. Hansryd, P. Hedekvist, P. Andrekson, and S. Knudsen, "300-Gb/s eye-diagram measurement by optical sampling using fiber-based parametric amplification," IEEE Photon. Technol. Lett., **13** (9), 987–989, September 2001.

30. J. Li, M. Westlund, H. Sunnerud, B.-E. Olsson, M. Karlsson, and P. Andrekson, "0.5 Tbit/s eye-diagram measurement by optical sampling using XPM-induced wavelength shifting in highly nonlinear fiber," in Proc. 29th Eur. Conf. on Opt. Comm. (ECOC'03), Rimini (Italy), September 21-25 2003, pp. 136–137, paper Mo4.6.4.

31. H. Ohta, N. Banjo, N. Yamada, S. Nogiwa, and Y. Yanagisawa, "Measuring eye diagram of 320 Gbit/s optical signal by optical sampling using passively modelocked fibre laser," Electron. Lett., **37** (25), 1541–1542, December 2001.

32. S. Nogiwa, N. Yamada, and H. Ohta, "Broad wavelength-bandwidth optical sampling system using wavelength-tunable soliton pulses," in *OSA Trends in Optics and Photonics (TOPS) Vol. 55, Optical Fiber Commun. Conf., Technical Digest, Postconference Edition*, Anaheim, CA (USA), March 17-22 2002, pp. 533–534.

33. N. Yamada, H. Ohta, and S. Nogiwa, "Jitter-free optical sampling system using passively modelocked fibre laser," Electron. Lett., **38** (18, pp. 1044–1045, 29th August 2002.

34. C. Dorrer, D. Kilper, H. Stuart, and G. Raybon, "Ultra-sensitive optical sampling by coherent-linear detection," in *OSA Trends in Optics and Photonics (TOPS) Vol. 55, Optical Fiber Commun. Conf., Technical Digest, Postconference Edition*, Anaheim, CA (USA), March 17-22 2002, pp. FD5–1 – FD5–3, postdeadline paper FD5.

35. S. Kawanishi, T. Yamamoto, N. Nakazawa, and M. Fejer, "High sensitivity waveform measurement with optical sampling using quasi-phasematched mixing in $LiNbO_3$ waveguide," Electron. Lett., **37** (13), 842–844, 1st June 2001.

36. I. Kang and K. Dreyer, "Sensitive 320 Gb/s eye diagram measurements via optical sampling with semiconductor optical amplifier-ultrafast nonlinear interferometer," Electron. Lett., **39** (14), 1081–1082, 10th July 2003.

37. I. Shake, R. Kasahara, H. Takara, M. Ishii, Y. Inoue, T. Ohara, Y. Hibino, and S. Kawanishi, "WDM signal monitoring utilizing asynchronous sampling and wavelength selection based on thermo-optic switch and AWG," in Proc. 29th Eur. Conf. on Opt. Comm. (ECOC'03), Rimini (Italy), September 21-25 2003, pp. 780–781, paper We4.P112.

38. I. Shake, H. Takara, and S. Kawanishi, "Simple Q factor monitoring for BER estimation using openend eye diagrams captured by high-speed asynchronous electrooptical sampling," IEEE Photon. Technol. Lett., **15** (4), 620–622, April 2003.

39. I. Shake and H. Takara, "Chromatic dispersion dependence of asynchronous amplitude histogram evaluation of NRZ signal," J. Lightwave Technol., **21** (10), 2154–2161, October 2003.

40. I. Kang and C. Dorrer, "Optical sampling source-free simultaneous eye-diagram monitoring and clock recovery up to 160 Gb/s," in Proc. 29th Eur. Conf. on Opt. Comm. (ECOC'03), Rimini (Italy), 21-25 September 2003, pp. 292–293, paper Tu4.2.4.

41. S. Kodama, T. Shimizu, T. Yoshimatsu, K. Yoshino, T. Furuta, and H. Ito, "Ultrafast optical sampling gate monolithically integrating a PD and EAM," Electron. Lett., **40** (11), 696–697, May 2004.

42. D. V. der Linde, "Characterization of the noise in continuously operating mode-locked lasers," Appl. Phys. B, **39**, 201–217, 1986.

43. C. Dorrer, C. Doerr, I. Kang, R. Ryf, and P. Winzer, "High-sensitivity high-resolution sampling using linear optics and waveguide optical hybrid," in *Proc. 29th Opt. Fiber Commun. Conf. (OFC 2004)*, Los Angeles, CA (USA), 22-27 February 2004, postdeadline paper PDP18.

44. N. Yamada, H. Ohta, and S. Nogiwa, "Optical sampling system using passively mode-locked fiber laser with KTP crystal," IEICE Trans. Electron., **E86-C** (9), 1816–1823, September 2003.

45. C. Schubert, S. Diez, J. Berger, R. Ludwig, U. Feiste, H.G. Weber, G. Toptchiyski, K. Petermann, and V. Krajinovic, "160 Gb/s all-optical demultiplexing using a gain-transparent Ultrafast-Nonlinear Interferometer (GT-UNI)," IEEE Photon. Technol. Lett., **13** (5), 475–477, May 2001.

46. C. Schubert, J. Berger, U. Feiste, R. Ludwig, C. Schmidt, and H.G. Weber, "160 Gb/s polarization insensitive all-optical demultiplexing using a gain-transparent Ultrafast-Nonlinear Interferometer (GT-UNI)," IEEE Photon. Technol. Lett., **13** (11), 1200–1202, November 2001.

47. C. Boerner, C. Schubert, C. Schmidt, E. Hilliger, V. Marembert, J. Berger, S. Ferber, E. Dietrich, R. Ludwig, B. Schmauss, and H.G. Weber, "160 Gbit/s clock recovery with electrooptical PLL using a bidirectionally operated electroabsorption modulator as phase comparator," Electron. Lett., **39** (14), 1071–1073, 10th July 2003.

48. C. Schubert, R. Ludwig, S. Watanabe, F. Futami, C. Schmidt, J. Berger, C. Boerner, S. Ferber, and H.G. Weber, "160 Gbit/s wavelength converter with 3R-regenerating capability," Electron. Lett., **38** (16, pp. 903–904, 1st August 2002.

49. S. Diez, R. Ludwig, C. Schmidt, U. Feiste, and H.G. Weber, "160-Gb/s optical sampling by gain-transparent four-wave mixing in a semiconductor optical amplifier," IEEE Photon. Technol. Lett., **11** (11), 1402–1404, November 1999.

50. K. Igawa, A. Otani, and Y. Tsuda, "Novel optical sampling oscilloscope without traditional trigger technique and measurement of optical short pulse modulated PRBS pattern," in *Proc. 29th Opt. Fiber Commun. Conf. (OFC 2004).* Washington, DC, USA: Opt. Soc. America, 2004, paper MF73.

51. C. Dorrer, D. Kipler, H. Stuart, G. Raybon, and M. Raymer, "Linear optical sampling," IEEE Photon. Technol. Lett., **15** (12), 1746–1748, December 2003.

52. O. Buccafusca and P. Hernday, "Time resolved characterization of the polarization state of optical pulses," in *OSA Trends in Optics and Photonics (TOPS) Vol. 86, Optical Fiber Commun. Conf., Technical Digest, Postconference Edition*, 2003, pp. 501–502, paper ThJ3.

53. M. Westlund, H. Sunnerud, B. Olsson, M. Karlsson, and P. Andrekson, "Time-resolved state-of-polarization measurement using all-optical sampling with sampling pulse polarization rotation," in Proc. 30th Eur. Conf. on Opt. Comm. (ECOC'04), Stockholm, SE, 2004, paper Mo3.5.6.

54. R. Essiambre, B. Mikkelsen, and G. Raybon, "Intra-channel cross-phase modulation and four-wave mixing in high-speed TDM systems," Electron. Lett., **35** (18), 1576–1578, 1999.

55. P. Mamyshev and N. Maysheva, "Pulse-overlapped dispersion-managed data transmission and intrachannel four-wave mixing," Opt. Lett., **24** (21), 1454–1456, 1999.

56. E. Hellström, H. Sunnerud, M. Westlund, and M. Karlsson, "Third-order dispersion compensation unsing a phase modulator," J. Lightwave Technol., **21** (5), 1188–1197, May 2003.

57. I. Shake, H. Takara, S. Kawanishi, and Y. Yamabayashi, "Optical signal quality monitoring method based on optical sampling," Electron. Lett., **34** (22), 2152–2154, 28th October 1998.

58. I. Shake, E. Otani, H. Takara, K. Uchiyama, Y. Yamabayashi, and T. Morioka, "Bit rate flexible quality monitoring of 10 to 160 Gb/s optical signals based on optical sampling technique," Electron. Lett., **36** (25), 2087–2088, 7th December 2000.

59. I. Shake, H. Takara, and T. Morioka, "Determination of the origin of BER degradation utilizing asynchronous amplitude histograms," in Proc. 4th Pacific Rim Conference on Lasers and Electro-Optics (CLEO/Pacific Rim 2001), 15-19 July 2001), II560–II561, paper ThB2-2.

60. I. Shake and H. Takara, "Averaged Q-factor method using amplitude histogram evaluation for transparent monitoring of optical signal-to-noise ratio degration in optical transmission system," J. Lightwave Technol., **20** (8), 1367–1373, August 2002.

61. M. Westlund, H. Sunnerud, M. Karlsson, J. Hansryd, J. Li, P. Hedekvist, and P. Andrekson, "All-optical synchronous Q-measurements for ultra-high speed transmission systems," in *OSA Trends in Optics and Photonics (TOPS) Vol. 55, Optical Fiber Commun. Conf., Technical Digest, Postconference Edition*, Anaheim, CA (USA), March 17-22 2002, pp. 530–531, paper ThU2.

62. C. Schmidt, C. Schubert, J. Berger, M. Kroh, H.-J. Ehrke, E. Dietrich, C. Börner, R. Luwig, H.G. Weber, F. Futami, S. Watanabe, and T. Yamamoto, "Optical q-factor monitoring at 160 Gb/s using an optical sampling system in an 80 km transmission experiment," in *OSA Trends in Optics and Photonics (TOPS) Vol. 73, Conference on Lasers and Electro-Optics, OSA Technical Digest, Postconference Edition.* Washington DC: Optical Society of America, 2002, pp. 579–580.